

Scramjet testing at high enthalpies in expansion tube facilities

Matthew McGilvray

A thesis submitted for the degree of Doctor of Philosophy at

The University of Queensland in September, 2008

Division of Mechanical Engineering, School of Engineering

Declaration by author

This thesis is composed of my original work, and contains no material previously published or written by another person except where due reference has been made in the text. I have clearly stated the contribution by others to jointly-authored works that I have included in my thesis.

I have clearly stated the contribution of others to my thesis as a whole, including statistical assistance, survey design, data analysis, significant technical procedures, professional editorial advice, and any other original research work used or reported in my thesis. The content of my thesis is the result of work I have carried out since the commencement of my research higher degree candidature and does not include a substantial part of work that has been submitted to qualify for the award of any other degree or diploma in any university or other tertiary institution. I have clearly stated which parts of my thesis, if any, have been submitted to qualify for another award.

I acknowledge that an electronic copy of my thesis must be lodged with the University Library and, subject to the General Award Rules of The University of Queensland, immediately made available for research and study in accordance with the Copyright Act 1968.

I acknowledge that copyright of all material contained in my thesis resides with the copyright holder(s) of that material.

Matthew McGilvray

List of Publications

Additional Published Works by the Author Relevant to the Thesis but not Forming Part of it

McGilvray, M., Austin, J., Sharma, M., Morgan, R.G. and Jacobs, P.A., “Condition investigation in University of Illinois HET expansion tube,” *16th Australian Fluid Mechanics Conference*, Gold Coast, Australia, 2007.

Dann, A.G., Morgan, R.G. and McGilvray, M., “Experimental study of two-dimensional shock wave/turbulent boundary layer interactions,” *26th International Symposium on Shock Waves*, Gottingen, Germany, 2007.

McGilvray, M., Morgan, R.G., Jacobs, P.A. and Ramanah, D., “Boundary layer transition in an expansion tube at a low enthalpy operating condition,” *45th AIAA Aerospace Sciences Meeting*, Reno, USA, 2007.

McGilvray, M., Jacobs, P.A., and Morgan, R.G., “Simulations of scramjet starting in an expansion tunnel,” *14th AIAA Space Planes and Hypersonic Systems and Technologies Conference*, Canberra, 2006.

Morgan, R.G., McIntyre, T.J., Gollan, R., Jacobs, P.A., Brandis, A., McGilvray, M., van Diem, D., Knoffo, P., Pulsonnetti, M.V. and Wright, M., “Radiation measurements in non reflected shock tunnels,” *24th AIAA Applied Aerodynamics Conference*, San Francisco, USA, 2006.

McGilvray, M., Teakle, P., Jacobs, P.A. and Morgan, R.G., “Geometric nozzle design for Wagtail rockets,” *5th Australian Space Sciences Conference*, Melbourne, Australia, 2005.

McGilvray, M., Morgan, R.G., Paull, A., Abdel-Jawad, M.M., Jacobs, P.A., McIntyre, T.J. and Scott, M.A., “Operating condition in UQs impulse facilities for scramjet testing,” *25th International Symposium on Shock Waves*, Bangalore, India, 2005.

Acknowledgments

I wouldn't have been given this opportunity if it weren't for the invite of Richard Morgan (*sneaky/player/Duke*). For this alone, I cannot begin to express my gratitude. It has definitely been an interesting and enjoyable four years of my life as your student and friend. As a supervisor I could not have really asked for more. Your ability to understand the most complex problems in such a broad range of fields still amazes me. From hypersonic flows to the correct eye contact and stance to deal with a venomous snake, you are a wealth of knowledge. I can only hope that a little of this may have rubbed off on me.

Secondly, I would like to express my gratitude to Peter Jacobs, my associate supervisor, for all the support and guidance he has given me in my thesis. Your generous help cannot be underestimated. If it wasn't for Peter, I would still be stuck pondering the reason behind the dips in the pitot pressure in the X3 flow condition. Your input has helped me past many road blocks in my thesis work, and your insistence on sending me for extra gym sets and runs kept me from burning out, not to mention helping me to dominate over Richard on the squash court!

To my fellow postgrads and X-Lab RA's, thanks for all the help in operating the expansion tubes, running the blackhole computer and all the great memories. In particular, a special thanks to Rowan Gollan for your selfless help with getting the CFD codes running has been invaluable. Special mention is also deserved for Eccy, Fabs and Doc. Thanks for the morning coffees, numerous trips to the local establishments, holidays, concerts, sporting events and various other functions which have kept me sane and in a constant hang over throughout my thesis.

Thanks to all the boys in the workshop, in particular, Brian Laughrey, for all their hard work on modifying and fixing the expansion tubes and manufacturing of the scramjet model. Apart from your gifted skills in both design and machining, your smiles have always been a welcome sight in the early hours of the morning.

To my parents, Noel and Dianne, thankyou for all your encouragement and support throughout my thesis, especially during my write up. I truly appreciate it all, and would have never been able to complete it without you.

Thanks also goes out to Roger and Susan for welcoming me into their home, offering me another place to escape to while I finalised my thesis.

A big thanks to David Gildfind, Jacko, David Buttsworth, Con Doolan and my parents for finding the many speelling mitsakes, and, grammatical errors throughout my thesis.

Gee, the joy you brought me over the years, while distracting in the short term, helped me to finish this thesis in the long run. Keep smiling, sweet pea.

Abstract

With the high costs of flight testing, especially at hypersonic speeds, ground based facility testing of scramjets becomes an attractive option. The expansion tube is the only facility currently that can offer full flight property duplication at the total pressures and total enthalpies required, while maintaining correct chemical composition. Due to difficulties with short test times and unsteady flow phenomena, scramjet testing in these facilities has not been thoroughly investigated. This study examines these issues, in order to explore the practicality of testing a full '*tip to tail*' scramjet engine at a true flight replication condition in an expansion tube facility.

An investigation was initially undertaken on the large X3 expansion tunnel facility to maximise test time and core flow, aimed at producing a 30 km altitude, Mach 10 flow condition. This was identified as the limitation point of the T4 reflected shock tunnel, which has generally been accepted to produce reliable scramjet data for propulsion tests. Using a condition that is also able to be produced in the T4 facility, will permit direct comparison of data between the two facilities in the future, providing confidence in results from expansion tube facilities. Both experimental measurements and numerical calculations showed that the limitation of the test time was due to large boundary layer growth after transition, which engulfed the entire core flow $200 \mu\text{s}$ into the test time. This phenomenon is likely to affect all scramjet duplication conditions in expansion tubes, as the flow properties are conducive to boundary layer transition occurring.

Two solutions were proposed and investigated in order to overcome the flow disruption caused by boundary layer transition; the use of a steady expansion nozzle at the acceleration tube exit; the use of hydrogen as an accelerator gas. Since the smaller X2 facility had a Mach 10 steady expansion nozzle and X3 was decommissioned for the free piston driver to be upgraded, the investigation was shifted to X2. Due to a restricted test time of $550 \mu\text{s}$, the static pressure of the flow condition was increased to allow a reduction in the length of the scramjet (*pressure-length scaling*). A combination of experimental and numerical calculations of the facility was used to define the flow properties. With the confidence of overcoming the phenomenon associated with boundary transition in the X2 facility, numerical modelling of the X3 facility with a steady expansion nozzle was then undertaken to show a 1 ms condition could be produced. Although initially promising, the hydrogen accelerator gas solution requires further investigation.

A two dimensional scramjet was designed with upstream injection for testing in X2. This was a three shock inlet with a constant area combustor and a planar thrust surface. Since the flow condition involved changes in flow properties during the test time, an

investigation of the appropriateness of a quasi steady analysis was undertaken. Using a fuel off simulation of the scramjet duct with the transient inflow properties from the X2 facility nozzle exit, the convective terms for pressure were shown to be two orders of magnitude larger than local terms indicating the dominance of the convective terms change in flow properties at any location allowing quasi-steady flow to be assumed. A normalisation procedure was developed to deal with the transient nature of the data and to accurately represent the axial progression of the gas through the duct. The numerical simulations were also used to show that both flow establishment was achieved and that impulsive starting of the intake would occur.

Experimentation with the scramjet using static pressure measurements throughout the body side of the engine provided verification of supersonic combustion. This was verified by the doubling of the static pressure from the start to the end of the combustor for an air test gas, whereas with a nitrogen test gas no significant change in pressure occurred. Effects of fuel equivalence ratio, injector size and cowl position were also investigated. A net inviscid thrust was predicted, using the quasi-steady flow analysis, indicating a specific impulse of 183 s.

This work provides evidence to validate the use of expansion tube facilities for experimental testing of scramjets at flight duplication conditions. Limitations due to boundary layer transition flow effects has been shown to be avoidable. Numerical simulations of the facilities showed good agreement with experimental measurements, allowing definition of freestream properties and can now be applied to further scramjet conditions with confidence. Stable, supersonic combustion was shown to be produced for these expansion tube conditions. Coupling the transient simulation of the flow condition with a numerical calculation of the fuel off experimental scramjet has been useful in both verification of the design and performance predictions. Appropriate techniques have been presented to analyse scramjet pressure and thrust measurements where transient effects are present in the freestream.

Keywords

expansion tube, scramjet, numerical simulation, experimental, transient flow, boundary layer transition

Australian and New Zealand Standard Research Classifications

090107 Hypersonic Propulsion and Hypersonic Aerodynamics (100%)

Contents

List of Publications	ii
Acknowledgments	iii
Abstract	iv
Keywords	vi
Australian and New Zealand Standard Research Classifications	vii
1 Introduction	1
1.1 Original scientific contributions of this study	5
2 Literature Review	6
2.1 Requirements for Ground Testing of Scramjets	6
2.2 Types of Facilities for High Mach Number Scramjet Testing	13
2.2.1 Heated blowdown type facilities	17
2.2.2 Long duration piston compression facilities	18
2.2.3 Reflected shock tunnels	19
2.2.4 Expansion tubes	21
2.3 Summary	24
3 Expansion Tube Literature Review	26
3.1 History and Development of Expansion Tubes	26
3.2 Expansion Tube Operation	29
3.2.1 Flow properties in an expansion tube	32
3.2.2 Driver options	34
3.3 Expansion Tunnel Operation	36
3.4 Establishment of free stream conditions in expansion tube/tunnel facilities .	39
3.5 Summary	43
4 Condition Development in the X3 Expansion Tube	45
4.1 X3 Facility Description	45
4.1.1 Measurement techniques	46
4.1.2 Buffer upgrade	50
4.1.3 Future driver and steady expansion nozzle upgrade	53

4.2	Scramjet Flight Condition	55
4.2.1	Estimation of fill conditions	57
4.3	Experimental measurements	58
4.3.1	Increase in reservoir pressure due to high percentage argon driver .	58
4.3.2	Pressure gauge offset and initial trials	58
4.3.3	Final condition	59
4.4	Numerical Simulation	64
4.4.1	One dimensional modelling	65
4.4.2	Axisymmetric modelling	68
4.5	Boundary Layer Transition	86
4.5.1	Review of expansion tube boundary layer studies	89
4.5.2	Theoretical predictions of boundary layer transition	91
4.5.3	Experimental measurements	94
4.5.4	Numerical simulations	96
4.5.5	Possible solutions to boundary layer transition	98
4.6	Summary	106
5	Condition Development in the X2 Expansion Tunnel	108
5.1	X2 Facility Description	108
5.1.1	Measurement techniques	109
5.1.2	Facility upgrades for scramjet testing	111
5.2	Experimentation	114
5.2.1	Low enthalpy scramjet condition	115
5.2.2	High enthalpy scramjet condition	124
5.3	Numerical Simulation	126
5.3.1	One dimensional modelling	127
5.3.2	Axisymmetric modelling	134
5.4	Summary	145
6	Scramjet Literature Review	147
6.1	Supersonic Combustion	147
6.2	Scramjet Engines - History and Development	148
6.3	Scramjet Flowpath Design for High Speeds	150
6.3.1	Fuelling options	152
6.3.2	Inlet	157
6.3.3	Hydrogen injection and mixing	162
6.3.4	Combustor	166
6.3.5	Thrust nozzle	170
6.4	Summary	171

7 Scramjet Flow-Path and Model Design	173
7.1 Flowpath Design	174
7.1.1 Inlet	174
7.1.2 Fuel injection	186
7.1.3 Combustor	192
7.1.4 Thrust surface	194
7.2 Model Design	194
7.3 Transient Simulation of Scramjet Model	197
7.3.1 Transient analysis of results	198
7.3.2 Simulation results	206
7.3.3 Inlet start up	213
7.3.4 Flow establishment	217
7.4 Summary	220
8 Scramjet Experiments in the X2 Expansion Tunnel	222
8.1 Experiment Setup and Calibration	222
8.1.1 Fuel system calibration	223
8.1.2 Pressure transducer calibration	224
8.2 Experimental Results	226
8.2.1 Effects of fuel injection	234
8.2.2 Effects of combustion	236
8.2.3 Variation in fuel equivalence ratio	239
8.2.4 High enthalpy condition	244
8.2.5 Larger diameter injector holes	246
8.2.6 Engine performance	252
8.3 Summary	253
9 Conclusion	255
9.1 Recommendations for Further Work	257
Bibliography	276
A Perfect Gas Theory for an Expansion Tube	277
A.1 Shock Tube	278
A.2 Shock tube with Area Change	279
B Gas Buffer Simulation	282
B.1 Pressure Relief Valve	282
B.2 Primary Piston	283
B.3 Gas Trap	284

C Fuel System Calibration	285
D Uncertainty Analysis	287
D.1 Uncertainty in X2 Flow Properties	287
D.2 Uncertainty in Scramjet Pressure Measurements	288
E Scramjet Physical Design Drawings	293
F Scramjet Pressure Transducer Calibration	312
G Scramjet Normalisation Pressure	314

List of Tables

2.1	Simulation requirements for supersonic/hypersonic combustion. Adapted from [1].	7
2.2	Approximate total pressure capabilities of various expansion tube facilities. Taken from [2].	22
3.1	Free stream properties of a scramjet flight trajectory for test time calculations.	38
4.1	Wall pressure sensor locations in X3 relative to the primary diaphragm (P.D. is primary diaphragm, S.D. is secondary diaphragm).	47
4.2	Nominal free stream conditions for planned Mach 10 condition.	56
4.3	Perfect gas results for initial estimate of Mach 10 condition for X3.	57
4.4	Fill conditions for final X3 condition.	60
4.5	Experimental properties for X3 Mach 10 condition.	60
4.6	Summary of $L1d$ flow properties in the shock tube for X3 condition.	67
4.7	Grid refinement properties for X3 in the acceleration tube and history point locations used for comparison.	76
4.8	Flow conditions for X3 Mach 10 condition.	85
4.9	Summary of flow values used in analytical prediction of transition location.	92
4.10	Summary of flow values for hydrogen acceleration gas condition.	103
5.1	Sample points from X2 nozzle contour. Taken from [3].	109
5.2	Wall pressure sensor locations in X2 operated in relative to the primary diaphragm (P.D. is primary diaphragm, S.D. is secondary diaphragm, TE is tube exit and NE is nozzle exit).	111
5.3	Fill conditions for the low enthalpy X2 condition.	116
5.4	Freestream conditions of numerical simulations of pitot cavity conducted by Jacobs [4] of a reflected shock tunnel condition using similar probes to that used in a expansion tube.	119
5.5	Fill conditions for the high enthalpy X2 condition.	125
5.6	Summary of $L1d$ flow properties in the shock tube for X2 condition.	132
5.7	Flow conditions for low enthalpy X2 Mach 10 condition.	139
5.8	Flow conditions for high enthalpy X2 Mach 10 condition.	142
6.1	Important chemical reactions between hydrogen and air for supersonic combustion. M is a third body reactant such as nitrogen. Taken from [5].	154

7.1	Wedge angles for inlet design.	178
7.2	Conditions after each shock on inlet.	180
7.3	Geometry of inlet designed for testing in T4.	181
7.4	Boundary layer separation limit on intake and combustor.	182
7.5	Geometry of scaled inlet for X2 scramjet design.	183
7.6	Magnitude of terms in the <i>total derivative</i> for static pressure for the scramjet intake.	201
8.1	Fuel system calibration results for scramjet model.	226
8.2	Experimental details for shots presented. For shots x2s159 and x2s160 the initial stagnation pressure and mass flow rate was estimated from calibration data.	228
8.3	Fuel equivalence ratio and pressure across combustor (p_2/p_3) at $400 \mu s$ calculated for various shots using air mass flow rate calculated from computational simulations.	244
8.4	Fuel equivalence ratio and pressure across combustor (p_2/p_3) at $400 \mu s$ calculated for large diameter injection hole experiments. This uses the air mass flow rate calculated from computational simulations.	249
8.5	Inviscid performance prediction of scramjet at various fuel equivalence ratio at $400 \mu s$ for larger hole injection experiments.	253
D.1	Relative uncertainties in derived flow quantities. Taken from [6].	288
E.1	List of drawings for scramjet.	293
F.1	Calibration results of Kulite pressure transducers used in scramjet testing. .	312
F.2	Calibration results of PCB pressure transducers used in scramjet testing. .	313
G.1	Pressure at IA-C1 used in normalisation for each shot presented.	314

List of Figures

1.1	Fuel specific impulse for various high speed propulsion devices. Taken from [7].	1
1.2	Atmospheric flight trajectories for airbreathing and rocket powered ascent to orbit. Taken from [8].	3
1.3	Initial temperatures for vibrational excitation, dissociation and ionization of air for various altitudes and flight speeds. Adapted from [9] and [10].	4
2.1	Total pressure and total enthalpy requirements for a high speed scramjet engine. Taken from [11].	8
2.2	Specific Impulse for an engine with freestream with air dissociation. Taken from [12]. Freestream conditions are as follows; Baseline - expected flight conditions; Pressure Limited Equilibrium - condition produced by RST if in chemical equilibrium (low total pressure); H _{ST} - RST produced conditions (low total pressure and chemical dissociation).	11
2.3	Variation in ignition and reaction time of hydrogen/air with dissociation level of oxygen. Taken from [11].	12
2.4	Different facility total pressure and total enthalpy capabilities. Taken from [1]. Note that the enthalpy capabilities of the facilities span the Mach number range.	14
2.5	Oxygen dissociation level from different types of impulse facilities.	15
2.6	Nozzle exit composition for facilities that stagnate test gas. Taken from [11].	15
2.7	Comparison of error in energy due to gas composition and static temperature for stagnation heated vs non-stagnated facilities. Taken from [1]. Freestream Mach number shown in solid lines and total pressures indicated by dashed lines.	16
2.8	Comparison of test time production for various hypersonic ground test facilities. Taken from [13].	16
2.9	Total pressure and total enthalpy predictions for ground test facilities. Adapted from [8].	24
3.1	Idealised distance-time diagram of a free piston driven expansion tube.	30
3.2	Schematic of energy addition process across an unsteady expansion (flow left to right). Taken from [14].	32
3.3	Flow between shock and contact surface in a shock tube for a shock steady co-ordinate system, U _s = 0 (flow right to left in the lab fixed frame of reference). Adapted from [15].	32

3.4	Schematic of alligator mouth extension for large inlets.	33
3.5	Performance of different expansion tube drivers. Taken from [16]. M_7^* is the driver equivalent flow Mach number and p_6/p_4 is the ratio of driver pressure at primary diaphragm rupture to shocked acceleration gas pressure.	36
3.6	Ideal distance-time diagram of an expansion tunnel.	37
3.7	Test time available at end of acceleration tube for variation in nozzle inlet Mach number.	38
3.8	Comparison of experimental and hybrid calculations of flow at nozzle exit for a 25 MJ/kg Mars condition in the X2 expansion tunnel. Taken from [17]	43
4.1	Schematic of the X3 expansion tube (not to scale). Taken from [18].	46
4.2	Pitot pressure mounting arrangement for X2 and X3 (dimensions in mm). . .	49
4.3	Thin film heat transfer gauge in mounting.	50
4.4	Dual piston arrangement in X3 through compression process (piston moves left to right).	51
4.5	Schematic of gas buffer as inner piston enters (piston moving right to left). Taken from [19].	52
4.6	Properties from gas buffer analysis.	53
4.7	Assembly drawing of gas buffer.	54
4.8	Valve design and spring design.	54
4.9	X3 steady expansion nozzle profile. Taken from [20].	55
4.10	X3 nozzle section view. Taken from [20].	56
4.11	Pressure in the driver through the free piston compression with high argon mass fraction (experiment s201 compared with calculation by Scott [21]). .	59
4.12	Position of interface after the passing of the shock.	61
4.13	Experimental static wall pressure close to tube exit for X3 Mach 10 condition (x3s253).	62
4.14	Experimental pitot pressure across at three radial locations at the acceleration tube exit for the X3 Mach 10 condition (x3s253).	62
4.15	Experimental pitot pressure across the tube exit for X3 Mach 10 condition at various times (x3s253).	63
4.16	Expanded view of experimental pitot pressure across at three locations at tube exit for X3 Mach 10 condition (x3s253).	64
4.17	Pitot pressure variation with Mach number, specific heat ratio and static pressure.	64
4.18	Geometry for <i>L1d</i> simulation for X3.	66
4.19	Comparison of static wall pressure in shock tube for X3 Mach 10 condition. Fluctuations before the shock is due to electrical noise in the data lines. .	68

4.20 Sound speed at st2 from <i>L1d</i> simulation in shock tube for X3 Mach 10 condition.	68
4.21 Axisymmetric setup for X3 simulation.	69
4.22 Properties at three locations at the tube exit for laminar simulation of X3 Mach 10 condition.	71
4.23 Properties at three locations at the tube exit for turbulent simulation of X3 Mach 10 condition.	73
4.24 Comparison of static and pitot pressure [Pa] various times from the turbulent simulation for X3 Mach 10 condition. Pitot pressure is shown in the top half of the tube and static pressure in the bottom half.	74
4.25 Contour plot of pitot pressure at 5 ms and 7 ms from the turbulent simulation for X3 Mach 10 condition. Pathlines are shown in the shock steady frame of reference ($U_s = 3122$ m/s).	75
4.26 Properties at tube exit on the midline for the turbulent simulation of X3 Mach 10 condition with differing grid resolution.	77
4.27 Pitot pressure across the acceleration tube exit at 8 ms for varying grid resolutions.	78
4.28 Temperature at tube exit at 8 ms for varying grid resolutions.	78
4.29 Cell based Reynolds number for simulations of X3 Mach 10 condition at tube exit.	79
4.30 Properties at tube exit compared for laminar and turbulent simulations with experimental measurements. Static pressure is at the wall whereas other properties are taken close the centreline.	80
4.31 Comparison of shocks speeds for Mach 10 condition between computational simulations and experiments.	81
4.32 Comparison of the pitot pressure axially along the acceleration tube for laminar and turbulent simulations at various times.	82
4.33 Comparison of contour plots of density and Mach number for laminar and turbulent simulations at 7 ms.	83
4.34 Pitot pressure contours for laminar and turbulent simulations of X3 Mach 10 condition at 7 ms.	84
4.35 Transition from laminar to turbulent boundary layer for a flat plate in hypersonic flow. Adapted from [9].	86
4.36 Transition from laminar to turbulent boundary layer for a flat plate in hypersonic flow with unsteady, shock initiated flow.	87
4.37 Distance-time diagram for a shock-induced boundary layer on a flat plate showing shock, transition and fully developed turbulent boundary layer locations including experimental data. Taken from [22].	88

4.38	Idealised heat transfer and temperature measurements for a shock-induced boundary layer on a flat plate. Taken from [22].	88
4.39	Transition from laminar to turbulent boundary layer in an expansion tube (shock steady frame of reference).	89
4.40	Pitot pressure in Langley pilot expansion tube for transitional condition. Taken from [23].	90
4.41	Schematic of particle integration process of Reynolds number in Weilmuenster's method [24] of calculating transition location in an Expansion tube. Particles A and B start in the shock tube, with particles C and D starting in the acceleration tube with the dotted lines showing their path through the flow processes, and crosses show transition locations.	92
4.42	Distance-time diagram of analytically predicted boundary layer transition location and time in the X3 Mach 10 condition. The Re_t are plotted with the lowest occurring first in time.	93
4.43	Heat transfer measurements taken in the Langley expansion tube. Taken from [23].	94
4.44	Experimental measurements of heat transfer from shot s349 vs van Driest flat plate predictions [25].	95
4.45	Distance-time diagram of Weilmuenster's [24] analytical prediction of X3 boundary layer transition versus experimental measurements.	96
4.46	Experimental measurements of heat transfer from s349 compared with computational simulations.	99
4.47	Heat transfer from CFD (turbulent and laminar) with turbulent pitot pressure at at8.	100
4.48	Distance-time diagram of Weilmuenster's [24] analytical prediction of X3 boundary layer transition versus CFD measurements.	100
4.49	X3 acceleration tunnel geometry for axisymmetric calculations. Taken from [20].	101
4.50	CFD of flow properties in X3 nozzle condition.	102
4.51	Static pressure from at7 and pitot pressure from the test section from X3 hydrogen acceleration gas shot (s289). The pitot pressure has been time shifted to show the shock arrival at the same time.	104
4.52	Properties along the length of the acceleration tube for hydrogen accelerator gas shot (s289).	105
4.53	Static pressure behind various shock speeds with air contamination for an ideal gas mixture of equilibrium gases. Initial conditions of the gas are 150 kPa and 300 K with no reactions.	106

4.54 Close up of acceleration gas region of static and pitot pressure from X3 hydrogen acceleration gas shot (s289). The pitot pressure has been time shifted to show the shock arrival at the same time.	107
5.1 Schematic of the X2 expansion tube. Taken from [26].	109
5.2 Schematic of the pressure transducer locations in X2 operating in tunnel mode. Taken from [17].	110
5.3 Insert piece for the X2 dumptank to fit smaller X2 nozzle.	113
5.4 Schematic of Ludwieg tube operation.	113
5.5 Diagram of hydrogen system on X2.	114
5.6 Experimental recoil of driver tube in X2.	116
5.7 Experimental acceleration tube static pressure for low enthalpy X2 condition.	117
5.8 Comparison of perfect gas and Mirels prediction for the time between the interface and shock.	117
5.9 Experimental nozzle static pressure for low enthalpy X2 condition.	118
5.10 Experimental pitot pressure measurements for X2 low enthalpy condition. .	119
5.11 Static pressure contour plots of pitot probes similar to those used in X2. Adapted from [4]. Times are from the start of the simulation.	120
5.12 Pitot pressure at transducer face for M7 simulation of pitot pressure mount. Adapted from [4]. Dashed line represents flush mounted transducer simulation.	121
5.13 Comparison of normalised pitot pressure and wedge static pressure for low enthalpy X2 condition. Pitot pressure is normalised by a factor of $\frac{1}{187}$ and wedge static pressure is by $\frac{1}{4.24}$	122
5.14 Effects of Mach number change on wedge and pitot pressure.	123
5.15 Average pitot pressure for low enthalpy condition across the nozzle at various axial locations.	123
5.16 Experimental acceleration tube static pressure for low enthalpy X2 condition with N ₂ test gas.	124
5.17 Average pitot pressure for low enthalpy condition across the nozzle with N ₂ test gas.	124
5.18 Experimental acceleration tube static pressure for high enthalpy X2 condition.	125
5.19 Experimental pitot pressure for high enthalpy X2 condition.	126
5.20 Comparison of wedge and pitot pressure in the high enthalpy X2 condition. Pitot pressure is normalised by a factor of $\frac{1}{186}$ and wedge static pressure is by $\frac{1}{3.29}$	127
5.21 Geometry for the L1d simulation (not scaled).	128
5.22 Static pressure in shock tube for one dimensional simulation of low enthalpy condition in X2.	129

5.23	Sound speed in shock tube for one dimensional simulation of low enthalpy condition in X2.	129
5.24	Distance-time diagram of static pressure contours in the shock tube for the low enthalpy condition simulation using <i>L1d</i> . Units are [Pa].	130
5.25	Distance-time diagram of static temperature contours in the shock tube for the low enthalpy condition simulation using <i>L1d</i> . Units are [K].	131
5.26	Distance-time diagram of static temperature contours of the secondary diaphragm rupturing for the low enthalpy condition simulation using <i>L1d</i> . Units are [K].	132
5.27	Static pressure in shock tube for one dimensional simulation of high enthalpy condition in X2.	133
5.28	Sound speed in shock tube for one dimensional simulation of high enthalpy condition in X2.	133
5.29	Geometry for the <i>MB_CNS</i> simulation of X2.	134
5.30	Properties at three locations across the nozzle exit for low enthalpy X2 Mach 10 condition.	136
5.31	Contours showing log of pitot pressure during nozzle start-up for low enthalpy X2 Mach 10 condition.	137
5.32	Comparison of <i>MB_CNS</i> simulation and experimental data for low enthalpy X2 Mach 10 condition.	138
5.33	Properties at three locations across the nozzle exit for high enthalpy X2 Mach 10 condition.	141
5.34	Comparison of <i>MB_CNS</i> simulation and experimental data for high enthalpy X2 Mach 10 condition.	143
5.35	Properties near centreline for X2 Mach 10 condition with varying grid resolutions.	144
5.36	Pitot pressure across nozzle exit for low enthalpy condition with varying grid resolutions.	145
5.37	Temperature across nozzle exit for low enthalpy condition with varying grid resolutions.	145
5.38	Cell Reynolds number comparison for low enthalpy condition with varying grid resolutions.	146
6.1	Schematic of Rayleigh line flow. Adapted from [27].	148
6.2	Schematic of scramjet engine incorporated into a spaceplane for transatmospheric acceleration. Taken from [28].	149
6.3	Equilibrium heat release of stoichiometric hydrogen/air mixture. Taken from [29]. T_3 is the final temperature and p_3 is both the initial and final pressure.	151

6.4	Different fuels thermal energy absorption capacity to meet total engine heat flux as a function of freestream Mach number and dynamic pressure. Taken from [28].	153
6.5	Isobaric batch reaction of stoichiometric hydrogen and air. Taken from [28]. Initial conditions of 2 atmospheres and 1500 K. Temperature labelled as T.	155
6.6	Ignition time for stoichiometric hydrogen/air mixture.	156
6.7	Reaction time for stoichiometric hydrogen/air mixture.	157
6.8	Inlet performance as a function of inlet pressure ratio and area ratio. Taken from [30]. Results are presented for a constant dynamic pressure flight path (47.8 kPa).	158
6.9	Thrust potential for a Mach 7 scramjet with either 30 degree flush wall injector or 10 degree swept ramp injector. Taken from [31].	164
6.10	Total pressure losses from injection and mixing of hydrogen parallel to an incoming airstream of of various Mach numbers. Taken from [32] which reproduced original [33]). Mixing is assumed to either occur in a constant pressure or constant area process.	166
6.11	Comparison of combustor shapes in terms of weight, strength, ratio of wetted area to flowpath area and ratio of length to duct height. Taken from [34].	168
6.12	Length of combustor required to complete hydrogen/air combustion using Huber et al. [35] ignition and reaction times. Initial stoichiometric mix of hydrogen/air at a pressure of 100 kPa and temperature of 1000 K.	169
6.13	Combustor performance with losses due to irreversibilities and frictional losses. Taken from [36].	170
6.14	Effect of Mach number profile in a nozzle on thrust production. Taken from [37].	171
6.15	Effect of skin friction in a nozzle on overall thrust. Taken from [38].	172
7.1	Schematic of two dimensional inlet for scramjet design (orientation to be mounted in expansion tunnel).	175
7.2	Heat transfer rate at stagnation location on blunted leading edges.	177
7.3	Minimum time required to melt an un-cooled, semi-infinite slab of copper at stagnation location.	178
7.4	Shock shape for first wedge with nose bluntness.	181
7.5	Geometry for scramjet inlet.	182
7.6	Contour of Mach number on inlet for inviscid design (scaled in transverse direction).	184
7.7	Contour of Mach number of combustor inlet for inviscid design (scaled in transverse direction).	184
7.8	Pressure along compression surface for inviscid design.	184

7.9	Contour of Mach number of combustor inlet for viscous design (scaled in transverse direction).	185
7.10	Pressure along compression surface for viscous design.	185
7.11	Properties across combustor for viscous scramjet design validation.	187
7.12	Mass flow rate requirement of hydrogen using data transient flow data at nozzle exit from <i>MB_CNS</i> simulation.	188
7.13	Stagnation pressure requirement for H ₂ system using transient flow data at nozzle exit from <i>MB_CNS</i> simulation.	189
7.14	Fuel equivalence ratio for H ₂ system using transient flow data at nozzle exit from <i>MB_CNS</i> simulation.	190
7.15	Change in fuel equivalence ratio across a 200 mm combustor.	191
7.16	Comparison of different methods to obtain fuel penetration from the third wedge.	191
7.17	Penetration distance as a function of time.	192
7.18	Mixing efficiency for hydrogen injection into air.	192
7.19	Estimated combustion efficiency of a true scramjet flow field	193
7.20	Predicted thrust performance of a combustor with heat addition and friction as a function of combustor length.	194
7.21	Schematic of thrust production from two dimensional nozzle.	195
7.22	Mach 10, X2 scramjet model.	196
7.23	Mounting arrangement for static pressure measurement. Taken from [7].	197
7.24	Picture of the fuel valve and transducers of scramjet model.	197
7.25	Schematic of flow domain and boundary conditions for transient simulation of scramjet.	198
7.26	Pathline path and static pressure for pressure derivative term evaluation. Starting position is x = 50 mm, y = -20 mm.	202
7.27	Evaluation of pressure derivative terms along a pathline through the intake.	203
7.28	Control volume used in analysing significance of rate of change in stored momentum.	204
7.29	Comparison of thrust production in a scramjet between flight and ground testing.	205
7.30	Schlieren images of scramjet from transient simulation at 600 μ s.	206
7.31	Log of pressure and pathlines within scramjet from transient simulation at 600 μ s. Scramjet is scaled by a factor of 2 in the transverse direction.	207
7.32	Flow properties along pathlines from transient simulation of scramjet at 600 μ s. Pathline initial position: solid = 10 mm, dash = 20 mm, dash-dot = 30 mm.	208
7.33	Comparison of wall pressure along the body side of the scramjet duct from numerical simulation at various times.	209

7.34 Normalised pressure down the scramjet duct from numerical simulation using the two normalisation methods.	210
7.35 Change in normalised pressure down the scramjet duct from numerical simulation using the two normalisation methods.	211
7.36 Effect of normalised velocity on pressure normalisation down the scramjet duct at 500 μ s. The pathline velocity was taken from the simulation at 600 μ s, with an initial position of 10 mm.	211
7.37 Heat transfer on first wedge from numerical simulation.	212
7.38 Normalised heat transfer down the scramjet duct from numerical simulation using the slug tracking method.	213
7.39 Variation in normalised pressure using slug tracking method with variation in grid resolution.	214
7.40 Schlieren images of inlet start up from transient numerical scramjet simulation (20 - 100 μ s).	215
7.41 Schlieren images of inlet start up from transient scramjet numerical simulation (120 - 200 μ s).	216
7.42 Transient inflow density taken from MBCNS simulation of X2.	217
7.43 Time for flow to establish down scramjet duct using static pressure.	218
7.44 Time for flow to establish down scramjet duct using static pressure.	219
7.45 Distance time schematic for startup of a scramjet combustor in an impulse facility where fuel is injected prior to the test flow arrival.	220
 8.1 Schematic of laser/photo diode fuel system trigger.	223
8.2 Timing of components in fuel system.	224
8.3 Stagnation pressure for several calibration trials.	225
8.4 Calculated mass flow rate for several initial Ludwieg tube fill pressures.	227
8.5 Comparison of pressure traces on thrust surface for fuel off shot.	228
8.6 Comparison of effects of nitrogen versus air test gas with computational simulations with fuel off.	230
8.7 Experimental pressure traces along the inlet compared with computational simulation data.	232
8.8 Experimental and numerical pressure traces at first location in combustor (CO-C1, x = 247.8 mm).	233
8.9 Comparison of effects of fuel injection using nitrogen as free stream gas to remove combustion effects.	235
8.10 Static pressure behind fuel injection location on third wedge for various Ludwieg tube fill pressures with nitrogen freestream gas.	236
8.11 Fuel equivalence ratio change during the test period for various initial Ludwieg tube fill pressures.	237

8.12	Combustion effects on normalised static pressure along the scramjet duct for a initial Ludwieg fill pressure of 380 kPa.	238
8.13	Combustion effects on normalised static pressure along the scramjet duct for a initial Ludwieg fill pressure of 730 kPa.	240
8.14	Combustion effects on normalised static pressure along the scramjet duct for a initial Ludwieg fill pressure of 1080 kPa.	241
8.15	Pressure ratio across combustion for one dimensional heat addition into a constant area duct for various fuel equivalence ratios. Using nominal inflow conditions of $M = 4.73$ and $T = 1000$ K.	242
8.16	Variation in fuel equivalence ratio on normalised static pressure along the scramjet duct at $400 \mu s$	243
8.17	Scramjet duct pressure for nitrogen test gas and fuel injection two different freestream conditions. Initial Ludwieg tube fill pressures of 1080 kPa and 1040 kPa were used for the high and low enthalpy shots respectively.	245
8.18	Penetration of four sonic jets for varying size holes with $\phi = 1$ using nominal freestream conditions on third wedge at $400 \mu s$	246
8.19	Fuel equivalence ratio change during the test period for various initial Lud- wieg tube fill pressures, large injector hole diameter tests.	247
8.20	Comparison of normalised static pressure for large hole injectors with vari- ation in freestream gas.	248
8.21	Comparison of normalised static pressure with medium fuel mass flow rate tests with variation in injection hole diameter.	250
8.22	Static pressure through scramjet duct for larger fuel injection holes of 2.8 mm diameter for various fuel equivalence ratios.	251
8.23	Inviscid net thrust predictions of scramjet at various times. Normalised by pressure on first wedge.	253
A.1	Wave diagram for a shock tube.	277
A.2	Reference frames for a shock wave passing through a stagnate gas.	278
A.3	Wave diagram for a shock tube with an area change at the primary diaphragm.	280
B.1	Schematic of pressure relief valve. Adapted from [19].	282
D.1	Example of normalised pressure data points over the measurement period. Taken for transducer location CO_6C_15 for x2s117.	289
D.2	Uncertainties in pressure measurements due to different effects for combus- tion effects, using an initial Ludwieg fill pressure of 730 kPa at $400 \mu s$	291
D.3	Combined uncertainties in pressure measurements due to different effects for combustion effects, using an initial Ludwieg fill pressure of 730 kPa at $400 \mu s$	292

Nomenclature

α	fuel injection constant
β	$\frac{dB}{dm}$
β	dispersive term
χ	molecular weight
δ	shock standoff, m
\dot{m}	mass flow rate
\dot{q}	heat transfer rate, W/m ²
η_c	combustion efficiency
η_m	mixing efficiency
η_{KE}	kinetic energy efficiency
γ	specific heat ratio, c_p/c_v
λ	flow property
μ	viscosity, Pa.s
ω	fundamental frequency, Hz
ϕ	fuel equivalence ratio
ρ	density, kg/m ³
θ	wedge angle, °
v', v''	stoichiometric mole numbers
A	Arrhenius pre-exponential constant, m ³ /mol.s
A	area, m ²

a	speed of sound, m/s
A^*	area at throat, m ²
B	flow property
c	pre-tension, m
C_H	Stanton number
c_p	specific heat at constant pressure, J/kg.K
c_v	specific heat at constant volume, J/kg.K
C_{μ_T}	Baldwin-Lomax transition constant, usually 14
CS	control volume
CV	control surface
D	diameter, m Drag, N
D_1	Damkohler's first number
D_2	Damkohler's second number
E_A	activation energy, J/kg
F	force, N
f	fuel to air ratio
G_s	constant, flow length requirement
GW	wall enthalpy ratio
H	stagnation enthalpy, J/kg
h	static enthalpy, J/kg
h_{alt}	altitude, m
K	thermal conductivity constant, W.K/m spring constant, N/m
k_b	backward reaction rate, m ³ /mol.s
k_f	forward reaction rate, m ³ /mol.s
L	length, m
M	Mach number

m	mass, kg
n	Arrhenius equation power constant normal
NE	nozzle exit
P	penetration distance, m
p	pressure, Pa
$P.D.$	primary diaphragm
p_{pitot}	pitot pressure, Pa
q	dynamic pressure, Pa
R	radius, m/specific gas constant, J/kg.K
r	radial distance, m
Re	Reynolds number
Re_θ	momentum thickness based Reynolds number
Re_l	unit Reynolds number, 1/m
s	spacing, m
$S.D.$	secondary diaphragm
T	temperature, K/thrust, N
t	time, s
TE	tube exit
U	velocity, m/s
V	volume, m ³
W	work, J
X	species/uncertainty
x	axial distance, m
y	radial distance, m

0	stagnation condition
δ	boundary layer
∞	free stream condition
ϕ	variable
<i>accel</i>	acceleration gas
<i>air</i>	air
<i>aw</i>	adiabatic wall
<i>c</i>	curvature/clearance
<i>com</i>	combustor
<i>eff</i>	effective
<i>ent</i>	entrance
<i>est</i>	flow establishment
<i>f</i>	fuel/final
H_2	hydrogen
<i>i</i>	initial/integrated/ignition
<i>inj</i>	injectors
<i>j</i>	jet
<i>lam</i>	laminar
<i>lud</i>	Ludwieg tube
<i>nom</i>	nominal
<i>p</i>	piston
<i>r</i>	reaction/radial
<i>ref</i>	reference
<i>s</i>	shock
<i>sep</i>	seperation
<i>st</i>	stoichiometric

T turbulent

t transitional

$test$ test gas

v valve

w wall

Introduction

The use of high speed propulsion engines has primarily been in the application of either missile technology, space access or aviation. The development of these propulsion devices over the past 100 years has seen some of the most difficult engineering challenges overcome. The choice of engine for use in an aerospace application is a balance between the performance aspects (usually quantified by specific impulse), the purpose of the engine and the cost involved in both development and construction of the engine. High speed propulsion has been dominated by the conventional chemical rocket not only due to its flexibility of operation both within and outside earth's atmosphere, but also due to its low cost of both design and production. The rocket however, is theoretically outperformed by the supersonic combustion ramjet (scramjet) for atmospheric travel, as the oxygen used in the combustion processes of the scramjet can be collected from the air. This reduces the amount of lift-off mass required by the vehicle as the oxidiser required by the engine does not have to be carried. The performance superiority of hydrogen fuelled scramjets from Mach 6 to Mach 20 over ramjets and rockets can be seen in Figure 1.1, gauged by the fuel specific impulse.

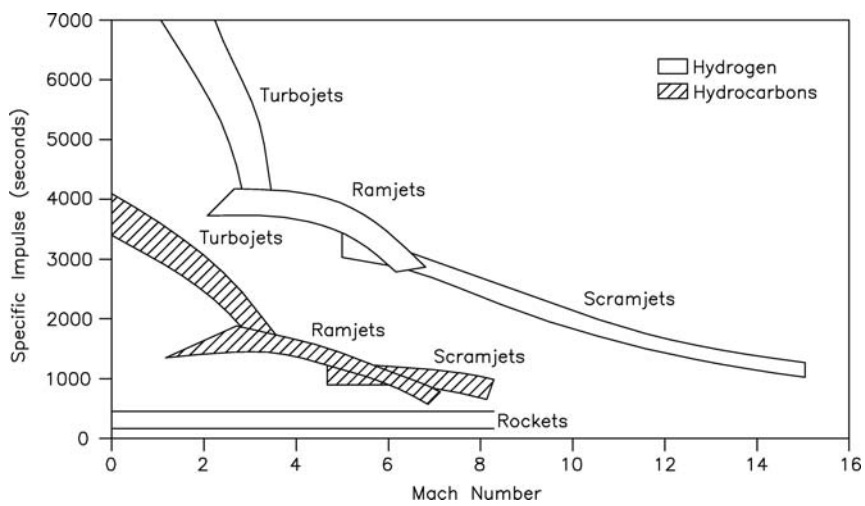


Figure 1.1: Fuel specific impulse for various high speed propulsion devices. Taken from [7].

Supersonic combustion ramjet technology today is still in the basic research phase of overall development. The basic fluid phenomenon of combustion at supersonic speeds was first proposed theoretically in 1949 [39] and realised experimentally in 1955 [40]. It was

proposed that this flow phenomenon would be suitable for high speed vehicles as the large flow losses and thermal/structural loading that slowing of the airstream causes in other air-breathing engines could be avoided. The scramjet engine, unlike its low speed predecessors, is required to be highly integrated into the vehicle itself to take advantage of compression on the airstream on the forebody. Since the discovery of supersonic combustion, research has focused on the ability to overcome the engineering challenges associated with using supersonic combustion to produce thrust in a vehicle. Some of these research areas include compressing the freestream air efficiently, fuel injection and mixing efficiency, dealing with the high structural heating and structural loading and integration of the engine into a useable vehicle.

Lu and Marren [10] stated,

“A successful research and development program in hypersonic flight technology requires wind tunnel testing, numerical simulation and ultimately, prototype testing, resulting in a validated integrated test and evaluation methodology.”

As the scramjet engine development moves forward towards realistion, ground testing provides a relatively cheap and quick platform to test both flow phenomenon and different aspects of the technology. Ground testing also offers the ability to measure many instream flow properties throughout the engine that would not be possible during a flight test. Component testing such as intake tests, allows for the simplification of one part of the engine so that improvements can be made while removing interaction effects of other components. This is a necessary step towards a functioning device, however the interactions between components must be addressed at some stage in the future to realize a functioning prototype. Ground testing can also provide validation data for numerical simulations, as these are still only developing to deal with the complex, coupled flow and chemistry.

As development continues to higher speed engines, the bulk of the flow through the combustor may remain hypersonic. In comparison to lower Mach number engines where combustor flows have a bulk Mach number close to one, the fully three dimensional nature of these higher speed engines is required to be understood. Additional effects of high compressibility on turbulent boundary layers and fuel/air mixing where the fuel velocity will be surpassed by the incoming air streams velocity are not well known. Currently there is very limited data to support the understanding of these effects that are seen in hypersonic combustion flows, which gives low confidence to engineers in the reliability of flow simulations. Therefore extensive experimental testing is required for the development of engines at higher Mach numbers.

Many types of facilities around the world have been used to test scramjets such as, heated blow-down facilities, long duration piston compression facilities and reflected shock tunnels. With the high total pressure and total enthalpy requirements at the higher Mach

number portion of the predicted transatmospheric scramjet ascent (Figure 1.2), these previously mentioned facilities are incapable of matching all flow properties above an approximate flight Mach number of 10. In order to create these flows, the test gas is required to reach very high stagnation conditions. Firstly, these facilities are not capable of producing both the higher total pressures and total enthalpies required. Secondly, as the total pressure of the test gas is realised before passing through a steady expansion nozzle, severe erosion of the shock tube reservoir and nozzle throat regions occurs. As a result, this limits the flow conditions total pressure to about 120 MPa [11]. Finally, the high temperatures seen during stagnation cause non-equilibrium gas composition to occur at the scramjet intake. As the gas is expanded from stagnation conditions, where the air is highly dissociated due to high temperatures (~ 3000 K at Mach 12 as shown in Figure 1.3), the dropping temperature drives the dissociated atoms to reform into binary molecules. However, due to the short transit times, some of the atoms will not have the time to reform and therefore will not reach equilibrium composition. This is one of the main reasons that most of the development of supersonic combustion propulsion technology has been focused on the lower Mach number range of their predicted usability.

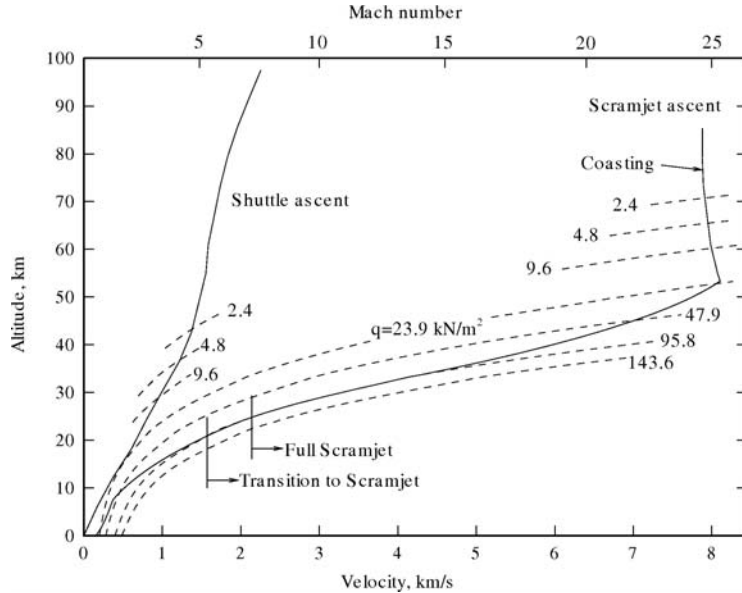


Figure 1.2: Atmospheric flight trajectories for airbreathing and rocket powered ascent to orbit. Taken from [8].

The expansion tube is capable of producing the high energy and density flows required for high speed development of scramjets. It avoids the issues of high total pressure containment and non-equilibrium gas composition seen in other hypersonic ground test facilities because the test gas is never stagnated once the energy has been added to it. Coupled with a high performance driver, the expansion tube is capable of producing total pressure to the order of tens of GPa. This is due to part of the energy addition to the test gas

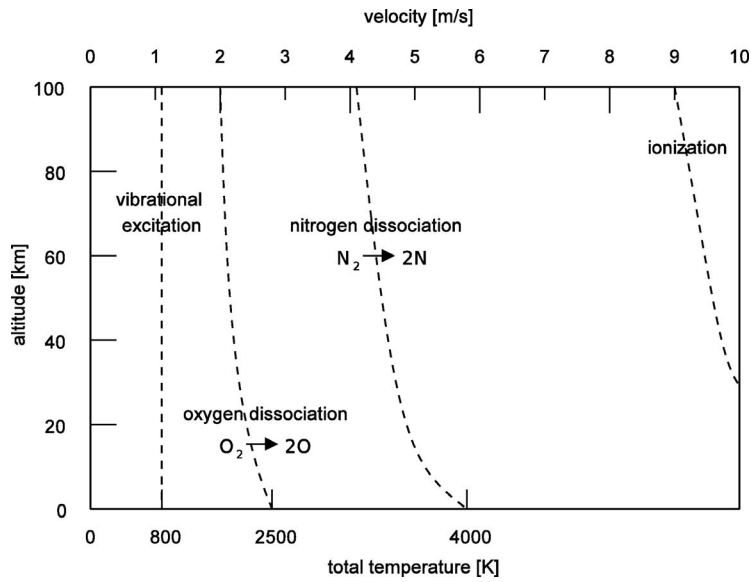


Figure 1.3: Initial temperatures for vibrational excitation, dissociation and ionization of air for various altitudes and flight speeds. Adapted from [9] and [10].

occurring through the unsteady expansion process after the test gas is initially processed by a shock wave. However, the expansion tube facility can only provide relatively short test times. Also, expansion tubes have been shown to produce inherently *noisy* flow [41] in the operating region where scramjets are to be tested. Conditions which are at the lower enthalpy end of the expansion tube likely operating range (below approximately 10 MJ/kg) and/or have a sound speed ratios over the test gas/driver gas interface close to unity exhibit this corrupted flow. If these short comings can be overcome, an expansion tube can provide a crucial ground testing capability for propulsion testing which is necessary for scramjet technology development to higher Mach numbers.

The topic of this doctoral thesis is to establish the practicality of undertaking a complete '*nose to tail*' test of a supersonic ramjet in an expansion tube ground test facility at a flow condition which replicates true flight. The work in this thesis targets the the high speed regime where a reflected shock tunnel fail to produce flow with correct gas composition, vibrational state and total pressure requirements, to allow future direct comparison of results between the two facilities. This is a a Mach 10, 100 kPa dynamic pressure condition. With this capability, investigations of scramjet performance can begin to be performed in expansion tube facilities on the upper theoretical limit of scramjets in terms of both total pressure and total enthalpy. These future studies can be performed on complete scramjet geometries without making implications like direct combustor testing which cannot capture all vehicle interaction effects.

1.1 Original scientific contributions of this study

This study has presented several original contributions to scientific knowledge, which are presented in this thesis as follows:

- Identification of limitations for duplicating a scramjet flow condition in expansion tubes due to boundary layer transition (Chapter 4).
- Presentation of solutions to overcome test flow disruption caused by boundary layer transition to produce a flight duplication condition in an expansion tube (Chapter 4).
- Production of test flow to replicate the expected freestream conditions for a *pressure-length* scaled scramjet in the X2 expansion tunnel facility (Chapter 5).
- Definition of transient flow properties across the tunnel exit using both experimental measurements and a hybrid numerical calculation (Chapter 5).
- Development of an analysis to deal with quasi-steady scramjet data where the freestream flow is known to be transient (Chapter 7).
- Use of numerical scramjet simulations with the transient inflow freestream flow predicted for the expansion tube to show meaningful measurements could be extracted using the quasi-steady analysis, and inlet startup and flow establishment could be achieved (Chapter 7).
- Testing of a ‘*nose to tail*’ scaled scramjet engine in a expansion tube and initial characterisation of its performance (Chapter 8).

Literature Review

A review is presented of the current needs and requirements of a ground test facility to conduct higher speed scramjet research and development. A comparison is made between currently established hypersonic ground test facilities, on how each addresses the requirements needed for high speed air-breathing engine testing. A description of each facility is presented, including a description of its capabilities and an overview of scramjet research conducted in each type of facility at higher Mach numbers.

At the 1992 workshop on high speed combustion sponsored by ICASE and NASA LaRC, directed towards the hypersonic propulsion requirements of NASA, the keynote speech by Bushnell [42] stated the following on hypersonic air-breathing propulsion.

“Although significant research is required for the ‘lower’ speed range ($M < 10$), the major research frontiers are in the hypervelocity arena, which has never been seriously addressed. Even the facility base is deficient for the high Mach number case.”

This statement highlighted the need in 1992 for high speed test facilities for aero-propulsion testing above Mach 10. The lack of scramjet test facilities for the simulation of conditions at Mach 10 and above remains to this day, evidenced by the recurrence of this same theme throughout the literature [10, 43, 28]. With this in mind, it seems pertinent that this thesis address the need for a higher Mach number test facility for air-breathing propulsion.

2.1 Requirements for Ground Testing of Scramjets

For duplication of flight conditions in ground testing, differing physical parameters must be maintained depending on the test performed [10]. In scramjets, the required types of testing are aerodynamic, aerothermal, aeropropulsion, structures and high temperature gas effects due to the integration of the engine in the body. For the propulsive tests however, the gas composition and flow variables (pressure, temperature and velocity) must be maintained [43]. As described by Anderson [1], for hypersonic combustion, the primitive variables to describe a flow during flight are shown in Table 2.1. For ground testing, these can be represented by simulation parameters, which are well known dimensionless groupings.

Table 2.1: Simulation requirements for supersonic/hypersonic combustion. Adapted from [1].

Primitive Variables		Simulation Parameters	
p	pressure (or density, ρ)	M	Mach number
T	temperature	Re	Reynolds number
U	velocity	C_H	Stanton Number
L	length	D_1	Damkohler's first number
ν_i	gas composition	D_2	Damkohler's second number
		GW	wall enthalpy ratio

Anderson [1] suggests that in general, to ensure faithful representation of the coupled chemical and flow processes that duplication of all primitive variables is required. Therefore all simulation parameters are met with the exception of wall temperature and wall reactivity which is hard to achieve in short duration tests. This would mean that flight scale must be preserved for ground testing. Morgan and Stalker [44] noted that for some conditions that a pressure-length scaling could be applied to a simple supersonic combustor. Using a pL scaling would satisfy most of the simulation parameters shown in Table 2.1, apart from the wall enthalpy ratio. An experimental investigation by Pulsonetti [45, 46] showed that the use of binary scaling of the density-length (ρL) or pressure-length (pL) would meet most of the requirements for subscale scramjet testing, although this could not match all effects. Mixing and viscous effects are matched well by either scaling law, with a slight underprediction of full scaled combustion pressure rises.

With increasing Mach number on a transatmospheric flight path, ground test facilities are required to supply rapidly increasing levels of both total pressure and total enthalpy to the scramjet [11, 47, 1, 31, 28] (Figure 2.1). The total enthalpy requirement of the freestream mainly consists of the kinetic energy and can reach levels of up to 30 MJ/kg. Therefore, the total enthalpy increases with the square of freestream velocity (Figure 2.1a). Only minor changes occur in the thermal energy component of the total enthalpy due to the low temperature variation through a space planes ascent [11]. Thus, there is little latitude in this requirement. However, the total pressure requirement is not as stringent, with lower dynamic pressure flight paths able to be tested. Also, the total temperature increases to levels, whereby if stagnated, will cause significant dissociation of the oxygen and nitrogen in the test gas.

The total pressure is seen to increase on a logarithmic scale (Figure 2.1b) with flight Mach number, to extreme levels of the order of GPa. If due to size or test limitations sub-scaled testing is required, this will increase the total pressure requirement linearly with decreasing model size (if pL scaling is adapted) [45]. Thus, the total pressure requirement may be even more extreme. On the other hand, to relieve the demands on ground test

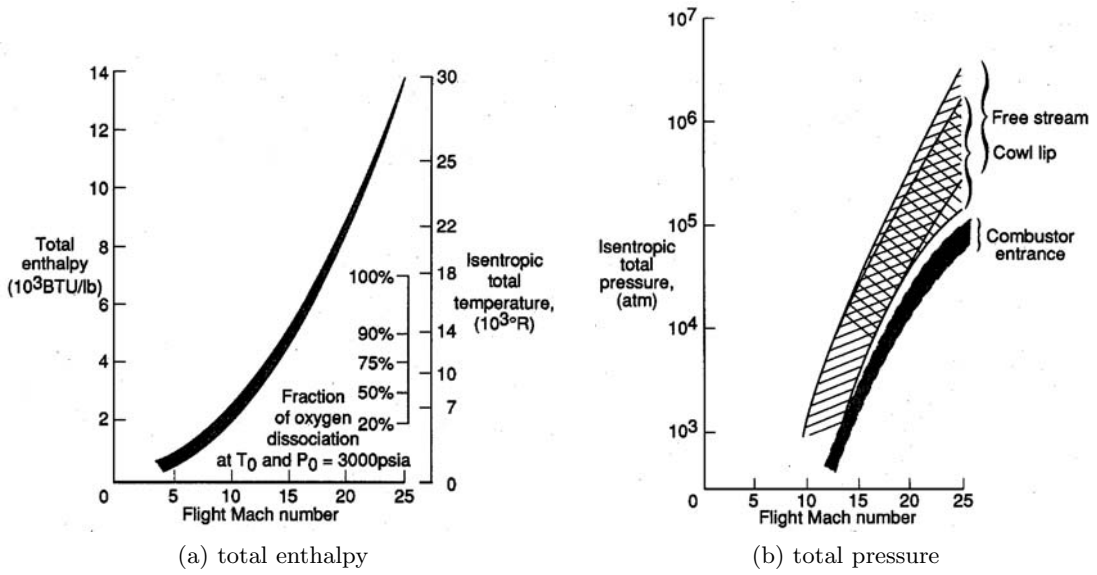


Figure 2.1: Total pressure and total enthalpy requirements for a high speed scramjet engine. Taken from [11].

facilities to produce these high total pressures, *direct* or *semi-direct* scramjet testing can be used or a lower dynamic pressure flight path chosen for ground testing. This can be seen in Figure 2.1b, where the conditions at the cowl tip (*semi-direct*) and combustor entrance (*direct*) are substantially lower by up to an order of magnitude [28]. This is due to the freestream's properties representing the flow properties after being processed by the intake where total pressure losses occur. This also has the added advantage of shortening the model which allows for more flow lengths of gas being processed by the scramjet. However, this comes at the cost that the true intake flow field is not created, including boundary layer development and non-uniform flow field.

The time of the experiment needs to be long enough for flow to establish at steady state conditions expected in flight. It is suggested by Bushnell [43] for hypersonic aeropropulsion tests that minutes are required for testing. Best [48] suggests that the operation time of a single stage to orbit will be of the order of ten seconds, though the total flight time is of the order of minutes. Chinitz et al. [11] makes the distinction between a '*propulsion research facility*' and an '*engine development facility*'. The first facility is needed to perform basic research and technology development relating to operability and performance of engine components and complete engine flow-paths. This is stated to be a relatively inexpensive facility as multiple facilities can be used that are tailored for the research aims. Its major use would be to verify CFD and perform evaluation of engine design parameters. In comparison, the engine development facility is an expensive facility with long test times to demonstrate durability and operability of a full scale, full weight flight verification test.

As will be shown in a later section (Section 2.2), currently it is impossible to generate flow for periods longer than of the order milliseconds at higher Mach number ground testing conditions. If wall temperature effects are ignored¹ due to the time taken for the associated properties to reach equilibrium, the test time requirement will be reduced. This still meets the requirements for a large range of possible testing that can be performed in the propulsion research facility. In this circumstance the time required for testing becomes the flow establishment time. Flow establishment is the time after the initial passing of the incident shock for the flow to reach steady state [49]. Steady state is defined as where the residual properties of the initial slug of gas, combustion effects, the growth of boundary layers and their resulting effects to reach equilibrium before the test period can start.

Correlations have been developed for the flow establishment times for flat plates in reflected shock tunnels at hypersonic speeds by Davies and Bernstein [22] and East et al. [50]. This correlation for establishment times is given by Equation 2.1 with G_s representing the number of flow lengths needed to reach steady state or the ratio of flow establishment time compared with the time taken for the flow to proceed over a particular flow feature. For pressure measurements, the value of G_s was found to be 2 for laminar flows and approximately 1 for turbulent flow [50]. For flow over a turbulent flat plate, approximately 3.3 flow lengths was required for skin friction measurements to reach steady state and 0.9 flow lengths for pressure measurements [22, 50]. Steady state was assumed to occur when pressure fluctuations reduced to below a small residual level within just under a flow length, however skin friction required over three flow lengths to settle. This is an expected outcome as the pressure will not fluctuate too much as the pressure changes due to viscous interactions of the boundary layer formation are low compared with the overall pressure. In comparison, the skin friction will change proportionally with boundary layer development and is significant compared to the total level.

$$t_{est} = t_i + \frac{G_s x}{U} \quad (2.1)$$

A numerical study performed by Jacobs et al. [49] on a high Mach number generic scramjet configuration showed that the flat plate predictions can be used to form a correlation of flow establishment times. This was performed using both a steady and transient inflow conditions of the flow expected in an idealised reflected shock tunnel² for a two dimensional simulation of a centrally injected scramjet without modelling the effects of injection or combustion. The correlation showed again that flow lengths of approximately 0.9 were required for pressure levels to reach steady state and 3 flow lengths for skin friction

¹The structure of the scramjet takes significant time to reach thermal equilibrium, on the order of seconds.

²The data had a smoothed profile with no high frequency perturbations.

and Stanton number for both the steady and transient inflow³ conditions at a reasonable distance from the leading edge. Close to the leading edge the number of flow lengths was higher to reach steady state, but the total flow time should not be effected due to the large time required for the flow establishment at the end of the scramjet combustor. Jacobs et al. also predicted that flow lengths of 80 and 140 were required for the recirculation regions behind the rearward facing step and injector strut respectively.

The analysis of Jacobs et al. was advanced by Rogers and Weidner [51] with the inclusion of hydrogen injection from a centrally located strut in the combustor. The boundary layer settling times were found to occur within 3 to 4 flow lengths for both the transient and steady inflow simulations. The mixing parameters however were established after 2 flow lengths in the steady state case, but more than 4 flow lengths were required for some of the parameters in the transient case. This indicates that mixing required similar amount of flow lengths to achieve steady state as those predicted for the boundary layer. It is also pointed out for the transient inflow simulation that although larger flow lengths for establishment of mixing parameters are predicted, that only two flow lengths are required for flow establishment of pressure after the peak pressure is reached (peak pressure indicates the starting of the test period).

For combustion effects, the time taken to reach equilibrium can be quite small, although the effects on the boundary layer can take some time to establish due to turbulent interactions and their effects on mixing.

The effects of having incorrect gas composition on scramjet performance has been explored and reviewed by many researchers [11, 12, 52, 1, 31] for different ground test facilities. One cause of incorrect gas composition is due to dissociation of the nitrogen and oxygen and further reactions. This is caused by the test gas dissociating while encountering high temperatures during the gas cycle of creating the test flow and very short expansion times not allowing the reformation back to the *clean air* composition. These high temperatures are usually unavoidable as most facilities use heating processes to increase the total pressure and total enthalpy of the test gas. The consequence is substantial levels of O, N, and NO in the freestream. Another cause for incorrect test gas composition is due to the creation of water vapour (and perhaps other contaminants in vitiated facilities) by sudden de-excitation of the vibrational mode and associated energy release. This again is due to the test gas obtaining high temperatures and obtaining energy in the vibrational mode and rapid expansion causing a time delay before the de-excitation can occur. Having incorrect inflow composition affects the thermal properties of the test gas, thus altering flow structures, boundary layer growths and combustion effects. Also the error in energy levels due to the incorrect gas composition increases third body reaction rates disrupting the flow further. As these changes to the scramjet are quite complex

³To reach steady state, these are normalised against the freestream using the hypersonic equivalence principle.

and difficult to decouple, it is advisable to minimise the amount of dissociation in the freestream. Bakos [12] showed by computationally modelling a generic scramjet, the total specific impulse measured in the presence of freestream dissociation would increase by approximately 100 s above the a similar condition if in chemical equilibrium (Figure 2.2). This was due to extra heat release when burning from O rather than O₂. However the performance above Mach 15 is lower than that expected in flight (Baseline condition) due to the total pressure limitation of the reflected shock tunnel.

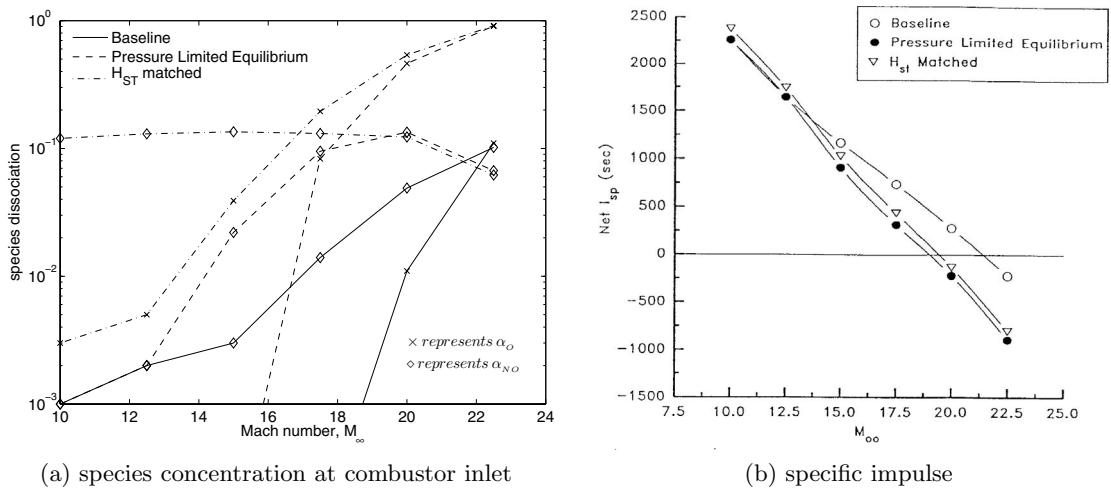


Figure 2.2: Specific Impulse for an engine with freestream with air dissociation. Taken from [12]. Freestream conditions are as follows; Baseline - expected flight conditions; Pressure Limited Equilibrium - condition produced by RST if in chemical equilibrium (low total pressure); H_{ST} - RST produced conditions (low total pressure and chemical dissociation).

As finite rate chemistry plays a dominant role in supersonic combustion, starting with a dissociated air freestream will significantly change the flow properties through the combustor. Having a dissociated airstream results in a decrease in the ignition and reaction times and alters the energy yield from combustion (and therefore pressure and temperature) as the flow passes down the combustor. Thus, all measurements throughout the engine will be incorrect. Shortening of ignition and reactions times was illustrated by Chinitz et al. [11], by investigating the effect of oxygen dissociation level on combustion stoichiometric composition of hydrogen air mixture at 1 atmosphere (Figure 2.3). With the increasing oxygen dissociation level, the ignition and reaction times drop dramatically by an order of magnitude. The effect of their differences will depend on the nature of the flame. For example, there will be negligible effects on a classical diffusion flame, whereas, there will be significant effects for a kinetically limited flame. Anderson [1, 31] highlighted the effect of dissociation on airstream energy levels by stating,

“The fundamental difficulty in generating hypersonic flows in a ground test facility is related to putting the energy into the proper mode in the test gas that is generated.”

The energy is mostly tied up in the NO and dissociated oxygen which would not be present in clean air. This has adverse effects on inlet boundary chemistry and nozzle expansion.

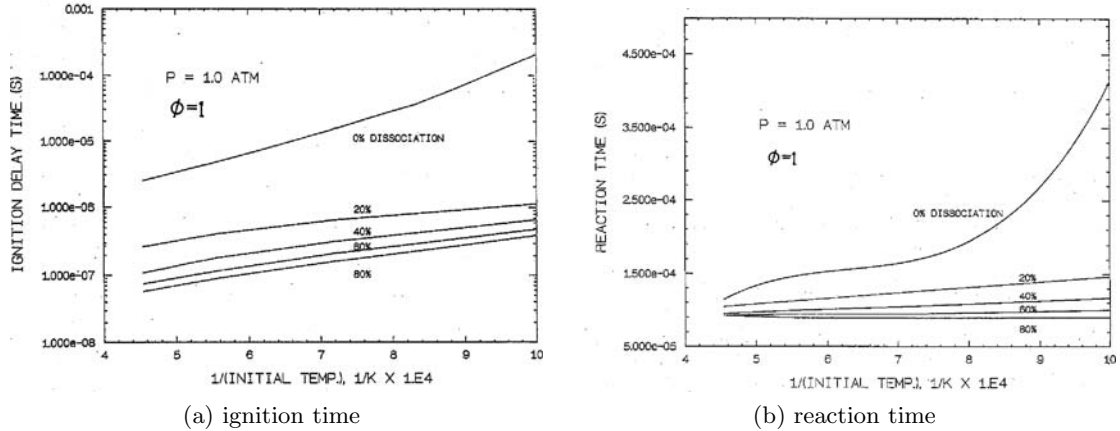


Figure 2.3: Variation in ignition and reaction time of hydrogen/air with dissociation level of oxygen. Taken from [11].

Small inaccuracies in the flow condition can have adverse effects on the overall performance of the engine. Willbanks [53] investigated the effects on combustion of small perturbations in combustor inlet temperature for both a constant pressure and a constant area combustor, with premixed hydrogen air in a quasi-steady analysis. That study established that perturbations in temperature had greater effects on constant pressure combustors than constant area combustion for high Mach numbers. Changes of the order of 15 K in free stream temperature can cause significant changes in peak pressure rises in the combustor. This work demonstrated the sensitivity of scramjet performance to inlet conditions throughout the test time.

Transient effects of perturbations in freestream properties in ground test facilities are expected due to the processes by which the flow is produced. Transient perturbations can enhance mixing by creating further turbulence in the freestream and oscillating shock waves [54]. Park [55] observes these transient perturbations can cause early transition of boundary layers. Currently, the quantitative extent of the effects of free stream perturbations in hypersonic wind tunnels on transition and turbulent mixing is largely unknown [11]. Regardless, meaningful measurements have been made in hypersonic/hypervelocity wind tunnels [56, 57].

2.2 Types of Facilities for High Mach Number Scramjet Testing

With the described requirements for aeropropulsion testing of scramjets detailed in Section 2.1, it is pertinent to review the capabilities of testing in each type of facility that has been used for moderate to high Mach number testing of scramjets. The high total pressure and enthalpy requirements of high Mach number scramjets limits the use of most conventional ground test facilities. This is reflected in the large power requirements to run continuous flow facilities (increasing from 93 MW at Mach 6 to 281 MW at Mach 10 and 1270 MW at Mach 20 [28]), which limits the selection to short flow duration blowdown facilities, piston compression facilities or impulse facilities (reflected shock tunnels (RST) and expansion tubes).

Anderson [1] explores what effects a short duration flow will have on testing a scramjet model and making meaningful measurements. With the high energy involved at the high Mach number conditions, the short flow duration of the flow means that cooling requirements can be met using simple heat sink approaches. Measurements such as local heat flux also become easier⁴ with short duration flows due to the use of semi-infinite conduction. However, all flow data must be recorded as soon as possible, to reduce any wasted flow through the model. Therefore, the measurements taken must have high frequency responses (in the order of 10^6 Hz). As alluded to previously, the model wall temperature will likely be close to room temperature. Hence, the wall enthalpy ratio will be less than that seen in flight which is approximately 0.2. However, both skin friction and heat transfer become virtually independent of the wall enthalpy ratio at values less than 0.3. Anderson states that the greatest concern is that without the duplication of wall temperature, wall reactivity will not be simulated.

As most short duration ground test facilities stagnate the test gas before expansion to the freestream pressure, this high total pressure will exist as static pressure and therefore presents a structural limit to achievable conditions. As discussed previously (Section 2.1), the total pressure requirement can be reduced with *direct connect testing* [11, 28]. Figure 2.4a presents a collection of facility capabilities collated by Anderson [1]. This shows that pulse facilities (like the reflected shock tunnels T5 and Calspan) can reach the total pressure requirements for above Mach 8 testing. This is due to the short duration in which the high total pressures have to be contained in a pulse facility. However, the expansion tube facilities (like upgraded HYPULSE) are the only current facilities that can reach the total pressures for above Mach 10 freejet testing or Mach 12 for direct connect testing. This is due to the fact that both the total pressure is never obtained in an expansion tube (the test gas is not stagnated) and the total pressure is increased through the unsteady expansion process.

⁴This is easier to measure an approximate result. However, this is still not a high precision technique.

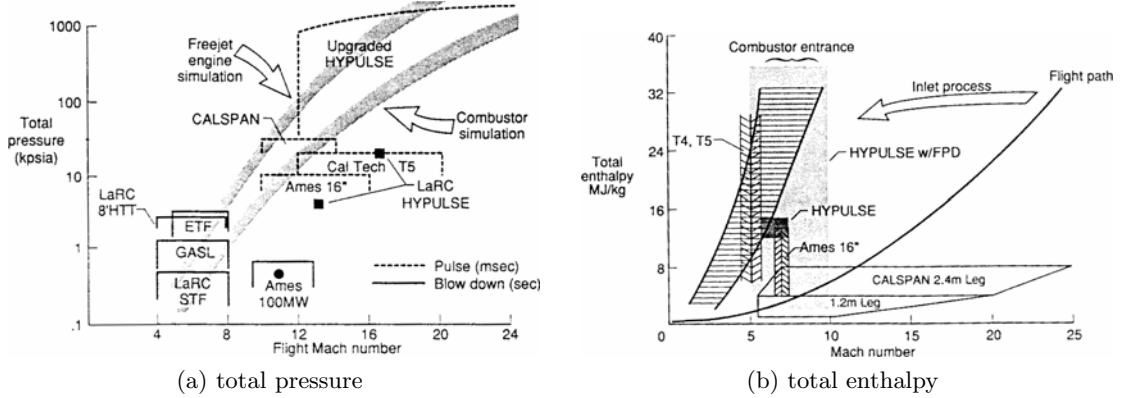


Figure 2.4: Different facility total pressure and total enthalpy capabilities. Taken from [1]. Note that the enthalpy capabilities of the facilities span the Mach number range.

Figure 2.4b shows the total enthalpy capabilities of various hypersonic test facilities against the requirements of flight. It can be seen that at low performance, conventional heated driver systems (like the Calspan reflected shock tunnels Leg I and II) limit enthalpy production in a RST to approximately a Mach 12 flight condition. In comparison, medium performance detonation drivers (used in the NASA Ames 16" and HYPULSE facilities) can provide an increase up to a Mach 15 flight condition with total enthalpies of 15 MJ/kg. The free piston driver (high performance driver used in the T4 and T5 facilities) can produce total enthalpies in reflected shock tunnels up to 30 MJ/kg. The expansion tube however, can easily produce the total enthalpies required, with or without a high performance driver due to the total enthalpy increase in the test gas through the unsteady expansion process.

For all current facilities apart from the expansion tube, the test gas realises its stagnation conditions at some point in the cycle. Therefore, the air reaches the temperatures where the oxygen and nitrogen molecules dissociate (total temperature seen in Figure 2.1a) and cannot reform in the short time periods once cooled through the nozzle expansion process [47, 1, 12, 52]. Figure 2.5 shows the production of dissociated oxygen for various facilities. This shows that the reflected shock tunnels produce a significant level of dissociated oxygen when simulating flight conditions above Mach 10 and that the addition of a free piston driver to an expansion tube can decrease the amount produced at high Mach number conditions.

Mass spectrometry measurements in a reflected shock tunnel at various total enthalpies were made by Skinner and Stalker [58] (and was also empirically modelled by Park [55]). These measurements showed similar trends as recorded above for levels of dissociated oxygen, and also showed that experimentally the composition level of NO/N₂ is consistently around 0.15 for all total enthalpies above 5 MJ/kg. Numerically, this was seen to rise from 0.2. The free jet composition of a gas produced by the steady expansion from a stagnated gas (Figure 2.6) was shown by Chinitz et al. [11] for a constant dynamic pressure

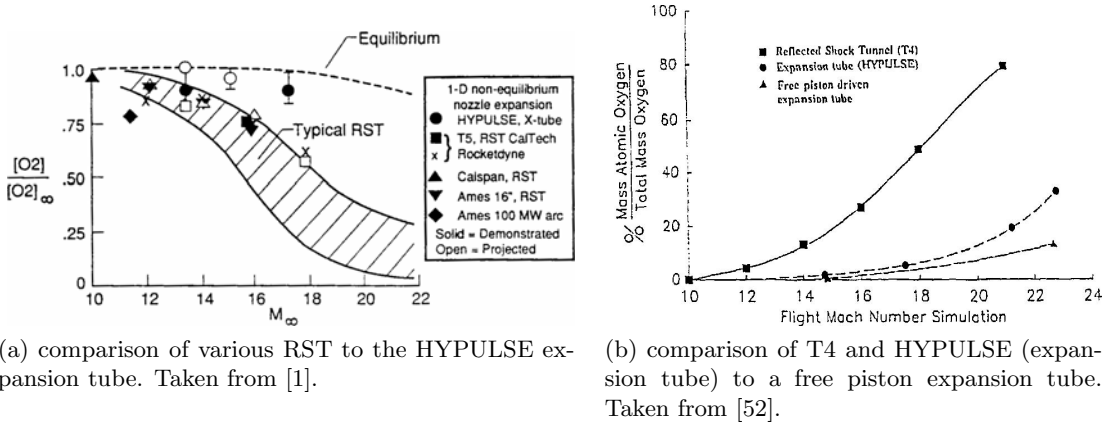


Figure 2.5: Oxygen dissociation level from different types of impulse facilities.

of 50 kPa. This also shows the level of NO was quite constant with increasing condition Mach number and the level of dissociated oxygen increasing quite rapidly.

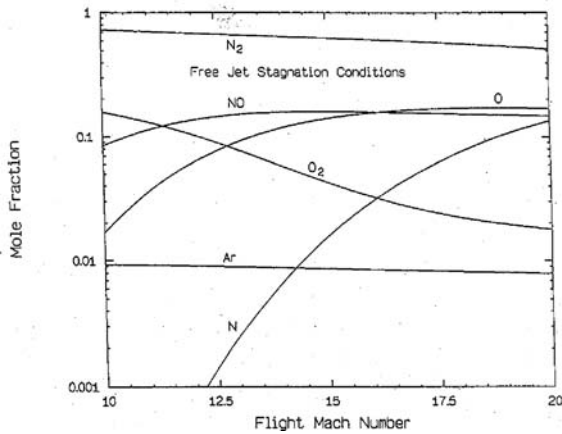


Figure 2.6: Nozzle exit composition for facilities that stagnate test gas. Taken from [11].

A comparison of the energy in the gas composition and static temperature for direct connect testing at a pressure of 0.5 atm and kinetic energy efficiency of the intake of 0.98 was given by Anderson [1] for facilities using stagnation heating and non stagnation methods for producing flows (Figure 2.7). This also shows the amount of error involved in the static temperature for expansion of the gas from a given total pressure and total enthalpy. Therefore, to minimise the error in the test gas, the position of the condition should be towards the bottom center of Figure 2.7. This shows that the stagnation heating has an order of magnitude higher energy error, although the static temperature is comparable between the two different types of facilities.

Smith et al. [13] shows that the facilities capable of supplying the high energy demands of the high total enthalpy conditions required with increasing flight Mach number, have diminishing test times (Figure 2.8). The expansion tube facility can create flows with test

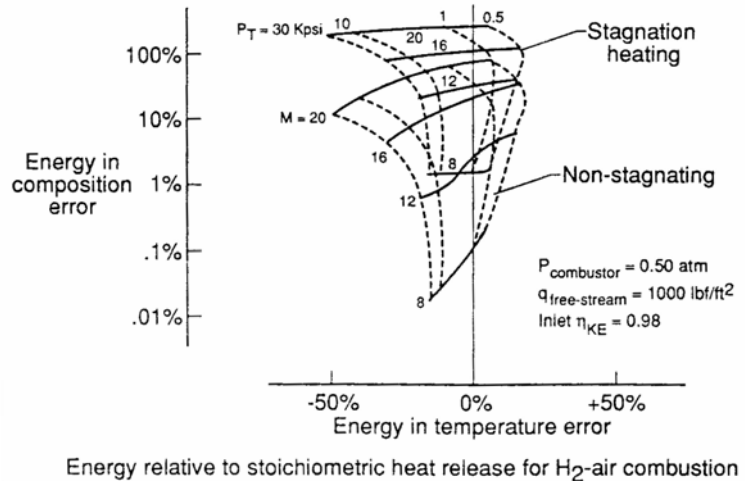


Figure 2.7: Comparison of error in energy due to gas composition and static temperature for stagnation heated vs non-stagnated facilities. Taken from [1]. Freestream Mach number shown in solid lines and total pressures indicated by dashed lines.

times of up to 1 millisecond at low velocities of 3-4 km/s and can produce high enthalpy flows up to superorbital speeds. Although the impulse type facilities can produce the highest speed flows, there is only minimal test time to conduct testing within. This limits the test capabilities in impulse type facilities to that of propulsion testing and flow phenomenon investigations.

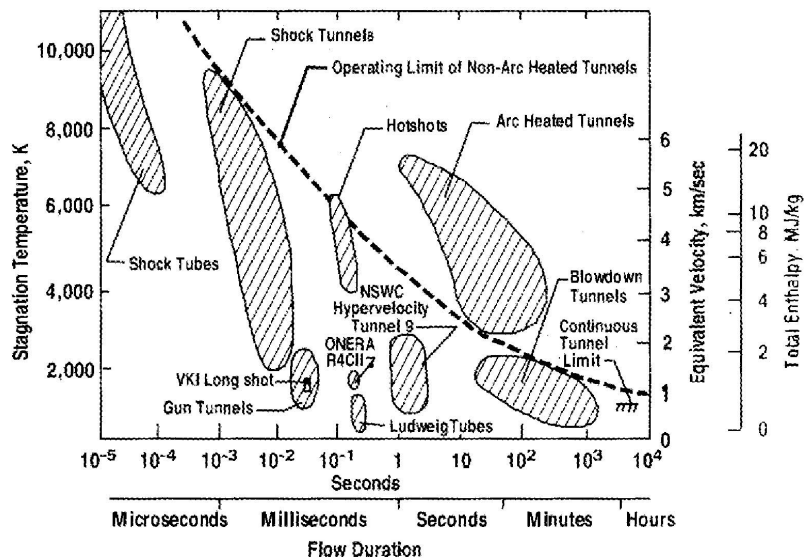


Figure 2.8: Comparison of test time production for various hypersonic ground test facilities. Taken from [13].

Currently, a trade-off between the total pressure, total temperature, gas composition and test times must be made when choosing a facility [10]. A review is presented of the possible hypersonic facilities indicating their advantages and disadvantages in producing suitable flow conditions. As differing facilities in each grouping of type can vary with performance, a brief overview is given for any suitable high Mach number scramjet conditions. A review is also presented of any scramjet testing at higher Mach numbers within each type of facility.

2.2.1 Heated blowdown type facilities

A blowdown facility can produce long duration, near continuous flow at a hypersonic condition by expansion of stored high pressure test gas through a near isentropic nozzle into a low pressure test section. Heat addition to the stagnated gas can increase the total enthalpy capabilities of these facilities to allow replication of expected freestream conditions and to prevent liquefaction from occurring after expansion [10]. Common forms of heating are combustion heating and electric arc heating. Pulsed arc-jet heated facilities are more commonly known as hotshot facilities, but cannot outperform the longer duration arc heated facilities.

Below Mach 8, heated blowdown facilities can be used for long test time scramjet testing. Bushnell states [42], that each heater will produce a particular type of molecular contaminant whose effect on the combustion process is largely unknown. The effect of this contaminant is also suggested to be dependent on the fuel used in supersonic combustion testing. NASA [42] has suggested,

“a series of round robin tests of a single experiment to gauge the effects of contamination. High levels of free stream turbulence can also be an issue in these facilities.”.

This contamination issue has also been noted by Anderson [1] and Lu and Marren [10].

The effects of air dissociation can also be a limitation to the use of heated blowdown facilities due to the extremely high temperatures needed before the stagnated gas is expanded as discussed in the previous section. Fischer et al. [59] studied the effects of nitric oxide on scramjet performance between flight Mach numbers of 6 to 8. It was predicted that although negligible levels of oxygen radicals would remain after recombination in the expansion process and mixing with unheated air, small levels of nitric oxide would remain. Nitric oxide was found both analytically and experimentally to be at a level of 3.6% at the nozzle exit. Performing numerical calculations, it was predicted that this level of nitric oxide would increase the performance of the scramjet by 4% which was considered negligible. This will become a greater issue with higher Mach number simulation conditions, as the nitric oxide level will be further increased.

Total pressure is another limitation of blow down type facilities for use in true propulsion tests at higher Mach numbers. Anderson [1], suggests the use of heated blowdown type facilities are limited to total pressures below 20 MPa, with arc heated facilities having an even lower capability due to nozzle throat cooling problems. Lu and Marren [10] reasoned this limitation of pressure is due to the time need to heat the mass of gas as it moves through the arc. Scramjet testing has been limited to around Mach 8 in this facility, for example the Mach 7 combustor testing of Hyper-X in the NASA AHSTF facilities [31, 13].

The US air force have put forward a new concept to produce flows of up to Mach 15 with true flight conditions and flow cores up to 1 m in diameter [48]. This system (RD-HWT/MARIAH II) has several challenges to overcome to become an operational facility which have to this point, not been satisfactorily solved. Firstly, it is based upon an ultra high air supply pressure of 2 GPa, with a significantly large volume. The next process is the addition of thermal energy to the flow after expansion into the test section (the flow is supersonic) through radiant heat transfer from a laser/electron beam. Requirements to reduce contamination chemical dissociation, heat transfer and erosion problems also requires the addition of a MHD (magnetohydrodynamic) accelerator for velocity augmentation. This project still requires substantial research and development to become an operational hypersonic wind tunnel [48, 11], which may not be achievable in the near-term.

2.2.2 Long duration piston compression facilities

The free piston compression tunnel, otherwise known as a ‘gun tunnel’, was initially developed after World War II with the use of old naval gun barrels [60]. The facility operates by driving a piston down the gun barrel and compressing the gas in front of it. Once the gas is sufficiently compressed, a diaphragm ruptures allowing the gas to be expanded through a nozzle and with tuned piston operation, maintains the stagnation pressure in the order of 10 ms. Total temperature and total pressure limitations of the facility are 2500 K and 20 MPa respectively. Thus, this facility is not often used in scramjet testing.

Another type is the Piston Gasdynamic units such as the PGU-11 at the TSNIIMASH facility in Russia [61]. Similar to a gun tunnel, it compresses the test gas with a piston but differs with the test gas being admitted to an additional chamber for further shock heating. This uses an entropy raising throttling process, which raises the stagnation temperature by a factor of the specific heat ratio in each stage. This gives the advantage that a given temperature ratio can be achieved at a smaller volume ratio and therefore increases the overall test time. The plenum section uses a mechanical valve instead of a diaphragm for starting and additionally stopping the test flow. This facility can produce test times of 1-3 s [11], but is restricted due to high heating loads experienced in the throat of the nozzle. This facility can be used to conduct scramjet tests at approximate free stream flight conditions up to Mach 10. This is accomplished by using a nitrogen test gas with a

pure oxygen fill in the cascade chambers, thus avoiding of the high temperature limit due to thermal loading when oxygen passes through the cascade section. Tests of the standard GASL supersonic combustion model (two dimensional model) with test flows lasting on the order of 25 ms have been conducted [62].

2.2.3 Reflected shock tunnels

The reflected shock tunnel is an extension of the shock tube with the ability to produce hypervelocity flows. The first experimental measurement of positive thrust from a scramjet in a pulse facility was measured by Paull et al. [63] in 1995 in the T4 reflected shock tunnel. This facility increases the test gases total pressure and temperature through 2 shocks (an initial shock followed by a reflected shock off the end of the shock tube). It produces hypervelocity true flight flows by then expanding the stagnated gas through a steady expansion nozzle to the desired condition [16]. The total enthalpy created is proportional to ratios of sound speed and pressure between the test gas and the driver gas. The maximum total pressure is limited by the mechanical strength of either the driver or the shock tube [11]. Also, with increasing total temperatures, nozzle throat erosion must be addressed [64]. The test time in the reflected shock tunnel is usually limited by driver gas contamination with times in the order of milliseconds available for testing. This short test time however becomes quite useful, as inexpensive models can be used and permit the use of large windows for flow visualisation. Some of the larger facilities able to produce flows for higher Mach number scramjets are the T4 facility in Australia, HYPULSE, Calspan LENS I, T5 and AEDC facility in the USA, HEG in Germany and HIEST in Japan.

Like other facilities described previously, the reflected shock tunnel is also restricted in use due to incorrect chemical composition of the freestream. This is caused by chemical dissociation at high temperatures once the flow is stagnated, with rapid expansion not allowing full recombination [11, 1]. This becomes significant in test conditions at Mach 10 and above [11]. Both Anderson [1] and Bakos et al. [65] show for a wide variety of facilities, the predicted oxygen dissociation levels increase rapidly with Mach number from Mach 12 for equivalent scramjet flight conditions. The production of atomic oxygen for this type of facility compared with other stagnating facilities can be minimal up to a higher Mach number of 10. This is due to larger nozzles allowing for more recombination and the production of high total pressures [11]. However, the formation of nitric oxide is of greater importance in reflected shock tunnels [11]. This is due to nitric oxide being quite stable through the expansion process with only minimal reductions from the stagnation region to the nozzle exit. Also the increase in total pressure which suppresses the production of atomic oxygen, enhances the production of NO. As discussed previously, nitric oxide is both a catalyst for ignition and increases the effective heat release from combustion.

The University of Queensland's T4 facility has been used to test several flow phenomenon of supersonic combustion at higher Mach numbers. Morgan and Stalker [66] performed experiments between a simple constant area combustor that was centrally injected to test the difference in performance between hypersonic and supersonic combustion. This testing was performed in the T4 reflected shock tunnel at a stagnation enthalpy between 3-25 MJ/kg, where lower total pressures had to be used due to the limitation in total pressure for the facility. Tests by Bakos et al. [12, 67] were conducted at Mach 17 equivalent, to examine the effect of oxygen dissociation on combustion. It was noted that the combustion efficiency was substantially increased due to the oxygen dissociation levels in the free stream. These are described in more detail in Section 2.2.4. Belanger et al. [68] also tested a similar scramjet combustor at high Mach numbers in the T5 facility, though did not record a large effect due to air dissociation.

More recently at the University of Queensland, a Mach 10 condition has been developed by Abdel-Jawad [69] for scramjet testing at a flight similarity condition. With the implementation of a new steady expansion nozzle and tailoring of the piston dynamics to the maximum extent possible given the structural limitations of the T4 facility, the total pressure and total enthalpy was able to be met for a 30 km altitude condition with a test time of just over 1 ms. However, the oxygen dissociation and nitric oxide levels are yet to be measured for this condition. Tip to tail testing was performed on a 2D scramjet design by Paull [70] in 2005 using this condition as part of the DARPA funded HyCause program. These results however, are yet to be published. Also, three dimensional inlet and combustor designs are being investigated using this condition by Smart [56].

The HIEST facility is currently capable of producing flows that replicate the free stream conditions required at the scramjet combustor entrance up to Mach 15 flight [71, 64]. Limitations of both nozzle throat melting and free stream dissociation for high density flows have been noted as limitations [64]. Recently, testing of a semi-direct Mach 12 flight geometry has been undertaken for both straight and diverging two dimensional geometries. This was undertaken at a free stream Mach number between 9 and 14 with varying enthalpies between 4 and 9 MJ/kg at a constant total enthalpy of 30 MJ/kg [72]. Stable combustion and flow development was achieved with an increase in performance seen over previous tests [71] due to larger pressures at the combustor entrance. Nozzle throat erosion and other tunnel maintenance requirements reduce the utility of such conditions as a routine research tool.

Propulsion testing was conducted in the HYPULSE facility for the HYPER-X scramjet demonstrator [31]. With the two flight tests being conducted at Mach 7 and Mach 10 conditions, flight equivalent conditions were created in the ground test facilities [73]. The Mach 7 condition was able to be approximately replicated with the scramjets intake and combustor combination being tested. However, for a Mach 10 condition, the facility is unable to produce the required total pressure of 24 MPa. To sidestep this problem, the

model was mounted at an angle as to produce a weaker shock from the intake ramp and the freestream conditions are set in order to match the required total enthalpy and Mach number. Therefore, the conditions can be reproduced at the combustor entrance with a reduced static pressure which can be accounted for in the geometrical scaling of the vehicle. The equivalent Mach 10 condition was estimated to have a NO level of 6%, reducing the freestream oxygen level to 19.5%.

Holden [74] has reported that the Calspan facility has been able to produce flows of up to Mach 12 with total pressures of 200 MPa and 6300 K total temperature and test times of up to 8 ms. Little dissociation of oxygen (less than 1%) is reported to be present in the free stream, and was detailed to be caused by the large stagnation pressures of the conditions. This is in contradiction to the estimates of Anderson [1] shown in Figure 2.5a, who projected the level oxygen dissociation would be significantly higher at approximately 10%. It is most likely that high levels of nitric oxide could be present due to the high stagnation pressures (as discussed previously). A generic two dimensional configuration was used for testing in the range between Mach 10 and 12 [75].

Van Wie and Auldt [76] conducted a numerical study of generic Mach 10 inlet with blunted edges, followed by experimentation in the Calspan reflected shock tunnel. The freestream conditions had total pressures up to 32 MPa and total temperatures up to 1883 K with test times of 6-9 ms. This investigated the interaction between the large boundary layer growth on the inlet and its interaction with a single return shock from the cowl to straighten the flow. Although the facility could not produce the equivalent flight total temperatures or test times needed to raise the wall temperatures, it allowed valuable experimental comparison of the flow effects with numerical calculations.

2.2.4 Expansion tubes

The expansion tube is an extension of the shock tube with an intermediate pressure section filled with the test gas, which after being initially shocked, is processed by an unsteady expansion. The principal advantages of an expansion tube over other hypersonic ground test facilities come down to four characteristics [77, 11]. Higher total pressure and total temperature performances can be achieved for a given driver gas pressure and sound speed compared with all other facilities due to the final unsteady expansion process. Also with the absence of a sonic throat, material degradation due to high heat transfer rates is avoided. The test gas is never contained at its total temperature, therefore it reduces problems of chemical dissociation. This is also the case with the total pressure, therefore the tube strength requirements are alleviated. Thus, when this facility is coupled with a high performance driver, it can produce flows with enthalpies high enough for re-entry aerodynamic studies. The current performance capabilities of the larger expansion tube test facilities can be seen in Table 2.2 [8]. This performance however comes at the cost of

test time [11, 16], with extremely long facilities (close to 100 m) required to produce test times larger than one millisecond [78]. Also there can be problems with both flow quality and noise due to acoustic waves and diaphragm effects [16]. A more detailed description of this type of facility can be found in Chapter 3.

Table 2.2: Approximate total pressure capabilities of various expansion tube facilities. Taken from [2].

JX1	300 MPa
HYPULSE	1.6 GPa
X3	8 GPa
X2	10 GPa
RHYFL-X (proposed)	40 GPa

The use of an expansion tube was stated by Leonard and Rose in 1968 as the most viable option for testing of scramjet engines above 30 km altitude and 3 km/s for flight condition duplication with equilibrium gas composition. With the expansion tube still in early development at the time of their paper, Leonard and Rose stated

“Extension to higher performance in terms of test time and flow conditions necessitates large diameter, long tubes, and very large energies.”

The large energy requirements has been solved with the development of both detonation and free piston drivers for coupling with impulse facilities, although small test times still remain a major drawback of this type of facility. The review of hypervelocity facilities for airbreathing engines by Chinitz et al. [11] suggests the expansion tube is the only single stage facility able to produce flows at above Mach 10 with the necessary attributes for propulsive testing. As shown previously, Anderson et al. [31] show a similar result for air dissociation effects on scramjets.

Increases in the test time capabilities of expansion tubes can be made by increasing the total length of the facility, up to limits dictated by viscous effects. However, this is quite expensive and increases in test times are limited due to attenuation of shock and interface to the same speed. Test times can be reduced with the component testing of scramjet combustors in direct connect testing, where the testing of a supersonic combustor can be undertaken using free stream conditions equivalent to those produced by a scramjet inlet at a given flight condition. Therefore, the equivalent combustor condition has a slightly decreased velocity with a large increase in pressure and temperature with an associated drop in Mach number when compared to the flight conditions flow parameters. This gives the advantage of either the model being closer in scale to the flight model or increased test time to establish the flow. Preliminary work by Rizikalla et al. [79] on the HYPULSE facility indicates that test conditions could be produced between Mach 15 to

20 for scramjet combustor tests with test times of approximately $200\ \mu s$ at a constant enthalpy of 15 MJ/kg. These conditions were extended to range between 10 to 20 MJ/kg, with total pressures of up to 400 MPa [80]. It was noted that there could be a limitation of low enthalpy conditions due to transition, though they could be avoided by increasing the Reynolds number.

An increase in both static pressure capability and test time was shown to be possible with the inclusion of a detonation driver to the HYPULSE facility [81, 82] running with a steady expansion nozzle. The design of a full capture nozzle by Chue et. al. [83] led to the creation of a flight enthalpy condition. This was a Mach 15, 47.8 kPa dynamic pressure flight replication condition with a free stream Mach number of 13.5. This is a semi-direct flow condition, requiring part of the intake to be removed to correctly ascertain the properties at the combustor entrance. This had a total enthalpy of 11.5 MJ/kg and was an extension of the Mach 7 and Mach 10 conditions in reflected shock tunnel mode, described in the previous section. A series of flight enthalpy conditions have now been produced between Mach 15 - 21 in the facility with test times of the order of 0.3 ms [84].

The work of Stewart [2, 8] showed the testing capabilities for the currently decommissioned RHYFL facility with a free piston driver in an expansion tube mode could greatly exceed all other current test facilities. With the extremely high total pressure capabilities shown in Figure 2.9, subscale models which are binary scaled using the pressure-length parameter can be used to increase the flow lengths processed by the scramjet model. Stewart indicates the limitation of scramjet testing in reflected shock tunnels is $3\ km/s$ (which is approximately Mach 10 flight) because of contamination of the test gas with driver gas.

The first tests of a scramjet in an expansion tube were performed in the HYPULSE facility as a comparison of performance due to oxygen dissociation effects at high Mach numbers [12, 85, 67, 1, 77, 31]. These compared tests run in the T4 reflected shock tunnel at Mach 17 total enthalpy replication where oxygen dissociation levels were estimated to be 48%. The experiment was an axisymmetric combustor with wall injection. This was followed by further numerical analysis to diagnose some of the flow phenomenon. This study showed that the dissociation effects in a reflected shock tunnel marginally enhances combustion and increases the overall energy yield.

While testing the generic HYPER-X scramjet shape in reflected shock tunnel mode at HYPULSE (as described above), Mach 15 equivalent tests were also performed on the model [73] in the expansion tunnel mode of operation. The condition was matched for total pressure and enthalpy, with a reduction in Mach number to 13.5 and an associated rise in static pressure and temperature. This allows for the correct conditions to be produced at the combustor entrance. Although measurements were not made, it is believed that there was little dissociation of the free stream due to the low static temperatures.

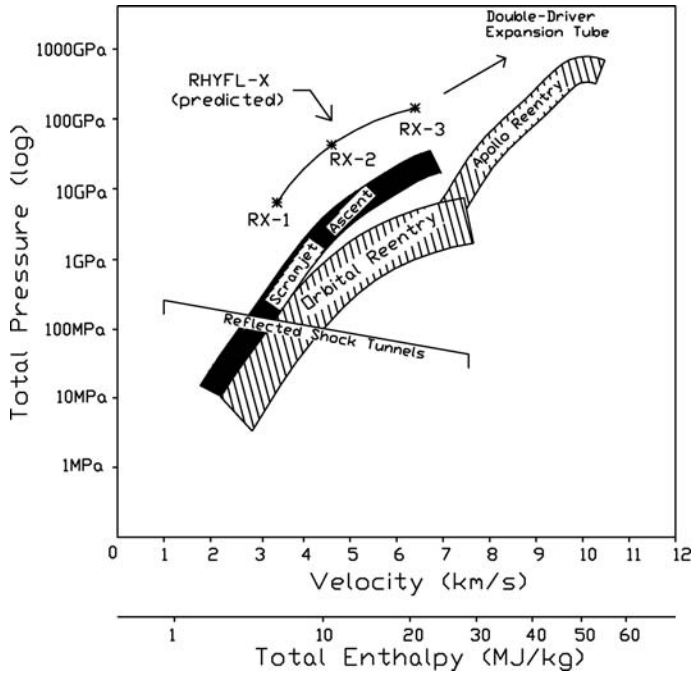


Figure 2.9: Total pressure and total enthalpy predictions for ground test facilities. Adapted from [8].

2.3 Summary

For high supersonic to hypersonic combustion ground testing, it becomes impossible to meet the performance requirements which have been used in the majority of facilities to date for low Mach number scramjet testing. Limitations for high Mach number scramjet propulsive testing are due to the requirement for duplication of most free stream properties, equilibrium chemical composition, full scale model and long test times to establish flow in any recirculation regions. Although some free stream perturbations and transient flow effects are acceptable, these need to be measured and the effects investigated.

An expansion tube/tunnel facility is currently the only viable near term option for integrated propulsive testing at true flight conditions above Mach 10. This is due to the high stagnation temperature requirement which has associated problems of dissociation and molecular contamination. In most hypersonic ground test facilities, the flow reaches these temperatures before expansion, with chemical freezing occurring preventing recombination. This can significantly alter ground test measurements of flow properties due to the freestream air having both errors in composition, static enthalpy and vibrational temperatures compared to flight. Also, as the freestream is already partly dissociated, an increase occurs in the energy yield through the combustor. This is due to the finite rate nature of the combustion reactions over the time scales that exist in a combustor, which initially involve dissociating oxygen. Also, the development of flows with increasing stagnation

pressures is unreachable in most facilities, although they can be reduced with either semi-direct or direct connect testing. These are not an issue in an expansion tube due to the high total pressure and total temperature capabilities, since the flow is never stagnated and therefore minimises losses. This however, comes at the cost of flow test time and flow quality that is capable to be produced in this facility.

Expansion Tube Literature Review

A review is presented of the history and operation of expansion tube/tunnel facilities including their limitations in producing flow for scramjet experiments. Description is also provided of the calculation of transient free stream properties in these facilities.

3.1 History and Development of Expansion Tubes

The expansion tube was first proposed by Resler and Boxsom [86] in 1952 to increase the abilities of the shock tunnel by replacing the steady expansion nozzle with an unsteady expansion through a tube. This creates a flow which has significant increase in the Mach number and Reynolds number while reducing the undesired dissociation and ionization levels. A detailed theoretical investigation on expansion tubes was conducted by Trimpli [87] in 1962. Motivation was due to the required capabilities to perform design experimentation on existing hypersonic wind tunnels insufficient for the upcoming lunar return mission. The analysis was performed for both perfect and real gases at equilibrium under the assumptions of ideal diaphragm rupture, centered expansion fans and continuum flow. A summary of the solution procedure proposed by Trimpli is given in Appendix A for the analytical calculation of the flow properties using a perfect gas. This also considered many design issues that would need to be addressed for a facility to be designed and built. These include tube diameters and lengths and the gas compositions of the driver and acceleration gases. Trimpli identified that the expansion tube would have numerous advantages over a shock tunnel. The velocities attainable were twice those possible in conventional shock tunnels for the same test section density, pressure and initial driver conditions. The degree of dissociation could be kept at a low level through all phases of the thermodynamic cycle and thus it was likely that the gas through the test time would be in equilibrium. Trimpli noted that the acceleration tube would need to have quite a large diameter to ensure that boundary layer growth would not engulf the core flow. The non-idealised secondary diaphragm rupture effects were recognised to be influential in test time as the test gas used would be that next to diaphragm. One major advantage over other hypersonic test facilities was that variations in freestream Mach number could be achieved just by variation in fill conditions without requiring geometrical changes. Further work was recommended into interface mixing and shock wave attenuation.

The first work experimentally was conducted at the NASA Langley Research Center on the Langley pilot facility, by conversion of an existing cold hydrogen driven shock tube [88]. The facility had a constant diameter of 95 mm, and the driver could be pressurised to 10 MPa. Initial results were compared with the theoretical predictions of Trimpf [87], with the differences stated to be moderate and tolerable. The facility could produce flow conditions in the hypervelocity range with test times which could be useful in testing aerothermodynamic models. Although the issues predicted by Trimpf were present, these were not considered to be serious enough when compared with the facilities overall capabilities. Other facilities were produced in the 1960's, though it appears much of the early work was completed at NASA Langley with the construction of a 150 mm diameter facility with an arc heated helium driver [89] named the Langley expansion tube. Many studies were conducted on establishing flow conditions and quantifying flow effects of flow establishment, diaphragm effects and boundary layer growth [90]. These showed that challenges could be overcome to produce repeatable test flows, with core flow and test times long enough to test reentry vehicles. The variety of flow conditions first thought possible was not achieved, with test conditions for each particular test gas only obtainable over a very narrow range. These were due to the limitations of the arc heated driver and other flow issues. A summary was presented of the facility and its operation in 1983 [90] marking the decommissioning of the facility due to financial issues at NASA and because of their disappointing performance envelope. This left a hole in the ground testing abilities with no other active facilities available that could produce hypervelocity flows.

After an eight year absence of expansion tubes, the University of Queensland has seen the development of three facilities in the last 20 years operating with free piston drivers. The first and the smallest of these was the now labelled X1 facility, converted from the TQ shock tube and initially titled the TQ expansion tube being 7.74 m in length [91]. A NASA grant was provided to determine the range of test conditions that could be produced from this facility, as the free piston driver offered an increase in the total enthalpy and total pressure from the arc heated driver in the Langley expansion tube. Experiments led to the establishment of flow conditions with both air and argon test gas with flow velocities in some conditions exceeding 9 km/s [92]. This used the initial work by Paull and Stalker [93], that prescribed to reduce the amount of unsteadiness in the test flow, the sound speed ratio of the expanded driver/test gas interface must be less than approximately 1. Studies were also undertaken by Paull and Stalker [94] and Gourlay [95] into test time prediction and maximisation.

The X2 facility was designed and constructed in 1995 at the University of Queensland using a two stage free piston driver [96]. The facility has been used to investigate several different aerothermal problems [14, 6] and expansion tube operational studies [97, 8]. It has been shown to be able to produce conditions up to 52 MJ/kg and total pressures of 6150 MPa. Recently this facility has been converted to include a single piston driver to

increase operability and performance [3]. It has also been fitted with a contoured steady expansion nozzle for use in tunnel mode to increase test time and core flow. This has been shown to be effective in producing flows for air re-entry conditions [3] and titan aerocapture flight paths [98]. With the introduction of the single piston driver, this has been shown to now produce total enthalpy flows of up to 75 MJ/kg.

The superorbital X3 facility was built using knowledge acquired from the X2 facility, adapting the two stage free piston driver concept to minimise costs [99]. The facility is 65 m in length and has an acceleration tube diameter of 182.6 mm and was designed to be capable of handling primary diaphragm rupture pressures up to 100 MPa [100, 16], with test gas total pressure capabilities up to 8 GPa. Conditions have only been tested up to total enthalpies of 100 MJ/kg. X3 is the largest, high performance expansion tube in the world. It is capable of duplicating super-orbital conditions for planetary re-entry studies. Currently, the facility is undergoing upgrades of both the nozzle and driver [20].

The HYPULSE shock/expansion tube facility at General Applied Science Laboratory (GASL) was recommissioned in 1989 as part of the NASP experiments [101]. This was originally the Langley 150 mm expansion tube, and was reinstated in response to the demand to test high total enthalpy scramjet experiments for the NASA/DARPA NASP program, where the conditions were not obtainable in other facilities. This was a change from other expansion tube facilities where the targeted test conditions were mainly for re-entry aerothermodynamic experiments. A free piston driver was considered on the facility, but it was determined in 1994 that a shock induced driver was more commercially viable and could produce the test conditions of interest [80, 102]. This facility has been used to test numerous scramjet configurations including the combustor for the HYPULSE flight tests [77, 73]. A summary of the facility can be found in [102].

The LENS-X facility at Calspan is an extension of the LENS II reflected shock tunnel [103, 75]. It employs a conventional heated driver, which limits its total pressure and enthalpy capabilities in comparison to UQ and GASL facilities. However, it can more readily avoid noise issues that can be involved with detonation and free piston drivers. The facility has been used for aerothermal testing [104, 105] at medium total enthalpies of 10 MJ/kg.

Japan has a small free piston expansion tube, JX-1, located at the Institute of Fluid Science and Tohoku University [106]. This facility is 13 m in length and has an inner diameter of 50 mm. The facility was built in order to produce the hypervelocity flows needed to test the MUSES-C capsule. Stagnation enthalpies of the order of 40 MJ/kg are possible and diaphragm rupture pressures of 20 MPa have been obtained. The facility has been used to investigate some of the issues with test time evaluation and flow quality associated problems with secondary diaphragm rupture.

Two smaller, low enthalpy expansion tube facilities have been built at Universities in the USA. The first of which is located at Stanford University [107], is a 12 m long, 89 mm

facility, built for investigation into flow diagnostic techniques, like PLIF and PIV of flow effects mainly in scramjet combustion. This facility is capable of producing flow total enthalpies equivalent to flight up to Mach 12, although are not able to match full flight conditions with high static temperatures of the order of 1400 K. This is due to the limitation of 4.24 MPa in the unheated driver gas, which limits the total pressure obtainable for the high density conditions. The University of Illinois have a similar unheated driven expansion tube with a length of 9.14 m and tube diameter of 152 mm [108]. The limitation in driver pressure is approximately 6 MPa, with preferred diaphragm rupturing occurring at 4.3 MPa. This is hoped to be used to study flow phenomenon in the hypervelocity range, where chemical non-equilibrium effects become dominant.

RHYFL was to be the worlds largest reflected shock tunnel being 96 m in length, but was never completed due to the funding cut for the NASP program at NASA and has been in storage since. The conversion of the decommissioned RHYFL facility to a free piston driven expansion tube was first proposed by Chinitz et al. [11] in 1994 for use in airbreathing propulsion testing. Further work has been completed by Stewart [8] suggesting that the total pressure limit for the facility is 40 GPa. Unfortunately though, this facility is still inactive and there are currently no plans to commission it.

3.2 Expansion Tube Operation

An expansion tube is a type of impulse facility, which can produce high speed flows up to super-orbital speeds [100] for short durations. Limitations of total enthalpy and total pressure production in other impulse facilities and other undesirable flow attributes discussed previously made the expansion tube a promising option. Energy is added in this facility to the test gas partly through a shock wave and then by accelerating the flow using an unsteady expansion. This alteration from shock tubes and reflected shock tunnels enables testing at higher enthalpies than in other facility types where flow dissociation occurs since in those all of the energy is transmitted to the flow with shock waves. The unsteady expansion process has an additional benefit of increasing both the total enthalpy and total pressure of the flow. This comes at the cost of a reduced test time produced compared with other hypersonic facilities.

The configuration for a free piston driven expansion tube can be seen in Figure 3.1. The entire facility is the same as a shock tunnel up to the secondary diaphragm, where the steady expansion nozzle is replaced by a constant area tube therefore allowing the formation of an unsteady expansion. From an initial compressed driver slug (region 4), the primary diaphragm is removed usually through rupture by increasing the pressure in the driver gas. A pressure differential across the interface between the test gas in the shock tube (region 1) and driver gas sends a shock wave down the shock tube. This shock

speed is increased if a temperature differential¹ is also present. The shock compressed test gas (region 2) and expanded driver gas (region 3) have the same static pressure and velocity. The secondary diaphragm is made of a *light* (low mass) material, so that as the shock wave reaches it, rupturing occurs with minimal flow disturbances. Like at the primary diaphragm, a pressure and temperature differential causes a shock wave to propagate down the acceleration tube. This secondary shock has a much higher shock speed than the primary shock. Once the shock compressed test gas undergoes an unsteady expansion process (region 7), it is used at the acceleration tube exit after the passing of the acceleration gas (region 6).

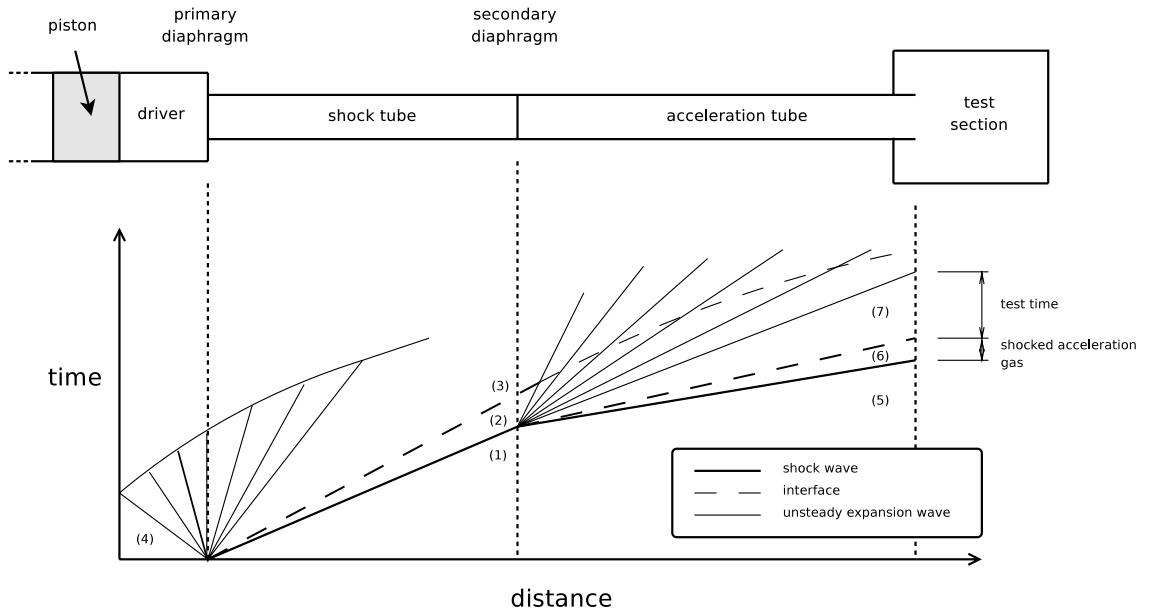


Figure 3.1: Idealised distance-time diagram of a free piston driven expansion tube.

Inspecting the increment in velocity change (dU) for a given reduction in static enthalpy (dh) for a steady expansion process (Equation 3.1) compared with an unsteady expansion process (Equation 3.2) highlights how an expansion tube can attain higher velocity flows [87]. The incremental velocity change in an unsteady expansion is larger than that of a steady expansion by a factor equal to the Mach number. This allows for larger velocity increases for the same drop in static enthalpy across the expansion process or for a lower initial temperature to be used before the unsteady expansion to achieve the same velocity and temperature after expansion. With the lower temperature realised in the shocked test gas, less dissociation will be seen relative to that of a facility that uses a stagnated gas with a steady expansion process.

¹This is dependent on whether the driver gas is heated.

$$dU = - \left(\frac{dh}{U} \right) \quad \text{steady expansion} \quad (3.1)$$

$$dU = - \left(\frac{dh}{a} \right) = - \left(M \frac{dh}{U} \right) \quad \text{unsteady expansion} \quad (3.2)$$

The change in total enthalpy is given by the change in static enthalpy with the addition of the velocity multiplied by the change in velocity ($dH = dh + UdU$). Therefore, no change in total enthalpy will be seen through a steady expansion with the inclusion of the velocity change from Equation 3.1. As total pressure can be related to the total temperature from an initial static pressure and temperature for an isentropic process (Equation 3.3), there will also be no change in total pressure through a steady expansion ($dT_0 = dH/c_p = 0$). This is in contrast to an unsteady expansion, where an increase is seen in the total enthalpy, given by Equation 3.4. This will also see an increase in the total pressure for this process. Both the total enthalpy and total pressure can be seen to dramatically increase through the unsteady process at high Mach numbers, for a much smaller drop in the static enthalpy needed to accelerate the gas to the desired velocity when compared with a steady expansion.

$$\frac{p_0}{p} = - \left(\frac{T_0}{T} \right)^{\frac{\gamma}{\gamma-1}} \quad (3.3)$$

$$dH = - (M - 1) dh \quad (3.4)$$

The mechanisms behind the multiplication of the total enthalpy and total pressure in an expansion tube were presented clearly by Morgan [16] in a review of expansion tubes of which a summary is presented here. Figure 3.2 shows a Lagrangian slug of test gas convecting through an unsteady expansion. The front of the slug does work on the gas downstream as it passes through the unsteady expansion. The work exerted is proportional to the pressure, distance integral ($W = \int p A dx$) through the unsteady process. As the rear of the slug reaches the unsteady expansion fan, the pressure drop will remain the same but the distance traversed increases due to growth in the expansion fan. Therefore the work exerted onto the slug by the upstream gas is larger than that at the leading face (downstream face). This means a net gain of total enthalpy is attained in the expanded gas and associated increase in total pressure.

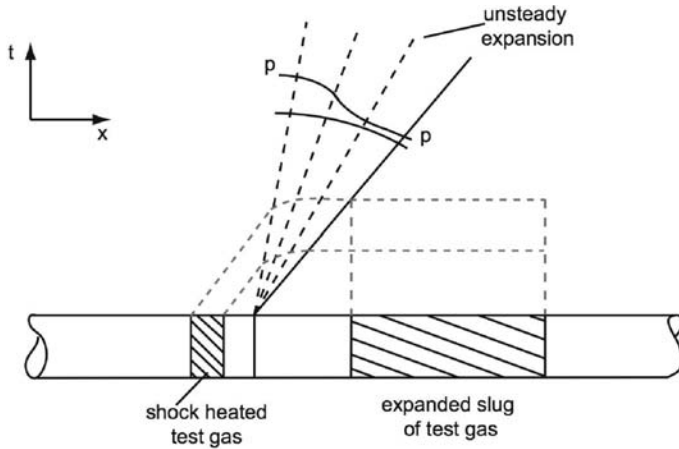


Figure 3.2: Schematic of energy addition process across an unsteady expansion (flow left to right). Taken from [14].

3.2.1 Flow properties in an expansion tube

For an ideal, inviscid expansion tube, the time between acceleration gas interface and secondary shock would increase linearly with distance down the tube. However, similar to shock tubes, the time (or distance) between the shock wave and interface attenuates due to mass entrainment into the boundary layer [15, 109]. This occurs with the shock decelerating and the interface accelerating causing a velocity gradient across the acceleration slug (Figure 3.3). Just behind the shock, the gas velocity is less than the shock speed. The gas in the freestream will begin to accelerate as mass is lost to the boundary layer to ensure that the conservation of mass and momentum is met across the system. With significantly lower pressures and densities in the acceleration tube, the boundary layer can be assumed to be laminar in the acceleration slug (region 6 in Figure 3.1). These effects become more pronounced for low initial pressures and large length to diameter ratios. In an expansion tube both these occur, with acceleration fill pressures between 1 - 100 Pa and long acceleration tube lengths to maximise test times. Mirels' prediction of shock/interface attenuation has been used successfully to predict distances between the shock and interface for various expansion tube conditions [110, 108, 18].

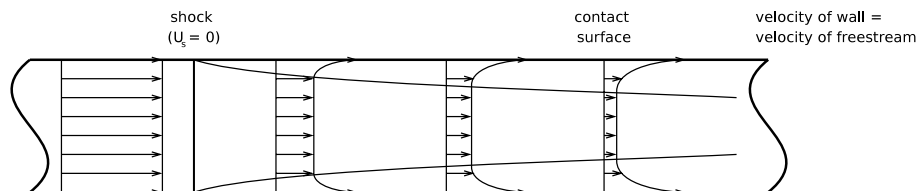


Figure 3.3: Flow between shock and contact surface in a shock steady co-ordinate system, $U_s = 0$ (flow right to left in the lab fixed frame of reference). Adapted from [15].

The test time in an ideal expansion tube is defined as the relatively steady period between the passing of the acceleration gas interface and the leading edge of the unsteady expansion fan centered at the secondary diaphragm (Figure 3.1). This can be cut short due to a $U + a$ wave from the driver or reflection of the $U - a$ wave from the test gas driver gas interface. The maximum test time in this case is upstream at the intersection of the $U + a$ wave and the leading edge of the $U - a$ wave. Paull and Stalker [94] state that estimations of the test times can be made using perfect gas theory (i.e. constant wave speeds) as long as the boundary layer mass entrainment effects are accounted for. They also note that pressure scaling will effect the test time due to boundary layer entrainment although will be minimal on moderate scaling. Other flow effects that can limit the test times are boundary layer transition [111], turbulent mixing at the interface and Rayleigh-Taylor instabilities at the driver test gas interfaces [95].

The core flow in an expansion tube is reduced from the inner diameter of the acceleration tube due to the boundary layer. At low pressures, which is usual for most expansion tube conditions, the boundary layer can grow to be quite large engulfing a large proportion of the tube. Thus it is necessary to measure the extent of this growth. Boundary layer transition has been shown to dramatically increase the size of the boundary layer quite rapidly. Therefore, it is advisable to either avoid transition by having low Reynolds numbers or ensure that this occurs close to the contact surface [24, 23, 41]. A further review of this phenomenon can be found in Section 4.5.1. It is also necessary to include the effects of the Mach cone developed at the acceleration tube exit from free jet expansion into the low pressure test section, in the same way as a hypersonic nozzle exit flow must be analysed. This is important for test models that are either a reasonable distance from the exit or use the gas at a significant distance from its leading edge such as a scramjet inlet (Figure 3.4). Thus for scramjet inlets, an “alligator mouth” extension piece might be required to increase the distance for the Mach cone to process the core flow [112].

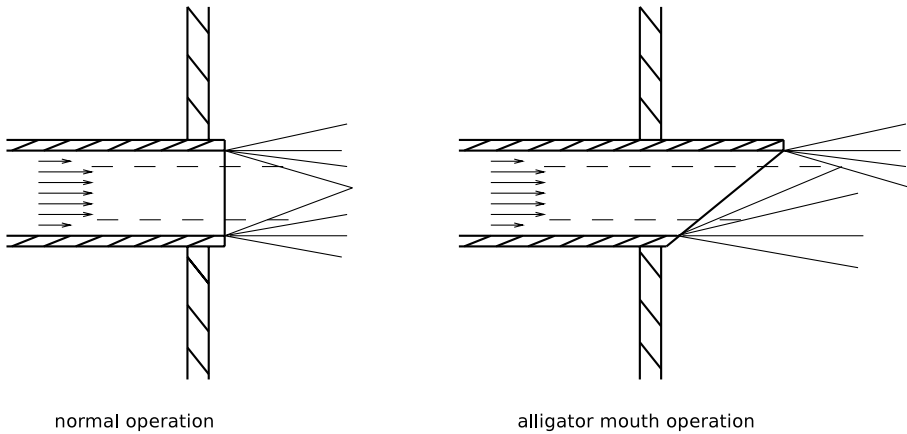


Figure 3.4: Schematic of alligator mouth extension for large inlets.

The interaction of the primary shock wave and the secondary diaphragm can cause adverse flow quality effects due to their finite rupture time and inertia [23, 113, 114]. This results in an initially strong reflected shock, but attenuates fast to become reasonably weak shock and is transmitted back upstream. Roberts et al [115] showed that wave reflections related to the finite holding time of the diaphragm causes early corruption of the test gas flow. Alleviation of any flow disturbances and reduction of opening time has been shown experimentally by using as thin as possible diaphragm² [115, 114]. Visualisation of the diaphragm rupturing process [116, 117] has shown there are strong three dimensional effects associated with the rupture of thick diaphragms having large interactions. Due to this reflected shock, dissociation of the test gas may remain frozen in the subsequent unsteady expansion. Bakos et al [52] showed using analytical and numerical schemes that for sub orbital air conditions, the effects on chemical recombination can be calculated using diaphragm properties and reflected shock conditions.

Test flow instabilities caused by acoustic waves has limited the available test conditions from the early experiments at Langley [118]. These acoustic waves are generated in the primary diaphragm rupturing process and are transmitted through the test gas/driver gas interface [119]. This noise source is also present in other types of shock tubes. However, analysis conducted by Paull and Stalker [93] showed that when passing through an unsteady expansion, the acoustic waves focused into finite frequencies of very large amplitude. This prevented the formation of a steady and useable core of test gas. A mechanism was identified by Paull and Stalker [93] to eliminate instabilities in the test gas by tailoring the sound speed ratio across the driver gas/test gas interface. If the wavelength of the acoustic waves is given by $2\pi a(\omega\beta)^{-1}$, an increase of sound speed across this interface ($a_2 > a_3$) the property β (given by Equation 3.5) can become imaginary and therefore cannot exist in the test gas. With waves of the lower possible frequencies holding the most energy, the intensity of the acoustic waves is greatly reduced in the test gas with this sound speed buffering. Although there is no clear cut off point, Morgan [16] suggests that the ratio of sound speed $\frac{a_2}{a_3}$ should be larger than 1.25. It is also noted that this may also be dependent on the tube diameter.

$$\beta = \sqrt{1 - \left(\frac{3.83a}{\omega r}\right)^2} \quad (3.5)$$

3.2.2 Driver options

The purpose of the driver is to supply a high pressure, high sound speed slug of gas for driving a shock down the shock tube [97]. There are many driver options to investigate, with tradeoffs between performance, operationability and cost. Choices for drivers can

²A given thickness is required to hold the pressure differential between the shock and acceleration tube fill pressures.

be based not only in terms of performance and flow quality but also the technical risk, cost and safety and operational issues [102]. Therefore this has spawned a wide variety of differing drivers on impulse facilities. As defined by Bakos and Erdos [120] in the review of driver options for the HYPULSE facility, the options for drivers are light gases, electrically heated light gases, combustion heated light gases and compressively heated gases.

A light gas driver has been used in the original Langley expansion tube [90] and more recently in the smaller US facilities [107, 108]. Gases of choice were either hydrogen or helium due to their low molecular weight. Although higher performance can be made by using a hydrogen driver (higher sound speed), problems raised due to safety concerns of detonation has limited its use and also limited performance benefits due to dissociation. A non-heated driver has the advantage of being quite simple, but performance is limited by achievable sound speed. An externally heated driver can increase the sound speed of the driver gas, allowing for higher performance. Compared with non heated drivers, a heated driver will allow the same shock speed at a lower driver pressure. This has been used in reflected shock tunnel facilities like Calspan [75] to have long test times with good repeatability and quality of flow.

A combustion driver can be an effective way of increasing the temperature of the driver gas, via the heat release from combustion of gases like hydrogen and oxygen. However, even using the lightest fuel (hydrogen), the combustion products (H_2O) are much heavier than compressed He, which can be used in other drivers. A detonation driver is also limited in pressure, as deflagrative combustion proves hard to establish at high pressures [121]. An increase in the performance can be obtained by using a detonation wave to initiate combustion [122]. The arrangements for initiating the detonation wave and the direction of travel are critical issues. Two common detonation modes are used; forwards or backward propagating [122]. Forward propagating detonation is accompanied by a following expansion wave which leads to severe shock attenuation, although current work by Liu et al. [123] is investigating mechanisms to alleviate this. Backward propagating detonation drivers are less effective but can produce steadier flow properties. This type of driver is capable of pressures in the order of 150 MPa with relatively short lengths required (in the order of 3 to 6 m for larger facilities). This driver concept offers reasonable performance, with a moderate initial cost. A thorough review of detonation drivers is presented by Olivier et al. [124].

The free piston driver has the ability to produce high total enthalpy and pressure gases and is one of the highest performing driver options. The free piston compression process was first introduced by Stalker [125] for use in driving shock tubes. The process of the compression can be seen in Figure 4.4 for a dual piston arrangement, whereby high pressure air is used to drive a piston down the driver compressing the light gas in front of it until the diaphragm rupture pressure is reached. In this process, the stored energy of the compressed reservoir gas is transferred to the piston in the form of kinetic energy and

then back to the light driver gas in the form of internal energy. With its use in reflected shock tunnels, it has the added performance of being able to maintain the driver pressure by further compression in a tailored or overtailored case. In comparison with the use of free piston drivers for reflected shock tunnels, the hold time for the pressure is not as critical [16]. Free piston drivers are currently in operation on the UQ X-series and the Japanese expansion tube facility [106].

Compound drivers offer the highest performance of all driver concepts, especially when creating large enthalpy flows. Often called a double-diaphragm arrangement [113, 97], this driver is coupled with one of the before mentioned drivers, creating a shock wave through a driver gas in a secondary driver section. For high values of flow speed behind the secondary shock with a given starting sound speed for the primary driver³, the compound driver can obtain larger static pressure ratios between the driver gas and test gas. Thus, this driver arrangement has been found useful in obtaining high speeds (above ~ 8 km/s) and high static pressure conditions (approximately above 2 kPa). This has been shown graphically by Morgan (Figure 3.5) for a helium/helium arrangement in comparison with a single piston (helium) and combustion (hydrogen, oxygen helium) drivers. The pressure recovery across the process is substantially higher for a given *driver equivalent flow Mach number* ($M_7^* = \frac{U_7}{a_4}$).

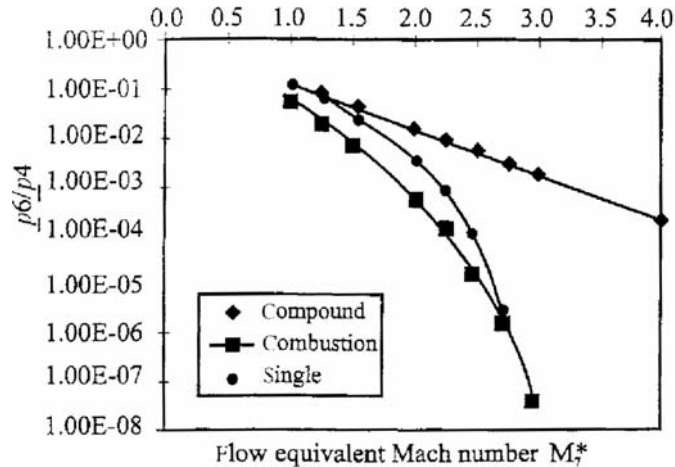


Figure 3.5: Performance of different expansion tube drivers. Taken from [16]. M_7^* is the driver equivalent flow Mach number and p_6/p_4 is the ratio of driver pressure at primary diaphragm rupture to shocked acceleration gas pressure.

3.3 Expansion Tunnel Operation

An expansion tunnel was first theoretically studied by Trimpli and Callis [126] in 1965 and consists of an expansion tube with a steady expansion nozzle placed at the acceleration

³This can be defined as the flow equivalent Mach number.

tube exit. This concept was explored in order to increase the test time and core flow size while solving operational issues like the high vacuum levels in the acceleration tube and secondary diaphragm rupturing. This area change alters the wave structure to include a steady expansion at the exit of the acceleration tube as seen in Figure 3.6. This takes the already shocked acceleration gas and expanded test gas and expands it through an area change increasing the Mach number and velocity of the flow while reducing the density and temperature. This area change reduces the total enthalpy, and also a small total pressure loss, decreasing the ' ρL ' testing capabilities in proportion to diameter, but increases the available core flow of the facility. This can be compensated for in an expansion tube, which can produce extremely high levels of these flow quantities as discussed in Section 3.2.

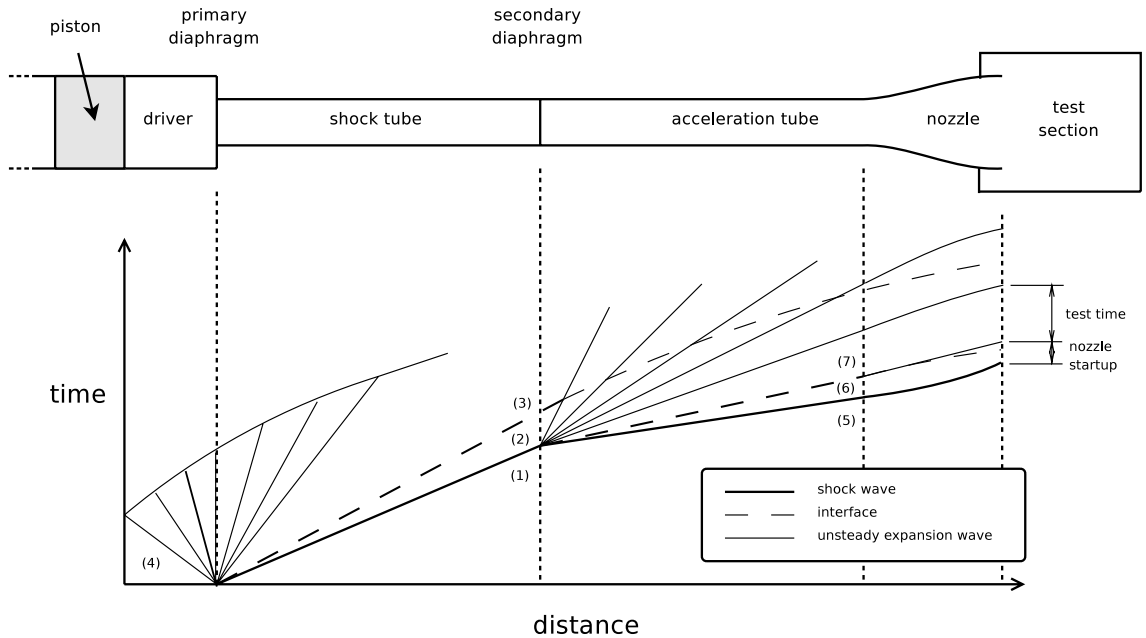


Figure 3.6: Ideal distance-time diagram of an expansion tunnel.

With the test time available in expansion tubes being the time between the unsteady expansion and the interface [95], there will be a test time increase over a non tunnel condition due to both the decrease in velocity and the increase in sound speed needed in the test gas before expansion. Even without this, with the addition of a nozzle to a known expansion tube condition, the test time is seen to increase with the addition of a nozzle, contrary to intuition [8, 3]. Assuming constant wave speeds, the test time in an expansion tube is given in Equation 3.6 for variation in length, x (in metres). For a given inlet Mach number into the nozzle to achieve a desired condition and assuming isentropic expansion, flow properties can be calculated for the expanded test gas. Doing this for conditions at higher Mach numbers along Billig's proposed scramjet flight trajectory [127], seen in Table 3.1, the acceleration tube test time can be calculated for these conditions before

entering the nozzle (Figure 3.7). This shows that a significant increase in available test flow time can be made by using a steady expansion nozzle with a decreasing Mach number.

$$t_{test} = \frac{x}{U_7 - a_7} - \frac{x}{U_7} = \frac{xa_7}{U_7^2 - U_7 a_7} \quad (3.6)$$

Table 3.1: Free stream properties of a scramjet flight trajectory for test time calculations.

Mach Number	Velocity [m/s]	Altitude [km]	Temperature [K]	Sound Speed [m/s]
10	3016.7	30	226.5	301.7
12	3659.8	32	231.5	305.0
14	4320.2	34	237.5	308.6

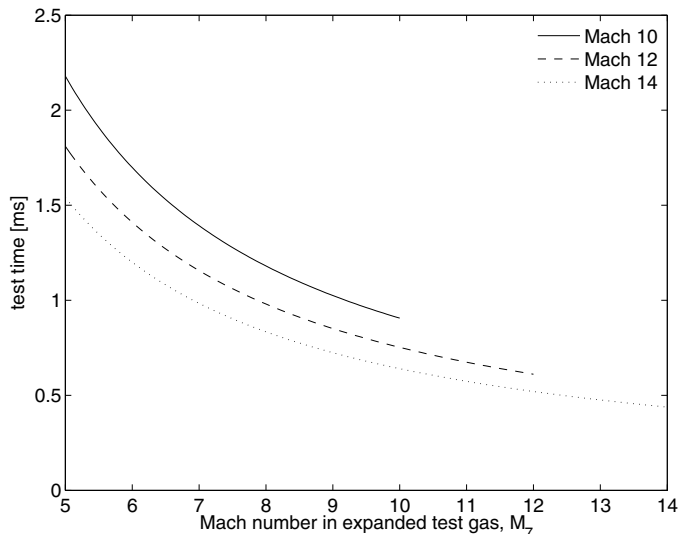


Figure 3.7: Test time available at end of acceleration tube for variation in nozzle inlet Mach number.

The inlet Mach number for the nozzle may be limited by interruption of reflected $U + a$ waves off the piston as the total time taken from the primary diaphragm rupture will increase by reducing the nozzle inlet Mach number. For a free piston driver with an area change, the Mach number of the driver gas at the throat and through the steady expansion will be quite low (~ 0.05 typically). This means for relatively low piston speeds ($\sim 100 - 200$ m/s) the $U - a$ wave created at primary diaphragm rupture can be cancelled to the first order without $U + a$ reflection. This enables the short slug of gas to act as a much longer driver tube. However, the piston deceleration will ensure that driver $U + a$ waves are eventually created, but for most free piston expansion tube conditions will not be the test flow termination event. The nozzle start up process and the increased speed of

the unsteady expansion will decrease the available test time if the acceleration slug is quite small [126]. At the relatively low velocity, low temperature conditions required to match scramjet flight trajectories, the acceleration slugs are quite long. Also, an extension to the test time may be possible due to the continuation of steady flow after the arrival of the unsteady expansion, qualitatively discussed by Scott [3]. This phenomenon was postulated to occur as the unsteady expansion reaches the inlet of the nozzle, the boundary layer will grow at the start of the nozzle a lot quicker than at the exit. Since the boundary layer at the end will take significantly longer to grow, the area ratio appears to increase sufficiently to offset the reduction in Mach number (and increase in density) of the underexpanded test gas.

As the flow is not stagnated as in the case of a reflected shock tunnel, the boundary layer is expanded through the nozzle, growing with the reduced pressure and possibly separating. Therefore, the area ratio of expansion is reduced from the geometrical nozzle to the viscous nozzle. Initial work with the Langley expansion tunnel, looked at using conical nozzles with an embedded nozzle inside with a smaller inlet diameter, termed as a '*skimmer nozzle*' [128, 118]. This provided a way of removing the boundary layer while keeping the flow uniform. These proved to be unworkable due to annular shocks created at the leading edge and initial expansion. The conical nozzle also provided further non-uniformities with no wave cancellation, divergent flow and had a lower Reynolds number than desirable.

Full capture nozzles require a design that accounts for the intital boundary layer at inlet and growth within the nozzle. More recently these have been designed to try to eliminate any disturbances with wave cancellation due to the geometrical profile. These have been designed and tested (numerically and/or experimentally) in the X2 facility [3], LENS facility [104], HYPULSE facility [121, 129] and proposed refurbishment of the RHYFL reflected shock tunnel [2]. The X2 nozzle appears to have the greatest success at achieving a desirable flow, with it design using a space marching parabolised Navier-Stokes solver, optimising the nozzle for minimal flow disturbances and divergence.

3.4 Establishment of free stream conditions in expansion tube/tunnel facilities

The accurate definition of free stream properties in any flow facility is vital to the experiment. This need is more acute in impulse type facilities, with very few experimental measurements of the free stream being able to be measured directly, due to the short flow durations and harsh flow environments. Here, numerical tools are relied upon to describe the full set of flow properties.

The simplest of these tools are inviscid post processing tools, such as the University of Queensland *JUMP* code [18, 14]. This code relies upon experimental measurements of static pressures and shock speeds to undertake shock and unsteady expansion calculations to describe the flow in each *steady* flow region of the test and acceleration gases, as shown in Figure 3.1. With this program, the chemical state of the gas can be varied between equilibrium and frozen states in the unsteady expansion to best fit the experimental data. This is critical for calculating the resulting flow conditions, as the total enthalpy multiplication process is directly dependent on the thermal component of static enthalpy. This is fundamentally different to the process of calculating conditions at the exit of a steady flow nozzle. In this situation, the errors in the chemical conversion rate will affect the calculated flow properties, but the total enthalpy will be correct. The balance between thermal and chemical enthalpy will just be incorrect. If the chemical enthalpy is not described correctly through the unsteady expansion process, a major error can occur.

Although this representation of the flow is sufficient to provide estimates of changes in flow conditions, it ignores several non-ideal processes and also the two dimensional nature of the flow, and is not truly predictive. It also, this ignores the transient behaviour of the flow, giving only a guide to conditions at one instant during the flow. Calculations using *JUMP* have been shown to be correct to the first order [130], but differences of 20% can occur for time averaged flow properties compared to more detailed two dimensional numerical calculations.

Full numerical simulations of the transient flow in the expansion tube can, of course, provide a closer representation of the flow than those based on quasi-steady flow. This approach allows for the prediction of the free stream conditions rather than requiring experimental measurements. However, these calculations are typically computationally expensive. Reasons for the computational expense include:

- the transient nature of the calculations compounds grid resolution issues, as the placement of small cells is required at various position throughout the calculation;
- the small axial cell sizes required to resolve shocks and gas interfaces while having enormous overall length scales of the facilities (usually 6 orders of magnitude larger);
- the small axial cell sizes required close to secondary diaphragm to accurately capture the Riemann problem of large pressure and temperature differences [131];
- the small radial grid sizing required near the tube wall to accurately resolve the boundary layer [131];
- the large difference in axial and radial distances leading to large aspect-ratio in cells [131];

- the need to model the non equilibrium thermochemistry of the expanded test gas [131, 132], where the gas is near equilibrium in the shock tube causing a high rate of reaction, thus decreasing the time step;
- the resolution of chemistry through an unsteady expansion to resolve total enthalpy multiplication;
- for free piston driven facilities, the long duration compression process [3];

Also, the numerical simulation of expansion tunnel flows using structured grids [3], require high radial and axial grid resolution to resolve the flow through the steady expansion with the increasing radius approaching the test section.

In order to reduce the size of the calculation, there have been a variety of approaches to simplify the problem. These include:

- simulating the flow one dimensionally [96, 106, 2, 26], using analytical correlations to deal with friction and heat transfer, and mass loss to the boundary layer [133];
- modelling using steady inflow conditions from shock calculations part of the way down the shock tube [131, 103];
- hybrid calculations, which use transient inflow conditions from one dimensional simulations of the driver, shock tube and secondary diaphragm and are placed uniformly across the tube upstream of the secondary diaphragm [8, 130, 26, 3, 17];
- the assumption of equilibrium, frozen or perfect gas chemistry [130, 26, 131];

Each of these simplifications have implications upon the flow field which have to be accepted to enable large scale simulations of the expansion tube flow.

Jacobs [132] made the first attempt at undertaking an axisymmetric simulation of the full NASA Langley expansion tube [132]. The simulation was limited to laminar, perfect gas flow to keep the study manageable. Although most of the bulk flow features computed were consistent with experimental measurements, shock speeds and pressure levels only roughly matched the experimental values. The largest discrepancies between the calculations and experiment were seen for a condition where experimentalists had attributed boundary layer transition to the cause of disruptive free stream flow effects. To obtain better results, Jacobs pointed to the immediate need to perform simulations with the inclusion of non-ideal thermal and chemistry effects, non-ideal diaphragm rupture dynamics, and a turbulent boundary layer model.

The next step in complexity of modelling was undertaken by Wilson [131], where the inclusion of turbulence and finite rate chemistry was implemented into an axisymmetric calculation of the HYPULSE facility. This study simplified the geometry by using the calculated post shock conditions uniformly across the inflow boundary at the mid point

of the shock tube (i.e. steady inflow). Even with this, the simulation was still computationally limited to a nitrogen test gas and was grid dependent (a moving grid used). Also, the transition of the boundary layer to turbulent was set using a fixed distance from the interface, requiring knowledge from experimental measurements. The numerical results captured the flow property levels and first order boundary layer effects compared well to experimental measurements. For a condition where boundary layer transition occurred during the test time, the simulation captured the bulk of the properties, which gave further confidence in the calculations. Wilson again pointed to the importance of including diaphragm rupture mechanics to better resolve key flow effects.

With the flow produced at the expansion tube exit being highly dependent on the secondary diaphragm rupture process [131, 132], mathematical models have been introduced into one dimensional calculations. However, it is difficult to include the intrusive effects of the diaphragms in a multi-dimensional models. Stewart et al. [2] showed that the introduction of a hold time of $5 \mu\text{s}$ onto the secondary diaphragm in the one dimensional simulation of the X2 facility, decreased the pitot pressure, and gave worse agreement with experimental data. An inertial diaphragm model, such as that explored recently by Potter et al [17] in the one dimensional code, *L1d*, can give a better representation of the flow field by comparing the flow produced further downstream in the acceleration tube. These have been used to capture the primary entropy raising processes which effect the flow. Use of these models in hybrid simulations of the University of Queensland facilities with various gas model assumptions, has been used to improve the agreement between the simulations and the experimental measurements [8, 130, 3, 17]. However, routine experimental measurements close to the secondary diaphragm (like those discussed in Section 3.2.1) are needed to validate the mathematical model chosen, such as those discussed in Section 3.2.1). Currently, only ideal diaphragm rupture has been dealt with in two dimensional axisymmetric simulations [132, 131, 103].

The most advanced simulation to date was completed by Potter et al. [17], on a 25 MJ/kg Mars ($\text{CO}_2\text{-N}_2$) entry condition in X2 in tunnel mode, using the hybrid approach with the University of Queensland codes. The advances made in this work on previous simulations included the use of a two temperature model with finite rate chemistry, whilst simulating the entire facility. Also, the entire dump tank was modelled, in an attempt to capture the axial variations of flow properties from the expansion tunnel nozzle. Even with use of 63 processors, this study could not claim full grid convergence with the finest grid being 43x5155 cells (1 mm squares on average). The simulation results showed very similar transient trends as the experimental static pressure data, though the pitot pressure whilst exhibiting a similar transient behaviour, was offset by up to 20% (Figure 3.8). However, this can be seen to be within the variation of the experimental measurements over the test time. Due to the loss of grid resolution through the steady

expansion nozzle, extra noise can be seen at the flow exit, with the worst being seen along the centreline, since grid clustering is used towards the wall.

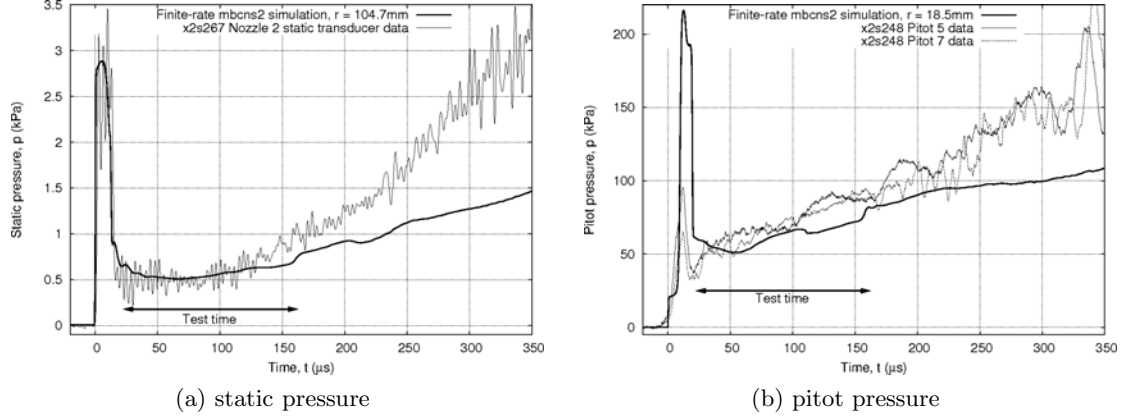


Figure 3.8: Comparison of experimental and hybrid calculations of flow at nozzle exit for a 25 MJ/kg Mars condition in the X2 expansion tunnel. Taken from [17]

As noted by Scott [3], a comparison of experimental and numerical data in expansion tube/tunnel facilities can become difficult as currently both sets of data suffer from significant levels of noise. In numerically modelling the flow, it becomes unclear how much of this noise is produced from the unsteady growth of the boundary layers, the upstream originating waves, and amplification of static enthalpy fluctuations through the unsteady expansion process, or as computed due to unresolved grids, modelling deficiencies in geometry, diaphragm rupture, gas state and turbulence. However, since the experimental data generally has an order of magnitude larger noise, numerical modelling of expansion tubes endeavours to match all experimental measurements as closely as possible and capture all transient flow effects to the first order

3.5 Summary

A review has been presented on the important flow processes, history, development and operation of expansion tube facilities. The expansion tube can create high velocity flows with large total pressures and total enthalpies. This is due to the use of an unsteady expansion instead of the common steady expansion in most hypersonic ground test facilities. Issues like secondary diaphragm mass entrainment, boundary layer transition and acoustic noise must be minimised to reduce the perturbations seen in the test flow. Following from the pioneering work of Trimpi, developments were made by NASA to establish the constraints on operation. More recently facilities like the University of Queensland's X3 facility have been able to produce conditions up to the superorbital regime. Expansion tubes can be operated with a variety of driver arrangements from low noise, low performance conventional heated drivers to moderate noise, high performance detonation and

free piston drivers. With the addition of a nozzle, the expansion tunnel can increase both the test time and core flow at the expense of pL component, which drops in proportion to the diameter in hypersonic flow. However the large total pressure capability of expansion tube facilities, allows high levels of pressure-length to be maintained. Due to lack of experimental measurements, definition of most free stream properties in expansion tube/tunnel facilities require a transient simulation of the whole facility to be undertaken. Although computationally expensive, these have been shown to give a reasonably time accurate representation of the flow.

Condition Development in the X3 Expansion Tube

Investigations were undertaken in the X3 facility to determine if a flow condition could be produced that fully replicated the flow properties that would be seen during a transatmospheric ascent of a scramjet. The targetted condition was at the crossover point between the capabilities of reflected shock tunnels and expansion tube facilities. A large drop was measured in the pitot pressure radially across the facility during the predicted test period. A theoretical, numerical and experimental investigation was undertaken of boundary layer transition in an expansion tube. Two different methods were investigated to avoid the effects of this phenomenon.

4.1 X3 Facility Description

The X3 facility is a free piston driven expansion tube located at the University of Queensland. It was developed and built by Morgan [100] in 2000 for simulating superorbital flows after promising flow measurements were obtained in the smaller X1 and X2 facilities. The development of X3 was undertaken to improve the simulation capability by increasing the facility size. This facility has been used for numerous aerothermodynamic testing over the past six years. These include measurements of radiation on reentry vehicles in the Titan atmosphere [14], viscous effects through ducts at superorbital speeds [18] and shock standoff measurements for re-entry vehicles [134]. In recent years it has also been used as a shock heated driver shock tube for radiation measurements where non-equilibrium chemistry effects are present [135].

The X3 facility has a total length of 65 m and an exit diameter of 182.7 mm with useable core flows up to 140 mm. Figure 4.1 shows a schematic of the entire tube, with the test models placed in the dump tank. This facility uses a dual free piston compressor to drive the hypervelocity flow production and is described further in Section 4.1.2. The first stage compression tube is 12 m long and 500 mm in diameter and the second stage is 12 m long and 200 mm in diameter. The primary diaphragm is held between the inner piston buffer cage and the shock tube and is usually thin steel of the order of 1 mm. The shock tube is 12.6 m in length with a bore diameter of 180 mm with the secondary diaphragm

(Mylar film) located at the end of this. The acceleration tube is 24.6 m in length and has a bore diameter of 182.7 mm. The test section of X3 also doubles as a dump tank to ensure pressures after a shot are sub-atmospheric to prevent the dump tank from moving off the acceleration tube. Filling of the different tubes and firing is all controlled from a control panel located near the primary diaphragm.

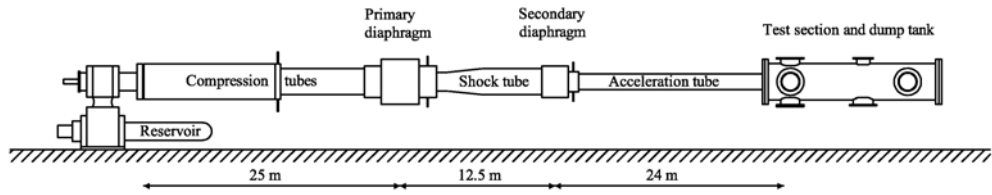


Figure 4.1: Schematic of the X3 expansion tube (not to scale). Taken from [18].

4.1.1 Measurement techniques

As in most wind tunnel facilities, refined measurements must be made of the freestream properties of the flow. In an expansion tube this becomes even more critical with the short duration, transient nature of the flow. The high total pressure and total enthalpy of the flow produced make it difficult to measure most properties as many measurement techniques cannot be used. Also, fast response times are required (in the order of microseconds) to capture all flow effects. This allows only a handful of measurements to be taken of the freestream. Due to the complex, unsteady flow processes which occur in creating the flow, it also becomes useful to measure properties such as shock speeds and static pressure in the early stages of the flow development. These upstream measurements provide additional information to predict the test flow properties.

Static pressure

Static pressure is measured at various locations along the wall in the shock and acceleration tube, as well as at one position close to the primary diaphragm in the driver tube. Measurements are taken using commercially purchased piezoelectric transducers, PCB type 112A with a PCB power supply. Calibration of each these sensors was undertaken by the manufacturer. They are flush mounted in brass sleeves which are mounted with o-rings to both seal the mount and to reduce any vibration effects on the transducers caused by stress waves in the tube produced by the driver compression/primary diaphragm rupture. This mounting arrangement for these transducers is similar to those shown in reference [96]. The shock speed can be calculated (Equation 4.1) between two transducers by taking the time of the shock arrival for both transducers and the distance between the transducers.

$$U_s = \frac{x_2 - x_1}{t_2 - t_1}, \quad x = \frac{x_1 + x_2}{2} \quad (4.1)$$

Table 4.1: Wall pressure sensor locations in X3 relative to the primary diaphragm (P.D. is primary diaphragm, S.D. is secondary diaphragm).

Transducer	Location [mm]
<i>compression tube</i>	
barrel	-18
<i>shock tube</i> (P.D. - 0 mm)	
st1	6440
st2	12520
<i>acceleration tube</i> (S.D. - 12660 mm)	
at1	14555
at2	18685
at3	22730
at4	26795
at5	30445
at6	34065
at7	35665
at8	36095

Pitot pressure

In supersonic flow, the pitot pressure is the pressure obtained when the flow is firstly shocked then brought to rest. Pitot pressure is a useful measurement, since it allows for the Mach number and flow uniformity to be estimated for a known static pressure and approximated specific heat ratio, γ^1 . The Rayleigh pitot pressure formula for perfect gases can be seen in Equation 4.2, where it can be noted the free stream static pressure is directly related to the pitot pressure measured. Pitot pressure has been measured in expansion tubes using either a shielded commercial pressure transducer or a stress wave bar gauge [136]. The shielded arrangement was used in condition testing due to re-usability and ease of use. In doing this though, the start up time of the sensor is diminished to the order of 15 μs and can also cause acoustic noise in the readings [136]. Another problem discussed in the literature for longer test time facilities which have a similar flow environment, like T4, is the false readings given by thermal stress induced forces on the front of the sensor. Due to the short test times though, this will be a minimal effect and has been explored using an hydraulic oil buffer in the cap of the sensor (Section 4.3.3).

¹This can be accurately estimated at low temperatures.

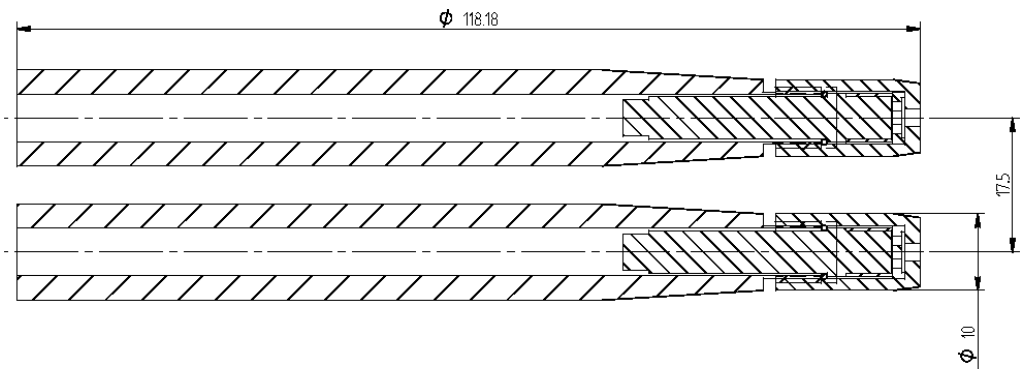
$$p_{pitot} = p_1 \left[\frac{(\gamma + 1) M_1^2}{2} \right]^{\frac{\gamma}{\gamma-1}} \left[\frac{\gamma + 1}{2\gamma M_1^2 - (\gamma - 1)} \right]^{\frac{1}{\gamma-1}} \quad (4.2)$$

The pitot pressure arrangement used in testing can be seen in Figure 4.2, where a shield is used in front of the sensor to ensure that no diaphragm fragments can damage the transducer. A line of 9 of these transducer arrangements were mounted in the test section as seen in Figure 4.2. Similar to the static pressure measurements, Pitot pressure is measured using commercial PCB 112A series piezoelectric transducers, using a PCB power supply. These are separated by 17.5 mm spanning a total of 140 mm of the exit. It is generally positioned off centre, to provide an estimate of the boundary layer edge due to a reduction of Mach number in this region. It is also noted that no attempt was made to reduce vibration in the sensor. Calibration of these sensors occurred in-situ using shop air supplied to a mounting piece that could be slid over the top of the brass mounting of each pitot. The compressed air is supplied to the mounting piece for a short duration by opening a solenoid valve that was triggered manually.

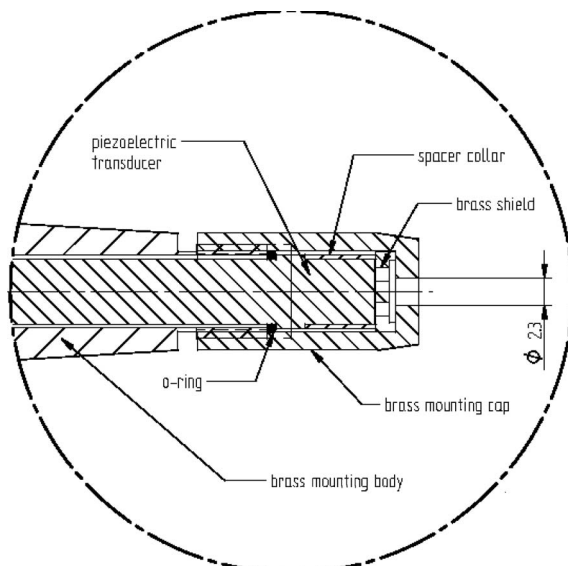
Heat transfer

Heat transfer gauges can also be mounted in the wall pressure locations shown in Table 4.1 to take measurements of the boundary layer development. With this type of measurement, the use of a fast response time transducer is required with high sensitivity for small temperature increases. For this, a thin film heat transfer gauge is most appropriate. The theory and design criteria of these gauges can be found in more detail in Schultz and Jones [137]. The gauges used were manufactured at the University of Queensland [138] consisting of a 1 mm x 0.3 mm nickel strip deposited to a quartz cylinder 2mm in diameter and length of 4 mm. The gauge has gold tabs painted down the sides of the gauge with the two leads are soldered to these. Due to the harsh environment seen during operation, a silicon dioxide layer is deposited over the top of the gauge. The $\sqrt{\rho c k}$ value for the gauges is given as $1540 \text{ J/m}^2/\text{K}/\text{s}^{1/2}$ and have a response time of $2\mu\text{s}$.

The gauges are mounted in a PCB style body (Figure 4.3), which is similarly mounted in a brass sleeve with o-rings for both sealing and vibration isolation as used in the static pressure sensors. They can be placed in any of the static pressure locations in Table 4.1. Calibration for these sensors follows the methods described by Hayne [138], using a computer controlled calibration oven before mounting into the tunnel wall. This calibration gives the sensitivity of the heat flux gauge, α by finding the rate of change of resistance with temperature, $d\Omega/dT$ divided by the gauge's resistance.



(a) pitot pressure mounting and spacing



(b) close up of transducer

Figure 4.2: Pitot pressure mounting arrangement for X2 and X3 (dimensions in mm).

Data Acquisition

Data acquisition is undertaken using locally developed “databoxes” which measure voltages and convert these from analog signals to digital data to be collected by a PC via an ISA or USB port². These have 7 cards with 3 recording channels on each which can have differing coupling (AC or DC), full scale voltages (0.1V to 0.5 V) and initial offset (-100% to 100%). Time bases can be set on each of these cards individually, with a maximum of 3 different time bases being able to be used in one test. Each time base can be triggered individually (AC or DC coupling, trigger level and trigger slope can be set on each), with 8192 samples recorded for each channel. The number of pre-trigger samples can also be set on each individually. An in-house built software code SON_OF_MONC [139], is used

²This has been a new addition to the databoxes as of 2006.

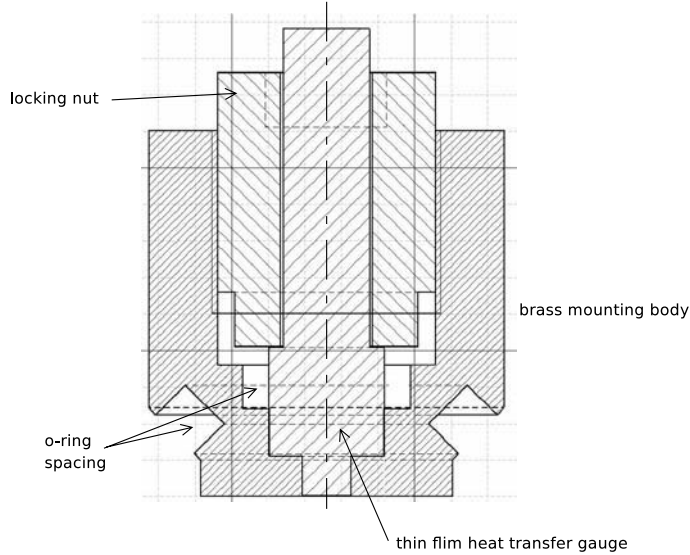


Figure 4.3: Thin film heat transfer gauge in mounting.

on the PC to collect the data from the databox and store each channel as an individual ASCII text file.

4.1.2 Buffer upgrade

Using the principles developed on the smaller X2 facility [96], a dual free piston driver was created for the larger X3 machine. The arrangement of the pistons can be seen within the tube in Figure 4.4, with a large diameter outer piston which has a mass of 80 kg and a heavier inner piston (360kg). The first stage of compression involves both pistons passing through a large volume with most of the work from the expanding reservoir gas imparted to both the pistons in the form of kinetic energy, but with little compression is accomplished on the driver gas. When the pistons reach the area change, the inner piston continues to move into the smaller diameter compression tube while the outer piston starts to decelerate due to the confinement and compression of the gas trapped in front of it. The bulk of the larger piston's kinetic energy though, is dissipated through a shock loading and deformation process on a polyurethane buffer [100] with the gas pressure relieved as the inner piston moves completely into the smaller tube. In the second stage of compression, the inner piston passes through a smaller volume where the driver gas compresses rapidly to the burst pressure of the diaphragm. With this scheme, a shorter driver can be obtained with additional financial savings made with the use of a thinner walled first stage for the compression tube due to lower pressures. However, the lack of a change in area at the primary diaphragm will result in a lower performance due to the first part of the unsteady expansion being subsonic (Equation 3.4)

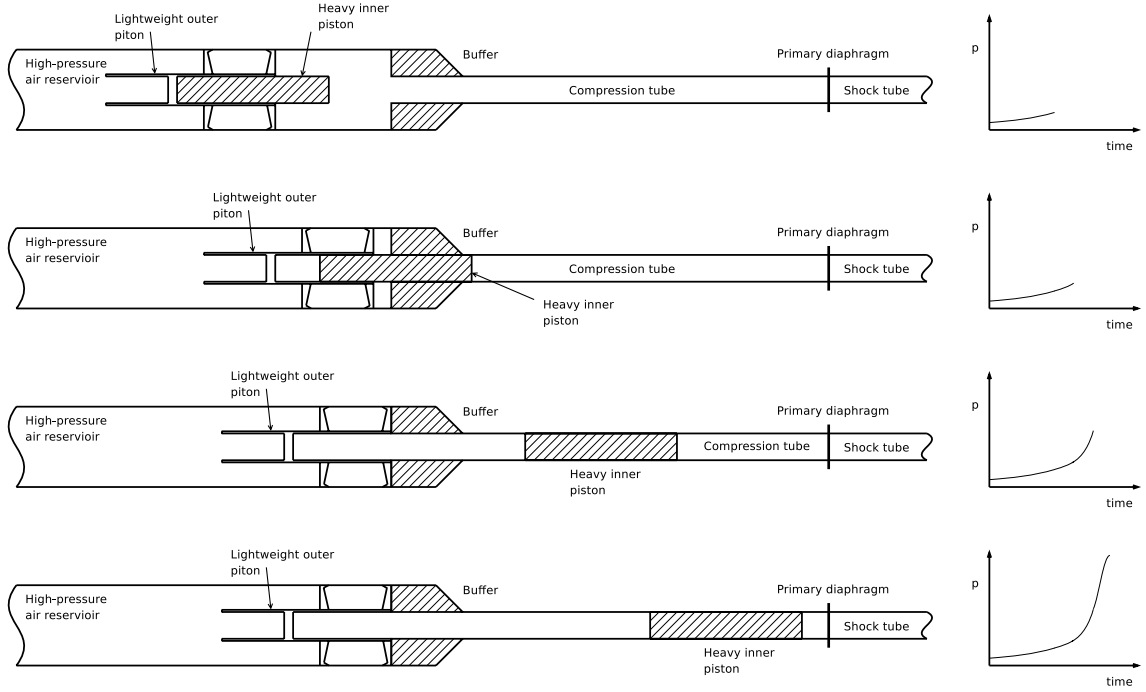


Figure 4.4: Dual piston arrangement in X3 through compression process (piston moves left to right).

The deceleration of the outer piston using the polyurethane buffer has been the limiting factor in X3's operation for increasing the total enthalpy and pressure in conditions the tunnel was designed to achieve. This is due to the polyurethane buffer reaching the upper limit of elastic deformation and limits the pistons velocity to approximately 50 m/s. To overcome this, several attempts were made at a design to use a hydraulic damping system [19] to slow the outer piston. This led to experiments by Silvester in 2002 [18], which proved to be unsuccessful. This was thought to be caused by a reduction in the predicted pressure due to cavitation in the oil. This led to an investigation into a gas buffer system by Lynch [19], which uses the regulated build up of pressure in front of the outer piston to decelerate the piston (Figure 4.5). The pressure is regulated with pressure relief valves set to not exceed 25 MPa due to both the material strengths of the outer piston and compression tube. This method has the additional bonus of recapturing some of the lost kinetic energy of the outer piston which is now transferred into the gas in the form of pressure and temperature. Some of this high temperature and pressure gas can move in front of the inner piston with the opening of the relief valves.

A simple quasi one dimensional model was implemented by Lynch[19] of the piston dynamics and buffer assuming isentropic compression throughout the process, starting at the point where the inner piston enters the buffer³ (Figure 4.5). Appendix B shows the

³This is 550 mm of gas trapped at this point.

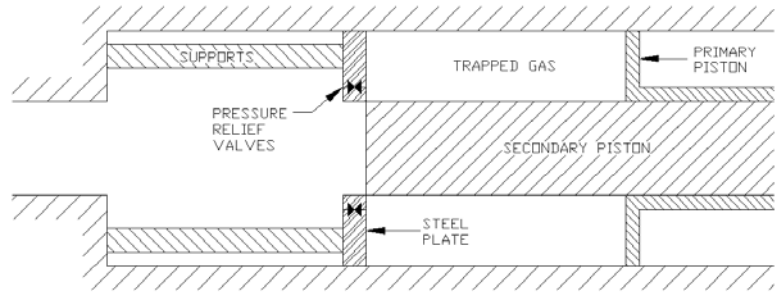


Figure 4.5: Schematic of gas buffer as inner piston enters (piston moving right to left). Taken from [19].

equations used in this model for the gas dynamics and its interaction with the piston and pressure relief valves. Initial conditions in front of the piston were estimated to be a temperature of 900 K, a pressure of 1 MPa for a pure helium driver and a piston velocity of 100 m/s. Piston and tube geometry is as shown above in Figure 4.5, with a clearance between the piston and buffer of 2 mm. The radius of valve openings was required to be 10 mm diameter due to valve seating size.

The preliminary design and analysis of Lynch's was modified to make a practical system for implementation in X3. A new spring constant was chosen of 800,000 N/m, which allowed for 16 valves to be placed in the gas buffer. With the pre-compression set to 6 mm on 12 of the springs and 5 mm on the remaining 4 set, it was possible to achieve both a soft landing of the piston and also restrict the pressure level to below 25 MPa. Using these new design parameters, the calculations produced the results shown in Figure 4.6. The results show that the piston actually stops before it reaches the buffer, so that once the trapped air is vented completely the piston should come to rest in the front of the buffer. It can also be noted that the peak pressure is limited to 24 MPa by the opening of the valves at a pressure of 10 MPa. The mass leakage around the piston is minimal compared with the level that is reached once the valve is completely opened.

The mechanical design was manufactured by the Division of Mechanical Engineering workshop at the University of Queensland and was completed in early 2004. This included practical design attributes such as nylon guide pieces for the inner piston and the buffer as it enters the larger compression tube during the turn around procedures. The valves used diesel engine valve seats due to their hardness and temperature resistant material properties. Coil springs were ordered from National Springs and a specification drawing can be seen in Figure 4.8. The buffer assembly drawing can be seen in Figure 4.7, with the piston travelling towards it from the right. The valve assembly is shown in more detail in Figure 4.8. The spring is held in place between the valve disc and the spring pre-tensioning disc which allows for up to a 12 mm precompression on the spring. The positioning of the

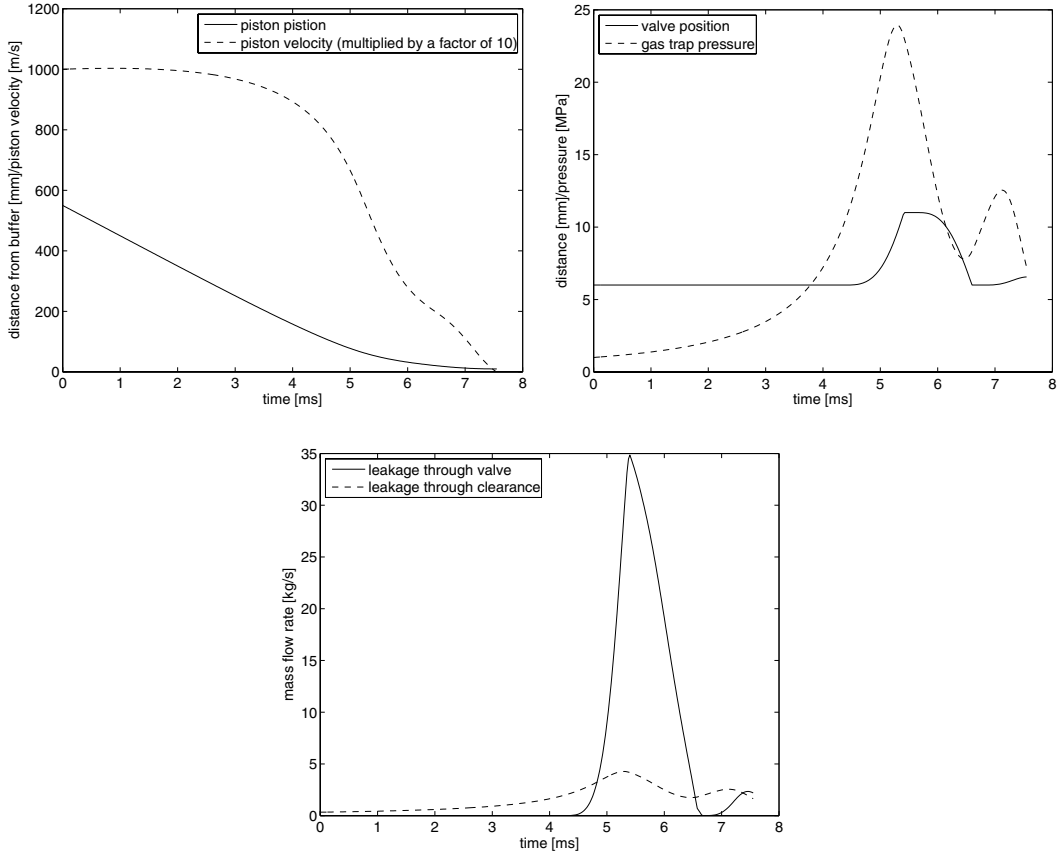


Figure 4.6: Properties from gas buffer analysis.

pretension disc is locked into place with a disc placed behind it. The valve disc seats on a 45 degree chamfer, on the machined diesel engine valve seats. A polyurethane buffer was also placed behind the valve disc to ensure the spring would never fully compress and to soften the landing of it.

the Lagrangian code, *L1d* used at the University of Queensland.

The gas buffer was built in the early stages of 2004, but was never trialled because work had commenced on the upgrade of the X3 facility to a single piston driver which does not require a complicated stopping mechanism as was designed 4.1.3.

4.1.3 Future driver and steady expansion nozzle upgrade

A single piston driver and steady expansion nozzle upgrade has been planned for the X3 facility after the successful development of these by Scott [3] for the X2 facility and financial support provided for the upgrade under a Queensland Smart State grant. A single piston driver can outperform a dual piston configuration as it removes the loss of energy required to stop the outer piston. This also mitigates the issue of stopping the outer piston which has been a continual issue in the X3 facility. The design incorporates

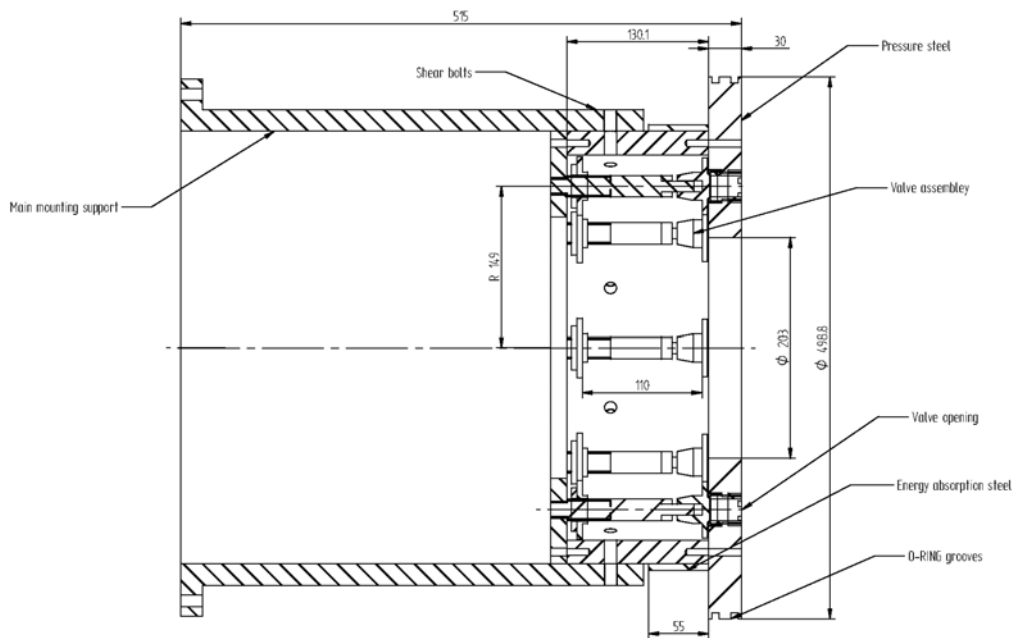
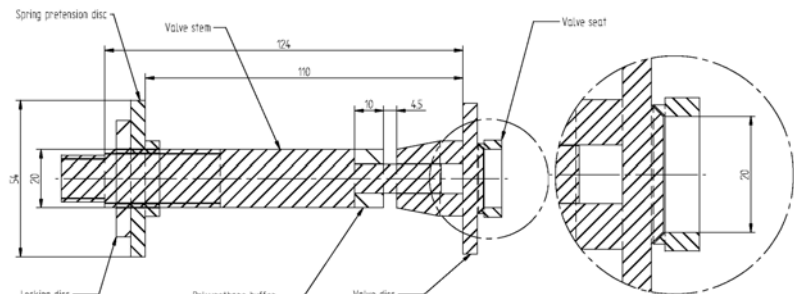
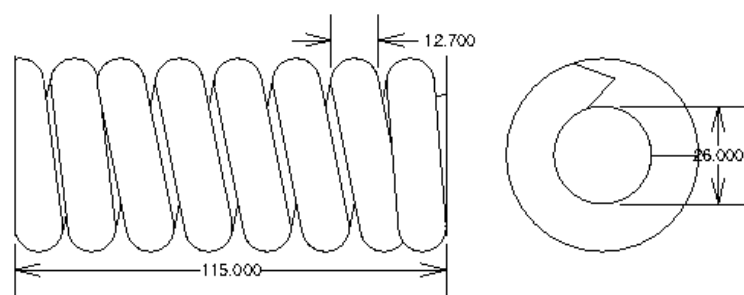


Figure 4.7: Assembly drawing of gas buffer.



(a) Valve dimensions



(b) spring dimensions

Figure 4.8: Valve design and spring design.

an area change which allows for higher total pressure and holding time as all unsteady expansions occur in the supersonic flow regime. Development work has been carried out on this design with a ~ 15 m long, 500 mm diameter driver is currently under construction.

The scaling of the X2 facilities Mach 10 steady expansion nozzle was both investigated and developed by Davey [20] for the larger bore diameter of X3. Numerical simulations with the *MB_CNS* Navier-Stokes solver [140] were used to validate the direct scaling using the Mach 10 scramjet conditions in the X2 facility as a test case (to be discussed in Chapter 5). This showed the contoured nozzle could be truncated to 2.5 m and maintain most of its core flow. The non-truncated nozzle profile and sample points for the contour can be seen in Figure 4.9. The nozzle has a geometrical area ratio of 23.2 with an exit diameter of 440 mm. The manufacture of this nozzle is to be completed in-house using a composite winding technique developed for manufacture of solid rocket casings and nozzles [141]. Currently, the nozzle mandrel and end fairings have been manufactured with the nozzle due to be wound using a carbon epoxy matrix in 2008.

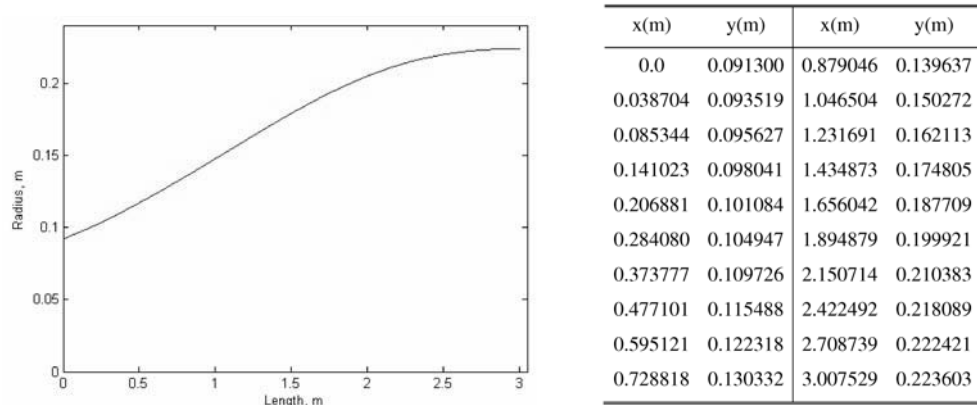


Figure 4.9: X3 steady expansion nozzle profile. Taken from [20].

4.2 Scramjet Flight Condition

As discussed, the first aim of this thesis was to produce a free stream condition that could also be produced in the T4 reflected shock tunnel so as to define the likely cross over point between the two types of facilities. Details of the T4 condition can be found in Abdel-Jawad [69]. Due to this reason, a free stream condition was chosen of Mach 10 at 30 km altitude, with flow properties shown in Table 4.2. Total pressures, enthalpies and temperatures have been calculated using a constant specific heat ratio of 1.4 and gas constant of 287 J/kg.K. The altitude was defined due to the dynamic pressure requirement suggested by Billig [127] for a transatmospheric launch vehicle flight path being between 25 - 125 kPa. A rather high dynamic pressure was chosen at 85 kPa, although this was

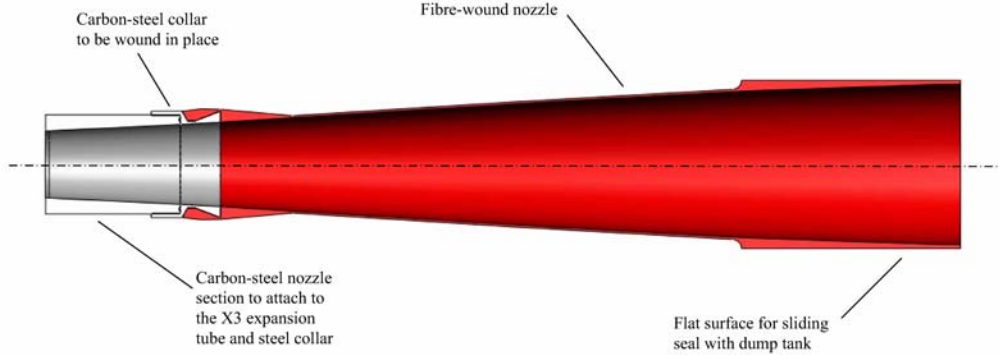


Figure 4.10: X3 nozzle section view. Taken from [20].

never achieved in the T4 facility. As X3 has quite a large exit area, this condition does not require scaling for the planned scramjet capture area needing a core of 120 mm diameter.

Table 4.2: Nominal free stream conditions for planned Mach 10 condition.

Property	Value
altitude, h_{alt} [km]	30.0
static pressure, p [Pa]	1197.0
dynamic pressure, q [kPa]	83.7
pitot pressure, p_{pitot} [kPa]	154.7
total pressure, p_0 [kPa]	50799.8
static temperature, T [K]	226.5
total temperature, T_0 [K]	4756.5
density, ρ [kg/m ³]	0.0184
Mach number, M	10
speed of sound, a [m/s]	301.7
velocity, U [m/s]	3016.7
static enthalpy, h [kJ/kg]	227.5
total enthalpy, H [MJ/kg]	4.778
viscosity, μ [Pa.s]	1.472e-05
unit Reynolds number, Re_l [10 ⁶ /m]	3.772

4.2.1 Estimation of fill conditions

Fill composition and pressures are required so that flow parameters for the desired condition can be estimated. The scramjet condition parameters (Table 4.2) can be seen to be quite cold and have a low total enthalpy compared with most conditions tested in the superorbital facility. However, this condition also has quite a high density which should enable relatively higher fill pressures in the shock and expansion tubes giving low shock speeds. A high percentage argon driver will also need to be used to produce such a low shock speed. With low enthalpy conditions, disturbances in the test flow can arise due to a low speed of sound buffer across the test gas/driver gas interface [142]. Therefore attention must be made to the ratio of sound speeds for this interface.

Calculations using the perfect gas method of Trimpli [87] (method shown in Appendix A), show that a condition is possible in the X3 expansion tube that will satisfy the criteria. Taking the diaphragm rupture pressure of 11 MPa and temperature of 1500 K from previous experiments [18], the fill conditions in the shock and expansion tubes can be manipulated to find the appropriate free stream conditions in the test gas slug (region 7 in Figure 3.1). The driver composition can also be manipulated to change the initial shock speeds by changing the gas constants which effect the overall shock speed. It was found that for a fill condition of 25 kPa air in the shock tube and 10 Pa of air in the acceleration tube and a driver fill composition of 80% argon and 20% helium (burst pressure of 11 MPa) could produce the correct flow parameters. These fill conditions could therefore be used for an initial experiment and tuned to give the correct flow parameters, as the physical flow in the expansion tube will be non-ideal. Flow calculations gave a primary and secondary shock speeds of 1420 m/s and 3783 m/s respectively.

Table 4.3: Perfect gas results for initial estimate of Mach 10 condition for X3.

Region	p [kPa]	T [K]	a [m/s]	U [m/s]	M	ρ [kg/m ³]	p _{pitot} [kPa]
(1)	25.0	300.0	347.2	0.0	0.00	0.29	0.0
(2)	483.7	1256.5	710.5	1112.5	1.57	1.34	1774.0
(3)	483.7	432.2	426.7	1112.5	2.61	4.42	5041.2
(4)	11000.0	1500.0	794.9	0.0	0.00	28.9	0.0
(5)	0.01	300.0	347.2	0.0	0.00	0.000116	0.0
(6)	1.384	7210.5	1702.1	3126.4	1.84	0.000669	6.7
(7)	1.384	235.8	307.8	3126.4	10.16	0.0205	184.5

4.3 Experimental measurements

To find the flow properties for the condition, a series of shots were performed using perfect gas estimations to give incremental changes in fill pressures, using the estimated fill conditions given in 4.2.1 as a starting point. The basic flow measurements taken in X3⁴ are wall static pressures (at locations given in Table 4.1), primary and secondary shock speeds ascertained from the static pressure measurements and pitot pressure at acceleration tube exit. Additional heat transfer measurements are presented later at positions given in Table 4.1.

4.3.1 Increase in reservoir pressure due to high percentage argon driver

Initial shots on X3 (s199-s202) failed to rupture the primary diaphragm due to a low peak pressure at the end of the free piston stroke. The only change between this condition and those used previously [134, 18, 14] was that the percentage of argon in the driver was minimal due to the high enthalpies of those flows. This process was thought to be caused by either flow choking at the area change of the driver or due to a significant difference in the piston dynamics caused by the change in the overall gas properties (specific heat ratio and gas constant) with the higher argon composition.

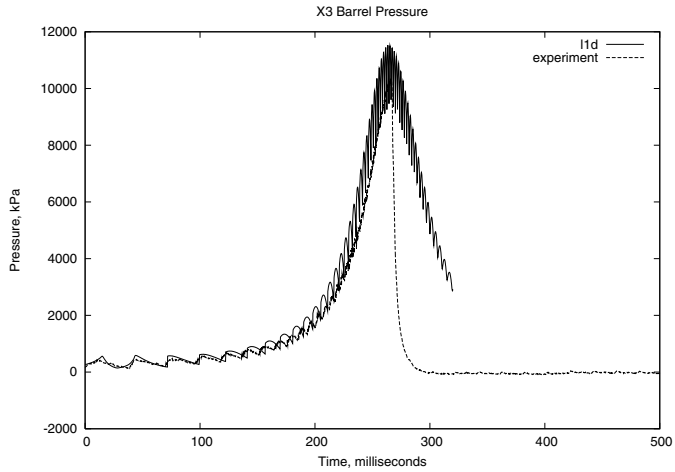
One dimensional modelling was completed by Scott [21] using the free piston modelling capabilities of *L1d* [143] to understand the flow processes. The rupture pressure in the simulation was set well above the expected peak pressures. Results of this can be seen in Figure 4.11, where the comparison is shown to be in good agreement between the experimental driver pressure for s201 and that computed for this condition. The peak pressure is shown to be approximately 10.5 MPa, which is lower than the diaphragm rupture pressure of 11 MPa. Also, the wave processes especially during the early part of the stroke are close in both magnitude and period. It was shown that by increasing the reservoir fill pressure to 1.55 MPa (Figure 4.11b) will increase the peak pressure during the stroke to the required rupture pressure of 11 MPa.

4.3.2 Pressure gauge offset and initial trials

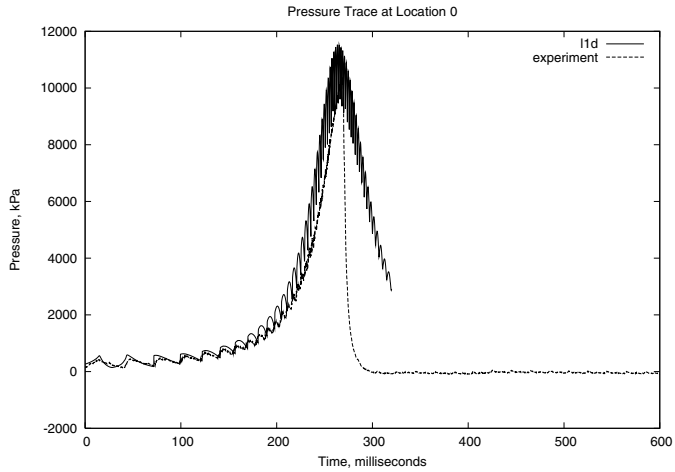
Initial trials of the condition showed shock speeds were much quicker than the original predictions from the perfect gas simulation in Section 4.2.1. This was due to two effects: the increase in the compressed driver gas temperature compared with previous conditions; and the acceleration tube fill pressure gauge appeared to have an offset of approximately 9 Pa at the pressure of around 12 Pa (i.e. the gauge was reading 21 Pa for a 12 Pa fill)⁵. This was diagnosed with use of a Barocel transducer which has a higher accuracy at the

⁴The techniques can be seen in Section 4.1.1.

⁵This has been seen in previous experiments



(a) 1.4 MPa reservoir fill pressure



(b) 1.55 MPa reservoir fill pressure

Figure 4.11: Pressure in the driver through the free piston compression with high argon mass fraction (experiment s201 compared with calculation by Scott [21]).

pressures above the Varians low range capabilities. Five shots were run to tune the shock speeds to the desired levels to achieve the Mach 10 condition at the correct pressure.

4.3.3 Final condition

The final condition trialled had the fill conditions seen in Table 4.4. This used a 1.6 mm cold rolled steel primary diaphragm and a 0.0005" thick Mylar secondary diaphragm. The primary shock speed was measured to be 1442 m/s and the secondary shock speed to be 3108 m/s. It is noted that the conditions are quite close to those originally predicted by a perfect gas simulation. A series of 12 shots were undertaken at this condition to reduce uncertainties in the flow properties.

Table 4.4: Fill conditions for final X3 condition.

Reservoir	1.55 MPa	air
Compression tube	17.2 kPa	70% argon 30% helium
Shock tube	33.0 kPa	air
Acceleration tube	12.0 Pa	air

Table 4.5: Experimental properties for X3 Mach 10 condition.

Rupture pressure, p_4	11.4 MPa
Primary shock speed, U_{s1}	1442 m/s
Secondary shock speed, U_{s2}	3108 m/s
Test gas static pressure, p_6, p_7	1.28 kPa
Test gas pitot pressure, p_{pitot}	168.1 kPa

The recorded flow properties detailed in Table 4.5 are quite close to those of the Mach 10 condition described in Section 4.2. The flow properties were averaged over 12 shots; acceleration tube static pressure and shock speed values presented are for the closest points to the end of the tube. The acceleration tube pressure is slightly higher than aimed, which in turn increases the pitot pressure directly. If an assumption of the specific heat ratio, γ is 1.4⁶, the test flow Mach number can be calculated to be 10.09. To check the appropriateness of the specific heat ratio chosen, an equilibrium calculation of the gas being shocked and brought to rest was conducted. Assuming a Mach number 9.97, with a velocity of 3100 m/s and temperature of 240 K, results in a pitot pressure of 169.5 kPa which compares well to the perfect gas and experimental pitot pressure.

The secondary shock speed is quite slow compared with the perfect gas predictions by 670 m/s or 18%. The effect on the flow would be to both slow the trailing flow and reduce the pressure and temperature of the flow processed by the shock. This is partly due to shock attenuation down the tube as can be seen in Figure 4.31. The test flow however, should have nearly the correct velocity due to the Mirels effect [15]. As discussed in 3.2.1, mass loss to the boundary layer accelerates the interface towards the shock increasing the velocity of the test gas. Figure 4.12 shows the time between the shock and interface calculated using a constant velocity interface and Mirels calculation, with post shock properties determined by perfect gas relations [144]. The laminar boundary layer solution was chosen as the diameter/pressure product (dp_∞), is less than 0.5 as prescribed Mirels [109]. This shows that by the end of the acceleration tube, the interface has nearly asymptoted to the point where it is at the same speed as the shock. It is a standard approach to do analytical calculations, expecting the real shock speed to be

⁶The stagnation temperature is approximately 5000 K, so a drop in the specific heat ratio is expected.

equal to the analytical predicted post shock flow speed due to these effects, which seems to apply here too. Thus, the test gas velocity can be assumed to be relatively close to the measured shock speed and therefore be close to the parameters defined in Table 4.2..

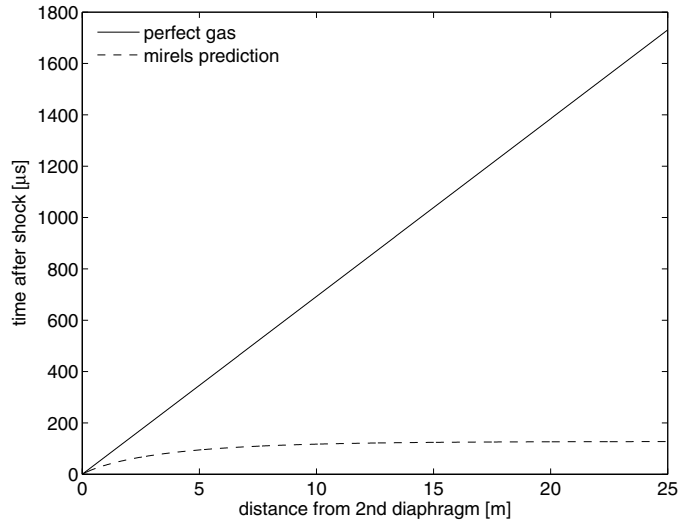


Figure 4.12: Position of interface after the passing of the shock.

The measured static pressure and pitot pressure can be seen for shot s237 in Figures 4.13 and 4.14 respectively, as a typical shot. The static pressure is taken at the last two locations, at7 and at8, which are in the last 2 m of the acceleration tube. These show a relatively steady trace for the initial $400 \mu\text{s}$ after the passing of the shock. After this, the pressure drops slightly before the $U - a$ wave passes at $520 \mu\text{s}$ after the shock arrival, increasing the pressure quite rapidly with large flow oscillations. With the acceleration slug taking $110 \mu\text{s}$ to pass according to Mirels calculations (Figure 4.12) assuming a laminar boundary layer and seen in the pitot pressure measurements at exit (Figure 4.13), there is steady pressure for $410 \mu\text{s}$, which is shorter than was hoped for with the theoretical prediction being approximately $800 \mu\text{s}$.

The pitot pressure was measured at the acceleration tube exit⁷ at nine different radial locations as mentioned in Section 4.1.1. This is shown at three of these radial locations in Figure 4.14. It can be seen that after the passing of the acceleration slug (a pressure of 13 kPa and slug length of $110 \mu\text{s}$) there is a further increase in the pressure to 165 kPa. This holds steady until $250 \mu\text{s}$ after the passing of the shock before sharply decreasing. Also, the levels are quite similar at all three locations across the tube, but the farthest pitot from the centreline at -62.5 mm shows a reduced pitot pressure, due to its proximity to the edge of the boundary layer. This is approximately half way through the predicted test time using the static pressure measurement. It can be seen that all three of the radial locations seem to match each other quite well, with no relative difference in timing of the

⁷This is as close as possible to tube exit assuming a nominal recoil.

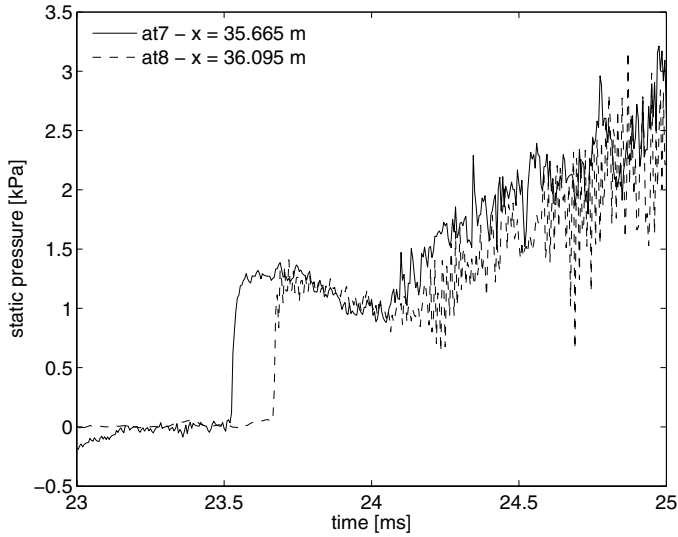


Figure 4.13: Experimental static wall pressure close to tube exit for X3 Mach 10 condition (x3s253).

passing of the shock, interface or the drop in pitot pressure. This can be further seen in Figure 4.15 where all nine pitot pressures are plotted together against radial distance for various times. As noted previously, the outer pitot pressure measurements are low compared with rest, indicating they are located within the boundary layer..

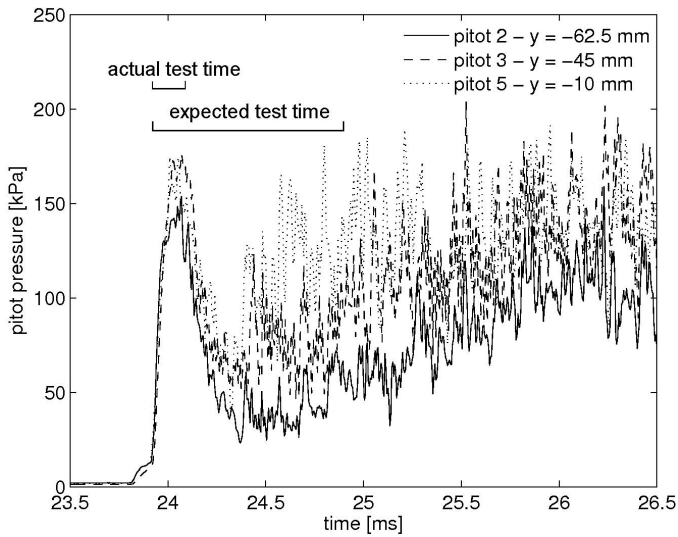


Figure 4.14: Experimental pitot pressure across at three radial locations at the acceleration tube exit for the X3 Mach 10 condition (x3s253).

The pitot pressure traces are explored more closely for the acceleration/test gas period (Figure 4.15), revealing that by $500 \mu\text{s}$ after the passing of the shock the pitot pressure level has dropped down to 60 kPa. Figure 4.17 shows the plotting of pitot pressure against

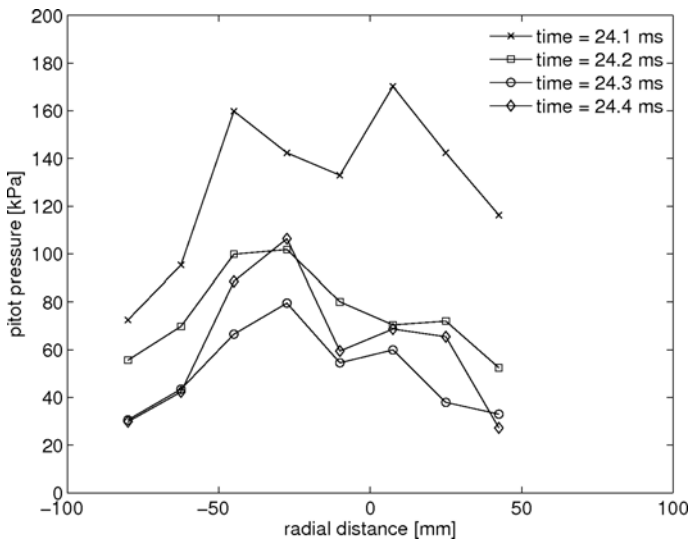


Figure 4.15: Experimental pitot pressure across the tube exit for X3 Mach 10 condition at various times (x3s253).

Mach number from Equation 4.2 for variations in static pressure and the specific heat ratio. The specific heat ratio will change from the cold free stream to the hot gas within the pitot from being shocked then stagnated. The equivalent specific heat ratio cannot be predicted easily as it will change in both the process of the gas being shocked then brought to rest. A range for the γ is expected between 1.3 and 1.4 and therefore chosen as the bounds for this variable. It can be seen that the effect of the specific heat ratio is marginal, and accounts for a change of less than 10 kPa. The static pressure is varied from the nominal value of 1.28 kPa, to 1 kPa and 1.5 kPa, to account for shot to shot variation and the dip in pitot pressure seen just before the unsteady expansion. Therefore, if the pitot pressure drops from the nominal value down to 1 kPa, as occurs in Figure 4.16 the pitot pressure should be 120 kPa if the Mach number holds constant. With the pitot pressure dropping to 60 kPa at 1 kPa static pressure, this corresponds to a Mach Number of approximately 6.7 with only minor variation due to the specific heat ratio.

The effect of thermal stress on the transducer can cause false readings and even negative pressure readings as shown by Silvester [18] well after the test time. This is due to the extremely high temperatures at stagnation for hypersonic flow, where the thermal energy is transferred into the top of the sensor which is exposed compared with the rest of the sensor. As discussed earlier (4.1.1), this effect has been mitigated through the use of hydraulic oil in the cap of the pitot. This creates both an acoustic wave dampening effect and while creating a thermal buffer to the transducer. The drop in pitot pressure can therefore only be accounted for by a drop in the Mach number of the flow, indicating there is no useable core flow.

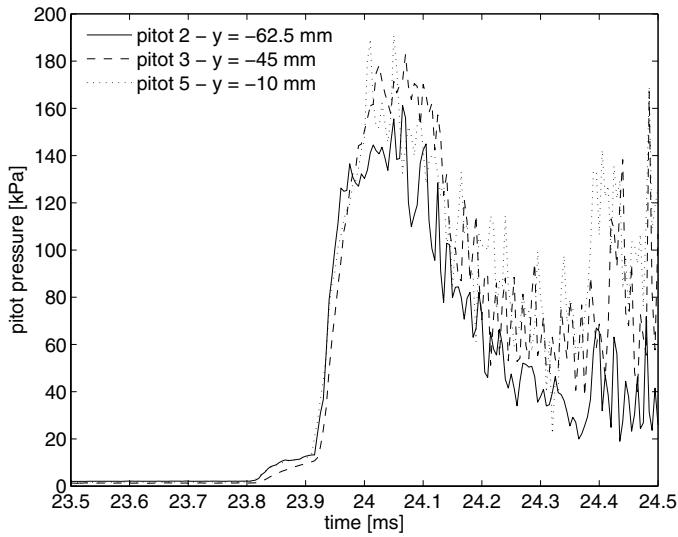


Figure 4.16: Expanded view of experimental pitot pressure across at three locations at tube exit for X3 Mach 10 condition (x3s253).

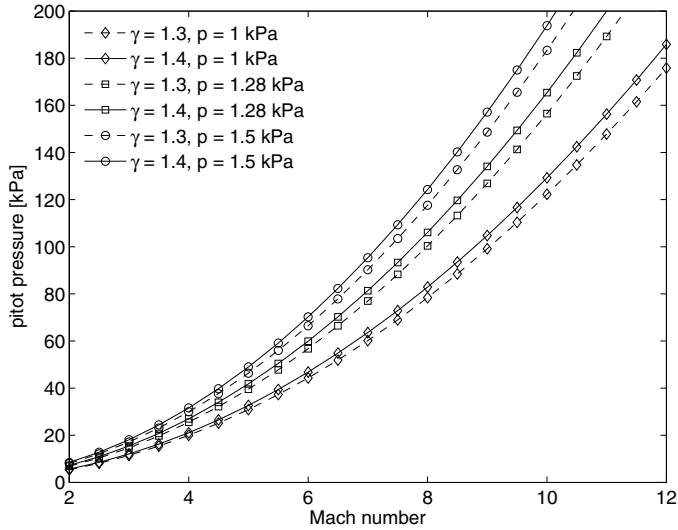


Figure 4.17: Pitot pressure variation with Mach number, specific heat ratio and static pressure.

4.4 Numerical Simulation

Computational fluid dynamics (CFD) provides a valuable tool for the analysis of expansion tube conditions as many properties cannot be easily measured experimentally due to the harsh environment and short test times. Experimental results (static pressure, pitot pressure and shock speeds) are used for both comparison and validation that the numerical work is capturing the bulk of the flow properties accurately, as grid independence is too expensive computationally and a minor effect when compared to the modelling deficiencies

(further discussion in Section 3.4). Once validated, the numerical simulations can provide extensive details of the flow which is unattainable from experiments. Details of the core flow at the acceleration tube exit is of most interest, with other data able to be used for both validation and diagnostics tool of flow development. One use of particular interest, was to uncover the flow phenomenon that caused the large drop in the pitot pressure of the test gas seen in experiments.

The modelling technique used in the analysis presented in this thesis has been previously utilised successfully at the University of Queensland in modelling higher enthalpy expansion tube conditions [130, 3, 14]. This uses a combination of both a one dimensional simulation of the shock tube and an axisymmetric simulation of the acceleration tube. This allows simplification of the calculation, as the boundary layer influences in the shock tube have only minor influences on the flow and enable simulation of some of the complex fluid/boundary interactions seen at the secondary diaphragm, such as reflected shocks and diaphragm rupture times. The acceleration tube flow though, is greatly affected due to the growth of large boundary layers caused by low pressures which leads to shock attenuation and acceleration of the interface. Also, variations will occur across the tube, which are of interest when accessing the usable core flow.

4.4.1 One dimensional modelling

Using the fill conditions found experimentally, a one dimensional simulation of the shock tube was performed on X3 using the transient *L1d* code [143]. This code uses a Lagrangian based description of the gas dynamics, with engineering correlations to adjust the momentum and energy of the gas for things such as viscous effects at walls and area changes due to the one dimensional nature of the code. The code can include multiple interacting gas slugs, pistons and diaphragms. Each gas slug is broken into multiple cells, with the interaction of each being dependant on neighbouring cell properties. The code uses a time stepping procedure which handles interactions with boundary conditions (walls, free ends, diaphragms and pistons) at the end of each time step. Each side of a diaphragm is modelled as a reflective boundary condition. For further information on modelling shock tubes with this code see [143].

For the work included within this thesis, the numerical simulations do not include the piston dynamics. This means conditions for the compressed driver gas are estimated at primary diaphragm rupture, when the piston velocity is assumed to be negligible [130, 3] so therefore is set to be a solid wall. In contrast to reflected shock tunnels, as the flow is not stagnated, any associated waves with the piston still moving will not have a strong effect on the test gas used during testing. The secondary diaphragm is modelled as a diaphragm with a rupture pressure of 200 kPa. The hold time is set to a low value of $5 \mu s$ as the effects of mass entrainment and reverse shocks will be minimal at the high density

and low shock speed condition being simulated. This geometry can be seen in Figure 4.18, where the major dimensions are shown for the tube. The change in diameter in the driver gas slug, is due to the buffer and pressure plate arrangement and is the same as that used by Jacobs et al. [130]. Viscous effects are incorporated using the Darcy-Weisbach engineering correlations for steady incompressible pipe flow and are explained in detail in [143].

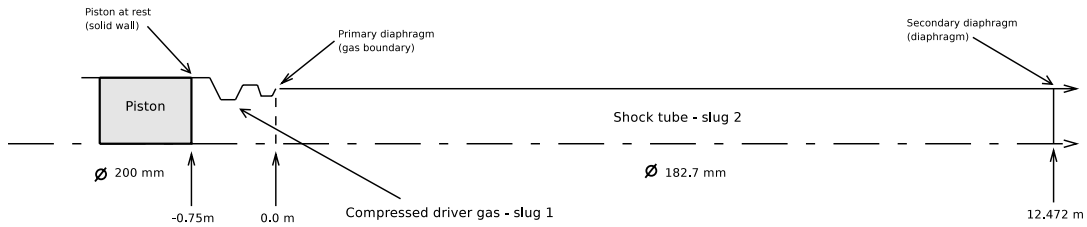


Figure 4.18: Geometry for *L1d* simulation for X3.

The driver gas is modelled as a perfect gas, with properties well known as both argon and helium are noble gases. The air in both the shock and acceleration tube however, will have a change in the gas properties due to the strong shock passing through, increasing its temperature significantly. In the one-dimensional simulations included within this thesis, the shock tube gas is modelled as a gas in chemical equilibrium. For speed of processing within the simulation, a table is made of gas properties for multiple pressures and temperatures expected within the simulation. The gas properties are calculated using the NASA *CEA* code [145], which has stable, widely used equilibrium characteristics for most gases and mixtures. Gas properties are therefore interpolated within *L1d* using a piecewise linear fit over a large table of data where the density coordinate is logarithmic in the look up table (LUT). The use of chemical equilibrium with a LUT has been used successfully to model a wide range of expansion tube conditions of different gases at lower enthalpies [18, 3]. This is different to the finite rate simulation requirements needed by Stewart [8] to simulate scramjet conditions in the RHYFL expansion tube. This is due to the relatively low temperatures seen throughout the X3 condition, as test gas behind the primary shock is also reasonably slow which would allow for further recombination.

Estimations of the compressed driver temperature have been made by using simulations conducted by Scott [21], to be 2000 K using a rupture pressure 11.45 MPa set by the diaphragm material. This can also be estimated by assuming the piston compression is a polytropic process with similar characteristics as other X3 flow conditions, except there will a change in the gas constant due to large Argon percentage. Fill pressures and compositions for the simulation are the same as seen in Table 4.4, with the shock tube initial temperature assumed to be at 296 K. The simulation was conducted on both a coarse initial cell sizing of 250 cells and 1500 cells and a fine grid of 500 cells and 3000 cells for the driver slug and test gas slug respectively. The simulation was conducted on

a single processor on the Blackhole Linux cluster at the University of Queensland [146]. Results of these simulations at the shock tube station st2⁸ can be seen in Table 4.6, where it can be noted that there are only minor changes seen between the two grid sizes.

Table 4.6: Summary of $L1d$ flow properties in the shock tube for X3 condition.

Property	$L1d$	$L1d$
	coarse	fine
Primary shock speed, m/s	1412.3	1440.8
Sound speed ratio across interface, a_2/a_3	1.176	1.181
Static pressure, kPa	639.9	642.6
Velocity, m/s	1110	1118.1
Temperature, K	1152	1164.0
Density, kg/m ³	1.935	1.928
Unit Reynolds number, [million/m]	47.71	47.59

To ensure that the simulation has modelled the condition accurately, a comparison can be made between the experimental measurements of static pressure and the simulation data at the same location. Figure 4.19 shows that the simulation appears to be modelling the static pressure reasonably well directly after the passing of the shock, which is of most importance. Further time after the passing of the shock, there is some variation between the experimental and numerical results. This could be due to the poor quality of the experimental measurements with variation in static pressure before the arrival of the shock. Also due to the one dimensional nature of the simulation, capturing of radial variations and mass loss to the boundary layer can cause discrepancies with the physical flow. But with the shock speed seeming to match reasonably well between the experiment and $L1d$ simulations, with a difference of 0.1%, it indicates that $L1d$ is modelling the flow within the error of the experimental measurements. This can then be used as a transient flow condition for the axisymmetric calculations.

The sound speed ratio across the driver/test gas interface is quite important in low enthalpy conditions due to its ability to buffer sound waves as discussed previously. The shock can be seen to pass the location at 4.2 ms with a sudden rise in sound speed and the interface is the next change at 5.2 ms, with a significant drop in sound speed. The perfect gas predictions of the initial condition have been quite good in keeping a favourable sound speed ratio (a_2/a_3) of approximately 1.18. This is taken from Figure 4.20, which shows the time history of the sound speed at st1.

⁸st1 is used for shock speed ratio and shock speed is taken between st1 and st2.

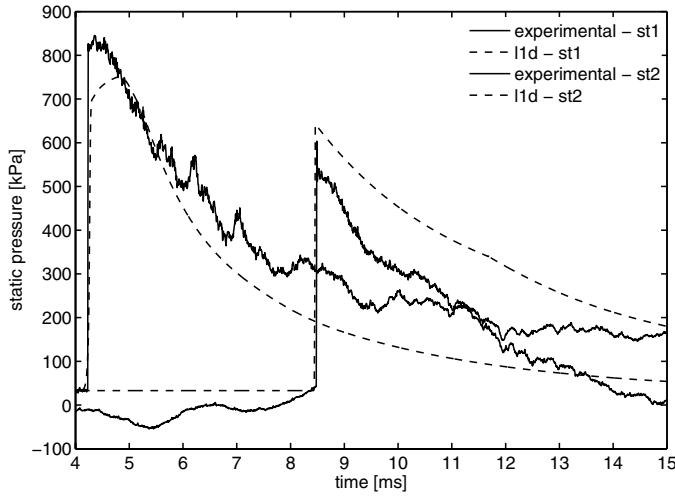


Figure 4.19: Comparison of static wall pressure in shock tube for X3 Mach 10 condition. Fluctuations before the shock is due to electrical noise in the data lines.

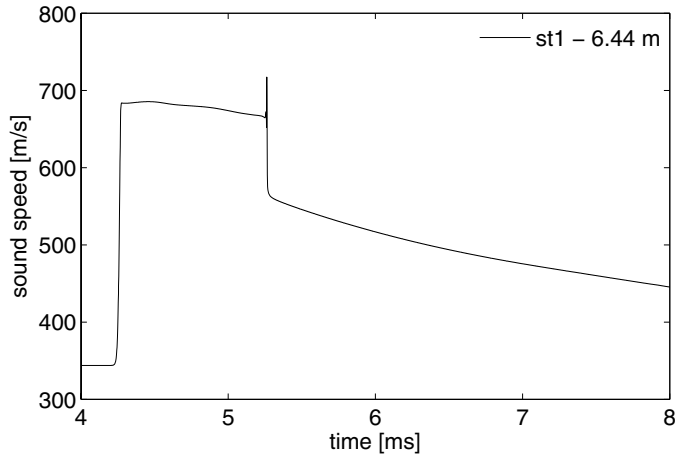


Figure 4.20: Sound speed at st2 from $L1d$ simulation in shock tube for X3 Mach 10 condition.

4.4.2 Axisymmetric modelling

With the one dimensional modelling completed of the shock tube, the next step in numerically modelling the expansion tube flow is an axisymmetric simulation of the acceleration tube. This uses the *MB-CNS* code [140], which is a multiblock, two dimensional/axisymmetric compressible flow solver using a cell centred finite volume approach to solving the Navier-Stokes equations. It utilises a structured grid, fixed in space. This was developed for solving transient hypersonic problems where strong shocks, high enthalpies and large gradients are present in the flow.

The time history of flow properties taken just behind the secondary diaphragm from the one dimensional $L1d$ model are used as a transient inflow condition. This is duplicated

for every cell across the entire tube in the axisymmetric calculation. The simulation uses the geometry represented in Figure 4.21 with the dimensions taken from Figure 4.1. It can be noted that there is a small slug of shock tube fill condition gas, being 150 mm long. This buffers the start of the simulation from having extremely large flow gradients initially, which decreases the allowable time step to extremely low values. The difference between the acceleration and shock tube fill conditions causes weak compression waves into the acceleration tube centered at the secondary diaphragm. These have a minimal effect on the flow exiting the tube due to the shock passing these quite close to the secondary diaphragm. The outflow boundary condition uses ghost cells and extrapolates the flow from the last cell in the simulation.

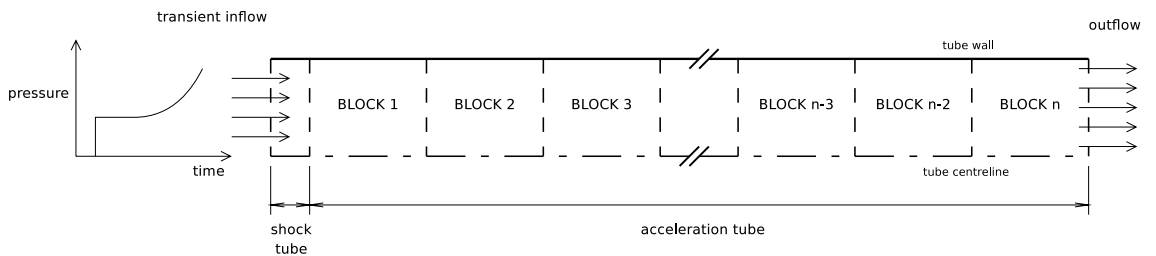


Figure 4.21: Axisymmetric setup for X3 simulation.

A version of the *MB-CNS* code that uses the message passing interface (MPI) method of splitting the flow field into blocks which can be computed on separate processors. This uses a different computer processor and separate local memory to solve and store the flow field. This also has the ability to pass information about the flow field between the processors or blocks. The major advantage of using this is that the clock time taken to run a simulation is decreased proportionally to the number of processors⁹. Another advantage of simulating expansion tubes in particular, is that processors can be brought on line once the shock reaches the end of each axial block. Each *MB-CNS* simulation conducted in this thesis utilises this by splitting the flow field into multiple blocks of equal size axially.

Equilibrium chemistry is again utilized as in the one dimensional simulation by using interpolation from a look up table generated using the *CEA* code [145]. This should be sufficient due to the relative low speeds of the secondary shock (~ 3 km/s) which therefore allows enough time in the experiment to allow chemical equilibrium to be reached. In some expansion tube conditions, the test gas becomes chemically frozen due to the temperature gradient with respect to time being too large [16]. However, the low speed and temperature gradient allows the expanded test gas to come back to chemical equilibrium over the large distances traversed through the acceleration tube. Viscous effects, block splitting and grid resolution are discussed for both the laminar and turbulent simulation cases within

⁹The factor is less than the number of processors because the time taken to pass information between processors increases with the number of processors.

the respective sections. All simulations were computed on the Centre for Hypersonics Blackhole Linux cluster located at the University of Queensland [146]. Typical run times of the finest grid simulations were 148 hours when using 35 processors.

Laminar simulation

A laminar simulation was conducted of the flow condition using a fixed temperature wall of 296 K and transient information taken from the upstream *L1d* simulation. The simulation was broken into 41 blocks axially, with 40 of these representing the acceleration tube. The acceleration tubes grid has a resolution of 10080 cells axially and 81 cells radially. There is a clustering of the grid using the *MB_CNS* parameter β of 1.05 towards the tube wall (See reference [140] for further details on clustering), with a cell height of 0.21 mm at the wall, to better resolve the boundary layer by having more cells located within it. The single shock tube block is made up of 30 cells and has the same radial distribution of cells. The fill properties are as stated in Table 4.5.

The time history of flow properties at three locations radially at the acceleration tube exit are shown in Figure 4.22. The locations correspond to the closest cell to the centreline, a third of the way across the grid and the closest cell to the wall. It can be noted that low amplitude oscillations occur at the centreline, which are not present at the next location. These disturbances have been seen in other modelling of the tubes, and are not believed to be true flow occurrences [130, 3]. These disturbances have been attributed to an amplification of slight waves at the centreline due to the low grid resolution in this region because of clustering of the grid towards the wall and centreline anomaly in axisymmetric simulations. The plot shows the condition is in quite good agreement with the flow properties between the centre and midline. The static pressure is at a similar level as the experimental measurements and has a similar time period before the interruption of the test time by the leading edge of the unsteady expansion. The values of Mach Number and therefore the pitot pressure are slightly higher than the ideal condition. This is due to a decreased static temperature and increased velocity of the flow. It can be noted that the dip in pitot pressure halfway through the test time is not present in this simulation. The time history near the wall shows that there is a significant jump in the temperature across this first cell of approximately 200 K, although this is not believed to have a great effect on the overall flow properties of the free stream. The shock speed at the end of the tube was 3131 m/s, slightly higher then expected. The results of the laminar simulation are discussed further in Section 4.4.2 when compared with experimental and turbulent simulation results.

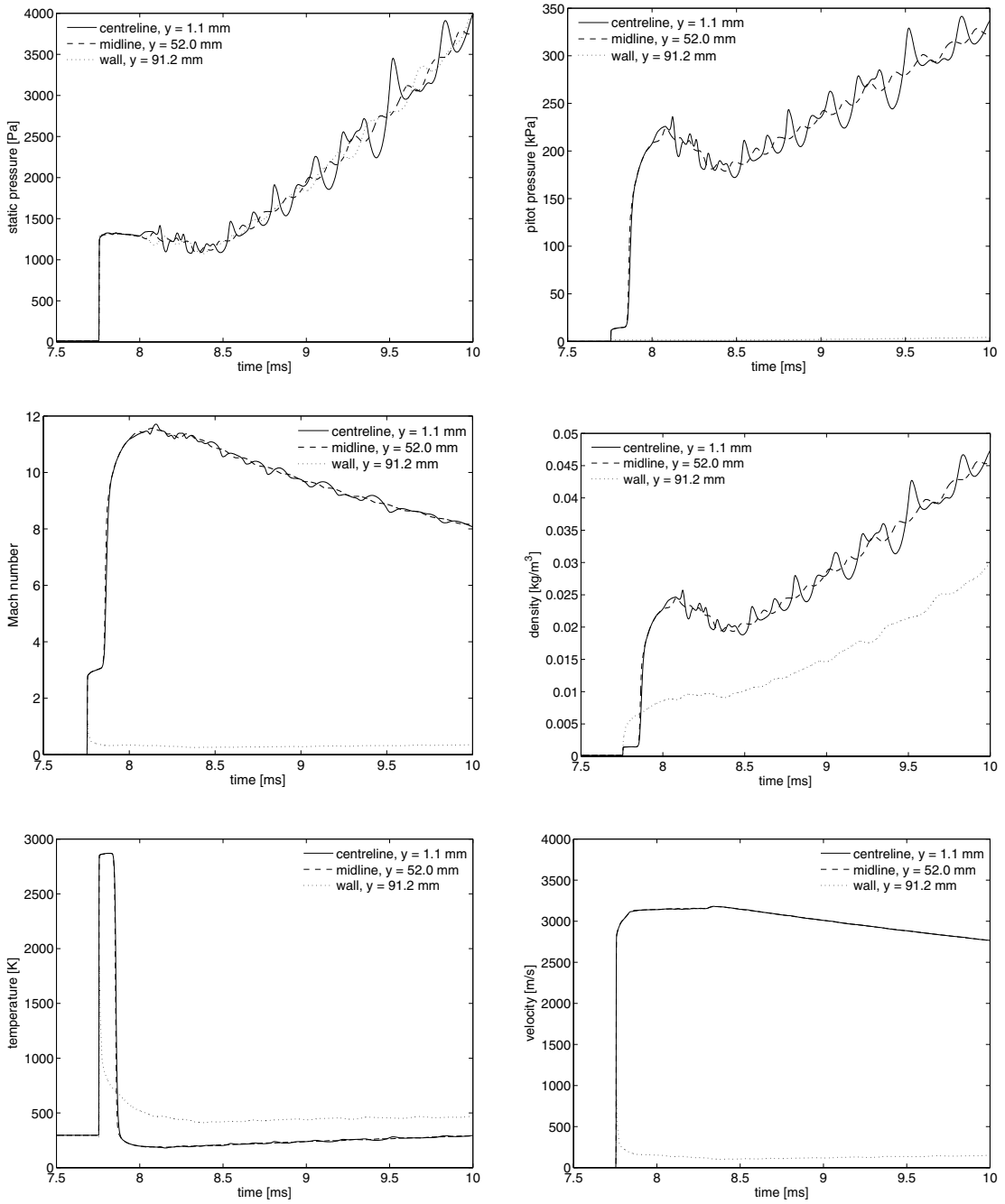


Figure 4.22: Properties at three locations at the tube exit for laminar simulation of X3 Mach 10 condition.

Turbulent simulation

With the targetted condition having a unit Reynolds number of 3.77 million/m, it is expected that the boundary layers should transition to become fully turbulent within the test time. This uses the observations made in the HYPULSE expansion tube, where if the

test gas unit Reynolds number exceeded 1.33 million/m, the boundary layer was fully turbulent [41]. Most conditions in expansion tubes are aimed at re-entry or upper-atmosphere flight, where the densities are low and therefore have low Reynolds numbers. This causes the boundary layers to remain laminar. Thus, not many simulations of expansion tube conditions need to investigate turbulent boundary layers. If the boundary layer does become fully turbulent in a hypersonic flow regime, it can swell to large sizes due to the high temperatures compared to the freestream.

The turbulence model used in the simulation is the Baldwin-Lomax eddy-viscosity model [147], which is included in *MB-CNS*. This model adds the effects of turbulence to the Navier-Stokes equations by simply adding an additional term to the transport coefficients for eddy viscosity, μ_T and eddy thermal conductivity, k_T . These terms are calculated using algebraic means from the flow properties. This is less accurate than the one and two dimensional models which solve partial differential equations for the convection, creation and dissipation of the turbulent kinetic energy. The Baldwin-Lomax turbulence model uses a free stream reference equation to calculate whether the boundary layer should transition. At each time step, the maximum turbulent viscosity for each radial profile is compared with the free stream viscosity and if it is more than the constant (C_{μ_T} , which is nominally set to be 14 according to original model), the turbulent viscosity is added to the laminar component (Equation 4.3b). This turbulence model has been shown in hypersonic flow regimes to be quite good at predicting transition location [148], although the boundary layer once turbulent can be significantly underresolved.

$$\mu_T = 0 \quad \text{if } (\mu_T)_{\max} < C_{\mu_T} \mu_{\infty} \quad (4.3a)$$

$$\mu_{eff} = \mu_{lam} + \mu_T \quad (4.3b)$$

The turbulent simulation used a structured grid comprising of 10110 cells axially with 30 cells in the shock tube (set to initial shock tube fill conditions) and 81 cells in the radial direction. It again used a clustering of the grid towards the tube wall, with a β factor of 1.05. Due to the number of processors available on the Blackhole linux cluster when this simulation started, it was broken into 25 blocks instead of 40 as used in the laminar simulation. One of these blocks was for the shock tube. The temperature was again set at a fixed temperature of 296 K and the simulation uses an equilibrium gas model for the air with fill properties from Table 4.5.

The results for this simulation can be seen in Figure 4.23, showing time histories for three radial locations at the acceleration tube exit. The large oscillations can be seen to be larger than those previously noted in the laminar simulations. This is due to the larger disturbances in the boundary layer due to the addition of turbulence in the transient flow.

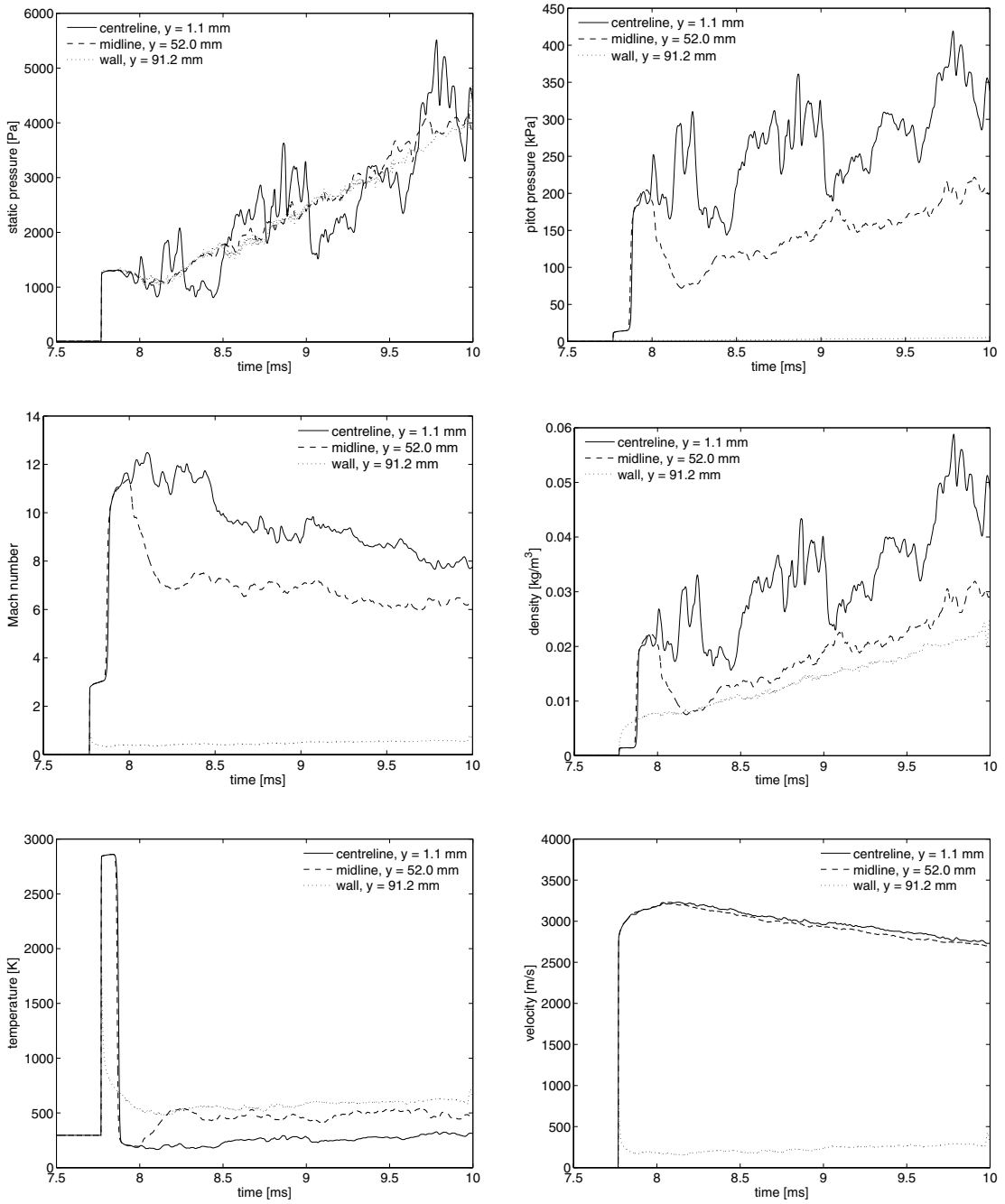


Figure 4.23: Properties at three locations at the tube exit for turbulent simulation of X3 Mach 10 condition.

The flow properties seem to be very similar to those calculated in the laminar solution up until $250 \mu\text{s}$ after the shock passes. Then, as can also be seen in the experimental results (Figure 4.16), a drop in pitot pressure occurs through the predicted test time. This drop however, only occurs at the midline (52 mm off centreline) and not all the way

across the tube as in the experimental results. Contour plots of the pitot pressure from the turbulent simulation in Figure 4.24 reveal that the transition to turbulence produces a rapid growth in the boundary layer towards the centreline while the static pressure remains relatively unchanged. This is not sufficient enough though to engulf the entire tube. The cause of this discrepancy is unknown. However, lower grid resolution simulations gave better agreement for the rate of boundary layer growth, pointing to inconsistencies in the mathematical modelling of boundary layer. With no other turbulence model implemented into the CFD code, this could not be investigated.

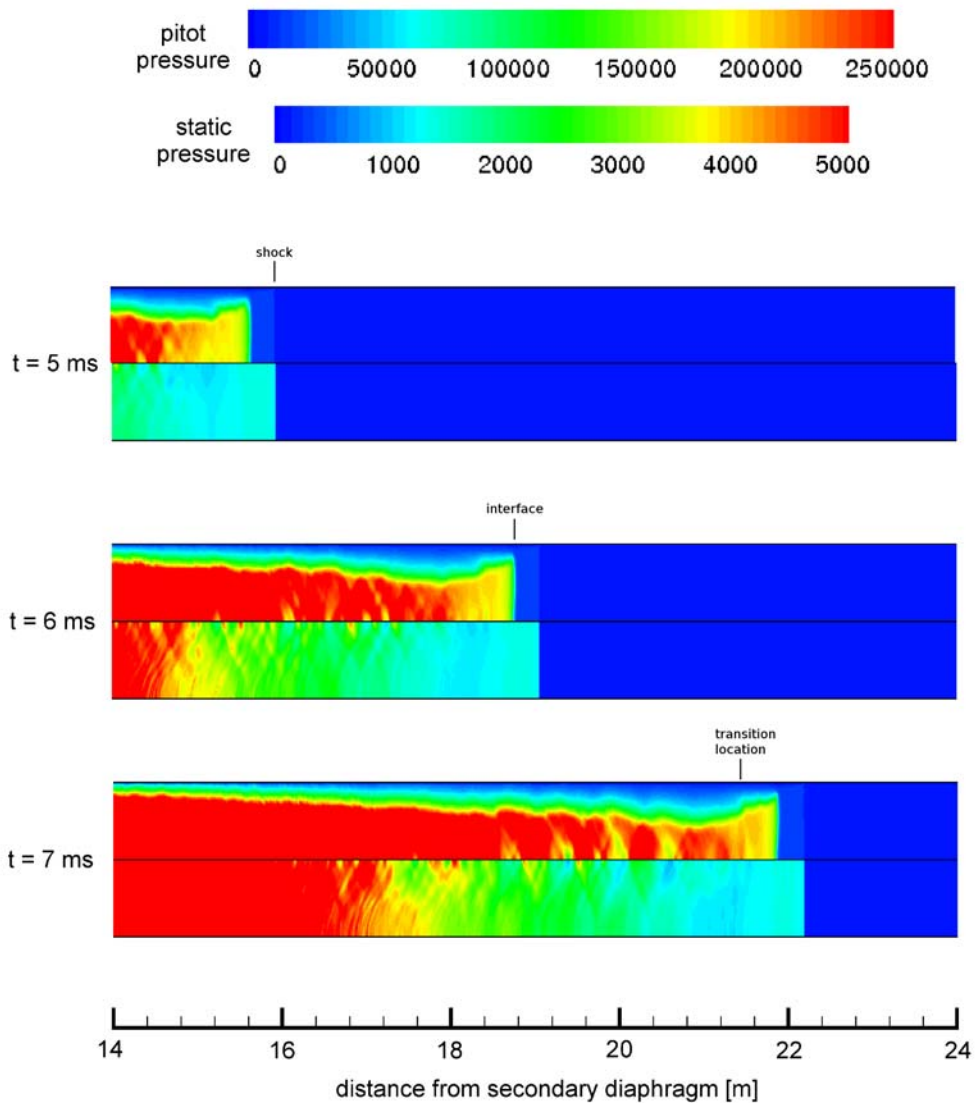


Figure 4.24: Comparison of static and pitot pressure [Pa] various times from the turbulent simulation for X3 Mach 10 condition. Pitot pressure is shown in the top half of the tube and static pressure in the bottom half.

The pitot pressure contour, Figure 4.24, revealed a large growth in the boundary layer at the point of transition. As the maximum separation between the shock and interface has been reached, it is of interest to establish whether this *bubble* of boundary layer is a build of acceleration gas being squashed between the wall and the test gas or whether this gas originates from the test gas. If this is originally acceleration gas, the use of a lower temperature gas may relieve the extent of boundary layer growth from occurring. Figure 4.25 shows the same pitot pressure contour with pathlines overlaid in the shock steady frame of reference (i.e. velocity in the axial direction is given by $U_s - U$). This reveals that this growth in boundary layer after transition is test gas, as the pathlines show that the acceleration gas will end up *squashed* against the wall. The results are discussed further in Section 4.4.2, where the turbulent results are compared against the experimental and laminar results directly. Also a more in depth investigation is given in Section 4.5 for boundary layer transition effects in expansion tubes and for this condition.

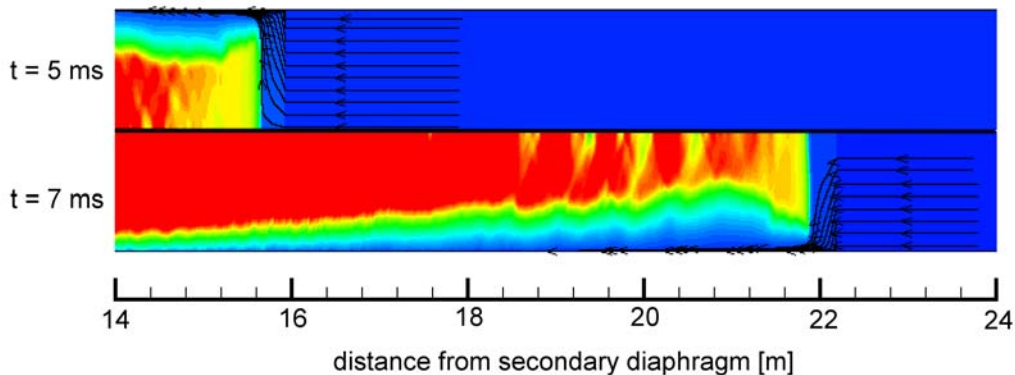


Figure 4.25: Contour plot of pitot pressure at 5 ms and 7 ms from the turbulent simulation for X3 Mach 10 condition. Pathlines are shown in the shock steady frame of reference ($U_s = 3122 \text{ m/s}$).

Grid refinement

As discussed in Section 3.4, grid resolution is limited due to the size of the calculations computational expense due to many different reasons, including resolution of large length scales of the facility and that of boundary layers and moving shocks. To gauge the degree of grid independence in this solution, a grid refinement study was undertaken. This was completed for the turbulent simulation only due to computational time limits, and is the case of most interest. The turbulent simulation was shown to capture the major flow effects more accurately, with some of the flow across the tube exhibiting the dip in pitot pressure seen experimentally. Table 4.7 shows the grid properties used in the simulations. It is noted that the axial grid resolution from the finest grid to the coarsest grid is larger

by a factor of 3. In the radial direction, the ratio of fine grid to coarse grid resolution is 2.25. All simulations use a clustering with a β factor of 1.05 towards the wall.

Table 4.7: Grid refinement properties for X3 in the acceleration tube and history point locations used for comparison.

	cells axially	cells radially	β	x_{hist} [m]	y_{hist} [mm]
Grid 1	3360	36	1.05	24.560	51.0
Grid 2	6720	54	1.05	24.580	51.6
Grid 3	10080	81	1.05	24.587	52.0

Figure 4.26 shows the time histories of flow properties at the acceleration tube exit along the midline. It can be noted that the locations of these points in the model are each slightly different (Table 4.7), as the cell-centered locations will shift with the size of the cell. All three grid resolutions capture the expansion process quite well, with the static pressure and velocity being similar for all simulations. The flow properties of the medium and fine grids show similar traces. The coarse grid simulation predicts the levels of temperature, density, Mach number and pitot pressure which are all significantly lower than the two finer grid simulations. As the grid resolution increases, the boundary layer is decreasing in size and its transition location (drop in Mach number) moves further away from the shock. The differences between the medium and fine grid appear to mainly reside with the timing of the transition of the boundary layer.

To examine the change in radial properties with grid refinement, Figure 4.27 shows the pitot pressure across the acceleration tube exit at 8 ms into the simulation. As shown in Figure 4.26, this is after the drop in pitot pressure has begun. The pitot pressure is seen to be quite different between the three simulations. This is due to differences in shock arrival times which will mean the boundary layer growth and associated effects are compared at different axial distances from the shock. However, grid effects, such as the growth of boundary layer and resolution of wave processes will also cause these discrepancies. The coarse simulation shows the effects of the boundary layer transition between the wall and the centreline, with decreasing pressure when moving towards the wall. As was noted previously, the boundary layer in the finest grid simulation had not grown to its maximum as compared to the other 2 simulations at the same time. To look at the effects of the boundary layer further, temperature is also plotted across the tube (Figure 4.28) with the second graph showing the temperature close to the wall. This reveals that the boundary layer growth is again slightly smaller in the finer grid compared with the medium grid. Near the wall though, the temperature is quite similar between the better resolved grids, although there exists a jump of 240 K from the wall to the first cell even in the finest grid simulation performed here.

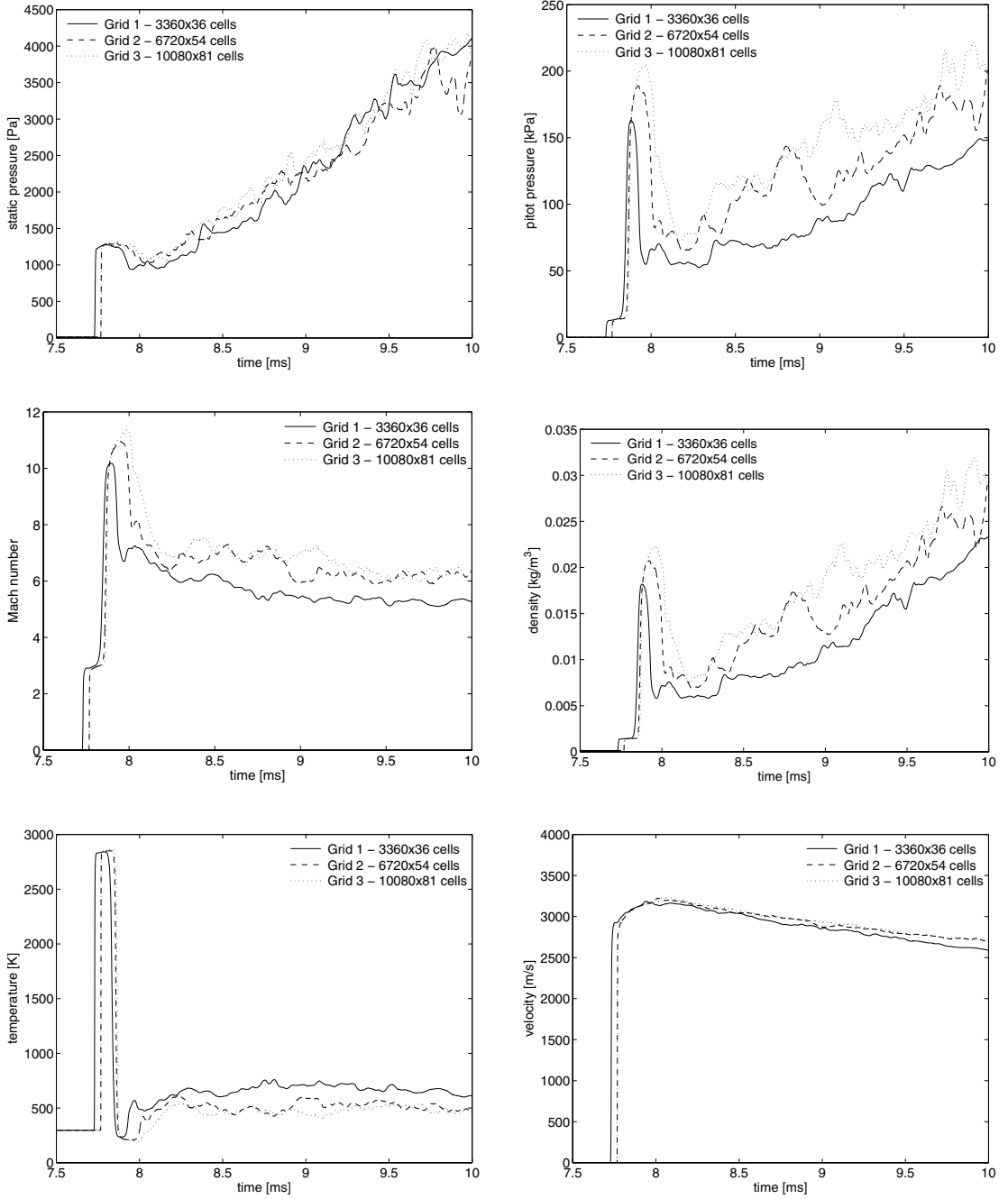


Figure 4.26: Properties at tube exit on the midline for the turbulent simulation of X3 Mach 10 condition with differing grid resolution.

For calculations of shock tubes, the cell based Reynolds number (Re_{cell}) at the wall has been used to describe whether the boundary layer is acceptably resolved [149]. As a *rule of thumb*, the Re_{cell} at the wall must be less than one for confidence to be taken in the grid [149]. However, Sharma and Wilson [149] showed this is difficult to achieve,

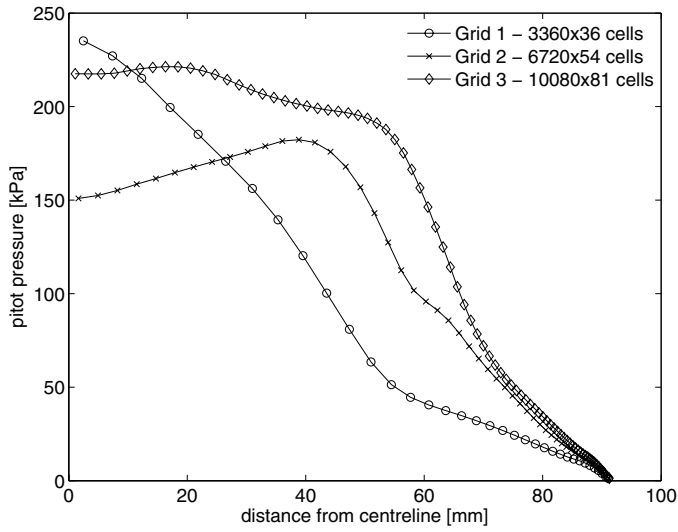


Figure 4.27: Pitot pressure across the acceleration tube exit at 8 ms for varying grid resolutions.

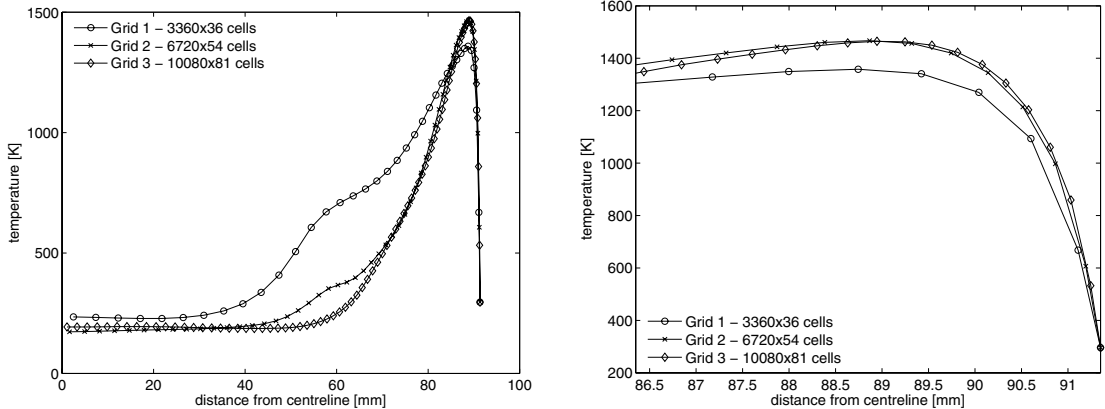


Figure 4.28: Temperature at tube exit at 8 ms for varying grid resolutions.

due to the small height of the boundary near the shock. Also, some latitude must be taken for the present calculations, as the flow encountered for this condition is an order of magnitude higher densities (increasing well above this in the underexpanded test flow) for a similar shock speed and gas. Therefore, this flow could be more comparable to the rule of thumb used in bluff body work where the cell Reynolds number needs to be below 10 for the grid to be trusted for heat transfer calculations. Figure 4.29 shows that the cell Reynolds number for the fine grid is just under 4 for the acceleration gas, and rises to 5 for the test gas. The divergence of the laminar and turbulent gas models indicates the point of transition as seen in the pitot measurements. Although the flow before the arrival of the unsteady expansion shows an acceptable level of grid resolution, the boundary layer through the expansion is not resolved.

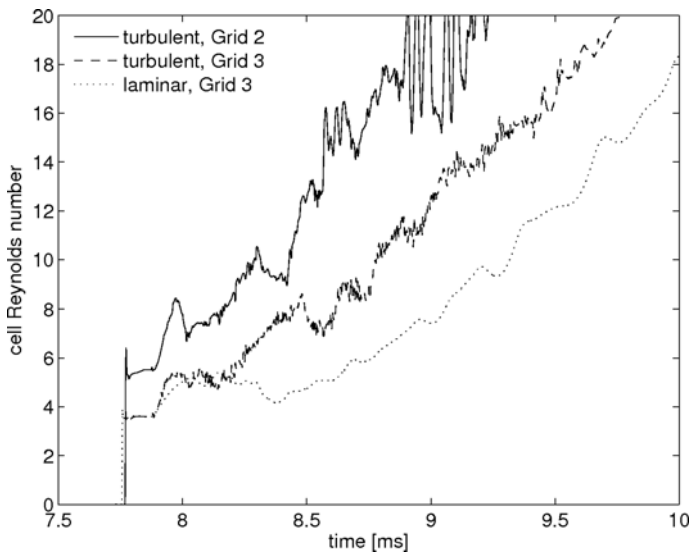


Figure 4.29: Cell based Reynolds number for simulations of X3 Mach 10 condition at tube exit.

Large increases in computational time (on the order of weeks, using 35 processors) are required to achieve a similar increase in grid resolution as shown between each of these grids. Comparing the results between the medium and fine grids, similar flow features and property levels are shown and are also within the experimental fluctuations (Section 4.4.2). Thus, the resolution of the grid was deemed to be adequate for the purposes of this study.

Comparison of experimental and computational simulations

This section gives a direct comparison between the experimental and the numerically obtained data for the flow properties. Flow properties for experimental measurements and both numerical simulation (turbulent and laminar) as shown earlier at the tube exit, are plotted against each other in Figure 4.30 at 52 mm from centreline in the numerical simulations and 45 mm in the experimental measurements¹⁰. The static pressure level is seen to be quite similar between the two numerical simulations where as the experimental measurement is slightly lower. The times of the interruption of the test time by the leading edge of the unsteady expansion are all quite similar. The higher static pressure in the numerical simulations can be seen to significantly increase the pitot pressure. Taking this into account, the turbulent simulation represents the experimental measurement quite well, with pressure matching in terms of both level, timing of the interface, dip in pitot pressure and the arrival of the unsteady expansion. Whereas, the laminar simulation can be seen to correspond well with the others until it diverges at 250 μs , where it follows a similar trend as the static pressure measurements of slightly dipping before the unsteady

¹⁰Static pressure is taken at at8.

expansion arrival. The plots of Mach number, density and temperature show clearly the effect of the turbulent boundary layer swelling compared with the laminar simulation. The velocity is seen to be quite similar between the two numerical simulations.

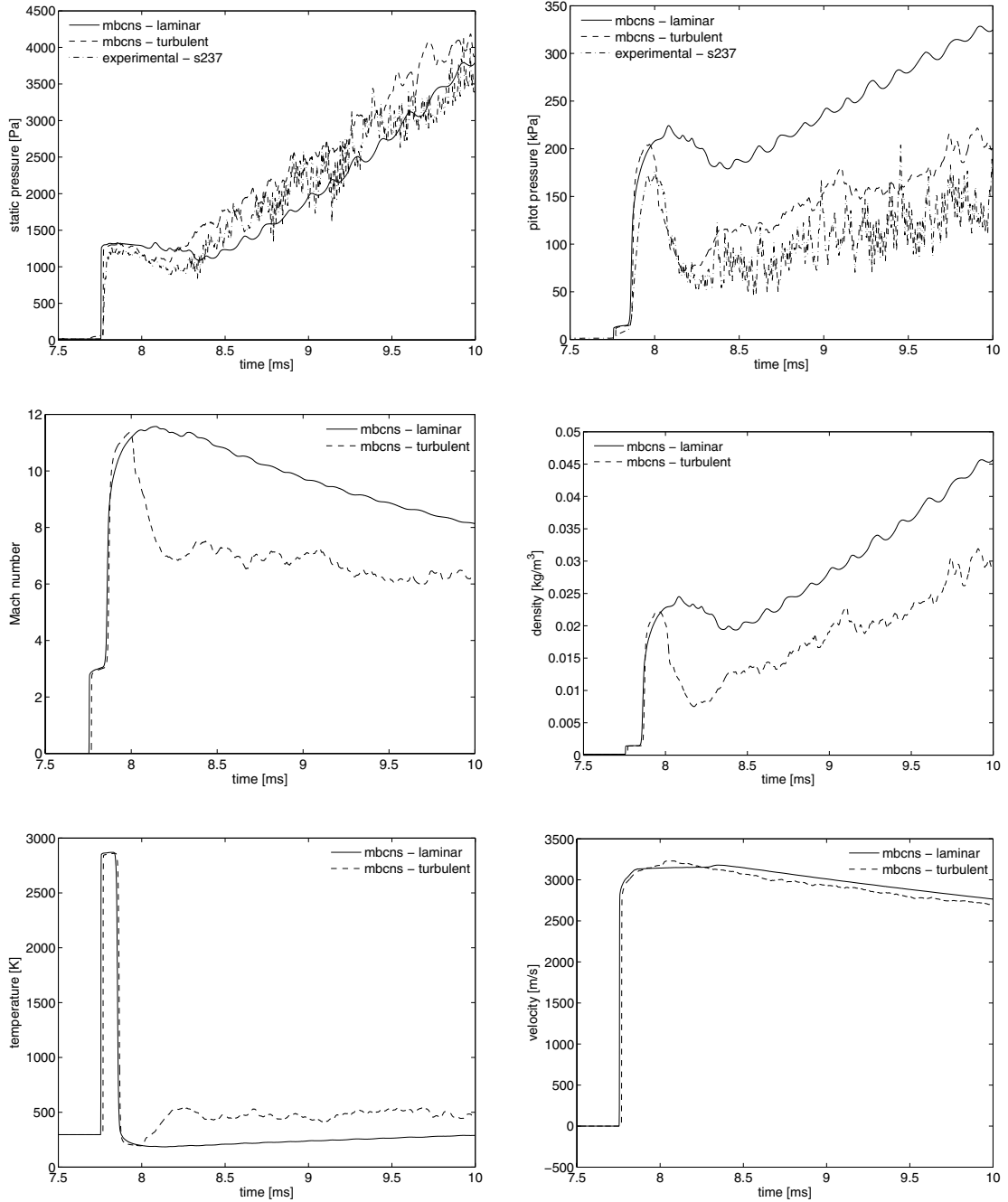


Figure 4.30: Properties at tube exit compared for laminar and turbulent simulations with experimental measurements. Static pressure is at the wall whereas other properties are taken close the centreline.

Shock speeds are shown down the acceleration tube in Figure 4.31. Good agreement is seen in the shock speed down the length of the tube between the experimental and turbulent simulation, with a difference of 20 m/s by at 8, where the laminar simulation is seen to have a slightly higher shock speed once attenuated by approximately 70 m/s. The two numerical simulations are higher than the experimentally measured shock speed, which would explain the lower static pressure measured experimentally. The shock attenuates rapidly as it moves down the acceleration tube, with a large decrease seen in the first 7 m. This same behaviour was theoretically predicted using Mirels [15] calculation of shock and interface attenuation to the same speed shown in Figure 4.12, where attenuation also occurs mostly in the first 7 m from the secondary diaphragm. High shock speeds are also expected initially due to the primary shock reflection off the secondary diaphragm (5 μ s hold time).

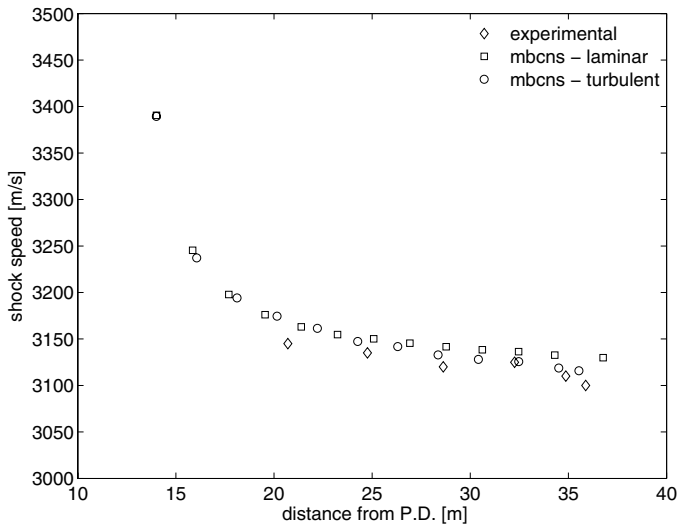
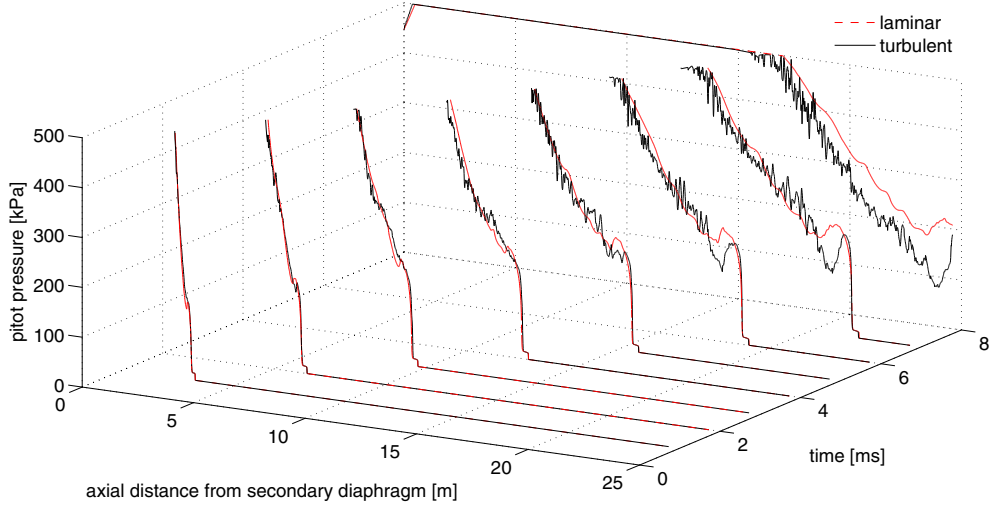
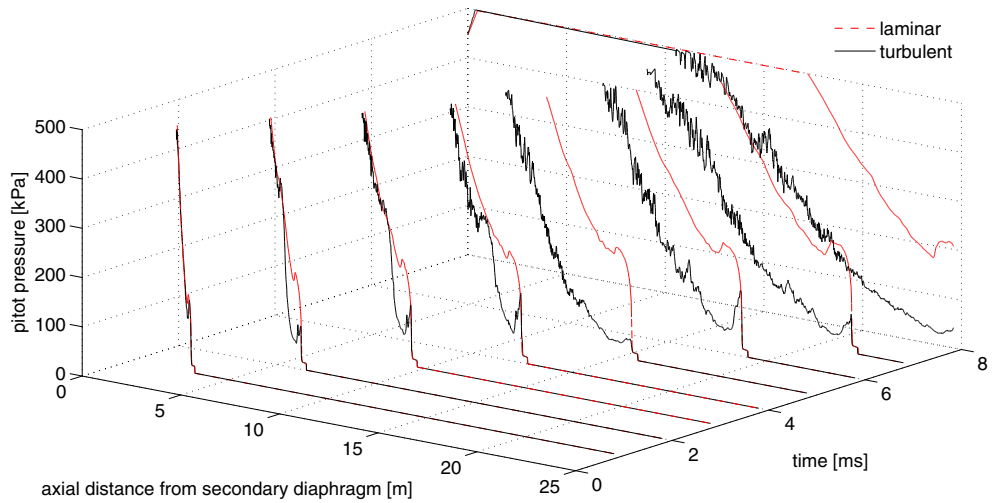


Figure 4.31: Comparison of shocks speeds for Mach 10 condition between computational simulations and experiments.

To explore how the development of the boundary layer occurs between the laminar and turbulent simulation, a comparison pitot pressure is shown axially along the acceleration tube at various times in Figure 4.32. For the radial location shown in previous sections at 52 mm, the difference in pitot pressure during the test flow is seen when the shock is at 5 ms, at 16 m from the secondary diaphragm. After this time, the drop in pitot pressure is seen to grow and is not reflected in the laminar simulation. Closer to the wall, at a position 70 mm from the centreline, the drop in pitot pressure within the test flow can be seen immediately in the turbulent simulation. This is due to the increase in boundary layer height behind the contact surface, where the laminar simulation boundary decreases immediately.



(a) 52 mm radially



(b) 70 mm radially

Figure 4.32: Comparison of the pitot pressure axially along the acceleration tube for laminar and turbulent simulations at various times.

Contour plots showing the Mach number and the log of density when the shock has reached 22 m from the secondary diaphragm (Figure 4.33) clearly show the differences in the laminar and turbulent simulations. Comparing the laminar and turbulent simulations¹¹, the two are similar until the interface. The growth of the boundary layer in the first 300 mm behind the interface in the turbulent solution is quite large compared with the laminar solution. This includes a region of lower Mach number gas sitting between

¹¹Laminar simulation is the top half of the tube and turbulent is the bottom half.

the boundary layer and the core flow. After this, there is then a quick growth in the low Mach number region of the turbulent simulation engulfing a significant portion of the tube (exterior 50 mm). The low density region can also be seen to be significantly larger in the turbulent simulation. Figure 4.34, shows line contours of pitot pressure at this same location. As measured experimentally, the decrease in pitot pressure due to boundary layer growth occurs quite rapidly in the turbulent simulation. Whereas the laminar simulation the pitot pressure is relatively constant across the entire tube. As explored previously, there is a large underestimation of the extent of boundary layer growth. Apart from the low pitot pressure region on the walls present in the turbulent simulation, it can also be noted the oscillations in the flow are less in the laminar simulation.

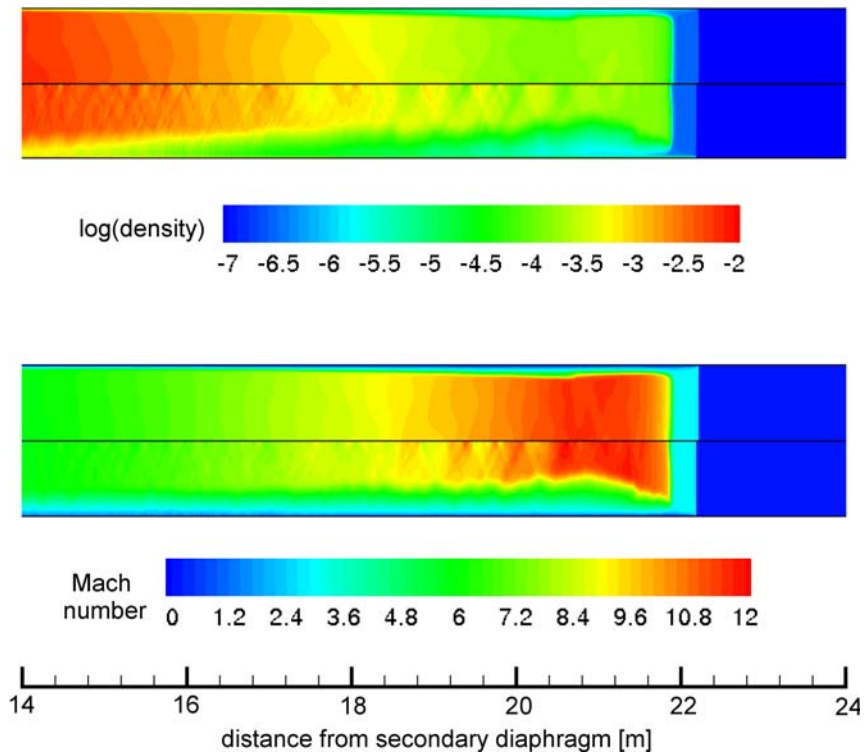


Figure 4.33: Comparison of contour plots of density and Mach number for laminar and turbulent simulations at 7 ms.

Table 4.8 shows a comparison of these flow properties measured half way through the predicted test time ($250 \mu\text{s}$ behind the interface). The turbulent simulation gives a better comparison of the flow properties seen in the experiment than the laminar simulation. However, the turbulent simulation does not predict the rapid growth of the boundary layer which engulfs the entire tube instantaneously in time, as seen in the experimental measurements. This could be better resolved with perhaps a finer grid, although this is not assured. The use of a different turbulence model like a two equation turbulent kinetic energy model might be more appropriate, although the simulation time would be further

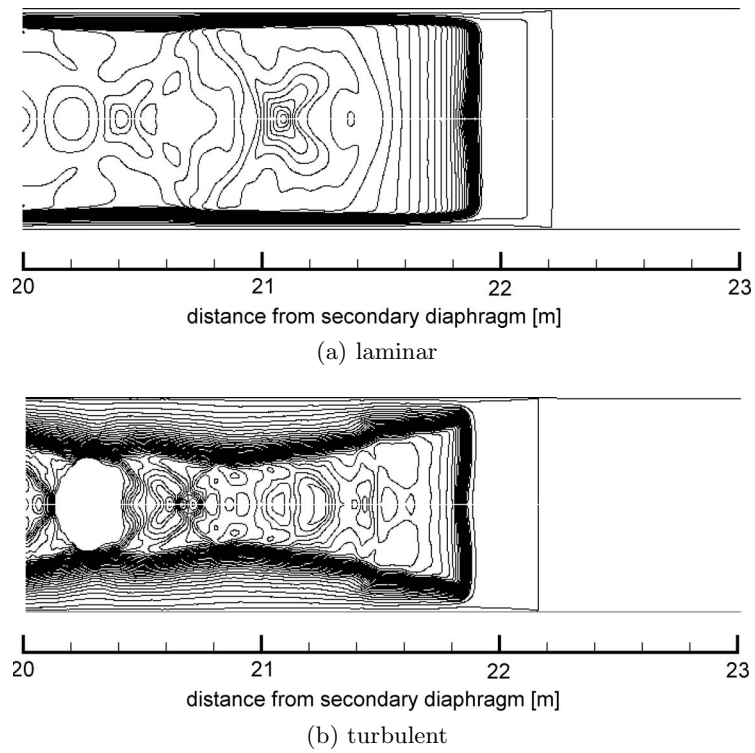


Figure 4.34: Pitot pressure contours for laminar and turbulent simulations of X3 Mach 10 condition at 7 ms.

increased. For the purpose of this work the Baldwin-Lomax model has been shown to give enough data to resolve the flow phenomena seen in the experiment.

Table 4.8: Flow conditions for X3 Mach 10 condition.

Property	Experimental	L1d	MB_CNS	MB_CNS
		Laminar	Turbulent	
<i>Shock tube</i>				
Primary Shock Speed [$m s^{-1}$]	1442	1441	-	-
Shock Tube Pressure [MPa]	592	613	-	-
<i>Acceleration tube</i>				
Secondary Shock Speed [$m s^{-1}$]	3108	-	3131	3122
Static Pressure [kPa]	1.28	-	1.32	1.30
Pitot Pressure [kPa]	168.1	-	212.2	204.1
Mach Number	-	-	11.5	11.2
Density [kg/m^3]	-	-	0.0232	0.0224
Static Temperature [K]	-	-	210	200
Velocity [$m s^{-1}$]	-	-	3129	3132
Stagnation Enthalpy [MJ/kg]	-	-	5.11	5.11
Unit Reynolds number [million/m]	-	-	5.25	5.29
Test Time [μs]	150	-	530	130

4.5 Boundary Layer Transition

With the likely cause of the drop in pitot pressure across the tube simultaneously attributed to boundary layer transition, this flow phenomena is investigated further. Prediction of boundary layer transition in hypersonics is still a large research area, as no single theory can accurately represent this phenomena for all flow cases and some phenomenon cannot be accurately predicted with any theory. Boundary layer transition in a expansion tube is quite different to that seen for a generic flat plate in hypersonic flow, as shown in Figure 4.35. In the case of flow over a flat plate, the transition location can usually be located by using a transition Reynolds number (Equation 4.4) based on past experimental measurements or analytical expressions.

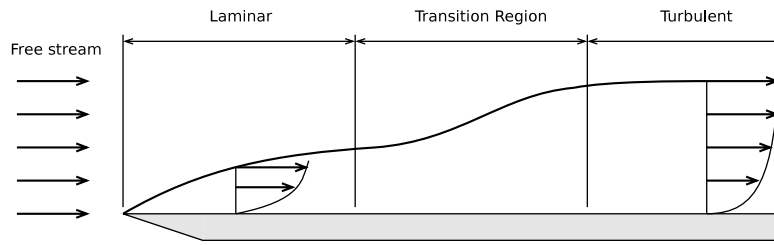


Figure 4.35: Transition from laminar to turbulent boundary layer for a flat plate in hypersonic flow. Adapted from [9].

$$x_t = \frac{Re_t \mu_\infty}{\rho_\infty U_\infty} \quad (4.4)$$

The time dependency of the development of a boundary layer along the wall of the flat plate is quite complex. Figure 4.36 shows the development of a shock initiated boundary layer over a flat plate. It can be seen although the boundary layer close to the leading edge may have reached steady state, the boundary layer initiated from the shock is still quite unsteady. As a similar dependency is shown in expansion tube boundary layer development, a review is presented of the unsteady development of a shock induced boundary layer over a flat plate¹². Figure 4.37 shows experimental data from Davies et al. [22] of the distance and time development of a boundary layer produced by hypersonic flow passing over the body, preceded by a shock wave. The value α relates to the path taken through the x - t plane of a gas particle compared to the path taken by the leading edge particle path ($\alpha = \frac{x}{U_2 t}$). The shock travels at a higher speed (w_1) than the flow behind it (U_2). Particles of gas that start on the plate itself (which will end up lying between the shock and the leading edge particle path), where $\alpha > 1$ from Equation 2.1 is precisely the boundary layer that would be formed on a plate without a leading edge in the shock stationary

¹²This is quite similar to the development of a boundary layer on a shock tube wall.

co-ordinate system [150] and therefore quasi-steadiness can be assumed. Transition occurs at the location and time were both the maximum momentum thickness (approximately $0.57 < \alpha < 0.6$) and transitional Reynolds number coincide. The transition location is seen to propagate downstream in a non-uniform manner, unless it crosses into the region where less than one flow length has passed and therefore it will stay at a constant distance from the shock.

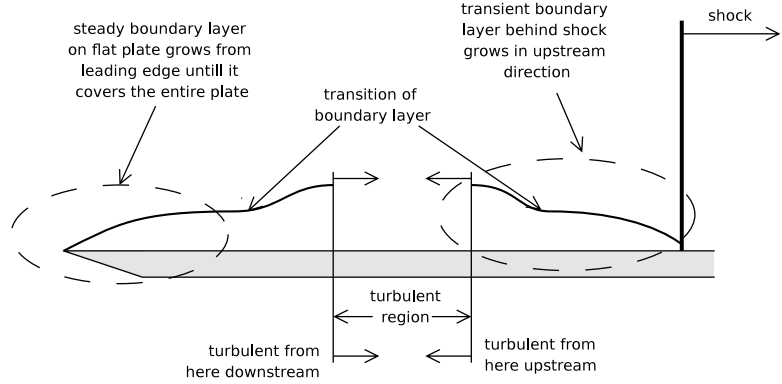


Figure 4.36: Transition from laminar to turbulent boundary layer for a flat plate in hypersonic flow with unsteady, shock initiated flow.

The heat transfer seen by a transducer at an axial location on the plate will initially jump to extremely high levels (dependant on the shock thickness) and diminish with $(t - t_s)^{-\frac{1}{2}}$ for a laminar boundary layer. This can be seen in the predicted heat transfer rates shown in Figure 4.38. For the locations upstream of transition, once slices of gas arrive that were not initially at rest on the flat plate, the heat transfer rate will take an indeterminate path and eventually come to a steady state value (for steady flow of incoming gas) after $\alpha = 0.3$ (or approximately three flow lengths). This is due to the gas coming from the freestream not being able to be processed in the quasi-steady, shock stationary system. If the axial location is past the transition location, the heat transfer rate will inflect (gradient is zero) and rise. If the location is far enough downstream, the heat transfer will reach a steady state level once the turbulent boundary layer is fully developed (which is usually one flow length after the passing of the shock).

To compare with the flat plate analogy, an expansion tube can be viewed in the shock steady frame of reference as seen in Figure 4.39. The boundary layer is allowed to develop from a single point as in the flat plate case. However, the flow velocity profiles in this reference frame, are reversed as if the wall is travelling at the same speed as the incoming flow of un-shocked acceleration gas. Transition of the boundary layer is affected by the incoming free stream turbulence and acoustic waves. This should not occur in the shocked acceleration gas¹³, assuming care has been taken in creating an acoustic buffer across

¹³This assumes mixing does not occur at the interface.

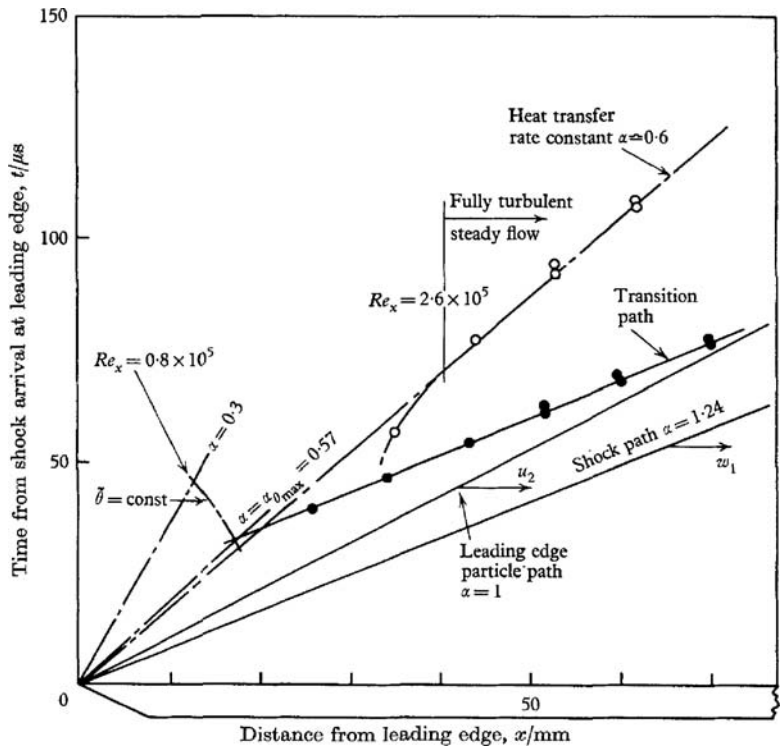


Figure 4.37: Distance-time diagram for a shock-induced boundary layer on a flat plate showing shock, transition and fully developed turbulent boundary layer locations including experimental data. Taken from [22].

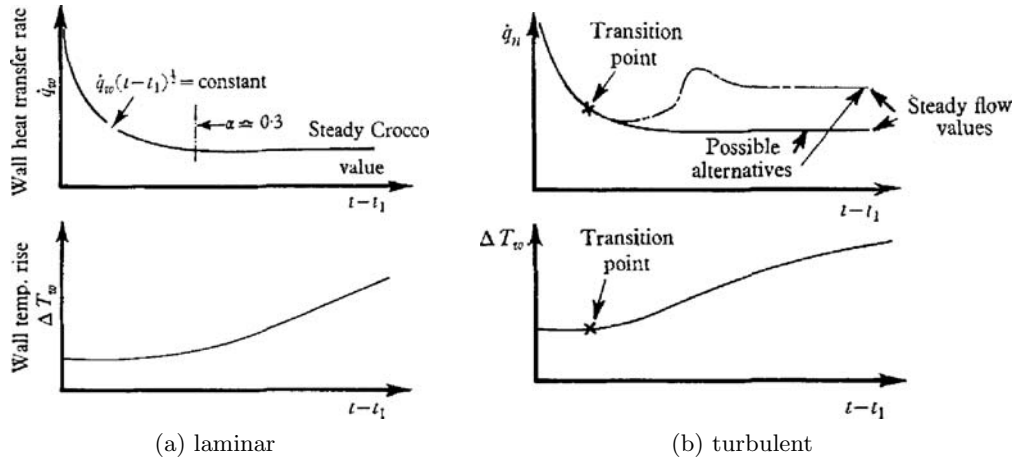


Figure 4.38: Idealised heat transfer and temperature measurements for a shock-induced boundary layer on a flat plate. Taken from [22].

the the driver/test gas interface [93]. Therefore, the boundary layer development should occur up until this point in a similar fashion to that in the flat plate described previously. This is the case in shock tubes, whereby transitional Reynolds numbers have been used successfully in predicting transition location. In expansion tubes however, the acceleration

slug has low Reynolds numbers before the interface due to very low densities and length scales making transition unlikely. After the interface, boundary layer development is influenced by the expanded test gas which has differing flow properties to the acceleration gas, including a much higher density. This would provide a distinct change in the heat transfer at the interface location (or where $\alpha = 1$). Also, this flow will have free stream turbulence from interaction with the diaphragm opening [41] and boundary layer interactions. Thus it makes it difficult to predict transition in a expansion tube due to the influences of both the developing boundary layer from the acceleration gas and expanded test gas boundary layer addition and flow history.

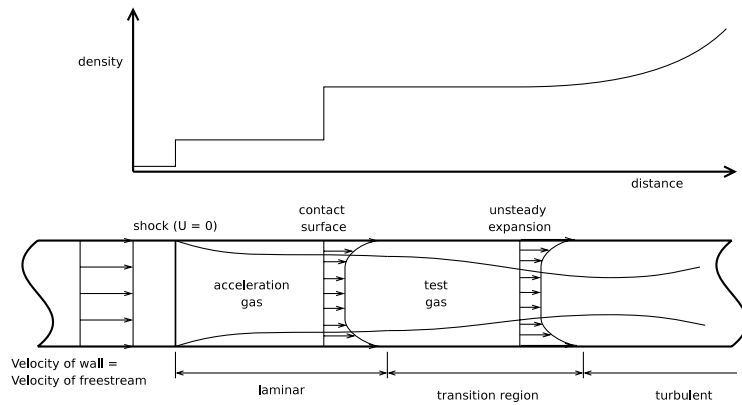


Figure 4.39: Transition from laminar to turbulent boundary layer in an expansion tube (shock steady frame of reference).

4.5.1 Review of expansion tube boundary layer studies

The relation between dip in pitot pressure and boundary layer transition was first hypothesised by Jones and Moore [88] following unexplained experimental measurements taken in the Langley pilot expansion tube. Weilmuenster [24] was the first to investigate this sudden decrease in pitot pressure (with constant static pressure) and determined that the phenomenon was caused by boundary layer transition occurring a *considerable* time after the passing of the contact surface of the acceleration/test gas. Experimental pitot surveys at different axial locations showed that a turbulent boundary layer can grow to engulf the entire tube diameter with increasing axial distance. A method was developed that used an integration of free stream Reynolds number based on particle tracking from the initially shocked test gas, then through the unsteady expansion to determine the transition time for various locations for a given transitional Reynolds number. A reasonable match was seen when compared with experimentally derived measurements of transition location for three different experimental conditions.

In surveying the Langley tubes performance, Shinn and Miller [23] recorded full pitot surveys at the tube exit of the flow for variances in acceleration tube fill pressure. The higher fill pressure conditions saw a drop in pitot pressure, where heat transfer measurements confirmed transition was occurring. Figure 4.40 shows pitot pressure presented by Shinn and Miller at various locations at the acceleration tube exit where boundary layer transition has occurred with an acceleration tube fill pressure of 52.6 Pa. This phenomenon has also been further documented on the Langley tube both experimentally and numerically and also attributed to the transition of the boundary layer[90, 132]. It was noted that due to test flow disturbances, including boundary layer transition, the range of conditions at low enthalpies was limited.

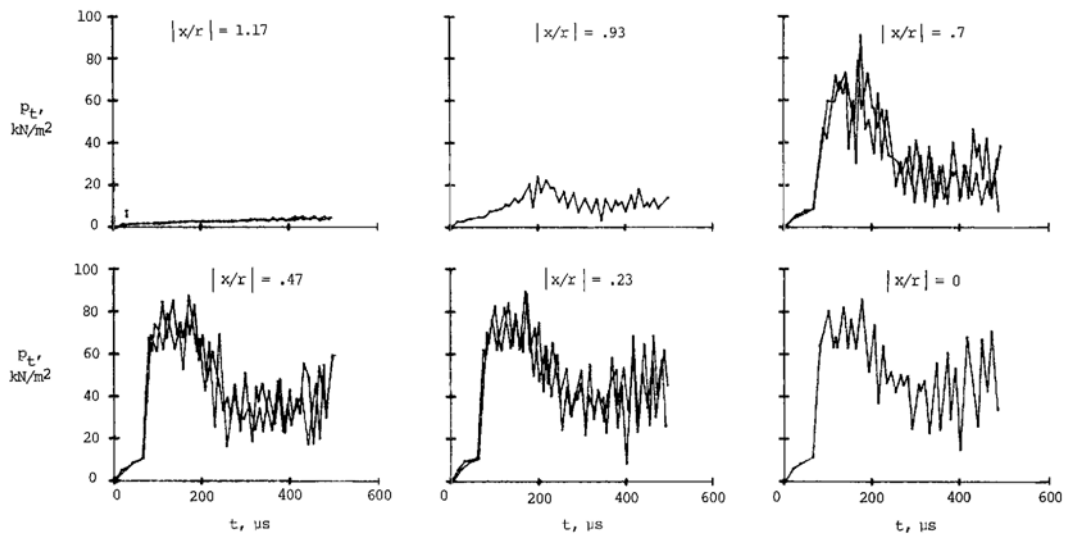


Figure 4.40: Pitot pressure in Langley pilot expansion tube for transitional condition. Taken from [23].

The refurbished Langley tube (HYPULSE facility at GASL) solved some of the other flow disturbance problems detailed in the Langley era, but again found the problem related to the boundary layer transition at low enthalpy conditions [80, 41, 131]. Work on this low enthalpy condition in the HYPULSE facility determined that increasing the unit Reynolds number of the test gas could mitigate some of the more severe effects of boundary layer transition by moving the transition location closer to the contact surface or decreasing the boundary layer thickness relative to the tube diameter, although the condition would have to differ in free stream properties (mainly density). A “rule of thumb” was created to determine whether a condition was viable due to being fully turbulent or laminar based on the unit Reynolds number of the expanded test gas. Later, computational simulations [131] using a turbulent boundary of these conditions used a fixed transition location determined by experimental data. This gave good agreement between the pitot pressure effects associated with boundary layer transition and those measured experimentally.

4.5.2 Theoretical predictions of boundary layer transition

The first method established to predict transition in an expansion tube was proposed by Weilmuenster [24] using experimental data from the Langley pilot expansion tube. It is based on an integrated Reynolds number method, given in Equations 4.6, whereby a particle's Reynolds number is tracked through its motion from initially being at rest in the shock tube, shocked and accelerated (region 2 on Figure 3.1) where flow properties are reasonably constant, variable conditions while passing through the unsteady expansion into the acceleration tube, where conditions are again constant (region 7 on Figure 3.1). By inverting this, for a given transitional Reynolds number (this was between 30-60 million for Langley tube conditions) for each axial location down the tube, the time of transition can be calculated by tracking particles integrated Reynolds numbers from their original state of rest. This is the opposite of conventional transition calculations such as those used in shock tubes, whereby the Reynolds number is calculated from the starting axial location of the shock. In expansion tubes however, this takes the gas through its full flow history in the bulk direction of travel. This process of predicting transition is the reverse of what would be undertaken for the flat plate case discussed previously.

$$Re_t = \sum Re_i \quad (4.5)$$

$$Re_i = \int_{x,i} Re_{l,i}(x)dx \quad (4.6)$$

This process is shown in Figure 4.41, where 4 slices of gas travel through tubes on the right of the diagram. The crosses indicate the position of transition for each gas slice during its travel towards the acceleration tube exit. On the left of the diagram, the gas slices intergrated Reynolds number is shown, where the test gas will have a much higher integrated Reynolds number due to the high density of the gas until expanded to the test flow density. Thus, transition can occur in either the shock or acceleration tube and will be condition dependant.

To investigate the likely transitional point down the tube for the X3 condition, the transitional Reynolds number has been varied from 100-200 million in Figure 4.42. Gas properties for the shock tube are used from the *L1d* computational simulation and acceleration tube properties are taken from the axisymmetric, turbulent computational simulation. The positioning of the shock wave and interface are assumed to be of constant velocity (i.e. straight line), with the time from the leading edge of the $u - a$ wave taken at the end of the tube obtained from the computational simulations. All the input information for the analytical calculations can be seen in Table 4.9. The plot shows that transition will occur during the test time within the transitional Reynolds number bounds given by Weilmuenster. For the transitional Reynolds number of 100 million, an increase in the

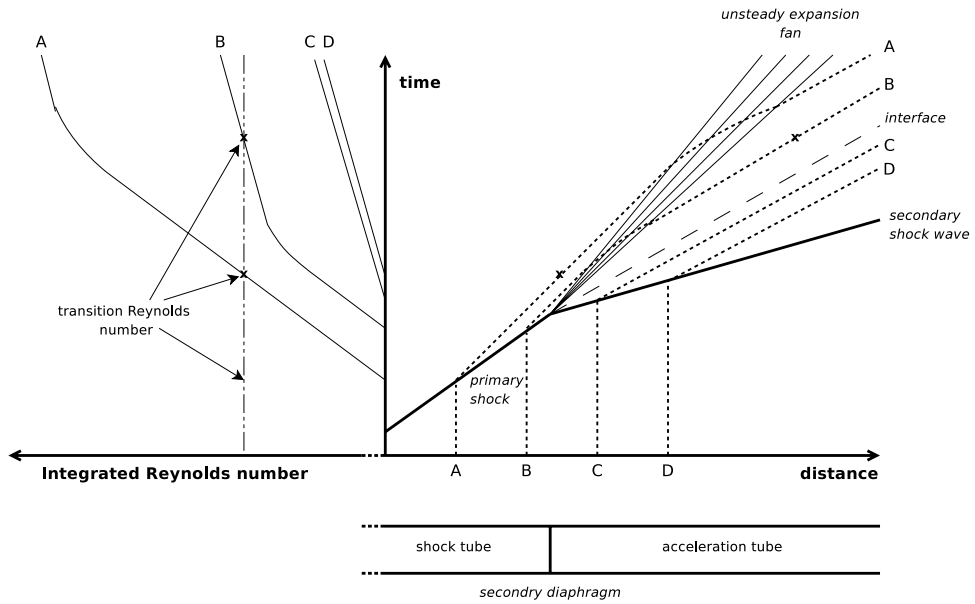


Figure 4.41: Schematic of particle integration process of Reynolds number in Weilmuenster's method [24] of calculating transition location in an Expansion tube. Particles A and B start in the shock tube, with particles C and D starting in the acceleration tube with the dotted lines showing their path through the flow processes, and crosses show transition locations.

test time may be possible by shortening the tube to where the transition point crosses the tail of the unsteady expansion, giving a slightly longer test time. It has also been noted by Erdos et al. [80] that if the transition of the boundary layer occurs just after the acceleration/test gas interface, as it does for the 200 million transitional Reynolds number case, the condition is not adversely affected directly by the transitioning. Rather, the test time can be terminated by the growth of the boundary layer into the test core, whereby shortening the acceleration tube, can maximise the test time. Therefore, it seems likely that if the transitional Reynolds number for the X3 facility is over 100 million, the condition will be unusable.

Table 4.9: Summary of flow values used in analytical prediction of transition location.

Velocity of primary shock wave, U_{s1}	1441 m/s
Velocity in shock tube, U_2	1118 m/s
Sound speed in shock tube, a_2	688 m/s
Density in shock tube, ρ_2	1.928 kg/m ³
Temperature in shock tube, T_2	1164 K
Velocity in acceleration tube, U_7	3132 m/s
Time between interface and $u - a$ wave, t_{test}	520 μ s
Time between interface and secondary shock wave, t_{accel}	110 μ s

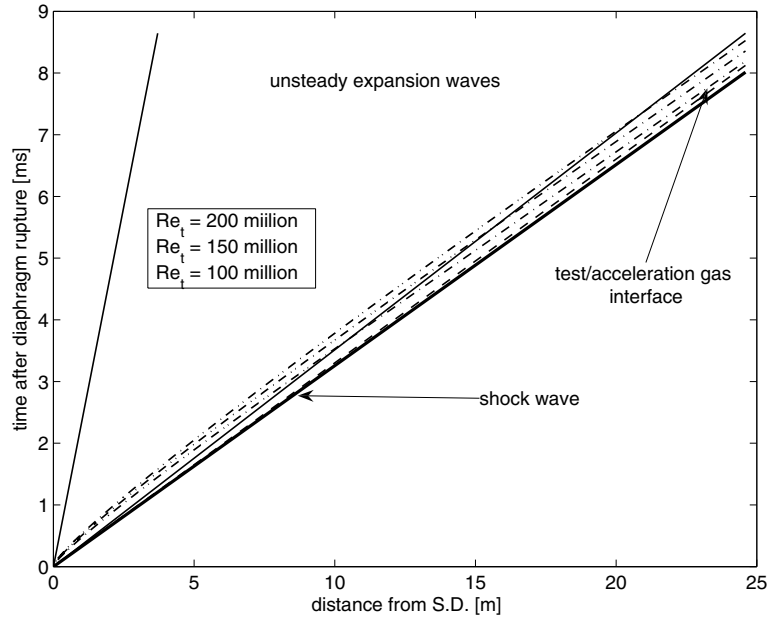


Figure 4.42: Distance-time diagram of analytically predicted boundary layer transition location and time in the X3 Mach 10 condition. The Re_t are plotted with the lowest occurring first in time.

A second simpler method has been used in the HYPULSE expansion tube by Erdos et al. [41], suggesting that the transitional region of operation can be predicted by the unit Reynolds number. The transitional region is stated to be between the fully turbulent lower boundary limit of 1.4 million per metre and the fully laminar upper boundary limit of 0.7 million per metre. It was established that for a 10.2 MJ/kg total enthalpy condition with a unit Reynolds number of 1.44 million per metre, the test gas slug was fully turbulent. However, this condition could still be used with a shortened acceleration tube to limit boundary layer growth. The unit Reynolds numbers of the transitional X3 condition was 3.44 million per metre which suggests a dependency on more than just the test gas Reynolds number for boundary layer transition. Intuitively, boundary layer transition Reynolds number should be facility and condition dependent and therefore be affected by such things as tube diameter and length, wall roughness, free stream turbulence and flow condition parameters.

The two methods described above are solely dependant on the test gas, with no consideration of the acceleration gas which makes up a significant part of the boundary layer (approximately 4mm). This would either imply that transition is only dependent on the properties of the test gas, with no consideration of the properties or composition of the boundary layer (different gas compositions or thicknesses) or that the boundary layer is mostly made up of test gas after the passing of the contact surface. This is of interest,

as the transition time can be derived in most shock tube work by taking the transition point for the Reynolds number based on the time after the arrival of the shock [151], as written in Equation 4.7, where the transitional Reynolds number is usually in the order of 650,000. The shocked conditions, which in an expansion tube is the acceleration gas are taken into account first and then the expanded test gas. Though as stated previously, using this method would imply the minor importance that the acceleration gas has on boundary layer transition due to its low density and small slug length.

$$Re = \frac{\rho U^2 t_s}{\mu} \quad (4.7)$$

4.5.3 Experimental measurements

To both diagnose and to locate the boundary layer transition time, heat transfer measurements were taken at various axial locations on the wall of the tube. A similar process was used in the Langley tube [24, 23, 41] to determine transition location. Figure 4.43 shows heat transfer measurements in a transitional condition taken by Shinn and Miller [23] in the Langley tube. They noted that transition occurred when there was a step rise in the heat after relaxing from the passing of the shock. The boundary layer has therefore transitioned at approximately $280 \mu s$ at 7.75 m and $210 \mu s$ at 12.23 m . This also shows the phenomenon of the transition location getting closer to the interface further down the tube, which is quite similar to the predictions of Weilmuenster [24] for expansion tubes and shock induced boundary layer growth on a flat plate.

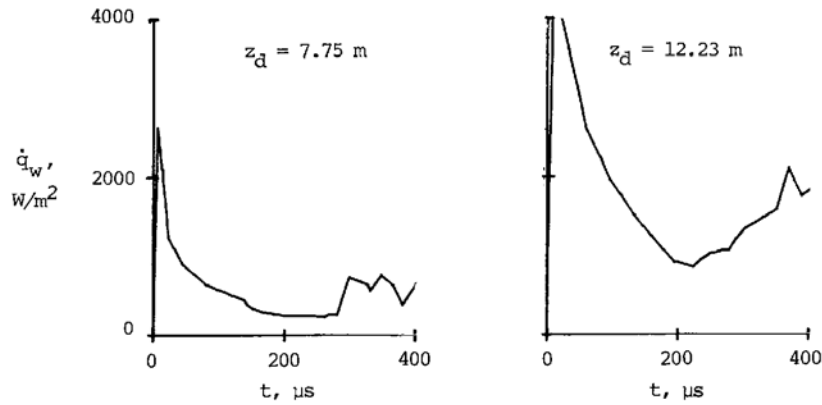
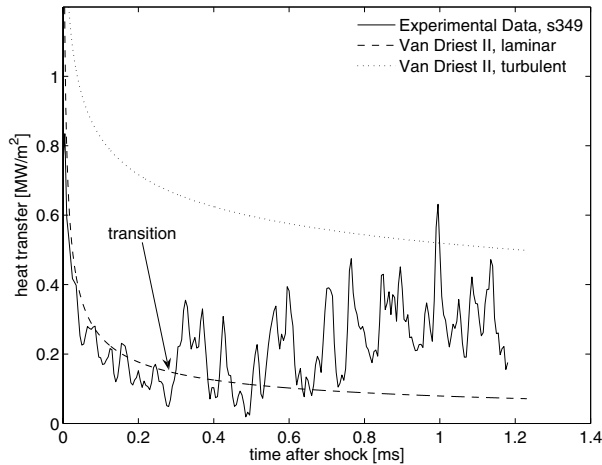


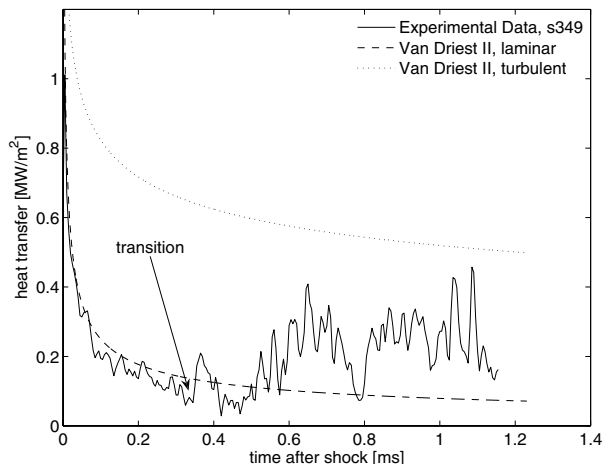
Figure 4.43: Heat transfer measurements taken in the Langley expansion tube. Taken from [23].

Measurements were undertaken in the X3 tube using thin film heat transfer gauges as described in Section 4.1.1. These were at positions at3, at5 and at7 in Table 4.1, although the heat transfer gauge at at7 failed to give reasonable data. These measurements are compared with theoretical values of both the laminar and flat plate predictions of

van Driest [25] in Figure 4.44. The freestream flow properties used in the calculation of heat transfer are those derived if the Mach number in the test gas of the experiments is assumed to be 10 and a wall temperature of 296 K. Although geometrically different and neglecting the acceleration slug gas effects, this gives a sensible guide to what heat transfer measurements may be expected. The heat transfer rates are transformed from distance to time by using the flow velocity. The experimental values are fairly consistent with the laminar predictions for the first section of flow. This is seen to change at a certain point, which is where the heat transfer level rises, but is still well below that predicted by van Driest for turbulent flow. This change though, could be significant enough to be caused by boundary layer transition although noise is quite significant in these measurements.



(a) 10.258 m from secondary diaphragm



(b) 17.967 m from secondary diaphragm

Figure 4.44: Experimental measurements of heat transfer from shot s349 vs van Driest flat plate predictions [25].

With the transition location occurring when the heat transfer diverges from the van Driest predictions in the two experimental measurements, the period for each is $280 \mu s$ and $345 \mu s$. Plotting this in Figure 4.45 the heat transfer predictions match reasonably well with the transition location calculated using Westminster's theory [24] with a transitional Reynolds number of 125 million. This uses the same properties as described in the previous section. From pitot measurements, the time after interface arrival to the drop in Mach number is $250 \mu s$, which corresponds well to that predicted using this method. From this, it can be concluded that the Weilmuenster theory works well for this condition in predicting transition location.

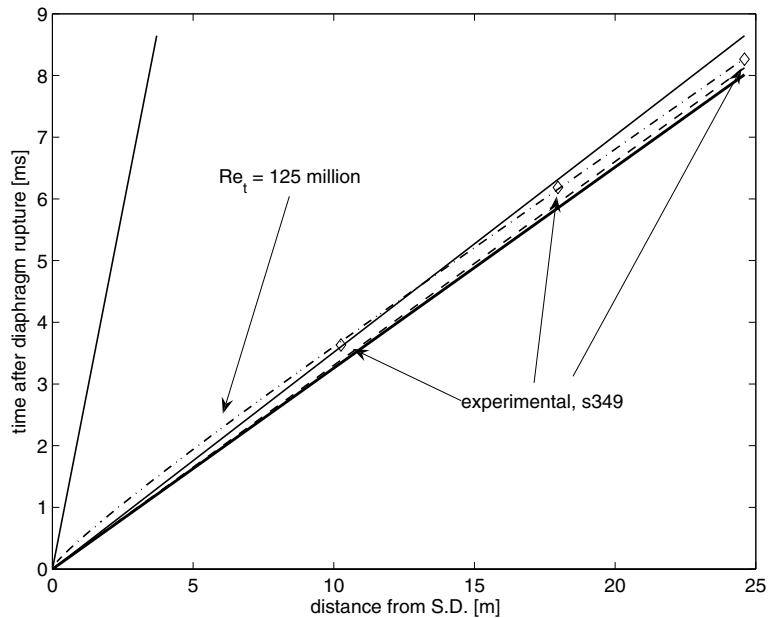


Figure 4.45: Distance-time diagram of Weilmuenster's [24] analytical prediction of X3 boundary layer transition versus experimental measurements.

4.5.4 Numerical simulations

Numerical simulations of an expansion tube with turbulent boundary layers have been conducted before [131, 103], though they haven't included a numerical transitional model. The calculations by Nompelis et al. [103] assumed that there was fully developed boundary layers throughout the facility, which will show incorrect results. The turbulence model used by Wilson et al. [131] in the simulations of the HYPULSE was the Cebeci and Smith model [152], which is another algebraic model. Wilson et al set the transition point at a certain distance from the shock, taken from experimental data. The results of this showed similar results to those found experimentally, although the simulated flow condition had

the transition location at the interface and had few problems with large scale boundary layer growth.

A numerical simulation has been completed of the X3 condition using the Baldwin-Lomax turbulence model [147], with the transition criteria of comparing freestream viscosities to that of the turbulent viscosity within the boundary layer. The turbulence model is a “switch” at each axial location, comparing the turbulent viscosity to that seen in the free stream. Therefore, to calculate the transition location, the simulation will take into account the flow history of both the expanded test gas from its original stagnation in the shock tube and the boundary layer composition from its start at the secondary shock back downstream through to the interface. A further description of this can be found in Section 4.4.2.

The axisymmetric, viscous simulations were undertaken with the *MB-CNS* [140] Navier-Stokes solver using both a turbulent boundary layer and a laminar boundary layer for comparison. The simulation procedure is described in more detail in Section 4.4, including initial conditions, geometry, grid resolution and boundary conditions. This also gives results for the simulations where it was seen that the boundary layer is underestimated. This could be due to the grid resolution used or the turbulence model selected.

The heat transfer can be calculated by transforming the temperature trace near the wall. Heat transfer at any point in a fluid flow can be derived by Equation 4.8a. An approximation near the wall can be made by Equation 4.8b, where the conductivity of the gas (air) which is dependent on the gas temperature. As a simplification, the thermal conductivity is assumed to be constant at 65 W/m K (value at 296 K). Comparing both a laminar and turbulent simulation to the experimental data (Figure 4.46), it can be seen that the experimental transition location is quite close and was previously diagnosed correctly. The turbulent heat transfer is seen to rise at this point and diverge from the laminar simulation at the experimental transition location. The level once turbulent, is seen to be lower than that measured experimentally. As mentioned previously, the boundary layer height once turbulent is underestimated in this simulation so therefore it is expected that the heat transfer predicted at the wall should be lower than that measured experimentally. Also, the simulation will not be able to resolve the thermal boundary very well at all, due to the high grid resolution required in any turbulence model close to the wall to resolve the laminar sublayer (unless “wall functions” are used to integrate the effect of the sublayer). This can explain some of the difference between the heat transfer measurements.

$$\dot{q} = -K \frac{\partial T}{\partial y} \Big|_y \quad (4.8a)$$

$$\dot{q} \approx -K \frac{\Delta T}{\Delta y} \Big|_{wall} \quad (4.8b)$$

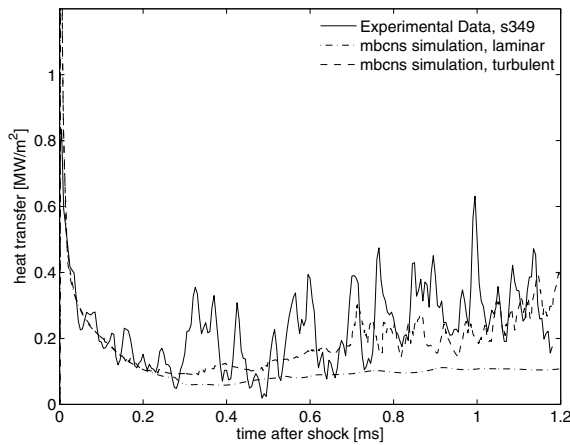
Comparing the location of the pitot pressure dip in the midline of the tube from the turbulent simulation and the wall heat transfer divergence from the laminar simulation (Figure 4.47), shows good agreement of transition location. The plateauing of the turbulent heat transfer also corresponds to the increase in pressure from the unsteady expansion. Comparing the location down the tube of where the heat transfer changes between the laminar and turbulent simulations with the analytical predictions in Figure 4.48, again shows good agreement with the experimental measurements. As the first measurement location of heat transfer (at3), transition is seen to occur earlier than the prediction and matches the time of the head of the unsteady expansion. The higher density flow could be tripping the boundary layer earlier due to free stream disturbances in this region.

4.5.5 Possible solutions to boundary layer transition

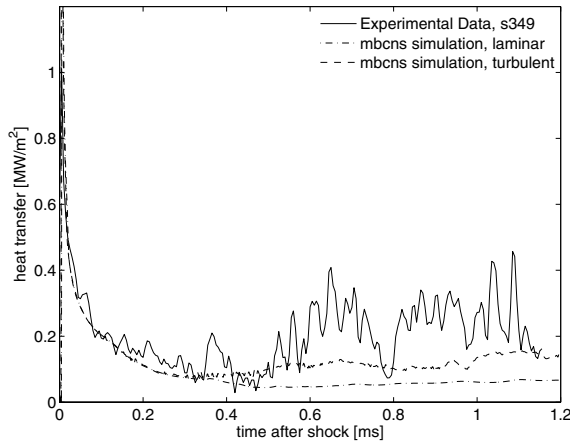
As expansion tube facilities are the only current facility capable of producing both the total enthalpy, total pressure and gas composition requirements above Mach 10 for hypersonic airbreathing ground testing, it is desirable to find a solution to the boundary layer transitioning problem. For some cases, the shortening of the expansion tube may be a possible compromise if the test time can be increased enough. Also, the increasing of Reynolds number as suggested by Erdos et al. [41] to promote early transition may be a suitable compromise in some conditions. However, it seems neither of these ideas can be used for the Mach 10 replication condition aimed for in X3. Two possible solutions are proposed; (1) use of a steady expansion nozzle to promote early transition by increasing the test gas unit Reynolds number while still replicating the condition or (2) use of a different acceleration gas to delay transition. These two solutions are both discussed and either explored experimentally or numerically to test whether the condition could still be achieved without adverse effects caused by boundary layer transition.

Tunnel mode of operation

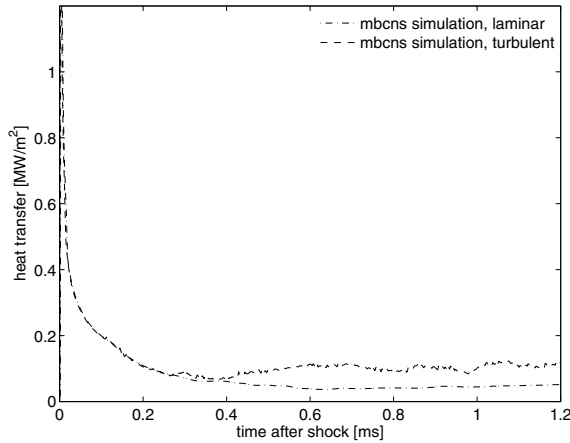
Steady expansion nozzles have been used previously to increase both flow core size and test time in an expansion tube [3, 129]. As the problem of boundary layer transition has been viewed to be relieved by having a high unit Reynolds number in the test gas and a short acceleration tube length[41], it is proposed that a steady expansion nozzle should enable both these criterion to be met while still matching the desired free stream properties. To achieve the same condition aimed for previously, a higher density, higher temperature condition must be produced in the acceleration tube and then expanded through a steady expansion nozzle thereby dropping the temperature and density to the desired level. With the high ρL scaling capabilities of an expansion tube, the loss in density can easily be met.



(a) 10.258 m from secondary diaphragm



(b) 17.967 m from secondary diaphragm



(c) 26.566 m from secondary diaphragm

Figure 4.46: Experimental measurements of heat transfer from s349 compared with computational simulations.

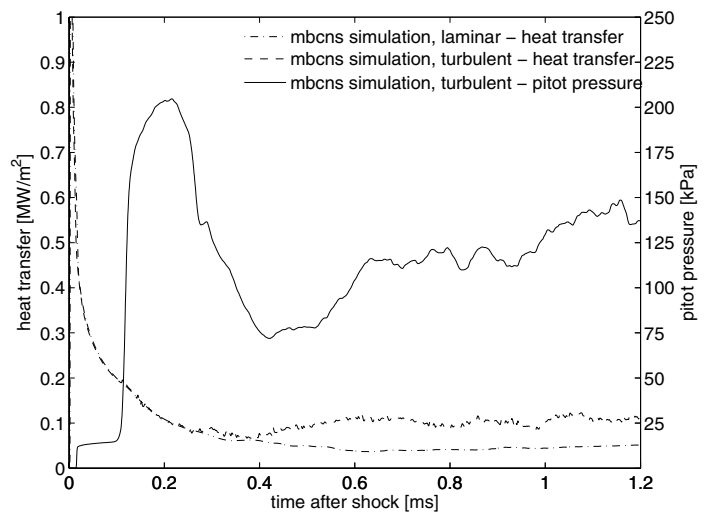


Figure 4.47: Heat transfer from CFD (turbulent and laminar) with turbulent pitot pressure at 8.

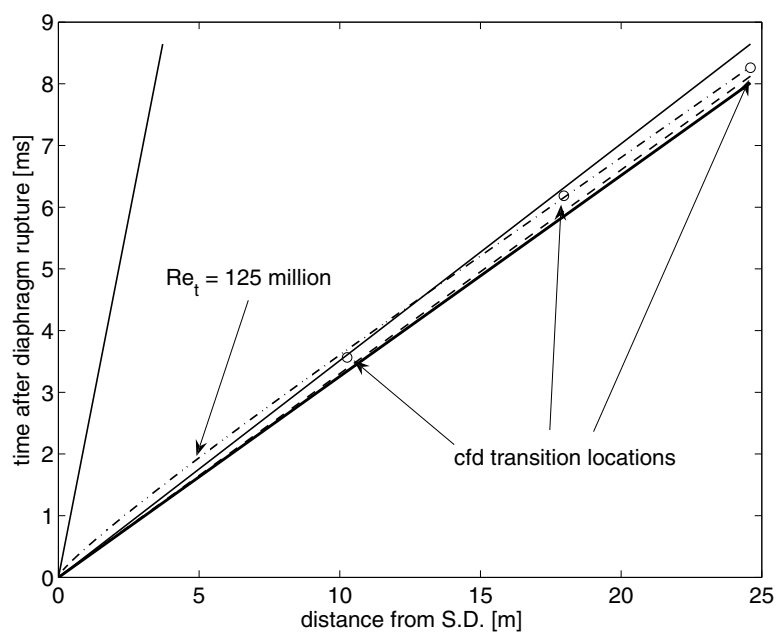


Figure 4.48: Distance-time diagram of Weilmuenster's [24] analytical prediction of X3 boundary layer transition versus CFD measurements.

After successful testing of a Mach 10 condition in the smaller X2 facility (Chapter 5) with a steady expansion nozzle this looked promising for the larger X3 facility. Davey [20] undertook a CFD study to investigate scaling the contoured steady expansion nozzle of X2 to the larger bore diameter of X3 and also the design and manufacturing aspects of putting the nozzle in place. This is described further in Section 4.1.3. As X3 is currently out of operation (2007) awaiting driver upgrades (as discussed in Section 4.1.3) and the nozzle is still to be manufactured, work on this has been purely a numerical study.

The numerical simulations were conducted in the same manner as described in Section 4.4.2 using the X3 tube configuration. The geometry used in the simulation is the same as used by Davey [20], seen in Figure 4.49 and described above in Section 4.1.3. The fill conditions are similar to those used in the X2 condition and copied for the X3 simulations by Davey [20]. These did have to be modified due to both differing boundary layer interactions (especially through the nozzle) and shock attenuations in the longer tubes with an increase in the acceleration tube fill pressure to 200 Pa. The simulation used a grid resolution of 401600 cells (5020 axially by 80 radially) and was parallelised into 40 blocks. An equilibrium chemistry model was once again used with a Baldwin-Lomax turbulent boundary layer model with a fixed temperature wall of 296 K. As this used a similar grid was used to that of previous calculations (Section 4.4.2), grid refinement was not undertaken. Apart from prediction of test time and approximation of likely flow properties, the purpose of this calculation was to show that boundary layer transition did not cause boundary layer to engulf the core flow.

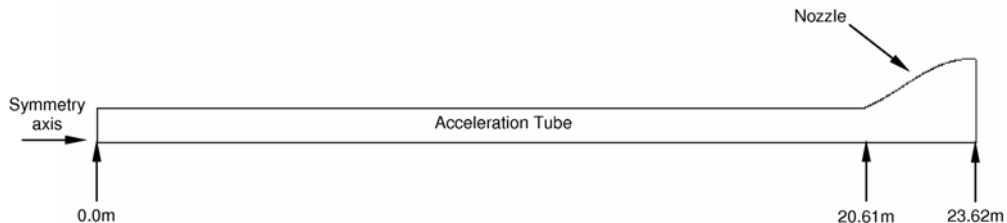


Figure 4.49: X3 acceleration tunnel geometry for axisymmetric calculations. Taken from [20].

The pitot and static pressure time histories at the nozzle exit in Figure 4.50, show that the condition is quite promising with a steady pressure profile throughout the test period of approximately 1 ms. The static pressure is reasonable, at a level of 1.7 kPa. In the pitot pressure trace, the unexpanded and expanded acceleration gas are quite visible and the starting process of the nozzle takes approximately $500 \mu s$. The pitot pressure is quite constant across the entire core flow during the test period, with a core flow of 220 mm. The calculated Mach number of the flow was 10.8, which is a little higher than wanted. However, further refinement can easily be made during experimentation to reduce both

the static pressure and Mach number back to the desired flight duplication condition. This shows that the X3 facility is capable of testing a Mach 10 scramjet of up to 1 m, assuming there needs to be three flow lengths passed through the engine during the test time to obtain quasi-steady supersonic combustion and fully start the exhaust.

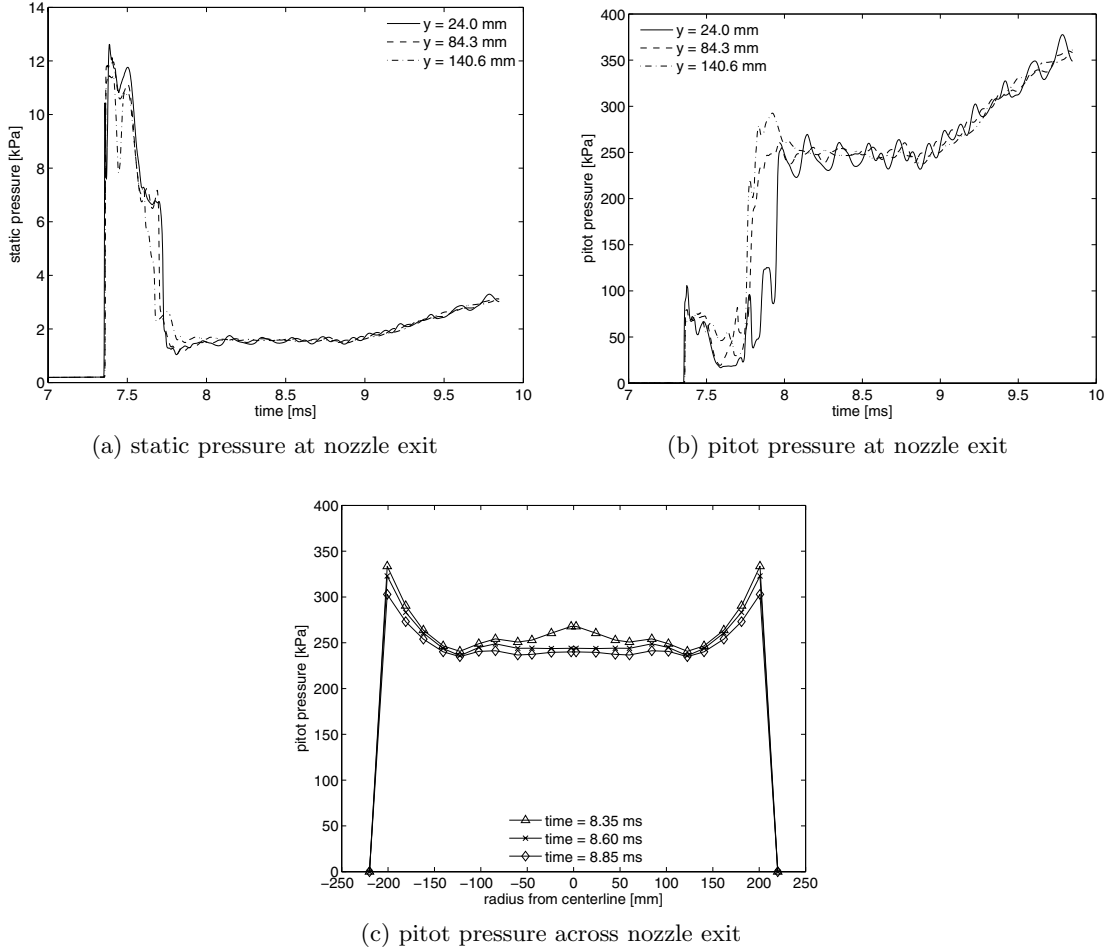


Figure 4.50: CFD of flow properties in X3 nozzle condition.

Accelerator gas selection

With just a standard acceleration tube, the use of an acceleration gas other than air could be used in two different ways to subdue the effects seen with boundary layer transition. The first is that a gas with a high Reynolds number effect (ie. high viscosity and larger slug length) could be used as the acceleration gas to promote earlier transition after the interface. This could be thought of as previous shock tube transition work [151], where the Reynolds number taken back from the shock to transition is of the order of 0.65 million. The second is a gas that would create a viscous sub-layer below the test gas, which has a low friction and subsequent entrainment could be reduced. Initial calculations showed

that hydrogen could meet both of these criteria, with a large Reynolds number produced by the interface due to a large slug length and very low viscosity.

An initial experiment (shot s289) has been undertaken for a hydrogen acceleration gas, aiming again for the Mach 10 scramjet condition. With hydrogen however, consideration must be made of the possibility of ignition and reaction. This could well occur in the acceleration gas, as it is likely that there will be some air contamination into the acceleration tube. With the low molecular weight of hydrogen, a small volume of air in the acceleration gas can account for a large mass fraction. Initial theoretical calculations using perfect gas relations (conducted in the same manner as those presented in Section 4.2.1) gave the flow conditions, which can be seen in Table 4.10. The shock speeds calculated were 1427 m/s and 4215 m/s for the primary and secondary shocks respectively.

Figure 4.51 shows the pitot pressure at the tube exit and the static pressure close to the end of the acceleration tube, which have been time shifted to give a direct comparison of times. Similar pitot and static pressures were recorded at these stations. The static pressure is seen to initially drop before it suddenly rises after 1 ms. This dropping static pressure was not recorded at the first five sensors in the acceleration tube, however it occurs at all of the last three. The rise in static pressure across the shock is approximately double that predicted from the theoretical predictions. The pitot pressure is seen to increase at approximately the same time as the rise in static pressure occurs, then after another microsecond, dramatically increases. While the pitot pressure is approximately similar to that expected in the acceleration gas from theoretical predictions, it seems to increase with time before 1 ms. This could be an indication that there is some combustion occurring, with the heat release having an initial ignition phase and then heat release over a certain distance. The pitot pressure is seen to plateau at the predicted theoretical pitot pressure 3 ms after the passing of the shock. This however appears to be where the static pressure is approximately 5 kPa and occurs after an increase in the static pressure. This would mean a drop in Mach number to approximately 5.5.

Table 4.10: Summary of flow values for hydrogen acceleration gas condition.

Region	p [kPa]	T [K]	a [m/s]	u [m/s]	M	ρ [kg/m ³]	p _{pitot} [kPa]
(1)	34.7	300.0	347.2	0.0	0.0	0.403	0.0
(2)	677.9	1266.8	713.4	1119.1	1.57	1.86	2493.9
(3)	677.9	526.8	499.4	1119.1	2.24	4.52	5305.5
(4)	11000.0	1600.0	870.4	0.0	0.0	24.1	0.0
(5)	0.15	300.0	1318.4	0.0	0.0	0.000121	0.0
(6)	1.767	884.8	2264.3	3161.6	1.40	0.00696	5.4
(7)	1.767	231.4	304.9	3161.6	10.37	0.00185	246.0

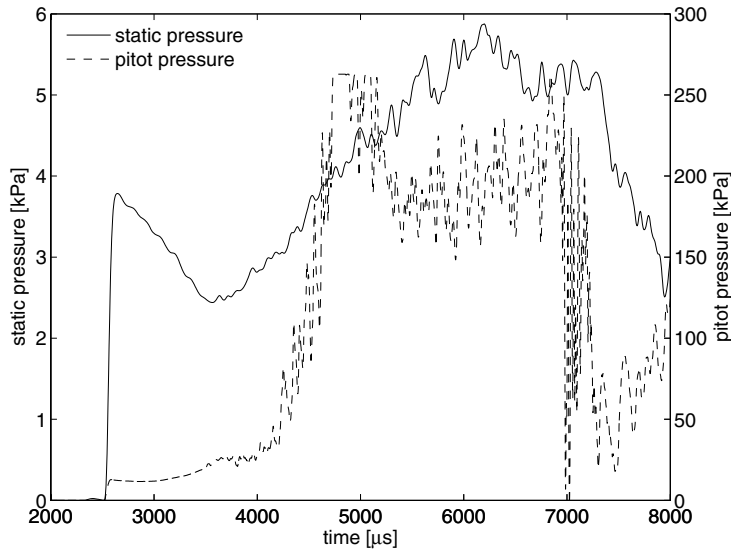


Figure 4.51: Static pressure from at7 and pitot pressure from the test section from X3 hydrogen acceleration gas shot (s289). The pitot pressure has been time shifted to show the shock arrival at the same time.

To explore further, properties are plotted at various locations down the tube in Figure 4.52. The time between the shock and the rise in static pressure (usually assumed to be the arrival of the unsteady expansion) initially increase to around 1 ms half way down the tube. This separation time is then seen to remain approximately constant throughout the rest of the process. It is noted that the shock speed is quite underpredicted (in comparison to theoretical predictions) but dramatically increases by 1000 m/s as it moves further down the acceleration tube. This is quite different to normal expansion tube operation, where the shock speed usually decreases due to boundary layer development. At the same time, the pressure rise across the shock is also seen to dramatically drop down the length of the tube. Usually an increasing shock speed would increase the static pressure ratio across the shock.

This interesting behaviour could be a by product of air contamination in the acceleration tube, which would cause a decrease in the shock speed initially. With combustion effects, the shock speed may increase due to further energy being added to the flow. The time taken for the gas close to the secondary diaphragm to reach the test section being milliseconds and relatively high temperature and pressures in the acceleration gas, if a suitable level of air is present, it is likely to react. Also the concentration of the air would be non-uniform through the tube due to the hydrogen being filled just prior to firing (on the order of seconds) which could also add to the increasing shock speed effect. The likelihood would be that the air will be at a higher concentration closer to the secondary diaphragm as the hydrogen is filled just before firing from the test section. Figure 4.53 shows for initial conditions of 150 Pa and 300 K, the static pressure behind a shock with

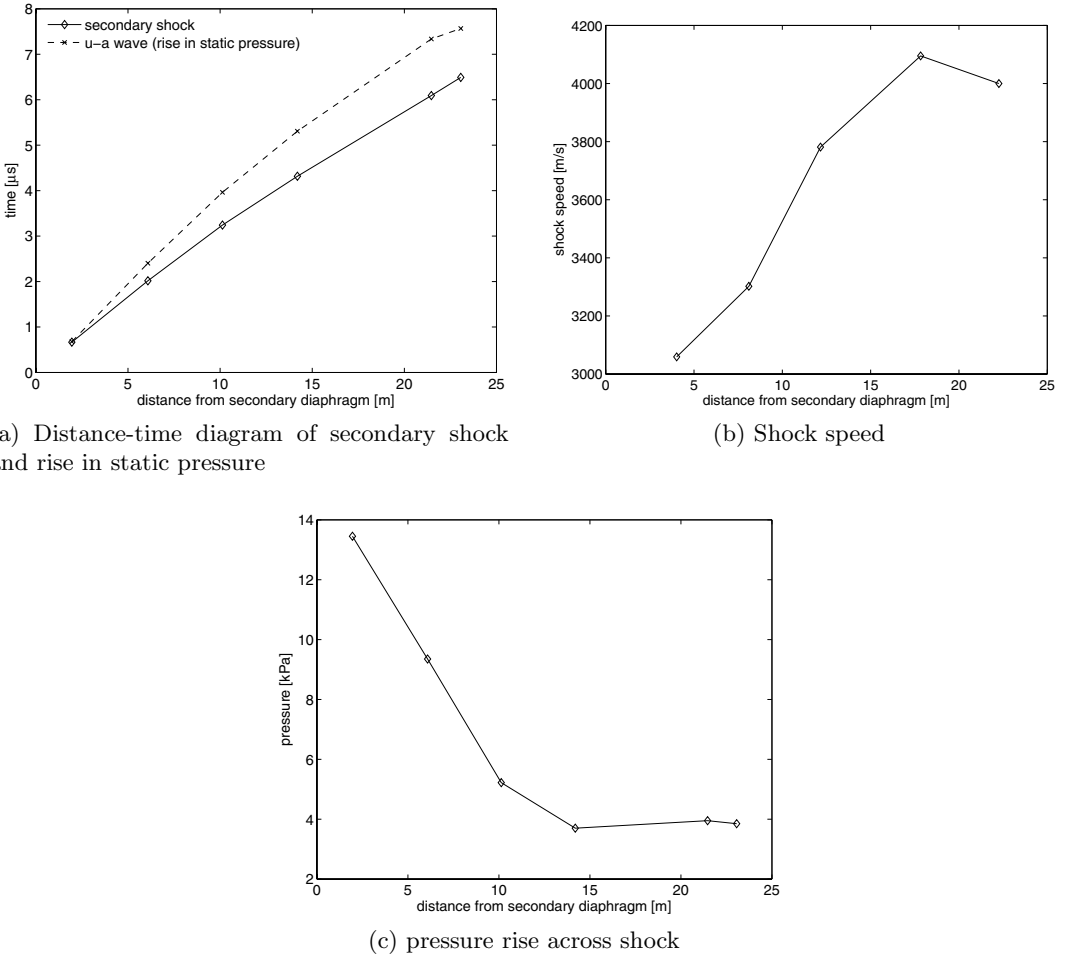


Figure 4.52: Properties along the length of the acceleration tube for hydrogen accelerator gas shot (s289).

various levels of air contamination into the hydrogen. This simulation was completed for an equilibrium gas using the *CEA* [145], assuming no reactions between the air and hydrogen. This shows that as the amount of air volume fraction increases, the static pressure rises across the shock. Also, as the shock speed increases the static pressure across the shock will also increase.

Investigating the interactions that were seen in the pitot pressure, a close up of this time region is given in Figure 4.54. At the end of the acceleration tube if no combustion effects are present, the shock speed would be 4000 m/s. Therefore, the jump in static pressure across the shock ($2500 \mu s$) of 3.8 kPa is best predicted by a volume fraction of air being 10%. Assuming a specific heat ratio of 1.35 and a pitot pressure is 12.5 kPa, the Mach number can be calculated using the Raleigh pitot formula (Equation 4.2) to be 1.5. However, using *CEA*, the Mach number after the passing of the shock should be 1.69. At the inflection point of the static pressure ($3500 \mu s$), the static pressure is 2.6 kPa and the

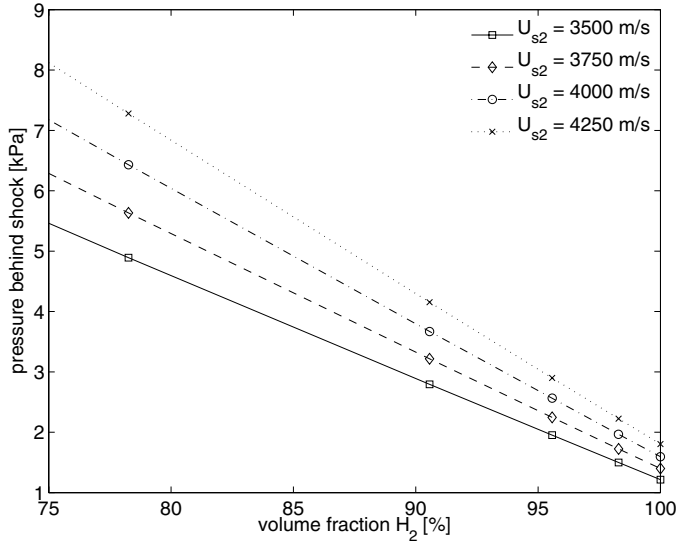


Figure 4.53: Static pressure behind various shock speeds with air contamination for an ideal gas mixture of equilibrium gases. Initial conditions of the gas are 150 kPa and 300 K with no reactions.

pitot pressure is 23.2 kPa. Again assuming a specific heat ratio of 1.3, the Mach number of the flow should be 2.6. Even if the contact surface has accelerated to the speed of the shock (4000 m/s) due to Mirels effects¹⁴, the sound speed would have to decrease from 2100 m/s to 1550 m/s, meaning a dramatic drop in temperature. Therefore, it would seem that there are other effects such as combustion occurring. This may also explain the reason for such a large interface between the two gases, with Mirels calculations using properties predicting an acceleration slug being 600 μ s long instead of the 2.5 ms when the test gas arrives.

Although this initial work has not been able to explain what is occurring in the gas, there appear promising aspects that could be applied to resolve some of the issues surrounding boundary layer transition in an expansion tube. Numerical calculations were attempted, although could not be completed due to current limitations in the code. With the Mach number of the flow being quite low, it may be able to be passed through a steady expansion nozzle to reduce the temperature and pressure, which would further increase the test time from the substantial 1.5 ms obtained.

4.6 Summary

Experimental and numerical work was conducted in the X3 expansion tube to obtain a relatively low enthalpy, high density condition for scramjet testing which would be

¹⁴Using Mirels formulations, the shock/interface will not attenuate until another 18 m from the exit of the acceleration tube.

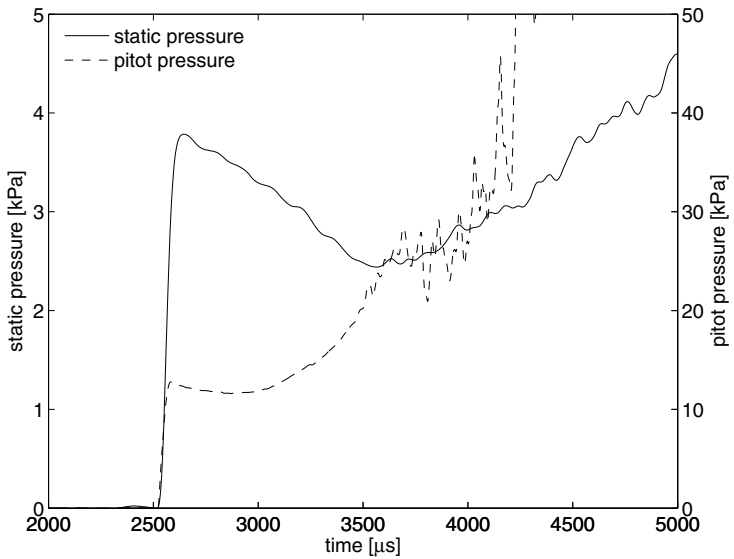


Figure 4.54: Close up of acceleration gas region of static and pitot pressure from X3 hydrogen acceleration gas shot (s289). The pitot pressure has been time shifted to show the shock arrival at the same time.

comparable to the T4 Mach 10 condition. Experimental work showed that a test time of $100 \mu\text{s}$ was possible before a large dip in the pitot pressure across the entire radius simultaneously cut the test time short. It was concluded that this must be caused by a significant drop in the Mach number of the condition. Numerical simulations of the facility with a transitional boundary layer showed similar flow features after the point of transition. Further experimental and analytical work verified that the test was being concluded early due to boundary layer transition occurring on the expansion tube walls.

Two possible solutions were explored to resolve this problem. The first was the addition of a steady expansion nozzle to the end of the acceleration tube allowing for an increase in the test gases unit Reynolds number and promote early transition. The second was the use of a hydrogen acceleration gas that would both reduce the amount of test gas that enters the boundary layer by creating a viscous sub layer and promoting earlier transition by increasing the Reynolds number taken from the shock to the interface. The use of a steady expansion nozzle looks like the most immediately promising option out of the two solutions, providing a total test time of 1 ms. Although the use of a hydrogen acceleration gas creates complex flow effects not currently resolved, this solution may be able to provide longer test times and ultimately coupled with a steady expansion nozzle would also increase the core flow. Because the X3 facility was unavailable for actual scramjet experiments, attention was shifted to the smaller X2 facility which had a nozzle that produced reasonable flow (with an adequate core diameter and flow duration).

Condition Development in the X2 Expansion Tunnel

This chapter provides an investigation into producing a flow condition which can be used for a 2/5 pL scaled, Mach 10 scramjet flight model in the X2 facility with a steady expansion nozzle, to overcome the boundary layer transition problems seen in the X3 facility. A higher enthalpy condition with the same Mach number is also produced. The freestream conditions are defined through both experimental measurements and numerical calculations of the facility.

5.1 X2 Facility Description

The X2 facility is located at the University of Queensland and was originally designed and constructed by Doolan [96] as a two stage free piston driven expansion tube. A review for this type of facility is discussed further in Section 3.2. The facility was able to produce total enthalpy flows of 120 MJ/kg and total pressures up to 10 GPa. This facility was used to investigate re-entry flows for balutes and aerocapture maneuvers in Jovian atmospheres [14] and for determining flow establishment times behind rearward facing steps [138]. It has also been used for many studies on secondary diaphragm effects [117] and higher enthalpy drivers [97]. In 2005, Scott [26] reconfigured the facility to a single piston driver to obtain better performance and easier operation. This configuration of the facility can be seen in Figure 5.1 with a total length of 17.3 m. The reservoir remained unchanged with a volume capacity of 0.277 m³. The facility has a driver tube 5 m in length and 256.8 mm in diameter and a contraction ratio of 9 at the primary diaphragm. The piston has a mass of 35 kg and 341 mm in length and does not have brakes. The shock tube was extended and now is 3.424 m in length and is 85 mm in diameter. This runs straight through to the acceleration tube with a length 5.155 m.

In 2005, Scott [3] also placed a steady expansion nozzle on the exit of the acceleration tube transforming the facility into an expansion tunnel. This gives the facility larger core flows and increased test time, although this comes with an associated drop in total pressure and density. A further description of the flow processes of an expansion tunnel can be found in Section 3.3. The nozzle is a full capture nozzle, that is a nozzle which

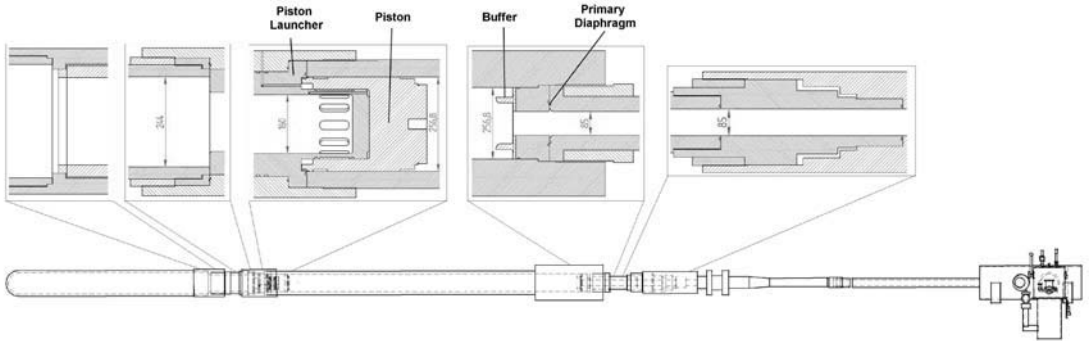


Figure 5.1: Schematic of the X2 expansion tube. Taken from [26].

takes the entire flow from the acceleration tube (Regions 2 and 7 in Figure 3.6) and expands it by a certain geometrical area ratio without boundary layer removal. Scott designed a contoured nozzle using an optimisation algorithm coupled with parabolised Navier-Stokes equations for minimal flow divergence and flow non-uniformity. For checking of the design contour, a transient viscous simulation was undertaken of the nozzle geometry for a single condition. The final nozzle geometry has an area ratio of 5.63 taking the flow to a diameter of 201.8 mm over a length of 1.4 m. Sample points for the nozzle contour can be seen in Table 5.1. The nozzle was designed to have an inlet Mach number of 7.6 and exit Mach number of 10.2. This nozzle configuration has been used to simulate Titan atmospheres [98] and extends the core flow diameter and test time by matching flow conditions used previously in the expansion tube mode [3].

Table 5.1: Sample points from X2 nozzle contour. Taken from [3].

axial [m]	radial [m]	axial [m]	radial [m]
0.0	0.0425	0.403471	0.058292
0.033843	0.044861	0.590938	0.076543
0.085036	0.046159	0.825679	0.100123
0.158080	0.047400	1.100956	0.104087
0.261443	0.050497	1.4	0.104087

5.1.1 Measurement techniques

The X2 facility is quite similar to the larger X3 facility in the techniques available to ascertain experimental measurements seen in Section 4.1.1. The three main types of measurements are wall static pressure (also used for shock speed calculations), pitot pressure and optical visualisation. Additional information can also be recorded on the recoil posi-

tion of the driver tube, which relates to the position of the piston. The pitot pressure again uses the same nine sensor rake as described in Section 4.1.1 mounted in the test section where the axial and radial position can be adjusted. The data is recorded as described for the X3 facility (Section 4.1.1) on in-house built ‘databoxes’.

Static pressure

The static pressure mounting is slightly different to that used in the X3 machine. This wall mounting arrangement for the PCB piezoelectric transducer can be seen in Scott [3]. The static pressure axial locations shown in Figure 5.2 are listed in Table 5.2. The three shock tube sensor locations are clustered towards the secondary diaphragm, to capture the shock speed just prior to diaphragm rupture. The acceleration tube contains 6 measurement locations, with the final two locations located at the same axial position close to the nozzle entrance. The nozzle has two external attachments if static pressure is required, which measure the wall static pressure for the nozzle 10 mm after the exit plane (10.126 m from the primary diaphragm). Unlike the X3 facility, the driver tube does not have a static pressure measurement to record the burst pressure of the primary diaphragm.

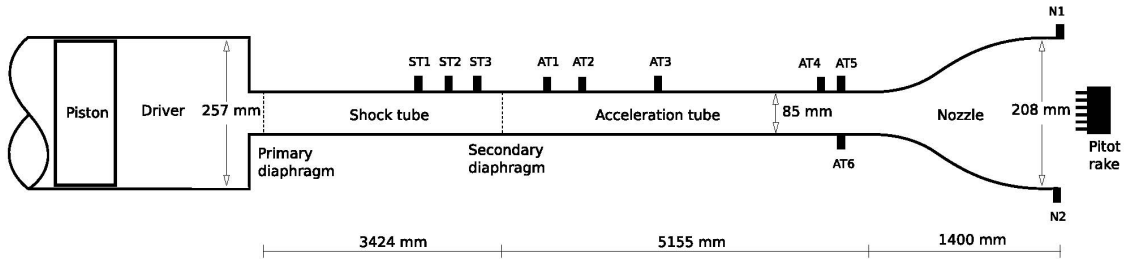


Figure 5.2: Schematic of the pressure transducer locations in X2 operating in tunnel mode. Taken from [17].

Pitot pressure

Pitot pressure measurements are taken in the test section of the facility, with 9 aerodynamically shielded probes mounted in a pitot rake. As the pitot rake is the same as that used in the X3 facility, refer to Section 4.1.1 for further information.

Recoil sensor

A linear differential gauge has been mounted between the driver tube and its support to record the recoil of the driver tube. Because no external forces act on the facility during operation (to the first order), driver recoil gives an indication of piston motion. This gauge requires a constant voltage input of 10 V, and gives a direct output voltage related to its position. This can be calibrated before and after if required, by taking readings at various

Table 5.2: Wall pressure sensor locations in X2 operated in relative to the primary diaphragm (P.D. is primary diaphragm, S.D. is secondary diaphragm, TE is tube exit and NE is nozzle exit).

Transducer	Location [mm]
<i>Shock tube (P.D. - 0 mm)</i>	
ST1	2572
ST2	2804
ST3	3036
<i>Acceleration tube (S.D. - 3424 mm)</i>	
AT1	3955
AT2	4205
AT3	6019
AT4	7865
AT5	8045
AT6	8045
<i>Nozzle exit (TE - 8579 mm, NE - 10136 mm)</i>	
N1	10.126
N2	10.126

linear positions. Recoil of the driver tube can give an estimate of piston position, which is a useful tool when diagnosing problems with the facility, like un-ruptured diaphragms or buffer damage.

Holographic laser interferometry

Holographic laser interferometry compares two laser pictures interferometrically, where at least one is holographically reconstructed [153]. This technique gives density gradients primarily and other flow properties like temperature and electron levels in a two dimensional plane. Three dimensional effects must be accounted for as these will affect measurements because they will be in the line of sight (i.e. across the test section). A detailed review of this technique can be found in [154].

5.1.2 Facility upgrades for scramjet testing

The size of the X2 dumptank/test section was too small to mount the planned scramjet experiments. The X3 dumptank was chosen to be modified and installed as the new X2 test section. This also gave the advantage of more room to access models and larger viewing windows for optics. Due to the larger size of the X3 dumptank, the entire X2 facility was required to be moved to be able to fit the dumptank onto the facility. This

gave an opportunity to raise the entire tunnel so that the laser tables used on the X3 facility could also be used on the X2 facility. Also, the tunnel frame could be aligned more accurately and totally secured to the ground in this moving process. A hydrogen system was required to perform scramjet testing. Therefore a Ludwieg tube system with solenoid valve actuation was designed and installed on the dumptank. These are discussed in further detail below.

Relocation

Relocation of the facility was required due to the need for a larger test section to mount the upcoming scramjet experiment. The facility was restricted in the axial direction so that a larger test section could not fit. Therefore, the entire tunnel was shifted across the X-lab to a larger space along the northern wall and positioned at an angle of 5 degrees to the wall. This orientation allowed for the placement of the laser tables on both sides of the dumptank. The tunnel was lifted by 130 mm to allow the laser tables to be used from the X3 facility. Anchoring of the entire facility was completed with a design that allows the tunnel to be aligned in all three directions if required.

Dumptank modifications

Pitot pressure measurements in the impulse facilities at the University of Queensland have been relatively noisy signals, with harmonic fluctuations. However, the average value of the measurement remains relatively stable. This oscillatory behaviour became prevalent in the quasi-steady Mach 10 scramjet condition in the X2 expansion tube. It was known that the test time would be relatively short compared to what would be available in the T4 reflected shock tunnel facility, so therefore the transient behaviour of the flow was

The dumptank was required to be modified from its X3 configuration, before fitting to the X2 expansion tunnel. This included modification of the front plate and sliding seal to fit the nozzle, adjustment of overall height and new optical windows. The front plate was modified by having an insert which took the internal diameter of the sliding seal from 294.0 mm to 230.6 mm. This plate can be seen in Figure 5.3. The height of the dumptank was modified by placing new caster wheels supports to the dumptank frame. The optical windows were offset from the centre of their mounting plates, to enable viewing closer to the nozzle exit. Also, a new rail system was incorporated into the dumptank to allow the fuel line to remain connected whilst the rail moved.

Hydrogen system

To fuel the scramjet, a constant pressure supply is required for a short period of time. The fuel system needs to be opened quickly, usually controlled by a fast acting solenoid valve. A Ludwieg tube was designed to be fitted to the X2 facility similar to that used on the

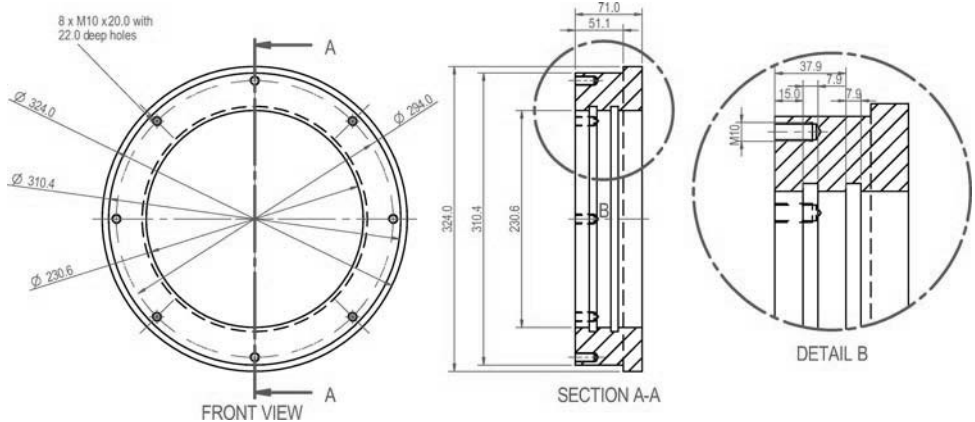


Figure 5.3: Insert piece for the X2 dumptank to fit smaller X2 nozzle.

T4 reflected shock tunnel [155]. This uses a long constant area tube (region 1) to supply a cavity behind the fuel injectors (region 3) as shown in Figure 5.4. When the valve is opened, the high pressure gas in the Ludwieg tube passes through an unsteady expansion into this cavity. A relatively steady pressure is held in the cavity until the reflection of the unsteady expansion from the end of the tube back to the cavity. The Mach number of the hydrogen in the Ludwieg tube can be calculated to be 0.125 from the area ratio A_2/A_t of 5. Therefore the temperature and also the sound speed will only change marginally from 300 K and 1318 m/s respectively and the velocity will be 165 m/s. With the length of Ludwieg tube being 5 m, the test time is calculated to be 6.8 ms, using the unsteady expansion time given in Paull [93].

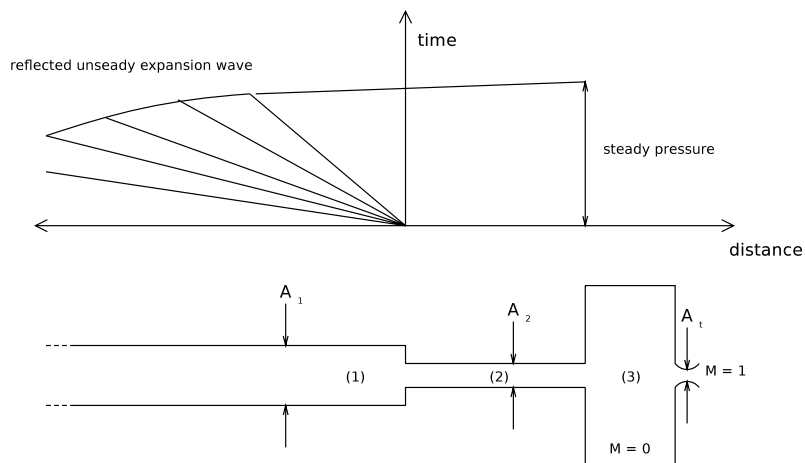


Figure 5.4: Schematic of Ludwieg tube operation.

The fuel system design incorporated both a digital and analog fill pressure gauge, manual vent and vacuum evacuation line through to the dumptank as shown in Figure 5.5. The Ludwieg tube was manufactured from 5/8" copper pipe (1/2" ID) and the pipe

between the valve and the supply cavity is 1/2" copper pipe (3/8"). The solenoid valve used in the system was a commercial ASCO high pressure pilot activated valve [156] which has a minimum area of a 1/2". To activate the solenoid valve, a triggering system uses a photo diode/laser system to detect movement of the driver to indicate the firing of the facility. This is due to the time required to open the valve is too long to use a pressure signal. The valve power unit was built originally for T3 in 1980 at the University of Queensland. This has a delay setting and voltage level control built in. The methods used in the calibration of the system are described in Appendix C, which allow for the conversion of the stagnation pressure recorded in the scramjet fuel cavity to the mass flow rate of hydrogen injected.

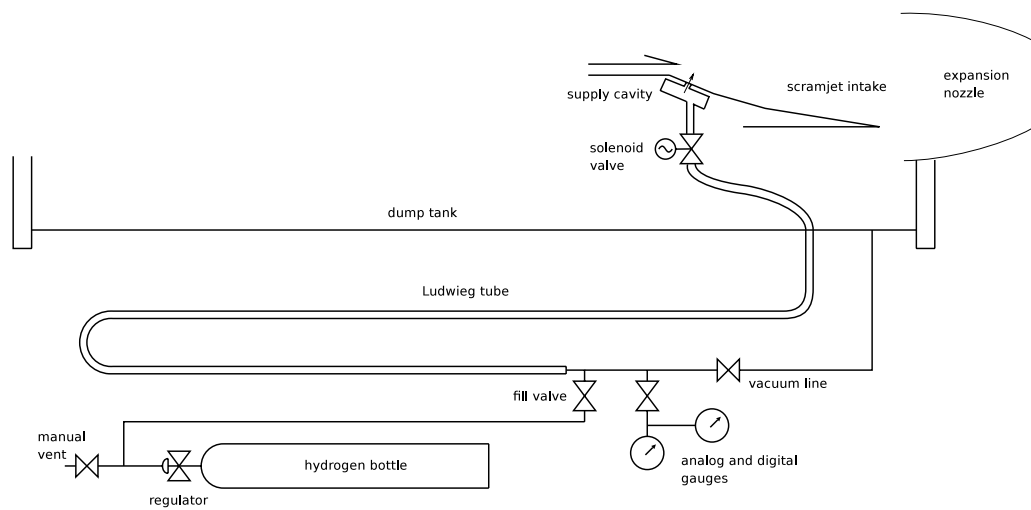


Figure 5.5: Diagram of hydrogen system on X2.

5.2 Experimentation

With boundary layer transition causing a large flow disruption in the test time of the X3 facility, it was proposed that operating in expansion tunnel mode could be used to avoid this phenomenon (Section 4.5.5). With the X2 facility having a nozzle with the correct attributes available (i.e. designed for exit Mach number of 10.2), the establishment of a Mach 10 scramjet condition was undertaken in this facility with the view of undertaking subscaled scramjet experiments. Initial estimates were made using perfect gas calculations as described in Section 4.2.1, targetting to duplicate the Mach 10 condition in Table 4.2 (page 56) with the exception of static pressure and related properties (density, pitot pressure, total pressure and unit Reynolds number). This condition was adjusted so the scramjet that could be tested would have a reduced test time from that established in T4 by reducing the overall length of the scramjet. Therefore, it was decided to use pL scaling and use a smaller scramjet with an increased static pressure. With the

scramjet being 2/5 of the original size, the condition required 2.5 times the static pressure and therefore density. This condition was labelled the “low enthalpy” condition. Also, a “high enthalpy” condition at the same Mach number was produced to investigate the effects of enthalpy on the scramjet performance.

A previously used condition [3] was modified for the experiments, adjusting driver gas and rupture pressure to reduce piston impact damage. This was due to a change in the piston dynamics whereby damage was inflicted on the buffer that stops the piston. The dynamics of the piston were altered due to changes in the gas composition and trimming of the piston causing it to travel at higher speed at the point of impact. This could not be relieved by increasing the reservoir and driver pressure, as the limit of sealing pressure was reached on the piston space. Moving to thinner diaphragms lowered the burst pressure from 24 MPa to 15.5 MPa. Using a 300 mbar initial fill pressure enabled the appropriate conditions in the driver at rupture to duplicate shock speeds from the first series of tests while removing the hard impacts of the piston.

These effects can be picked up in the recoil of the driver seen in Figure 5.6. The recoil relates the position of the piston due to the conservation of momentum in the facility. The tunnel movement is seen to have a minimum, just after diaphragm rupture when the piston impacts the buffer. The piston then moves backwards due to the high pressure in front of it and then impacts a second time once the pressure drops in the compressed driver slug. In the larger free piston shock tunnels, brakes are often used to stop the piston from impacting twice. Figure 5.6 shows that a larger second impact occurs (the second dip) in x2s103 compared with x2s98 due to the piston dynamics described previously. Increasing the driver and reservoir pressures as seen in x2s113 reduces the impact, though it is still quite *hard* impact and the shock speeds were not able to be reached with higher temperatures in the compressed driver slug. The reduction is quite noticeable in x2s117 where it is difficult to pick up the second impact. Thus the piston does not have a hard second impact and the shock speeds could be matched to the original experiments.

5.2.1 Low enthalpy scramjet condition

The low enthalpy condition has the fill conditions given in Table 5.3, with the uncertainty analysis given in Appendix D. This condition has a relatively high shock tube fill pressure and is a pure argon driver. This used a 1 mm steel diaphragm (un-scored), which was estimated to have a rupture pressure of 15.5 MPa, scaling from previous conditions. Shock speeds for this condition were averaged over 27 shots, some of which were scramjet tests. The primary shock was 1629 ± 41 m/s and the secondary shock shock speed was 3550 ± 89 m/s. Shock speed variations down the tube are shown in Figure 5.32a. The traces for the acceleration tube static pressure at at4 and at5 for shot x2s253 can be seen in Figure 5.7. The variance between the two signals is quite small, with the time between

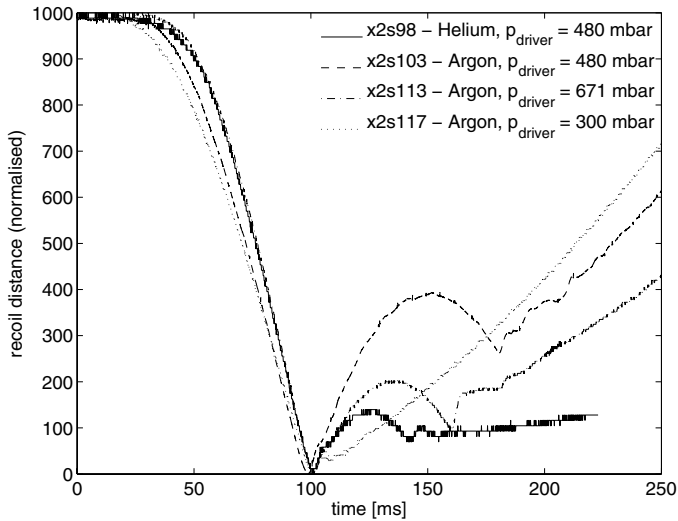


Figure 5.6: Experimental recoil of driver tube in X2.

the shock and the rise in pressure approximately $120 \mu s$. The average pressure level over the series of shots was 17.2 kPa over the period between the shock and unsteady expansion.

Table 5.3: Fill conditions for the low enthalpy X2 condition.

Reservoir	1.15 MPa	air
Compression tube	30.0 kPa	argon
Shock tube	95.0 kPa	air or nitrogen
Acceleration tube	140.0 Pa	air

quite

To investigate the location of the interface, a Mirels calculation was undertaken for a laminar boundary layer¹ using perfect gas calculations based on the fill conditions. This is compared to the perfect gas prediction down the length of the acceleration tube in Figure 5.8. This shows that at at5, the time between interface and shock should be $110 \mu s$ according to the Mirels prediction. This is the same time that an increase in the static pressure is seen in the experimental measurements (shown in Figure 5.7). Using the perfect gas sound speed prediction (410 m/s) and the interface speed predicted by Mirels (3480 m/s) the time between the interface and unsteady expansion at at5 is estimated to be $175 \mu s$. This is around the same time that a noisier static pressure is recorded. The cause of the early rise in the static pressure may be due to the transition of the boundary layer, but is unclear.

¹Can be assumed to be laminar due to the low unit Reynolds number and slug size for the acceleration gas slug.

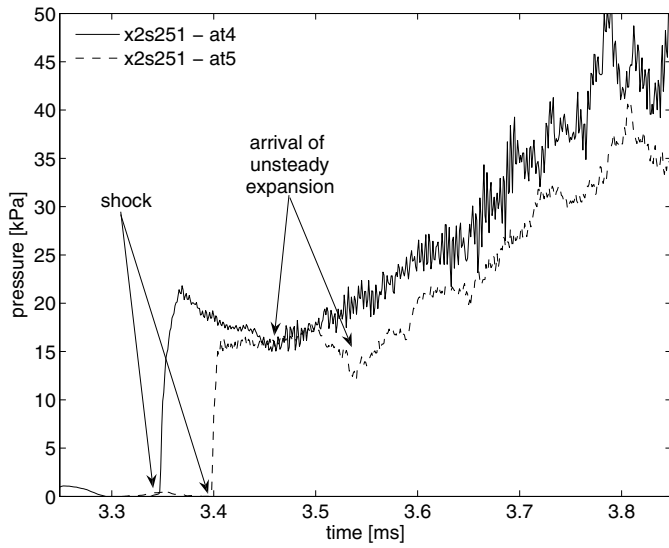


Figure 5.7: Experimental acceleration tube static pressure for low enthalpy X2 condition.

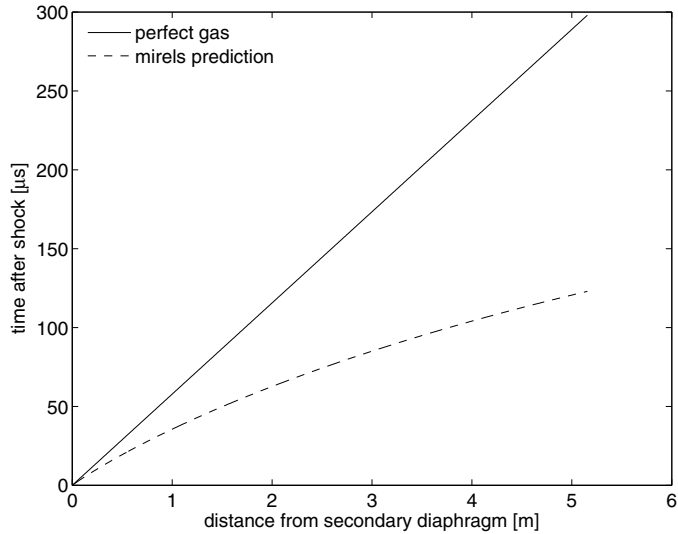


Figure 5.8: Comparison of perfect gas and Mirels prediction for the time between the interface and shock.

Flow properties at the end of the nozzle exit were measured using 9 pitot and 2 static pressure measurements at the nozzle wall. The time histories for 3 pitot and both static pressure sensors from the nozzle are shown in Figure 5.9 and Figure 5.10. These were taken from two different shots because the static pressure mounts were difficult to install with the attachment of the new test section. The nozzle start up is seen to take approximately $150 \mu\text{s}$. This takes more than the entire period seen in the acceleration tube before the unsteady expansion cuts the available test time. The static pressure then drops to a pressure of 1.8 kPa at the start of the test time and then steadily rises until

4.45 ms to 3 kPa. This gives approximately $550 \mu\text{s}$ of test time. After this point, the pressure rise is too high for accurate scramjet experiments. To estimate the effects of this increase in pressure on the quasi-steadiness of the flow in a scramjet model, an analysis is completed using the computed values seen in the axisymmetric simulation of the condition in Section 5.3.2.

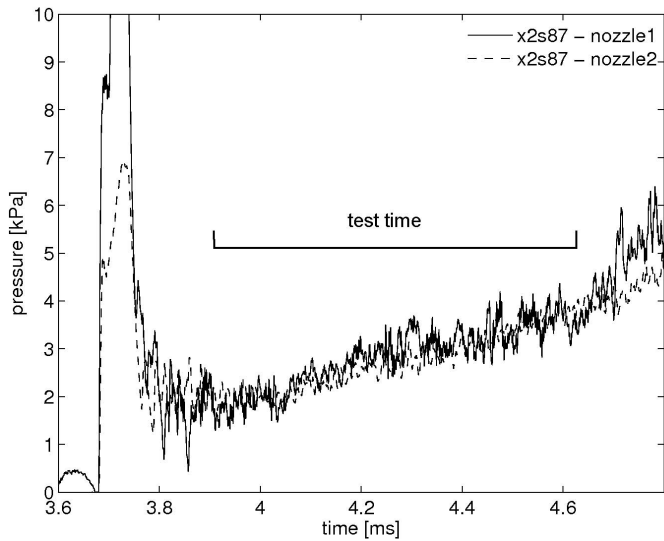


Figure 5.9: Experimental nozzle static pressure for low enthalpy X2 condition.

During the starting process seen in the first $150 \mu\text{s}$ after the passing of the shock in the pitot pressure trace (Figure 5.10), large pitot pressures are measured due to the shock created at the entrance to the nozzle [3]. The initial low pitot pressure is the unexpanded acceleration gas. The pitot pressure has quite a large, low frequency oscillation throughout the entire flow of approximately 100 kPa amplitude and a frequency of 30 kHz. Similar behaviour is recorded in all three positions, and seems to have a similar frequency and amplitude. One possible cause of these flow perturbations would be due to acoustic waves. Acoustic waves may disrupt the velocity of the flow due to focusing through the unsteady expansion of the driver gas [93]. This is described further in Section 3.2.1. However in this case, it is not believed to be an actual free stream flow phenomenon but rather is a flow effect within the pitot cavity itself as discussed further in the proceeding section.

Pitot pressure fluctuations

Fluctuations in pitot cavities were explored numerically by Jacobs [4] for a simplified pitot configuration, with the same dimensions as used in the expansion tube facilities. This was after large fluctuations where seen experimentally in pitot pressure measurements from the Drummond reflected shock tunnel facility. This study was undertaken in *MB-CNS*, with an axisymmetric geometry and initial conditions in the numerical simulation of 286 K and

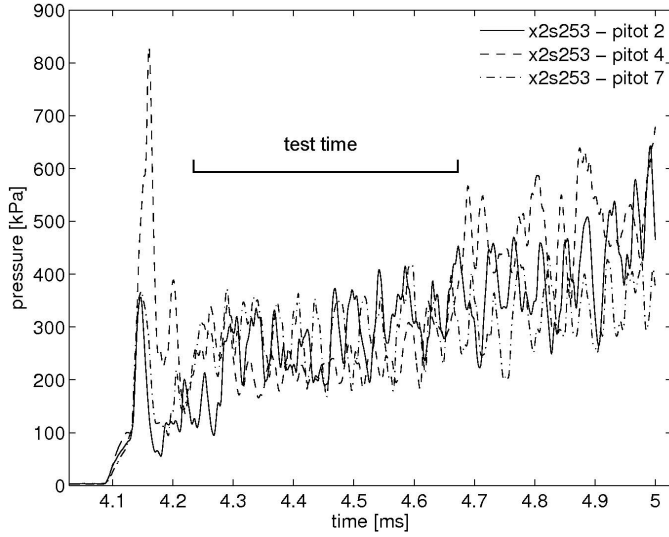


Figure 5.10: Experimental pitot pressure measurements for X2 low enthalpy condition.

400 Pa. The simulation used a perfect gas with a specific heat ratio of 1.3, with a steady inflow boundary condition. Simulations were undertaken for two different flow conditions, a Mach 7 and a Mach 4 condition with freestream properties as shown in Table 5.4. These conditions have quite a low freestream total enthalpy, however the temperature and pressure of the Mach 7 case is quite similar to the Mach 10 case being investigated for X2.

Table 5.4: Freestream conditions of numerical simulations of pitot cavity conducted by Jacobs [4] of a reflected shock tunnel condition using similar probes to that used in a expansion tube.

	M4	M7
velocity [m/s]	1980	1890
static pressure [kPa]	21.2	0.586
temperature [K]	644	210
Mach number	3.75	6.8
total enthalpy [MJ/kg]	2.47	2.17
pitot pressure [kPa]	392.4	35.72

Figure 5.11 shows the simulations using the Mach 7 flow properties for two configurations of the pitot probe; how it is mounted experimentally in X2 with a cavity in between the transducer and protective brass casing and with the transducer mounted flush so therefore no cavity is present. The flow field in front of the cavity in both is seen to vary greatly over the quite long time period of $300 \mu s$, due to the large flat surface. It is unclear whether this behaviour is only a numerical result (as for blunt bodies 3 diameters of flow length is required to reach flow establishment $\sim 30 \text{ mm} = 10 \mu s$) or whether this behaviour

can exist in a physical experiment. If this is possible experimentally, it suggests the time required for the flow to settle in front of the pitot is too long for use in an expansion tube, where the test times are less than one millisecond. For the cavity mounted transducer, it can be seen that there is a change in the contour lines within the cavity at each of the times.

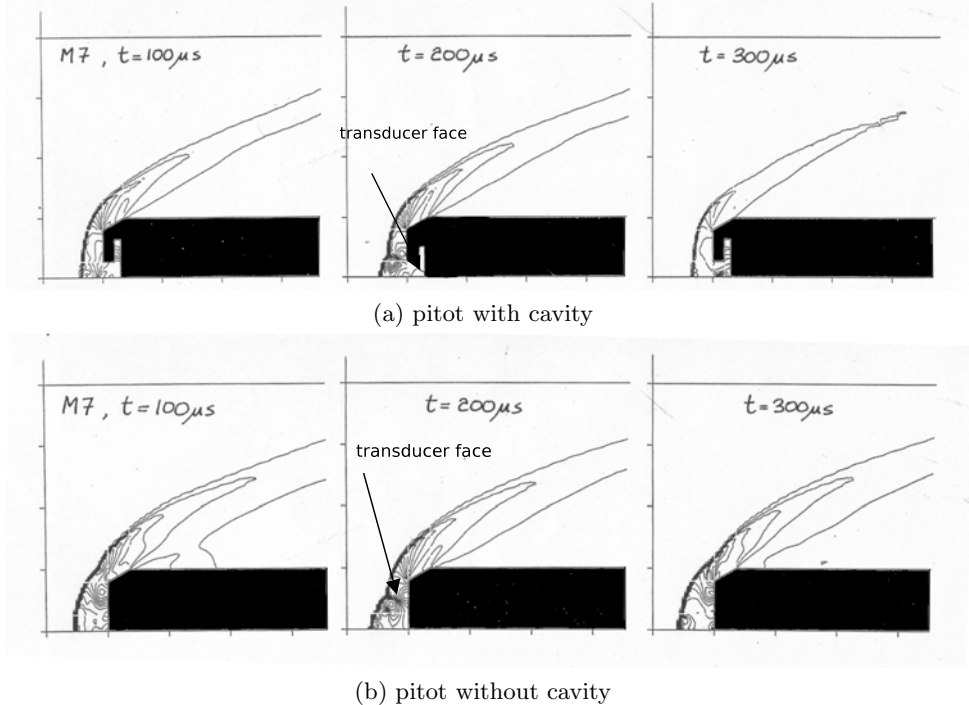


Figure 5.11: Static pressure contour plots of pitot probes similar to those used in X2. Adapted from [4]. Times are from the start of the simulation.

The pitot pressure at the front of the transducer is plotted in Figure 5.12 where both show large oscillations in the stagnation region in front of the shielding. After the starting pulse (approximately $30 \mu s$), the pitot pressure in both arrangements has an average level of approximately 35 kPa, which is similar to that of the freestream. For the cavity mounted case, large fluctuations with a frequency of 30 kHz and amplitude of 15 kPa are present. A similar behaviour is seen in the flush mounted simulation, but less pronounced. Although the frequency is similar, the amplitude is reduced to between 6-9 kPa. Although not shown here, the M4 flow condition case with the cavity mounted transducer had a frequency of 40 kHz and amplitude of 150 kPa (approximately half the average pitot pressure). This shows that pitot pressure measurements using this type of arrangement are quite difficult and are exacerbated by the presence of a cavity in front of the transducer. The coupling of the unsteady flow produced at both the front of the pitot cap and cavity is seen to cause large fluctuations of 50 - 100% from the expected pitot pressure. It may be that the

numerical simulation is not capturing the effects in front of the pitot correctly, however, if noise is present in the condition this can be amplified by the cavity.

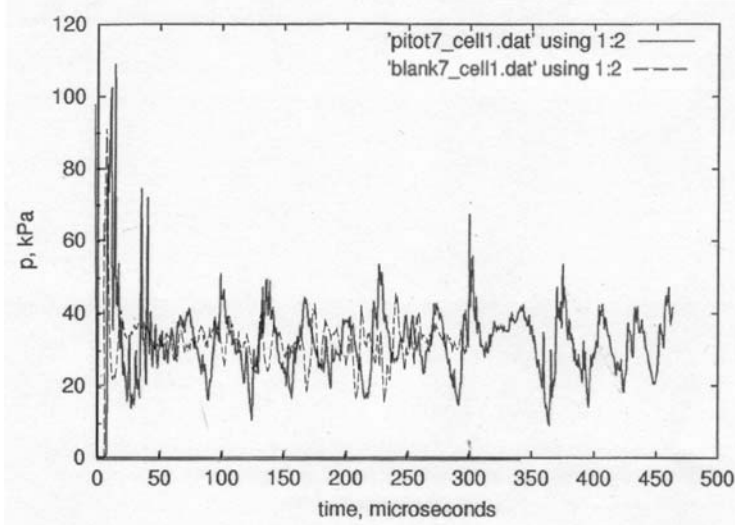


Figure 5.12: Pitot pressure at transducer face for M7 simulation of pitot pressure mount. Adapted from [4]. Dashed line represents flush mounted transducer simulation.

To investigate whether the pitot gauges are giving sensible responses, further information is required. Scramjet “tare”² results intake static pressure measurements can be used to demonstrate that the oscillatory behaviour is not in the free stream. Description of the scramjet intake and experimentation can be found later in Sections 7.1 and 8.2. Figure 5.13 shows the static pressure recorded from x2s119 on the first wedge in the scramjet intake and is compared with the pitot recorded at the approximately the same radial and axial location. This is normalised by the expected wedge (oblique shock theory) and pitot pressure (Rayleigh pitot formula) using perfect gas free stream properties of a specific heat ratio of 1.4, p_{static} of 1.8 kPa, velocity of 3250 m/s and temperature of 250 K. This gives a normalising pitot pressure of 244.5 kPa and wedge pressure of 4.85 kPa. It can be seen that the pitot pressure fluctuates by 20%, whereas the wedge static pressure variation is negligible. The wedge pressure and pitot pressure for an inviscid, perfect gas flow [144] are both directly related to the pre shocked static pressure (i.e. $p_{wedge} \propto p_{static}$ and $p_{pitot} \propto p_{static}$). Therefore, any differences in the magnitude of the fluctuations between the wedge and pitot pressure must be caused by the fluctuations in velocity of the freestream, which may come from fluctuations in the static enthalpy of the test gas before passing through the unsteady expansion process.

Figure 5.14 shows the normalised wedge and pitot pressure with variation in free stream Mach number, calculated for a perfect gas and the nominal freestream properties previously presented. This is again normalised by the average pressure during the test

²Tare refers to experiments run where no fuel was injected and air was used as the test gas.

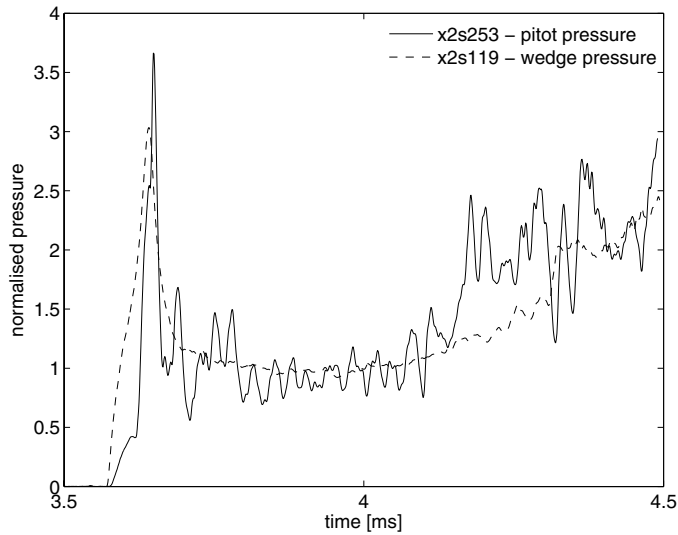


Figure 5.13: Comparison of normalised pitot pressure and wedge static pressure for low enthalpy X2 condition. Pitot pressure is normalised by a factor of $\frac{1}{187}$ and wedge static pressure is by $\frac{1}{4.24}$.

time. This is also shown for a change in velocity were total enthalpy is conserved. For a drop in flow velocity of 50 m/s to 3200 m/s, the pitot pressure is seen to change by 40%, which is approximately that seen experimentally. Also, this change in velocity would also affect the wedge static pressure by approximately 20%, which is not seen experimentally. The analysis assumes viscous and non-perfect gas effects are negligible and also the effects should be seen in the mounting arrangement of the static pressure measurement. With this in mind, the analysis shows that the measurements of pitot pressure are most likely to be incorrect and the probable cause is due to waves traversing the cavity in front of the pressure transducer in the pitot. It can also be noted that the wedge static pressure has a less dramatic rise during the test time than seen in both the static nozzle wall measurement and the pitot.

Although pitot pressure measurements may be aerodynamically noisy, they can still be useful in estimating the average pitot pressure and the size/position of the flow core. Figure 5.15 gives the variation in pitot pressure across the nozzle with variation in axial position. The pitot pressure is averaged over the entire test period. If the apparent error in the measurement is ± 80 kPa, the pitot pressure may increase with axial position. The core flow diminishes though, with an initial core of approximately 100 mm down to 40 mm by 250 mm away from the nozzle exit.

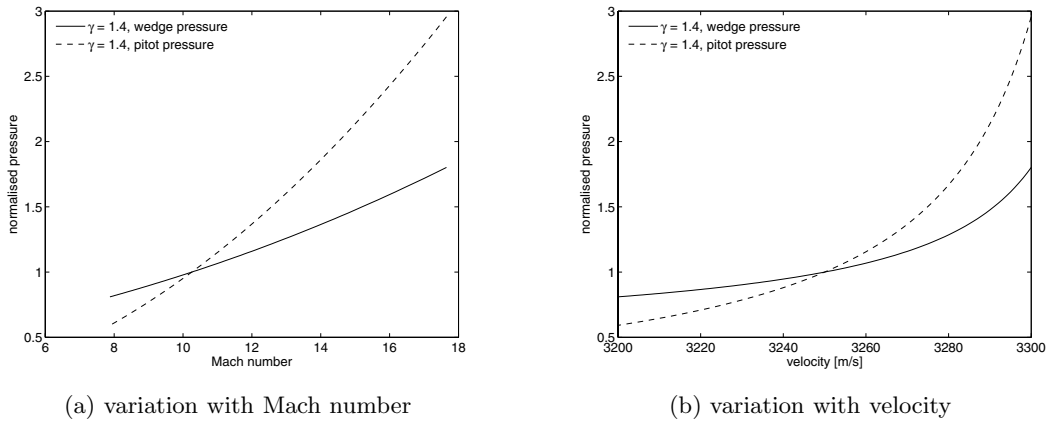


Figure 5.14: Effects of Mach number change on wedge and pitot pressure.

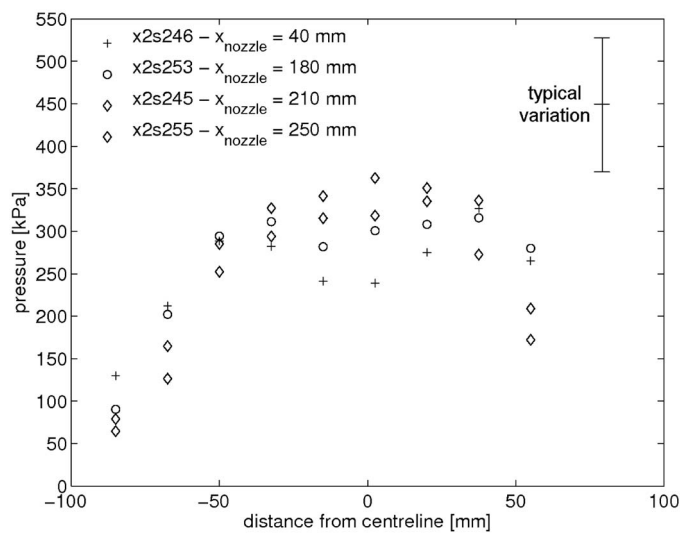


Figure 5.15: Average pitot pressure for low enthalpy condition across the nozzle at various axial locations.

Nitrogen test gas

With scramjet testing, it is convenient to test the effects of not having combustion although still retaining the effects of fuel injection and mixing. This is achieved by using nitrogen as the test gas. As nitrogen is the main component of air and has similar gas attributes at low to medium temperatures (less than 2000 K) it is expected that the flow conditions will be nearly the same as the air condition. To investigate this, a pitot shot was taken with a nitrogen test gas (x2s252). The shock speed taken at the end of the acceleration tube matches reasonably well with the air test gas experiments, being 3530 m/s. The acceleration tube static pressure time history is also seen to match the air test gas case (shot x2s253) quite well with both the quasi-steady test time and pressure level. Although

pitot pressures are again quite noisy, the averaged time histories of the test time across the nozzle (Figure 5.17) show similar trends seen in the air test gas shots.

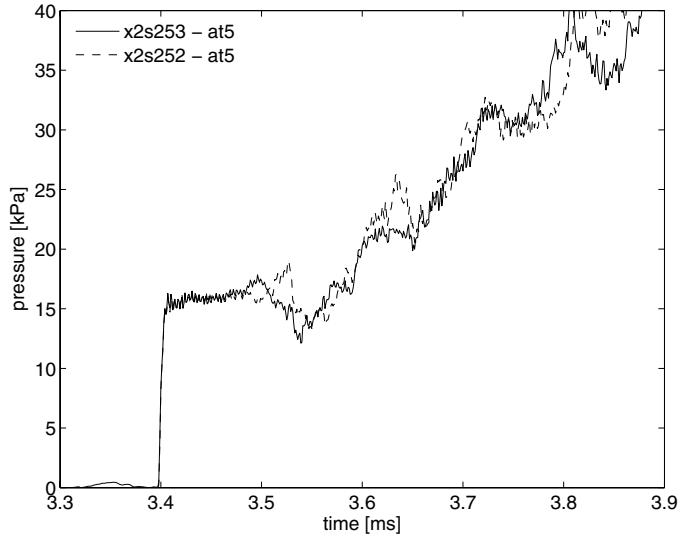


Figure 5.16: Experimental acceleration tube static pressure for low enthalpy X2 condition with N_2 test gas.

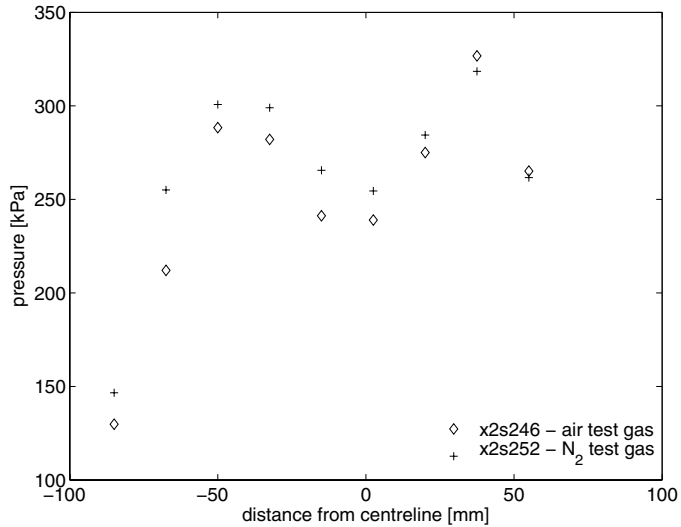


Figure 5.17: Average pitot pressure for low enthalpy condition across the nozzle with N_2 test gas.

5.2.2 High enthalpy scramjet condition

A higher enthalpy test condition was produced to test the scramjets performance with variation in the free stream enthalpy. To achieve this, the static pressure and Mach

number were aimed to be held consistent with the low enthalpy condition. Therefore the velocity had to be increased in line with the speed of sound to ensure the Mach number was held constant. The fill conditions can be seen in Table 5.5. The driver now has a 30% helium composition (by volume) to increase the initial shock speed, though it was found that no increase was required in the reservoir fill pressure. There is also a slight decrease in the fill pressures of both the shock and acceleration tubes. This again used a 1 mm steel primary diaphragm with an approximate rupture pressure of 15.5 MPa.

Table 5.5: Fill conditions for the high enthalpy X2 condition.

Reservoir	1.15 MPa	air
Compression tube	30.0 kPa	30% helium and 70% argon
Shock tube	63.0 kPa	air or nitrogen
Acceleration tube	104.0 Pa	air

Averaged over nine shots, the primary shock speed was 1848 ± 46 m/s and the secondary shock speed was 3912 ± 98 m/s. A large increase in the primary shock speed is seen with a similar increase in the secondary shock compared to the low enthalpy condition. The acceleration tube static pressure can be seen to have slightly decreased to an average level of 15.4 kPa, with the time histories of at4 and at5 shown in Figure 5.18. The time between the shock and the unsteady expansion has slightly increased from the low enthalpy condition to 130 μ s. This is due to the interface going at a significantly faster speed, but the unsteady expansion wave travelling only a slightly increased speed.

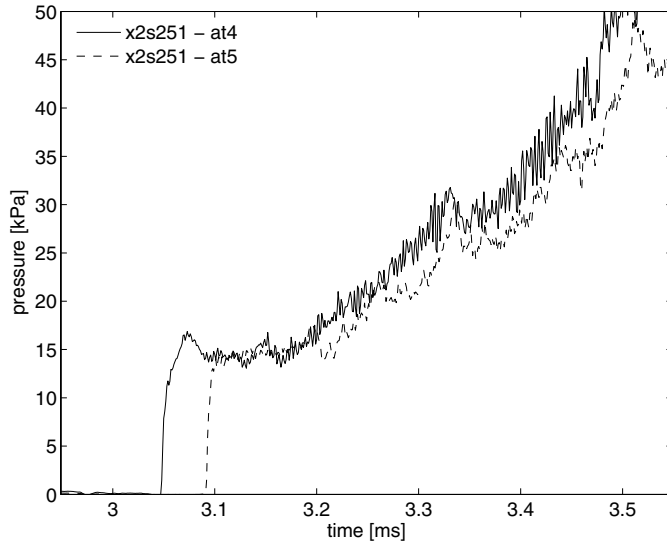


Figure 5.18: Experimental acceleration tube static pressure for high enthalpy X2 condition.

As stated for the low enthalpy condition the pitot measurements have large scale oscillations possibly caused by perturbations of the flow within the pitot cavity. This can be seen in Figure 5.19, where time histories of pitot pressure are given at three radial locations. The pitot pressure is lower than seen in the low enthalpy case by approximately 30%. This is consistent with the same Mach number and lower static pressure as the low enthalpy condition. As in Section 5.2.1, the static pressure recorded at the surface of the first wedge in the scramjet experiment can be used for comparison with the pitot measurements to investigate the pitot pressure fluctuations. Figure 5.20 shows the normalised pitot pressure and static wedge pressure. The normalising pressures are calculated from the Rayleigh (pitot) and oblique shock (wedge) formulas from [144] using free stream flow properties of a Mach number of 10.2, γ of 1.4 and a static pressure of 1.2 kPa. The two measurements have similar trends through the entire test period, including a rise in pressure caused by the arrival of the unsteady expansion. The free stream static pressure is one third lower than that used for the low enthalpy condition which indicates that the Mach number has been held constant. This is due to the Mach number influencing the pitot pressure level approximately twice as much as it affects the wedge static pressure. The issue of the rise in static pressure on the “quasi-steadiness” of the flow is investigated further in Section 5.3.2

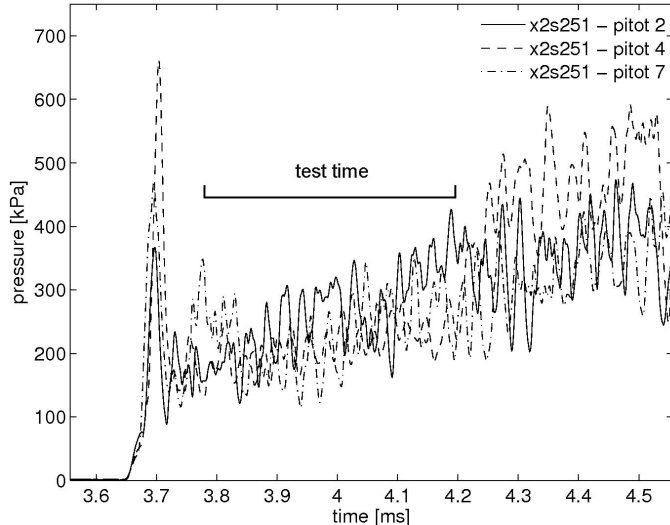


Figure 5.19: Experimental pitot pressure for high enthalpy X2 condition.

5.3 Numerical Simulation

Numerical simulations were conducted to establish flow properties that are not able to be measured experimentally. Validation of the calculations uses the few experimental measurements taken. This uses the same procedure described in Section 4.4 for the X3 facility,

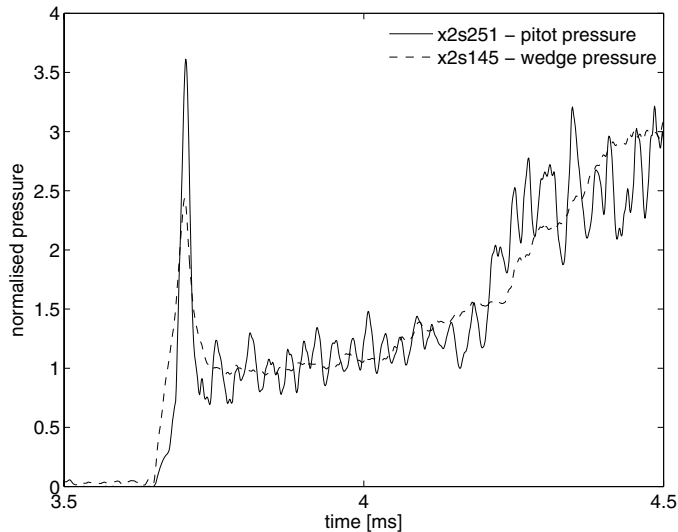


Figure 5.20: Comparison of wedge and pitot pressure in the high enthalpy X2 condition. Pitot pressure is normalised by a factor of $\frac{1}{186}$ and wedge static pressure is by $\frac{1}{3.29}$.

whereby a one dimensional simulation is conducted of the driver and shock gases at primary diaphragm rupture. Exit flow from the shock tube is used as a transient inflow condition across the acceleration tube in an axisymmetric calculation. This procedure of simulation of conditions of the X2 expansion tunnel have been shown to match conditions satisfactorily [3, 98]. This again assumes equilibrium chemistry throughout, with long times in the order of milliseconds for the shocked test gas to reach the end of the acceleration tube and relatively low temperatures in the gas throughout (below the dissociation temperature for air at one atmosphere pressure).

5.3.1 One dimensional modelling

The one dimensional simulations use the *L1d* program[143], as described in Section 4.4.1 for the X3 facility. The geometry for the simulation can be seen in Figure 5.21, where the compressed driver slug enters an area change to the smaller shock tube diameter at 110 mm from the primary diaphragm. The slug length was taken from Scott [3], which was found to model a pure helium driver correctly, for a higher enthalpy condition. The acceleration tube is included in the simulation unlike the X3 work, as the wave structures through the entire flow processes required investigation, although the steady expansion nozzle was neglected since it cannot be resolved satisfactorily in a one dimensional, Lagrangian simulation. The secondary diaphragm was set with a burst pressure of 120 kPa and a holding time of 5 μs . This is due to the thick Mylar required due to an extremely high shock tube pressure of 95 kPa compared with most other expansion tube fill conditions. The viscous effects were included in this simulation, where the flow will be turbulent as

determined by the local Reynolds number based on diameter. For the two grids, the initial number of cells in the driver, shock and acceleration tube are 75, 1500, and 1000 respectively for the coarse grid and 150, 3000, and 2000 cells for the fine grid. There was clustering placed on the cells towards the secondary diaphragm in the acceleration tube using a factor of 1.02. Fill conditions for the simulation were taken from Table 5.3 and Table 5.5 for the two different enthalpy conditions.

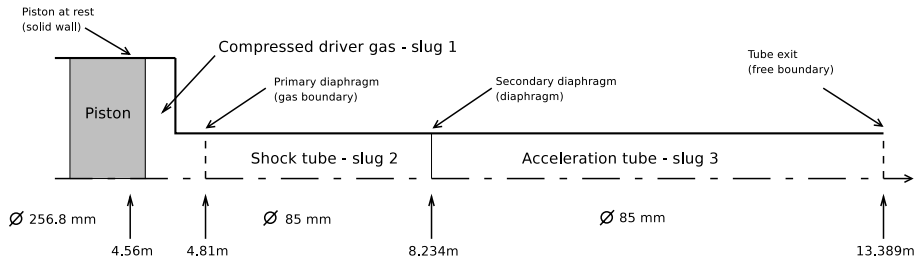


Figure 5.21: Geometry for the *L1d* simulation (not scaled).

Low enthalpy scramjet condition

An estimation of the final driver temperature of 2800 K and a driver pressure of 15.8 MPa was made using a combination of a perfect gas analysis and compared to experimental measurements. This temperature is slightly higher than the value estimated by Scott [3] for a pure helium condition. A comparison of the calculated static pressure with that measured experimentally in s119 can be seen in Figure 5.22 using the computational time base. This shows both have similar levels of static pressure and decay rates, showing the simulation has captured the driver slug correctly. There is an overshoot measured experimentally at both st2 and st3, which are thought to be caused by gauge response issues. This has also been shown by Scott [3] to occur at various conditions. Also, the initial rise in pressure caused by the shock occur at similar times which indicate the shock speed is correctly calculated. The properties just before the diaphragm at position st3 for the fine grid simulation are shown in Table 5.6. The sound speed buffer (a_2/a_3) is seen to be 0.892 which is not able to remove acoustic wave interference for the condition. There is a noticeable difference in the flow properties between the two grid sizes, though further refinement has shown that the fine grid was converged enough to define the wave structure and shock tube flow properties for the axisymmetric simulation.

To investigate the speed of sound buffer in this condition, Figure 5.23 shows the time history of this property at st1 and st3. The initial jump to 730 m/s is due to the passing of the shock, with the second rise back to 730 m/s being the passing of the interface. With the region between the interface and the shock theoretically having constant flow properties, the sudden dip in sound speed is unexplained. The two traces show this dip occurring at a consistent time before the interface and both show a drop of 55 m/s. As

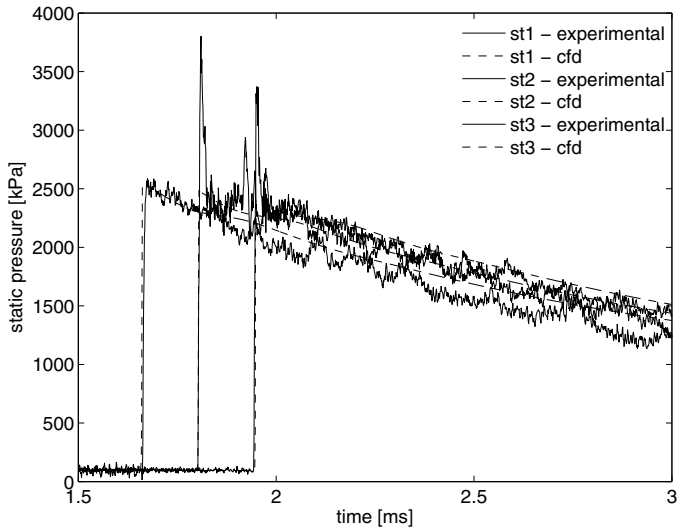


Figure 5.22: Static pressure in shock tube for one dimensional simulation of low enthalpy condition in X2.

the Reynolds number based on diameter is 12.9 million, this cannot be caused by heat transfer effects as *L1d* assumes turbulent boundary layers at a Re_d of 3000.

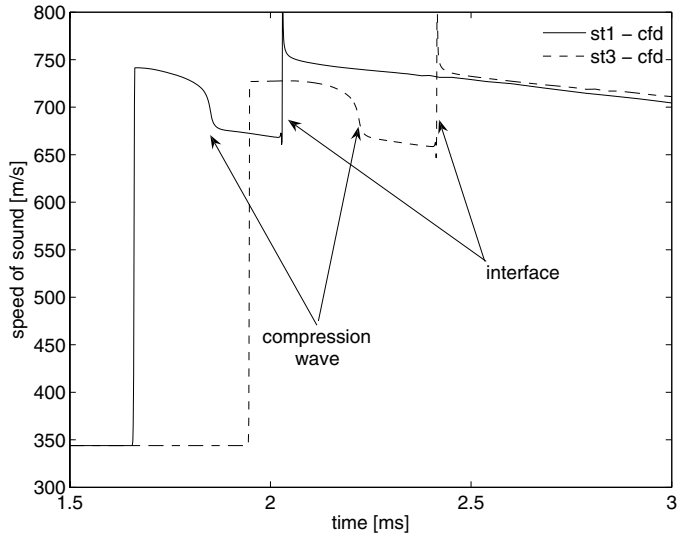


Figure 5.23: Sound speed in shock tube for one dimensional simulation of low enthalpy condition in X2.

To explore the dip in sound speed further, distance-time (XT) plots of temperature and pressure contours of the shock tube can be seen in Figures 5.24 and 5.25. There is a distinct bend in the shock at 6.07 m where an increase in shock speed occurs from 1479 m/s to 1583 m/s. This is caused by a compression wave initiated at the area change seen in the pressure plot. This is due to the initial shock being produced through the

constant area section, which has a lower expanded pressure than that of the driver gas that passes through the area change. In the physical tube however, this effect will likely be de-focused due to the finite opening time of the primary diaphragm. Therefore, once the $U - a$ wave reaches the area change a compression wave causes all the gas in front to be compressed further with little change in pressure. Therefore, after this point the gas that is originally compressed by the lower shock speed will have a lower temperature than that processed by the higher shock speed. This was also noted by Scott [3], although the effects of the temperature drop in the unexpanded test gas on the final condition were not explored. This creates a distinct temperature gradient in the test gas, bounding the gas processed before the compression wave, and after the area change compression wave. As the unsteady expansion process will only use a small slug of gas which is processed just before the secondary diaphragm, the effects of this process should be negligible on the flow condition. Having the lower sound speed test gas at the interface may help to buffer any acoustic waves as the ratio of sound speed at the interface will be larger.

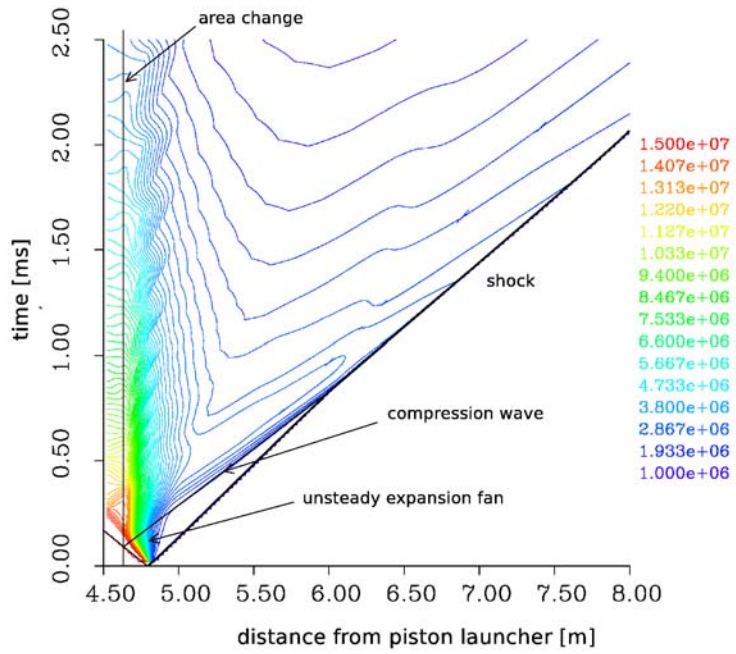


Figure 5.24: Distance-time diagram of static pressure contours in the shock tube for the low enthalpy condition simulation using *L1d*. Units are [Pa].

The reflected shock at the secondary diaphragm is expected to be quite strong, as the thickness of the Mylar used was quite large (1 thou) compared with other conditions tested in expansion tubes with similar pitot pressures. This was due to the large pressure differential which had to be held between the shock and acceleration tubes. The contour plot of temperature can be seen in Figure 5.26 for the time and position of the secondary diaphragm rupture. The reflected shock can be seen to initially propagate backwards

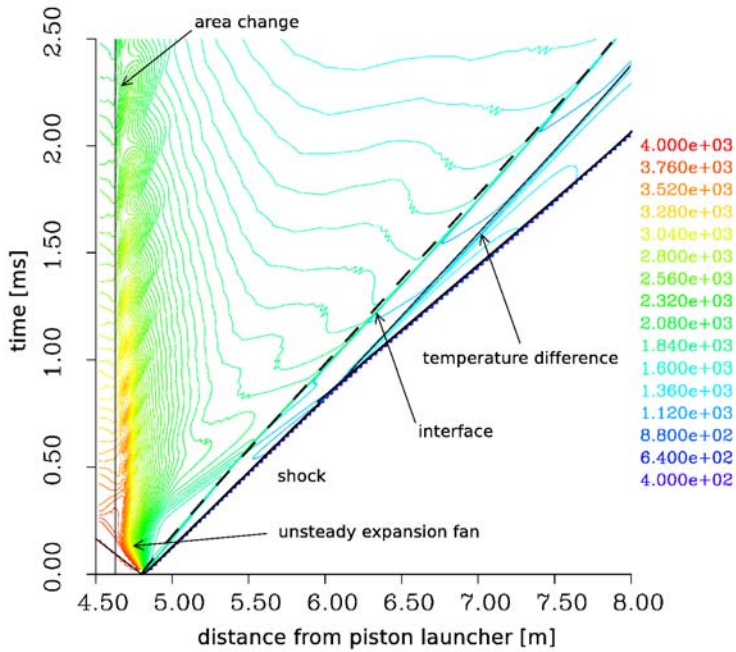


Figure 5.25: Distance-time diagram of static temperature contours in the shock tube for the low enthalpy condition simulation using *L1d*. Units are [K].

before being turned back downstream. As the gas used in the test time will be processed by this shock, temperatures could increase and large scale reactions can occur as in reflected shock tunnels. However, as shown here the temperatures are still below 2000 K where oxygen starts to dissociate. However, at higher Mach number conditions the reflected shock off the secondary diaphragm will require further analysis, as the thickness of the diaphragm will still need to be quite large.

High enthalpy scramjet condition

The high enthalpy condition final driver temperature and pressure was found to be larger than that required in the low enthalpy condition, being 16.2 MPa and 3100 K. It is unclear why this requires a 300 K higher temperature, although it is still under the isentropic limit of 3500 K. This was investigated by comparing numerical results with experimental shock speed and static pressure. This comparison can be seen in Figure 5.27. The shock speed is matched quite well by the simulation, with the timing of the shock arrival consistent with experimental measurements from shot x2s251. The time histories are also seen to match, with st1 showing the same initial drop in pressure which plateaus for $50 \mu\text{s}$ then continues to drop. The flow properties at the passing of the shock at st3 are given in Table 5.6. There is a slight change between the two grid sizes, but this is minimal. Between the two

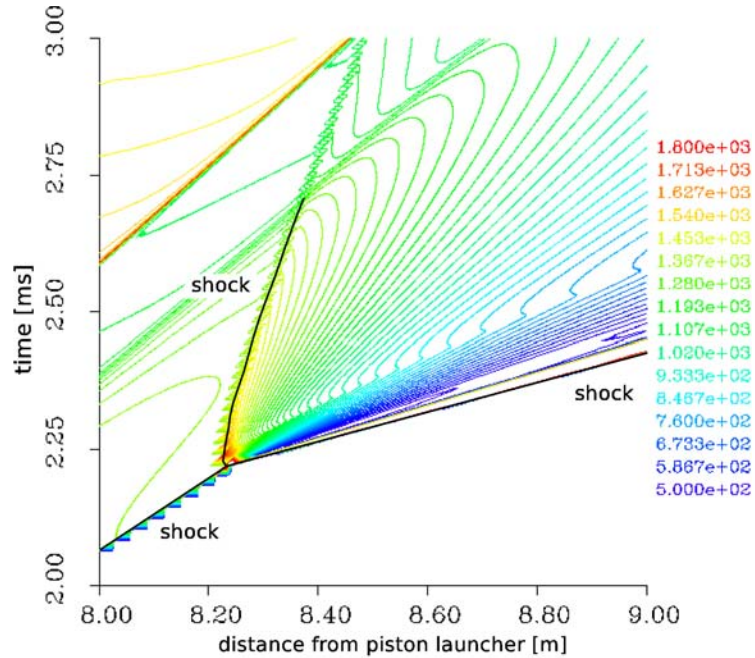


Figure 5.26: Distance-time diagram of static temperature contours of the secondary diaphragm rupturing for the low enthalpy condition simulation using *L1d*. Units are [K].

flow conditions the static pressures are similar, where both the temperature and velocity have significantly increased to meet the higher enthalpy.

Table 5.6: Summary of *L1d* flow properties in the shock tube for X2 condition.

Property	Low enthalpy		High enthalpy	
	coarse	fine	coarse	fine
Primary shock speed, [m/s]	1593	1584	1886	1902
Sound speed ratio across interface, a_2/a_3	0.892	0.871	0.844	0.846
Static pressure, [kPa]	2372	2368	2222	2213
Velocity, [m/s]	1293	1286	1555	1552
Temperature, [K]	1395	1378	1787	1785
Density, [kg/m^3]	5.98	5.98	4.33	4.32
Unit Reynolds number, [million/m]	152.3	151.4	116.2	115.7

The sound speed ratio across the interface is 0.846, which is again marginal in buffering any acoustic waves generated in the driver slug. This is helped however, by a sudden drop in sound speed in the compressed test gas, due to compression waves generated once the primary diaphragm centered unsteady expansion waves reach the area change. This same behaviour was noted in the low enthalpy condition and is explored further in this section. Figure 5.28 shows the time history of sound speed for st1 and st3, where the drop of sound

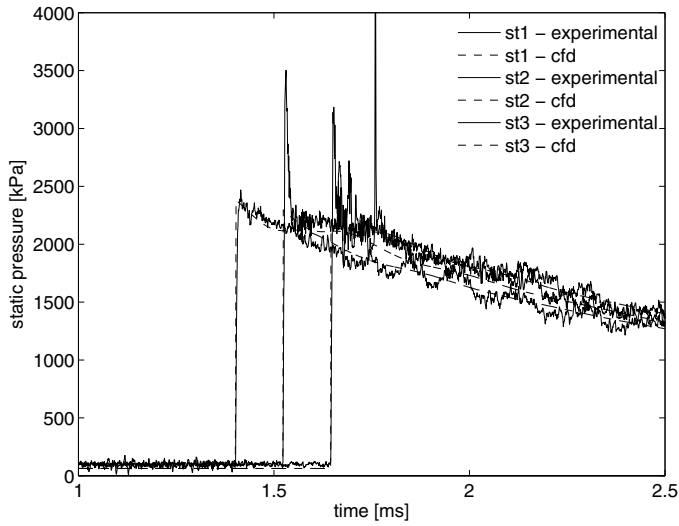


Figure 5.27: Static pressure in shock tube for one dimensional simulation of high enthalpy condition in X2.

speed has a ratio across it of 0.844. The reflected shock wave comes from the area change and propagates back down the tube and catches up with the primary shock which then accelerates. A new interface is created between the gas which has been processed by two different shock speeds. This provides a favourable sound speed buffer which may help in maintaining clean flow. The sharp rise indicates the arrival of the interface with the driver gas.

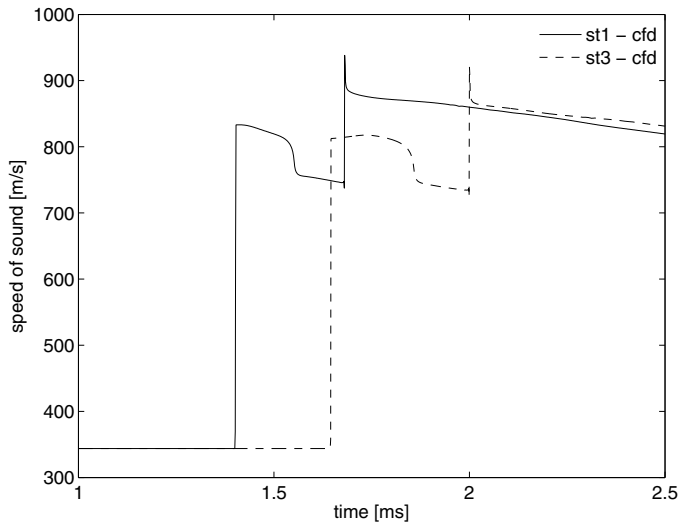


Figure 5.28: Sound speed in shock tube for one dimensional simulation of high enthalpy condition in X2.

5.3.2 Axisymmetric modelling

Axisymmetric simulations are undertaken on the acceleration tube and steady expansion nozzle using the Navier-Stokes solver *MB-CNS* [140] as part of a hybrid simulation of the whole facility. A detailed description of the code and simulation procedure can be found in Section 4.4.2. The axisymmetric modelling as used in the simulation for the X3 facility, uses a transient inflow boundary condition. The boundary condition information is taken from the one dimensional flow just before the secondary diaphragm rupture and placed across the radius of a short section of the shock tube and filled with the un-shocked initial conditions. Thus, the interactions of the reflected shock will be included in the flow. This is connected to the acceleration tube and nozzle which is set at the initial fill conditions. The nozzle exit plane boundary condition is assumed to be supersonic. A schematic of this is shown in Figure 5.29 with the geometry for the facility given in Section 5.1. As shown in the schematic, the *MB-CNS* code allows the tube to be broken into blocks and run in parallel to reduce the computing time.

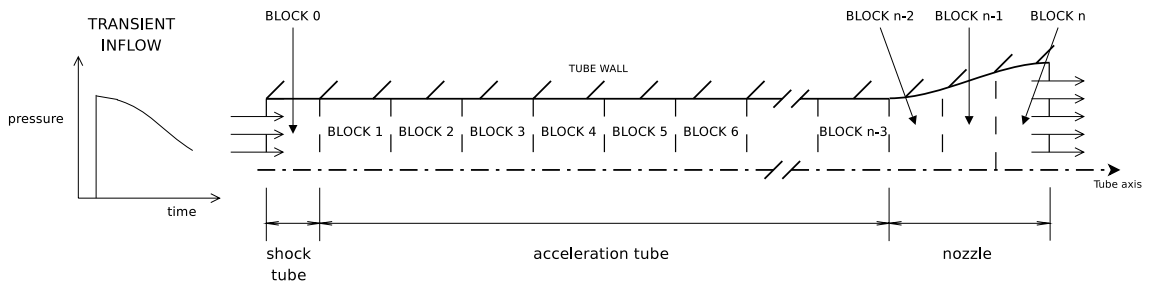


Figure 5.29: Geometry for the *MB-CNS* simulation of X2.

The simulation models the tube and nozzle wall using a fixed temperature wall (298 K) with the Baldwin-Lomax turbulence model. The work on boundary layer transition on X3 in Section 4.5 suggests that the flow will become turbulent close to the interface for this condition. An equilibrium gas model based on *CEA* [145] was used to reduce computational time taken in using a more complex finite rate gas model. With low temperatures and flow speed, any chemical reactions will not occur fast enough for the effects on the flow to be noticeable in the test flow. The grid used in the simulations was 4928 cells axially and 160 cells radially using a Roberts clustering factor of 1.05 towards the wall. The geometry used is as described by Scott [3] and is shown in Section 5.1. Again, the simulations were conducted on the Centre for Hypersonics cluster, Blackhole.

Low enthalpy scramjet condition

Using an initial pressure for the acceleration tube of 140 Pa air found experimentally, simulations were undertaken of the low enthalpy X2 condition. Figure 5.30 shows flow properties at three locations across the flow exit. The first two locations are within the

core flow of the condition, with the final being at the nozzle wall. The first is off centre line by 18.8 mm, to avoid the noise due to large cells and focusing seen in the X3 simulations. After an initial start up process taking 140 μs , the flow is seen to gradually increase in static pressure, density and temperature, with an associated drop in velocity and Mach number. If the test time is taken between 2.1 and 2.7 ms, the average of these properties match the targetted condition quite well. The static pressure at the wall is seen to take a lot longer to drop to the values seen at the start of the nozzle and also rises earlier. This is due to the longer time required for boundary layer development on the nozzle. The reason for the earlier rise is not clear. The Mach number is seen to be quite noisy, especially at the start of the test time. This is thought to be caused by the turbulent transition in the flow just after the interface. This however, should not be as severe in experiments as the numerical simulation shows large gradients in temperature which would not occur.

To investigate both the nozzle start up process and the discrepancies in the flow histories, contour plots of the log of pitot pressure are given for the end of the expansion tube and steady expansion nozzle between 1.4 ms and 2.2 ms. These are taken from the medium grid resolution simulation (4928x80 cells), which has more flow perturbations than the high grid resolution simulation. The plot at 1.4 ms shows the shock at the nozzle entrance with strong gradients around the interface upstream of this. A bulge in the boundary layer just upstream from the interface is the location of the transition to a turbulent boundary layer. This causes waves to be sent through the test gas. As the flow proceeds through the nozzle, a distinct wave can be observed to be travelling upstream of the interface. This is due to the initial under expansion of the test gas due to the low density acceleration gas being caught at the edge of the nozzle. Once this has been passed out of the nozzle, the core flow is allowed to pass through. There is a significant amount of noise seen in the middle of the flow, although it has been found in other simulations that this is due to a lack of grid resolution near the centreline because of the tradeoff with clustering towards the walls [8, 3] (see Section 3.4 for further details).

A comparison is needed with experimental measurements to ensure the simulation reflects the flow development correctly. Figure 5.32 shows a comparison between the *MB_CNS* axisymmetric simulations and experimentally measured shock speed down the acceleration tube and static pressure in the acceleration tube, static pressure at nozzle exit and pitot pressure at the nozzle exit. Also, Table 5.7 gives the time averaged properties for the experimental versus the calculated results (*L1d* for the shock tube and *MB_CNS* for the acceleration tube). The method of calculating the uncertainties in the experimental and numerical simulations is given in Appendix D. Firstly, the shock speed appears to be overestimated in the numerical simulation by approximately 110 m/s. With the shock speed predicted quite well in the shock tube, the likely causes of the underestimation are incorrect fill conditions, non equilibrium chemistry effects or overestimation of reflected shock affects in shock tube simulation. This high shock speed causes the static pressure to

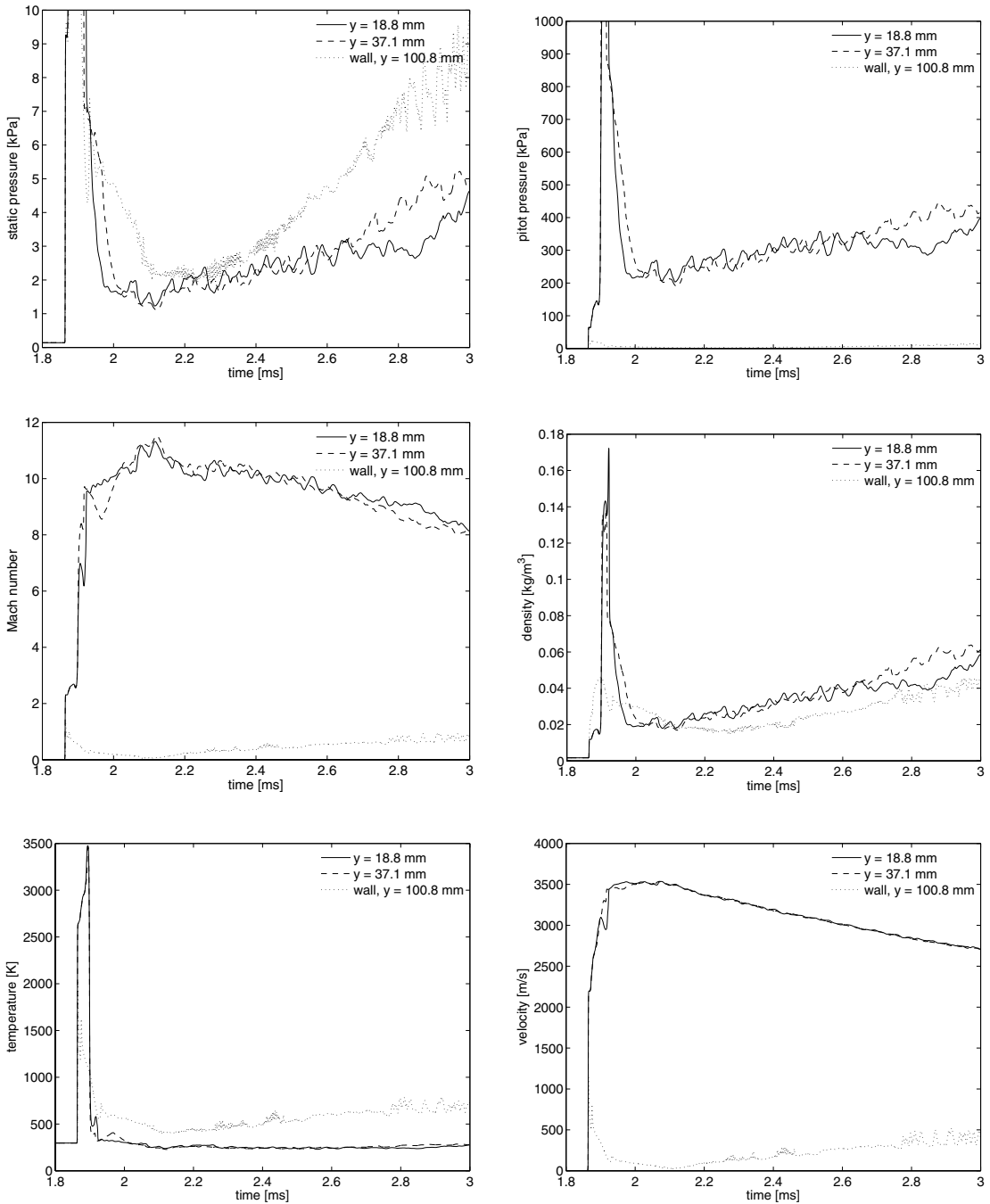
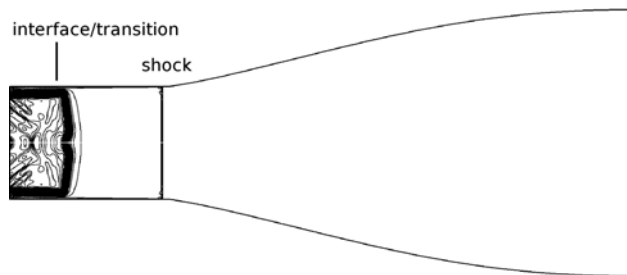
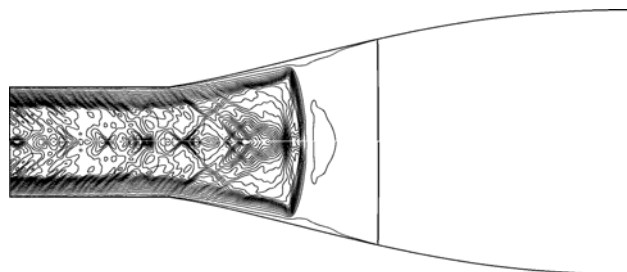


Figure 5.30: Properties at three locations across the nozzle exit for low enthalpy X2 Mach 10 condition.

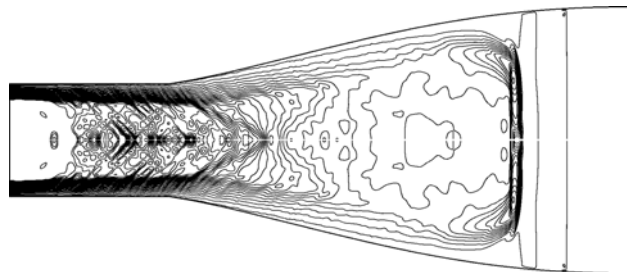
be overestimated by approximately 3 kPa. The numerical simulation does not predict the compression that is associated with the transition, and has a slight decrease in pressure whereas the experimental measurement increases. This discrepancy however, does not seem to affect the flow out of the nozzle with good agreement between the numerical



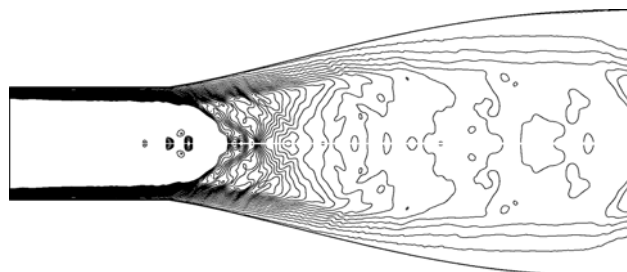
(a) 1.4 ms



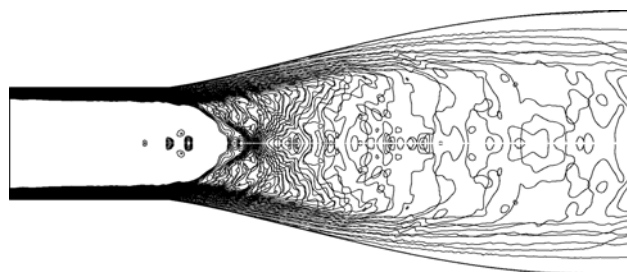
(b) 1.6 ms



(c) 1.8 ms



(d) 2.0 ms



(e) 2.2 ms

Figure 5.31: Contours showing log of pitot pressure during nozzle start-up for low enthalpy X2 Mach 10 condition.
137

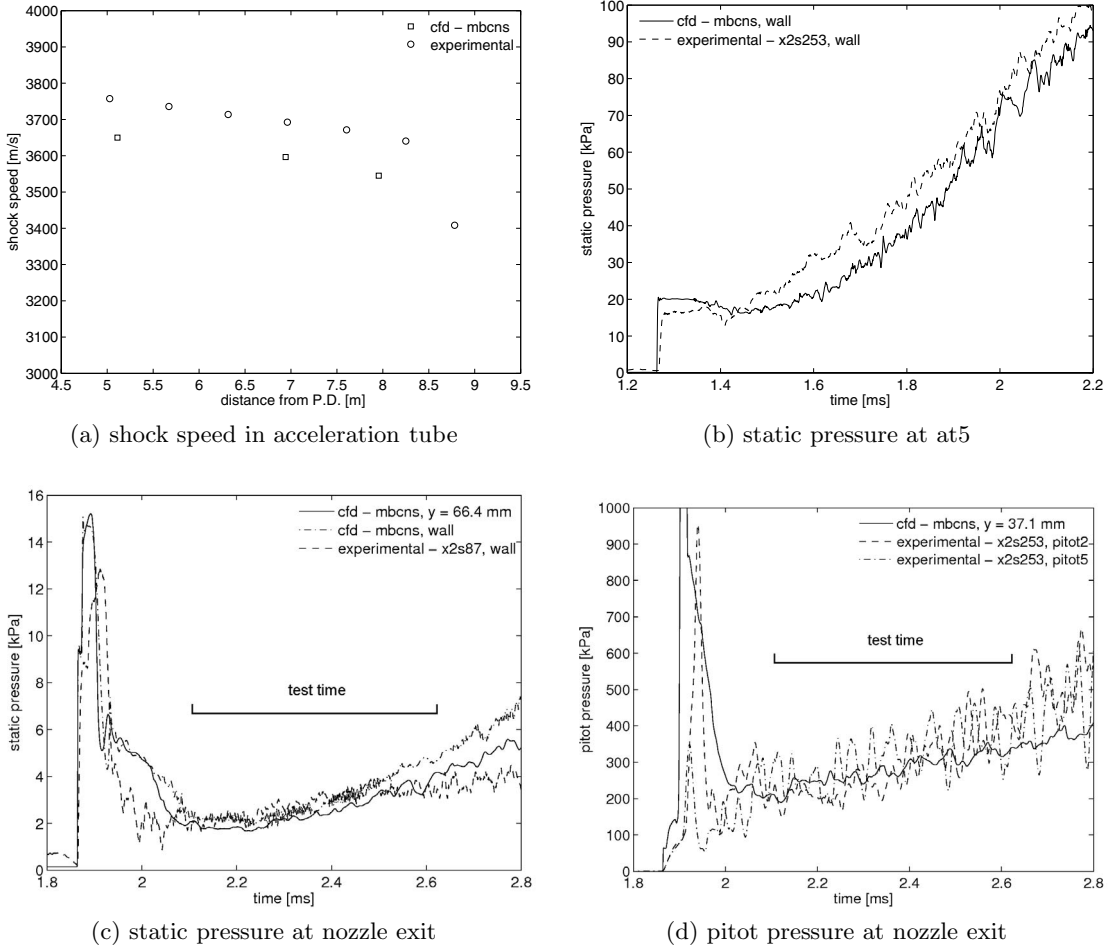


Figure 5.32: Comparison of *MB_CNS* simulation and experimental data for low enthalpy X2 Mach 10 condition.

and experimental predictions of pitot and static pressure at the nozzle exit. The static pressure at the wall is overpredicted in the numerical simulation, with a longer time for the passing of the accelerator gas. Thus, the wall measurement of static pressure is in better agreement with the static pressure of the core flow in the numerical simulation. The static pressure however, does increase a little more rapidly towards and after the test time. This can also be seen in the pitot pressure measurements. The poor experimental rise time of the pitot measurements can also be noted. Although the numerical simulation and the experimental values show some discrepancies, all the flow phenomena are captured relatively well.

High enthalpy scramjet condition

The high enthalpy condition simulation used the same grid and setup as the low enthalpy condition, with the fill pressure of 104 Pa in the acceleration tube and the transient inflow

Table 5.7: Flow conditions for low enthalpy X2 Mach 10 condition.

Property	Experimental	L1d	MB-CNS	Turbulent
<i>Shock tube</i>				
Primary Shock Speed [$m s^{-1}$]	1629 ± 41	1593 ± 51	-	-
Shock Tube Pressure [MPa]	2.42 ± 0.17	2.37 ± 0.31	-	-
<i>Acceleration tube</i>				
Secondary Shock Speed [$m s^{-1}$]	3550 ± 89	-	3640 ± 120	-
Static Pressure [kPa]	17.2 ± 1.2	-	19.7 ± 2.5	-
<i>Nozzle exit</i>				
Static Pressure [kPa]	2.4 ± 0.17	-	2.31 ± 0.30	-
Pitot Pressure [kPa]	-	-	295 ± 46	-
Mach Number	-	-	10.1 ± 0.42	-
Density [kg/m^3]	-	-	0.029 ± 0.0037	-
Static Temperature [K]	-	-	245 ± 15	-
Velocity [$m s^{-1}$]	-	-	3190 ± 100	-
Stagnation Enthalpy [MJ/kg]	-	-	5.33 ± 0.39	-
Unit Reynolds number [million/m]	-	-	5.89 ± 0.73	-
Test Time [μs]	550 ± 20	-	560 ± 20	-

conditions from the fine grid resolution one dimensional simulation. The histories of the flow properties at three radial locations are given in Figure 5.33. These show a very similar flow trend to that of the low enthalpy condition. The average of these properties can be seen in Table 5.8. The average Mach number is 9.9, with an increase in both velocity and temperature resulting in the increase in the total enthalpy. The test time is significantly longer, with no distinct rises apart from the increase in noise for static pressure and density at 2.1 ms into the simulation.

A comparison is made between the experimental and numerical simulations in Figure 5.34 for shock speed, acceleration tube static pressure and nozzle exit pitot pressure. As with the low enthalpy simulations, the shock speed is overpredicted by 160 m/s resulting in an increase in the acceleration tube static pressure, although this in itself is not large enough to cause this discrepancy. The late increase in the static pressure is again attributed to not resolving the effects of boundary layer transition rather than the unsteady expansion wave. The pitot pressure matches the experimental measurements quite well, although the large fluctuations of these measurements are not seen in the CFD result. This would be the case, as previously discussed, the experimental fluctuations were caused by acoustic noise in the pitot cap or fluctuations in flow structure in front of the pitot. In all, the simulations give a good approximation of the experiment and the calculated test conditions provide a basis of the freestream flow properties.

Grid refinement

To check the grid refinement of the simulation, two lower grid resolutions were used to simulate the low enthalpy condition. These grid refinements were made in the radial direction, with 57 cells, 80 cells and 160 cells while maintaining 4928 cells axially along the tube. The time history of flow properties close to the centreline at nozzle exit are shown in Figure 5.35, where the history locations are at axial locations of 1.7 mm, 1.2 mm and 9.2 mm for the low, medium and fine grids respectively. Although there are slight differences due to fluctuations due to the transient nature of the calculation (Section 3.4), the levels and timing of all major fluid phenomena are similar for all flow properties. It is also noted that with increasing grid resolution, that shock speed increases which causes a slightly greater discrepancy between experimental and numerical simulations.

To compare the flow across the nozzle exit for varying grid resolutions, pitot pressure and temperature profiles are given in Figures 5.36 and 5.37 at 2.2 ms into the simulation. The pitot pressure is seen to fluctuate quite dramatically across the core flow, with little comparison apart from the mean level between the three grids. This is due to the differences in shock speeds causing a change in the axial position behind the shock of the slice taken. The core flow size (before drop in pitot pressure) is similar between the two finer grid resolutions. The temperature profiles seem very similar between the three, with a

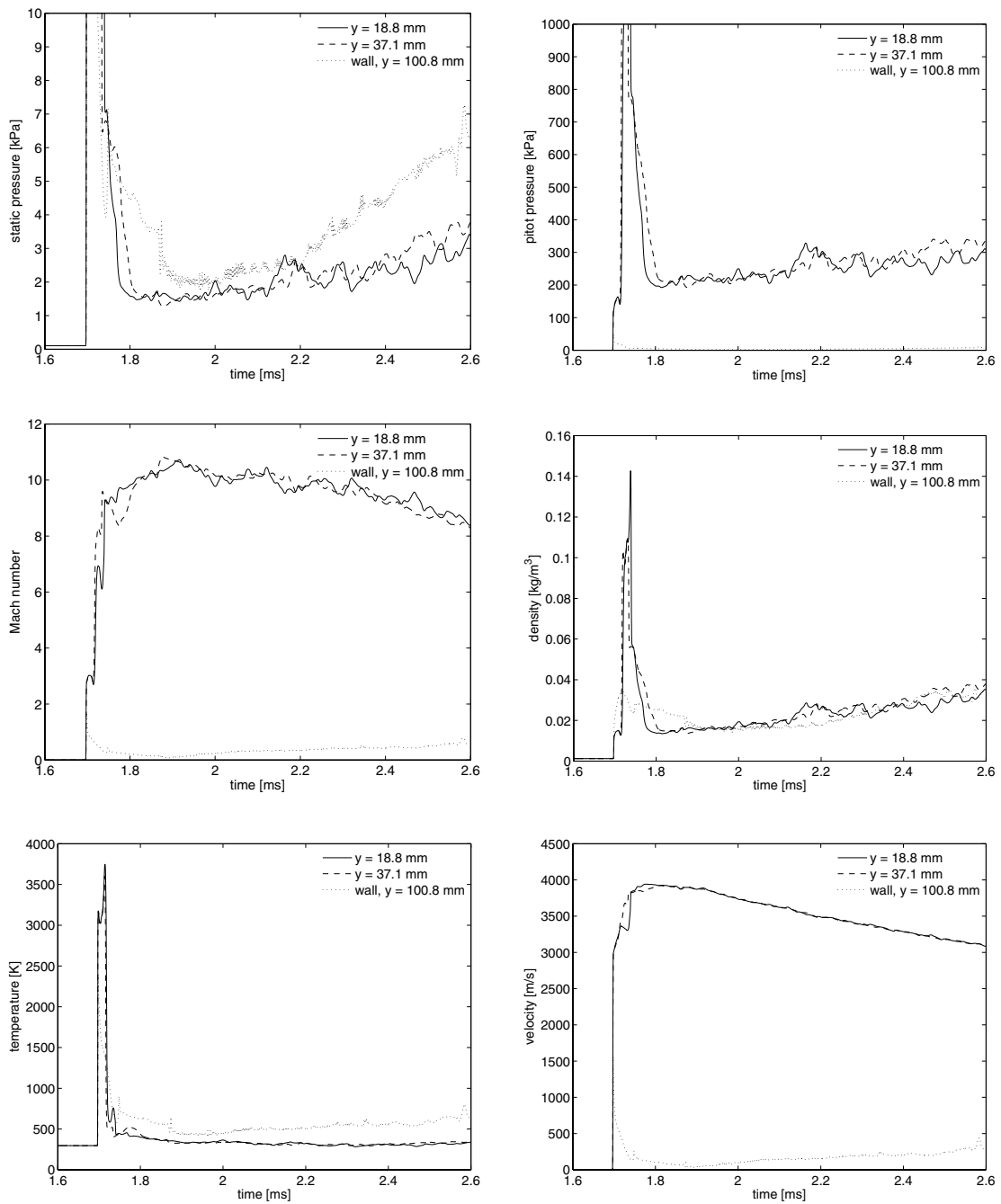


Figure 5.33: Properties at three locations across the nozzle exit for high enthalpy X2 Mach 10 condition.

Table 5.8: Flow conditions for high enthalpy X2 Mach 10 condition.

Property	Experimental	L1d	MB_CNS	Turbulent
<i>Shock tube</i>				
Primary Shock Speed [$m s^{-1}$]	1848 ± 46	1902 ± 61	-	-
Shock Tube Pressure [MPa]	2200 ± 150	2213 ± 280	-	-
<i>Acceleration tube</i>				
Secondary Shock Speed [$m s^{-1}$]	3912 ± 98	-	4070 ± 130	-
Static Pressure [kPa]	15.4 ± 1.1	-	19.5 ± 2.5	-
<i>Nozzle exit</i>				
Static Pressure [kPa]	-	-	2.05 ± 0.3	-
Pitot Pressure [kPa]	242 ± 17	-	245 ± 37	-
Mach Number	-	-	9.9 ± 0.4	-
Density [kg/m^3]	-	-	0.021 ± 0.00027	-
Static Temperature [K]	-	-	320 ± 19	-
Velocity [$m s^{-1}$]	-	-	3550 ± 110	-
Stagnation Enthalpy [MJ/kg]	-	-	6.62 ± 0.49	-
Unit Reynolds number [million/m]	-	-	3.86 ± 0.48	-
Test Time [μs]	500 ± 20	-	320 ± 20	-

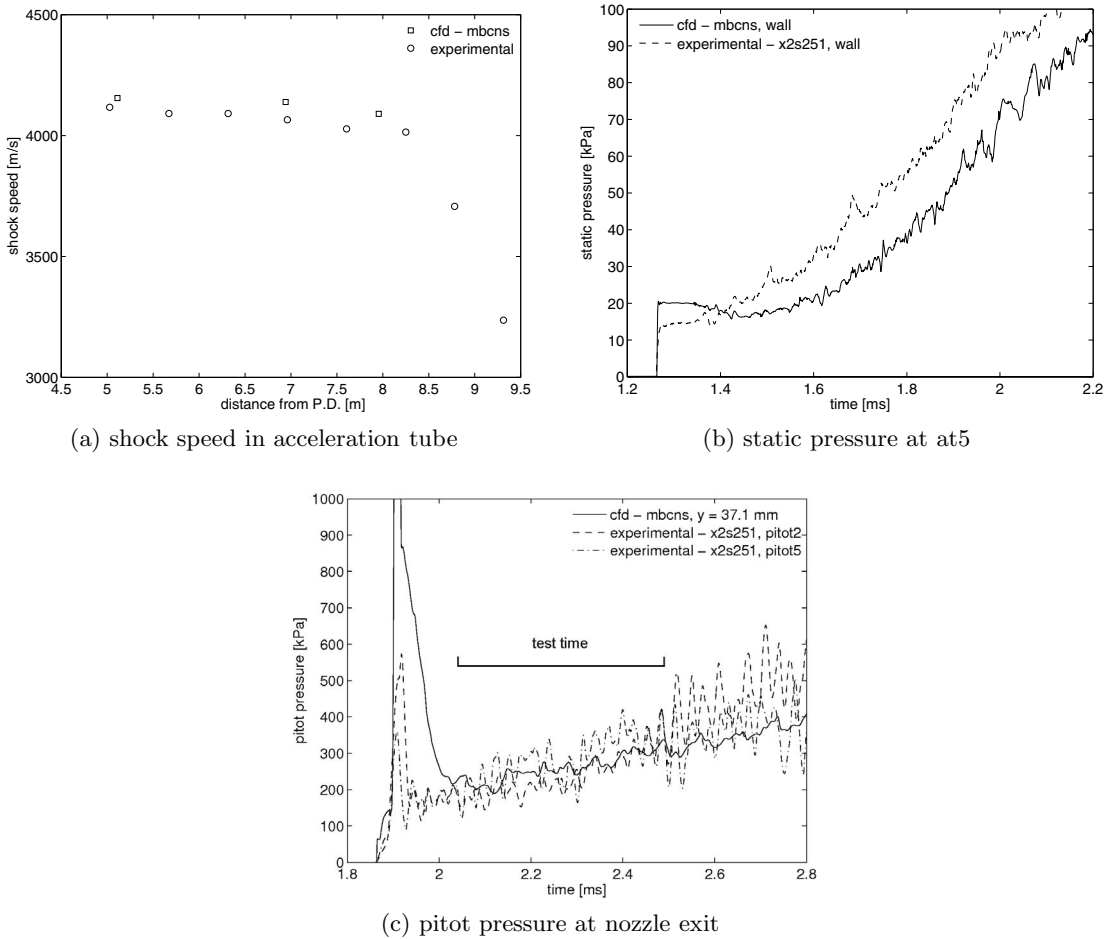


Figure 5.34: Comparison of *MB_CNS* simulation and experimental data for high enthalpy X2 Mach 10 condition.

larger boundary layer prediction in the coarser grid as seen in the pitot pressure. Close to the wall the profiles are a little different, although the gradient (related to the heat transfer) is quite similar between all three grids.

A check on the grid sizing near the wall in hypersonic flows can be made by using the cell size based Reynolds number, where the length is given by the distance between the wall and the cell centre (as discussed in Section 4.4.2). A comparison of the cell Reynolds number close to at5 in the acceleration tube and at the steady expansion nozzle exit is given in Figure 5.38 for both the medium and fine grids. The acceleration tube is close to being resolved, if the rule of thumb of less than 10 is used, during the acceleration slug and the test gas. However, as the unsteady expansion passes, the cell Reynolds number increases dramatically well above this level. The medium grid however has a cell Reynolds number of approximately 20 before the unsteady expansion, so therefore is not resolved far enough. Again, at the nozzle exit the fine grid resolution is below 10 during the test time, whereas the medium grid resolution is not. The start-up flow boundary layer may

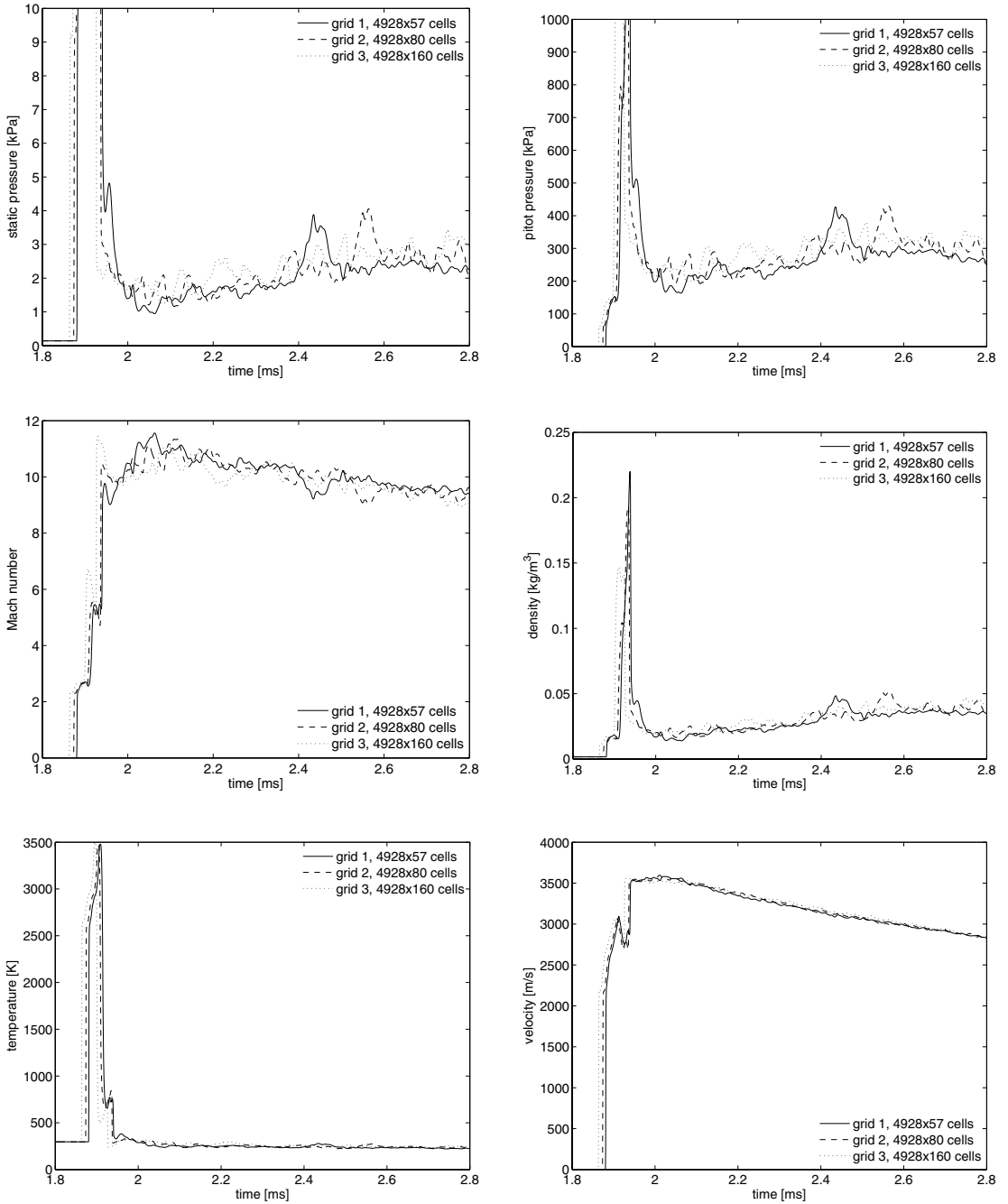


Figure 5.35: Properties near centreline for X2 Mach 10 condition with varying grid resolutions.

not be resolved far enough, although this will be difficult with a structured grid with a large expansion in the radial direction. Although perturbations can still be seen close to the centreline, the boundary layer resolution is seen to be acceptable for the purpose of this simulation.

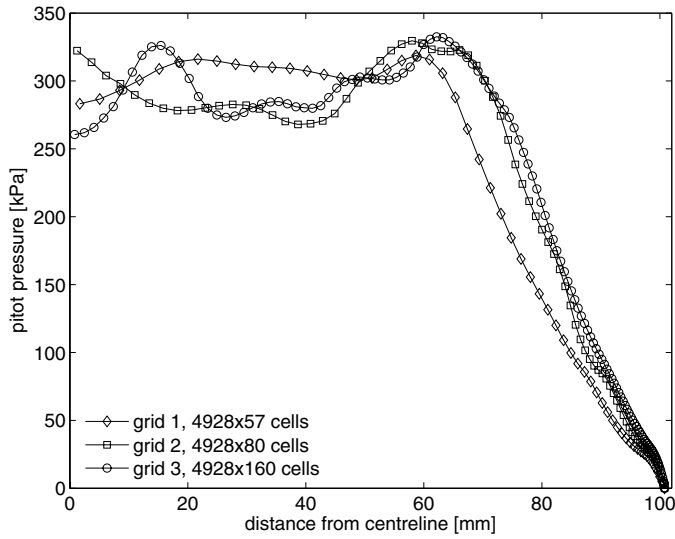


Figure 5.36: Pitot pressure across nozzle exit for low enthalpy condition with varying grid resolutions.

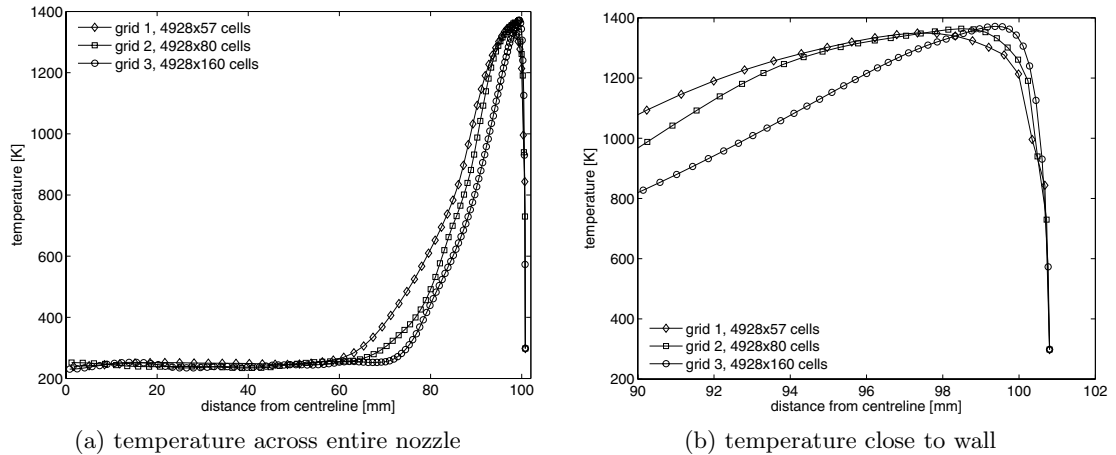


Figure 5.37: Temperature across nozzle exit for low enthalpy condition with varying grid resolutions.

5.4 Summary

Alterations of the X2 expansion tunnel facility have been presented to allow scramjet testing within the facility. Investigation both experimentally and numerically has been used to create two Mach 10 flow conditions. A pL scaled condition was explored to replicate flow properties expected from flight at 30 km (designated low enthalpy condition). Also a higher enthalpy condition was also explored. Experimentally, both conditions flow properties matched the desired flow properties reasonably well, although after $150 \mu\text{s}$ there is some transient behaviour in the flow. Experimentation revealed large fluctuations in pitot pressure were present in both flow conditions. Using measurements taken on the

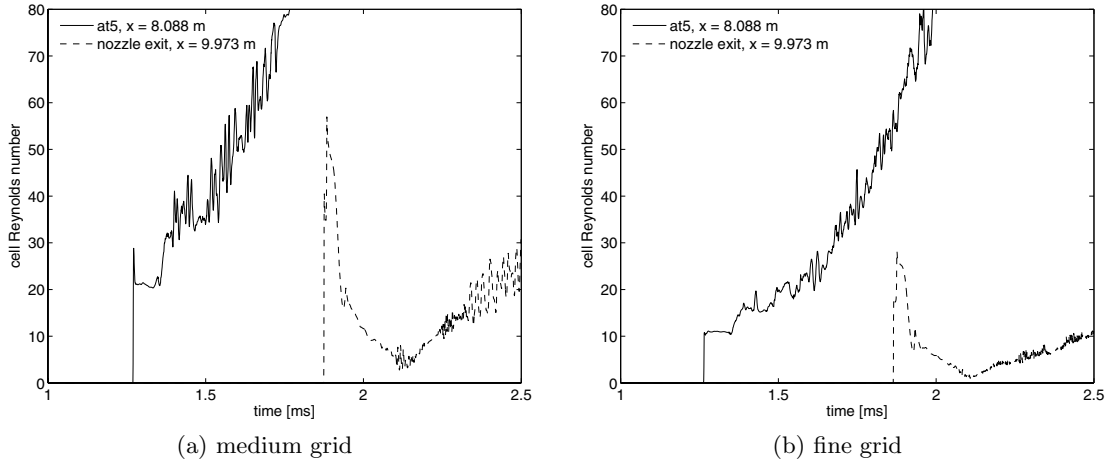


Figure 5.38: Cell Reynolds number comparison for low enthalpy condition with varying grid resolutions.

scramjet intake and previous numerical simulations, it has been shown this behaviour is most likely caused by oscillatory behaviour both in front of the pitot shielding and in the cavity between the shielding and the transducer. One dimensional simulations showed good agreement with both shock speed and static pressure. Although the sound speed ratio across the driver gas/test gas interface was too high to prevent acoustic waves being able to be transmitted across it, due to a re-compression wave from the area change in the driver, a second sound speed buffer is created. Axisymmetric calculations gave fair agreement with experimental measurements, although fluctuations occur in properties close to the axis of the facility due to poor grid resolution.

Scramjet Literature Review

A review is presented of the highest speed airbreathing engine, the scramjet and the physical phenomenon of supersonic combustion. A brief discussion is presented of the main research developments of scramjet engines. Scramjet design is reviewed, with a focus on engine design for high Mach numbers, intended for use in a transatmospheric ascent trajectory. Attention is paid to fuelling options and the design of the intake, fuel injection, combustor and thrust surface.

6.1 Supersonic Combustion

Combustion is a series of chemical reactions of a fuel and oxidant producing heat. Supersonic combustion is the occurrence of these chemical reactions while maintaining the core flow above sonic conditions. Supersonic combustion was first analysed by Tsien and Beilock [39] theoretically, by the addition of a heat source term to the steady state energy equation solved simultaneously with the other conservation equations for a supersonic flow. This was verified by experiments conducted at NACA by Fletcher et al. [40] in 1955 with supersonic combustion of aluminium borohydride within a wind tunnel. Hypersonic combustion is where the combustor entrance airflow Mach number is greater than approximately Mach 5 (i.e. hypersonic), corresponding to free stream Mach numbers of above approximately 12 [31, 42, 1, 157]. At these Mach numbers, the addition of thermal energy through the combustion of even the most energetic fuels becomes a small fraction of the overall energy level of the flow.

Heat release from supersonic combustion differs greatly from subsonic heat release in its effect on the flow properties. This can be examined by taking a simple Rayleigh line approach, whereby stagnation enthalpy is plotted against entropy (shown schematically in Figure 6.1) for a constant area, constant momentum flow with heat addition. In heating a subsonic flow (increasing the static enthalpy), the Mach number increases towards the sonic location. In supersonic flow, the opposite occurs with a decrease in Mach number with heat addition. Also, in supersonic combustion, with the use of the conservation of momentum and continuity equations, the static pressure must increase whereas it decreases in subsonic flow. In scramjet engines, the addition of enough thermal energy for the flow stream to reach the sonic location is termed “thermal choking”. Addition of more heat causes breakdown of the intake flow, resulting in intake spillage and ultimate collapse of

supersonic combustion. Thus, the addition of heat must be avoided if close to reaching sonic conditions in the combustor.

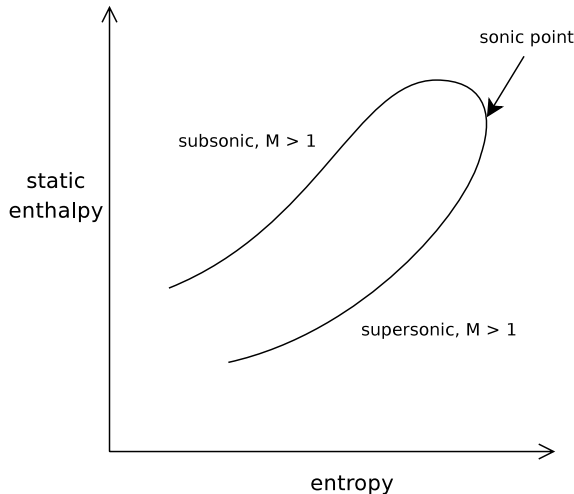


Figure 6.1: Schematic of Rayleigh line flow. Adapted from [27].

Application of the supersonic combustion phenomenon can be divided into four categories [127]: 1) External burning devices for thrust production or drag reduction and/or lateral control; 2) primary propulsion for missiles; 3) primary propulsion for hypersonic airplanes and transatmospheric accelerators; 4) thrust augmentation for fuel-rich rockets. Each of these uses have differing design considerations and limiting issues. For the scope of this thesis, the focus will be on the use of supersonic combustion for a hypersonic transatmospheric accelerator.

6.2 Scramjet Engines - History and Development

Supersonic combustion becomes a good option for thrust production at the hypersonic speeds required in a transatmospheric ascent. This is due to the bulk of the energy of the incoming flow, in the frame of reference of the vehicle, being in the form of kinetic energy. In a ramjet, this kinetic energy is converted to internal energy by decelerating the flow to subsonic speeds for use in combustion. At hypersonic speeds this conversion of kinetic energy to internal energy induces large flow losses, increases the flow temperature to a point whereby combustion has large losses to chemical dissociation. Also, large wall heat transfer rates and pressures induce excessive structural and thermal loads [28, 31, 30, 29]. In supersonic combustion ramjets (scramjets), keeping the flow supersonic allows for the addition of heat to the flow, increasing its internal energy with only minor reductions in the kinetic energy. This however, comes at the cost of time allowed for the combustion of the fuel and air mixtures.

At these high speeds, it is necessary to integrate the engine into the vehicle's body in order to minimise drag and to deal with extremely high heating loads. A simple schematic of the perceived configuration for a transatmospheric accelerating scramjet can be seen in Figure 6.2. The intake compression is integrated into the vehicle forebody, as oblique shocks emanating from upstream of the engine are unavoidable. Fuel is injected into the airstream where rapid mixing is required due to the short times of flight through the combustor. Combustion creates both large heat loads and skin friction drag due to the high density and high energy of the incoming airstream. The nozzle is purely divergent, as the accelerating flow is already supersonic and some of the expansion can occur as a free jet outside the confinement of the engine to maximise thrust compared with drag.

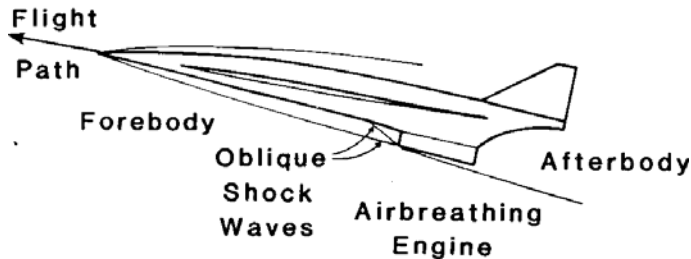


Figure 6.2: Schematic of scramjet engine incorporated into a spaceplane for transatmospheric acceleration. Taken from [28].

Early work on scramjets was conducted by Ferri, beginning in the late 1950's at the Brooklyn Polytechnic University and GASL to establish the chemistry between hydrogen/air and analyse key turbulent mixing issues in an attempt to match heat release to combustor design, as cited in [158]. With this, he set about establishing a fixed geometry scramjet that could operate over a wide range of Mach numbers. Other early work includes that of Switzenbank at McGill University on various scramjet components and Avery, Dugger and Billig at the John Hopkins University on the development of scramjets for use in missiles, as cited in [158, 127]. Some of the more major projects and achievements that have been accomplished since the initial scramjet work of the late 1950's are briefly discussed. A more detailed review of early scramjet work can be found in the review works of Curran [158], Heiser and Pratt [28], Curran et al. [159], Northam and Anderson [160], Billig [127] and Ferri [161, 5]. Stalker et al. [162] presents details of the wide variety of scramjet research that has been conducted at the University of Queensland, beginning in 1980. Reviews of high speed combustion are presented by Anderson et al. [47, 1, 31] and Bushnell [42].

Commencing in 1986, the joint NASA/DARPA National Aerospace Plane (NASP) program has been the best funded program in terms of scramjet technology development [158]. The major goal was to develop and demonstrate the feasibility of a single

stage to orbit (SSTO) vehicle. This developed the technology in five major areas: air-breathing engines; high specific material strength; high temperature materials; vehicle aerodynamics and airframe/propulsion integration. This also developed supporting capabilities in computational fluid dynamics, computational structural mechanics and ground testing infrastructure. Although cancelled in 1995, major test programs were conducted across the entire range of areas for scramjet technology and possible flight regimes.

Ground test development work has culminated in three recent flight programmes to test supersonic combustion. These are the University of Queensland HyShot program [163], the NASA Hyper-X program [164] and the single launch of the HyCause [165]. These programs had varying degrees of difficulties and different objectives. The Hyper-X configuration has been the most ambitious of these flight tests. This tested a fully configured thrust producing scramjet in a free flight scenario (detached from the booster rocket) with a constant dynamic flight path. This program aimed at operating the scramjet for 10 seconds. Out of the three tests completed, the last two were successful at flight Mach numbers of 6.83 and 9.6. The University of Queensland HyShot program was a combustor test primarily to validate ground test data from the T4 facility. This had 4 flights in total, the last two in conjunction with JAXA and QinetiQ had similar configurations as the first two. These flights were to take place on the return of the vehicle from a parabolic trajectory, taking it out of the earth's atmosphere up to 300 km altitude and re-orientated the payload so it is pointed downwards with minimal spin and yaw. The most successful of these was HyShot 2 with recovery of the data, which was used in validation of test data obtained in a reflected shock tunnel [163]. The data is yet to be released from the joint DSTO/DARPA HyCause flight.

6.3 Scramjet Flowpath Design for High Speeds

The optimisation of scramjet design becomes more critical with increasing flight Mach number, as the performance benefits reduce as seen in the specific impulse shown in Figure 1.1. This is highlighted by Anderson [1], stating,

“At high speed, component efficiency becomes critical as a consequence of the increasing kinetic energy in the air processed by the engine.”

A rule of thumb was presented by Anderson to explain this remark, known as the *rule of 69*. This is shown in Equation 6.1, which relates the possible heat release compared with the incoming airstream's kinetic energy. At the lower bound of predicted scramjet capability (at a Mach number of 6), this ratio is approximately 2. With increasing Mach number this ratio will decrease, for example at a M_∞ of 12 the ratio becomes 0.5. Thus, diminishing percentages of energy can be added to the flow. As energy is proportional to the velocity squared, adding a given energy to the flow at high speeds gives a small change in

velocity. Thrust is proportional to the change in velocity, so therefore the resulting thrust production capability of a scramjet will drop with increasing flight speed. These characteristics have been shown to result in the flow mixing and diffusive burning as described by Ferri [5, 1].

$$\left[\frac{\text{stoichiometric heat release}}{\text{kinetic energy of airstream}} \right] \approx \frac{69}{M_\infty^2} \quad (6.1)$$

Also, at high speeds, the amount of heat release possible diminishes [29]. This is due to two reasons; increased difficulty in achieving adequate mixing with low losses while maintaining a significant axial component of the fuel momentum and increased endothermic reactions (heat absorbing dissociation) in the combustor. Since the vehicle will likely have a fixed geometry inlet over a large flight Mach number range, as the flight Mach number increases the temperature at the start of the combustor will increase and the pressure will decrease (due to an increase in altitude). As can be seen in Figure 6.3, lower pressures and higher post combustion temperatures cause the amount of heat release to decrease due to endothermic reactions. The use of higher fuel to air ratios than required will be necessary above Mach 10 in order to provide adequate cooling of the freestream to ensure endothermic reactions do not occur [127]. This also has the additional compensation of providing more thrust, as the fuel axial momentum is a major contributor to the overall thrust [29].

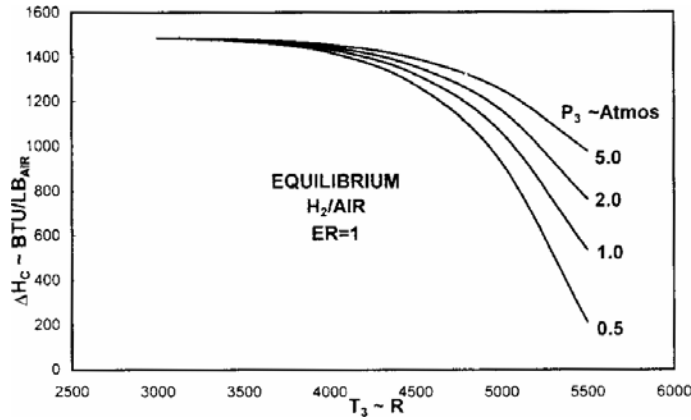


Figure 6.3: Equilibrium heat release of stoichiometric hydrogen/air mixture. Taken from [29]. T_3 is the final temperature and p_3 is both the initial and final pressure.

A review is undertaken of each major component of the supersonic combustion ramjet with specific attention paid to those critical in high Mach number scramjets. These components are the inlet, fuel injection, combustor and expansion nozzle. It is simpler to deal with each of the components separately, but their interactions are also quite important [28, 31]. For example, adjustment of the inlet compression will reduce the inlet flow losses, but this will require a lengthening of the combustor to have complete combus-

tion, which increases the overall skin friction. Additionally, integration of the engine with the flight vehicle becomes an important requirement at hypersonic speeds, to maximise the thrust potential of the vehicle. Therefore, attention is paid to each component for effects on other system components. Several schemes have been developed for flow path optimisation. These range from the quite simple methods which compile efficiencies from each component [166], unified cycle analysis methods [167, 168, 169] and to quite complex methods which can be applied to three dimensional CFD [170].

6.3.1 Fuelling options

With the flow being supersonic, the reaction residence times and ignition properties of the flow become quite critical to scramjet performance. This was acknowledged in the first experiments on supersonic combustion performed [40], whereby a highly reactive fuel was used. The nature of combustion can vary greatly over the postulated scramjet flight envelope. Some applications resemble the classic diffusion flame, where reaction rates are very fast and heat release is mixing controlled (typically high enthalpy). In some applications, ignition delay is critical and combustion, when it occurs has a large amount of premixing achieved. With minimal thrust being produced, another major consideration of fuel choice is the amount of heat release obtainable per unit mass of fuel. This is sometimes offset by the structural weight that is required to hold the fuel at high pressures. The choice of fuel is also dependent on the mission scenario for the scramjet, such as military operations where the fuel may be left in the rocket for long periods. Also, the fuel within the scramjet must be used as a thermal sink to ensure heat loads on the structure do not exceed material limitations. The two main choices for fuels in scramjet engines are hydrocarbon fuels such as ethylene and JP-7 or hydrogen. Although hydrogen can deliver a higher fuel specific impulse, larger thermal energy capacity and easier to ignite [28], hydrocarbons have 11 times the storage capacity over hydrogen, require less structural weight to contain the fuel as the tanks are smaller and therefore can be stored in any shaped container.

Lewis [171] stated,

“At near orbital speeds of a transatmospheric ascent, the only fuel that may be able to produce positive thrust is hydrogen.”

Lewis predicts the useful range of hydrocarbon powered scramjets is likely limited to be below Mach 10. More recent work by Tetlow and Doolan [172], explored a three stage vehicle on an orbital mission using a rocket/scramjet/rocket flight phase, where the scramjet was fueled by either hydrogen or the hydrocarbon JP-A. They discovered that the hydrogen scramjet configuration out-performed the hydrocarbon system, and was capable of having a similar payload mass fraction compared to a fully rocket based system. Heiser and Pratt [28] also point out that the only fuel with the thermal energy

capacity to deal with the system cooling requirements above Mach 10 is hydrogen, as seen in Figure 6.4. Hydrocarbon fuels have similar specific thrust to hydrogen. Therefore, for low speed applications, hydrocarbon may be a preferable fuel due to energy density and storage considerations despite lower specific impulse.

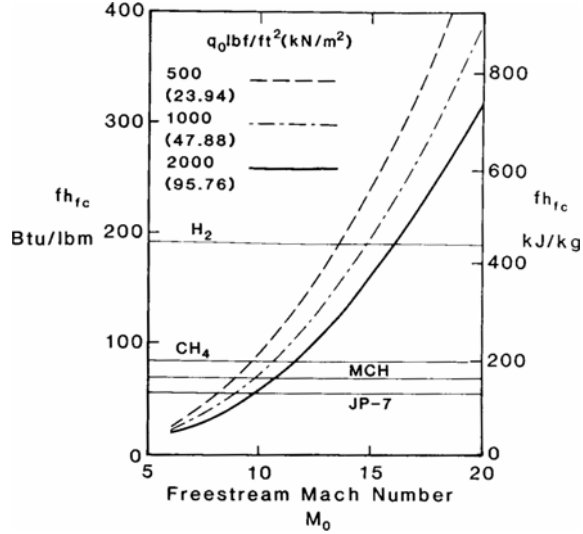


Figure 6.4: Different fuels thermal energy absorption capacity to meet total engine heat flux as a function of freestream Mach number and dynamic pressure. Taken from [28].

Hydrogen fuel combustion

The combustion process comprises a set of reactions between fuel (hydrogen) and an oxidiser (oxygen in air) which produces a net addition of thermal energy. There are many intermediate reactions that can occur between air and hydrogen, although the main combustion product is H₂O. Therefore, every oxygen molecule requires two hydrogen molecules (i.e. stoichiometric mixture) to reach complete reaction. The reaction rate for any chemical reaction is a function of the species concentration and the local temperature. With many different chemical reactions acting simultaneously, the rates of reactions in combustion become quite complex. The generalised form of a reaction involving n species is given by Anderson [9] in Equation 6.2. With this, the rate of production of any species can be calculated using Equation 6.3 for the forward and reverse reaction rates (k_f and k_b respectively) for the specific reaction. These reaction rates can generally be calculated by use of the modified Arrhenius equation [9] (Equation 6.4), where the dependence of reaction rates on temperature is introduced. The rate of reaction and therefore the rate of heat release is dependent on both the local temperature and local pressure (i.e. concentration).

$$\sum_{i=1}^n v'_i X_i \Leftrightarrow \sum_{i=1}^n v''_i X_i \quad (6.2)$$

$$\frac{d[X_i]}{dt} = (v''_i - v'_i) \left\{ k_f \prod_i [X_i]^{v'} - k_b \prod_i [X_i]^{v''} \right\} \quad (6.3)$$

$$k = A \left(\frac{T}{T_{ref}} \right)^n e^{-E_A/RT} \quad (6.4)$$

There are various reaction schemes available for the air/hydrogen interaction. One of the more popular schemes has been the Jachimowski “9 species, 33 reaction” scheme [173]. Jachimowski suggests that the species containing nitrogen only become important at flight Mach numbers above 12 due to the high dissociation temperature required for nitrogen. As this scheme is quite complex and numerically intensive, this is not explored within the context of this thesis. A simpler reaction scheme proposed from Ferri’s [5] early experimental work, suggests the most important hydrogen-air reactions are those seen in Table 6.1 involving seven species: H, O, H₂, O₂, OH, H₂O and M (a third body molecule). These important reactions include the breaking down of both the O₂ and H₂ molecules into chain-carriers and the creation of OH and H₂O molecules. The reaction rates of both the forward and reverse reactions have been obtained over the past 60 years using shock tubes. As Jachimowski [173] and Ferri [5] both concluded, the amount of concentration of free radicals in the initial flow can greatly vary the reaction rates. As discussed in Chapter 2, this is the reasoning behind the use of an expansion tube to conduct higher Mach number scramjet tests, as other hypersonic test facilities produce chemical dissociation of the air due to stagnation of the gas and the high total enthalpies.

Table 6.1: Important chemical reactions between hydrogen and air for supersonic combustion. M is a third body reactant such as nitrogen. Taken from [5].

(1)	H + O ₂	\iff	OH + O
(2)	O + H ₂	\iff	OH + H
(3)	OH + H ₂	\iff	H ₂ O + H
(4)	2OH	\iff	H ₂ O + O
(5)	H ₂ + M	\iff	2H + M
(6)	H ₂ O + M	\iff	H + OH + M
(7)	OH + M	\iff	H + O + M
(8)	O ₂ + M	\iff	2O + M

Ferri [5] describes the hydrogen-air combustion process as taking place in two steps; an initial step called the induction phase where the temperature does not substantially change and chain carriers are produced (H, O, OH, HO₂ and H₂O₂), followed by a second phase where the heat is released and the temperature increases quite rapidly due to the exothermic reactions occurring extensively. This can be seen in Figure 6.5. Heiser and

Pratt [28] define a third period where all the species mole numbers decay to their equilibrium concentrations, although as seen in Figure 6.5, the temperature does not change significantly. Huber et al. [35] defines the time taken in the initial phase of ignition to be once the temperature of the mixture has risen to 5% of the complete reaction temperature rise. In terms of the chemical reactions this is mostly the induction phase. The reaction time is defined as the time following ignition to reach 95% of the heat release from the formation of H_2O has occurred.

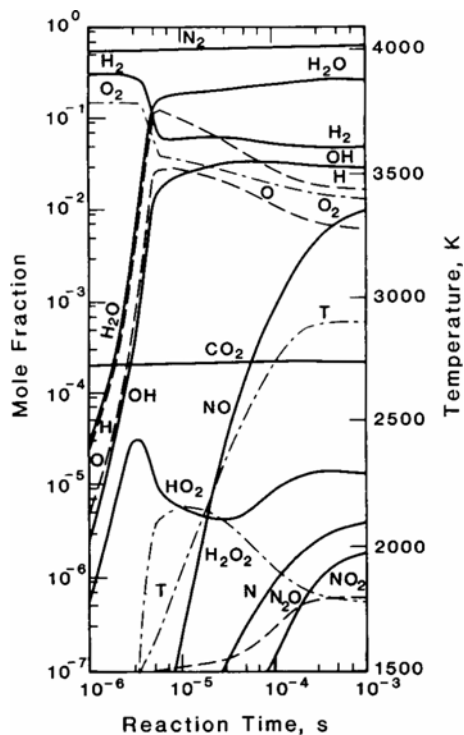


Figure 6.5: Isobaric batch reaction of stoichiometric hydrogen and air. Taken from [28]. Initial conditions of 2 atmospheres and 1500 K. Temperature labelled as T.

Analytical expressions for the time to ignition (ignition delay time) and reaction as a function of initial temperature and pressure (Equations 6.5 and 6.6) was proposed by Pergament [174]. These expressions apply for a perfectly mixed stoichiometric hydrogen-air mixture. It can be noted that the ignition delay time is an exponential function of temperature. This accommodates the fact that colliding reactants must possess sufficient energy to start the chain reactions. Also, the time for ignition is inversely proportional to the pressure. This is because the reactions involved in the induction phase are mostly two body reactions [35]. Plotting the ignition delay time for various temperatures over a pressure range between 0.5 to 1.5 atmospheres (Figure 6.6), reduction of ignition delay time is seen to occur with increasing initial temperature and pressure. The reaction time however, is not so dependant on the local temperature, as the highly reactive chain-carriers

have been formed. However the reaction time is inversely proportional to $p^{1.7}$ as the reaction system has many three body reactions where the reaction rates are proportional to the square of pressure. Figure 6.7 shows the reaction time as a function of temperature and pressure. It can be seen that the reaction time for temperatures less than 1300 K are shorter than those involved in igniting the flow. This is why silane has often been used to increase the temperature of the mixture to ignite the hydrogen/air mixture [160].

$$t_i = \frac{l_i}{U} = \frac{8 \times 10^{-14} e^{\frac{9600}{T}}}{p} \quad (6.5)$$

$$t_r = \frac{l_r}{U} = \frac{1.05 \times 10^{-9} e^{\frac{-1.12T}{1000}}}{p^{1.7}} \quad (6.6)$$

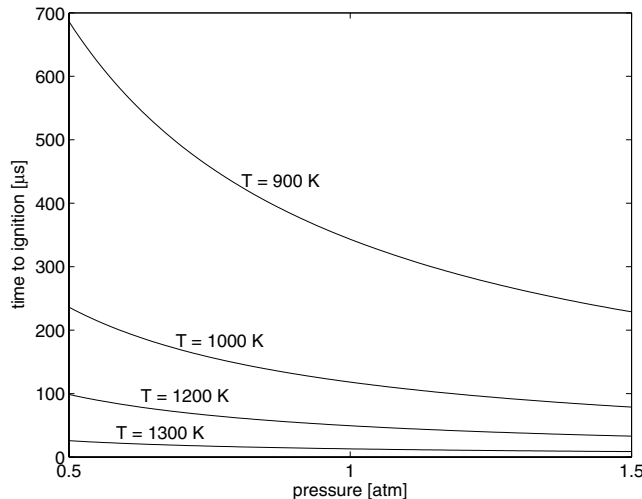


Figure 6.6: Ignition time for stoichiometric hydrogen/air mixture.

It is often desirable due to various design reasons, to have either a fuel rich or a fuel lean mixture (i.e. more or less fuel than used in a stoichiometric mixture). The ratio of actual fuel/air ratio to the stoichiometric fuel/air ratio is the fuel equivalence ratio¹ [28, 35]. The definition of this can be seen in Equation 6.7, which also shows the mass ratio of air to hydrogen required for a given fuel equivalence ratio. For a homogeneous hydrogen/air mixture, ignition is quite insensitive to the fuel equivalence ratio [35]. However, in a scramjet, temperatures of the fuel may be less than that of the freestream. Therefore, ignition is more likely to occur in lower equivalence ratio regions as the mixed temperature will be higher [35]. Huber et al. [35] also point out that the subsonic regions that are created behind perpendicular/angled injection are also a likely ignition position due to the long residence times and high temperatures.

¹Also known as equivalence ratio.

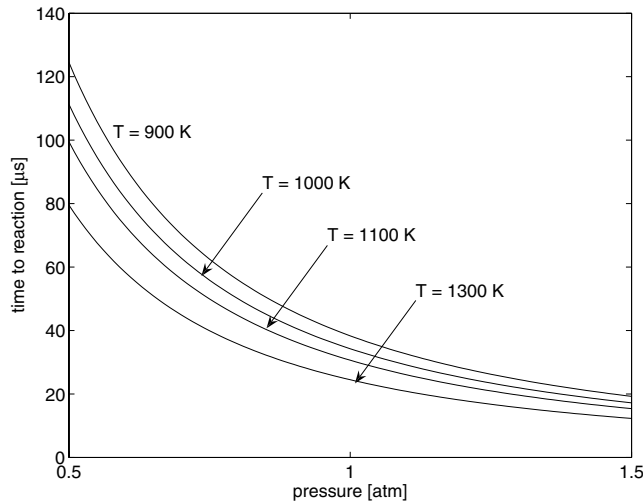


Figure 6.7: Reaction time for stoichiometric hydrogen/air mixture.

$$\phi = \frac{f}{f_{st}} = \frac{\dot{m}_f}{0.0292\dot{m}_{air}} \quad (6.7)$$

6.3.2 Inlet

As in low speed flight, the purpose of the intake of an engine is designed to both capture the incoming airstream for use in combustion and compress the flow to increase the entire cycle efficiency of the engine [30]. At hypersonic speeds, the compression required for combustion can be achieved without the use of a mechanical compressor as in conventional jet engines. In hypersonic inlets, the design aims to provide low flow losses, minimise weight and produce low drag. The design is complicated by many aerothermodynamic constraints (i.e. starting of the inlet, boundary layer separation) and mechanical/thermal constraints (i.e. leading edge heating rates). For scramjets, the inlet is also designed to provide supersonic flow to the combustion process, opposed to the subsonic flow requirements of a ramjet engine.

At hypersonic speeds, there will be inevitable flow compression caused by oblique shocks emanating from the vehicle forebody. A scramjet inlet can take advantage of some of this to reduce the compression required by the intake [28]. This has been seen in the use of the entire underbody of a scramjet vehicle as part of the intake in programs such as NASP and Hyper-X [158]. This also allows for the collection of large volumes of air which are needed to produce the required thrust due to the relatively low densities encountered at high altitudes compared with sea level. However, intakes are going to generally have to operate over a large Mach number range and require high efficiency across this range. Also, due to the difficulty in making joints and hinges that will survive the heating and aerodynamic loads, the geometries of these are likely to be relatively fixed.

The amount that the inlet should compress the flow will again depend on the integration into the complete system. As a rule of thumb, the pressure at combustor entrance should have a pressure of least 50 kPa and high enough temperatures to ensure auto-ignition of the fuel/air mixture (approximately above 900 K) [29]. At higher speeds, the required compression increases due to a reduction in freestream static pressure. This is illustrated in Figure 6.8, where for a given inlet area ratio, higher flight speeds result in a higher pressure ratio required across the inlet [30] while still achieving the same efficiency (shown here as kinetic energy efficiency). Higher inlet contraction ratios allow for higher pressure ratios across the inlet for the same inlet efficiency and reduce the combustor size, which is beneficial in minimising skin friction drag and flow losses associated with fuel injection. However, high inlet contraction ratios also result in higher temperatures at the combustor entrance (seen in the form of Mach number in Equation 6.8, as velocity change is small) which may decrease the heat release possible due to endothermic reactions (Section 6.3). This will become a greater issue at higher Mach numbers where large pressure rises are required.

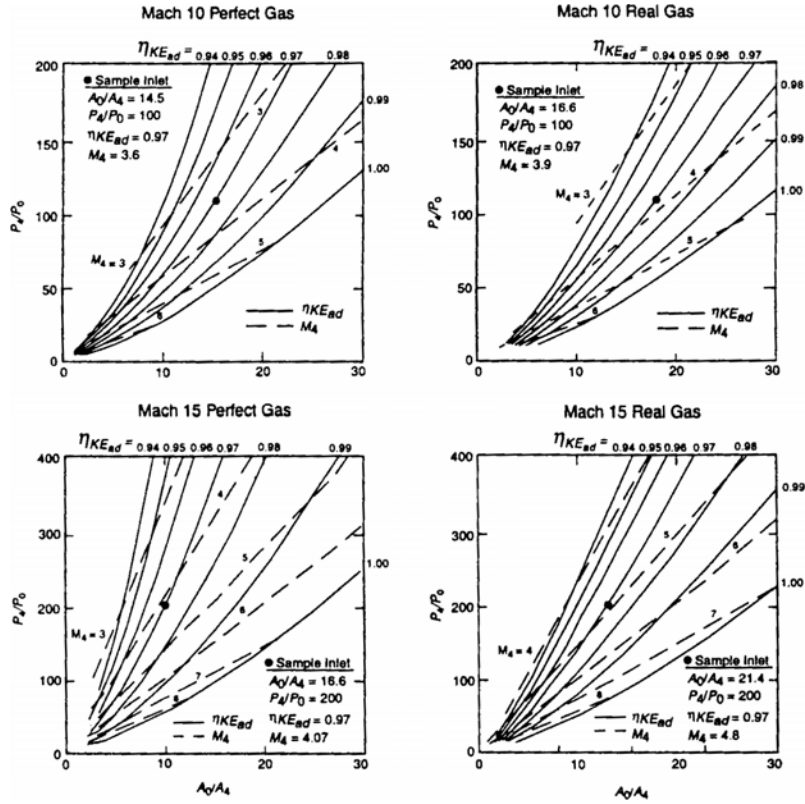


Figure 6.8: Inlet performance as a function of inlet pressure ratio and area ratio. Taken from [30]. Results are presented for a constant dynamic pressure flight path (47.8 kPa).

$$\eta_{KE} = 1 - 0.4 \left(1 - \frac{M_{com,ent}}{M_\infty} \right)^4 \quad (6.8)$$

A good review of different types of inlet design for a wide variety of scramjet configurations is presented by Van Wie [30]. Basic two dimensional inlets are generally quite inefficient as they use a series of oblique shocks as a compromise between the inviscid losses associated with the shocks, and high viscous losses that are associated with very long isentropic compression [175]. Planar two dimensional inlets offer the advantage of ease of design (although three dimensional flow effects exist, the flow remains predominately two dimensional) and are capable of functioning over a wide range of operating conditions with the possibility of variable geometries [30]. Full capture inlets like Busemann type inlets are highly efficient, although have full internal compression which can lead to unstart [30]. Sidewall compression inlets offer higher performance although they can result in large spillage drags at off design conditions due to narrow openings [30]. Due to geometrical constraints it makes sense to initially capture a rectangular area, but as will be seen in Section 6.3.4, low to medium aspect ratio combustors are most practical. Work by Smart et al. [176, 177] has shown that rectangular to elliptical transition inlets can be efficient and operate through a large range of conditions. This also takes advantage of a crotch area², which can allow spillage to start the inlet although is quite efficient at capturing the flow during normal operation.

Several of the aerothermodynamic constraints mentioned previously and their implications to inlet design are discussed here in further detail.

Inlet starting constraints

Intake starting is a critical issue to the operation of scramjets. At many flow conditions both started and unstarted inlets are theoretically possible. In scramjets, the ‘unstarted’ conditions are generally associated with flow spillage past the leading edges of the inlet, choking at points of restriction and extended subsonic regions in the combustor. Also in scramjets, unstart can be caused by large separated region forcing the expulsion of the shock system from the combustor duct and having subsonic entrance flow and spillage [30]. The fundamental cause of unstart is the inability of the ducted regions of the combustor to pass the mass flow captured by the intake under steady flow conditions. Some of the important issues are stream tube compression, flight Mach number and Reynolds number, and the flight history up to where combustion is initiated[30]. Unstarted flows established before reaching flight conditions may preclude correct operation at the design condition.

In ramjets, estimates of the allowable internal contraction can be made using the Kantrowitz limit, which is an isentropic calculation of the internal contraction area that

²The cowl side notched area in many scramjet intake designs to allow mass loss during intake start-up.

will produce sonic flow at the throat. For an ideal gas, the Kantrowitz limit can be calculated using Equation 6.9. Van Wie [30] suggests that at Mach numbers between 2.5 and 10, the limit is closer to that permitted by isentropic compression based on experimental data, with the limit defined by Equation 6.10. This is due to the flow through to the combustor at hypersonic speeds not being processed by a single normal shock, but rather by oblique shock waves caused by large separation on the external contraction surface. The contraction allowable however is less than the isentropic limit due to losses caused by shock waves and viscous interactions. It is noted that both of these theoretical limits depend primarily on the Mach number and not on the Reynolds number or boundary layer effects.

$$\frac{A_1}{A_2} = \frac{1}{M_1} \left(\frac{(\gamma + 1) M_1^2}{(\gamma - 1) M_1^2 + 2} \right)^{\frac{\gamma}{\gamma-1}} \left(\frac{\gamma + 1}{2\gamma M_1^2 - (\gamma - 1)} \right)^{\frac{1}{\gamma-1}} \left(\frac{1 + \gamma - 0.5 M_1^2}{\gamma + 0.5} \right)^{\frac{\gamma+1}{2(\gamma-1)}} \quad (6.9)$$

$$\frac{A_1}{A_2} = \left(0.05 - \frac{0.052}{M_\infty} + \frac{3.65}{M_\infty^2} \right)^{-1} \quad (6.10)$$

The process of flow establishment is very different in an impulsive test facility than seen in flight, so much so that impulsive facilities are not really very suitable for the study of inlet starting problems [30]. The mass flow immediately behind the starting shock in an expansion tube accelerator gas for instance, is much lower than that in the subsequent steady flow regime, thus making it easier for the starting pulse of gas to pass through the duct. Using computational simulations, Atkins [178] showed that, when testing in reflected shock tunnels, the minimum inlet area ratio for start is lower than that defined by traditional methods of Kantrowitz [179] used in steady flow. McGregor et al. [180] showed for simple two dimensional inlets that the starting limit is increased with the reduction of the initial test section pressure. In general, intakes are easier to start in impulse facilities than in flight.

Boundary layer transition and separation

Boundary layer development on a scramjet intake can influence both performance and the operability [30]. At hypersonic speeds, the boundary layer growth causes both large frictional losses, loss of mass entrapment through displacement thickness effects, and unstarting of the engine due to boundary layer separation. Because of this, separation regions need to be predicted within the engine design. In a two dimensional compression corner, a correlation (Equation 6.11) was proposed by Korgegi [181, 182] to predict the separation limit in terms of a pressure rise seen for $M_1 > 4.5$. This correlation has been validated against experimental data up to Mach 9, which should be sufficient for most of the regime of the operation of this inlet. However, Dann et al. [183] argue that at higher Mach

numbers, the pressure ratio could be higher than the Korgogi relationship predicts due to effects of Reynolds number and wall temperature. These factors were included by Dann et al. into a similar function by inclusion of the momentum flux of the boundary layer into the formulation.

$$\frac{p_{sep}}{p_1} = 0.17M_1^{2.5} \quad (6.11)$$

Transition of the boundary layer is required on the inlet, because a turbulent boundary layer can sustain much larger pressure gradients without separation. However, a turbulent boundary layer will also increase heat transfer and frictional losses. Therefore, to minimise losses it would be optimal to have the boundary layer transition to turbulent, before likely separation points. As the location of transition is an important parameter in scramjet intake design [30], this needs to be predicted early in the design stage. Van Wie [30] proposed a correlation (Equation 6.12) from experimental data on the likely transition location on an inlet. This shows that boundary layer transition location for a given Mach number can be calculated by using the momentum thickness Reynolds number

$$\frac{Re_\theta}{M_{eff}} > 150 \quad (6.12)$$

Aerodynamic heating

Aerodynamic heating loads are an important design constraint for scramjet inlets, especially at leading edges [30, 28]. At hypersonic speeds, the heat transfer rates are extremely high at locations where thermal energy is passed from the boundary layer to the body due to thermal differences. At or near stagnation regions, the heat transfer rates are at a maximum where the gas around the body has had the kinetic energy of motion converted to thermal energy. The thermal energy of a stagnation region increases with the square of the freestream velocity, which therefore increases the heat transfer rate accordingly. Heat transfer from the boundary layer to the body at hypersonic speeds can be written in terms of the Stanton number as shown in Equation 6.13.

$$\dot{q}_w = \rho_\delta U_\delta C_H (h_{aw} - h_w) \quad (6.13)$$

Due to the fact that the stagnation point heat transfer at hypersonic speeds is proportional to the inverse square of the radius ($\dot{q}_{w,0} \propto \frac{1}{\sqrt{R}}$) [9, 25], having a “sharp edge” on a scramjet leading edges will result in an enormous heat transfer rate. To counteract this, a blunted leading edge can be used to reduce the amount of heat transfer. Therefore, at small radii (i.e. sharp leading edges) the heating rate is too high for structural components compared with larger radii. Also, the conduction of thermal energy away from the stagnation point for a larger radii is increased due to the larger cross sectional area of material.

This thermal constraint leads to overall performance losses for the scramjet vehicle. Higher pressure losses on the inlet are caused by viscous interactions, entropy layer entering the combustor and higher losses across the bow shock due to shock curvature [30]. As the shock will be detached and normal at the stagnation point, the entire shock structure will be affected. This should asymptote back to the original shock angle, moving the shock location further away from the vehicle [9]. Billig [184] showed that the shock location for both sphere-cones and cylinder-wedges will move further away from the body for decreasing Mach number and increasing radius. As the shock generated will have greater angles than the attached oblique shock before it asymptotes, the flow will have greater losses across it. This results in higher pressures at the tip of the scramjet. Another flow effect of having a blunted leading edge is the movement of the transition location further downstream. This is due to the reduction in Reynolds number on the outer edge of the boundary layer due to a detached shock [185].

6.3.3 Hydrogen injection and mixing

In a scramjet engine, the fuel is added to the supersonic flow and ignited generally through shock heating or diffusive burning which in some circumstances is added by the addition of a highly reactive ignition gas like silane [160]. The momentum in the axial direction of the free stream air dominates any flow interaction with the incoming fuel stream. Any effort to induce mixing is met with penalties of larger total pressure losses and therefore reduction in overall thrust potential [54, 186]. The ideal design for effective injection of the fuel would provide a high mixing rate and limit any thermodynamic losses that occur due to this process. Also, it is envisioned that mixing rates will decrease in flight when compared to ground tests, due to the favourable high freestream air turbulence levels produced in ground test facilities [54]. It is suggested that injection will be quite fuel rich, with fuel equivalence ratios of up to 3 or 4 at the higher Mach numbers [127]. This is to reduce the amount of dissociated species in the nozzle expansion due to the high temperatures expected. It additionally increases thrust due to fuel momentum. Anderson [186] explores the relation between injector design (parallel and perpendicular) and heat release distribution from direct connect wind tunnel testing. In a review, Anderson states that at higher speeds (Mach 8 to 10 and above) that thermal choking is not an issue, even with quite rapid heat release and low combustor area changes due to the increased Mach number present in the combustor.

At flight Mach numbers larger than 10, the fuel momentum becomes an important element of the overall thrust [127, 187] and is therefore required to become more coaxial (i.e. aligned with the thrust direction). However, parallel injection relies upon free shear layer mixing [188] which has extremely long mixing lengths [160]. Inducing higher mixing rates has been achieved by using various techniques that include; provision of increased mixing

area through spanwise convolutions, control of initial shear layer dynamic vorticity production, imposition of longitudinal vortex motions, combustor design to ensure turbulence augmentation, shock interaction, operation close to the mixing zone where initial boundary layer or low Reynolds number turbulence structures are present, increased turbulence production through provision of multiple inflection points [54]. Various injection strategies have been employed in scramjet engines to maximise mixing rates and penetration while at the same time minimising any flow losses. Some of the main passive techniques for increasing fuel mixing through injection are:

- perpendicular injectors
- slot injectors
- angled injectors
- aeroramp injectors (array injectors)
- ramp injectors/hypermixing

A review of most of these and further passive and interactive techniques for enhanced mixing techniques is presented by Seiner et al. [188]. Perpendicular injection is not really viable at higher Mach number flight due to the overall losses of rotating the fuels momentum so it is parallel to the incoming airstream and the dependence on the addition to axial thrust [47, 54, 127, 160].

Differential data is available for the performance of the two most obvious choices of swept ramp injectors and angled injection. As neither exceeds the other in terms of performance, this indicates that the integration into the system is quite important. The mixing efficiency of ramp style injectors was shown to be higher than those available for flush wall injections at the same incidence angle of 30 degrees for freestream conditions of Mach 6 and 10 flight energy [47]. Again, for a Mach 7 flight scramjet the ramp style injectors were seen to have an increased mixing efficiency, at least in the near field [31] (Figure 6.9). However, the ramps are seen to impact on the flow with marginally larger flow losses just after the injection, which by the end of the combustor is the slight increase in thrust of the angled injectors over the swept ramps. By introducing thrust potential³, an indication of both mixing and flow losses can be combined. It is pointed out that, at higher Mach numbers this marginal difference can become a larger fraction of the net thrust. Use of different arrays of flush wall injectors (aeroramp) have been shown to be useful in both limiting flow losses and increasing mixing rates [188, 189].

The penetration and mixing efficiency with injection angle is quite critical. McClinton [190] showed that as the injection angle decreased towards 30 degrees from perpendicular to the incoming airstream, both the mixing rate and penetration increased. At

³The amount of thrust that could be produced by isentropically expanding the flow to the freestream pressure.

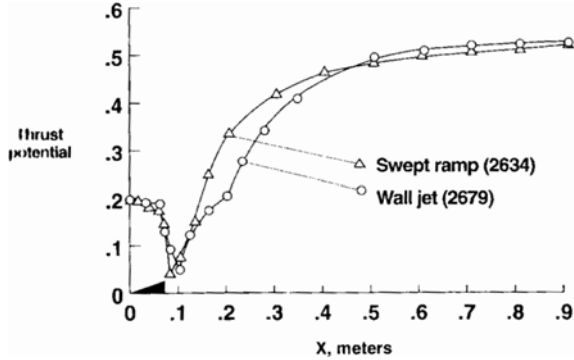


Figure 6.9: Thrust potential for a Mach 7 scramjet with either 30 degree flush wall injector or 10 degree swept ramp injector. Taken from [31].

the same time, less of a flow disturbance was recorded with an associated decrease in flow losses. Predictions of the penetration distance were shown to give quite good results by modifying the Vortz model (reviewed by McClinton [190]) and including the effective dynamic pressure ratio in the radial direction shown in Equation 6.14. Recently, a more comprehensive model has been suggested by Portz et al. [191] which includes the effects of boundary layer thicknesses (Equation 6.15, where the constants A to G given in [191] as a function of Mach number).

$$\frac{P}{D} = 3.385 \left(\frac{q_j}{q_\infty} \right)_{eff}^{0.09} \left(\frac{x}{D} \right)^{0.18} \quad (6.14)$$

$$\frac{P}{D} = A \left(\frac{q_j}{q_\infty} \right)^B \left(\frac{x}{D} + C \right)^E \left(\frac{\delta}{D} \right)^F \left(\frac{\chi_j}{\chi_\infty} \right)^G \quad (6.15)$$

Anderson [47] also showed that increasing the injection angle from 0 to 30 degrees, increases the mixing efficiency quite rapidly for a high speed engine. The spacing and interaction between jets can be quite influential on the mixing rate, as seen in the perpendicular injection experiments by Rogers [192] where a larger cross-stream injector spacing increased the mixing efficiency. McClinton [190] showed that the mixing efficiency equations that Rogers derived (Equation 6.17), could be used with the effective dynamic pressure ratio for angled injection.

$$\eta_m = 0.485 \left(\frac{x}{D} q_{r,eff}^{-0.671} \right)^{0.149} \frac{s}{d} = 12.5 \quad (6.16)$$

$$\eta_m = 0.297 \left(\frac{x}{D} q_{r,eff}^{-1.51} \right)^{0.210} \frac{s}{d} = 6.25 \quad (6.17)$$

Mixing can be enhanced by the interaction of a mixing region and various oblique shock waves. Buttsworth [193] notes that if a mixing region has a significant Mach number variation, vorticity will be amplified by passing through an oblique shock if the velocity

and density gradients lie in the same directions. Thus, at higher flight speeds being tested in this experiment, shock induced mixing should be effective as the velocity and density gradients will be aligned. Kumar et al. [54] reviews the flow phenomena that produce these effects. For a nonreacting case, the influence of shock interaction on turbulence is through direct amplification of incident dynamic vorticity; production of velocity fluctuations due to acoustic and entropy fluctuations, production of intense turbulent “*spottiness*”, direct production of fluctuations in energy, provision for local pressure gradients and streamline curvature which provides additional destabilization. For a heterogeneous/reacting flow an interacting shock can also act as a detonation wave adding additional embedded shear layers, an excitation source for interfacial waves in macromixing, a vorticity production source in connection with local concentration gradients. The creation of these shocks can be from fuel injection and associated structures, incident and reflected shocks most commonly originating from the intake, boundary layer separation regions, wall injection for cooling purposes. The amount of increase in turbulence and mixing rates due to shock stems appears to be in the order of 2 - 5 [54].

Upstream injection is a technology that has been explored for use in detonation wave ramjets [32], to both inject and mix the fuel before the steady state detonation wave positioned at the combustor entrance in a scramjet. Using upstream injection should allow the shortening of the combustor length and therefore reduce the major component of viscous drag in the scramjet engine cycle [194, 195]. This takes advantage of increased mixing length before the combustor, therefore decreasing the diffusive mixing process required within the combustor. Also, it can take advantage of further turbulent mixing by passing the mixture through the strong shock created from the flow straightening required after the inlet. This increases the turbulent mixing due to the oscillatory behaviour when a fluctuating Mach number flow passes through it [54, 188, 193].

However the balance for this technique between benefits in increased mixing allowing further heat addition to the flow and allowing for the use of shorter combustors and losses encountered due to injection of a secondary stream is yet to be investigated. Kumar et al. [54] states,

“The production of unsteady shock motions through up-stream fuel injection has many advantages and also a major drawback. The drawback is the retroaction of the injection momentum. Major benefits include automatic device cooling/survivability and production of large-amplitude shock motions at high frequencies.”

These losses were studied analytically by Dunlap et al. [33] for the supersonic, parallel injection of hydrogen on an inlet (Figure 6.10) where mixing was assumed to either occur as a constant pressure or constant area interaction. It can be seen that with increasing Mach number of the local freestream, these losses, shown as total pressure, increase.

Therefore, it is advisable for upstream injection to occur at the lowest possible Mach number. As the flight speed increases, the skin friction losses in the combustor and flow losses due to upstream injection will both increase. Therefore, a balance once again must be sought between these conflicting issues to optimise thrust in the scramjet.

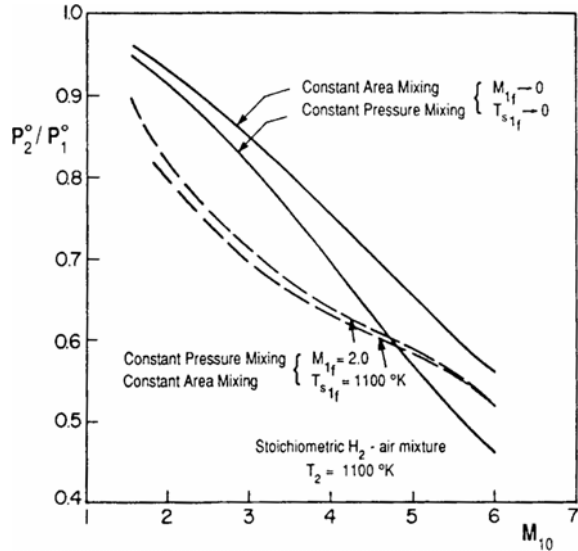


Figure 6.10: Total pressure losses from injection and mixing of hydrogen parallel to an incoming airstream of various Mach numbers. Taken from [32] which reproduced original [33]). Mixing is assumed to either occur in a constant pressure or constant area process.

In flight, it is expected that the fuel will be heated to remove thermal energy from the structure of the scramjet and to possibly improve performance [31]. For ease during ground testing, this flight effect will be ignored and the fuel storage will be at room temperature (i.e. approximately 300 K). Jet stagnation temperature appears to be independent of the penetration distance into the free stream [196]. However, an increase in the strength of the bow shock was noted with increasing stagnation temperature. Huber et al. [35] suggested that use of a relatively cold hydrogen stream in comparison to the heated air stream could limit the self ignition of the combustion. Also, the likely ignition points will occur where there is a low equivalence ratio as there will be a higher temperature. With the design suggested, the likely ignition point will occur after the return shock from the cowl. This pocket close to the cowl is where the highest temperature and lowest equivalence ratio occur.

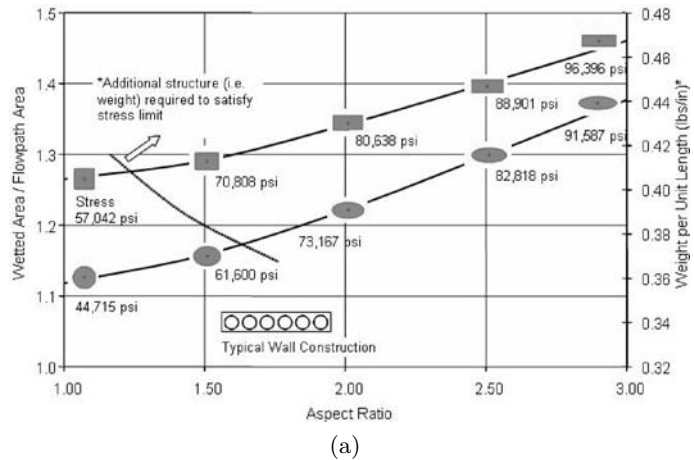
6.3.4 Combustor

Many different challenges arise when combustor design choices are considered for higher Mach number scramjets. Although a considerable amount of data exists for preliminary combustor design choices for Mach numbers less than 8 [47], the movement towards the

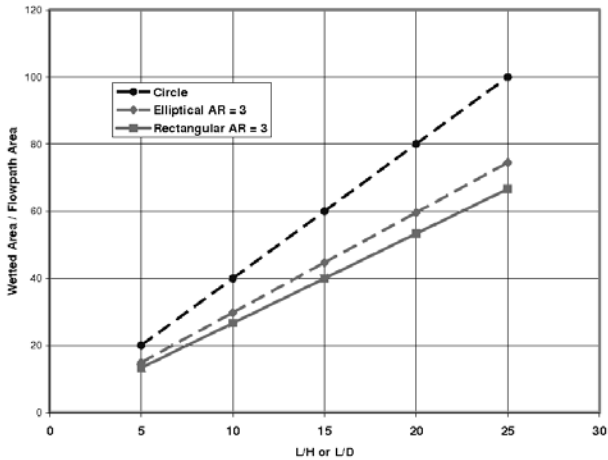
higher Mach numbers reveals the importance of such design issues. These include large peak heating and wall cooling requirements, minimisation of losses and increased mixing efficiencies. The trade off between mixing efficiency and the losses that promote the mixing will need to be addressed. This will in fact dominate most design issues. This is in contrast to lower Mach number scramjets, where the losses due to mixing can reduce the local Mach number which can be enough to offset these initial losses by a reduction in the Rayleigh losses. As the free stream Mach number increases, the Rayleigh losses are harder to offset due to the reduction in overall heat release. Also, the skin friction losses are highest in the combustor due to the high densities [28], so therefore this component's length must be kept to a minimum.

Anderson [47] suggests that shock waves that can originate from the intake should be kept to a minimum in the combustor to minimise losses. They should not be allowed to coalesce and strengthen and should be damped by expansion waves. This highlights the critical nature of the inlet/combustor interaction if waves are not to enter the combustor. With off design conditions likely, this criteria becomes even more difficult to complete. At lower speeds, combustor divergence is required to both prevent thermal choking [186] and to relieve the pressure to ensure boundary layer separation does not occur [29]. However, at higher Mach numbers this divergence can be decreased. The use of constant pressure combustors (i.e. expansion of the flow during heat release to maintain a constant pressure) can limit the structural weight required to contain the pressure loads. This expansion of the flow can also cool the flow to ensure that the temperature remains below that where combustion product dissociation will occur.

The cross sectional shape of combustors is dependent on the ratio of wetted surface area to flowpath area, structural weight, weight per unit length, ratio of combustor length to combustor height [34] and boundary layer effects. Smaller ratios of wetted area to flowpath area benefit the design by reducing skin friction drag and heat transfer concerns. It is obvious that a lower structural weight and weight per unit length reduce the overall vehicle mass. However the length to height ratio becomes important as many characteristics such as mixing and combustion efficiencies are related to this ratio. This is due to the shorter distances required to inject fuel. For rectangular shaped combustors, corner effects must be dealt with and their influences on boundary layers [18]. Also, they have lower performance characteristics. Using figures taken from Beckel et al. [34] (Figure 6.11), it becomes obvious that there are conflicting trade-offs in combustor design between circular and higher aspect ratio elliptical designs. Although the circular combustor offers a lower ratio of wetted area to flow path area, lower structural weight and lower overall weight per unit length, the elliptical design offers much better L/H ratios. Therefore, it will probably be preferable to have low to medium aspect ratio elliptical combustors, that fall below the limit where additional backing structure is required to contain stresses within the combustor (i.e. approximately at an aspect ratio of 1.6).



(a)



(b)

Figure 6.11: Comparison of combustor shapes in terms of weight, strength, ratio of wetted area to flowpath area and ratio of length to duct height. Taken from [34].

Odam [197] has presented an engine configuration which utilizes the strong mixing enhancement which was termed *radical farming*. This term refers to the use of discretised areas formed within the non-uniform flow where the pressure and temperature are higher than the average levels throughout the combustor and promote rapid reaction rates in these regions. As the strong waves are encouraged to be present throughout the combustor (contrary to the thoughts of Anderson [47] stated previously), the use of upstream injection can be used to promote early mixing if the offset losses can be managed. This engine requires much thought regarding the interaction of flow losses due to shock waves, injection and mixing, frictional losses, injection thrust production and probable high peak heating rates. A similar design of allowing the inlet shocks to pass into the combustor has been used in conjunction with Smart's three dimensional REST inlets [198]. This has been

shown to have high pressure increases, although accurate estimates are yet to be made of the actual thrust production [199].

One of the primary concerns with combustor design is to ensure that the length required to achieve sufficient mixing and combustion is accurate so that avoidable losses are minimised. An estimate can be made of likely combustor lengths by multiplying the time required for both mixing and combustion by the freestream velocity. Assuming the flow is premixed, the time required can be estimated by the ignition and reaction times. Using the approximations of these by Huber et al. [35] (shown in Equations 6.5 and 6.6), the likely length of combustors is shown in Figure 6.12 is shown for a stoichiometric hydrogen/air mixture at 100 kPa and 1000 K. The length of the combustor is seen to linearly increase with freestream velocity, as expected. The length of combustor required for only ignition is approximately a third of that required for full reaction, which can be over 1 m at higher speeds.

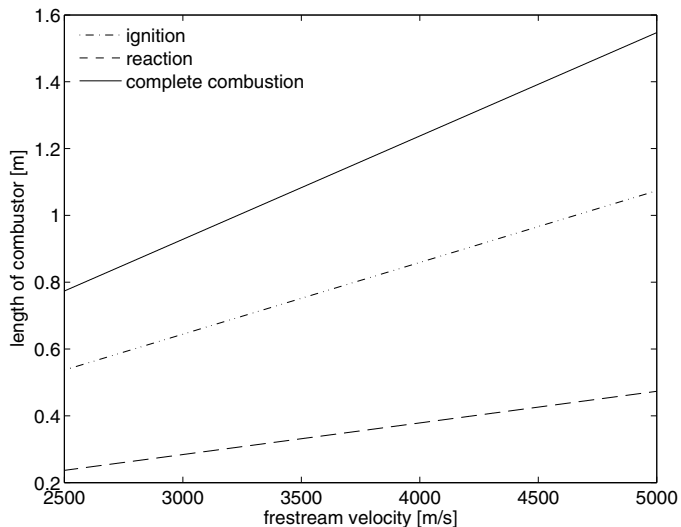


Figure 6.12: Length of combustor required to complete hydrogen/air combustion using Huber et al. [35] ignition and reaction times. Initial stoichiometric mix of hydrogen/air at a pressure of 100 kPa and temperature of 1000 K.

However, the length of combustor also depends on the frictional losses throughout the engine. This was shown simply by Riggins [36], in examining methods for estimating performances of high speed engines. A simple scramjet configuration, shown in Figure 6.13a, was examined for the optimal length of combustor when consideration was made of time dependency of heat and skin friction in the combustor for a Mach 12 flight condition. A simple exponential function was chosen to represent the time dependency for the heat release due to time required for mixing and reactions to occur. Figure 6.13b shows the results of the optimal combustor length to maximise performance. Although a significantly

larger amount of heat release can be obtained by having a larger combustor, the optimal length is shorter due to frictional losses.

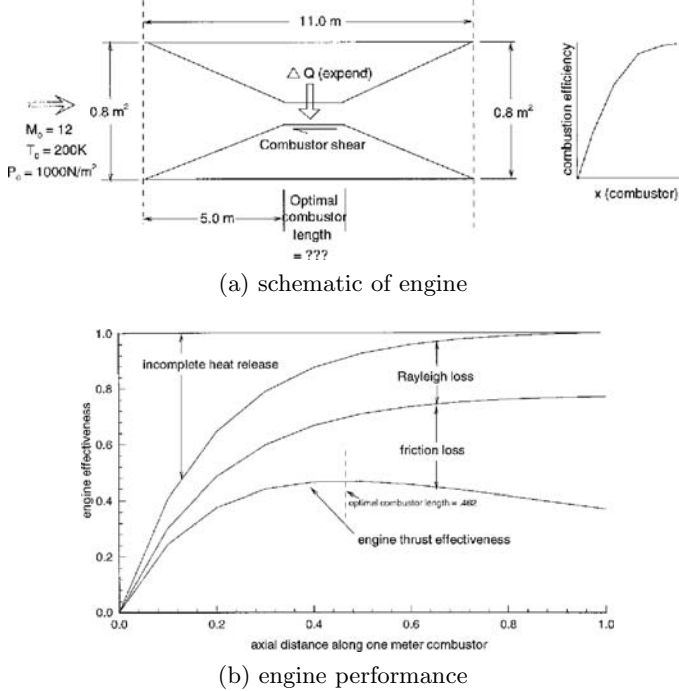


Figure 6.13: Combustor performance with losses due to irreversibilities and frictional losses. Taken from [36].

Wall cooling requirements in a flight vehicle may dominate the design of high speed scramjet combustors [47]. Not only must the overall cooling requirement be satisfied, but also localised peak heating must be withstood by the structure. It is envisioned that the bulk of the thermal energy may be able to be transferred to the fuel (as discussed in Section 6.3.3). However at higher heat loads the use of film cooling may also need to be used. Sureweera et al. [200] show that boundary layer combustion of hydrogen may be able to lower heat transfer to the structure and if injected parallel to the flow, increase the overall thrust. Also new generation carbon-carbon materials in combustors may be able to take advantage of radiation transfer to the external surfaces of the engine [201].

6.3.5 Thrust nozzle

Exhausting of the flow in a scramjet is quite difficult compared to conventional engines. The thrust produced by a nozzle can be maximised if the flow can be expanded isentropically to the freestream pressure and the flow is parallel and uniform. With the flow being supersonic, nozzle configurations can avoid the difficult transonic/sonic conditions at the throat and use sharp corner expansion [28]. However, the flow produced in a scramjet combustor is quite non-uniform and therefore requires sophisticated design to create par-

allel flow by exit [31]. Figure 6.14 shows that due to the flow having a low Mach number in the core of the flow (centrally injected) that as this flow is expanded a significant amount of the thrust will be focused in one area rather than across the entire nozzle. Another performance loss that will require consideration, is the optimisation of a configuration in non-equilibrium chemistry effects due to rapid expansion [169].

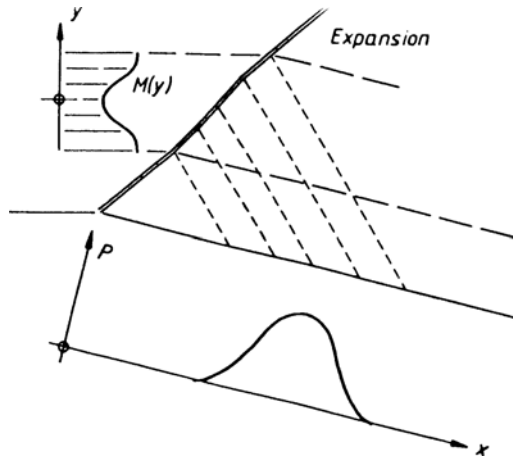


Figure 6.14: Effect of Mach number profile in a nozzle on thrust production. Taken from [37].

As the expansion of the flow to the freestream pressure requires a greater area than the intake area, the expansion nozzle will create an increase in the cross sectional area of the vehicle increasing both the inviscid and viscous external drag [28]. Also the skin friction losses within the nozzle itself can become quite large and produce an overall loss in thrust. Figure 6.15 shows the thrust able to be produced by a nozzle with variation in the skin friction coefficient from the example examined in Section 6.3.4. The total thrust is seen to decrease quite rapidly with increasing skin friction coefficient in the nozzle. Therefore, to optimise thrust a balance is sought between the thrust produced by expanding the flow to the freestream pressure and associated drag losses (internal skin friction and external inviscid/viscous losses). This is of most concern at higher flight Mach numbers, where the available thrust potential will be quite minimal [29]. Various scramjet concepts use single sided nozzle configurations (otherwise known as free expansion nozzles) due to the reasoning above [28], where the flow on the cowl side of the spaceplane can be expanded rapidly and become parallel to the vehicle.

6.4 Summary

A review is presented both of supersonic combustion and integration into a flight vehicle. Also a brief review is presented of some of the major achievements and work involving scramjets. The flow path design is reviewed, including the individual components of the

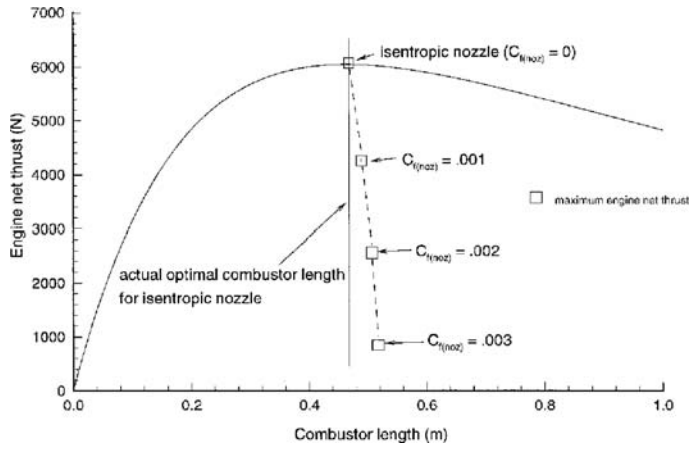


Figure 6.15: Effect of skin friction in a nozzle on overall thrust. Taken from [38].

system. These are the intake, fuel injection, combustor and thrust surface. Particular attention is paid to the integration of the component into an overall vehicle to optimise thrust.

Scramjet Flow-Path and Model Design

The design of a 2/5 pL scaled scramjet for testing in the X2 expansion tunnel is presented using analytical approaches. Investigation of transient inflow into the scramjet is provided. Transient numerical calculations of the engine, without fuel, are used with the time history calculated for the freestream, to analyse the appropriate use of quasi-steady flow analysis. Results from these calculations are also used in investigating intake startup and flow establishment, as well as provide comparative results for the experimental work.

Ground testing is used to test flight components for both direct design and/or to provide validation data for numerical work. The major goal of this work was to test the ability of an expansion tube to produce stable supersonic combustion in a scaled model of a flight scramjet. Hence a complete ‘nose to tail’ scramjet was designed. To reduce both the complexity in designing the scramjet and also the analysis of experimental data, a simple pseudo two dimensional scramjet configuration was chosen to be designed and tested. Therefore, a flight model was designed using an estimate of 0.01 m^2 capture area, and then scaled down to 2/5 the size for testing in X2. This scaling factor was chosen due to the ‘pL’ scaling of the test condition, a test time of only $500 \mu\text{s}$ and a core flow of 60 mm diameter. The scaling factor was used on all the components with a slight adjustment made on the intake to match the shock structure with viscous interactions.

A design philosophy was chosen to minimise losses due to entropy generation throughout the scramjet cycle to maximise thrust while maintaining likely flight scramjet parameters such as combustor alignment with the freestream. The sequential system of compression on the intake through a chain of shocks, provides many possible locations and conditions to initiate fuel injection. Following the discussion in Section 6.3.3, it was chosen to inject in the lowest Mach number part of the intake (i.e. close to the combustor), but still maintain a decrease in distance required for mixing in the high pressure combustor. A simple two dimensional planar design was chosen to be tested, due to the simplicity with both design and manufacture. Although the flow will be three dimensional throughout the engine, two dimensional predictions of the flow from analytical and computational methods should provide useful benchmark data to compare if a three dimensional scramjet was to be tested at a later date.

Hydrogen was chosen for use in the experiments described in this current study. This was decided due to the time of reaction being relatively less than that encountered with

hydrocarbon fuels (Section 6.3.1). The use of an ignition promoting gas such as silane was not necessary due to the large enthalpies produced in the flow condition. Also, it has been shown that hydrogen fuel is the better option for scramjets on a transatmospheric flight path, which the current study is investigating. The injection of hydrogen can be provided with a much simpler system than required for hydrocarbon testing, which would require preheating of the fuel to crack the carbon chains as would be required in flight.

7.1 Flowpath Design

The design of a scramjet model flow path involves consideration of many different aspects including drag losses, flow losses, fuel ignition, fuel mixing length and efficiencies and thrust production. Currently, some external factors are ignored such as mass balancing of the engine, reduction of external drag, thermal loading of the entire vehicle and integration details¹. These factors are influenced by every upstream design choice for the scramjet. Therefore, these have to be considered together in order to produce both an operational scramjet while still maximising the performance of the engine.

Due to the objectives of this research, the model was chosen to be a simple two dimensional design which could provide supersonic combustion. This was undertaken in conjunction with work in the T4 RST on the same targeted Mach 10 condition. The design of the scramjet is completed mostly with the use of two dimensional analytical tools and empirical formulas. However, verification is completed with the use of two dimensional numerical simulations of the flow path, un-fuelled. Although it will be evident that three dimensional effects like side wall shock interactions, corner effects and boundary layer growth will be present in experimental testing, these were not included in the design process.

7.1.1 Inlet

It was decided that three external shock and a single return shock be used for the scramjet intake design, shown in schematic in Figure 7.1². This provides a moderate performance inlet by minimising the amount of total pressure loss across the inlet (as shown in Chapter 6 and described in [175, 30]) while still being relatively simple enough to design and build for the scope of this thesis. For an inlet involving a number of entropy raising processes, the minimum increase in entropy is given by sharing the total entropy rise equally across each shock³. The design chosen comes close to this and was expected to be a reasonably efficient intake (yet practical) intake. Practical issues which must be considered during the design

¹The design is assumed to be incorporated into the underside of a hypersonic vehicle.

²This is orientated to the way it is mounted in the expansion tunnel.

³This cannot occur due to the criteria of re-orientating the flow entering the combustor to that of the freestream.

process include start/un-start, bluntness of leading edges to reduce temperature to avoid warping during flight, boundary layer separation and skin friction. Also, the influence of the side walls must be considered, as three dimensional effects will alter the flow through the development of boundary layers and weak waves entering the combustor.

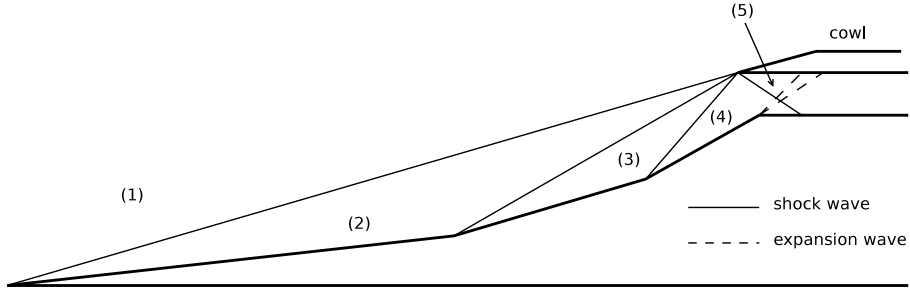


Figure 7.1: Schematic of two dimensional inlet for scramjet design (orientation to be mounted in expansion tunnel).

To design the inlet it is necessary to establish requirements for the flow properties for use in combustion. A static temperature of 1000 K (T_5) and a pressure of 100 kPa (p_5) were the targeted levels of compression at the combustor entrance. As discussed in Sections 6.3.1 and 6.3.2, the temperature and pressure dependencies on the ignition and residence time are quite critical. As shown in Figures 6.6 and 6.7, setting the conditions at this level ensures a reasonably short ignition and reaction time of 118 μs and 34 μs respectively for combustion. The change in these times by increasing the pressure above 100 kPa is quite minimal, however, increasing the temperature will cause a significant decrease to the ignition and residence times. This is avoided though, due to the increase in entropy that would be required which will decrease overall performance and the excessively high temperature that would limit heat release. These combustor inlet conditions compare well to those suggested by the equilibrium scramjet performance calculations of Kerrebrock [169] at Mach 10, being Mach 4.8 at a static pressure of 100 kPa and static temperature of 1020 K. These conditions are much higher than those used by Smart [175], but the conditions at the combustor entrance in Smart's design would be too low for auto-ignition of the hydrogen (i.e. below 800 K).

The inlet area ratio with this two dimensional inlet design can be considered an independent variable, which can be tuned by adjusting duct height. The selection of this parameter is influenced by the viscous effects of a growing boundary layer, skin friction and thermal energy losses, the starting ability of the inlet and the effects of combustor height. An area ratio of 0.1 (A_{com}/A_{inlet}) was chosen, to give a sufficient height for the boundary layer to develop in the combustor, although this is an arbitrary choice. This is well above the starting limit proposed by Van Wie [30] at Mach 10 of 0.0345, although as already discussed, there should not be an issue with the impulsive starting nature dur-

ing testing. Also, the internal compression as calculated using the Kantrowitz limit [179] should be quite small given the positioning of the cowl.

A conscious decision was made to let the return shock enter the combustion chamber as shown in Figure 7.1. This was made to ensure the effects of the return shock such as boundary layer separation on the inlet are completely avoided. However, this could mean that separation of the flow would occur in the combustor, and effects could creep back onto the inlet. A Prandtl-Meyer expansion fan was created at the combustion chamber entrance (body side) to straighten the flow to be parallel with the free stream. This would mean a series of expansion waves and shock waves enter and travel down the combustion chamber. In deciding to allow the wave generation into the combustor instead of occurring due to off design free stream conditions, the size of the hot and cold regions can be designed by combustor height and cowl positioning.

Leading edge and cowl bluntness

The blunting of leading edges is required in scramjet flight vehicles to obtain acceptable heating loads at hypersonic speeds (Section 6.3.2). This can be seen in the approximate stagnation point heat transfer taken from Anderson [9] in Equation 7.1, whereby the heat transfer increases inversely with the square root of nose radius. It is noted that this becomes a greater issue at high flight speeds, increasing with the power of 3 for velocity. Experimental data at Mach 8 [202] shows that at a blunted cowl tip where shock impingement occurs, the heat transfer rate can be up to 40 times greater than the undisturbed stagnation point heat transfer rates. Due to other adverse effects like large shear layers and flow losses due to curvature of the bow shock, this radius should be kept to a minimum. Although the problem of heating loads is not an issue in short duration ground testing due to short flow periods, the model was designed to reflect a true flight engine⁴.

$$\dot{q}_{w,0} \approx \frac{1.83 \times 10^{-8} \rho_{\infty}^{0.5} U_{\infty}^3 (1 - \frac{h_w}{H})}{\sqrt{R}} \quad (7.1)$$

To estimate the size of radius required, an assumption can be made that a flight vehicle will use copper as a leading edge material due to its high conduction rates. Podesta [203] gives the melting temperature for copper at 1356.6 K, and an enthalpy of formation of 204.7 kJ/kg. Using the free stream conditions, the heat transfer rates for differing radii of leading edges can be plotted using a wall temperature set at the melting point for copper shown in Figure 7.2. This shows that as the radius decreases, the heat transfer rate dramatically increases. Also plotted are the heat transfer rates of 20 and 40 times the amount of heat transfer at stagnation to show an estimate of the heat transfer rates if the inlet shocks impinge the cowl tip.

⁴This was due to the possibility of flight in the larger, T4 model.

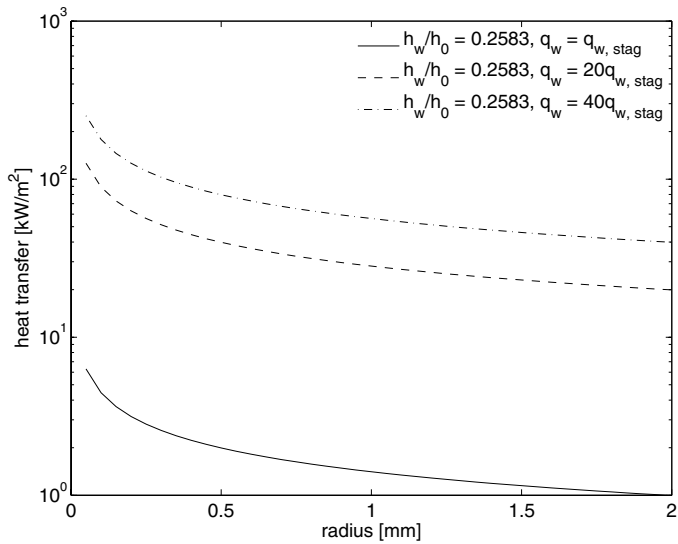


Figure 7.2: Heat transfer rate at stagnation location on blunted leading edges.

By taking a worse case scenario, an estimate can be made of the minimum time required to melt a copper tip with a given radius. This can be made by calculating the time for a semi-infinite block of copper at its melting temperature at the heated surface. In reality this time will be increased as the wall temperature will initially be below the melting temperature and will also conduct some of the thermal energy away to the rest of the scramjet structure. Figure 7.3 shows this minimum time to melt the copper tip. Using this, a decision was made to use a tip radius of 0.5 mm. This allows at least 100 s of flight time at the nose of the scramjet. It should be noted though, it is preferable even with the mass flow losses, to pass the inlet shocks outside the cowl tip as the time required to melt the copper could drop to the order of tens of seconds if shock impingement occurs. The effects of shock curvature, increase in pressure and shear layer development is explored further later in this section.

Geometry design

The geometry was designed using perfect gas relations [144], assuming inviscid flow, which was later verified by two dimensional viscous CFD (see Section 7.1.1). The inviscid assumption is reasonable as thin boundary layers are expected, with the pressure increasing with the distance from the front nose of the scramjet to maintain a thin boundary layer. Leading edge bluntness affects the curvature of the shock and will also be unaccounted for in this design method, though explored later in the design. The real gas effects should be minimal except for vibrational effects where the gas temperature is above 800 K, such as in the boundary layers [30]. The free stream conditions as given in Table 4.2 (page 56), were slightly modified to have a lower static pressure as the T4 condition where the

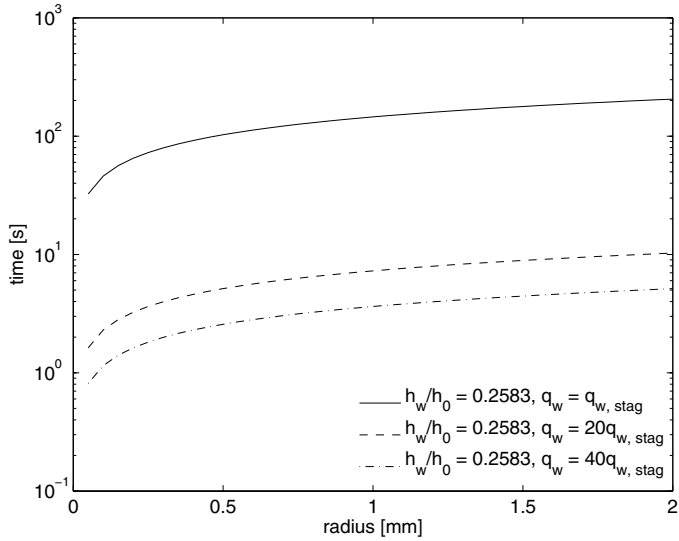


Figure 7.3: Minimum time required to melt an un-cooled, semi-infinite slab of copper at stagnation location.

scramjet was also to be tested [69] could only produce a static pressure of 1 kPa. Using these, the inlet was designed for a capture area of 100 x 100 mm, area ratio of 0.1 and combustor entry conditions of 100 kPa static pressure and 1000 K static temperature.

An iterative optimisation approach based on minimising the entropy rise, was used to design each of the external wedge angles⁵. This will give an equal entropy rise over each of the external shocks [175, 30] with the greatest losses coming from the return shock from the cowl. The wedge angle optimisation procedure gives the angles in Table 7.1, shown as the angle from the local flow direction to the ramp. The properties given for each region detailed in the schematic of Figure 7.1 are given in Table 7.2. The entropy rise across the last shock is approximately eight times greater than that seen across any of the wedges. Thus, the final turning shock is the strongest in the chain.

Table 7.1: Wedge angles for inlet design.

<i>Optimum Design</i>	<i>Final Design</i>
θ_1	4.00°
θ_2	4.85°
θ_3	5.69°
θ_4	14.54°
	θ_1 4.31°
	θ_2 4.99°
	θ_3 5.39°
	θ_4 14.69°

The exact optimised values were not used in the final scramjet design because the scramjet designed, in conjunction with Paull and Frost [70, 204] had slightly different wedge angles as also shown in Table 7.1. It can be noted that the flow is deflected through

⁵The fourth wedge angle is the summation of the first three.

larger angles on the first two ramps but slight less on the last ramp. Using these angles gives the properties across each shock shown in Table 7.2. The properties are quite similar to those presented for the optimised design, with a slight increase in temperature and pressure and therefore entropy. The Mach number is only negligibly affected between the two designs. The overall entropy factor difference is marginal between the two designs. It can be noted that combustion should only occur within the combustor as the temperature before the cowl shock (524.6 K) is too low for auto-ignition, although it could be induced by shock heating effects around the fuel jet.

The inclusion of curved shock effects were introduced using a relationship for shock curvature due to a blunted nose given in Equation 7.2, outlined by Billig [184]. The correlations for radius of curvature and shock standoff are taken from the experimental data and given by the correlation in Equation 7.2. This uses the radius of curvature (Equation 7.3) and the shock standoff (Equation 7.4). This is undertaken for the given shock angle from Table 7.1 for the final design. Figure 7.4 shows the shock shape from the first wedge for various radii of nose bluntness. It can be seen that the change occurs close to the nose, and only varies slightly. With a nose radius of 1 mm, the shock asymptotes to a position 10 mm higher than if the shock was produced by a sharp wedge. The variation in shock shape for a nose radius of 2 mm is quite small, of the order of 1 mm.

$$x = R + \delta - R_c \cot^2 \beta \left[\left(1 + \frac{y^2 \tan^2 \beta}{R_c^2} \right)^{\frac{1}{2}} - 1 \right] \quad (7.2)$$

$$R_c = 1.386 R e^{1.8/(M_\infty - 1)^{0.76}} \quad (7.3)$$

$$\delta = 0.386 R e^{4.67/M_\infty^2} \quad (7.4)$$

Using the shock shape given for a nose radius of 0.5 mm and the shock angles from Table 7.1, the locations of each ramp corner can be calculated. The results of this process give the geometries detailed in Table 7.3. This is shown in the schematic of the inlet in Figure 7.5. It can be noted that all the shocks meet at the cowl tip, with the return shock entering the combustor and intersecting the underbody at 50 mm past the flow straightening corner (position 4). To ensure that the external shocks don't enter inside the cowl at increased Mach numbers, the cowl can be positioned further downstream.

Boundary layer separation

Flow disturbances produced by the effective increased size of the inviscid forebody due to boundary layer growth was investigated in a computational refinement study of the geometry design undertaken in Section 7.1.1. Using the Korkegi relationship (Section 6.3.2), the pressure required at each compression corner on the inlet for separation is given in

Table 7.2: Conditions after each shock on inlet.

Position	Mach Number	Temperature [K]	Static Pressure [kPa]	Density [kg/m ³]	Velocity [m/s]	Entropy Factor $\Delta s/c_p$
<i>Optimum Design</i>						
(1) - Free Stream	10.00	226.5	1.00	0.018	2995.12	0.000
(2) - First Ramp	8.68	295.8	2.45	0.035	2970.42	0.020
(3) - Second Ramp	7.45	392.0	6.26	0.067	2936.53	0.023
(4) - Third Ramp	6.36	520.9	16.12	0.129	2889.98	0.024
(5) - Behind Cowl Shock	4.28	1010.8	100.00	0.412	2707.29	0.160
<i>Final Design</i>						
(1) - Free Stream	10.00	226.5	1.00	0.018	2995.12	0.000
(2) - First Ramp	8.58	302.3	2.61	0.036	2968.61	0.025
(3) - Second Ramp	7.34	402.7	6.76	0.070	2933.03	0.024
(4) - Third Ramp	6.34	524.6	16.45	0.131	2889.53	0.020
(5) - Behind Cowl Shock	4.25	1022.8	102.96	0.420	2703.60	0.163

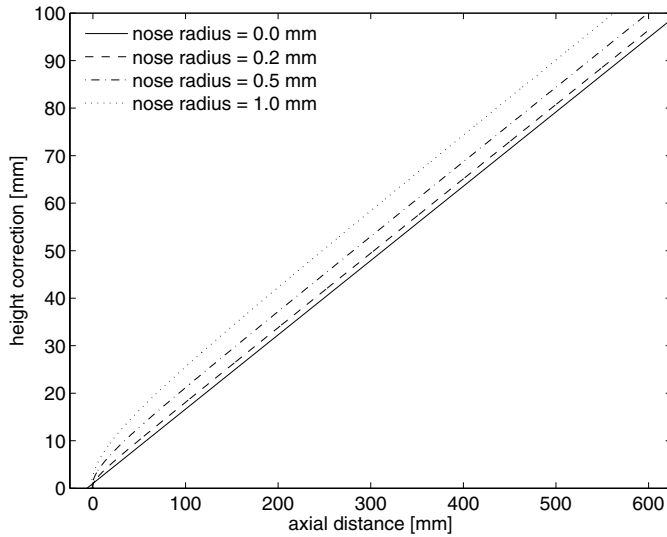


Figure 7.4: Shock shape for first wedge with nose bluntness.

Table 7.3: Geometry of inlet designed for testing in T4.

co-ordinate	axial position [mm]	height [mm]
1	0.00	0.50
2	306.00	23.56
3	472.29	50.79
4	621.84	90.00
5	600.18	100.00
6	680.50	90.00

Table 7.4. An additional value is given using the conditions, 5b, after the expansion from the third wedge into the combustor before the return cowl shock using a Mach number of 8.9 and a pressure of 17.4 kPa. Comparing the separation pressures to those calculated for each region in Table 7.4 shows that boundary layer separation is only likely to occur after the return cowl shock impinges the boundary layer expanded around the corner of the combustor. This will be seen in the computational simulations conducted later.

Computational simulation of inlet design and scaling for X2 experiment

A computational simulation using the *MB_CNS* code was completed on the scaled inlet for the experiment to provide qualitative information on the inlet. This simulation uses a steady inflow condition with the nominal free stream conditions in Table 4.2. The simulation was run for 2 ms, which was long enough to provide steady state results. The gas composition is pure air, modelled using an equilibrium gas model in the same way as described in Section 4.4.2. The simulation was run for two different geometries, based on

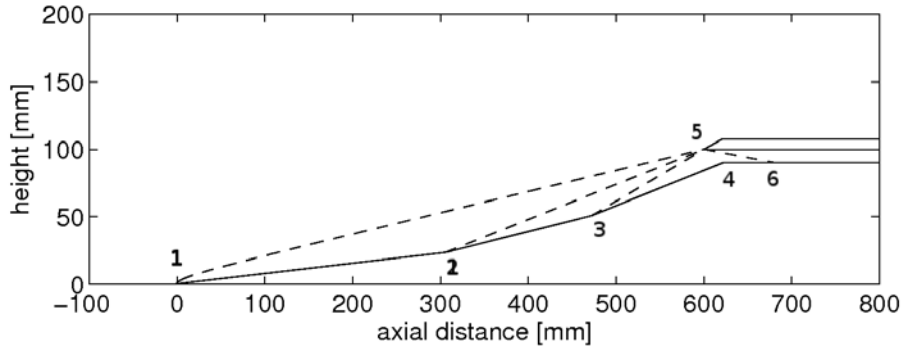


Figure 7.5: Geometry for scramjet inlet.

Table 7.4: Boundary layer separation limit on intake and combustor.

position	separation pressure	static pressure
	p_{sep} , [kPa]	p_1 , [kPa]
2	53.76	2.61
3	95.56	6.76
4	168.07	16.45
5a	282.89	102.95
5b	69.64	102.95

the full scale design presented previously. The full scale T4 inviscid design geometry is shown in Table 7.3 and the scaled geometry for the inviscid X2 scramjet inlet can be seen in Table 7.5.

As the bluntening of the leading and cowl tips are quite small (0.2 mm), it was neglected in the simulation as this would require a very fine grid to resolve the flow effects sufficiently on a structured grid, due to the large differences in distance scales between the nose and the inlet. This will mean that both the effects of the entropy layer and the leading edge shock will not be simulated directly. However, with such a small nose radius, the entropy layer created on a sharp leading edge due to growth of the boundary layer from a point will be similar to that expected for a blunted nose. Also, most of the freestream gas will still be processed by a leading shock strength. A second geometry defined as the viscous design was also simulated, where the design can be seen to be slightly adjusted, with the lengths of the wedges shifted to account for the leading edge shock position being moved outwards due to the bluntening of edges. This inlet design is that which was implemented for the experiment run in X2.

The inlet was modelled with 48000 cells, with 120 cells in the normal direction and 400 cells axially. Clustering was implemented towards the surface using a Roberts clustering function of 1.05. Although labelled as an inviscid designed inlet, both calculations were

Table 7.5: Geometry of scaled inlet for X2 scramjet design.

co-ordinate	inviscid design		viscous design	
	axial position [mm]	height [mm]	axial position [mm]	height [mm]
1	0.00	0.20	0.00	0.20
2	122.38	9.42	114.27	8.61
3	188.90	20.32	173.49	18.309
4	237.28	33.00	229.2	33.0
5	240.06	40.00	230.5	40.0
6	296.29	33.00	285.8	33.0

viscous simulations. The first wedge surface was set as a laminar boundary layer on a fixed temperature wall of 300 K. After the first wedge, all other surfaces were implemented as fixed temperature walls (300 K) with the Baldwin-Lomax turbulence model, which has an in built transition criterion. However, boundary layer transition was predicted at this location by using the empirical relationship discussed in Section 6.3.2.

Streamlines and Mach number contours can be seen for the inviscid designed inlet in Figure 7.6. This shows the three shocks generated by the wedges, which drop the Mach number as the flow moves further downstream of the inlet. These shocks meet and pass outside the cowl edge. There is a separation region that occurs where the expansion of the where the cowl shock meets the boundary layer developed from the body side surfaces of the inlet. This is as predicted in the inviscid calculations presented in Section 7.1.1. To investigate this further, a close up view of the cowl section is shown in Figure 7.7. This shows that the bulk of the flow is not being processed by the steady expansion at the inlet/combustor interface, due to both the presence of the separation region acting as a continuation of the wall, and the passing of the bulk of the flow through the return cowl shock.

The static pressure along the external compression surface is plotted in Figure 7.8 for various times. These are recorded at the first cell from the wall, at approximately 0.0025 mm. This shows that the simulation takes some time for the flow to establish, especially in the separation region and also the turbulent boundary layer on the third wedge. The viscous effects can be seen on the first wedge with a drop in pressure along the surface. A large temperature increase, as expected, is found in the separated region (not plotted). This peaks at a temperature of 1272 K, at 253 mm from the leading edge.

The viscous design showed that the three shocks generated from the external surfaces met below and in front of the cowl (Figure 7.9), but the steeper merged shock produced passed outside the cowl. This is to be expected with the nose radius not being modelled, but if the first shock is located another 1.5 mm higher, the shocks would pass outside

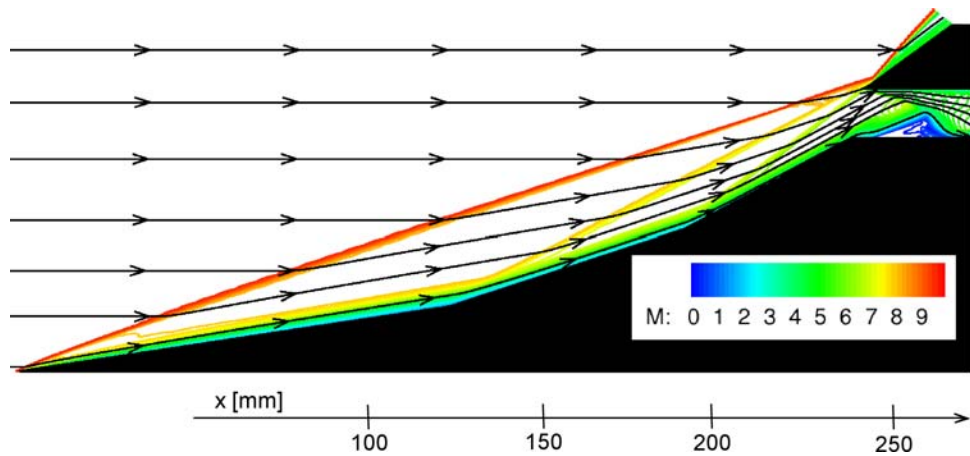


Figure 7.6: Contour of Mach number on inlet for inviscid design (scaled in transverse direction).

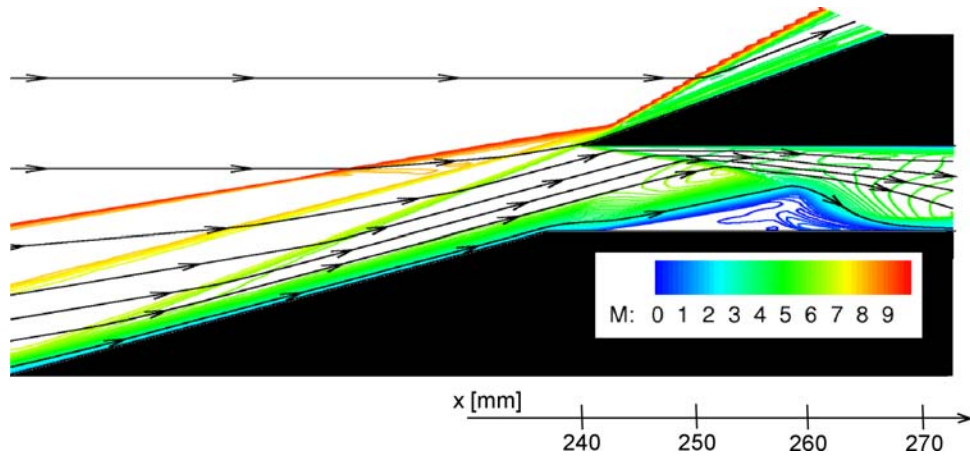


Figure 7.7: Contour of Mach number of combustor inlet for inviscid design (scaled in transverse direction).

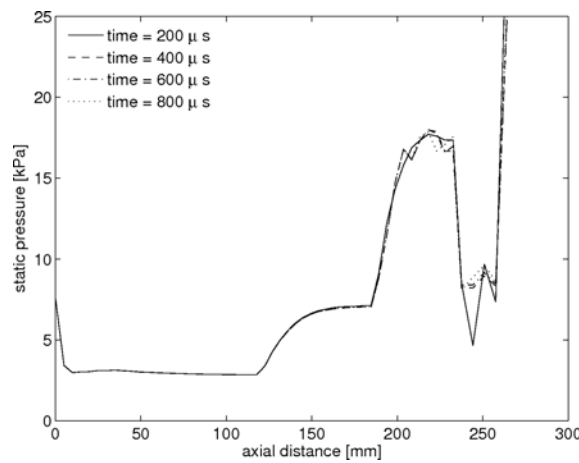


Figure 7.8: Pressure along compression surface for inviscid design.

the cowl. The static pressure in the closest cell along the external compression surface (Figure 7.10) shows similar effects as seen for the inviscid designed geometry.

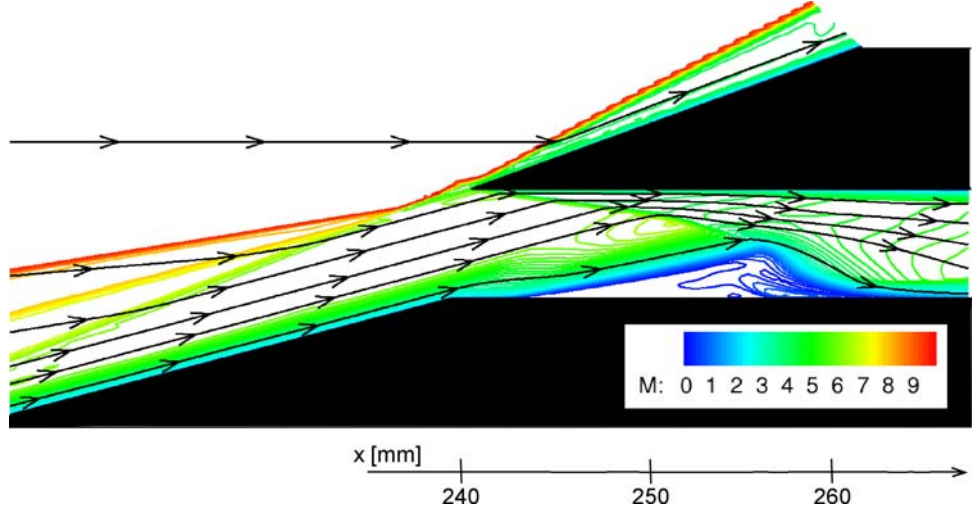


Figure 7.9: Contour of Mach number of combustor inlet for viscous design (scaled in transverse direction).

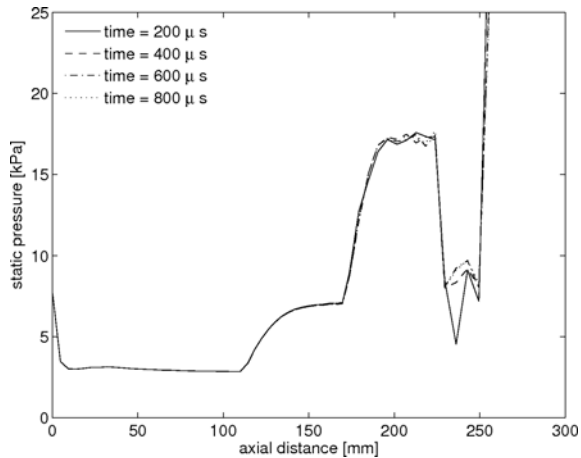


Figure 7.10: Pressure along compression surface for viscous design.

To explore the flow that exits the inlet, plots across the combustor are shown in Figure 7.11 for various flow properties at several axial locations. This has been shown for the viscous design geometry at a time of 2 ms. In general, the flow can be seen to be quite non-uniform, varying both in the normal and axial directions due to wave reflections through the duct. The Mach number plot shows the flow entering the combustor quite uniformly at above Mach 6 with the cowl shock dropping the Mach number of the flow on the far edge to Mach 4. The next axial location indicates that the separation region has a very low Mach number. Close to the combustor wall, the axial velocity in the flow is moving

upstream, as expected in a separated region. The last axial location shows a relatively uniform temperature and velocity and therefore Mach number, whereas the pressure and density plots indicate that there is a shock reflection starting to move back across the duct. Whilst the bulk of the flow passes through regions of temperatures of above 900 K and pressures above 80 kPa, these flow properties are, on average, less than these values. This however, will ensure ignition occurs from the production of radicals, then with the onset of combustion, temperature and pressure will increase down the combustor.

7.1.2 Fuel injection

Discrete orifice, wall injection at 45 degrees to the free stream was chosen as the injection method for the hydrogen in the scramjet. The position of the injection was chosen to be on the third ramp of the scramjet. The main influence for this decision was the desire to limit the ignition delay time by injection before the strongest shock in the scramjet and also reduce the mixing time. This will allow a reduction in the overall length of the scramjet. It is noted that this will lead to higher overall total pressure losses as discussed in Section 6.3.3. However, these losses could be less influential than the viscous drag encountered with long combustors. Using angled injectors which have a large component of axial momentum, will also increase the available total thrust of the engine.

A row of circular sonic hole injectors was placed on the third wedge. These holes were to direct fuel into the airstream at 45 degrees to the local flow, which is at an overall angle of 59.69 degrees to the scramjet's flight direction. As discussed in the scramjet literature review in Section 6.3.3, this is usually close to an optimum angle for both mixing, flow losses and thrust addition for a medium to high flight Mach number of 10. However, it may produce more overall thrust if a shallower angle is used. These injectors are to be supplied by a stagnation region of high pressure hydrogen in a plenum chamber. Creating a steady pressure in the plenum chamber will be supplied by the Ludwieg tube as described in Section 5.1.2. Therefore, to design the fuel injection system, the penetration, mixing and supply pressures must be investigated.

A prediction of the mass flow rate requirement throughout the test time can be made using Equation 6.7 for the mass flow rate of air for a given equivalence ratio. Using the outflow data 9 mm above the centreline at nozzle for the simulation of X2 for both conditions, the mass flow rate of hydrogen can be predicted with time. Using the timing from computational simulation, the transient mass flow rate requirement is shown in Figure 7.12. The amount of hydrogen required over the test period is shown to approximately double. The mass flow rate in the high enthalpy condition is lower as the mass flow rate of air is reduced for this condition due to the reduction of free stream density.

The stagnation pressure can be approximated for sonic injection by using the properties at the sonic point, the area of injection and the hydrogen mass flow rate. This is provided in

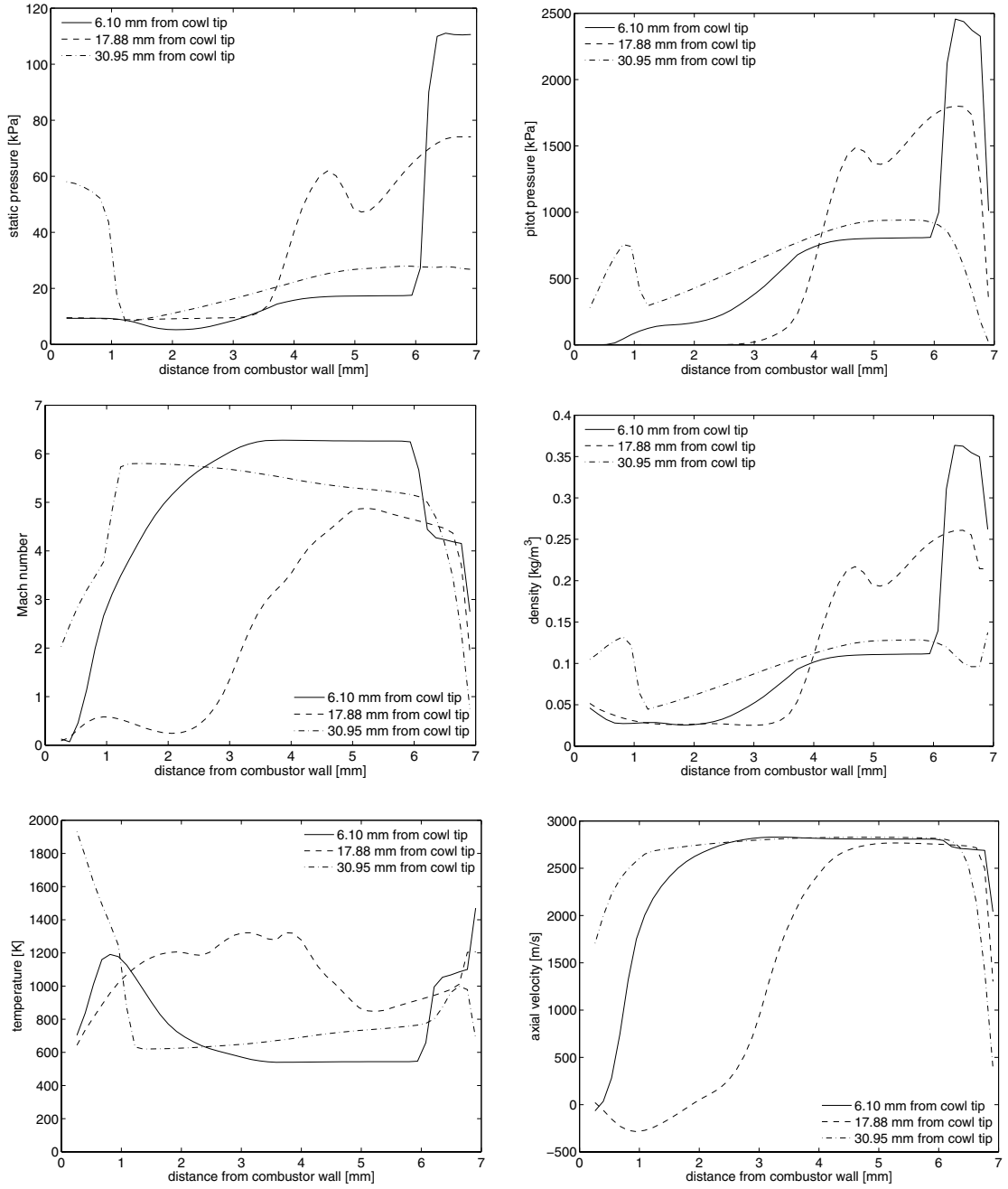


Figure 7.11: Properties across combustor for viscous scramjet design validation.

Equation 7.5. Using the mass flow rate results, a prediction can be made of the stagnation pressure requirement in the plenum chamber. This is shown in Figure 7.13 for both hole arrangements, 4 holes with diameters of 2 mm or 2.8 mm, using the predicted free stream properties. Stagnation pressures of up to 2 MPa are required for testing the scramjet at an equivalence ratio of 1 late in the test period. Earlier in the test time, 1 MPa is sufficient for testing of equivalence ratios up 1.5.

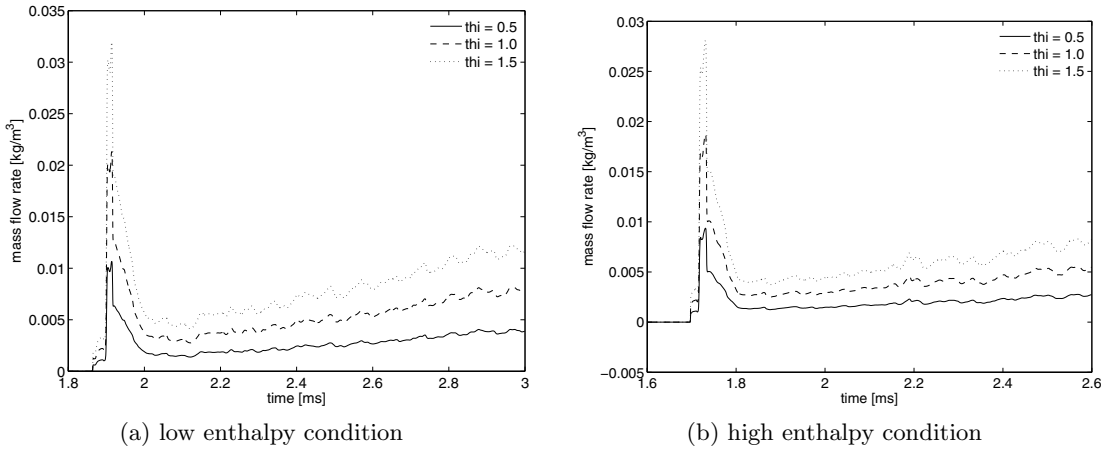


Figure 7.12: Mass flow rate requirement of hydrogen using data transient flow data at nozzle exit from *MB_CNS* simulation.

$$p_0 = \frac{\dot{m}_f RT^*}{0.5283\sqrt{\gamma RT^*} A_{inj}} \quad (7.5)$$

As pointed out previously, the stagnation pressure will be held relatively constant over the millisecond of flow shown here. It is more important therefore to review the change in equivalence ratio over the test period. This is shown in Figure 7.14, using the mass flow rates of hydrogen calculated for the two conditions and different hole configurations. It can be seen that there is quite a significant drop in equivalence ratio over the test period. For example, the low enthalpy condition with 2 mm diameter injector holes has a drop from an initial equivalence ratio of 1.1 to 0.7 over the test period. Therefore, careful attention must be taken when analysing data to include the time varying specific fuel equivalence ratio.

As this drop in fuel equivalence ratio will effect the pressure change across the combustor, it is of more importance to analyse it across the time flight of the gas through the combustor. Taking the change in fuel equivalence ratio in time to be linear at $0.001 s^{-1}$ (determined from Figure 7.14), the change in fuel equivalence ratio across a 200 mm combustor (time of flight is $64\mu s$ at 3100 m/s) is shown in Figure 7.15. At the start of the test time, this is shown to be 4%, but increases to 8% by the end. With such a significant change, this may be on the limit of what a quasi-steady analysis (Section 7.3) could handle. With the physical impracticalities (due to the short period of flow) of implementing a fuel system which increased the mass flow rate proportionally to the freestream, this cannot be avoided.

Penetration distance can be estimated using various different methods, as discussed in the literature review. Figure 7.16 shows a comparison between the three methods of McClinton, Vranos and Portz [190, 191] of penetration with axial distance downstream from injection. The flow properties used at the third wedge (where the hydrogen is injected)

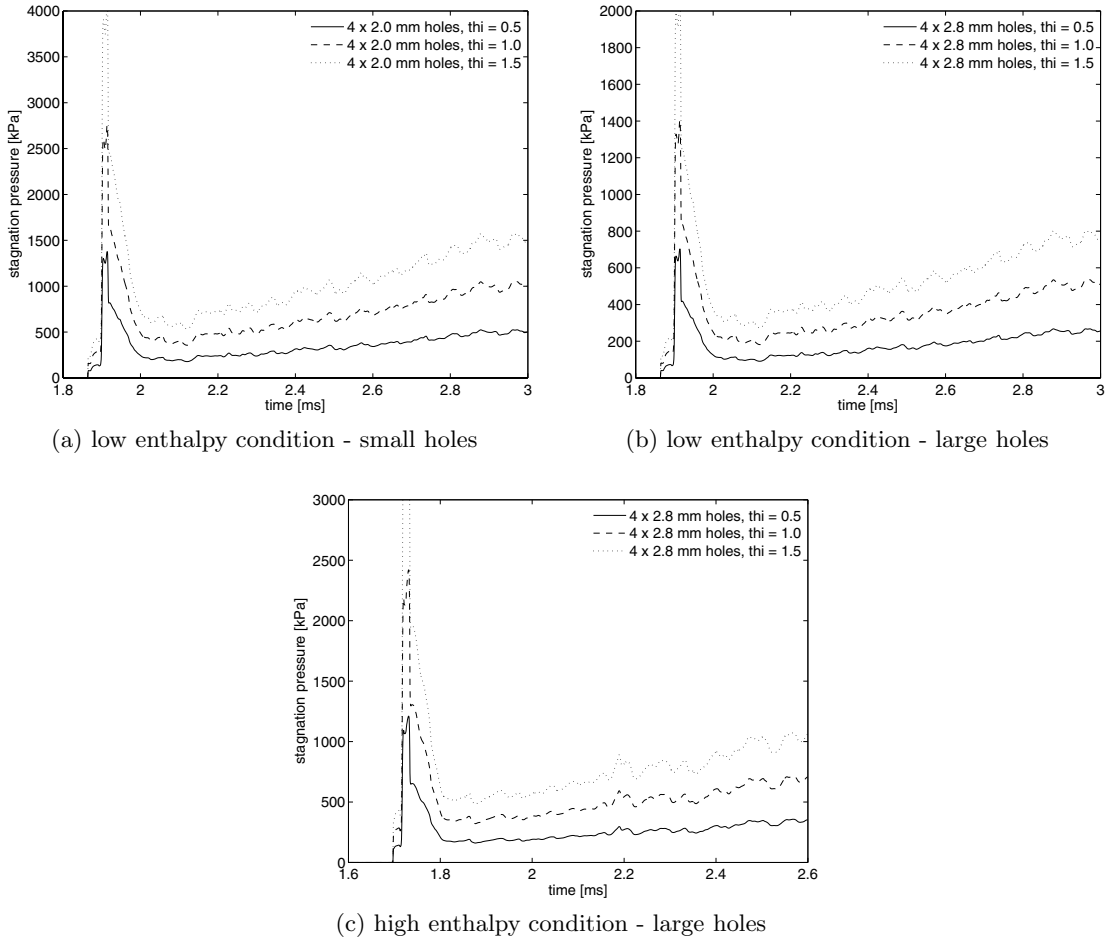


Figure 7.13: Stagnation pressure requirement for H₂ system using transient flow data at nozzle exit from *MB_CNS* simulation.

were estimated using perfect gas relationships from the initial freestream conditions at 2.4 ms from the simulation of the X2 condition (from Section 5.3.2). These properties were 3050 m/s, 0.221 kg/m³ and Mach 6.5. A stagnation pressure of 600 kPa was used, with an injector diameter of 2 mm and a boundary layer thickness of 1.5 mm for the Portz model. There is quite a large discrepancy between the models, with penetration distances varying from 16 mm to 4 mm at 50 mm downstream from the injection location. As McClinton's method is the only one to account for the fuel's initial injection angle, this is assumed to give the most accurate result. As the fuel is injected at 45 degrees to the air flow direction, none of the penetration calculation methods offer a valid estimation of the penetration distance close to the injector. The maximum concentration estimate of McClinton shows that this occurs quite close to the surface.

As the the freestream properties are transient, the fuel penetration can be explored as a function of time. Using the McClinton method, the maximum penetration of the hydrogen is investigated for different hole diameters and hydrogen plenum chamber pressures with

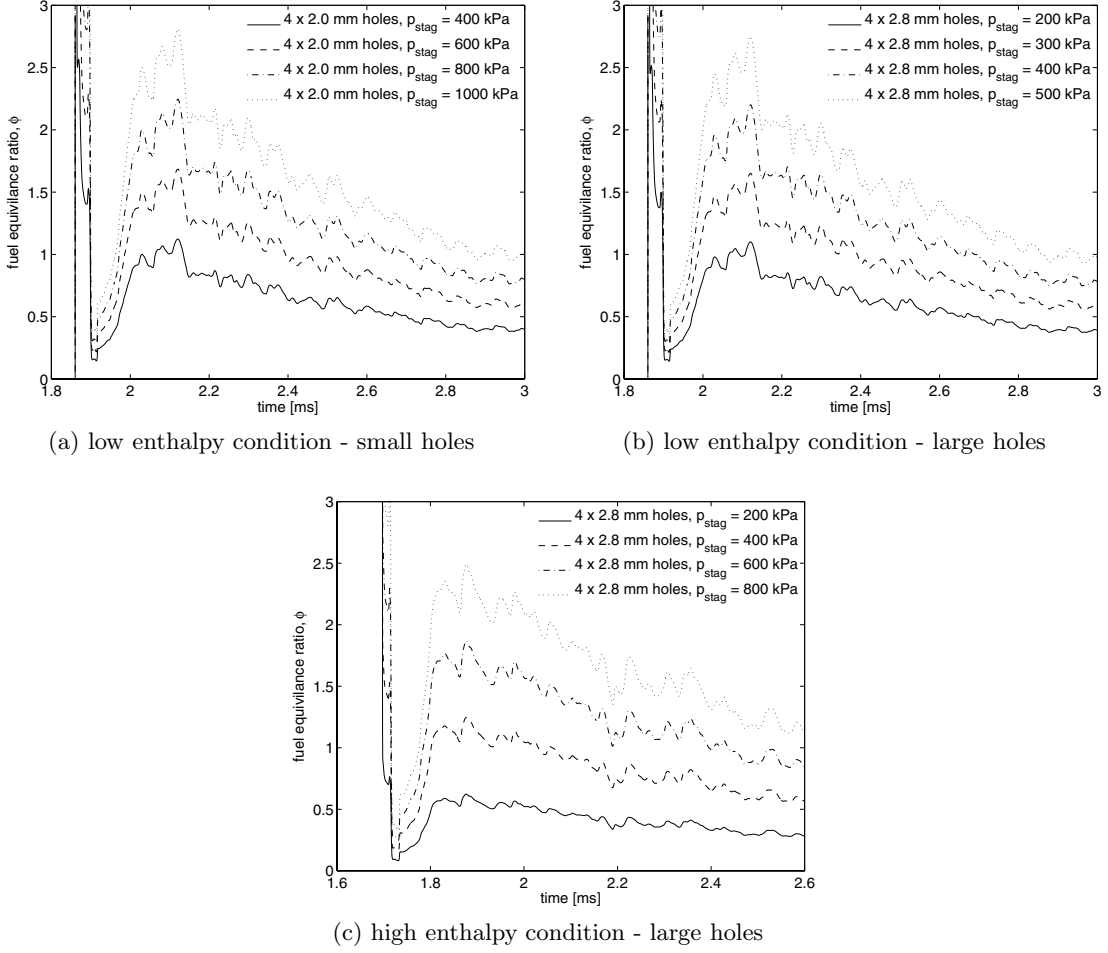


Figure 7.14: Fuel equivalence ratio for H₂ system using transient flow data at nozzle exit from *MB_CNS* simulation.

a transient freestream. This is presented in Figure 7.17 assuming a hole diameter of 2 mm, supply pressure of 600 kPa; a constant axial distance of 20 mm is used unless otherwise varied. There is shown to be only a minimal difference of approximately 5% in penetration distance during the test time. The variation is quite significant when using different injector diameters, with the penetration increasing with hole diameter. There is only minimal difference in penetration height with the likely range of hydrogen plenum chamber pressures considered, as the momentum of the freestream is significantly larger than that of the jets. This suggests that a reasonable penetration height should be obtainable using 2 mm diameter holes and stagnation pressures that allow variation of the equivalence ratio from 0.5 to 2.

The mixing efficiency can be approximated using a modified method for multiple jet perpendicular injection at an incident angle shown in Equation 6.17 for both spacings detailed. Using the same properties described previously from the X2 expansion tube

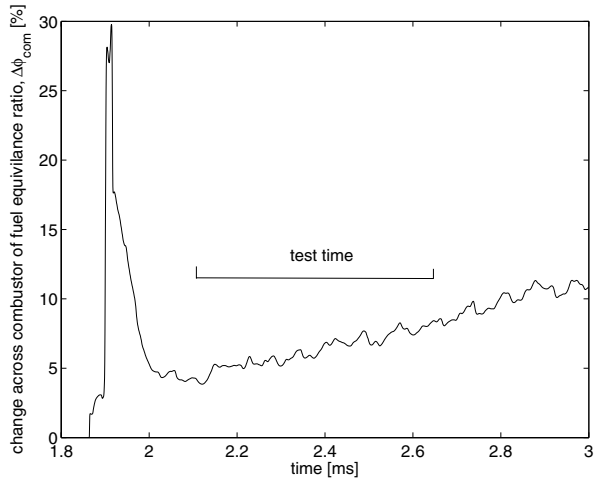


Figure 7.15: Change in fuel equivalence ratio across a 200 mm combustor.

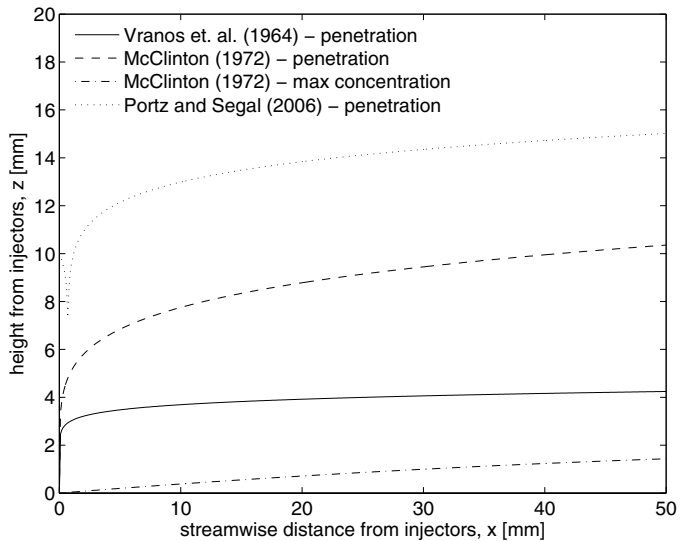


Figure 7.16: Comparison of different methods to obtain fuel penetration from the third wedge.

simulation at 2.4 ms, the mixing efficiency is estimated for a hydrogen supply pressure of 600 kPa. Figure 7.18 shows that the predicted mixing efficiency should reach 0.9 by the likely ignition point. As the spacing in the designed engine will be closer than those for which the correlations are given for (S/D of 4), the near field mixing is likely to be slower [192].. However, the far field mixing will likely improve.

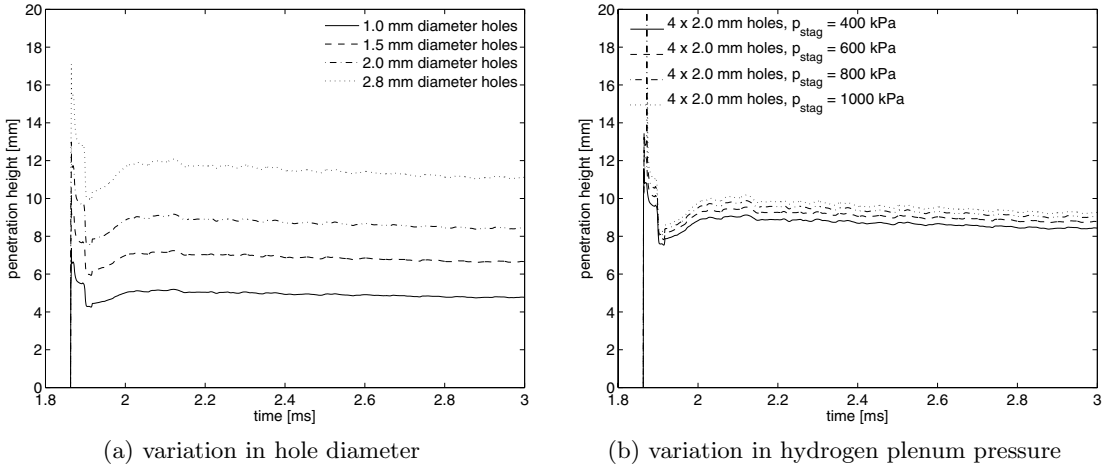


Figure 7.17: Penetration distance as a function of time.

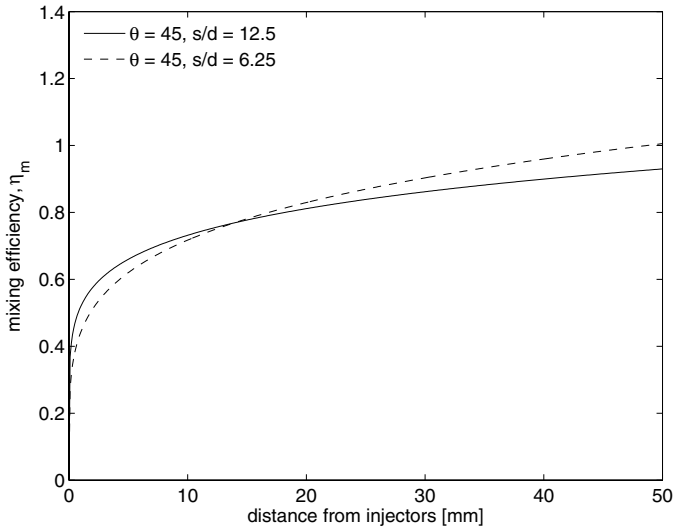


Figure 7.18: Mixing efficiency for hydrogen injection into air.

7.1.3 Combustor

It was decided that the combustor for the scramjet should be a constant area duct, with the allowance for shock waves emanating from the inlet into the combustor. To achieve combustion as quickly as possible, the temperatures and pressures need to be kept as high enough to ignite the fuel quickly. This however, may lead to performance decreases overall. The implication of combustor heating rates on flight vehicles was not considered, as the test times in the expansion tunnel are relatively small.

The combustor inlet area is 40 mm wide and 7 mm high. This is quite a small height, therefore mixing rates and combustion should occur in short lengths. To estimate the optimised combustor length, both the skin friction and the combustion must be modelled

together. This is because the maximum thrust potential may occur at a combustor length shorter than that required to reach complete reaction of the fuel/air mixture. John [27] describes a method for analytically modelling the heat addition and friction in a constant area duct based on the conservation of mass, momentum and energy. This requires knowledge of the heat release along the length of the combustor. The combustion efficiency can be used to model both the mixing and combustion effects where total heat release is achieved when this reaches unity. This relationship is estimated to follow an exponential curve as suggested by Riggens [36] with Equation 7.6. With an overall heat addition of 1 MJ/kg⁶, the total length to achieve complete combustion was predicted to be 0.9 m using the ignition and reaction times presented in Section 6.3.1, for the initial flow properties of 3000 m/s, 100 kPa and 1000 K. The change in the combustion efficiency can be seen in Figure 7.19.

$$\eta_c = 1 - e^{-6x} \quad (7.6)$$

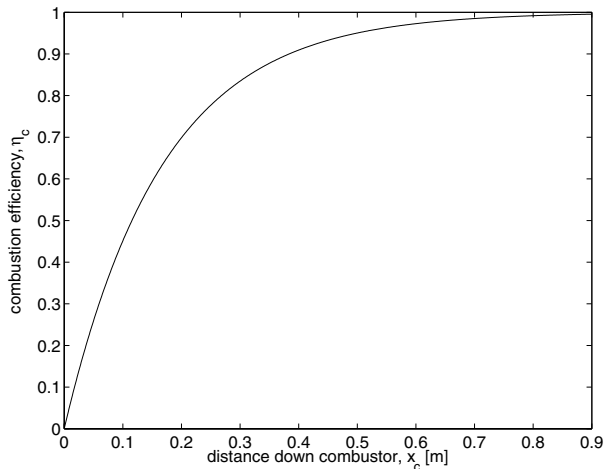


Figure 7.19: Estimated combustion efficiency of a true scramjet flow field

The thrust performance of the combustor can be seen in Figure 7.20, ignoring losses at both the inlet and expansion surfaces (i.e. non-isentropic processes) and assuming constant gas properties throughout the process ($\gamma = 1.4$ and $R = 287 J/kg.K$). It should be noted that for the Mach 10 condition being investigated, the flow properties used at the combustor entrance produce losses as previously shown and would result in negative thrust at the start of the combustor. The thrust potential by the end of the combustor is seen to be approximately 29 kN for a 1 m² capture area. Applying skin friction to the combustor shows that the thrust drops dramatically with increasing skin friction coefficient

⁶This relates to an equivalence ratio of 0.38, not accounting for losses due to incomplete mixing and combustion.

as expected. It also shows that an optimal combustor would have a shorter length than required to achieve full combustion. Given these findings, the combustor length chosen was set to 200 mm, which corresponds to a skin friction coefficient of just over 0.001 to give optimal thrust performance.

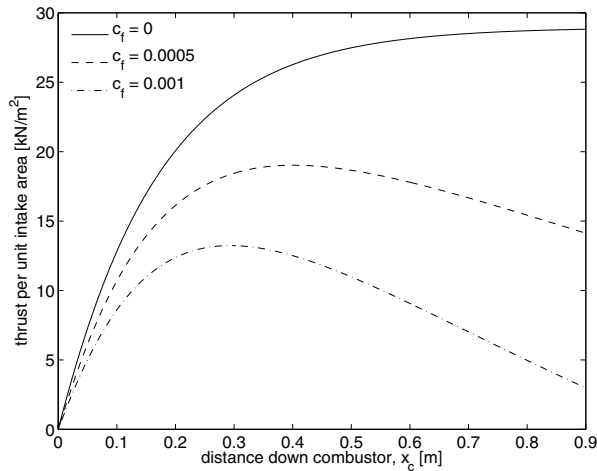


Figure 7.20: Predicted thrust performance of a combustor with heat addition and friction as a function of combustor length.

7.1.4 Thrust surface

A relatively simple approach was taken to design the thrust surface, due to lack of knowledge of both the flow profile and the chemical composition of the flow exiting the combustor. A planar two dimensional design was chosen, and as thrust was not to be directly measured (although the inviscid thrust may be estimated from pressure measurements), the cowl was extended to the exit plane of the exhaust. The exit area was matched to that of the intake area. Figure 7.21 shows a schematic of the likely pressure recorded along the thrust surface. Using the recommendations made by Stalker [205], an angle of 12 degrees was chosen for the thrust surface.

7.2 Model Design

The physical model design for the intended flow path design presented previously was undertaken as part of the testing of the scramjet for the larger T4 model. With the physical design completed for the T4 model by Frost et al. [204], this allowed for the same design principles to be used. As the model was not required to have similar properties to that required in flight due to weight thermal loading considerations, mild steel plates were used for most of the model. The total model was required to be positioned in the

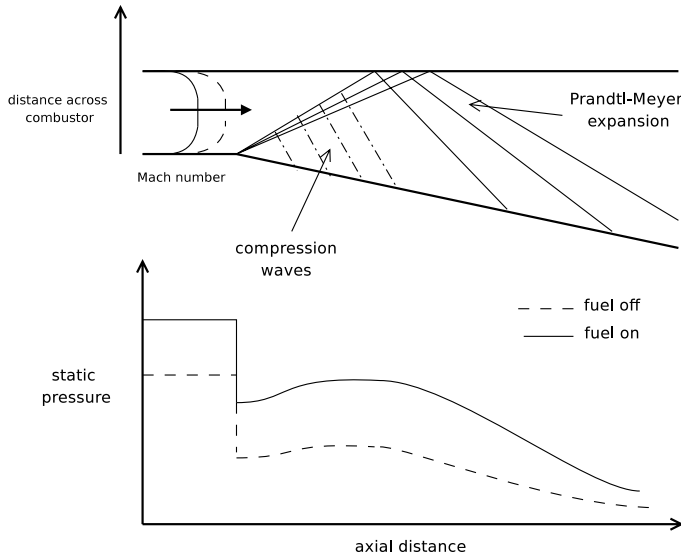
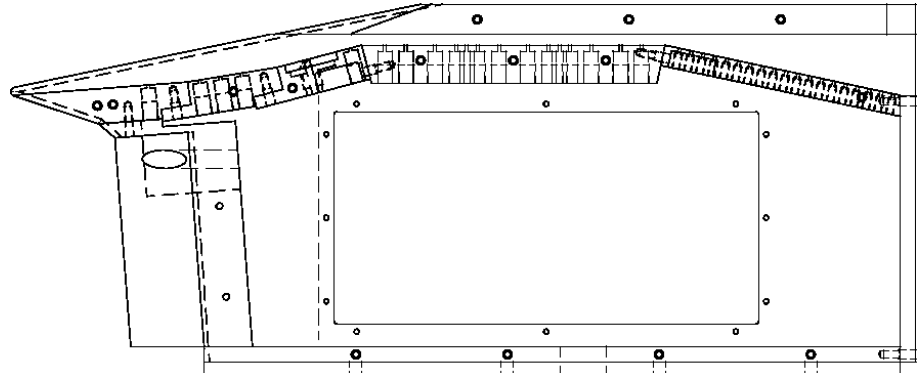


Figure 7.21: Schematic of thrust production from two dimensional nozzle.

centre of the core flow, and mounted to the slide rail of the X2 dumptank (described in Section 5.1.2). The scramjet was mounted upside down from the floor of the test section, with the cowl being the uppermost component. This allowed mounting both the solenoid valve as close as possible to the plenum chamber located behind the third wedge and connecting this to the Ludwieg tube located at the base of the dumptank. Also, external edges are machined backwards at an acute angle to prevent detached shocks occurring in front of the intake. The side walls on the inlet are also flared axially, following the shock line from the leading edge to the cowl. This decreases the effects of both the side wall viscous effects and weak shock waves. Figure 7.22 shows both an assembly drawing of the model and a picture of the model mounted in the dumptank. The workshop drawings for the each piece of the model can be seen in Appendix E.

Static pressure was the only flow property measured in the scramjet. The scramjet was designed to be able to support 28 PCB transducers along the inlet and combustor and thrust surface. These were all located along the bottom wall, to use the protective shroud provided with the scramjet. These were all mounted with a recess mounting arrangement with a 2 mm long, 2 mm diameter hole as described in Rowan [7] and shown in Figure 7.23. On the inlet, this was limited to centreline measurements, however in the combustor, measurements were taken at off centre locations. All these locations can be found in Appendix E. On the thrust surface, 2 PCB mountings were made off centre to ensure that the after shot pressure did not exceed the limit of the Kulite pressure transducers. These were also recess mounted, with the mounting using the M5 thread on the transducer. Two pitots were located below the bottom edge, with the pitot arrangement used in the T4 shock tunnel [155].



(a) model drawing of scramjet (sidewall removed)



(b) picture of scramjet mounted in X2 dumptank on modified rail

Figure 7.22: Mach 10, X2 scramjet model.

The fuel system was fed to the solenoid valve with a flexible tube from a connection point on the bottom of the dump tank. The solenoid was located below the combustor as shown in Figure 7.24. This allowed for a short distance of copper piping required to supply the plenum chamber behind the third wedge. Also, to measure stagnation pressure, a transducer was mounted to the plenum cavity. To allow access to both the transducers and fuel valve without having to disassemble the entire model, cover plates were made for the outer edge of the side walls.

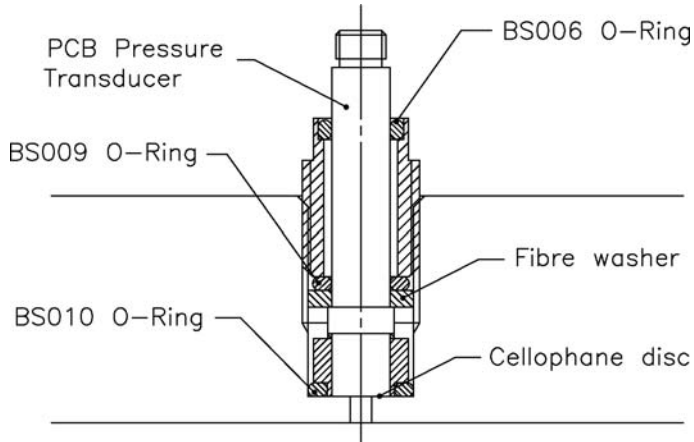


Figure 7.23: Mounting arrangement for static pressure measurement. Taken from [7].

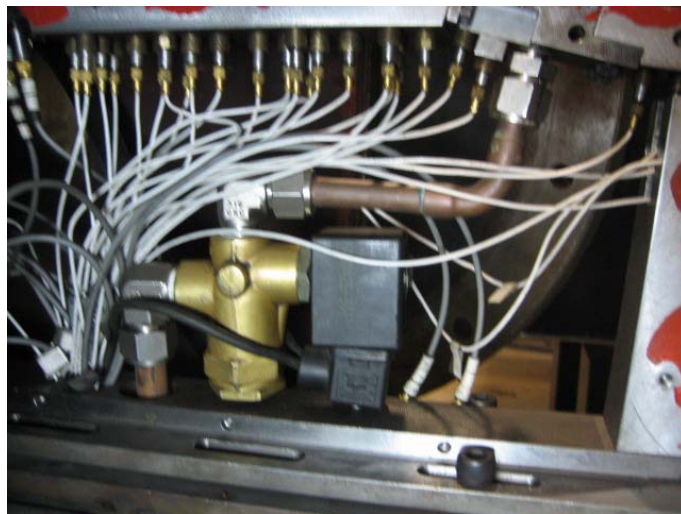


Figure 7.24: Picture of the fuel valve and transducers of scramjet model.

7.3 Transient Simulation of Scramjet Model

Because the X2 conditions flow parameters are transient in nature, it is important to ensure the scramjet will still operate over the complete test time. As Jacobs et al. [49] showed for a generic scramjet configuration with transient inflow, flow establishment times can be estimated via numerical simulations of the scramjet. This is especially important given the short test time considered here. A numerical simulation of the scramjet will also be useful in comparison with the fuel off data taken experimentally. Although the inlet is thought to start impulsively, this has not been explored for transient flow produced in an expansion tube, where the test flow is preceded by the high temperature accelerator gas. Using the time evolving inflow conditions expected from the expansion tube, this can also be explored.

The simulation again uses the Navier-Stokes solver *MB-CNS* [140], disregarding the effects of fuel injection and combustion. The flow data calculated at 18.8 mm off centre from the nozzle exit of X2 in the axisymmetric calculations of Section 5.3.2, a transient numerical simulation was undertaken of the scramjet configuration (shown in Figure 7.25) with the transient data applied uniformly across the entire inflow boundary. The analytically determined geometry used all the dimensions of the physical scramjet model apart from the inlet which uses the inviscid design geometry without the blunting on the leading edge and cowl tip. The simulation assumes equilibrium chemistry of air and uses a Baldwin-Lomax turbulence model on the body surface apart from the first wedge on the inlet⁷. The simulation uses a total of 187000 cells, with the scramjet capturing 1540 cells axially and 100 cells radially. All walls are assumed to be at a fixed temperature of 300 K. Further details of the use of transient inflow boundaries, turbulence model and the equilibrium chemistry in the *MB-CNS* code can be found in Section 4.4.2. Due to the fluctuations in flow properties given by the simulations, time averaging was used to smooth the flow that is coming into the scramjet.

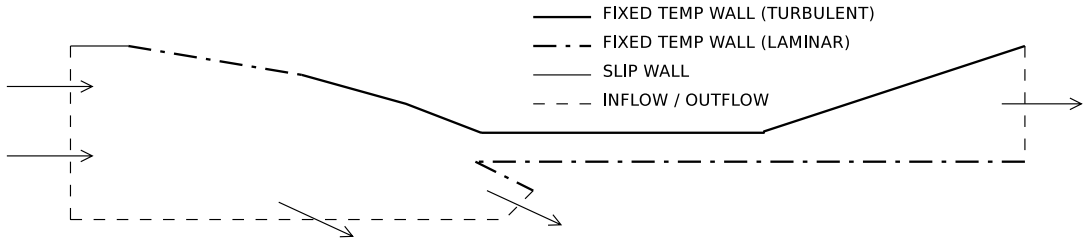


Figure 7.25: Schematic of flow domain and boundary conditions for transient simulation of scramjet.

7.3.1 Transient analysis of results

Due to the transient nature of the flow produced by X2, analysis of results must be undertaken, which takes proper account of the unsteady terms. These transient effects are similar to those seen in the flow establishment studies of Jacobs et al. [49] and Rogers and Weidner [51], based on a T4 reflected shock tunnel Mach 5 condition. Point location measurements such as static pressure and heat transfer will be dependent on the time derivative change at that particular location, whereas integrated properties such as axial momentum which effect total thrust will be affected by the time derivative change in the property integrated within the control volume of the engine. It is these later measurement that are difficult to reconcile in the presence of a time evolving inflow. However, some

⁷Current limitations in the code only allowed for the turbulence model to be applied to the north boundary.

correction may be made to the experimental measurements that mitigate the transient effects.

For the analysis of conserved properties, the integral form of the flow properties is taken, as shown in Equation 7.7. Investigation of the importance of the transient effects can be made by evaluating the time derivative term, $\frac{d}{dt} (\int_{CV} \beta \rho dV)$, compared with the magnitude of the other term (where $\frac{d}{dt} (B_{syst})$ is an external input).

$$\frac{d}{dt} (B_{syst}) = \frac{d}{dt} \left(\int_{CV} \beta \rho dV \right) + \int_{CS} \beta \rho (U \cdot n) dA, \quad \beta = \frac{dB}{dm} \quad (7.7)$$

When considering the effects of unsteadiness on the flow through a scramjet for point location measurements, it is useful to consider the *total derivative* of the flow properties from the Lagrangian point of view of a particle convecting through the flow field (given in Equation 7.8) [206]. The *total derivative* of a given property, λ , contains both a local term ($\frac{\partial \lambda}{\partial t}$) and the convective terms ($U \frac{\partial \lambda}{\partial x}, V \frac{\partial \lambda}{\partial y}, W \frac{\partial \lambda}{\partial z}$). The local term represents the transient nature of the flow property at a given point in space. The convective terms indicate, how the flow property changes with time as a fluid particle moves to locations with different flow properties. If the local term is zero, the flow is steady.

$$\frac{D\lambda}{Dt} = \frac{\partial \lambda}{\partial t} + U \frac{\partial \lambda}{\partial x} + V \frac{\partial \lambda}{\partial y} + W \frac{\partial \lambda}{\partial z} \quad (7.8)$$

If the local term is non zero, but much smaller than the convective terms, then particles will propagate through the flow field in much the same way as they would in steady flow. Due to the coupling of any changes of velocity with changes in thermodynamic properties, the gas will have almost the same properties (i.e. pressure, temperature, density). Such flows are termed *quasi steady* and the local flow properties can be used at any point in time to calculate the flow field using a steady flow analysis.

The “*hypersonic equivalence principle*” [9] postulates for flows with high Mach numbers, significant changes in Mach number may occur with only a small change in velocity, allowing for the flow field to be described as unsteady flow in one less space dimension. As a planar slice of gas passes through a scramjet, different areas of the section will be processed differently as they pass down the duct, due to waves having a small radial component of velocity. However, the bulk of the particles within a slice will all have similar axial velocities and will stay adjacent (or close) to each other. Therefore, a single velocity can be assumed as it passes through the entire scramjet process. Also, as the flow only undergoes small deflections in its velocity vector, the original axial speed (which is normal to the intake plane) can also be used to follow the slice of gas. Therefore, the convective terms in the *total derivative* can be based purely on the axial direction term ($U \frac{\partial \lambda}{\partial x}$).

If there are only minimal changes in intake flow properties (< 1%) in the time it takes a slice of gas to pass through the scramjet duct (one flow length), the flow can be analysed using a steady flow analysis using the average intake flow properties. This

is due to the minimal change it will have on any flow properties within the scramjet. For the case of *weak* transient inflow, it is useful to normalise values down the duct using the inlet flow parameter, so that comparisons may be made to axial distributions of properties between varying times (i.e. All the pressure measurements relate to the times when the same physical slug of gas was at the transducer). Using the “*hypersonic equivalence principle*”, (i.e. constant axial velocity) the normalised flow property, $\hat{\lambda}(x, t)$, is calculated using Equation 7.9, where the time delay Δt is given as the nominal transit time from the reference position (Equation 7.10). Thus, each individual fluid parcel is normalized against its initial state, which therefore removes most of the influence of the change in inflow conditions. This type of normalisation has been labelled the *initial reference method* [9].

$$\hat{\lambda}(x_n, t) = \frac{\lambda(x_n, t)}{\lambda(x_{ref}, t - \Delta t)} \quad (7.9)$$

$$\Delta t = \frac{(x_n - x_{ref})}{U_{norm}} \quad (7.10)$$

Where gradual changes in inflow properties are significant ($> 1\%$) along the length of the scramjet, further analysis is required. For these *stronger* transient changes in inflow, a *quasi steady* analysis may be used where the change in the local term of a flow property is insignificant compared with the convective term ($\frac{\partial \lambda}{\partial t} \ll U \frac{\partial \lambda}{\partial x}$). This is where data can be compared to a steady flow analysis by gathering the flow property for the same slice of gas at all relevant axial locations as it travels through the scramjet (i.e. the time of entrance, t , plus an offset time, Δt). If a quasi steady analysis can be applied, transient inflow can allow for multiple different inflow conditions to be tested during one test. Also, the normalisation procedure will need to be altered for a quasi steady analysis to be Equation 7.11. This normalisation method has been labelled the *slug tracking method*. Both these methods normalise the gas slices at the measurement locations by there initial values at the normalisation location. The difference being, the slug tracking method presents the normalised data for a single slice of gas with a set of initial properties, rather than multiple gas slices which had different initial properties, which at a single point in time are at the measurement locations.

$$\hat{\lambda}(x_n, t) = \frac{\lambda(x_n, t + \Delta t)}{\lambda(x_{ref}, t)} \quad (7.11)$$

Nature of pressure measurements

As static pressure measurements are the only flow property to be measured experimentally, the nature of this flow property is important. In scramjets, large pressure changes will occur through the intake, combustor and thrust nozzle. Therefore substantial convective

terms are expected throughout the entire engine. To determine if a quasi steady analysis can be used in analysis of both the experimental and calculated static pressure, local and convective terms in the *total derivative* are compared from the computational simulations of the engine described in Section 7.3. The intake was chosen for evaluation, as it shows a representative part of the engine which will exhibit changes due to both the local and convective terms.

As the flow through the scramjet intake of this study is dominated by discrete shock waves, the change in the convective terms will be large at the shock locations and small in between. Therefore, evaluation of the the convective terms is undertaken along a pathline at a given time (in a laboratory reference, which assumes steady flow), using the initial position, velocity and pressure as a reference. The local term is then evaluated for pathlines originating at the same position at two different times. The pathline used originates in the middle of the capture area and in the freepath, which then passes through the series of oblique shocks on the intake (Figure 7.26a). The change in the location of the streamline over the time that will be taken for the local term will be evaluated is shown to be negligible. However the change in pressure over this time is significant, with a rise of 25% (Figure 7.26b).

The comparison of the axial convective terms and the local terms along the pathline are shown in Figure 7.27a, where these results are summarised in Table 7.6. The convective terms throughout the engine are seen to be two orders of magnitude larger than the local time derivative terms. The change in the convective term across the intake 0.67 kPa/ μ s compared to the temporal change in the combustor entrance was 0.012 kPa/ μ s. Also, each increase in the convective term across each shock is at least an order of magnitude larger than the local term. This shows that the convective terms are much larger than the local terms along the intake and therefore quasi steady analysis should be applicable.

Table 7.6: Magnitude of terms in the *total derivative* for static pressure for the scramjet intake.

term	$\frac{dp}{dt}$ [kPa/ μ s]	location	$\frac{\text{convective term}}{\text{local term}}$
local, $\frac{\partial p}{\partial t} \propto$	inflow	0.0025	268
local, $\frac{\partial p}{\partial t}_{\text{combustor}}$	combustor	0.012	67
convective, $U \frac{\partial p}{\partial x}$	third wedge	0.67	-

The two convective terms ($U \frac{\partial p}{\partial x}$ and $V \frac{\partial p}{\partial y}$) through the intake are compared by analysing the same pathline through the intake. Figure 7.27b shows that the transverse direction convective term is similar across the intake to the axial term as it was taken in the middle of the capture area. However, if a pathline was taken closer to the body side of the scramjet, this term would be reduced as the velocity and pressure difference would remain

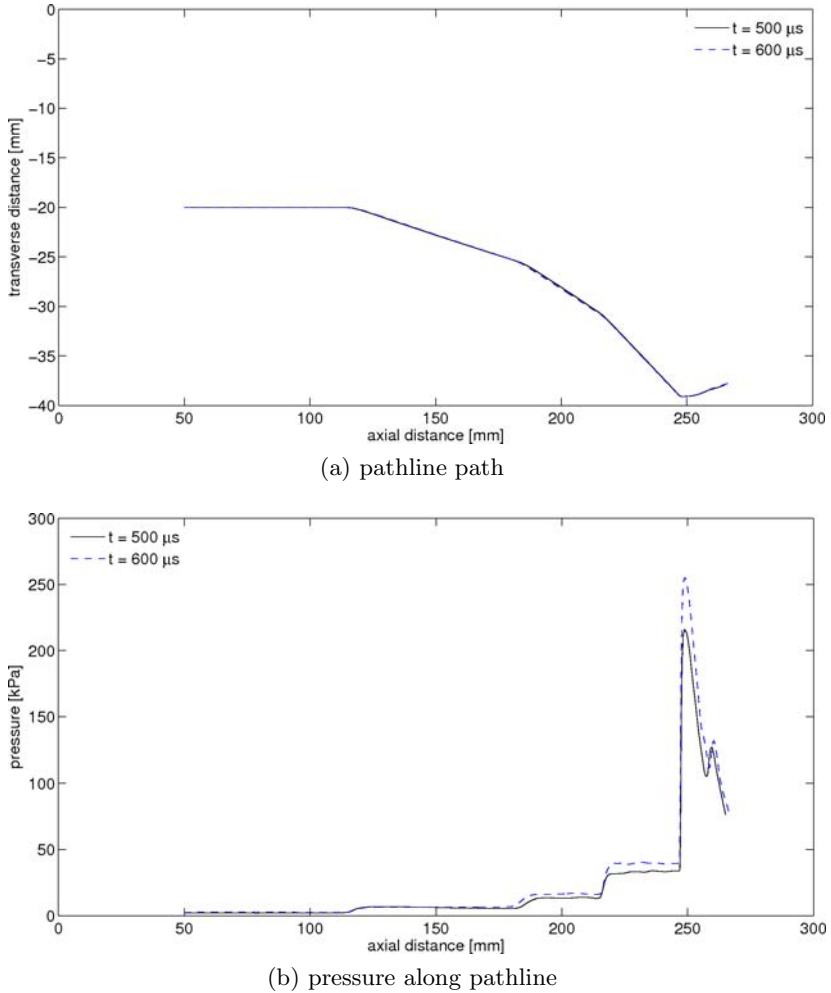


Figure 7.26: Pathline path and static pressure for pressure derivative term evaluation. Starting position is $x = 50$ mm, $y = -20$ mm.

constant whilst the change in transverse position would increase. Once the flow enters the combustor however, the transverse component is reduced to negligible levels as the average overall change in the transverse position is zero, whereas the axial position changes significantly. Therefore, any increase in pressure across the combustor will only increase the axial convective term which will dominate the *total derivative*.

Applying this method to a scramjet engine experiment where there is a transient freestream, can allow the experimenter to provide quasi-steady estimates of pressure field through the duct. This method of analysis could be limited however, when the effects of fuel injection and combustion are considered. The fuel injection process is separate to that of the freestream flow generation and is steady over a much longer period. Also, supersonic combustion in constant area ducts, is associated with significant decreases in velocity. This can be overcome, with a description of the velocity change throughout the

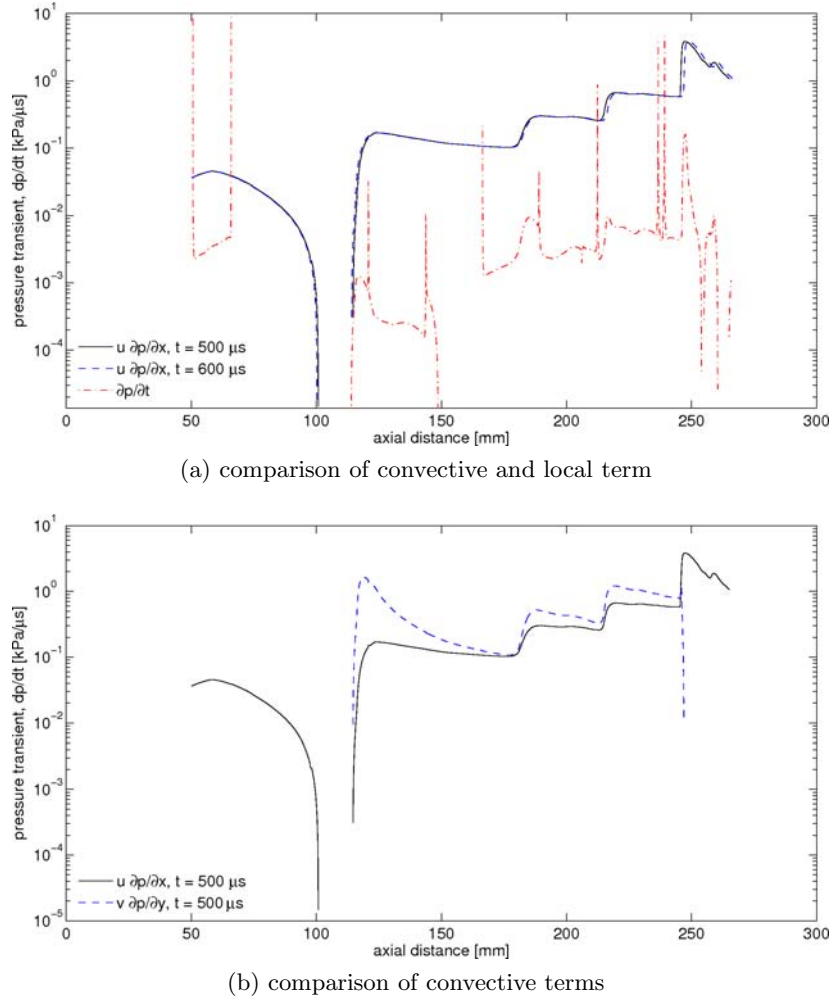


Figure 7.27: Evaluation of pressure derivative terms along a pathline through the intake.

engine as to ensure that the same slice of gas is analysed, but, the coupling of the chemical reaction rates to the incoming flow properties will be harder to deal with. However, in the absence of time accurate computational simulations of the engine, which include the temporal inflow, fuel injection and combustion, this method will at least give a first order representation of the flow.

Effect on thrust prediction

Thrust is a principal quantity in determining a scramjets performance and will need to be measured during ground tests. Despite the local flow properties being given quite accurately by a steady flow analysis, the effects of the transients can significantly alter the thrust development because it is an integrated effect across the entire engine.

The effect of transient inflow on thrust predictions can be investigated by taking the integral form of the momentum equation (Equation 7.12). This shows that thrust is

developed from a combination of the net flux properties out of the control volume plus the rate of change in momentum in the control volume (Figure 7.28). Taking a control volume around the whole vehicle, the linear momentum equation can be compared between flight and ground testing (shown in Figure 7.29). In flight (Figure 7.29a), there are no external forces acting on the control volume around the vehicle, although there are drag and thrust forces acting on the body of the scramjet. The change in momentum fluxes and forces due to pressure across the control volume is balanced by the rate of momentum change in the control volume. Therefore, for the vehicle to accelerate (i.e. $\frac{dU_\infty}{dt} > 0$), the momentum flux and pressure force exiting the control volume must be greater than that entering it ($(\rho_{out}U_{out}^2 + p_{out}) A_{out} > (\rho_{in}U_{in}^2 + p_{in}) A_{in}$).

$$\mathbf{F}_{ext} + \int_{CS} p(-\mathbf{n}) dA = \frac{d}{dt} \left(\int_{CV} \mathbf{U} \rho dV \right) + \int_{CS} \rho \mathbf{U}^2 dA \quad (7.12)$$

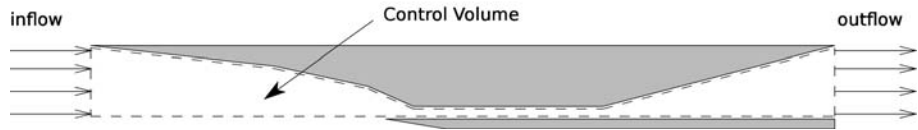
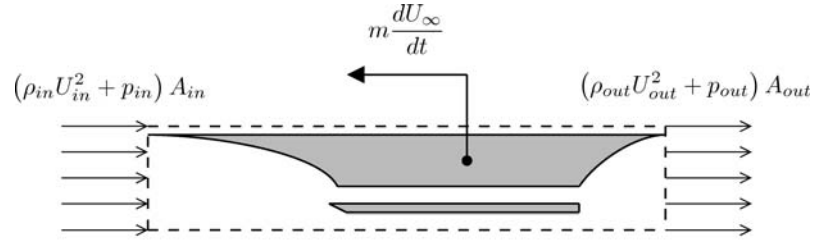


Figure 7.28: Control volume used in analysing significance of rate of change in stored momentum.

A ground test varies from flight, as the vehicle is constrained ($\frac{dU_\infty}{dt} = 0$) as shown in Figure 7.29b). With steady inflow conditions, the vehicle simulation will have a constant level of stored momentum within the control volume. Therefore, any change in momentum flux and pressure force across the control volume is counteracted by an external force by the supports of the scramjet and can be measured as a net thrust ($T - D$). Therefore, the net acceleration of the vehicle can be directly predicted for a single freestream (or vehicle) velocity. If the ground test facility produces a transient flow, there will be a net change in the stored momentum of the control volume. If the net thrust is much larger than the rate of change in stored momentum, this measurement can be used for the average original freestream conditions for the slices of gas within the scramjet. If the rate of change of stored momentum is significant, this term must be subtracted from the measured net thrust to predict the flight net thrust.

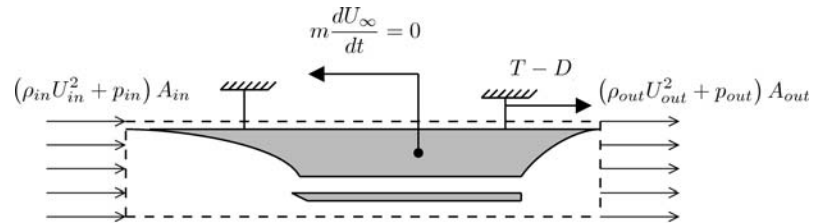
To evaluate the change in stored momentum term, the difference in integrated momentum throughout the control volume of the scramjet capture area (as shown in Figure 7.28) must be evaluated between two different times. A representation of the likely flow in the scramjet is taken from the fuel off CFD data which uses the transient inflow conditions of the expansion tunnel flow. Using the two dimensional simulation results for a constant width of 40 mm, the time derivative term was evaluated between results at 480 μs and 520 μs . This is found to be a 108 N increase in thrust. The average momentum term



$$F_{ext}^{(0)} = \frac{d}{dt} \left(\int_{CV} U \rho dV \right) - m \frac{dU_\infty}{dt} + (\rho_{out} U_{out}^2 + p_{out}) A_{out} - (\rho_{in} U_{in}^2 + p_{in}) A_{in}$$

$$m \frac{dU_\infty}{dt} = (\rho_{out} U_{out}^2 + p_{out}) A_{out} - (\rho_{in} U_{in}^2 + p_{in}) A_{in}$$

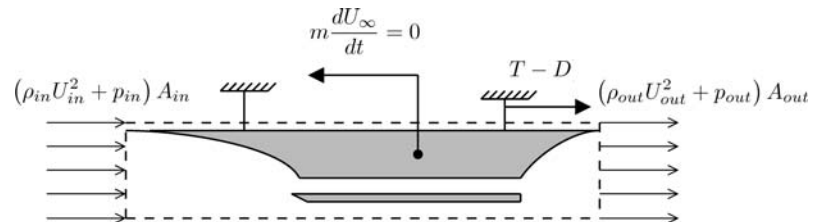
(a) flight testing - scramjet steady frame of reference



$$F_{ext}^{(T-D)} = \frac{d}{dt} \left(\int_{CV} U \rho dV \right) + (\rho_{out} U_{out}^2 + p_{out}) A_{out} - (\rho_{in} U_{in}^2 + p_{in}) A_{in}$$

$$T - D = (\rho_{out} U_{out}^2 + p_{out}) A_{out} - (\rho_{in} U_{in}^2 + p_{in}) A_{in}$$

(b) ground testing (steady inflow)



$$F_{ext}^{(T-D)} = \frac{d}{dt} \left(\int_{CV} U \rho dV \right) + (\rho_{out} U_{out}^2 + p_{out}) A_{out} - (\rho_{in} U_{in}^2 + p_{in}) A_{in}$$

$$T - D = \frac{d}{dt} \left(\int_{CV} U \rho dV \right) + (\rho_{out} U_{out}^2 + p_{out}) A_{out} - (\rho_{in} U_{in}^2 + p_{in}) A_{in}$$

(c) ground testing (transient inflow)

Figure 7.29: Comparison of thrust production in a scramjet between flight and ground testing.

$(\int_{CS} \rho \mathbf{U}^2 dA)$ between these times across the inlet and outlet boundaries was calculated to be -128 N (515 N at the inflow boundary and 387 N at the outflow boundary) and the pressure term $(\int_{CS} p(-\mathbf{n}) dA)$ was -4.5 N (3.5 N at the inflow boundary and 8 N at the outflow boundary). This gives a net drag of 15.5 N for the scramjet without combustion. It can be seen that the time derivative term is of the same order as the other terms, which indicates that thrust measurements cannot be evaluated as steady state values and the experimental measurements must be corrected to give the values that would be expected to be achieved in steady flight.

7.3.2 Simulation results

Flow properties down the engine

The transient numerical simulation of the scramjet experiment showed that supersonic flow was established within the duct. The flow is passed through a series of shocks and expansions within the constant area combustor and is then expanded out through the nozzle without any choking effects. To give an overview of the flow, Figure 7.30 shows the numerically produced Schlieren image of the scramjet at $600 \mu s$. The Schlieren image is produced by taking a combination of the density gradient in both the vertical and horizontal directions ($\sqrt{\frac{d\rho}{dx}^2 + \frac{d\rho}{dy}^2}$) to get the absolute density gradient. The intake shows three shocks being produced and passing just outside the cowl edge. The combustor flow is quite non-uniform with shock and expansion waves crossing the combustor. These are seen to become weaker by the end of the combustor, which could be an indication of the loss of grid resolution. No major waves can be seen on the thrust surface, as by the combustor exit most of the strong waves have been damped out and the low pressures in this region.

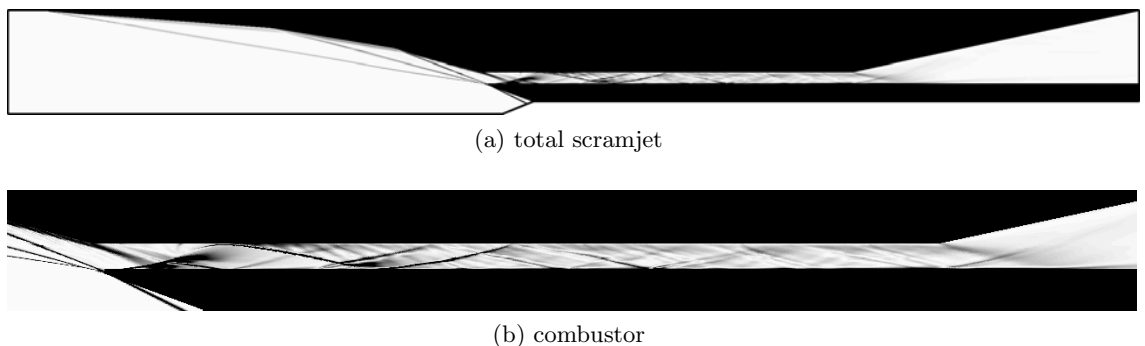


Figure 7.30: Schlieren images of scramjet from transient simulation at $600 \mu s$.

The flow properties will vary greatly through the scramjet due to a series of expansion and shock waves and will also vary in time. To give an indication of the change in flow properties, pathlines are taken from the inflow boundary at three radial locations at $600 \mu s$.

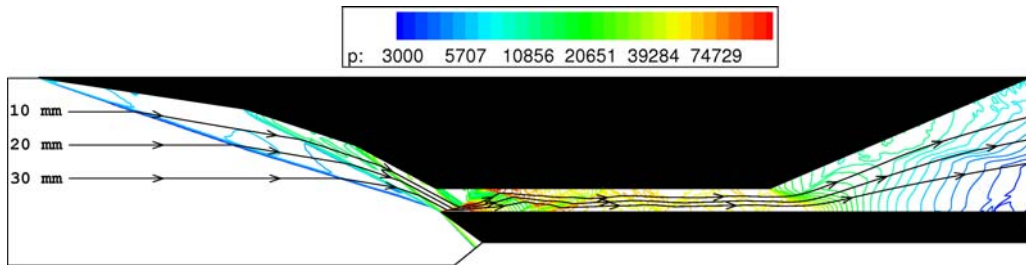


Figure 7.31: Log of pressure and pathlines within scramjet from transient simulation at $600 \mu s$. Scramjet is scaled by a factor of 2 in the transverse direction.

These pathlines are overlaid on top of a contour plot of the log of pressure in Figure 7.31. The flow properties are given along these in Figure 7.32. Each of the pathlines intercepts the shocks and expansions at differing axial locations, with the furtherest radial location from the body side of the engine intercepting the leading edge shock last. The bulk of the flow through the combustor is at an average pressure of 60 kPa and 1000 K, which is high enough for ignition of hydrogen. The axial flow speed does not change significantly through the entire engine (200 m/s), therefore the assumption of a constant velocity in the normalisation procedure shown above is appropriate. The average flow Mach number seen through the combustor is 4.8. The flow on the body side of the scramjet has a higher temperature by approximately 300 K and has a lower axial velocity by 50 m/s . This difference appears to be related to pathlines closer to the body side of the engine see the full reflection of the cowl shock before it starts to attenuate. There is also a laminar boundary layer on the cowl side due to limitations in the coded Baldwin-Lomax turbulence model.

As the bulk of the measurements to be taken in the experiment are static pressure along the wall, these are investigated in greater depth. Figure 7.33 shows a comparison of the static pressure from the body side wall along the length of the scramjet at various times throughout the simulation. At each time the pressure is averaged for $10 \mu s$ to mitigate the effects of noise of the inflow condition. At $250 \mu s$, the flow is still quite transient with a large pressure on the thrust surface as the expansion tube nozzle start up flow is still present. By $350 \mu s$ the flow throughout the entire engine is seen to stabilise, with the shock pattern seen at $450 \mu s$. The main difference between the flow at $450 \mu s$ and $650 \mu s$ is the overall pressure level.

As discussed previously, a normalisation procedure can be used to remove some of the long time duration effects caused by the transient inflows rise in static pressure. Two procedures were suggested in Section 7.3.1 to complete the normalisation, the slug tracking method and the initial reference method. Figure 7.34 shows a comparison at three different times of the normalisation of pressure for the two methods along the body side wall of the scramjet. Again at each time, the pressure is averaged over $10 \mu s$ and the normalisation

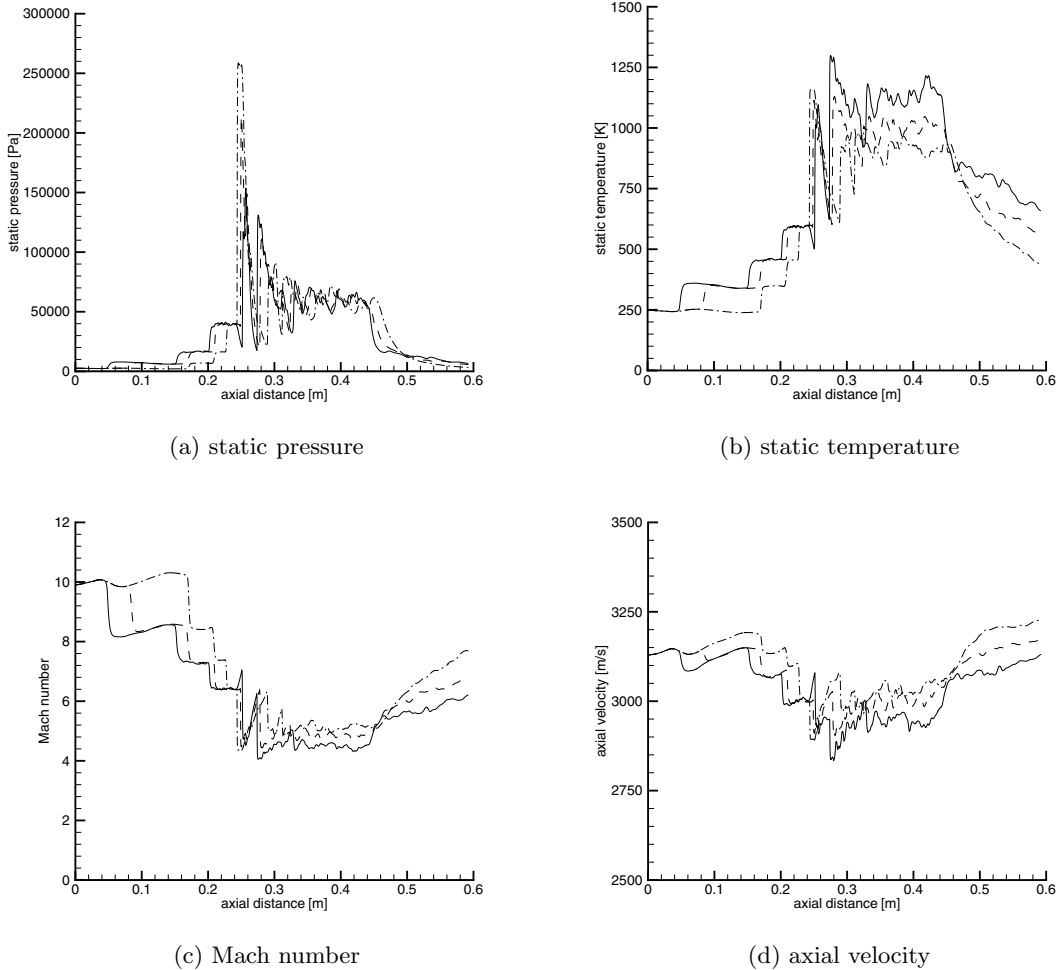


Figure 7.32: Flow properties along pathlines from transient simulation of scramjet at $600 \mu\text{s}$. Pathline initial position: solid = 10 mm, dash = 20 mm, dash-dot = 30 mm.

velocity is taken to be 3100 m/s. To give a representative comparison, the slug tracking method is given for an earlier time so as to compare the same slug of gas. In comparison to the actual static pressure along the body side wall (Figure 7.33), the normalised pressure gives a similar reflection of the wave pattern and strength throughout the scramjet. Both methods are seen to perform quite well, with it being difficult to pick differences especially at later times.

Figure 7.35 shows the differences at each location between two of the time steps for both methods. Comparing the two methods, the slug tracking method performs better with smaller differences in the normalised pressure level at the downstream end of the scramjet. In both, the intake shows the largest overall differences, with the combustor only having smaller differences due to a wave moving across one or two locations over the time. Although it is possible to numerically track the velocity of the gas slices through

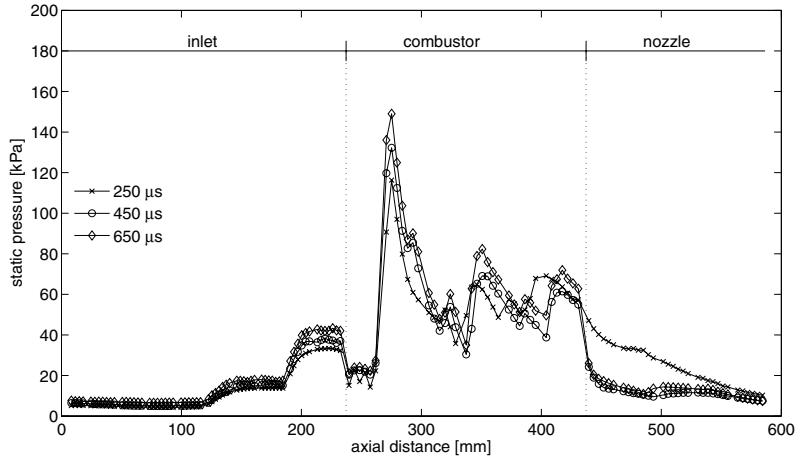


Figure 7.33: Comparison of wall pressure along the body side of the scramjet duct from numerical simulation at various times.

the scramjet to give a better approximation, this technique would not be able to be easily applied to the experimental scramjet flow.

The accuracy of these methods rely upon the accurate definition of the velocity of the gas through the scramjet. As shown in Figure 7.32d, the velocity will not remain constant through the engine, as assumed in the normalisation methods. Also, the inflow velocity will change in time, calculated to be 12% over the test time (Section 5.3.2). The errors in these methods will increase for measurements moving further downstream from the normalisation location, as the time differences will increase. To investigate this, a comparison is made between three constant normalisation velocities (which range over the axial velocities minimum and maximum through the engine) and a varying normalisation velocity taken from a pathline for the slug tracking method in Figure 7.36. As the pathline is taken from the scramjet at one time (i.e. a snapshot is taken of the flow, as if the engine was in steady state at that time), the time this is taken from the solution is approximately half of the time of flight of a particle through the engine. The difference between the time delay (Equation 7.10) through the engine, shows that the variation for 3100 m/s is quite small, less than 5 μs throughout the engine. Also, both the other normalisation velocities show relatively small time delay differences, by the end of the duct becoming less than 15 μs . The comparison between the normalised pressure if using the varying normalisation velocity to the constant 3100 m/s, shows there are only minor differences. On the intake this difference is less than 1%, and only increasing to 4% by the thrust surface, ignoring the large spikes due to movement in waves. Thus, the time of flight through the engine is quite small and the errors associated with the constant normalisation velocities are also small.

Heat transfer at the wall is useful in predicting whether the boundary layer has been fully established. Figure 7.37 shows the heat transfer at three locations along the first

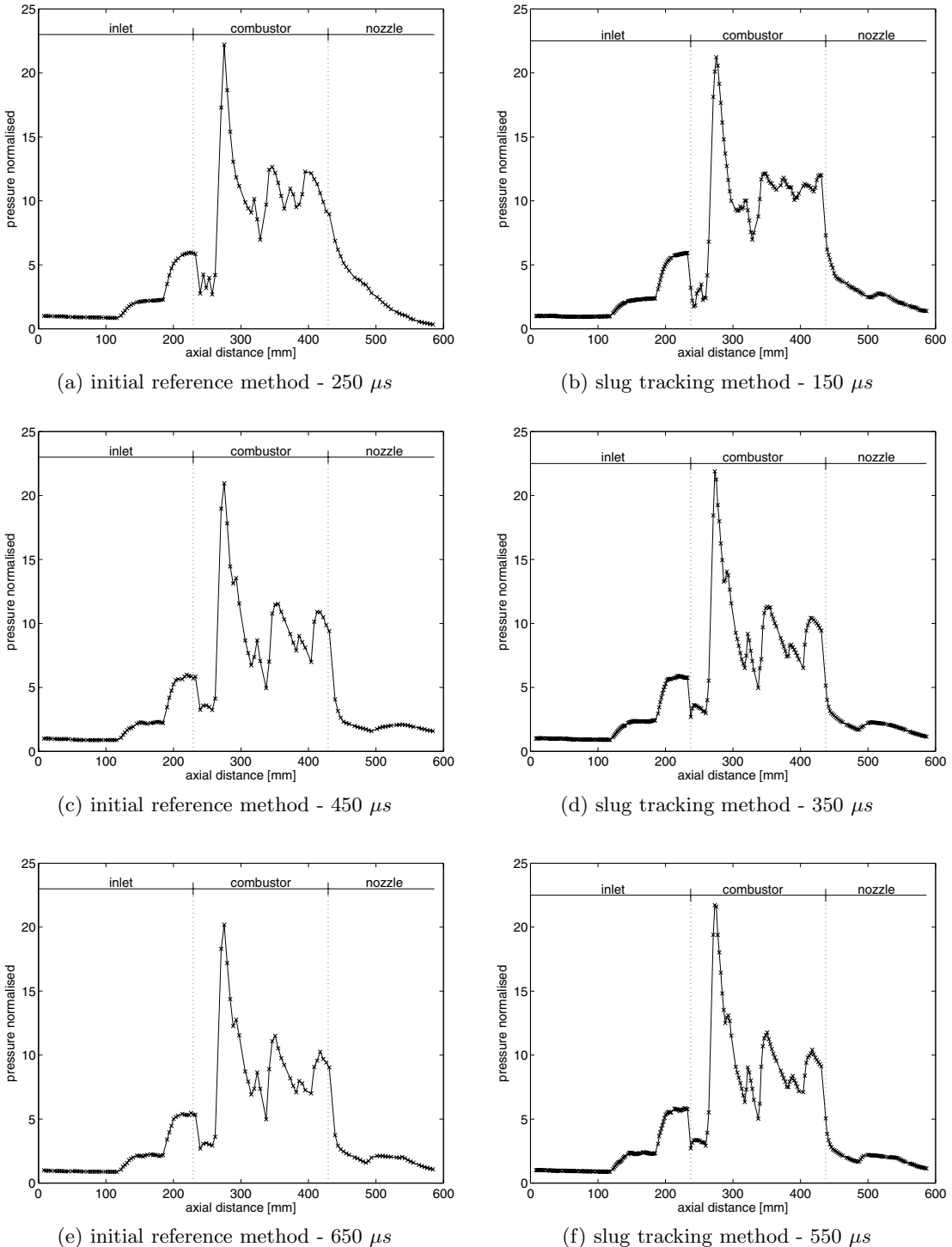


Figure 7.34: Normalised pressure down the scramjet duct from numerical simulation using the two normalisation methods.

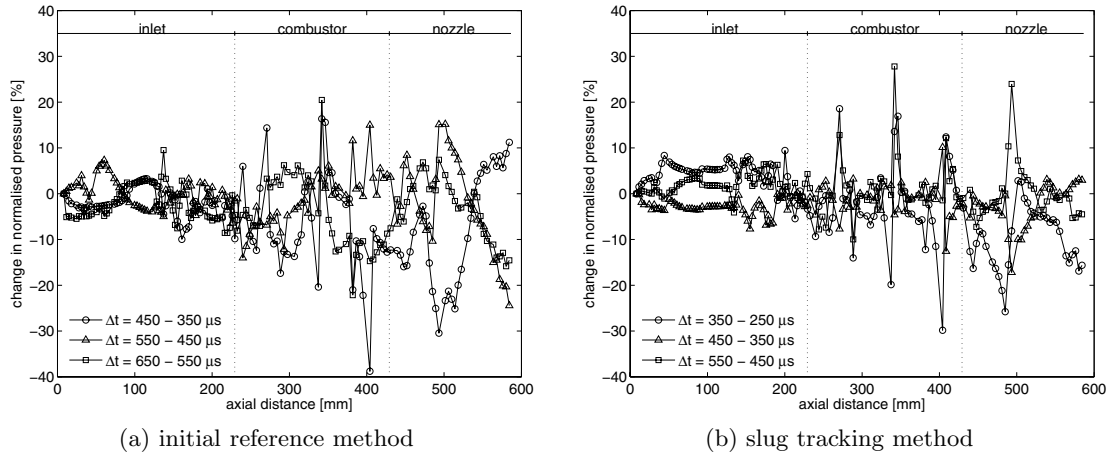


Figure 7.35: Change in normalised pressure down the scramjet duct from numerical simulation using the two normalisation methods.

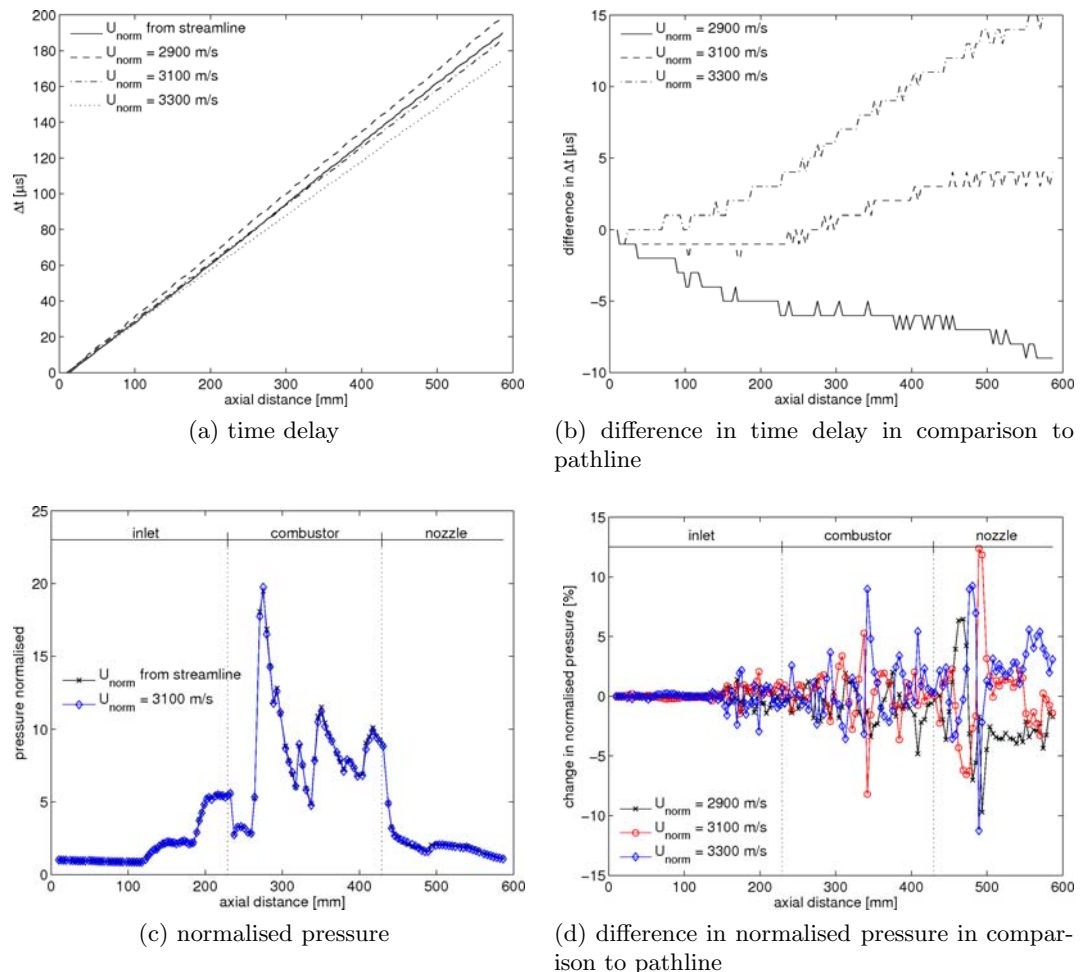


Figure 7.36: Effect of normalised velocity on pressure normalisation down the scramjet duct at $500 \mu s$. The pathline velocity was taken from the simulation at $600 \mu s$, with an initial position of 10 mm.

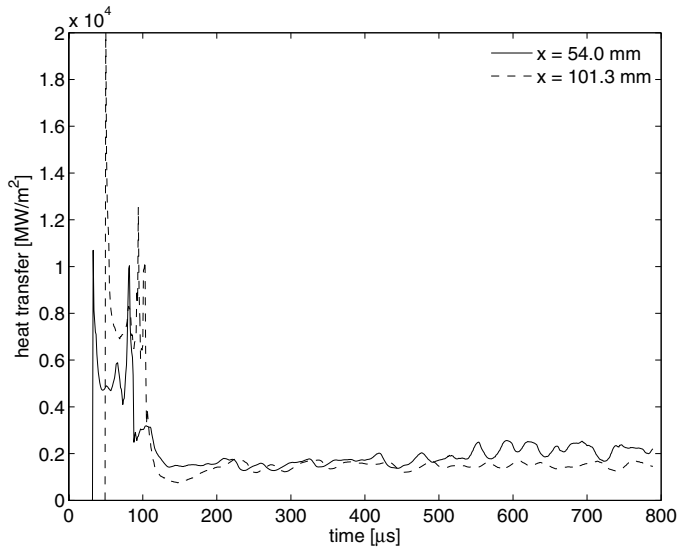


Figure 7.37: Heat transfer on first wedge from numerical simulation.

wedge of the inlet. Although small perturbations can be seen after the initial start up, the heat transfer at both locations becomes relatively steady at a level of 2000 MW/m^2 . Using the slug tracking method of normalisation, the normalised heat transfer down the scramjet duct is plotted in Figure 7.38. At $150 \mu\text{s}$ the effects of only the return cowl shock separation region is of major influence through the combustor. At later times, the points at which shocks and expansion waves meet the body side become more apparent. Also, the region of high pressure on the thrust surface is seen to have increased heat transfer at this point. Overall however, the level of heat transfer is seen to increase as the flow establishes. The transient nature of inlet flow causes shifts in the peaks of heat transfer through the engine.

Grid resolution

A simple grid resolution study was undertaken on the simulation by taking $2/3$ of the grid resolution in both the radial and axial directions. This meant a grid of 1540 cells in the axial direction and 100 cells in the radial direction through the scramjet. A comparison between this medium resolution grid and the higher resolution grid for normalised static pressure at $450 \mu\text{s}$ is shown in Figure 7.39. There are no large scale differences between the two simulations, with waves hitting at similar axial locations and pressure levels quite similar within 5%. The change between time steps for the two simulations seems quite similar in level, with the medium grid having a larger difference on the intake. Through the combustor and thrust nozzle, the finer grid resolution simulation actually has a larger difference between time steps. The finer grid resolution would appear to have enough

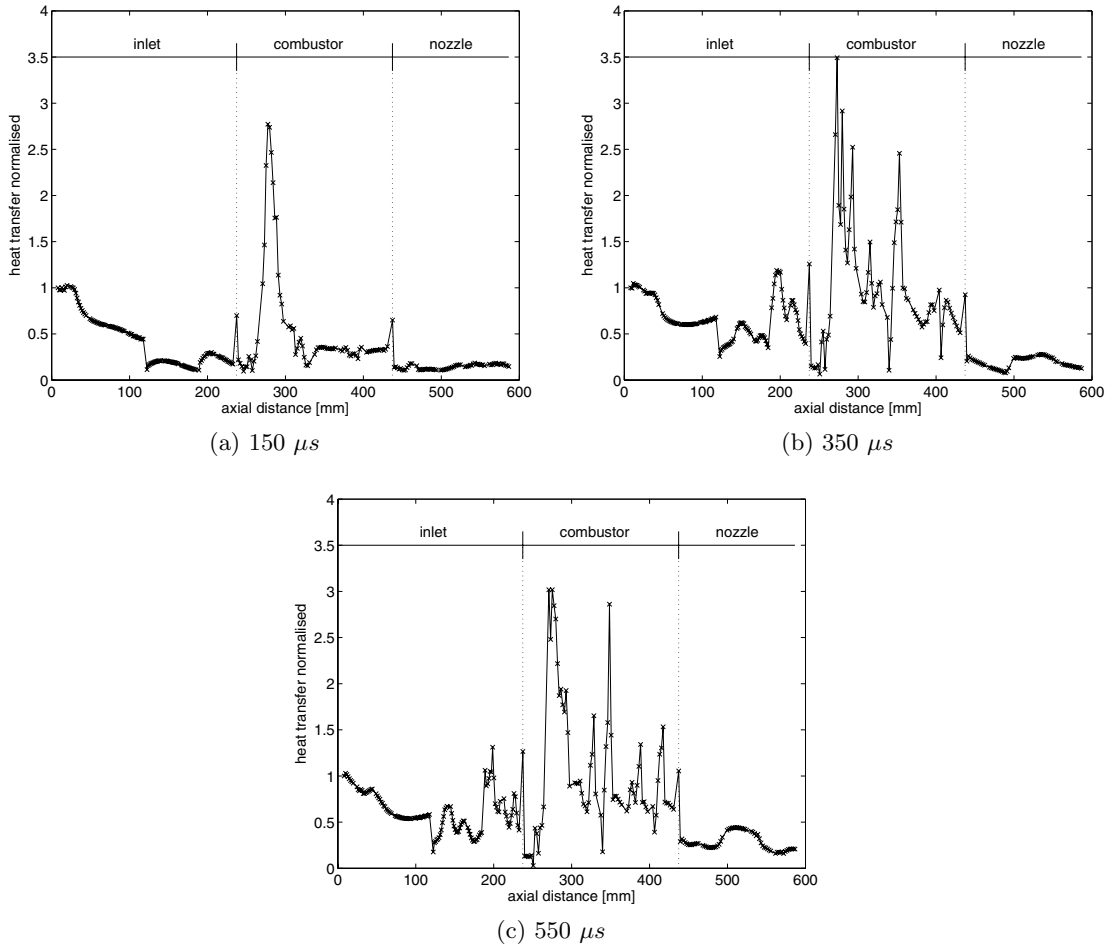


Figure 7.38: Normalised heat transfer down the scramjet duct from numerical simulation using the slug tracking method.

cell refinement to capture the flow phenomena which affect the static pressure within the scramjet.

7.3.3 Inlet start up

Intake starting is a critical issue in the operation of scramjets. At many flow conditions both started and unstalled intakes are theoretically possible. The ‘unstalled’ conditions are generally associated with flow spillage past the leading edges of the intake, choking at points of restriction, and extended subsonic regions in the combustor. The fundamental cause of unstart is the inability of the ducted regions of the combustor to pass the mass flow captured by the intake under steady flow conditions. Some of the important issues are stream tube compression, flight Mach number and Reynolds number, and the flight history up to where combustion is required. Unstalled flows established before reaching flight conditions may even preclude correct operation at the design condition. As discussed

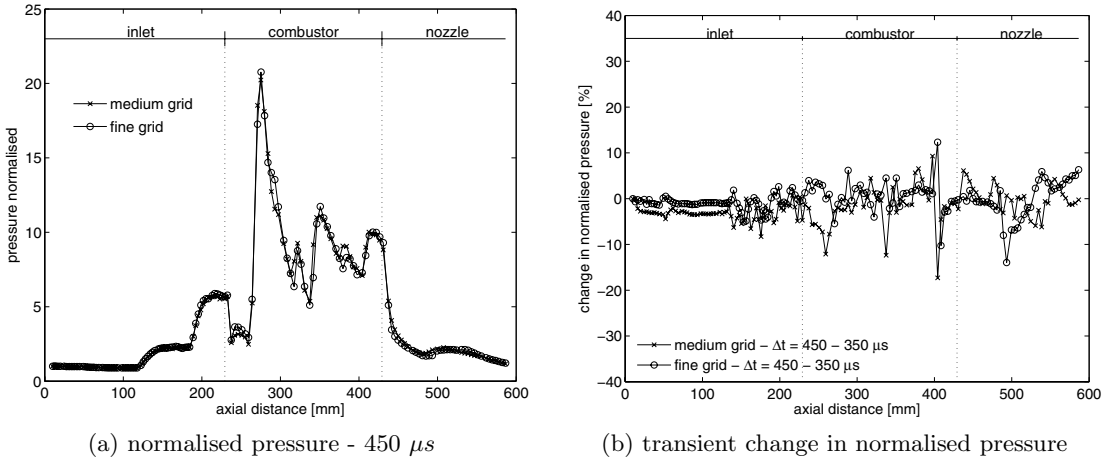


Figure 7.39: Variation in normalised pressure using slug tracking method with variation in grid resolution.

in Section 6.3.2, impulsive starting has been used for larger area contractions than possible if choked flow is established. As this has not been explored with the expansion tube flow operation of high temperature acceleration gas preceding the test gas, it is uncertain that an expansion tube can achieve this impulsive starting. The computational simulation is used here to investigate the starting of the engine for the transient flow condition produced by X2. This ignores any three dimensional effects which might either contribute to or alleviate unstart of the scramjet intake.

Using the absolute density gradient on the inlet ($\sqrt{\frac{\delta\rho^2}{\delta x} + \frac{\delta\rho^2}{\delta y}}$) to view the position of the wave motion in a simulated Schlieren image, the startup of the inlet can be seen in Figures 7.40 and 7.41. The cause of the unsteadiness seen in the shocks is the perturbation in the inflow data. This unsteadiness of the inflow is seen in Figure 7.42 showing the time history of the inflow density. The initial shock is seen to pass through the engine in the first $100 \mu s$. Weak shock waves can be seen to be generated from each of the wedges. As this passes through the throat on the inlet, there are no visible signs that any flow blockage occurs. This is then followed by an increase in the flow density as the expansion tube nozzle expands the acceleration gas where a reflected shock wave is created. Stronger waves can be seen to be created as this passes through the inlet, but as the flow is quite transient these are non-linear. As this reaches the inlet at $140 \mu s$, there are multiple shock and expansion interactions causing some of the flow to be spilt externally outside the edge of the cowl. If started in steady flow operation, this gas would have to be processed by the throat and may cause the engine to unstart. At approximately $70 \mu s$, the test gas/acceleration gas interface begins to propagate into the inlet. As this moves through the inlet, the oblique shocks are seen to be a lot straighter due to steadier inflow Mach number. Again, when the interface reaches the throat, at $160 \mu s$, spillage outside of the cowl helps prevent inlet unstart. There is negligible difference between the last two

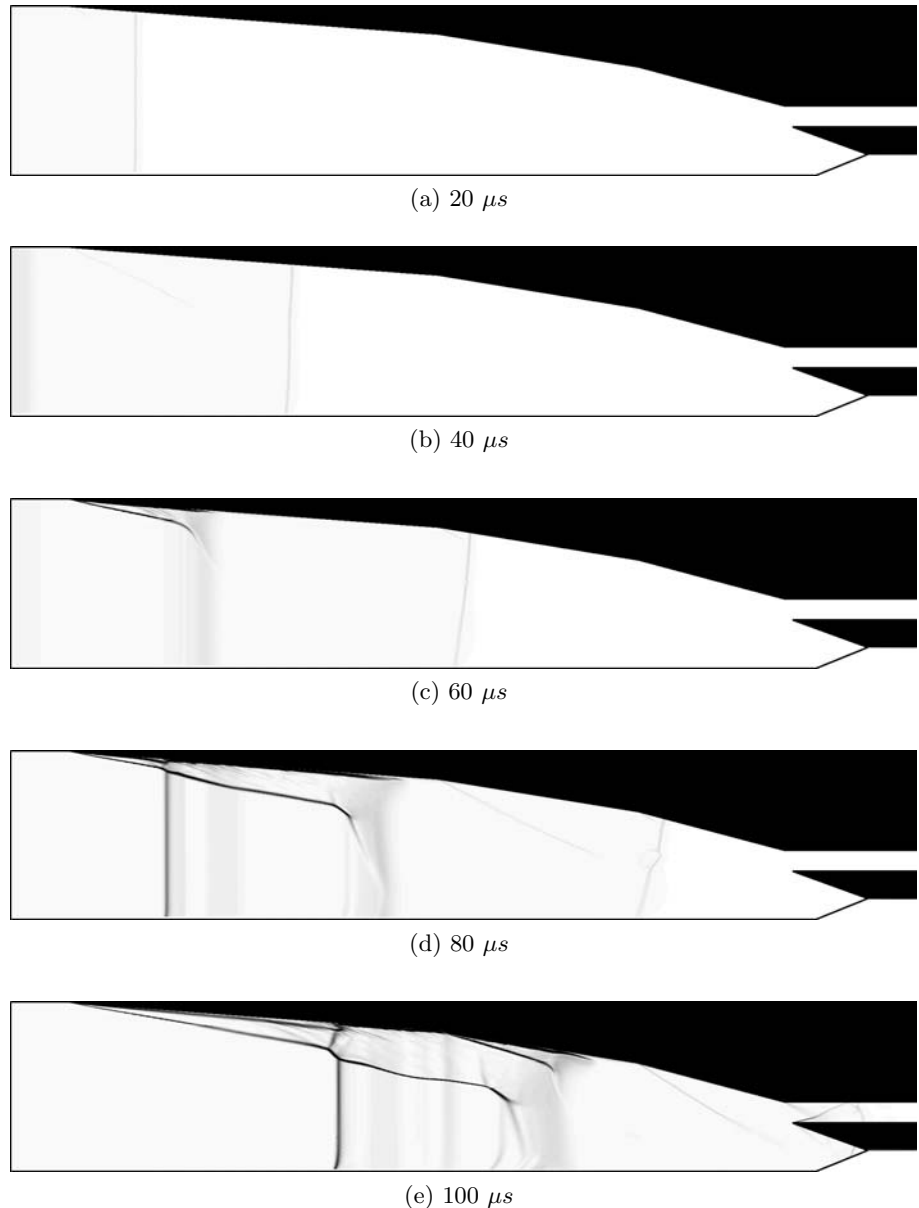
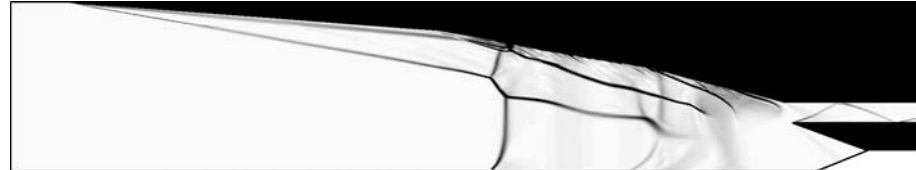


Figure 7.40: Schlieren images of inlet start up from transient numerical scramjet simulation (20 - 100 μs).

images at 180 and 200 μs where the intake has started and the acceleration gas has been completely passed.

This has shown that, at least for this condition, the inlet for the Mach 10 engine is likely to start. Also, it is likely that this same effect would be mirrored for all conditions created for scramjet testing in the expansion tube facility. This is due to the low density of the accelerator gas starting the inlet. It is also helped by large mass losses due to spillage outside the cowl caused by the compression waves created on the inlet, which pass well



(a) $120 \mu s$



(b) $140 \mu s$



(c) $160 \mu s$



(d) $180 \mu s$



(e) $200 \mu s$

Figure 7.41: Schlieren images of inlet start up from transient scramjet numerical simulation ($120 - 200 \mu s$).

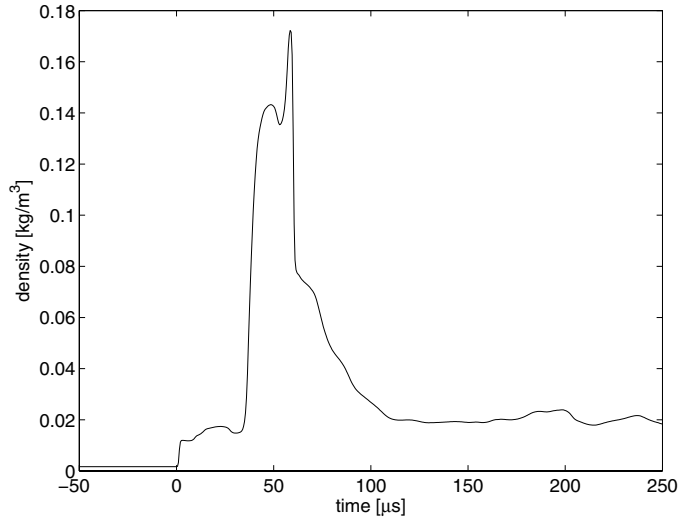


Figure 7.42: Transient inflow density taken from MBCNS simulation of X2.

outside the cowl due to the low Mach number of the acceleration gas. Even with a rise in density caused by a reverse shock due to the expansion tunnel mode of operation, the spillage of air outside the cowl is enough to ensure the inlet does not unstart.

7.3.4 Flow establishment

Flow establishment within a scramjet requires the residual levels of the starting processes including the growth of boundary layers to reach equilibrium before the steady test period can start. As discussed in Section 2.1, correlations have been developed (Equation 2.1) to estimate flow establishment times in generic scramjets for transient flow conditions in a reflected shock tunnel. Because an expansion tunnel flow is subtly different (with high temperature acceleration gas involved with the nozzle startup process), it is worth re-examining the flow establishment times for scramjets in this type of facility.

Using the computational flow data produced for the two dimensional scramjet with the transient inflow conditions computed for the X2 expansion tunnel, estimates of the flow establishment times can be predicted. Flow establishment can be gauged by using various flow properties. As stated previously, the static pressure is the measurement tool to be used in experimental testing so therefore is of most interest. Heat transfer is regularly used as it is the most effective diagnostic for flow establishment predictions, however, the numerical results presented have not fully resolved the boundary layer. Figure 7.43 shows the static pressure and normalised static pressure (normalised by the static pressure calculated at the first wedge of the intake using a flow velocity of 3100 m/s and the slug tracking method) at three locations through the scramjet duct. After passing the initial acceleration gas and the nozzle startup flow, the static pressure is seen to increase. This increase in the flow is reduced by the normalisation of the data. However, it can also be

noted that large oscillations are now seen in the flow. This is caused by the perturbations in the flow not matching due to variation of the velocity through the scramjet and in time causing the normalisation to not correctly capture the correct slug of gas. However the overall flow is seen to be reasonably steady.

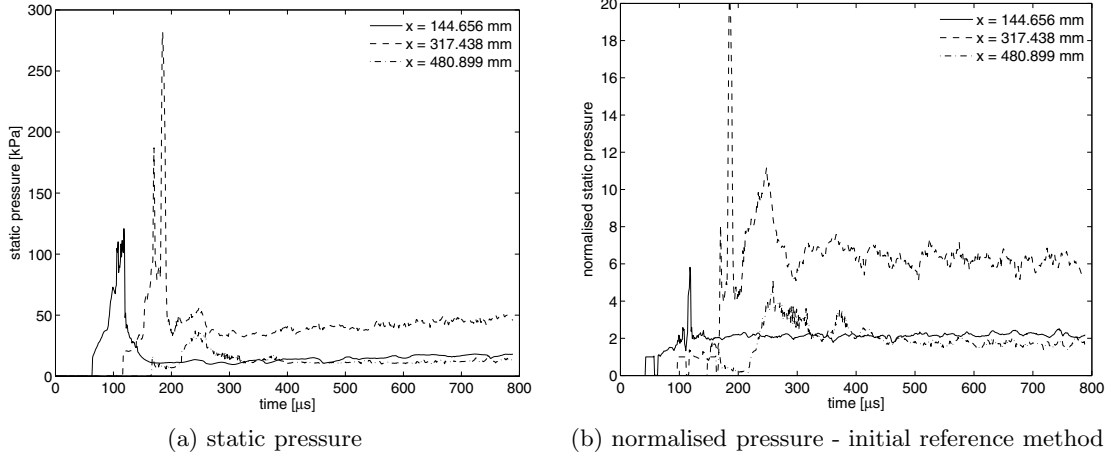


Figure 7.43: Time for flow to establish down scramjet duct using static pressure.

A new method was developed to determine the flow establishment time, to exclude the perturbations seen in the normalised static pressure traces. In it, the static pressure was used, but the rise in static pressure was also included. Using time averaging for each location over $4 \mu s$, the change in the static pressure was determined over a $50 \mu s$ period. The period of $50 \mu s$ (the flow travels $\sim 150 \text{ mm}$) was chosen since it should filter any small time period perturbations. Working back in time from $500 \mu s$ at each location, if the gradient of the pressure is greater than the specified level ($\left[\frac{dp}{dt} \right]_{limit}$), calculated using Equation 7.13, then the flow is assumed to have been established. Using limiting values of 20, 40 and $100 \text{ Pa}/\mu s$, the predicted flow establishment time down the scramjet duct using this method is shown in Figure 7.44. This shows that all three of these values show similar results, with a fairly linear trend for the establishment time through the scramjet. Due to changes in the wave locations, there is some scatter in the flow establishment times within the combustor especially for the $20 \text{ Pa}/\mu s$ limiting case. Also, due to the low pressures on the thrust surface, the flow establishment time is quite unreliable in that region.

$$\frac{dp(x,t)}{dt} \geq \left[\frac{dp}{dt} \right]_{limit} \quad (7.13)$$

The predicted estimate of the time to establish flow down the scramjet is given by Equation 7.14. This accounts for the initial startup flow of the expansion tunnel of $120 \mu s$ and shows that 1.2 flow lengths after this is required until flow establishment is reached. Thus the flow establishment is comparable with the work of Jacobs et al. [49] of 0.9 flow lengths after the passing of the upstream facing shock in the nozzle startup process. That

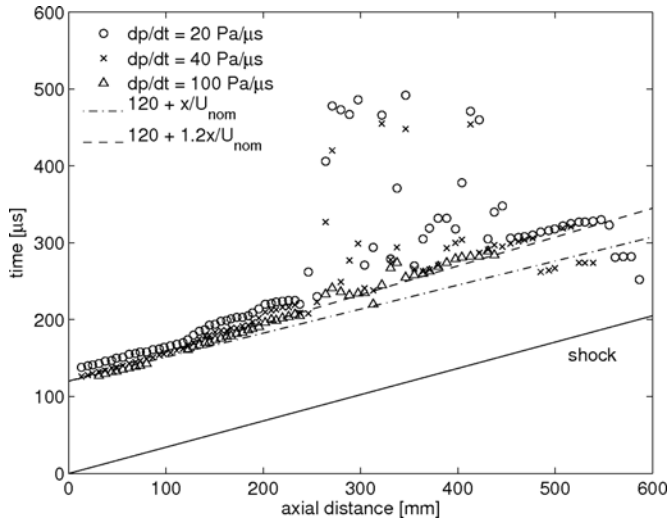


Figure 7.44: Time for flow to establish down scramjet duct using static pressure.

study used a stricter method to predict the flow establishment time, although the transient inflow was created with smooth data that avoided issues seen in the present study.

$$t_{est} = 120 + \frac{1.2x}{U_{nom}} \quad (7.14)$$

In the scramjet experiments, flow establishment of mixing properties is also required, which Rogers and Weidner [51] calculated to be of the order of 3-4 flow lengths in numerical simulations of a centrally injected combustor (no intake). With the injection of the fuel occurring just upstream of the combustor, the time flight through the combustor is $64 \mu s$ which creates an establishment time of $192 \mu s$ for three flow lengths or $256 \mu s$. When testing in impulse type facilities, the number of flow lengths required to achieve established mixing after the start of the test flow time can be reduced as the startup flow can also be used [51] to establish the mixing process. As can be seen in Figure 7.45, the fuel is injected before the arrival of the incident shock. Once the bulk of the fuel has been cleared (with the contact surface exiting the duct), the final establishment of mixing properties can proceed. Before the arrival of the start of the test time, flow with the approximately the same velocity will pass through the duct trailing the gas slug of fuel. This flow will establish some of the mixing structure between the fuel and the test gas before the arrival of the test time, however some extra time will be required before the mixing variables will become fully steady. With $120 \mu s$ of startup flow, if scramjet duct measurements are analysed for flow that originates later than $250 \mu s$ after the initial shock, four flow lengths, which is that suggested by Rogers and Weidner to achieve flow establishment with transient inflow, will be achieved.

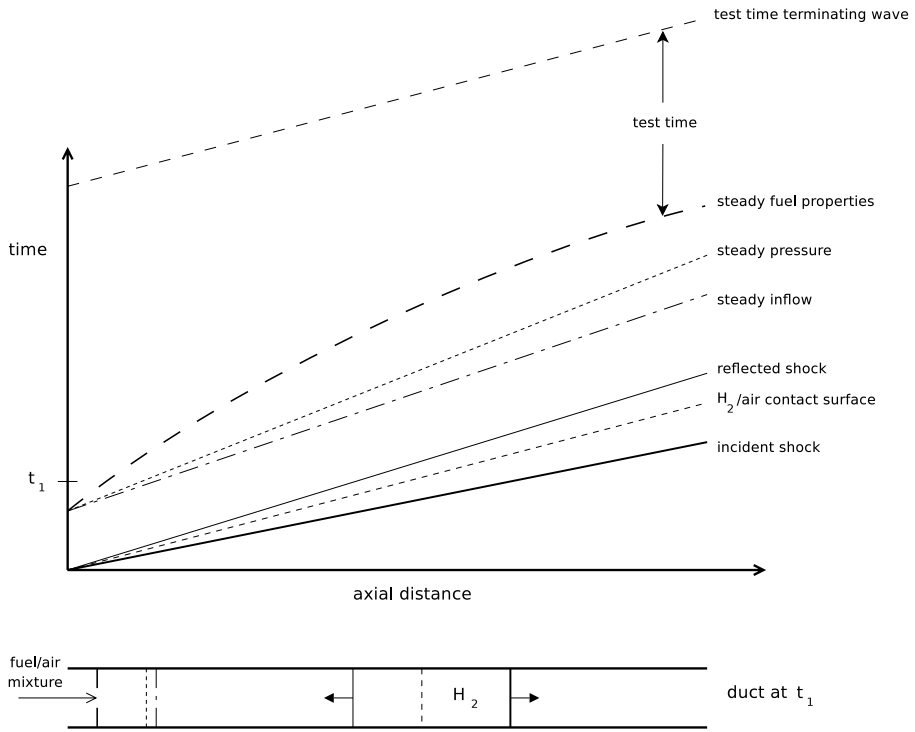


Figure 7.45: Distance time schematic for startup of a scramjet combustor in an impulse facility where fuel is injected prior to the test flow arrival.

7.4 Summary

A scramjet has been designed using analytical means for testing in the X2 expansion tube facility. A two dimensional design was chosen due to ease in both duct design and the analysis of results from experimentation. The inlet used a four shock compression process (three from ramps, one from cowl), designed to minimise flow losses but also produce flow conditions in the combustor able to auto ignite the fuel. The flow was also allowed to be quite non-uniform, as the use of upstream injection will cause large disturbances in the flow. Two dimensional simulations were conducted on the inlet to verify that the inviscid design was still consistant with the introduction of a boundary layer. Discrete hole injectors were investigated and found to achieve the desired mass flow rate and achieve good mixing and penetration. The constant area combustor was designed to achieve maximum thrust potential, by shortening the length from that required to achieve full heat release where skin friction losses are greater. Using drawings provided for the full scale model tested in T4, the subscale model was designed for manufacture.

Two dimensional, fuel off, transient simulations of the scramjet were conducted using inflow conditions from the simulation of X2. This allowed for the prediction of the performance of the scramjet without fuel injection. An investigation of found the effects of the transient flow could be accounted for in point location measurements by use of a quasi

steady analysis. However, as the time derivative term in the linear momentum equation was significantly large, thrust measurements require modification to predict the thrust expected in steady flight. It was shown that a quasi-steady analysis can be applied to transient pressure data along the scramjet. A method was developed for the normalisation of the flow data to allow the comparison of axial distributions at various times. The “impulsive starting” ability of an expansion tube facility has been demonstrated via simulation for a Mach 10 condition, which should apply to most conditions in an expansion tube. The flow establishment time was predicted, and showed that steady flow could be produced within the amount of test time available.

Scramjet Experiments in the X2 Expansion Tunnel

Results from the propulsion testing of a two dimensional scramjet in the X2 expansion tunnel is provided. With the transient inlet flow produced in the X2 facility, measurements within the scramjet are normalised using a slug tracking method. Effects of fuel injection and combustion are investigated with the parameters of fuel equivalence ratio, freestream enthalpy, injector hole diameter and cowl position investigated. Initial characterisation of engine performance is also provided.

8.1 Experiment Setup and Calibration

The two dimensional scramjet described in Section 7 was mounted in the X2 expansion tube facility. The scramjet was mounted to the rail of the test section such that the leading edge of the scramjet was 20 mm away from the nozzle exit plane. Location of the scramjet was referenced to the rail of the test section and was horizontally and axially aligned with the expansion tunnel nozzle. Within the scramjet, 28 PCB sensors were mounted along the wall throughout the testing, with up to 6 Kulite sensors on the thrust surface. The Kulites were omitted during the first series of testing to ensure that the maximum pressure (usually the driver gas reaching the test section) was not large enough to damage the Kulite sensors (limited to a maximum pressure 50 psi). All sensors throughout the facility and in the scramjet duct were recorded across two databoxes (described in Section 4.1.1) on a $1 \mu\text{s}$ sampling period. The data acquisition boxes were triggered by the first transducer in the shock tube (st1). Due to the pre-triggering sample rate being set to different levels between the two databoxes, databox B was $1040 \mu\text{s}$ delayed from databox A.

The setup of the plumbing for the Ludwieg tube fuel system is described in Section 4.1.1. The solenoid valve in the system (ASCO high pressure pilot operated valve [156]) requires a high voltage to be sent to the solenoid to open the inner pilot valve. Once the pilot valve has opened this allows the high pressure to pass in front of the main piston of the valve. To supply this voltage, an in-house built capacitor timing box was used to produce the high voltage ($\sim 50 \text{ V}$) for the solenoid. This uses a break in an external line (i.e. trip wire) from an external source to trigger the system. A laser pointed at a photo-diode was used to provide the signal to the capacitor timing box (this was passed

through a simple circuit to turn a 1 V signal into a trigger signal). A plate mounted to the driver tube wheel separates the laser and photo diode. As the tunnel recoils, the plate moves allowing the laser to be exposed to the photo diode (Figure 8.1).

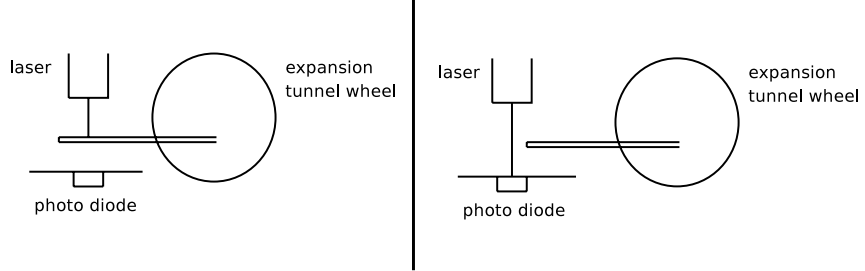


Figure 8.1: Schematic of laser/photo diode fuel system trigger.

Delay timing was required to provide the fuel injection just before the arrival of the flow at the scramjet model. The fuel system requires a pre-trigger at least 15 ms before the arrival of the flow. This is due to timing delays of the capacitor timing of at least 5.5 ms and an opening time of the main piston in the solenoid valve of approximately 6 ms. The capacitor timing box pre-trigger delay in conjunction with axial placement of the photo diode blanking plate was used to set the overall pre-trigger time delay. The overall timing for shot x2s117 is shown in Figure 8.2 for all the components in the fuel system. The signals of the system were recorded on a separate databox (Tektronix digital storage oscilloscope) to other work. These signals were the recoil sensor, laser diode trigger for the fuel system, stagnation pressure of the fuel plenum chamber and the first pressure transducer on the intake of the scramjet. This recorded timing of when the fuel is injected, to ensure that the timing was correct and the fuel stagnation pressure for use in calculating the fuel mass flow rate.

8.1.1 Fuel system calibration

Although an estimate was able to be obtained for the likely fill pressures required in the Ludwieg tube during the design of the scramjet (see Section 7.1.2), experimental calibration of the Ludwieg tube is required to ascertain the constant α in Equation C.3 to determine the fuel mass flow rate. Theoretically, α can be estimated to be 7.7359e^{-09} kg/Pa.s for the small holes and 1.5162e^{-08} kg/Pa.s for the larger holes. A more accurate calculation can be made by measuring the loss in hydrogen for a given stagnation pressure trace (using Equation C.4). This has been completed for a range of Ludwieg fill pressures up to 1 MPa for the 2 mm injectors and 1.2 MPa for the larger injectors. The stagnation pressure traces for these tests can be seen in Figures 8.3. It is noted that the small diameter traces have a significant amount of electrical noise, though this was unavoidable at

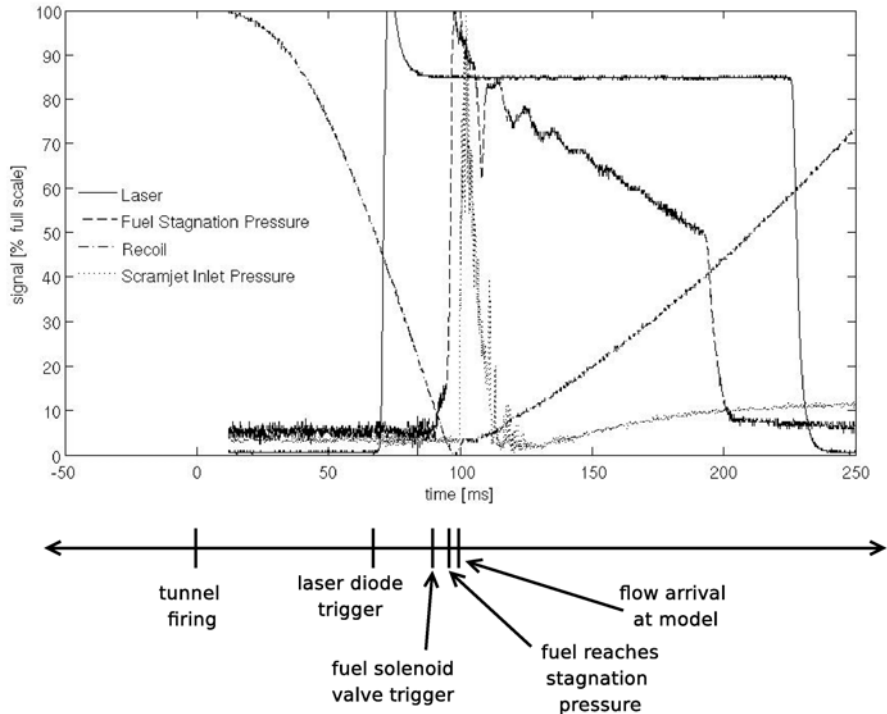


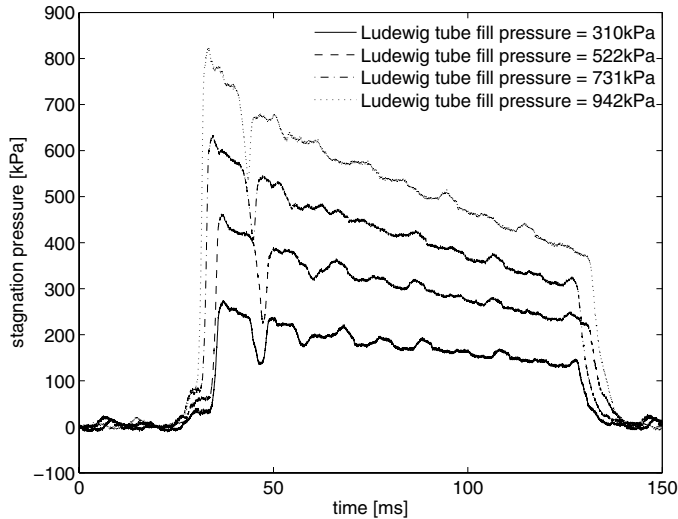
Figure 8.2: Timing of components in fuel system.

the time of testing. As would be expected, the stagnation pressure is lower for the large diameter tests for a given initial fill pressure.

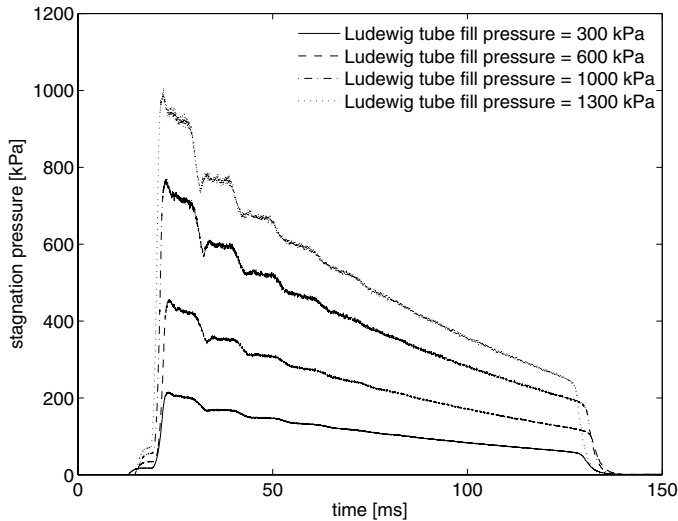
Using the initial stagnation pressure and the post trial Ludwieg tube pressure, the mass flow rate of fuel can be calculated as shown in Table 8.1.1. With the mass flow rate of fuel calculated, the constant α can also be calculated. The experimentally derived values for α shown in Table 8.1.1 are approximately $4.65e^{-09}$ kg/Pa.s for the small holes and $8.35e^{-09}$ kg/Pa.s for the large holes, which is significantly different to that estimated theoretically. The mass flow rate of hydrogen with initial Ludwieg tube fill pressure is shown in Figure 8.4. This is seen to vary linearly as expected, with much larger mass flow rates for the larger diameter holes.

8.1.2 Pressure transducer calibration

The pressure transducers used during the test campaign were mainly PCB type transducers, with some Kulites. Due to the variation of the transducers sensitivities from the manufacturers calibrations and also to check for any human error or mounting effects, recalibration was undertaken of all PCB transducers after testing. This was done by placing the transducers into a block with a single reference transducer and air is then passed into the block at 200 kPa (absolute) by opening of a solenoid valve. The calibration



(a) small injectors - 2.0 mm



(b) large injectors - 2.8 mm

Figure 8.3: Stagnation pressure for several calibration trials.

factor is therefore calculated by comparison with a reference transducer. This method of calibration is described in more detail by Odam [197]. The locations, manufacturer and experimental calibration for the PCB transducers can be found in Appendix F. The Kulites however, can be calibrated in-situ as they are an absolute gauge. This allows for calibration during the evacuation of the test section, which is required in the expansion tube operation. The calibration values for these can be seen in Appendix F. The axial locations of all the transducers used can be found in Appendix F and further details on locations can be found in the manufacturing drawings in Appendix E.

Table 8.1: Fuel system calibration results for scramjet model.

$P_{lud,i}$ [kPa]	$P_{lud,f}$ [kPa]	$p_{p,i}$ [kPa]	α [kg/Pa.s]	\dot{m}_{H_2} [kg/s]
small holes - 2.0 mm				
310.0	156.0	230.0	4.717e-09	1.132e-03
310.0	156.0	239.3	4.560e-09	1.132e-03
522.0	260.0	394.0	4.534e-09	1.860e-03
522.0	261.0	406.7	4.335e-09	1.827e-03
731.0	351.0	540.0	4.813e-09	2.714e-03
731.0	352.0	565.0	4.624e-09	2.711e-03
942.0	455.0	730.0	4.636e-09	3.510e-03
942.0	457.0	738.0	4.520e-09	3.454e-03
large holes - 2.8 mm				
305.4	83.8	207.0	8.480e-09	1.856e-03
295.1	79.9	206.0	8.244e-09	1.788e-03
386.6	104.4	271.3	8.389e-09	2.394e-03
380.1	105.7	269.0	8.313e-09	2.349e-03
488.4	126.3	354.0	8.321e-09	3.084e-03
489.7	125.0	350.0	8.277e-09	3.039e-03
599.2	148.2	429.0	8.359e-09	3.761e-03
981.9	268.0	721.3	8.275e-09	6.237e-03
996.1	246.1	726.1	8.352e-09	6.345e-03
1282.1	314.4	942.3	8.342e-09	8.215e-03
1283.4	323.4	938.2	8.413e-09	8.255e-03

8.2 Experimental Results

The scramjet test program involved varying the parameters of test gas (air or nitrogen), fuel equivalence ratio, fuel injection diameter and free stream condition. Results are analysed using the slug tracing method described in Section 7.3.1, in order to correctly couple the data with the transient free stream condition. Results presented have been time filtered using a $nhalf^1$ value of 2, to reduce any high frequency noise in the traces. All plots showing the axial distributions at a given time are averaged results over 10 μs (or slug lengths of approximately 30 mm), to dampen shifting in the wave structure within the scramjet. The normalisation pressure for each shot and time can be found in Appendix G. A constant normalisation velocity is used, with 3100 m/s used for the low enthalpy condition and 3500 m/s for the high enthalpy condition. This corresponds to the average

¹Number of passes over the data.

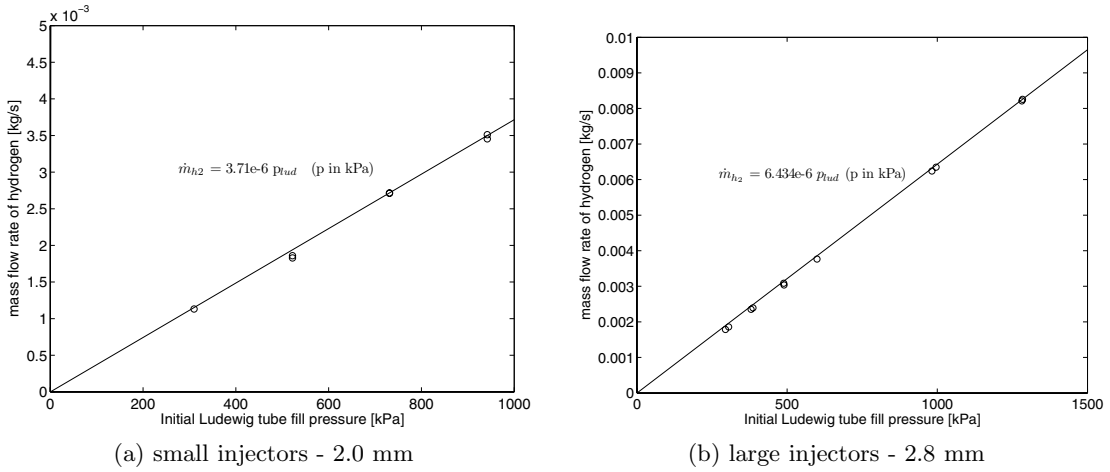


Figure 8.4: Calculated mass flow rate for several initial Ludwieg tube fill pressures.

velocity through the scramjet as calculated numerically in Section 7.3. All pressure traces used are zeroed against the pre shock values to remove any offset in the traces. Shots were ignored where anomalies such as incorrect shock speeds or static pressures were measured in the expansion tube gas cycle, or incorrect timing of hydrogen injection occurred.

With the complex processes in this engine in both space and time dimensions, an accurate uncertainty level cannot be quoted for the pressure levels presented. To give confidence in the data, however, a study is presented in Appendix D of an approximation of uncertainty levels through the engine which shows the differences caused by combustion. This shows that the effects of supersonic combustion can be clearly defined. However, this analysis can only give an indication of the uncertainties, with no account of changes in fuel mass flow rates and changes in freestream properties (apart from freestream pressure).

Several tests were attempted with glass side walls to allow holographic laser interferometry to view shock locations and density gradients in the flow. This was to be used to investigate the separation region expected at the start of the combustor and to look at the spillage past the cowl tip. However, due to the glass breaking in the side walls, this never produced meaningful results.

Pressure recorded on the Kulite transducers (located on the thrust surface) have been found to give four times the pressure recorded on both the PCB transducer and computational results for fuel off shots. Although calibration of these transducers produced correct calibrations, post analysis has shown that the Kulites indicated approximately 4 times the expected pressure. This can be seen in Figure 8.5, showing the large discrepancy in the data. It is unclear whether this was human error (possibly in the voltage supply or amplifier) or this is a true measurement, but all Kulite measurements on the thrust surface are presented using the modified calibrations by dividing by 4. This is exacerbated by the lower pressures on the thrust surface, causing a lower voltage in the transducer signals.

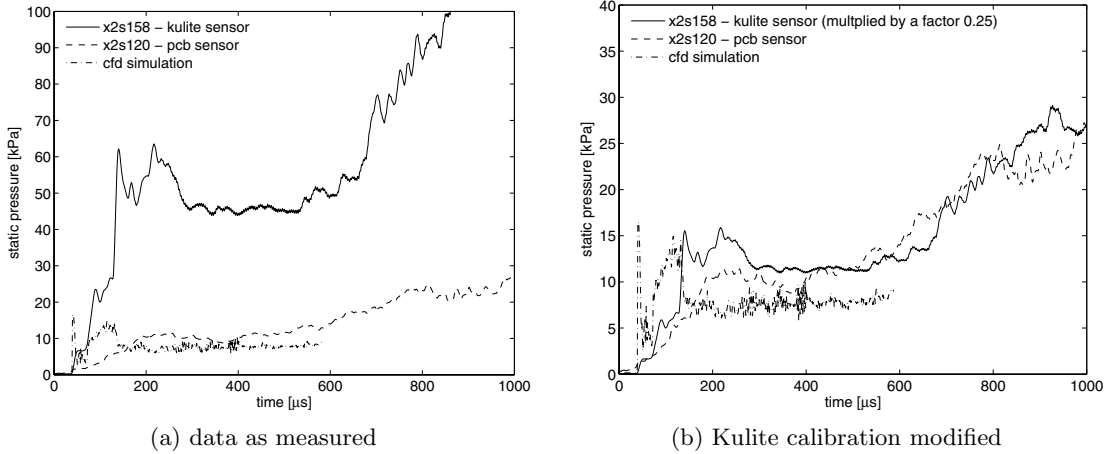


Figure 8.5: Comparison of pressure traces on thrust surface for fuel off shot.

A list of the successful shots is presented in Table 8.2, showing the test gas, freestream condition, injector hole diameter, initial Ludwieg tube fill pressure, fuel stagnation pressure and the mass flow rate of the fuel. Fuel equivalence ratio is not shown, as this will change for slug of gas due to the transient mass flow rate of the freestream air. This section details all the tests which were completed using the low enthalpy condition apart from the single high enthalpy shot. Fill properties and flow conditions can be found for this in Chapter 5.

Table 8.2: Experimental details for shots presented. For shots x2s159 and x2s160 the initial stagnation pressure and mass flow rate was estimated from calibration data.

shot number	test gas	condition [km/s]	D_{inj} [mm]	$p_{lud,i}$ [kPa]	$p_{0,i}$ [kPa]	\dot{m}_{H_2} [kg/s]
x2s117	air	3.1	2.0	730	595	2.774e-3
x2s118	N ₂	3.1	2.0	730	595	2.849e-3
x2s119	air	3.1	2.0	1080	877	4.201e-3
x2s121	N ₂	3.1	2.0	0	0	0
x2s122	N ₂	3.1	2.0	1080	875	4.193e-3
x2s124	air	3.1	2.0	380	302	1.451e-3
x2s125	N ₂	3.1	2.0	380	300	1.443e-3
x2s128	air	3.1	2.0	1400	1170	5.582e-3
x2s137	air	3.1	2.0	940	666	3.236e-3
x2s149	N ₂	3.5	2.0	1040	822	3.952e-3
x2s155	air	3.1	2.8	940	656	5.746e-3
x2s156	N ₂	3.1	2.8	670	485	4.241e-3
x2s158	air	3.1	2.8	0	0	0
x2s159	air	3.1	2.8	650	475	4.133e-3
x2s160	air	3.1	2.8	320	215	1.893 e-3

Fuel off

Results are presented for the scramjet configuration without injection of the fuel into the air test gas, where the cowl has been repositioned further forward for the x2s158 shot. This also allows a direct comparison to the computational simulation results presented in Section 7.3, where fuel was also not injected. The computational results have to be modified as the geometry is different on the intake to that of the experimental scramjet. The difference in geometry was so that computational simulations did not have to account for the small nose blunting, which would require a much finer grid to resolve. The computational data was reduced on each wedge on the intake, by removing the data points from the end of each length. This is expected to give similar data as seen experimentally, with any differences being caused by minor boundary layer effects.

Figure 8.6 shows a comparison of the normalised pressure down the scramjet duct at the start, middle and end of the test period. Throughout the scramjet, there is good agreement between all of the data, especially between the two experimental measurements. The mean level of pressure in the combustor agrees well between all three sets of data. However the shock/expansion locations are slightly different between all three. This is to be expected, with slightly different geometries of the intakes. The computational simulation can also be seen to *smooth* the flow towards the end of the combustor. This is probably due to the coarseness of the grid and over-prediction of the boundary layer. It can be noted that there is a large discrepancy between the experimental air traces for the first measurement in the combustor. This is caused by the moving of the cowl position forward by 26 mm, thus sending the return cowl shock onto the bottom wall of the combustor earlier. The two experimental measurements show a lower pressure on the third wedge of the intake. This is explored further in Section 8.2. The pressures measured on the thrust surface agree reasonably with the computational simulation results. In the air shot, the second measurement is higher than predicted by CFD (note: there is no data available at this point for the nitrogen shot). With the computational data being relatively uniform by the end of the combustor (see Figure 7.30), no waves of any great strength reach the thrust surface. Whereas, the experimental measurements will still have strong shocks and expansions at this point.

Comparing the flow at the three times shown, it can be seen that there is no major difference in the overall pressure level or flow structure through the scramjet. Only minor differences can be seen, due to variation in the axial location of shock/expansion wave structure caused by variations in the free stream properties. This shows that the flow establishment predictions made from the CFD are appropriate for flow with no fuel injection. The large drop in pressure from the combustor is due to a Prandtl-Meyer expansion, but then remains relatively steady. Once this has been reflected off the cowl, the pressure is seen to drop again towards the end of the thrust surface.

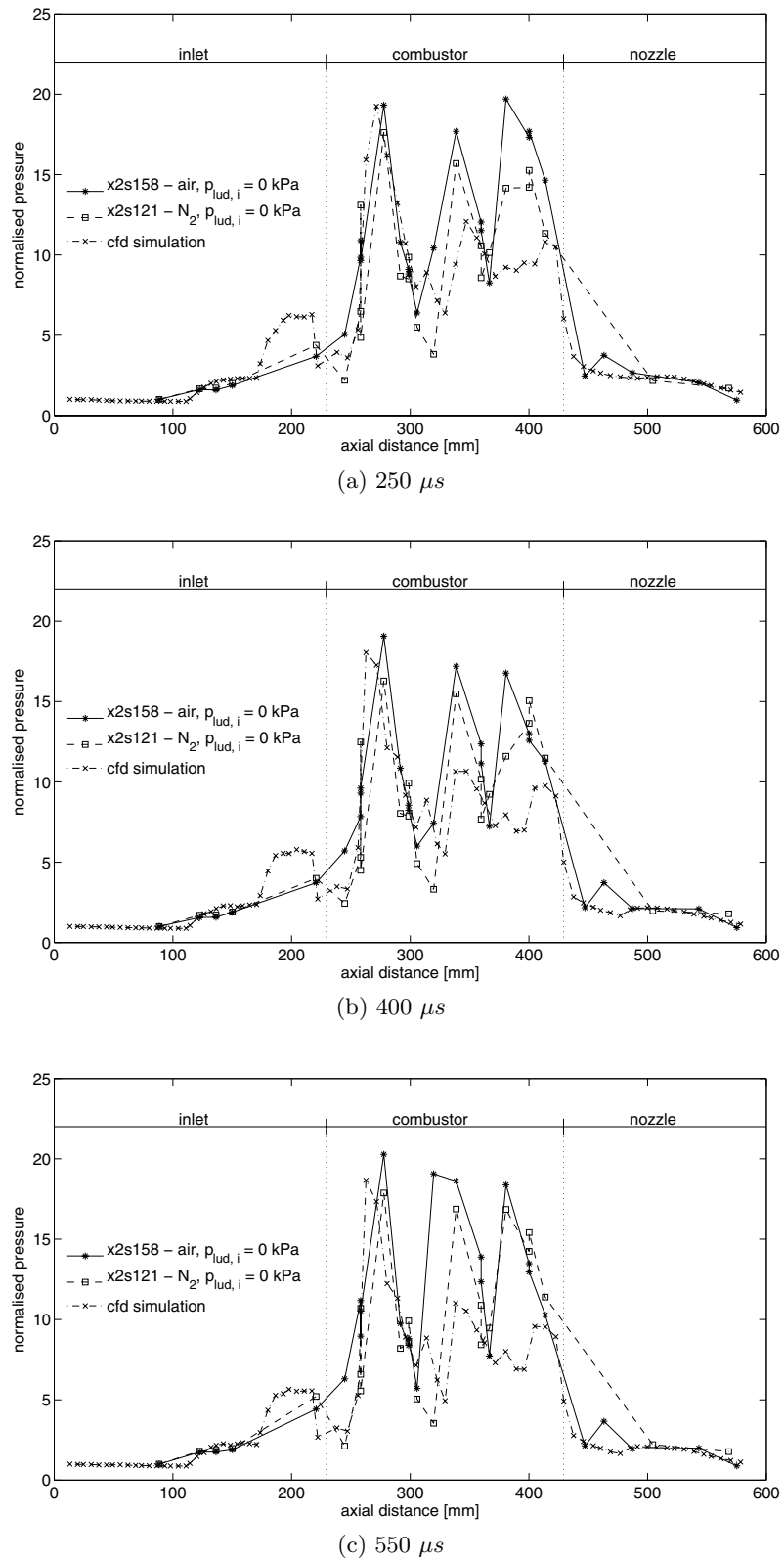


Figure 8.6: Comparison of effects of nitrogen versus air test gas with computational simulations with fuel off.

Inlet performance

A direct comparison may be made of time histories of pressure measurements on the intake, as the level will only be influenced by the shot to shot variation, apart from the last transducer, which will be affected by fuel injection. Figure 8.7 shows the time histories of the five pressure transducers located on the inlet for fuel off tests with both a nitrogen and air test gas and time histories at reflective locations from the computational simulation. The first position shown, IA-C1 is the location of the normalisation pressure used in the analysis of the scramjet. The static pressure at this location is seen to match quite well between the three experimental measurements and also the computational simulation result. It can be noted however, that the amount of noise in the time history of pressure in the computational simulation is substantially higher than the experimental measurements. As discussed in Section 7.3, the computational simulation has a large increase in the overall noise level due to the large oscillations in the inlet flow produced by computationally modelling the expansion tunnel flow.

Further downstream, the agreement is seen to be quite good between the two experimental measurements. The three measurements from the second wedge demonstrate reasonably close agreement with both the pressure level and the time until the arrival of the unsteady expansion (200 - 700 μ s) between the experimental results. On the third wedge, the pressure trace is seen to have some oscillations in the pressure level. This occurred in a few of the earlier tests, with the likely cause being a loose micro-dot cable connection. The computational simulation substantially overestimates the pressure at both the second and third wedge locations. It seems that the most likely cause for this discrepancy is due to the overestimate of static pressure in the numerical simulation of the expansion tunnel flow (seen in Chapter 7.3). In conclusion, the two dimensional inlet works well by both starting impulsively and providing steady intake conditions to the combustor. It in fact performs better than indicated by CFD.

Cowl repositioning

The repositioning of the cowl in the later shots (after x2s145) causes the return cowl shock to meet the bottom wall of the combustor further upstream. This can be seen experimentally in the first pressure measurement in the combustor 15.5 mm from the start of the combustor. Figure 8.8 compares the pressure traces with the cowl set in the two different positions. It shows that, with the cowl further upstream (x2s158), the pressure level is a lot higher. This is even higher than the computational simulation pressure (cowl positioned downstream), which has been shown previously to be high. Also, the flow measurement is seen to have more oscillations than the measurement where the cowl is further downstream. This behaviour could be an interaction of some or all of the oblique shocks reflecting off the cowl and entering the combustor.

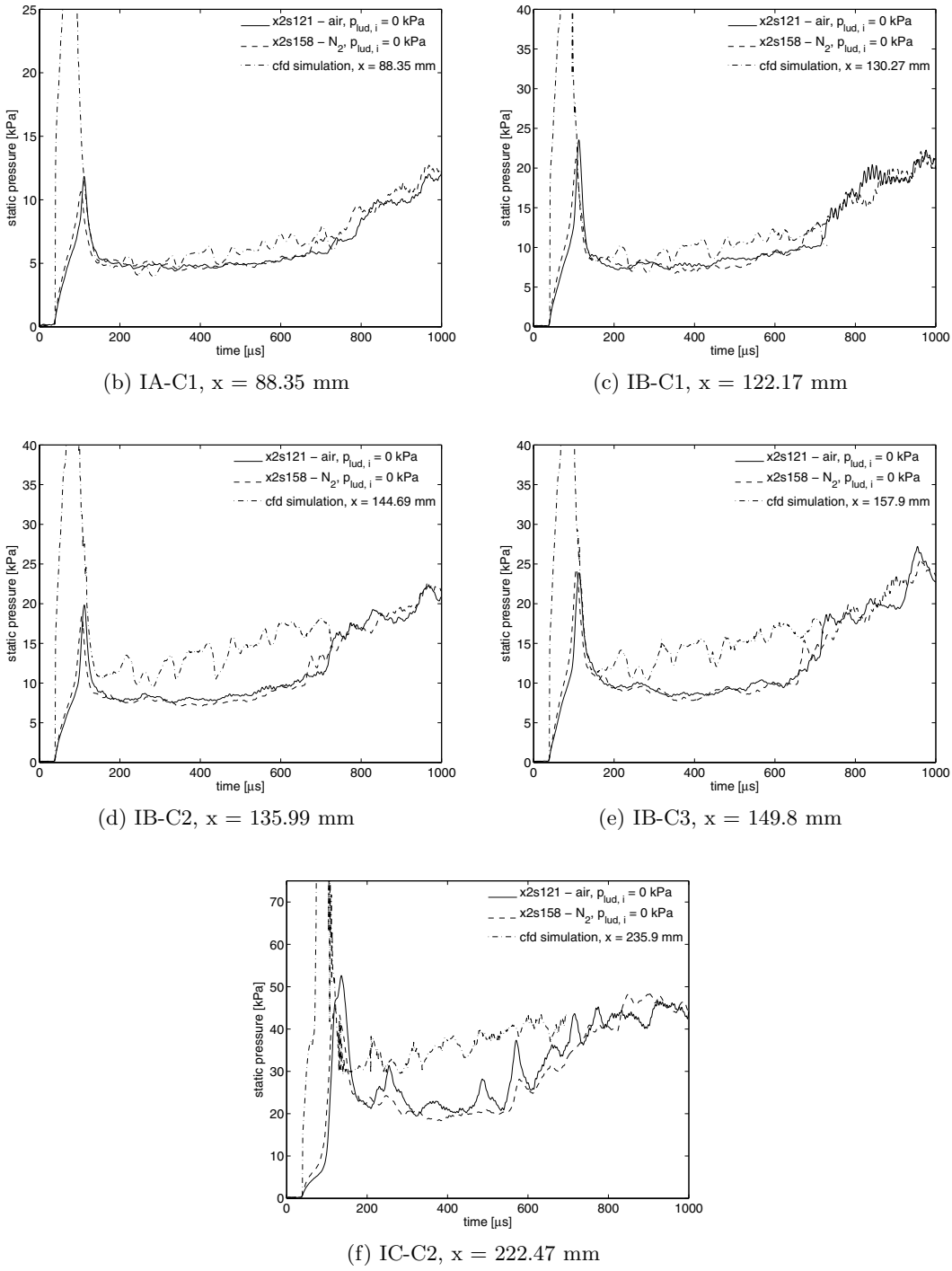
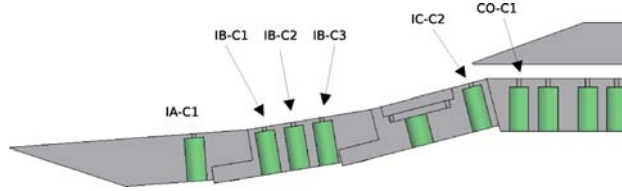


Figure 8.7: Experimental pressure traces along the inlet compared with computational simulation data.

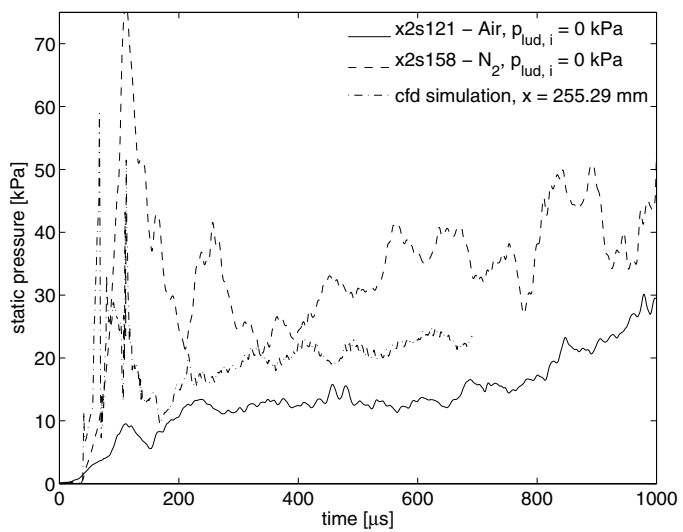


Figure 8.8: Experimental and numerical pressure traces at first location in combustor (CO-C1, $x = 247.8 \text{ mm}$).

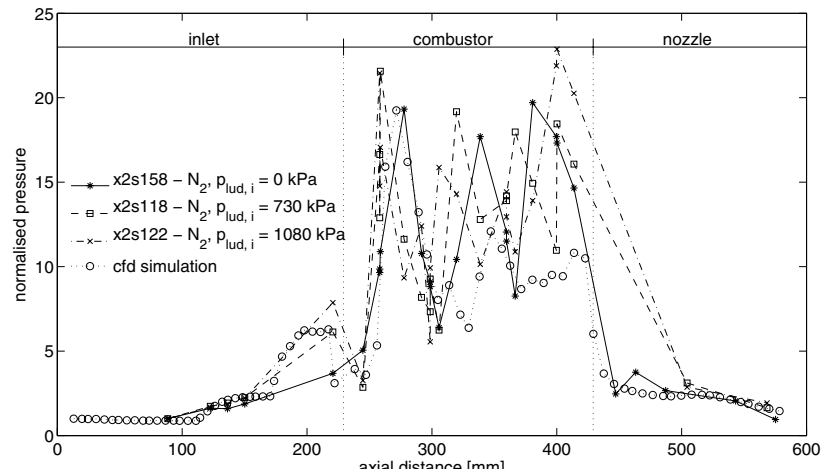
8.2.1 Effects of fuel injection

The use of a nitrogen test gas enables a decoupling of the effects of injection by removing the combustion since no oxidiser is present. To accomplish this, a nitrogen test gas is used in the expansion tube operation as a replacement to the air. As shown in Chapter 5), there is negligible variation in the free stream gas properties and 2) nitrogen is the main component of air and no dissociation occurs in these conditions. The variation of the flow structure down the scramjet duct can vary greatly with the amount of fuel injected. This is firstly due to greater losses in total pressure as discussed in Section 6.3.3, which therefore alters the cowl shock strength and all other flow interactions down the scramjet. Also, the shock structure that is present in front of the injection will slightly vary due to greater penetration of the fuel into the freestream.

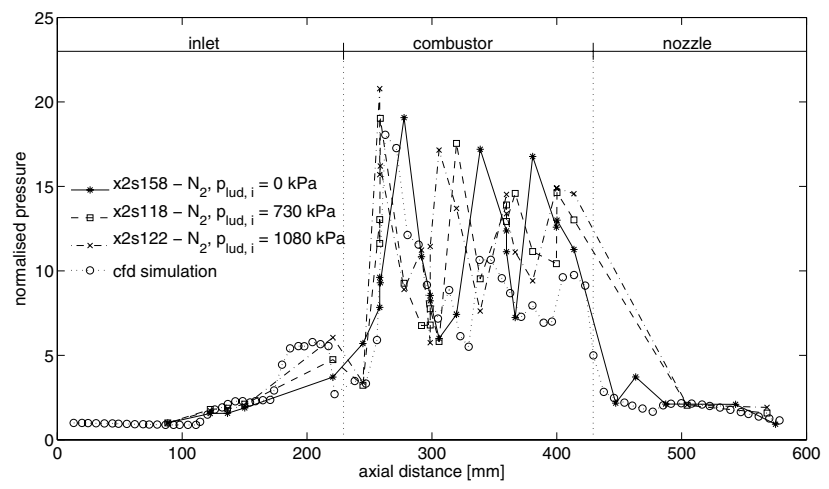
The effect of fuel injection is shown in Figure 8.9, which compares the normalised pressure down the scramjet duct for various fuel mass flow rates. Also shown is the calculated normalised pressure from CFD presented in Section 7.3. There is good agreement between the CFD and the zero fuel injection test at the start of the combustor, showing a similar shock/expansion pattern. This weakens as the shock and expansion pattern is smeared in the CFD, as described in the previous section. As the mass flow rate of fuel increases, the shock pattern is seen to move upstream. The first two points of measurement after the injection, (the first is on the third wedge of the inlet and the second is within the separation region predicted by CFD in the start of the combustor) show an increase in pressure due to the fuel injection causing shocks and mixing of the fuel. However, the mean pressure level throughout the combustor is seen to remain relatively stationary, with similar pressures measured at the end of the thrust surface.

Between all the times shown, there is not a great change in the overall level of the normalised static pressure. The transient effects of reduction in fuel equivalence ratio with time do not appear to be of great significance. The same amount of variation in the wave structure down the scramjet duct with time was seen in the fuel off shot (Section 8.2). This suggests that although the fuel equivalence ratio is dropping significantly, this is still a minor effect in comparison to the change in the freestream conditions.

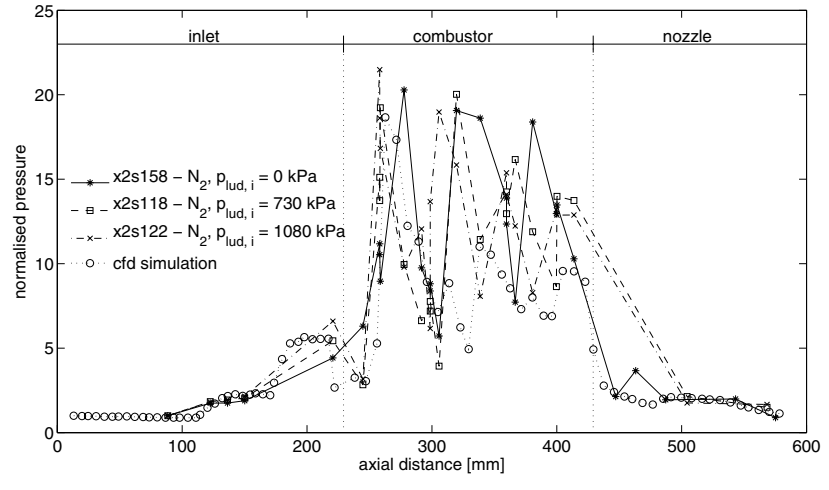
To examine the direct effects after the injection location, Figure 8.10 shows the static pressure at the two locations downstream of injection for various fuel mass flow rates. At the measurement location IC-C2 on the third wedge of the intake, the pressure is seen to increase with initial Ludwieg tube fill pressure as expected due to both the increase in mass injected and stronger shocks created in front of the discrete injectors. Also, the flow seems more disturbed, with large oscillations occurring at a period of approximately $70 \mu s$. The increase in pressure with fuel mass flow rate is also evident in the first transducer located in the combustor. This is with the exception of the fuel off signal, as the cowl had been shifted forward moving the return shock further upstream (Section 8.2). The flow at



(a) $250 \mu\text{s}$



(b) $400 \mu\text{s}$



(c) $550 \mu\text{s}$

Figure 8.9: Comparison of effects of fuel injection using nitrogen as free stream gas to remove combustion effects.

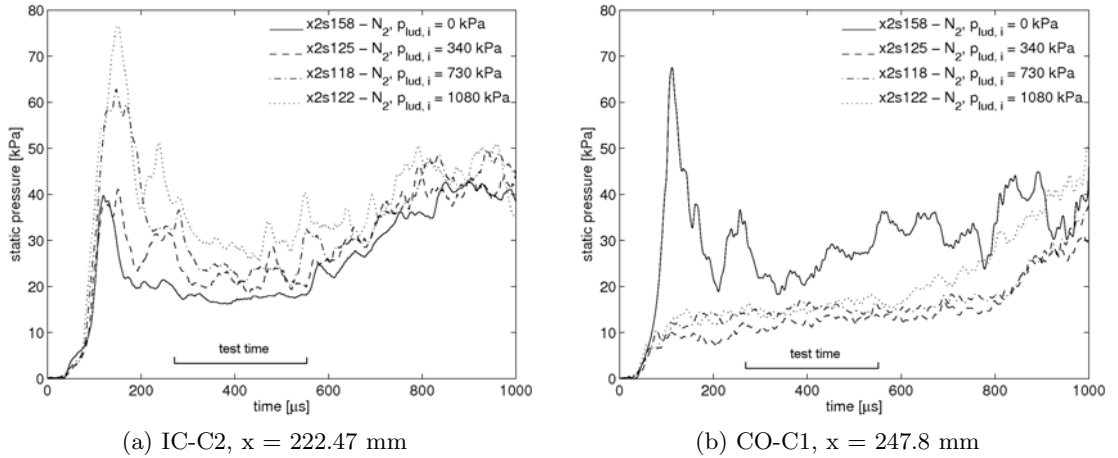


Figure 8.10: Static pressure behind fuel injection location on third wedge for various Ludwieg tube fill pressures with nitrogen freestream gas.

this location does not exhibit the same large oscillations as the last measurement on the intake (IC-C2). The rise from the unsteady expansion occurs at a later time than seen at IC-C2 as well and is more closely comparable to the other intake pressure measurements shown in Section 8.2.

8.2.2 Effects of combustion

Combustion effects can be investigated by a comparison of normalised static pressure distributions down the scramjet, between shots with a nitrogen test gas (*tare* shots) and those with an air test gas for a similar fuel mass flow rate. Therefore, the only significant change between the two should be due to the combustion of the fuel. For supersonic combustion in a constant area duct, the static pressure should, on average, increase down the combustion chamber. This increase in pressure is reflected by a large thrust surface pressure level variation caused by the wave structure within the engine. This has been undertaken for three different fuel mass flow rates, set by the initial fill pressure in the Ludwieg tube. As the mass flow rate of air is transient, the equivalence ratio with time has been calculated for each of the comparisons (Figure 8.11), using Equation C.4 and the calculated mass flow rate constant α found via the calibration discussed in Section 8.1.1. This shows there is a drop of approximately 50% in the fuel equivalence ratio over the useable test period, mainly due to the increasing density of the air at the expansion tunnel exit.

The first comparison presented of nitrogen to air shots was to investigate combustion effects is for an initial Ludwieg tube fill pressure of 380 kPa (shots x2s124 and x2s125) shown in Figure 8.12. There is quite good agreement seen between the normalised static pressure on the inlet and the start of the combustor. This firstly shows that the two

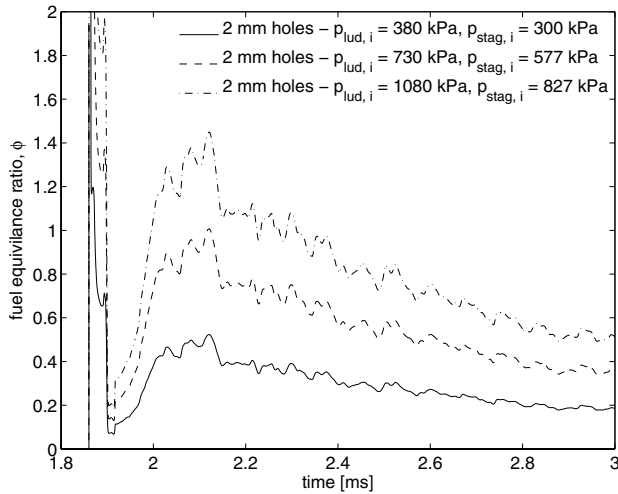


Figure 8.11: Fuel equivalence ratio change during the test period for various initial Ludwieg tube fill pressures.

shots are comparable, with matching freestream conditions and fuel injection parameters. Secondly, there is no sign of the initiation of bulk combustion effects on the intake. Combustion effects are not found until after the second shock (second large rise in pressure within the combustor) meets the bottom wall. In the computational simulation presented in Section 7.3.1, the highest pressure and temperature region was found on the cowl side of the combustor behind the initial cowl shock. With this being the likely location for ignition, it seems reasonable that the effects are not seen on the opposing wall until further downstream.

The rise in static pressure level seems to increase after ignition by approximately 75% and remains approximately level. However, although the average pressure seems not to increase any further, this cannot be verified with the amount of transducers located downstream of this location. The time variation in the measurements is minimal, although the drop in the fuel equivalence ratio is quite high. There is only a small variation in the pressure measured on the thrust surface. As these measurements are taken at the end of the thrust surface, it is not expected that the pressure level will be noticeably different on the scale of the plot.

The combustion effects for an initial Ludwieg tube fill pressure are presented in Figure 8.13 by comparing shots x2s117 and x2s118. This shows again, like for the first comparison, that there is a good agreement between both of these shots normalised pressure on the intake, apart from at $250 \mu s$, where there is some discrepancy downstream of the injection location on the third wedge of the intake. As discussed previously, this shows that both the freestream conditions are in reasonable agreement and there are no signs of combustion before the combustor. This second case however, shows signs of the combustion occurring earlier; after the cowl tip shock is reflected off the bottom wall the

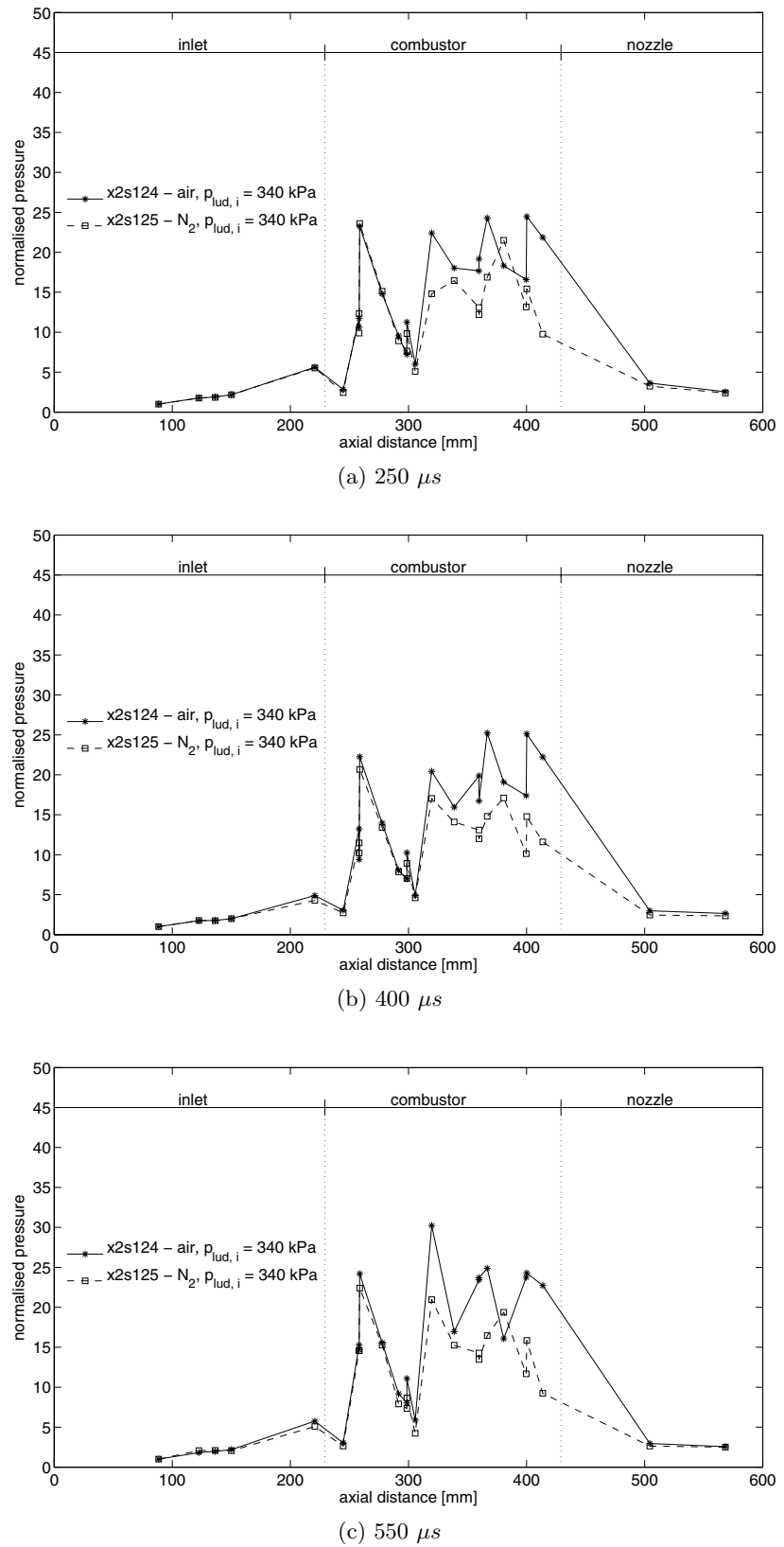


Figure 8.12: Combustion effects on normalised static pressure along the scramjet duct for a initial Ludwieg fill pressure of 380 kPa.

air test gas shot (x2s117) starts to increase from the normalised static pressure of shot x2s118. The normalised static pressure is seen to increase with axial distance down the duct and is double the normalised pressure at the last measurement location. The normalised static pressure on the thrust surface is slightly larger in the test with combustion. Again, there is no discernable difference due to the drop in fuel equivalence ratio during the test apart from movement in the wave structure. However, it appears at the first time shown that the combustion effects are still establishing, thus causing the wave structure to change quite significantly between time steps.

The final comparison of scramjet normalised pressure for nitrogen (x2s124) to air (x2s119) shots is shown in Figure 8.14 for an initial Ludwieg tube fill pressure of 1080 kPa. The combustion effects shown are very similar to those presented errorfor the previous comparison which had a lower fuel mass flow rate. There is no indication of combustion occurring on the inlet and the normalised static pressure on the intake is quite similar indicating that the freestream conditions are in good agreement. The ignition location appears on the bottom wall of the combustor at the reflection location of the unsteady expansion fan created at the intake/combustor corner. The rise in normalised static pressure is quite similar to that of the previous case, with a 100% pressure rise by the end of the combustor. The thrust surface however, shows quite a large increase in normalised static pressure of 50% for the shot with combustion effects.

8.2.3 Variation in fuel equivalence ratio

The amount of pressure rise available in a scramjet engine is limited by how well mixed the air and fuel is before reaching the thrust nozzle and how much heat release can be obtained, ensuring the flow remains supersonic. Thus, a scramjet can be either mixing limited or thermally limited, as explored in Chapter 6. Further performance may be obtained in these engines by injecting more fuel than the stoichiometric limit. This is both to overcome deficiencies in mixing performance for the given length of combustor and also to cool the overall flow to allow less losses due to high temperature effects of chemical dissociation. However, this can also decrease overall performance by further flow losses due to injection of more fuel (not investigated within this experimental study) or thermally choke the flow causing the flow to become subsonic.

The pressure rise by the end of the combustor can be calculated by simple Rayleigh line heat addition to a constant area duct. Using average values of the flow properties (Mach number of 4.73 and a static temperature of 1000 K) at the start of the combustor from the computational simulation (discussed in Section 7.3.1), a heat release for hydrogen of 90 MJ/kg and nominal freestream gas properties ($\gamma = 1.4$ and $R = 287 \text{ J/kg.K}$) the pressure change across the duct is calculated. This is shown in Figure 8.15 for variation in fuel equivalence ratio and combustion efficiency. The combustion efficiency combines

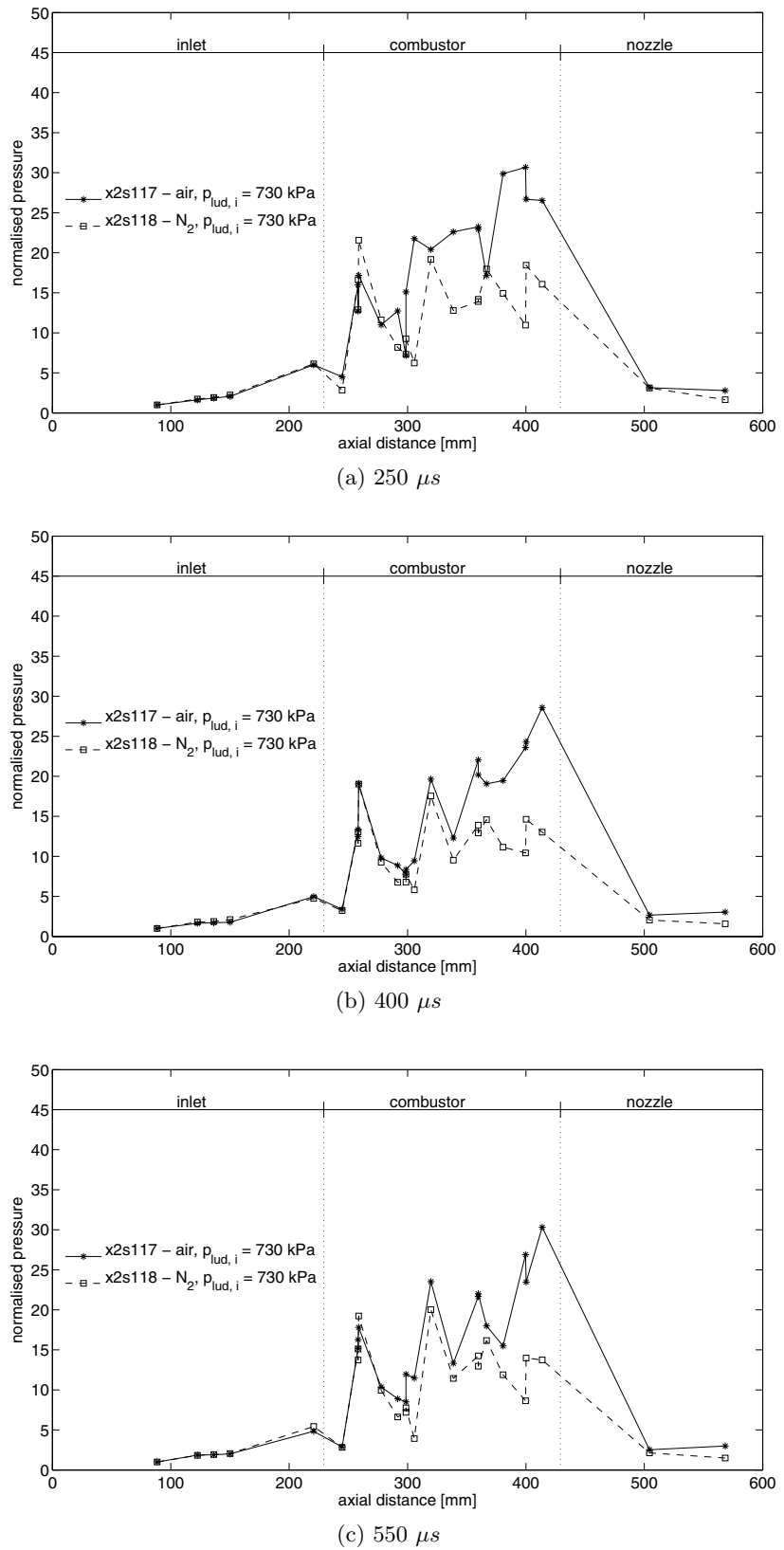


Figure 8.13: Combustion effects on normalised static pressure along the scramjet duct for a initial Ludwieg fill pressure of 730 kPa.

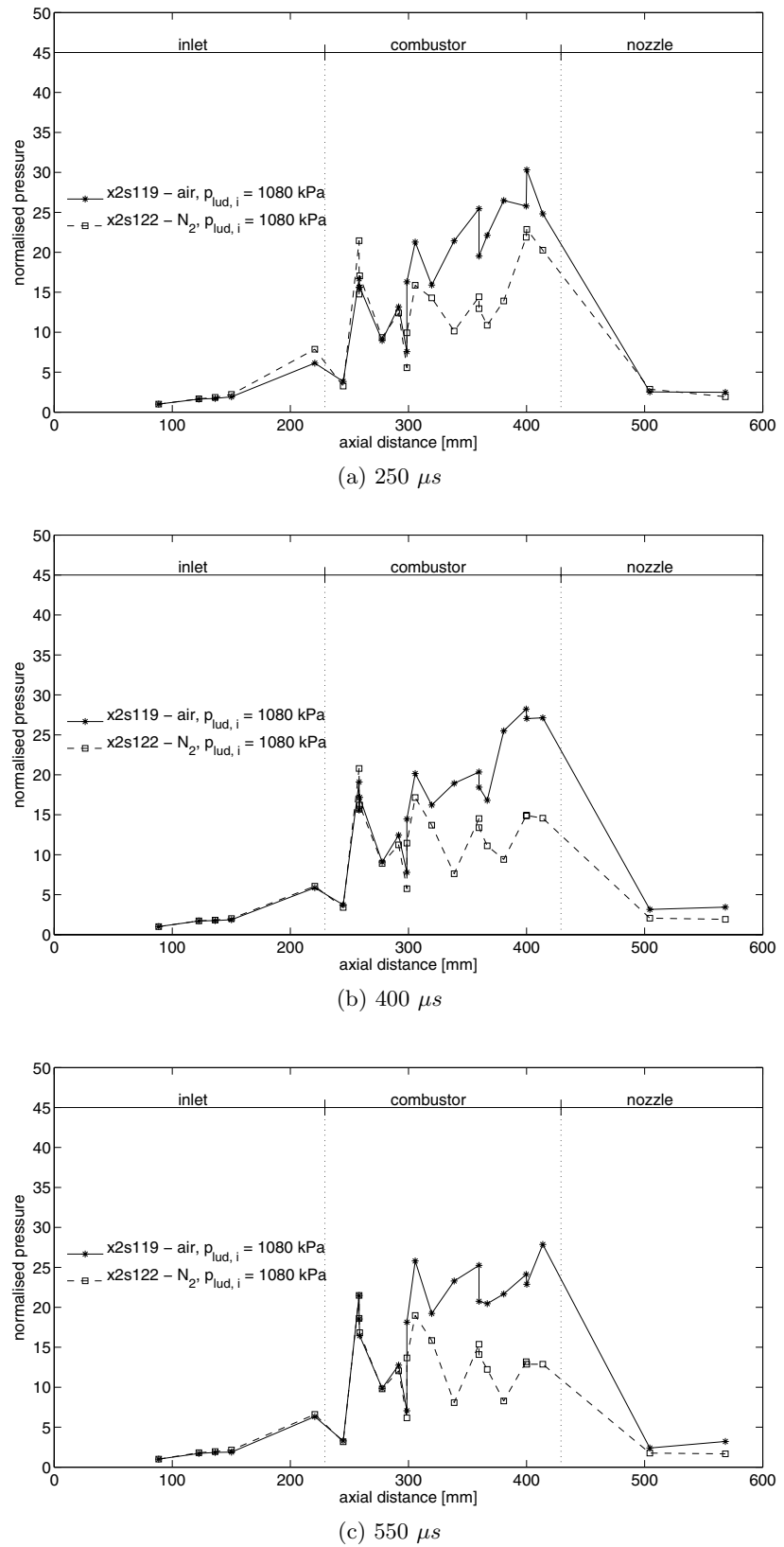


Figure 8.14: Combustion effects on normalised static pressure along the scramjet duct for a initial Ludwieg fill pressure of 1080 kPa.

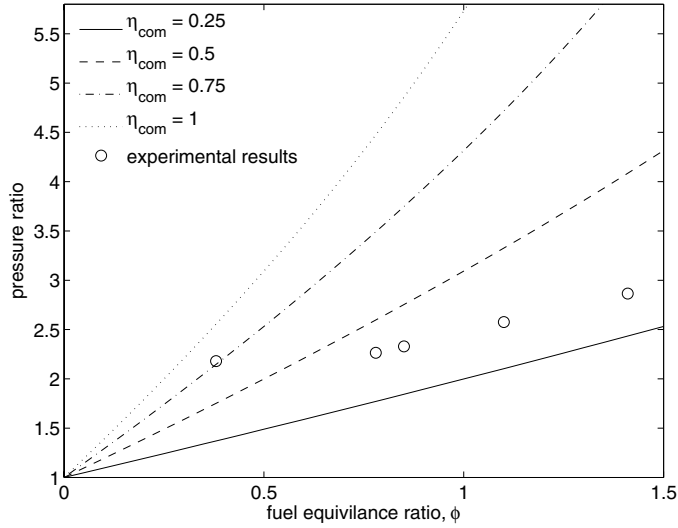
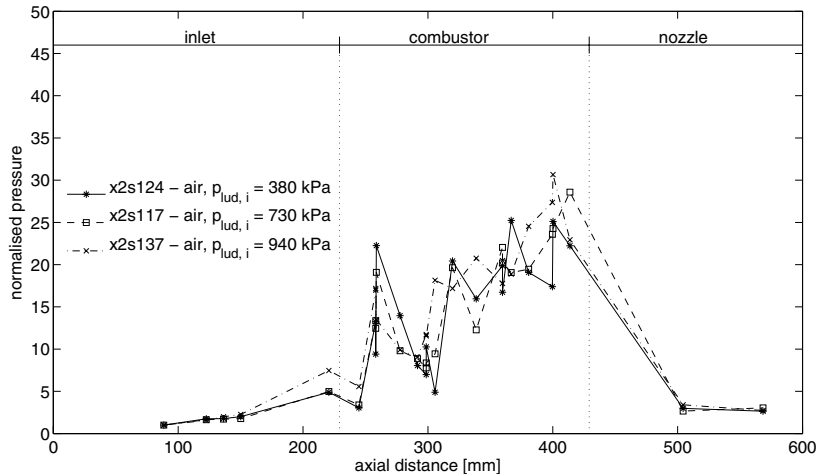


Figure 8.15: Pressure ratio across combustion for one dimensional heat addition into a constant area duct for various fuel equivalence ratios. Using nominal inflow conditions of $M = 4.73$ and $T = 1000$ K.

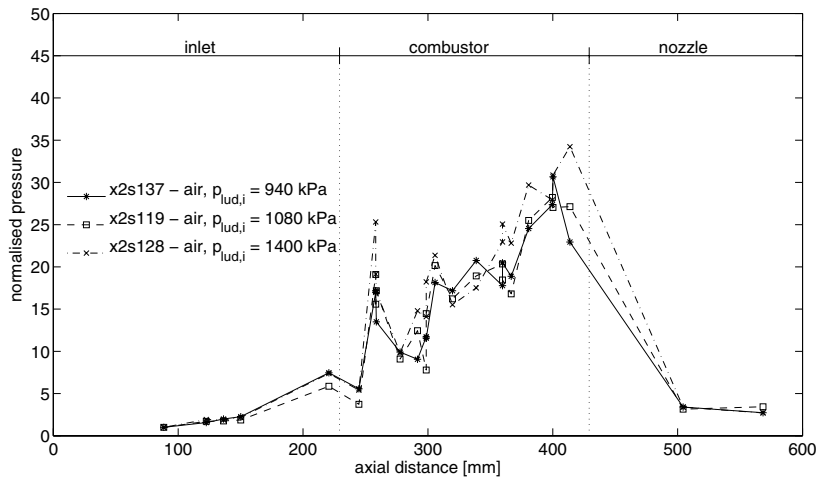
both the deviation from perfect mixing of the fuel/air and not achieving the desired heat release due to either limitation in combustor length or thermal losses in the experiment. This shows that as the equivalence ratio increases the pressure ratio across the combustor should increase quite noticeably. Also, there is an increasing gradient of pressure ratio with increasing combustion efficiency.

A comparison of the effects of fuel equivalence ratio of all the scramjet tests using the low enthalpy air freestream condition and where the scramjet had 2 mm injector holes is presented in Figure 8.16. This shows the normalised static pressure distributions of six different shots at $400 \mu\text{s}$. The same trend of rising pressure through the combustor can be seen with all fuel equivalence ratios. All shots exhibit similar pressures on the thrust surface. The normalised pressure through the combustor does increase with fuel equivalence ratio, although the amount it rises by is not as large as expected between each increment. Therefore, the limitation of the combustion can be theorised to be caused by mixing limitation in the length of combustor chosen, as long as all the fuel injected on the inlet enters the duct. This is also based on the assumption that the time of the test period is long enough for most of the significant effects of combustion which alter pressure measurements are established. Thus, no thermal choking point was found during the experimentation. As discussed in Section 6.3.1, the pressure rise due to combustion after ignition is not linear due to the finite rate chemistry effects. However, it can be seen that over the 80 mm of the combustor, the rise appears to be quite linearly in all shots.

To investigate the increase in combustor static pressure with fuel equivalence ratio, this property must be calculated at $400 \mu\text{s}$ for the six shots. Using the calculated mass



(a) low equivalence ratios



(b) high equivalence ratios

Figure 8.16: Variation in fuel equivalence ratio on normalised static pressure along the scramjet duct at $400 \mu\text{s}$.

flow rate of air at $400 \mu\text{s}$ after the passing of the secondary shock from computational simulations of the freestream condition (Section 5.3.2), the fuel equivalence ratio can be calculated using the mass flow rate of fuel for each shot (Table 8.3). It can be seen the fuel equivalence ratios range from 0.38 up to 1.41 across the six shots. Also given in Table 8.3 is the ratio of normalised static pressure axially across the combustor. It is assumed using the computational simulations of the scramjet and fuel into nitrogen experimental data, that the average normalised static pressure is 12.5 for all shots. This is used as the inflow combustor pressure, p_2 , to remove effects of the shock and expansion waves. To calculate the normalised pressure at the end of the combustor of each shot, a linear trend line is taken over the last 80 mm of the combustor. The corresponding value of normalised pressure of the trendline at the end of the combustor (429.2 mm) is taken to be p_3 .

Table 8.3: Fuel equivalence ratio and pressure across combustor (p_2/p_3) at $400 \mu s$ calculated for various shots using air mass flow rate calculated from computational simulations.

shot number	$p_{lud,i}$ [kPa]	ϕ	p_3/p_2
x2s124	380	0.38	2.18
x2s117	730	0.78	2.26
x2s137	940	0.85	2.33
x2s119	1080	1.10	2.58
x2s128	1170	1.41	2.86

There is a near linear increase of pressure ratio across the combustor with increasing fuel equivalence ratio. This is plotted in Figure 8.15 over the theoretical pressure rise due to combustion. For the lowest fuel equivalence ratio of 0.38 in shot x2s124, the combustion efficiency is quite high, at a value of 0.76. As the fuel equivalence ratio increases however, the combustion efficiency (which includes the mixing efficiency) decreases remarkably. One possibility for this behaviour is that the mixing could be length limited, therefore causing negligible increases in performance with increased fuel equivalence ratio. Another possibility investigated during testing for the underperformance at higher fuel equivalence ratios was that fuel was being injected over the top of the cowl. This would get worse at higher fuel equivalence ratios, as the penetration distance of the fuel jet would be greater, causing the increased mass of fuel to pass externally from the scramjet duct. This was explored in shot x2s149 by shifting the cowl tip forward, although no increase in performance was found. A less likely cause is the trapping of some hydrogen through the start up procedure in the boundary layer which therefore increases the overall fuel equivalence ratio during the test period. However, the mass that could be trapped should be quite small as expansion tunnel start up flow should clear most of the pre-test flow hydrogen from the scramjet duct. This behaviour remains unexplained at this point, with further investigation presented for the testing of larger injection ports in Section 8.2.5.

8.2.4 High enthalpy condition

Reliable combustion data was not obtained for the scramjet for the high enthalpy condition. This was due to problems with both pre-triggering the fuel system (caused by the tunnel shifting within its supports) and also the fuel valve not opening reliably (due to foreign material stuck in the pilot valve). However, data was obtained for the condition using a nitrogen test gas and fuel injection with an initial Ludwieg tube fill pressure of 1080 kPa. This data may still be of interest, so therefore is presented as a comparison to the low enthalpy condition in Figure 8.17. It shows that there is a similar flow structure and pressure level within the scramjet for both the high and low enthalpy freestream con-

ditions. However, the testing with the high enthalpy condition shows a higher pressure both on the third wedge of the intake and the start of the combustor. As the pressure recorded on the first wedge which is used for the normalisation are very close, this result seems to be an anomaly. However, it is quite interesting to note that the shock and expansion structure are quite similar. If combustion data was obtained, it is expected that the comparison between the two conditions would be quite valuable.

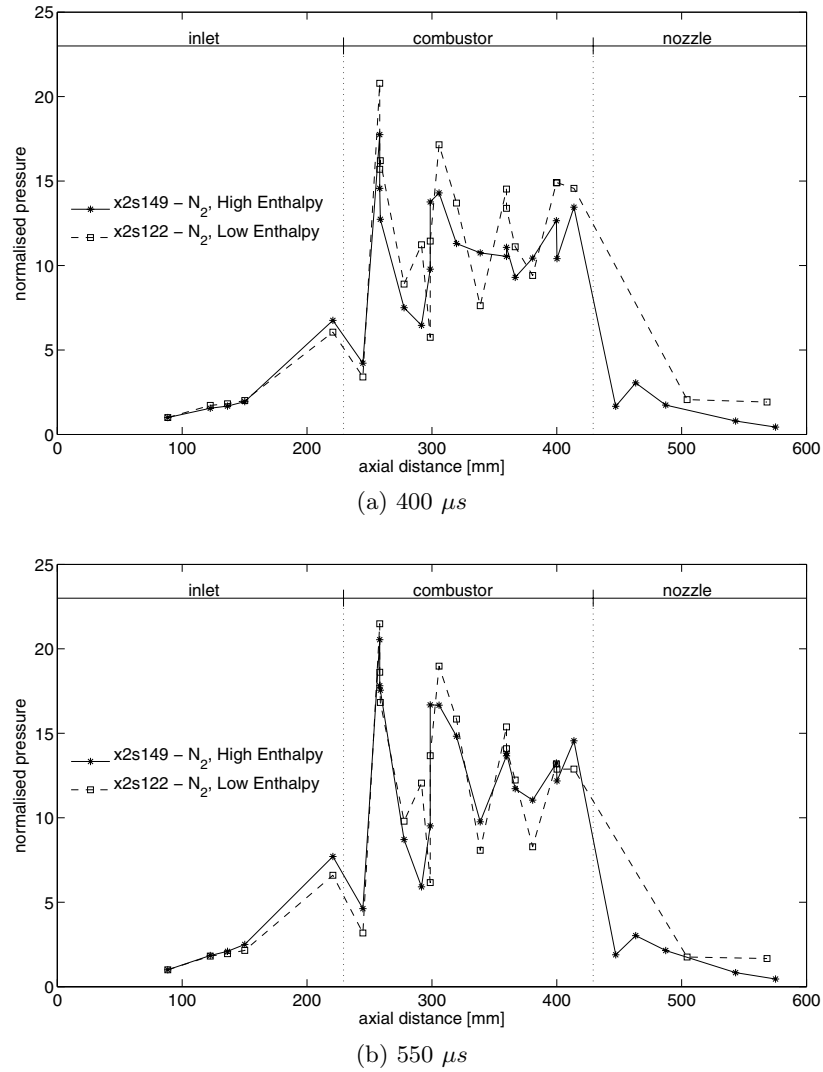


Figure 8.17: Scramjet duct pressure for nitrogen test gas and fuel injection two different freestream conditions. Initial Ludwieg tube fill pressures of 1080 kPa and 1040 kPa were used for the high and low enthalpy shots respectively.

8.2.5 Larger diameter injector holes

The fuel injection holes were altered for shot x2s155, to be a larger diameter of 2.8 mm. This alteration affects the hydrogen injection by increasing the penetration distance into the freestream while also lowering the stagnation pressure required for injection. The spacing between the injectors will decrease, which can affect the rate of mixing [192]. This modification was primarily undertaken as the fuel valve had begun leaking hydrogen into the test section before the shot, and was significantly worse for higher initial Ludwieg tube fill pressures. Due to the low fill pressures in the acceleration tube, this leakage can affect the flow condition produced by the expansion tube. Using the properties of the freestream over the third wedge at 400 μ s of 3050 m/s, 0.221 kg/m³ and Mach number of 6.5, penetration distance was calculated for the sonic jets of hydrogen with a mass flow rate ensuring the equivalence ratio was set to 1. Figure 8.18 shows the penetration height as a function of distance downstream from the injector for various fuel hole diameters using McClintock correlation [190] (Equation 6.14). It can be seen that at the combustor entrance (20 mm downstream) that the increase in penetration is 0.8 mm to 5.7 mm, increasing the penetration of hydrogen closer to the cowl, with the distance from the third wedge orientation being 6.76 mm. As more fuel should reach the ignition region, the combustion efficiency through the engine should therefore increase.

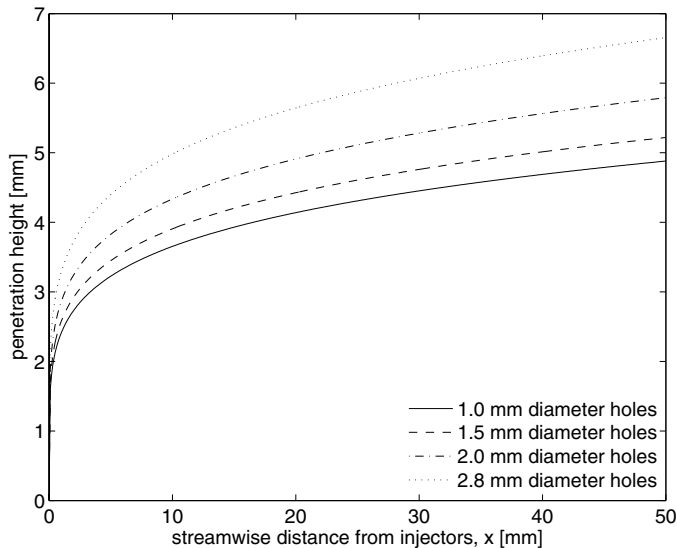


Figure 8.18: Penetration of four sonic jets for varying size holes with $\phi = 1$ using nominal freestream conditions on third wedge at 400 μ s.

It must also be noted that during these tests, the cowl was moved forward by 18 mm. This was to ensure that the jet could not overshoot the cowl and pass outside the combustor. As seen in Section 8.2.1, the overall average pressure in the combustor is not noticeably different, but the first sensor located 15.5 mm into the combustor is now af-

fected by the return cowl shock. With combustion tests, this will mean that the ignition source of the return cowl shock will be further upstream. Also, it is uncertain whether the leading edge shock may now be reflected and enter the combustor, although this looks unlikely due to the same pressure rise in the fuel off shot x2s158 as that recorded when the cowl was further downstream. Figure 8.19 shows the time variance of the equivalence ratio for the three experimental shots explored in this section. These tests are have similar fuel equivalence ratios as those explored for the smaller diameter injector tests.

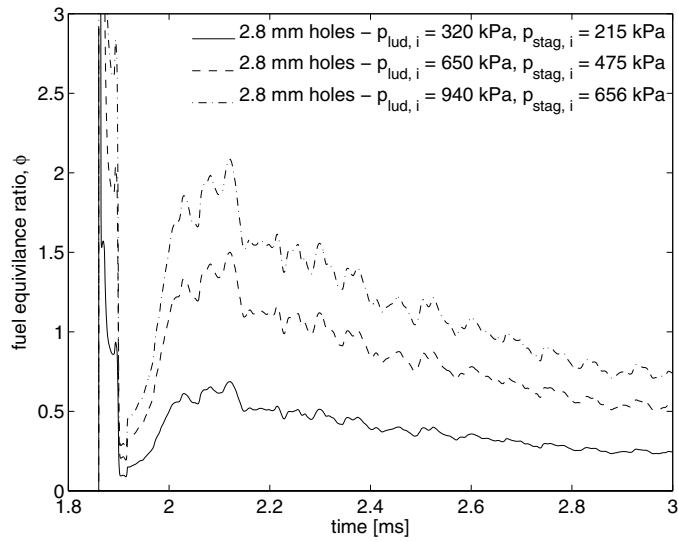


Figure 8.19: Fuel equivalence ratio change during the test period for various initial Ludwieg tube fill pressures, large injector hole diameter tests.

As was done for the smaller hole investigations, a comparison is required between the fuel off shots to fuel on shots into nitrogen to calculate the pressure rise from injection. This is shown in Figure 8.20, for a initial Ludwieg tube fill pressure of 650 kPa. This shows that there is quite a large rise in the pressure due to the injection of the hydrogen into the nitrogen test gas (x2s156) compared with the fuel off shot. The pressure is also seen to increase quite dramatically at the first axial transducer in the combustor. The normalised static pressure is seen to rise from 15 to 22.5. This also shows that having the cowl forward also increases the pressure at the start of the combustor. The fuel on shot into an air test gas (x2s159) shows a similar pressure rise as seen in shot x2s156 at the start of the combustor. Ignition of the fuel is seen 29 mm into the combustor, where the two pressure traces diverge. The results change a lot more with time taken in the test period, compared with previously presented results. This may be an effect of having the cowl positioned further forward, whereby more waves are captured into the combustor.

The comparison for the effects of injector diameter on the medium fuel equivalence ratio experiment is shown in Figure 8.21. That is, the increase in hole diameter combined with shifting the cowl position further forward, has moved the location of the first signs

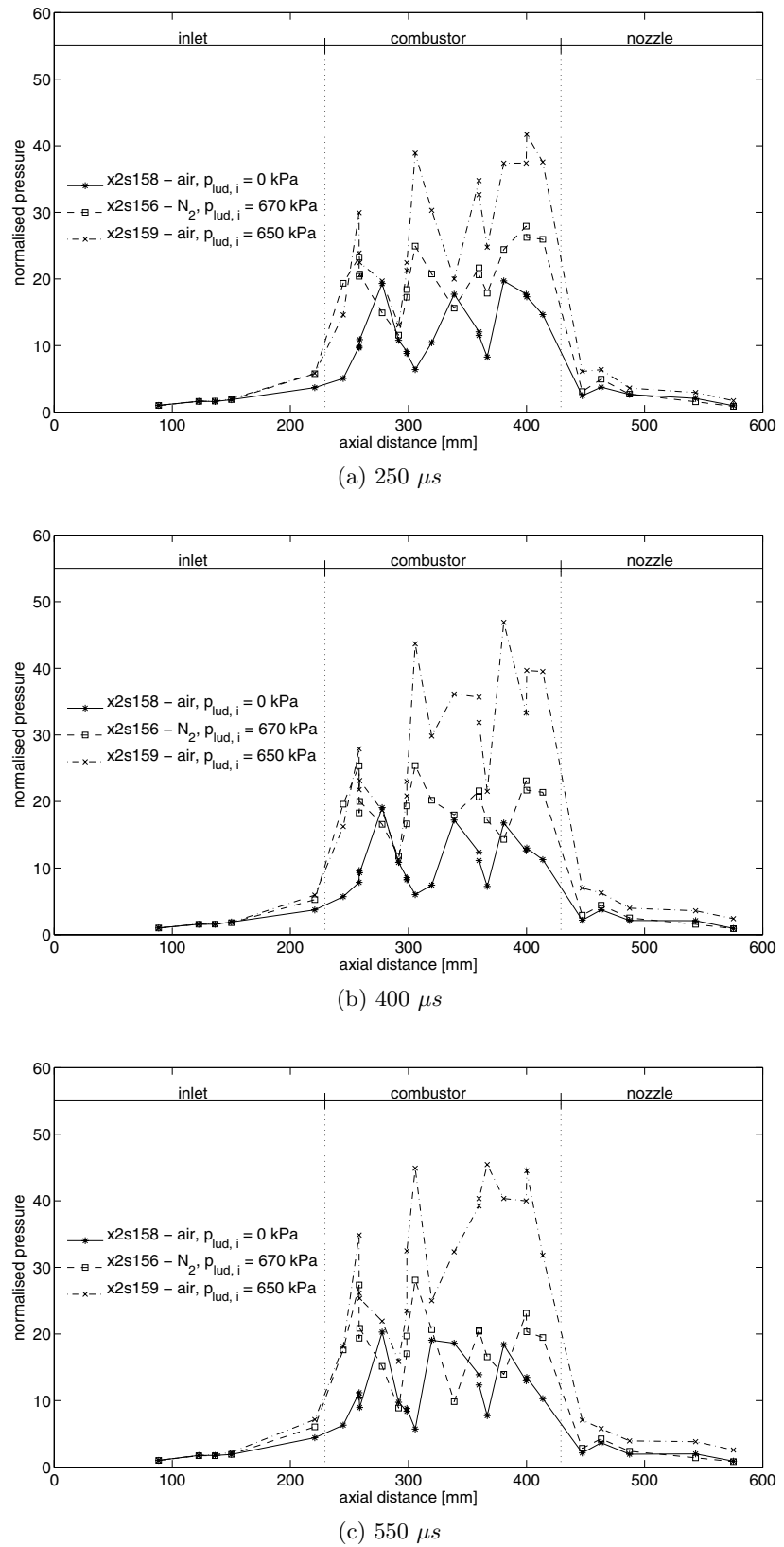


Figure 8.20: Comparison of normalised static pressure for large hole injectors with variation in freestream gas.

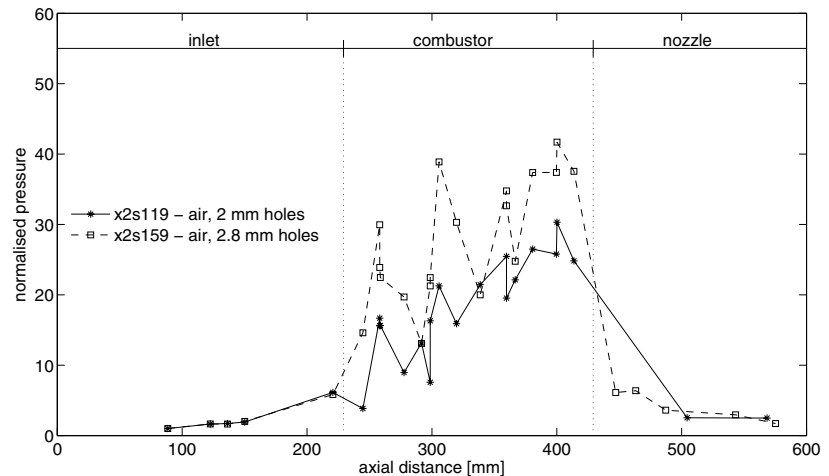
Table 8.4: Fuel equivalence ratio and pressure across combustor (p_2/p_3) at $400 \mu s$ calculated for large diameter injection hole experiments. This uses the air mass flow rate calculated from computational simulations.

shot number	$p_{lud,i}$ [kPa]	ϕ	p_3/p_2
x2s160	380	0.49	1.53
x2s159	730	1.09	2.27
x2s155	940	1.51	2.42

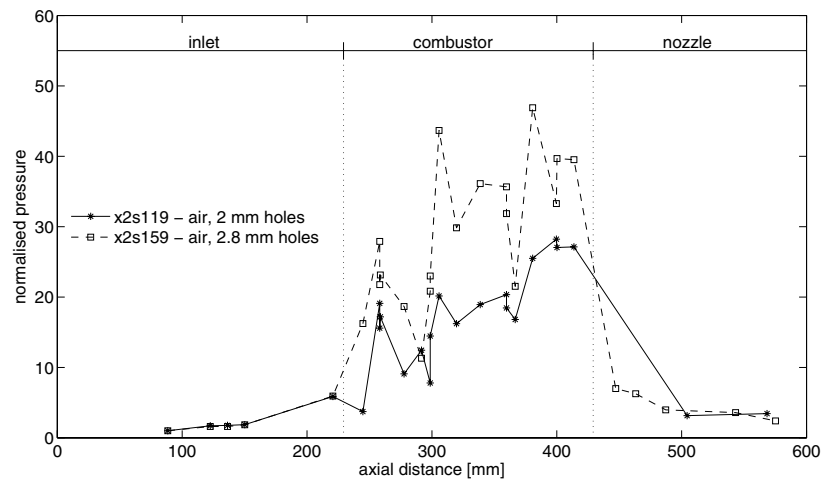
of combustion upstream and the overall pressure level throughout the scramjet combustor and thrust surface has increased. A larger increase in the normalised static pressure is measured at the first combustor location, which corresponds to the increased effects of having larger injector holes and also the cowl being positioned further forward. Although there is a larger pressure by the end of the combustor, the overall pressure rise across the combustor is quite similar. The static pressure measured on the thrust surface is also quite close agreement between the two shots.

The increase in normalised pressure across the combustor has been shown to be quite evident for the larger hole diameter tests. Figure 8.22 shows a comparison for the three tests with larger injector holes, with various fuel mass flow rates. From the first measurement taken in the combustor, the pressure is seen to increase with fuel equivalence ratio as it did with the smaller injector tests. This suggests that the pressure rise due to combustion is occurring quite rapidly, whereas theoretical predictions suggest a slower heat release just after ignition. The trend of higher pressure continues throughout the combustor and rises close to linearly with distance down the combustor. The pressure rise by the end of the combustor is seen to increase with equivalence ratio. However, the pressure initially measured at the start of the combustor is also higher. As there were no successful shots with a nitrogen test gas for the low and high equivalence ratios, the initial pressure cannot be attributed to either combustion or the injection of the fuel.

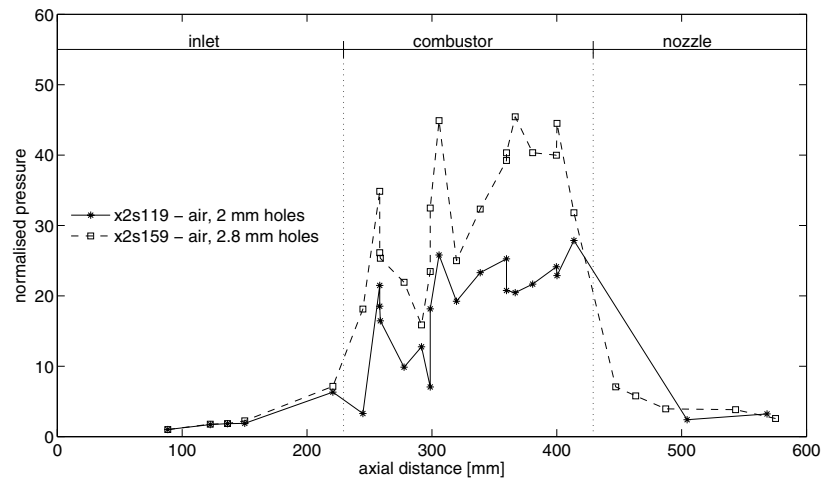
To calculate the pressure ratio change across the combustor, as was done in Section 8.2.3, a linear curve fit is taken over the last 80 mm to find the normalised pressure at the end of the combustor using the nominal value of 22 for the start of the combustor. Values for the pressure ratio across the combustor can be found in Table 8.4, along with the fuel equivalence ratio at $400 \mu s$. This shows that the change in pressure ratio is significantly lower than that predicted for the smaller diameter tests. Although there is a large change in combustor pressure ratio between the first two tests, there is only a small change between the last two. This would suggest that the combustion pressure level is limited by either mixing or thermodynamic effects. Again, the theoretical combustion efficiency drops with fuel equivalence ratio assuming constant thermodynamic properties.



(a) 250 μ s



(b) 400 μ s



(c) 550 μ s

Figure 8.21: Comparison of normalised static pressure with medium fuel mass flow rate tests with variation in injection hole diameter.

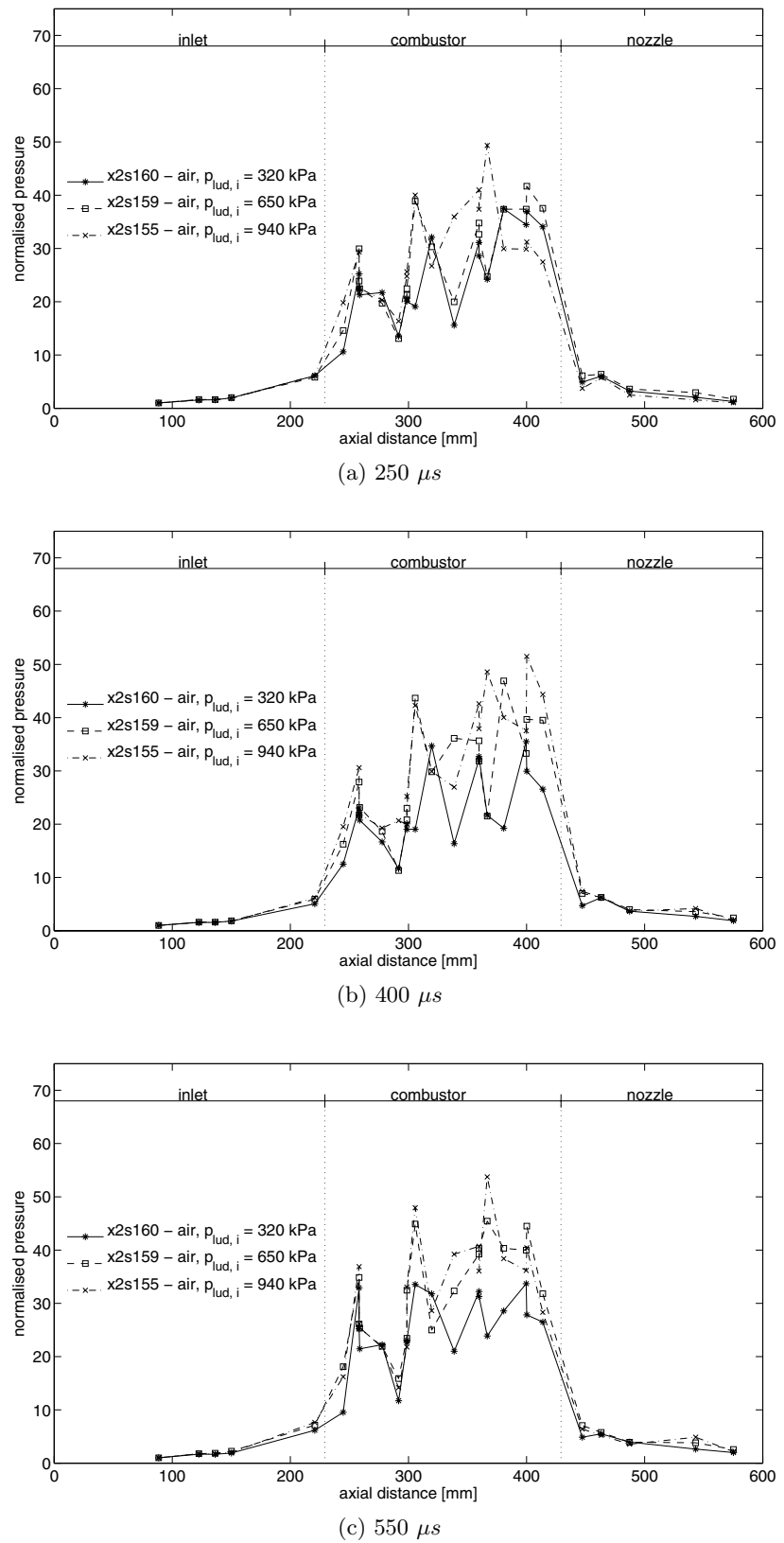


Figure 8.22: Static pressure through scramjet duct for larger fuel injection holes of 2.8 mm diameter for various fuel equivalence ratios.

8.2.6 Engine performance

Inviscid net thrust predictions can be made of the scramjet by integrating the pressure transducer data through the engine ($T - D = \int p dA$) for the area normal to the axial direction. Turner [207] compared inviscid thrust resolved from fuel-off scramjet experimental pressure distributions to that derived in a similar fashion from computational simulations of the engine. This showed that due to the poor resolution of pressure measurements, an overestimate of up to 100% of thrust was found experimentally. Therefore, the use of thrust data from this method should only be used as an estimate of performance. However, this analytical tool for prediction of the drag/thrust can be useful in predicting general trends for variations in fuel equivalence ratio or freestream conditions. Also, it avoids the issue seen in Section 7.3.1 where a direct thrust measurement cannot be analysed without the inclusion of the rate of change in stored momentum.

The net inviscid thrust was investigated for the pressure distributions presented in Figure 8.20. This compares the results of fuel off, fuel on into nitrogen and fuel on into air shots. This should show a worst case as the pressure is taken for the whole third wedge (which has the largest planar area) from the pressure transducer behind the injector and the first pressure transducer on the thrust surface is a significant distance from the turning corner where the highest pressure is likely to occur. The inviscid net thrust is presented for these shots at various times in Figure 8.23. This shows the fuel off experiment produces a substantial net drag, with increasing drag with the increase in freestream pressure as expected. The fuel on into nitrogen shot shows there is a substantial increase in the net thrust over the fuel off case due to fuel injection, however the scramjet is still producing drag. The effects of combustion in the fuel on into air shot gives a net positive thrust, of approximately the same magnitude of the drag shot. A peak is seen in the fuel on net thrust at 400 μs , however the net thrust is seen to vary substantially over the test time.

To investigate the inviscid performance of the scramjet at various fuel equivalence ratios, Table 8.5 presents normalised net inviscid thrust and specific impulse. The axial pressure distributions can be seen in Figure 8.22. The maximum thrust is found to occur at the near stoichiometric fuel equivalence ratio (1.09). The net thrust is quite similar to that found for the higher fuel equivalence ratio. However, due to the smaller fuel mass flow rate, the maximum specific impulse occurs at the lowest fuel equivalence ratio and substantially outperforms the other two fuel equivalence ratios. This is not surprising, as a similar thrust is present to that recorded in the higher fuel equivalence ratio tests and is divided by a small mass flow rate.

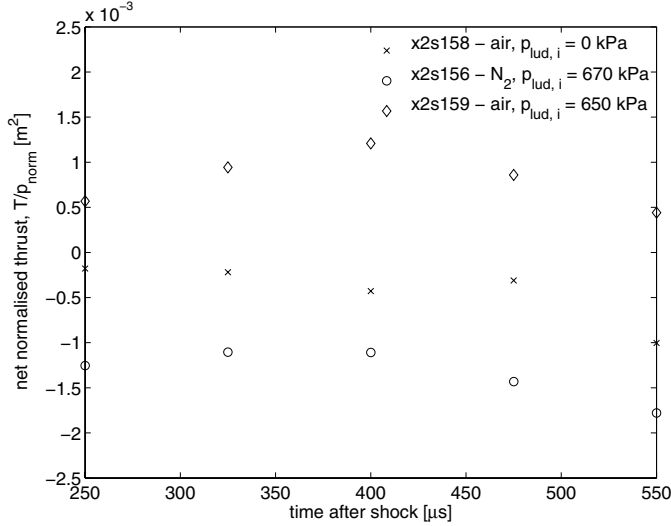


Figure 8.23: Inviscid net thrust predictions of scramjet at various times. Normalised by pressure on first wedge.

Table 8.5: Inviscid performance prediction of scramjet at various fuel equivalence ratio at $400 \mu\text{s}$ for larger hole injection experiments.

shot number	ϕ	$\frac{T-D}{p_{norm}} [\text{m}^2]$	T [N]	I _{sp} [s]
x2s160	0.49	0.705e ⁻³	3.30	182.9
x2s159	1.09	1.208e ⁻³	5.57	137.4
x2s155	1.51	1.186e ⁻³	5.51	97.7

8.3 Summary

Supersonic combustion was achieved for the two dimensional scramjet in the X2 expansion tunnel facility. Comparison of a fuel off shot with CFD showed good agreement apart from at the end of the combustor where the pressures predicted in the calculations were higher than measured. Comparison of fuel off to tare shots indicated that there was a slight rise in the static pressure due to injection. The use of the normalisation method showed that the results even with combustion, remained relatively steady through the testing. The engine appears to be mixing limited with no signs of subsonic regions or unstart noticed throughout the test campaign. The maximum pressure rise achieved across the combustor was 2.8, using 2 mm fuel injection holes at an equivalence ratio of 1.42. With larger injector holes and also the cowl moved forward, a much larger increase in the pressure was seen in the combustor than originally investigated. However, the overall pressure rise was less due to a higher pressure occurring at the start of the combustor. Estimates of net inviscid thrust on the large diameter injector experiments indicates there is thrust being

produced, with a maximum inviscid based specific impulse of 182 s at a fuel equivalence ratio of 0.49.

Conclusion

An investigation was undertaken on the large X3 facility to duplicate flow parameters of a Mach 10 flight condition at 30 km altitude. This is the highest Mach number, at which a scramjet duplication condition possible in the T4 reflected shock tunnel and therefore an overlap point between the two facilities. Effects of boundary layer transition during the test time reduced the measured pitot pressure significantly across the tube, allowing only $\sim 200 \mu\text{s}$ of test time. The pitot pressure drop was determined to be caused by boundary layer transition by using hybrid one/two dimensional simulations of the facility using the Baldwin-Lomax turbulence model from the time of the primary diaphragm rupture. This was later verified experimentally by measuring heat transfer at the expansion tube wall at various axial locations.

To avoid the drop of Mach number in the core flow, two different approaches were explored. The first solution was the use of a steady expansion nozzle at the end of the acceleration tube. Indirectly, this allows for a higher density and Reynolds number test flow to be produced before steady expansion to the designed condition. The net result is that transition will occur closer to the interface, which dampens the disruptive flow effects seen in the core flow. This approach was investigated numerically using the same hybrid simulation approach, showing that flow parameters could be replicated and had a test time of ~ 1 ms with a 300 mm of core flow diameter. The second solution was the use of a hydrogen acceleration gas, to produce a low viscosity sub-layer in the boundary layer. The corruption of the core flow could be avoided using this due to the reduction of the amount of test gas that enters the boundary layer and promoting early transition by increasing the Reynolds number from the shock to the interface. Initial experimentation with the hydrogen as the acceleration gas produced a flow of approximately the correct conditions, however many interesting flow phenomena still need to be explored, including probable combustion in the accelerator gas due to air contamination prior to firing.

At this time of the project, the smaller X2 facility has just been fitted with a contoured Mach 10 nozzle. Therefore condition investigation continued on this facility so that scramjet experimentation could be undertaken. Due to the reduced size of the X2 facility compared with X3, the test time available decreased from the 1 ms predicted by CFD for X3. Therefore, a replicated condition was chosen by decreasing the size of the scramjet and increasing the static pressure by a factor of 2.5 (maintaining the pL product) to ensure steady flow was established in the lower available test time. A condition was

established experimentally with the appropriate flow properties, a test time of $500 \mu\text{s}$ and with 110 mm diameter of core flow. However, there was a steady increase in the static pressure after the first $150 \mu\text{s}$ of the test time. Calculation of the other flow properties was again accomplished using a hybrid numerical calculation procedure using experimental data as validation.

A two dimensional scramjet was designed using analytical methods, with a capture area of 40 mm by 40 mm and a length of 629 mm. The scramjet was designed to have an optimised triple external shock intake, with upstream discrete hole injection of hydrogen, constant area combustor and a planar thrust surface. A time accurate, computational simulation (two dimensional with viscous effects) was used to verify the flow path of the design, using the transient inflow predicted from simulating the X2 facility condition. This also allowed flow establishment times and inlet start-up to be verified and a comparison was made with the fuel off experimental data. Investigation of the transient behaviour of wall static pressure showed a quasi-steady analysis could be applied, as the convective term was much larger than the local term of the *total derivative* of pressure with respect to time. A normalisation procedure was proposed in order to deal with the transient nature of the data to accurately represent the axial progression of the gas through the duct.

Experimentally, static pressure measurements in the scramjet were taken at various equivalence ratios with both nitrogen and air test gas. Combustion effects produced approximately double the wall static pressure across the combustor. It was shown that combustion was moderately affected by increasing the fuel equivalence ratio. The combustor was found to be primarily mixing limited. Experimentation was also undertaken with larger injection holes, higher enthalpy inflow condition and re-positioning of the cowl edge. The highest rise of static pressure across the combustor achieved was 2.8, with the configuration of small injectors with the cowl in its original position and for an equivalence ratio of 1.41. Using a quasi steady analysis of the pressure data, a significant positive net inviscid thrust, corresponding to a specific impulse of 183 s was estimated for the larger diameter fuel injection holes.

This work has validated experimental scramjet conditions and verified CFD approaches to model the expansion tube flow. This computational capability can now be applied to further high total pressure and total enthalpy scramjet conditions with confidence. Experimental testing has shown that stable, supersonic combustion can be produced using these expansion tube conditions. Coupling the transient simulation of the flow condition with a numerical calculation of the fuel off experimental scramjet has been useful in both verification of the design and performance predictions. Also, data from this simulation allowed development of appropriate techniques to analyse scramjet pressure and thrust measurements where transient effects are present in the freestream.

9.1 Recommendations for Further Work

Out of the research conducted in this thesis, some further work can be foreshadowed which is relevant to both increase the confidence and capability of testing scramjets in expansion tube facilities. Future studies might include:

- Experimental confirmation of the numerical results presented in this thesis, that with the addition of a steady expansion nozzle on X3, a 1 ms test time condition can be achieved. This could provide a flow condition with further test time at steady conditions and larger diameter core flow. A direct comparison could be then made between the effect of operating in tunnel mode on boundary layer transition.
- Further investigation of the use of hydrogen as an accelerator gas to reduce flow effects of boundary layer transition for expansion tube conditions. Initial investigation showed promise to resolve some of these issues and could be more effective than operating in tunnel mode.
- Developing the capability to produce flight duplication conditions with higher total pressure and total enthalpy in order to assess scramjet performance along likely flight paths.
- Assessment of direct connect conditions whereby flow properties are matched at the combustor entrance to order to increase model sizes.
- Investigation of source of noise in pitot pressure measurements in impulse facilities and prediction of freestream noise levels.
- Investigating techniques to reduce secondary diaphragm effects due to the high pressure ratios between the shock and acceleration tubes requiring large diaphragm thicknesses.
- Further quantification of transient inflow effects and the validity of the quasi-steady analysis method in the presence of fuel injection and combustion.
- Comparison of scramjet performance data between the full scale model tested in the T4 reflected shock tunnel and the scaled model tested in this thesis in the X2 expansion tunnel.
- Testing of the full scale scramjet model in the X3 expansion tunnel to provide a direct comparison of expansion tube and reflected shock tunnel scramjet data.
- Further qualification of scaled scramjet model performance by repeat tests and verification of thrust surface pressure.

- Testing of the scramjet model with fuel injection, using the developed higher enthalpy condition in X2.

Bibliography

- [1] G.Y. Anderson. *Combustion in High-Speed Flow*, chapter Hypersonic Combustion - Status and Directions. ICASE/LaRC Interdisciplinary Series in Science and Engineering. Kluwer Academic Publishers, 1994.
- [2] B.S. Stewart, R.G. Morgan, and P.A. Jacobs. Rocketdyne hypersonic flow laboratory as high-performance expansion tube for scramjet testing. *AIAA Journal of Propulsion and Power*, 19(1):98–103, January-February 2003.
- [3] M.P. Scott. *Development and modelling of expansion tubes*. PhD thesis, University of Queensland, St. Lucia, Australia, 2006.
- [4] D.R. Buttsworth and P.A. Jacobs. Measurement of fluctuations in a Mach 4 shock tunnel nozzle flow. *7th Australasian Heat and Mass Transfer Conference*, James Cook University, Townsville, July 2000. (Oral presentation).
- [5] A. Ferri. Mixing controlled supersonic combustion. *Annual Review of Fluid Mechanics*, 5, 1973.
- [6] M. Hayne. *Hypervelocity flow over rearward facing steps*. PhD thesis, University of Queensland, St. Lucia, Australia, 2004.
- [7] S. Rowan. *Viscous drag reduction in a scramjet combustor*. PhD thesis, University of Queensland, St. Lucia, Australia, 2003.
- [8] B.S. Stewart. *Performance predictions of the proposed RHYFL-X expansion tube*. PhD thesis, University of Queensland, St. Lucia, Australia, 2004.
- [9] J.D. Anderson. *Hypersonic and High Temperature Gas Dynamics*. McGraw-Hill, 1989.
- [10] F.K Lu and D.E. Marren. *Advanced Hypersonic Test Facilities*, volume 198 of *Progress in Astronautics and Aeronautics*, chapter 2: Principles of Hypersonic Test Facility Development. AIAA, 2002.
- [11] W. Chinitz, J.I. Erdos, O. Rizkalla, G.Y. Anderson, and D.M. Bushnell. Facility opportunities and associated stream chemistry considerations for hypersonic air-breathing propulsion. *AIAA Journal of Propulsion and Power*, 10(1):6–17, 1994.

- [12] R.J. Bakos, J. Tamagno, O. Rizikala, M.V. Pulsonetti, W. Chinitz, and J. Erdos. Hypersonic mixing and combustion studies in the HYPULSE facility. *AIAA Journal of Propulsion and Power*, 8(4):900–906, July-Aug 1992.
- [13] D.M. Smith, E.J. Felderman, F.L. Shope, and J.A. Balboni. *Advanced Hypersonic Test Facilities*, volume 198 of *Progress in Astronautics and Aeronautics*, chapter 10: Arc-Heated Facilities. AIAA, 2002.
- [14] B.R. Capra. *Aerothermodynamic simulation of subscale models of the FIRE II and Titan Explorer vehicles in expansion tubes*. PhD thesis, University of Queensland, St. Lucia, Australia, 2007.
- [15] H. Mirels. Test time in low-pressure shock tubes. *The Physics of Fluids*, 6(9):1201–1214, 1963.
- [16] R.G. Morgan. *Handbook of Shock Waves*, eds Ben-Dor, G., Igra, O. and Elperin, T., volume 1, chapter 4.2: Shock Tubes and Tunnels: Facilities, Instrumentation, and Techniques, Free Piston Driven Reflected Shock Tunnel, pages 587–601. Academic Press, San Diego, 2001.
- [17] D.F. Potter, R.J. Gollan, T. Eichmann, P.A Jacobs, R.G. Morgan, and T.J. McIntyre. Simulation of CO₂-N₂ expansion tunnel flow for the study of radiating blunt-body shock layers. *16th Australasian Fluid Mechanics Conference*, December 2007.
- [18] T.B. Silvester. *Multidimensional viscous flows at superorbital speeds*. PhD thesis, University of Queensland, St. Lucia, Australia, 2005.
- [19] M Lynch. *The X3 primary piston buffer*. Bachelor thesis, University of Queensland, St. Lucia, Australia, 2003.
- [20] M Davey. *A hypersonic nozzle for the X3 expansion tube*. Bachelor thesis, University of Queensland, St. Lucia, Australia, 2006.
- [21] M.P. Scott. Personal communications, 2004.
- [22] W.R. Davies and L. Bernstein. Heat transfer and transition to turbulence in the shock-induced boundary layer on a semi-infinite plate. *Journal of Fluid Mechanics*, 36:87–112, 1969.
- [23] J.L. Shinn and C.G Miller III. Experimental perfect-gas study of expansion-tube flow characteristics. Technical Paper 1317, NASA, December 1978.
- [24] K.J. Weilmuenster. An experimental investigation of wall boundary-layer transition Reynolds numbers in an expansion tube. Technical Note NASA TN D-7541, NASA, May 1974.

- [25] E.R. van Driest. The problem of aerodynamic heating. *Aeronautical Engineering Review*, 1956.
- [26] M.P. Scott, R.G. Morgan, and P.A. Jacobs. A new single stage driver for the X2 expansion tube. *43rd AIAA Aerospace Sciences Meeting and Exhibition*, Reno, Nevada, AIAA paper 2005-0697, June 2005.
- [27] J.E.A. John. *Gas Dynamics*. Allyn and Bacon, second edition, 1983.
- [28] W.D. Heiser and D.T. Pratt. *Hypersonic Airbreathing Propulsion*. AIAA Education Series. AIAA, 1994.
- [29] P. Kutschenreuter. *Scramjet Propulsion*, volume 189 of *Progress in Astronautics and Aeronautics*, chapter 8: Supersonic Flow Combustors. AIAA, 2000.
- [30] D.M. Van Wie. *Scramjet Propulsion*, volume 189 of *Progress in Astronautics and Aeronautics*, chapter 7: Scramjet Inlets, pages 447–511. AIAA, 2000.
- [31] G.Y. Anderson, C.R. McClinton, and J.P. Weidner. *Scramjet Propulsion*, volume 189 of *Progress in Astronautics and Aeronautics*, chapter 6: Scramjet Performance. AIAA, 2000.
- [32] J.P. Sislian. *Scramjet Propulsion*, volume 189 of *Progress in Astronautics and Aeronautics*, chapter 13: Detonation-Wave Ramjets, pages 823–889. AIAA, 2000.
- [33] R. Dunlap, R.L. Brehm, and J.A. Nicholls. A preliminary study of the application of steady-state detonation combustion to a reaction scheme. *Journal of Jet Propulsion*, 28(6):451–456, 1958.
- [34] S.A. Beckel, J.L. Garrett, and C.G. Gettinger. Technologies for robust and affordable scramjet propulsion. *AIAA/AHI 14th International Space Planes and Hypersonics Systems and Technologies Conference*, AIAA paper 2006-7980, November 2006.
- [35] P.W. Huber, C.J. Shenayder Jr, and C.R. McClinton. Criteria for self-ignition of supersonic hydrogen-air mixtures. Technical Paper 1457, NASA, 1979.
- [36] D.W. Riggins. Evaluation of performance loss methods for high speed engines and engine components. *AIAA Journal of Propulsion and Power*, 13(2):296–304, March–April 1997.
- [37] R.G. Morgan. *Combustion in High-Speed Flow*, chapter Supersonic Combustion Experiments in Free Piston Reflected Shock Tunnels. ICASE/LaRC Interdisciplinary Series in Science and Engineering. Kluwer Academic Publishers, 1994.

- [38] D.W. Riggins. Thrust losses in hypersonic engines part 2: Applications. *AIAA Journal of Propulsion and Power*, 13(2):288–295, March-April 1997.
- [39] H.S. Tsien and M. Beilock. Heat source in a uniform flow. *Journal of the Aeronautical Sciences*, 16(12):756, 1949.
- [40] E.A. Fletcher, R.G. Dorsch, and M. Gerstein. Combustion of aluminium borohydride in a supersonic wind tunnel. Technical Report RM E55DO7a, NACA, 1955.
- [41] J.I. Erdos and R. Bakos. Prospects for a quiet hypervelocity shock-expansion tunnel. *18th AIAA Aerospace Ground Testing Conference*, Colorado Springs, AIAA paper 94-2500, June 1994.
- [42] D.M. Bushnell. *Combustion in High-Speed Flow*, chapter Mixing and Combustion Issues in Hypersonic Air-Breathing Propulsion. ICASE/LaRC Interdisciplinary Series in Science and Engineering. Kluwer Academic Publishers, 1994.
- [43] D.M. Bushnell. *Advanced Hypersonic Test Facilities*, volume 198 of *Progress in Astronautics and Aeronautics*, chapter 1: Hypersonic Ground Test Requirements. AIAA, 2002.
- [44] R.G. Morgan and R.J. Stalker. Pressure scaling effects in a scramjet combustion chamber. *8th ISABE Symposium*, Cincinnati, Ohio, ISABE paper 87-7080, 1987.
- [45] M.V. Pulsonetti. *Scaling laws for scramjets*. PhD thesis, University of Queensland, St. Lucia, Australia, 1995.
- [46] M.V. Pulsonetti. Experimental methods for a scramjet scaling. Departmental Report 7/95, Department of Mechanical Engineering, University of Queensland, St. Lucia Qld 4072., 1995.
- [47] G.Y. Anderson, A. Kumar, and J.I. Erdos. Progress in hypersonic combustion technology with computation and experiment. *AIAA 2nd International Aerospace Planes Conference*, AIAA paper 90-5254, 1990.
- [48] J.T. Best. *Advanced Hypersonic Test Facilities*, volume 198 of *Progress in Astronautics and Aeronautics*, chapter 21: A New Mach 8-15 True Temperature Test Facility. AIAA, 2002.
- [49] P.A. Jacobs, R.C. Rogers, E.H. Weidner, and R.D. Bittner. Flow establishment in a generic scramjet combustor. *AIAA Journal of Propulsion and Power*, 8(4):890–899, 1992.

- [50] R.A. East, R.J. Stalker, and J.P. Baird. Measurements of heat transfer to a flat plate in a dissociated high enthalpy laminar airflow. *Journal of Fluid Mechanics*, 97(4):673–699, 1980.
- [51] R.C. Rogers and E.H. Weidner. Scramjet fuel-air mixing establishment in a pulse facility. *AIAA Journal of Propulsion and Power*, 9(1):127–133, January–February 1993.
- [52] R.J. Bakos and R.G. Morgan. Chemical recombination in an expansion tube. *AIAA Journal*, 32(6):1316–1319, June 1994.
- [53] C.E. Willbanks. Sensitivity of pre-mixed compression-initiated supersonic combustion to small perturbations in inlet flow variables. *AIAA Journal*, 8(1):115–119, 1970.
- [54] A. Kumar, D.M. Bushnell, and M.Y. Hussaini. Mixing augmentation technique for hypervelocity scramjets. *AIAA Journal of Propulsion and Power*, 5(5):475–476, Sept-Oct 1989.
- [55] C. Park. Experimental evaluation of real gas phenomena in high enthalpy impulse test facilities: A review. *19th Advanced Measurement and Ground Testing Technology Conference, New Orleans, LA*, AIAA paper 96-2234, 1996.
- [56] M.K. Smart. Personal Communication, 2007.
- [57] R.J. Stalker. Personal Communication, 2007.
- [58] K.A. Skinner and R.J. Stalker. Mass spectrometer measurements of test gas composition in a shock tunnel. *AIAA Journal*, 34(1):203–205, 1996.
- [59] K.E. Fischer and Rock K.E. Calculated effects of nitric oxide flow contamination on scramjet performance. *31st AIAA Joint Propulsion Conference*, AIAA 1995-2524, July 1994.
- [60] K.N.C. Bray. *Evaluation of the Hypersonic Gun Tunnel*, pages 547–700. ARS Progress in Astronautics and Rocketry. Academic Press, New York, 1962.
- [61] V.V. Kislykh. *Advanced Hypersonic Test Facilities*, volume 198 of *Progress in Astronautics and Aeronautics*, chapter 9: Piston Gasdynamic Units with Multicascade Compression. AIAA, 2002.
- [62] R.C. Orth and V.V. Kislykh. Data analysis from hypersonic combustion tests in the TSIIMASH PGU-11 facility. *7th International Space Planes and Hypersonic Systems and Technologies Conference, Norfolk, VA*, AIAA paper 96-4584, 1996.

- [63] A. Paull, R.J. Stalker, and D.J. Mee. Experiments on supersonic combustion ramjet propulsion in a shock tunnel. *Journal of Fluid Mechanics*, 296:158–183, 1995.
- [64] K. Itoh. *Advanced Hypersonic Test Facilities*, volume 198 of *Progress in Astronautics and Aeronautics*, chapter 8: Characteristics of the HEIST and its Applicability for Hypersonic Aerothermodynamic research and Scramjet Research. AIAA, 2002.
- [65] R.J. Bakos. *An investigation of test flow nonequilibrium effects on scramjet combustion*. PhD thesis, University of Queensland, St. Lucia, Australia, 1994.
- [66] R.G. Morgan and R.J. Stalker. Hypersonic combustion of hydrogen in a shock tunnel. ISABE paper 89-7059, 1989.
- [67] R.J. Bakos, R.G. Morgan, and J. Tamango. Effects of oxygen dissociation on hypervelocity combustion experiments. *17th AIAA Aerospace Ground Testing Conference*, Nashville, Tennessee, AIAA paper 1992-3964, 1992.
- [68] J. Belanger and H. Hornung. Transverse jet mixing and combustion experiments in hypervelocity flows. *AIAA Journal of Propulsion and Power*, 12(1):186–192, January–February 1996.
- [69] M. Abdel-Jawad. The Mach 10, 30 km altitude condition in the T4 shock tunnel using a new Mach 10 nozzle. Mechanical Engineering Report 2005/05, University of Queensland, 2005.
- [70] A. Paull. Personal Communication, 2007.
- [71] M. Takahashi, T Komuro, K. Sato, T. Sunami, H. Tanno, and K. Itoh. Performance characteristics of a scramjet engine at high speed condition over Mach 10. *25th International Symposium on Shock Waves*, Bangalore, India, July 2005.
- [72] M. Takahashi, T Komuro, K. Sato, M. Kodera, H. Tanno, and K. Itoh. Effect of combustor shape on scramjet characteristics at hypervelocity condition over Mach 10 flight. *14th AIAA/AHI Space Planes and Hypersonic Systems and Technologies Conference*, Canberra, Australia, AIAA paper 2006-8024, June 2006.
- [73] R.C. Rogers, A.T. Shih, C.Y. Tsai, and R.O. Foelsche. Scramjet tests in a shock tunnel at flight Mach 7, 10 and 15 conditions. *37th AIAA/ASME/SAE/ASEE Joint Propulsion Conference and Exhibit, Salt Lake City, UT*, AIAA paper 2001-3241, 2001.
- [74] M.S. Holden. Studies of scramjet performance in the LENS facility. *36th AIAA/ASME/SAE/ASEE Joint Propulsion Conference and Exhibit, Huntsville, AL*, AIAA paper 2000-3604, 2000.

- [75] M.S. Holden and R.A. Parker. *Advanced Hypersonic Test Facilities*, volume 198 of *Progress in Astronautics and Aeronautics*, chapter 4: LENS Hypervelocity Tunnels and Application to Vehicle Testing at Duplicated Flight Conditions. AIAA, 2002.
- [76] D.M. Van Wie and D.A. Auldt. Internal flowfield characteristics of a scramjet inlet at Mach 10. *AIAA Journal of Propulsion and Power*, 12(1):158–164, 1996.
- [77] J.I. Erdos. *Combustion in High-Speed Flow*, chapter Recent Experiments on Hypersonic Combustion in an Expansion Tube Test Facility. ICASE/LaRC Interdisciplinary Series in Science and Engineering. Kluwer Academic Publishers, 1994.
- [78] R.L. Leonard and P.H. Rose. Feasibility of a high-performance aerodynamic impulse facility. *AIAA Journal*, 6(3):448–457, March 1968.
- [79] O. Rizkalla, R.J. Bakos, Pulsonetti M.V., W. Chinitz, and J.I. Erdos. Use of an expansion tube to examine scramjet combustion at hypersonic velocities. *AIAA/ASME/SAE/ASEE 25th Joint Propulsion Conference*, Monterey, AIAA paper 89-2536, June 1989.
- [80] J. Erdos, J. Calleja, and J. Tamango. Increase in the hypervelocity test envelope of the HYPULSE shock-expansion tube. *18th AIAA Ground Testing Conference*, Colorado Springs, AIAA paper 94-2524, June 1994.
- [81] R.J. Bakos, J.I. Calleja, and J.I. Erdos. An experimental and computational study leading to new test capabilities for the HYPULSE facility with a detonation driver. *19th AIAA Advanced Measurement and Ground Testing Conference*, AIAA paper 96-2193, June 1996.
- [82] J.I. Erdos, R.J. Bakos, and Castrogiovanni. Dual mode shock expansion/reflected shock tunnel. *AIAA 35th Aerospace Sciences Meeting*, AIAA paper 97-0560, January 1997.
- [83] R.S.M. Chue, R.J. Bakos, C.Y. Tsai, and A. Betti. Design of an expansion tunnel nozzle in HYPULSE. *Shock Waves*, 13:261–270, 2003.
- [84] C.Y. Tsai and R.J. Bakos. Mach 7-21 flight simulation in the HYPULSE shock tunnel. *23rd International Symposium on Shock Waves*, Fort Worth, Texas, July 2001.
- [85] C.J. Jachimowski. An analysis of combustion studies in shock expansion tunnels and reflected shock tunnels. Technical Paper NASA TP-3224, NASA Langley Research Center, 1992.
- [86] E.L Resler and D.E. Boxsom. Very high Mach number principles by unsteady flow principle. *Cornell University Graduate School of Aerodynamic Engineering*, 1952.

- [87] H.L. Trimpli. A preliminary theoretical study of the expansion tube, a new device for producing high-enthalpy short duration hypersonic test gas flows. Technical Report R-133, NACA, 1962.
- [88] J.J. Jones and J.A. Moore. Exploratory study of performance of Langley pitot model expansion tube with a hydrogen driver. Technical Note D-3421, NASA, 1966.
- [89] J.A. Moore. Description and initial operating performance of the Langley 6-inch expansion tube using a heated helium driver. Technical Memorandum X-3240, NASA Langley Research Center, 1975.
- [90] C.G. Miller III and J.J. Jones. Development and performance of the NASA Langley research center expansion tube/tunnel, a hypersonic-hypervelocity real-gas facility. *14th International Symposium on Shock Waves*, Sydney, Australia, 1983.
- [91] I.A. Stringer. “TQ” free piston expansion tube - design and operation. Departmental Report 4/89, Department of Mechanical Engineering, University of Queensland, St. Lucia Qld 4072., 1989.
- [92] A.J. Neely, R.J. Stalker, and A. Paull. High enthalpy, hypervelocity flows of air and argon in an expansion tube. *Aeronautical Journal*, 1991.
- [93] A. Paull and R.J. Stalker. Test flow disturbances in an expansion tube. *Journal of Fluid Mechanics*, 245:493–521, 1992.
- [94] A. Paull and R.J. Stalker. Theoretical and experimental test times available in an expansion tube. *Tenth Australasian Fluid Mechanics Conference*, 1990.
- [95] C.M. Gourlay. Expansion tube test time predictions. Departmental Report 8/88, Department of Mechanical Engineering, University of Queensland, St. Lucia, Qld 4072., 1988.
- [96] C. Doolan. *A two-stage free-piston driver for hypervelocity expansion tubes*. PhD thesis, University of Queensland, St. Lucia, Australia, 1997.
- [97] M. Kendall. *A Study of high-enthalpy, entropy raising drivers for impulse facilities*. PhD thesis, University of Queensland, St. Lucia, Australia, 1998.
- [98] A. Brandis, R. Gollan, M.A. Scott, R.G. Morgan, P.A. Jacobs, and P. Gnoffo. Expansion tube operating conditions for studying nonequilibrium radiation relevant to Titan aerocapture. *42nd AIAA/ASME/SAE/ASEE Joint Propulsion Conference and Exhibit, Sacramento, California*, AIAA paper 2006-4517, December 2006.

- [99] C.J. Doolan and R.G. Morgan. Hypervelocity simulation in a new large scale experimental facility. *18th AIAA Ground Testing Conference*, Colorado Springs, AIAA paper 94-2492, June 1994.
- [100] R.G. Morgan. Development of X3, a superorbital expansion tube. *38th Aerospace Sciences Meeting and Exhibit*, AIAA paper 2000-0558, 2000.
- [101] J. Tamango, R. Bakos, M. Pulsonetti, and J. Erdos. Hypervelocity real gas capabilities of GASL's expansion tube (HYPULSE) facility. *16th AIAA Aerodynamic Ground Testing Conference*, Seattle, Washington, AIAA paper 90-1390, June 1990.
- [102] R.S.M. Chue, C.Y. Tsai, R.J. Bakos, J.I. Erdos, and R.C. Rogers. *Advanced Hypersonic Test Facilities*, volume 198 of *Progress in Astronautics and Aeronautics*, chapter 3: NASA's HYPULSE Facility at GASL - A Dual Mode, Dual Driver Reflected-Shock/Expansion Tunnel. AIAA, 2002.
- [103] I. Nompelis, G. Candler, and M. Holden. Numerical simulation of high-enthalpy experiments in the LENS X expansion tube facility. *42nd AIAA Aerospace Sciences Meeting and Exhibit*, Reno, Nevada, AIAA paper 2004-1000, 2004.
- [104] M.S. Holden, T.P. Wadhams, and G.V. Chandler. Experimental studies in the LENS shock tunnel and expansion tunnel to examine real-gas effects in hypervelocity flows. *42nd AIAA Aerospace Sciences Meeting and Exhibit*, Reno, Nevada, AIAA paper 2004-916, January 2004.
- [105] M.S. Holden, T.P. Wadhams, M. MacLean, and E. Mundy. Experimental studies in the LENS I and X to evaluate real gas effects on hypervelocity vehicle performance. *45th AIAA Aerospace Sciences Meeting and Exhibit*, Reno, Nevada, AIAA paper 2007-204, January 2007.
- [106] A. Sasoh, K. Ohnishi, K. Koremoto, and K. Takayama. Operation design and performance of a free piston driven expansion tube. *37th AIAA Aerospace Sciences Meting and Exhibition*, Reno, Nevada, AIAA paper 99-0825, January 1999.
- [107] A. Ben-Yakar and R.K. Hanson. Characterization of expansion tube flows for hypervelocity combustion studies. *AIAA Journal of Propulsion and Power*, 18(4):943–952, July-August 2002.
- [108] A. Dufrene, M. Sharma, and J.M. Austin. Design and characterization of a hypervelocity expansion tube facility. *45th AIAA Aerospace Sciences Meeting*, AIAA paper 2007-1327, January 2007.
- [109] H. Mirels. Shock tube test time limitation due to turbulent-wall boundary layer. *AIAA Journal*, 2(1):84–93, January 1964.

- [110] M. McGilvray, P.A. Jacobs, R.G. Morgan, and D. Ramanah. Boundary layer transition in an expansion tube at a low enthalpy operating condition. *45th AIAA Aerospace Sciences Meeting*, AIAA paper 2007-1328, January 2007.
- [111] M. McGilvray, R. G. Morgan, A. Paull, M.M. Abdel-Jawad, P. A. Jacobs, T. J. McIntyre, and M. A. Scott. Operating condition in UQ's impulse facilities for scramjet testing. *25th International Symposium on Shock Waves*, Bangalore, India, ISSW paper 1294-1a, July 2005.
- [112] R.G. Morgan. Personal Communication, 2007.
- [113] R.G. Morgan and R.J. Stalker. Double diaphragm driven expansion tube. *18th International Symposium on Shock Waves*, Sendai, Japan, 1991.
- [114] G.T Roberts, M.A. Kendall, and R.G. Morgan. Shock-diaphragm interaction in expansion tubes. *21st International Symposium on Shock Waves*, July 1997.
- [115] G.T Roberts, M.A. Kendall, and R.G. Morgan. Influence of secondary diaphragm influence on flow quality in expansion tubes. *Shock Waves*, pages 203–208, 1995.
- [116] T. Furukawa, T. Aochi, and A. Sasoh. Expansion tube operation with thin secondary diaphragm. *AIAA Journal*, 45(1):214–217, January 2007.
- [117] M. Wegener, M. Sutcliffe, and R.G. Morgan. Optical study of a light diaphragm rupture process in an expansion tube. *Shock Waves*, 10(3):167178, 2000.
- [118] C.G. Miller III. Operational experience in the Langley expansion tube with various gases and preliminary results in the expansion tunnel. *AIAA 9th Aerodynamic Conference*, Arlington, Texas, June 1976.
- [119] R.J. Stalker, A. Paull, and A.J. Neely. Comparative features of free piston shock tunnel and expansion tube facilities. *Tenth National Aero-Space Plane Technology Symposium*, April 1991.
- [120] R.J. Bakos and J.I. Erdos. Options for the enhancement of the performance of shock-expansion tubes and tunnels. *AIAA 33rd Aerospace Sciences Meeting*, AIAA paper 95-0799, January 1995.
- [121] R.J. Bakos, J.I. Calleja, A.H. Auslender, M.A. Sussman, and Wilson G.J. Design, calibration and analysis of a tunnel mode of operation for the HYPULSE facility. *19th AIAA Advanced Measurement and Ground Testing Conference*, AIAA paper 96-21964, June 1996.

- [122] F.K. Lu, R.J. Wilson, D.R. Bakos, and J.I. Erdos. Recent advances in detonation techniques for high-enthalpy facilities. *AIAA Journal*, 38(9):1676–1684, September 2000.
- [123] C.L. Liu, Z.M. Hu, D.L. Zhang, and Z. Jiang. Numerical simulations of forward driven detonation drivers for high enthalpy shock tunnel. *24th International Symposium on Shock Waves*, Beijing, China, July 2004.
- [124] H. Olivier, J. Zonglin, H.R. Yu, and F.K. Lu. *Advanced Hypersonic Test Facilities*, volume 198 of *Progress in Astronautics and Aeronautics*, chapter 6: Detonation-Driven Shock Tubes and Tunnels. AIAA, 2002.
- [125] R.J. Stalker. An investigation of the free piston compression of shock tube driver gas. Technical Report MT-44, Division of Mechanical Engineering, National Research Council, Canada, 1961.
- [126] H.L. Trimpi and T.J. Callis Jr. A perfect-gas analysis of the expansion tunnel, a modification to the expansion tube. Technical Report R-233, NACA, 1965.
- [127] F.S. Billig. Research on supersonic combustion. *AIAA Journal of Propulsion and Power*, 9(4):499–514, July-Aug 1993.
- [128] L.B. Callis Jr. An analysis of supersonic flow phenomena in conical nozzles by a method of characteristics. Technical Note D-3550, NASA, 1966.
- [129] R.S.M. Chue, R.J. Bakos, C.Y. Tsai, and A. Betti. The design of an expansion tunnel nozzle in HYPULSE. *23rd International Symposium on Shock Waves*, Fort Worth, Texas, July 2001.
- [130] P. A. Jacobs, T. B. Silvester, R. G. Morgan, M. P. Scott, R. J. Gollan, and T. J. McIntyre. Super-orbital expansion tube operation: Estimates of flow conditions via numerical simulation. *43rd AIAA Aerospace Sciences Meeting*, AIAA paper 2005-694, January 2005.
- [131] G.J. Wilson, M.A Sussman, and R.J. Bakos. Numerical simulations of the flow in the HYPULSE expansion tube. Technical Memorandum 110357, NASA, June 1995.
- [132] P.A. Jacobs. Numerical simulation of transient hypervelocity flow in an expansion tube. *Computers Fluids*, 23(1):77–101, 1994.
- [133] C.J. Doolan and P.A. Jacobs. Modeling mass entrainment in a quasi-one-dimensional model. *AIAA Journal*, 34(6), 1996.

- [134] M. Abdel-Jawad. *Stability assessment of planetary entry vehicles in the X3 super-orbital expansion tube*. PhD thesis, University of Queensland, St. Lucia, Australia, 2005.
- [135] R. Morgan, T. McIntyre, R. Gollan, P. Jacobs, A. Brandis, M. McGilvray, D. van Diem, P. Gnoffo, M. Pulsonetti, and M. Wright. Radiation measurements in non reflected shock tunnels. *36th AIAA Fluid Dynamics Conference and Exhibit*, San Francisco, AIAA 2006-2958, June 2006.
- [136] M.A. Sutcliffe and R.G. Morgan. The measurement of Pitot pressure in high enthalpy expansion tubes. *Journal of Measurement Science and Technology*, 19:327–334, 2001.
- [137] D.L. Shultz and T.V. Jones. Heat transfer measurements in short-duration hypersonic test facilities. AGARDograph 165, Department of Engineering Science, University of Oxford, Great Britain, 1973.
- [138] M. Hayne. The manufacture and mounting of thin film heat transfer gauges. Departmental Report 20/2003, Department of Mechanical Engineering, University of Queensland, St. Lucia, Qld 4072., 2003.
- [139] P.A. Jacobs. Databox manager: Device driver and user interface program. Departmental Report 14/2004, Department of Mechanical Engineering, University of Queensland, St. Lucia Qld 4072., 2004.
- [140] P.A. Jacobs. MB_CNS: A computer program for the simulation of transient compressible flow. Departmental Report 10/96, Department of Mechanical Engineering, University of Queensland, St. Lucia, Qld 4072., 1996.
- [141] F. Zander, P. Teakle, and R.G. Morgan. Automated manufacture of composite aerospace components at the UQ Centre for Hypersonics. *5th Australian Space Sciences Conference*, Melbourne, Australia, 2005.
- [142] R.G. Morgan. *Handbook of Shock Waves*, eds Ben-Dor, G., Igra, O. and Elperin, T., volume 1, chapter 4.3: Shock Tubes and Tunnels: Facilities, Instrumentation, and Techniques, Free Piston Driven Expansion Tubes, pages 603–622. Academic Press, San Diego, 2001.
- [143] P.A. Jacobs. Shock tube modelling with L1d. Departmental Report 13/98, Department of Mechanical Engineering, University of Queensland, St. Lucia Qld 4072., 1998.
- [144] Ames Research Staff. Equations, tables and charts for compressible flow. Technical Report 1135, NACA, 1953.

- [145] B.J. McBride and S. Gordon. Computer program for calculation of complex chemical equilibrium compositions and applications II. Users manual and program description. Reference Publication 1311, NASA, 1996.
- [146] R. Gollan, A. Denman, and M. Hankel. Clustering Is Not Rocket Science. *Linux Journal*, 28th August 2006.
- [147] B. Baldwin and H. Lomax. Thin-layer approximation and algebraic model for separated flows. *16th AIAA Aerospace Sciences Meeting*, AIAA paper 78-257, January 1978.
- [148] S.A. McKell. *Numerical simulation of the transition region in hypersonic flow*. PhD thesis, Virginia Polytechnic Institute and State University, Blacksburg, Virginia, USA., 1996.
- [149] S.P. Sharma and G.J. Wilson. Computations of axisymmetric flows in hypersonic shock tubes. *AIAA Journal of Thermophysics and Heat Transfer*, 10(1):169–176, 1996.
- [150] H. Mirels. Boundary layer behind a shock or thin expansion wave moving into a stationary fluid. Technical Note 3712, NACA, 1956.
- [151] E.L. Peterson and R.K. Hanson. Improved turbulent boundary-layer model for shock tubes. *AIAA Journal*, 41(7):1314–1322, 2003.
- [152] T. Cebeci and A.M.O. Smith. Analysis of turbulent boundary layers. *Academic Press, New York*, 1974.
- [153] T.J. McIntyre, M.J. Wegener, A.I. Bishop, and H. Rubinsztein-Dunlop. Simultaneous two-wavelength holographic interferometry in a superorbital expansion tube facility. *Applied Optics*, 36(31):8128–8134, 1997.
- [154] H. Kleine. *Handbook of Shock Waves*, eds Ben-Dor, G., Igra, O. and Elperin, T., volume 1, chapter 5.1 Measurement Techniques and Diagnostics: Flow Visualization, pages 683–740. Academic Press, San Diego, 2001.
- [155] M.J. Robinson, S.A. Rowan, and J.. Odam. T4 free piston shock tunnel operator's manual. Departmental Report 1/2003, Department of Mechanical Engineering, University of Queensland, St. Lucia Qld 4072., 2003.
- [156] ASCO valves. ASCO pilot operated solenoid valve. <http://www.ascovalve.com>, 2006.
- [157] R.J. Stalker and R.G. Morgan. The University of Queensland free piston shock tunnel T4 - initial operation and preliminary calibration. *4th National Space Engineering Symposium*, Adelaide, Australia, June 1988.

- [158] E.T. Curran. Scramjet engines: The first forty years. *AIAA Journal of Propulsion and Power*, 17(6):1138–1148, November-December 2001.
- [159] E.T. Curran, W.H. Heiser, and D.T. Pratt. Fluid phenomena in scramjet combustion systems. *Annual Review of Fluid Mechanics*, 28:323–360, 1996.
- [160] G.B. Northem and G.Y. Anderson. Supersonic combustion ramjet research at Langley. *24th AIAA Aerospace Sciences Meeting*, Reno, Nevada, AIAA paper 86-0159, January 1986.
- [161] A. Ferri. Review of scramjet propulsion technology. *Journal of Aircraft*, 5(1):3–10, 1968.
- [162] R.J. Stalker, A. Paull, R.G. Mee, D.J. Morgan, and P.A. Jacobs. Scramjets and shock tunnels: The Queensland experience. *Progress in Aerospace Sciences*, 41:471–513, 2005.
- [163] M.K. Smart, N.E. Hass, and A. Paull. Flight data analysis of the HyShot 2 scramjet flight experiment. *AIAA Journal*, 44(10):2366–2375, October 2006.
- [164] V. Rausch, C. McClinton, and J. Sitz. Hyper-X program overview. *Proceedings of the 14th International Symposium on Air Breathing Engines*, ISABE paper 99-7213, September 1999.
- [165] S. Walker and F. Rodgers. The Hypersonic Collaborative Australia/United States Experiment (HyCAUSE). *13th AIAA/CIRA International Space Planes and Hypersonic Systems and Technologies Conference*, Capua, Italy, AIAA paper 2005-3254, May 2005.
- [166] E.T. Curran, J.L. Leinang, L.R. Carreiro, and D.P. Petters. Further studies of kinetic energy methods in high speed ramjet cycle analysis. *28th Joint Propulsion Conference*, Nashville, Tennessee, AIAA paper 92-3805, July 1992.
- [167] P.J. Waltrup, F.S. Billig, and R.D. Stockbridge. A procedure for optimizing the design of scramjet engines. *AIAA Journal of Spacecraft and Rockets*, 16(3):163–171, 1979.
- [168] H. Ikawa. Rapid methodology for design and performance prediction of integrated supersonic combustion ramjet. *AIAA Journal of Propulsion and Power*, 7(3):437–444, May-June 1991.
- [169] J.L. Kerrebrock. Some readily quantifiable aspects of scramjet performance. *AIAA Journal of Propulsion and Power*, 8(5):1116–1122, Sept.-Oct. 1992.

- [170] D.W. Riggins, C.R. McClinton, and P.H. Vitt. Thrust losses in hypersonic engines part 1: Methodology. *AIAA Journal of Propulsion and Power*, 13(2):281–287, March-April 1997.
- [171] M.J. Lewis. Significance of fuel selection for hypersonic vehicle range. *AIAA Journal of Propulsion and Power*, 17(6):1214–1221, November-December 2001.
- [172] M.R. Tetlow and C.J. Doolan. Comparison of hydrogen and hydrocarbon-fueled scramjet engines for orbital insertion. *AIAA Journal of Spacecraft and Rockets*, 44(2), March-April 2007.
- [173] C.J. Jachimowski. An analytical study of the hydrogen-air reaction mechanism with application to scramjet combustion. Technical Paper 2791, NASA Langley Research Center, 1988.
- [174] H.S. Pergament. A theoretical analysis of non-equilibrium hydrogen-air reactions in flow systems. *AIAA/ASME Hypersonic Ramjet Conference*, 63113, 1963.
- [175] M.K. Smart. Optimization of two-dimensional scramjet inlets. *AIAA Journal of Aircraft*, 36(2):430–433, March-April 1999.
- [176] M.K. Smart. Design of three-dimensional hypersonic inlets with rectangular-to-elliptical shape transition. *AIAA Journal of Propulsion and Power*, 15(3):408–416, May-June 1999.
- [177] M.K. Smart. Calculation of stream-traced hypersonic inlet performance on and off design. *21st International Symposium on Shock Waves*, Great Keppel Island, Australia, July 1997.
- [178] H.D. Atkins. Numerical and analytical study of inlet processes in a shock tunnel environment. *AIAA conference*, AIAA paper 88-0601, 1988.
- [179] A. Kantrowitz and C. Donaldson. Preliminary investigation of supersonic diffusers. Technical Report ACR L5D20, NACA, 1945.
- [180] R.J. McGregor, S. Molder, and T.W. Paisley. Hypersonic inlet flow starting in the Ryerson/University of Toronto gun tunnel, *Investigations of Scramjet Inlets*. Technical report, Ryerson Polytechnical University and University of Toronto, Canada, July 1992.
- [181] R. H. Korkegi. Comparison of shock-induced two and three dimensional incipient turbulent separation. *AIAA Journal*, 13(4):534–535, April 1975.
- [182] R. H. Korkegi. A lower bound for three-dimensional turbulent seperation in super-sonic flow. *AIAA Journal*, 23(2):475–476, March 1985.

- [183] A. Dann, A. Denman, P. Jacobs, and R.G. Morgan. Study of separating compressible turbulent boundary layers. *AIAA/AHI 14th International Space Planes and Hypersonics Systems and Technologies Conference*, Canberra, Australia, AIAA paper 2006-7943, November 2006.
- [184] F.S. Billig. Shock wave shapes around spherical and cylindrical nosed bodies. *AIAA Journal of Spacecraft and Rockets*, 4(6):822–823, June 1967.
- [185] W.E. Moeckel. Some effects of bluntness on boundary-layer transition and heat transfer. Technical Report 1312, NACA, 1957.
- [186] G.Y. Anderson. An examination of injector/combustor effects on scramjet performance. *ISABE conference*, Sheffield, England, 1972.
- [187] D.W. Riggins, C.R. McClinton, R.C. Rogers, and R.D. Bittner. Investigation of scramjet injection strategies for high Mach number flows. *AIAA Journal of Propulsion and Power*, 11(3):409–418, May-June 1995.
- [188] J.M. Seiner, S.M. Dash, and D.C. Kenzakowski. Historical survey on enhanced mixing in scramjet engines. *AIAA Journal of Propulsion and Power*, 17(6):1273–1286, November-December 2001.
- [189] R.P. Fuller, P. Wu, A.S. Nejad, and J.A. Schetz. Comparison of physical and aerodynamic ramps as fuel injectors. *AIAA Journal of Propulsion and Power*, 14(2):135–145, March-April 1998.
- [190] C.R. McClinton. The effect of injection angle on the interaction between sonic and secondary jets and a supersonic free stream. Technical Note D-6669, NASA, 1978.
- [191] R. Portz and C. Segal. Penetration of gaseous jets in supersonic flow. *AIAA Journal*, 44(10):2426–2429, October 2006.
- [192] R.C. Rogers. Mixing of hydrogen injected from multiple injectors normal to a supersonic airstream. Technical Note D-6476, NASA, 1971.
- [193] D.R. Buttsworth. Interaction of oblique shock waves and planar mixing regions. *Journal of Fluid Mechanics*, 306:43–57, 1996.
- [194] A.D. Gardiner, A. Paull, and T.J. McIntyre. Upstream porthole injection in a 2D scramjet model. *Shock Waves*, 11:369–375, 2002.
- [195] A Kovachevich, A Paull, and McIntyre TJ. Investigation of an intake injected hot-wall scramjets. *42nd AIAA Aerospace Sciences Meeting and Exhibit*, Reno, Nevada, AIAA paper 2004-1037, January 2004.

- [196] L.J. Charns and D.J. Collins. Stagnation temperature and molecular weight effects in jet interaction. *AIAA Journal*, 8(2):287–293, 1970.
- [197] J. Odam. *Scramjet experiments using radical farming*. PhD thesis, University of Queensland, St. Lucia, Australia, 2004.
- [198] J.C. Turner and M.K. Smart. Experimental investigation of inlet injection in a scramjet with rectangular to elliptical shape transition. *26th International Symposium on Shock Waves*, Gottingen, Germany, 2007.
- [199] M.V. Suraweera and M.K. Smart. Shock tunnel experiments with a Mach 12 REST scramjet at off-design conditions. *46th AIAA Aerospace Sciences Meeting*, January 2008.
- [200] M.V. Suraweera, D.J. Mee, and R.J. Stalker. Skin friction reduction in hypersonic turbulent flow by boundary layer combustion. *43rd AIAA Aerospace Sciences Meeting*, AIAA paper 2005-613, January 2005.
- [201] R.G. Morgan and F. Zander. Radiatively cooled scramjet combustor. *26th International Symposium on Shock Waves*, Gottingen, Germany, 2007.
- [202] A.R. Wieting. Multiple shock-shock interference on a cylindrical leading edge. *AIAA Journal*, 30(8):2073–2079, 1992.
- [203] M.P. Podesta. *Understanding the Properties of Matter*. CRC Press, 2nd edition, 2002.
- [204] M. Frost and A. Paull. Mach 10 T4 scramjet model drawings. Personal Communication, 2005.
- [205] R.J. Stalker. Thermodynamics and wave processes in high Mach number propulsive ducts. *27th AIAA Aerospace Sciences Meeting*, AIAA paper 89-0261, January 1989.
- [206] F.M. White. *Fluid Mechanics*. McGraw Hill, Boston, fourth edition, 1999.
- [207] J.C. Turner. Personal Communication, 2007.
- [208] D. Mee. Uncertainty analysis of the conditions in the test section of the T4 shock tunnel. Departmental Report 4/93, Department of Mechanical Engineering, University of Queensland, St. Lucia, QLD, 4067, 1993.
- [209] N. Takashima, B.R. Hollis, E.V. Zoby, K. Sutton, J. Olejiniczak, M. Wright, and D. Prabhu. Preliminary aerothermodynamics of Titan aerocapture aeroshell. *39th AIAA/ASME/SAE/ASEE Joint Propulsion Conference and Exhibit, Huntsville, Alabama*, AIAA paper 2003-4952, 2003.

- [210] G.B. Whitham. *Linear and Nonlinear waves*. Wiley, 1974.
- [211] Baby Gee J. Morgan. *Lessons on removing rotten dead animals for any weary boyfriends*. PhD thesis, University of Queensland, St. Lucia, Australia, 2005.

APPENDIX A

Perfect Gas Theory for an Expansion Tube

The analytical calculations of an expansion tube using q perfect gas assumption is the same as a shock tube. These were used in evaluating an expansion tube, made by Trimpf [87]. The form of the equations used in work in this thesis are formulated here. These make use of the compressible flow equations from John [27] and the Ames research group [144]. These were used to predict the flow conditions shown in Figure A.1 using the fill conditions as an input for the calculations. This required the Mach number to be iteratively predicted until the constraint that the static pressure must be the same in the shocked test gas and the expanded driver gas.

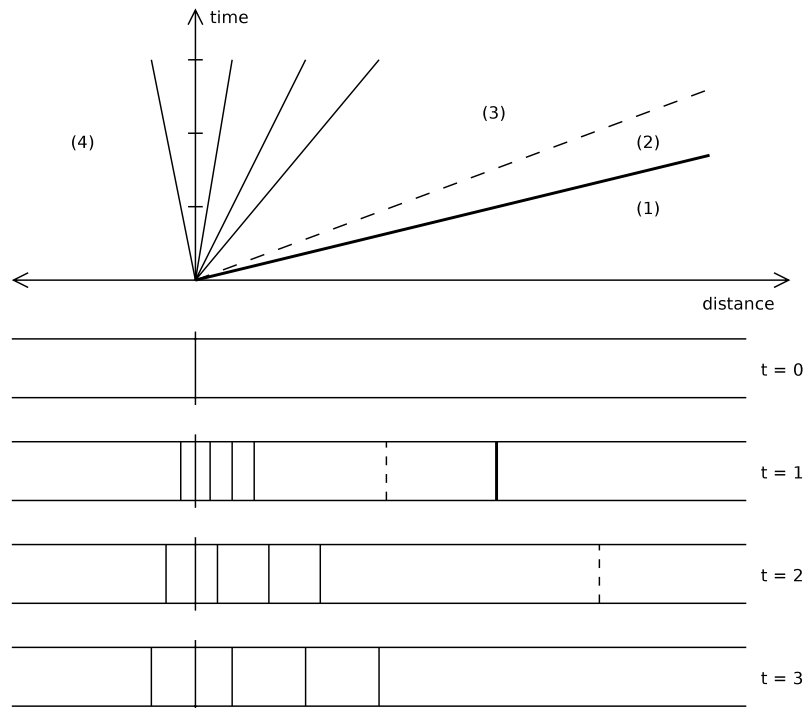


Figure A.1: Wave diagram for a shock tube.

A.1 Shock Tube

To calculate the flow properties, two constraints are placed that the pressure and velocity must be equal in the expanded driver gas and the shocked test gas ($U_2 = U_3$ and $p_2 = p_3$). Firstly looking at a shock passing through the tube as an observer, so that the tube is stationary and the shock passes down the tube is known as the lab frame of reference. This is seen in Figure A.2. As the formulation of the equations for a shock wave are usually in the form of a shock steady frame of reference, were the shock is stationary. Thus, stagnate gas in region 1 is given a velocity of equal to that of the shock and the shock processed gas now travels in the opposite direction at a speed equal to the difference of the shock speed and its lab frame speed. All other flow properties remain unchanged.

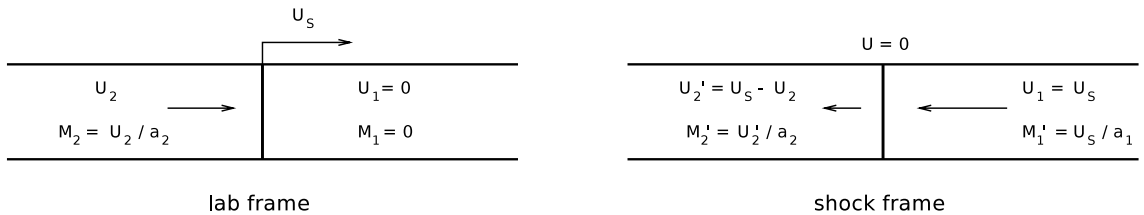


Figure A.2: Reference frames for a shock wave passing through a stagnate gas.

The Mach number after the shock in the shock steady reference (M'_2) can be formulated from the shock speed change across a shock.

$$M'_2 = \left\{ \frac{1 + \frac{\gamma_1 - 1}{2} M_s^2}{\gamma_1 M_s^2 - \frac{\gamma_1 - 1}{2}} \right\}^{\frac{1}{2}} \quad (\text{A.1})$$

The sound speed ratio across the shock is given by

$$\frac{a_2}{a_1} = \left(\frac{T_2}{T_1} \right)^{\frac{1}{2}} = \left\{ 1 + \frac{2(\gamma_1 - 1)}{(\gamma_1 + 1)^2} \frac{(\gamma_1 M_s^2 + 1)}{M_s^2} (M_s^2 - 1) \right\}^{\frac{1}{2}} \quad (\text{A.2})$$

Using these two equations (Equations A.1 and A.2) the velocity can be found for the shocked test gas

$$U_2 = U_s - U'_2 = M_s a_1 - M'_2 a_2 = M_s a_1 - M'_2 \left(\frac{a_2}{a_1} \right) a_1 \quad (\text{A.3})$$

The pressure rise through a shock is given by

$$\frac{p_2}{p_1} = \frac{2\gamma_1 M_s^2 - (\gamma_1 - 1)}{\gamma_1 + 1} \quad (\text{A.4})$$

Now looking at an unsteady expansion, $a + \frac{\gamma-1}{2}U$ must remain constant through the entire expansion. Therefore equating this for properties in regions 3 and 4, a rearrangement can give the equation for the sound speed ratio across the unsteady expansion fan. It can be noted that the velocity from the shocked test gas can be used here as $U_2 = U_3$

$$\frac{a_3}{a_4} = 1 + \left(\frac{\gamma_2 - 1}{2} \right) \frac{(U_4 - U_3)}{a_4} \quad (\text{A.5})$$

U_4 will equal zero if stagnated, as is the case across the primary diaphragm but will be equal to shocked test gas velocity across the secondary diaphragm. As the unsteady expansion is an Isentropic process, the pressure ratio across it can be calculated from the sound speed ratio

$$\frac{p_3}{p_4} = \left(\frac{a_3}{a_4} \right)^{\frac{2\gamma_2}{\gamma_2 - 1}} \quad (\text{A.6})$$

Therefore, for a given shock speed the ratio of the two fill pressures can be calculated, as $p_2 = p_3$.

$$\frac{p_4}{p_1} = \left(\frac{p_4}{p_3} \right) \left(\frac{p_2}{p_1} \right) \quad (\text{A.7})$$

A.2 Shock tube with Area Change

An area change is often used at the primary diaphragm to increase the performance of the driver. The wave diagram for this can be seen in Figure A.3. This will only consider the case where the flow is stagnated in region 4. The driver gas undergoes a steady expansion to Mach 1 at the throat. A weak $U - a$ wave is seen to propagate through the stagnated driver gas, but this can be ignored as the change in total pressure and temperature is negligible. From the throat, where the Mach number is 1, the flow can be calculated in the same way shown for a constant area tube.

The sound speed ratio across an unsteady expansion for a constant area ratio shock tube (Equation A.5) can be rewritten for starting from Mach 1 at for region 3'.

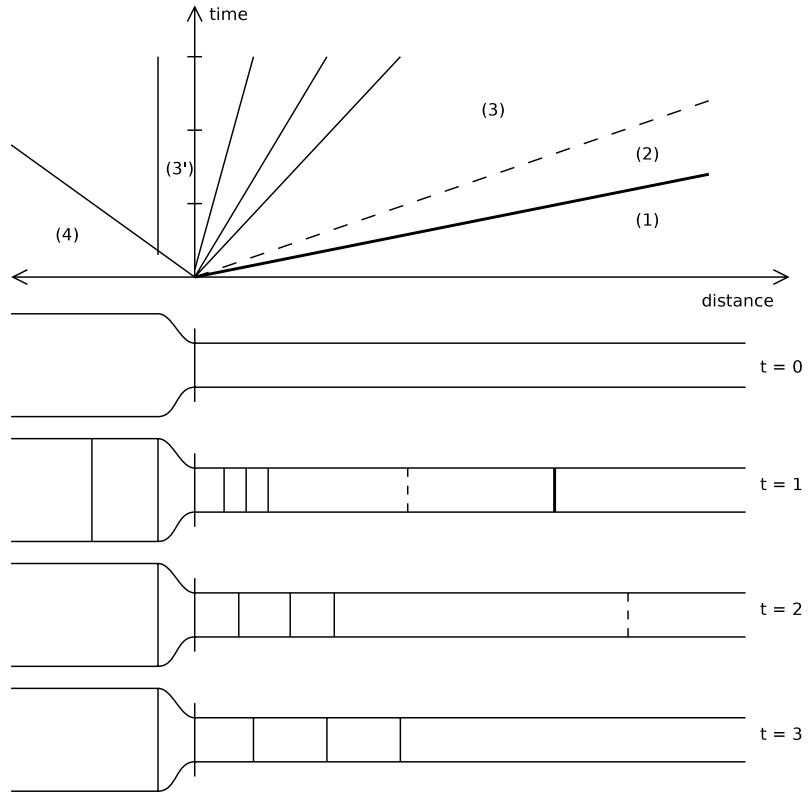


Figure A.3: Wave diagram for a shock tube with an area change at the primary diaphragm.

$$\frac{a_3}{a'_3} = 1 + \left(\frac{\gamma_2 - 1}{2} \right) \left(1 - \frac{U_3}{a'_3} \right) \quad (\text{A.8})$$

As in the constant area shock tube the process is Isentropic, so therefore the pressure ratio will be

$$\frac{p_3}{p'_3} = \left(\frac{a_3}{a'_3} \right)^{\frac{2\gamma_2}{\gamma_2 - 1}} \quad (\text{A.9})$$

The steady expansion process from the stagnated driver gas is also assumed to be isentropic. Therefore, knowing the Mach number is 1 in region 3' the sound speed ratio can be calculated

$$\frac{a'_3}{a_4} = \left(1 + \frac{\gamma_2 - 1}{2} M_3'^2 \right)^{-\frac{1}{2}} = \left(\frac{\gamma_2 + 1}{2} \right)^{-\frac{1}{2}} \quad (\text{A.10})$$

Therefore the pressure ratio can be calculated using the sound speed ratio

$$\frac{p'_3}{p_4} = \left(\frac{a'_3}{a_4} \right)^{\frac{2\gamma_2}{\gamma_2-1}} = \left(\frac{\gamma_2+1}{2} \right)^{\frac{-\gamma_2}{\gamma_2-1}} \quad (\text{A.11})$$

Therefore the pressure ratio for the driver gas from stagnation to the expanded gas can be derived from Equations A.9 and A.11.

$$\frac{p_4}{p_3} = \left(\frac{p_4}{p'_3} \right) \left(\frac{p'_3}{p_3} \right) \quad (\text{A.12})$$

Gas Buffer Simulation

A simple one dimensional model was taken by Lynch [19] for the piston dynamics, gas trap and pressure relief valves. The gas is assumed to both compress and expand isentropically in this analysis. This analysis uses gas dynamic equations taken from [27, 144, 206]. The simulation starts with the piston inserted into the gas trap (as shown in Figure 4.5). It then takes small time steps and redetermines all the parameters of the simulation.

B.1 Pressure Relief Valve

A simple model was taken of the pressure relief valve as shown in Figure B.1, whereby the flow through is assumed to be all in the axial direction before the dotted line and in the radial direction afterwards. This simplification permits the use of simple analytical tools to calculate the flow properties through the valve.

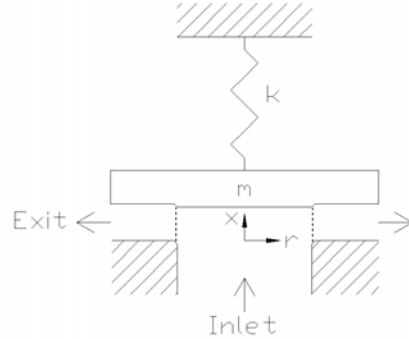


Figure B.1: Schematic of pressure relief valve. Adapted from [19].

The valve is assumed to be choked flow, with the throat situated at the dotted line. Therefore the mass flow rate passing through the valve is given by

$$\dot{m}_v = \gamma^{\frac{1}{2}} \left(\frac{2}{\gamma + 1} \right)^{\frac{\gamma+1}{2(\gamma-1)}} \frac{p_0 A^*}{\sqrt{RT_0}} \quad (\text{B.1})$$

where the throat area is

$$A^* = 2\pi R_i x \quad (\text{B.2})$$

The force acting on the disc can be broken into two terms seen in Equation B.3. The first is the force on the central part of the disc whether it is open or closed due to stagnation. Once the valve is opened, the second term is the force on the outer part of the disc which is dependant on how much the gas expands.

$$F_v = p_0 \pi R_i^2 + \int_{R_i}^{R_o} 2\pi p(r) dr \quad (\text{B.3})$$

To determine the pressure across the outside of the disc as the gas accelerates from stagnation, the following equation of Isentropic expansion can be used where Mach number can be found using the area ratio at each point.

$$p = \frac{p_0}{\left(1 + \frac{\gamma-1}{2} M^2\right)^{\frac{\gamma}{\gamma-1}}} \quad (\text{B.4})$$

The position of the valve from the buffer can therefore be determined quite easily for a given spring constant, K , and pre-compression c using Equation B.5. This will be zero while the force on the valve, F_v , is less than $K \times c$.

$$x_v = \frac{F}{K} - c \quad (\text{B.5})$$

B.2 Primary Piston

The model for the piston assumes frictionless movement with the only force acting on the piston is due to the build of pressure in front of it. This is justified as the pressure behind the piston at this stage of the compression process is quite low as most of its work has been transferred to the pistons. The force on piston can be written as

$$F_p = p_0 A_p \quad (\text{B.6})$$

where the pistons acceleration, velocity and displacement can be determined by

$$a_p = \frac{F_p}{m_p} \quad (\text{B.7})$$

$$U_p = U_0 - \int a_p(t) dt \quad (\text{B.8})$$

$$x_p = \int U_p(t) dt \quad (\text{B.9})$$

B.3 Gas Trap

The gas slug trapped between the piston is isentropically compressed by the piston therefore reducing its volume at each time step by $A_p \int U_p(t)dt$ from the starting length L . However there is mass leakage both through the clearance around the secondary piston and through the pressure relief valves. The mass flow rate through the clearance m_c is also assumed to be choked and therefore determined by Equation B.1, where the area is taken to be the clearance area A_c . The overall mass in the gas trap is

$$m = \frac{p_0 A_p L}{RT_0} - \int (\dot{m}_v + \dot{m}_c) dt \quad (\text{B.10})$$

The stagnation pressure can be determined from the volume V by

$$p_0 = \frac{mRT_0}{V} \quad (\text{B.11})$$

and the stagnation temperature from the enthalpy of the gas

$$H = c_p T_0 \quad (\text{B.12})$$

$$= m c_v T_{0,i-1} + \int p_0 dV \quad (\text{B.13})$$

APPENDIX C

Fuel System Calibration

Before conducting a series of tests with fuel injection, the fuel valve has to be calibrated so that the mass flow rate of fuel can be calculated. Full details of the theory involved can be found in the report by Pulsonetti [46].

The theoretical mass flow rate of fuel, \dot{m}_{H_2} , of specific heat, γ , and gas constant, R , at a Mach number of M through a nozzle of cross-sectional area, A , from a reservoir (the Ludewig tube) at pressure, P , and temperature, T , is given by,

$$\dot{m}_{H2} = \sqrt{\frac{\gamma}{R} \left\{ 1 + \frac{\gamma - 1}{2} M^2 \right\}^{\frac{\gamma+1}{\gamma-1}}} \frac{p}{\sqrt{T}} A M. \quad (\text{C.1})$$

Assuming choked flow through the nozzle throat and an Isentropic expansion of the fuel in the Ludewig tube, Equation C.1 can be modified to,

$$\dot{m}_{H_2} = \sqrt{\frac{\gamma}{R} \left\{ \frac{2}{\gamma + 1} \right\}^{\frac{\gamma+1}{\gamma-1}} \frac{A^*}{\sqrt{T_{lud,i}}} p_{lud,i} \left\{ \frac{p_{H_2}}{p_{lud,i}} \right\}^{\frac{\gamma+1}{2\gamma}}}, \quad (\text{C.2})$$

where,

A^* effective area of the throat of the nozzle,

$p_{lud,i}$ initial pressure in the Ludewig tube,

p_{H_2} measured fuel pressure after expansion of the fuel during test time,

$T_{lud,i}$ measured initial temperature in the Ludewig tube.

Typically, this is written as,

$$\dot{m}_{H_2} = \alpha p_{lud,i} \left\{ \frac{p_{H_2}}{p_{lud,i}} \right\}^{\frac{\gamma+1}{2\gamma}} = \alpha p_{lud,i} p_{H_2}^{\frac{\gamma-1}{2\gamma}}, \quad (\text{C.3})$$

where,

$\alpha = \sqrt{\frac{\gamma}{R} \left\{ \frac{2}{\gamma+1} \right\}^{\frac{\gamma+1}{\gamma-1}}} \frac{A^*}{\sqrt{T_{lud,i}}}$, and is obtained from calibration of the fuel injectors.

In an injection calibration test, the fuel valve is opened for a short period of time and the initial pressure and temperature in the Ludewig tube, the final pressure in the Ludewig tube and the time history of P_{H_2} are measured. Since only \dot{m}_{H_2} and P_{H_2} vary with time,

Equation C.3 can be integrated and the mass flow rate of fuel replaced with the quantity $\frac{p_{lud}V_{lud}}{RT_{lud}}$ from the ideal gas law $PV = mRT$ where m is the mass unit. Hence,

$$\alpha = \frac{(p_{lud,f} - P_{lud,i})V_{lud}}{RT_{lud}p_{lud,i}^{2/\gamma} p_{int,H_2}}, \quad (\text{C.4})$$

where,

- $p_{lud,f}$ is the final Ludewig pressure,
- $p_{lud,i}$ is the initial Ludewig pressure,
- R is the gas constant of fuel (for H_2 , $R = 4127 \text{ J/(kg.K)}$),
- t_f is the final time,
- t_i is the initial time, and
- p_{int,H_2} is equal to $\int_{t_i}^{t_f} p_{H_2}^{\frac{\gamma+1}{2\gamma}} dt$
- V_{lud} is the volume of the Ludewig tube.

Uncertainty Analysis

D.1 Uncertainty in X2 Flow Properties

Uncertainty occurs in both the prime experimental measurements and numerical simulations presented for the X2 facility. Numerical simulations rely upon inputs such as fill pressures and fill temperatures which are secondary experimental measurement. Hayne [6], conducted a thorough uncertainty analysis on experimental measurements and numerical simulations of the X2 facility. This was based upon the original work of Doolan [96] and used the guidelines presented by Mee [208]. This was conducted for both a sub orbital conditions and a super orbital condition, therefore the lower speed sub-orbital uncertainties are presented here.

Prime experimental measurements are both primary and secondary shock speeds, static pressure in the shock tube and acceleration tube, pitot pressure in the test section and test time. The shock speed is reliant on both the accuracy of the timing of the shock arrival and the distances between the sensors. Flush wall mounted pressure transducers are used to define the time of shock arrival. Electrical noise, vibrations caused by stress waves in the facility and rise time of the sensors can lead to inaccuracies in this measurement. With these factors, the shock timing accuracy was estimated to be $\pm 2\%$. As shown in Section 5.1, the distance between transducers is variable. Overall a level of $\pm 0.5\%$ is given by Hayne as the accuracy of the distances between the sensors. Therefore, the nominal accuracy of the shock speed measurement is $\pm 2.5\%$. The time is given a base inaccuracy of $30 \mu s$ in both the numerical and experimental measurements, as both have microsecond resolution of data and require human estimation of the time period.

Both static and pitot pressure measurements use the same type of gauges, although the mounting is different they will be considered together. The pressure measurements have both a calibration uncertainty and also a mounting uncertainty. These were estimated by Hayne to be $\pm 1\%$ and $\pm 4\%$ respectively. Therefore the overall accuracy of the pressure measurements were estimated to be $\pm 7\%$.

As numerical simulation use physical quantities as inputs, the inaccuracies of these on the final flow quantities can vary. These secondary experimental measurements include fill pressures of each section, initial temperatures, tube dimensions, diaphragm burst pressures and hold times. To judge the effect of each of these on the final flow quantity the least

squares method is used. That is, the uncertainty of a final property is related to the gradient of final quantity to each input through Equation D.1. The sensitivities of each can be found by initially perturbing the simulation and checking the end quantities. Using Haynes values for this, the final uncertainties for each variable can be seen in Table D.1.

$$X_f = \sqrt{\left(\frac{\partial X_f}{\partial X_{\phi_1}}\right)^2 (X_{\phi_1})^2 + \left(\frac{\partial X_f}{\partial X_{\phi_2}}\right)^2 (X_{\phi_2})^2 + \dots + \left(\frac{\partial X_f}{\partial X_{\phi_n}}\right)^2 (X_{\phi_n})^2} \quad (\text{D.1})$$

Table D.1: Relative uncertainties in derived flow quantities. Taken from [6].

Property	Uncertainty ($\pm\%$)
Shock Speed	0.5
Static Pressure	12.8
Pitot Pressure	15.1
Mach Number	4.2
Density	12.9
Static Temperature	5.9
Velocity	3.2
Stagnation Enthalpy	7.4
Unit Reynolds number	12.4

D.2 Uncertainty in Scramjet Pressure Measurements

The effects of combustion are indicated through measurements on pressure sensors with quantified accuracy. Each individual pressure measurement will have an associated uncertainty due to the confidence in calibration, recording and mounting. As they are flush mounted and are similar transducers to those used in the X2 facility, the uncertainty is as presented in Section D.1 of $\pm 7\%$. When normalised pressures are used, uncertainty is present in both the normalising sensor and the local measurement, where the total uncertainty in the actual measurement technique (X_{meas}) will be given by the root mean squares. Therefore, the error due to the measurement technique for the normalised static pressure at each location is $\pm 10\%$ being the combined uncertainty in the normalising sensor and the direct measurement of interest.

Uncertainty is also introduced by presenting the average of a turbulent fluctuating signal over a finite sample period. The uncertainty due to sampling the mean over a certain period can be calculated for a 95% confidence level, using twice the standard deviation over the measurement period ($X_\sigma = 2\sigma$). As a worse case, this uncertainty will be treated as being independent of the other sources discussed. With the time taken (being

quite small at $10 \mu\text{s}$) due to the normalisation procedure of the quasi-steady analysis used for the transient inflow, can be quantified. An example of the normalised pressure used for a gas slug is shown in Figure D.1. This shows, that although there is a rise in the pressure over the test period, the 2σ band encloses this already. This will give a greater uncertainty than may be present in the flow.

An additional uncertainty is introduced by using the slug tracking normalisation method, as the timing of the slug as it travels through the engine must be accurately defined. However, this is a second order effect, as minor errors in speed are only coupled through temporal gradients which are much less than the convective terms. As the method assumes a constant velocity where the flow has minor axial velocity perturbations, some error is present. Using the computational analysis of the scramjet with transient inflow in Section 7.3.2, the error in pressure due to changes in the normalisation velocity was shown to be reasonably small ($< 5\%$). The uncertainty in the normalisation velocity for the experiment was estimated to be $\pm 200 \text{ m/s}$. The uncertainty level in the normalised pressure due to this ($X_{U_{norm}}$), is accounted for by the maximum deviation at any axial location of the normalised pressure with the perturbed normalisation velocity to the nominal normalised pressure.

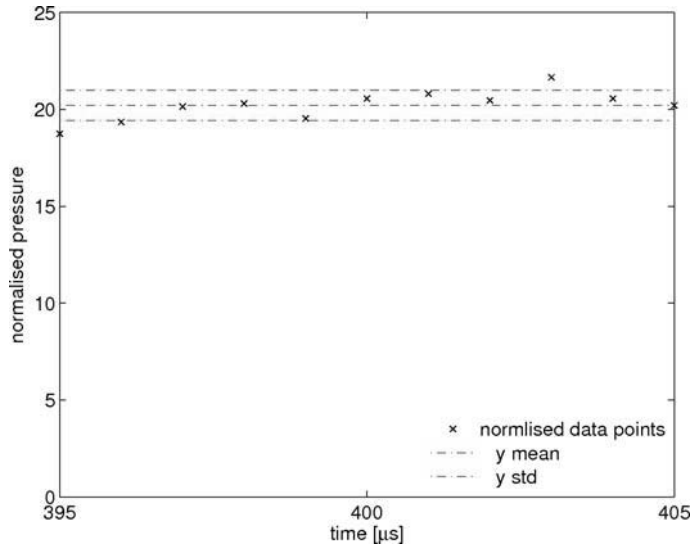
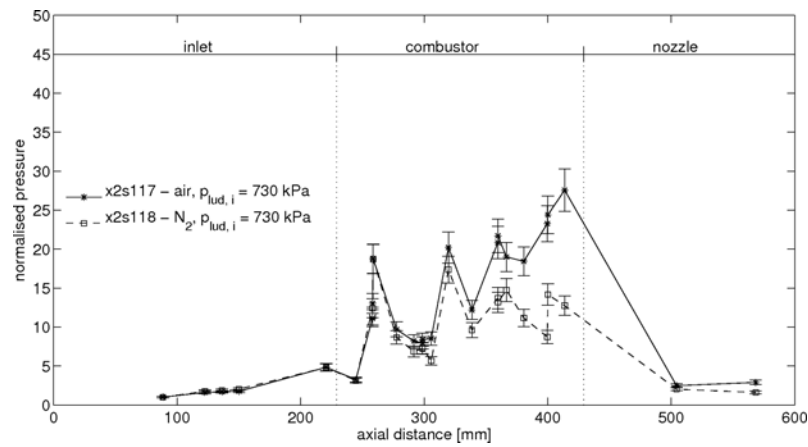


Figure D.1: Example of normalised pressure data points over the measurement period. Taken for transducer location CO_6C_15 for x2s117.

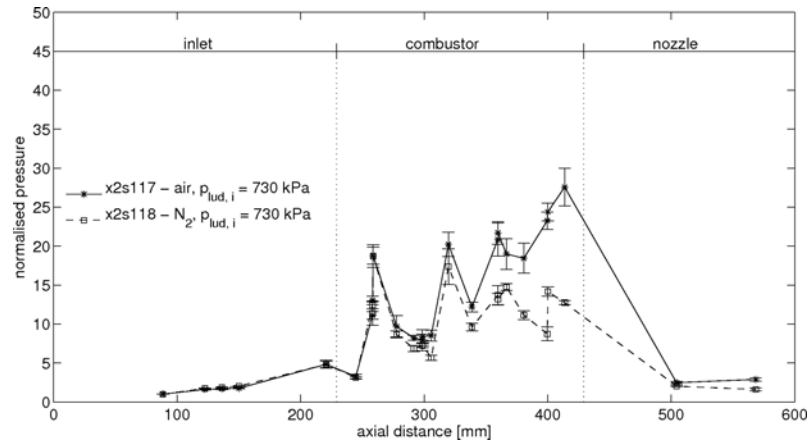
A test case is taken for where combustion effects are investigated, using the data presented for an initial Ludwieg fill pressure of 730 kPa at $400 \mu\text{s}$. The data for this is presented in the main text in Figure 8.13. Calculations of the uncertainties due to the individual measurement, finite sampling time and normalisation velocity are shown in Figure D.2. The error due to individual measurement is seen to be the greatest source of uncertainty in the engine. Both the uncertainty due to sampling and normalisation

velocity is seen to vary in magnitude throughout the engine, with the shift in the wave structure within the engine attributed to most of the uncertainty. These effects are seen to be greatest in the combustor, which is a zone of multiple wave reflections. In this region, shifts in the wave pattern with time can noticeably perturb pressure measurements from sensors located at fixed axial locations. The pressure rise in the experiment due to combustion is noticeably above that of the fluctuations of the flow. Combining these errors using the root mean square approach (Equation D.2) is shown in Figure D.3. Including the possible error bands, the difference between the air test gas to nitrogen by the end of the combustor is quite significant, thus demonstrating that supersonic combustion is clearly achieved. This is in light of the pressure along the intake corresponding well between the two shots, demonstrating that the freestream properties are similar.

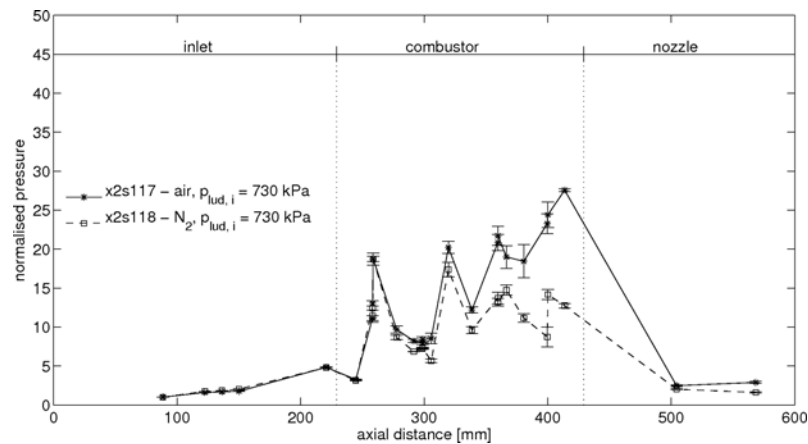
$$X_{p_{norm}} = \sqrt{X_{meas}^2 + X_{\sigma}^2 + X_{U_{norm}}^2} \quad (\text{D.2})$$



(a) Uncertainty due to individual measurement



(b) Uncertainty due to sampling



(c) Uncertainty due to normalisation velocity

Figure D.2: Uncertainties in pressure measurements due to different effects for combustion effects, using an initial Ludwieg fill pressure of 730 kPa at 400 μs .

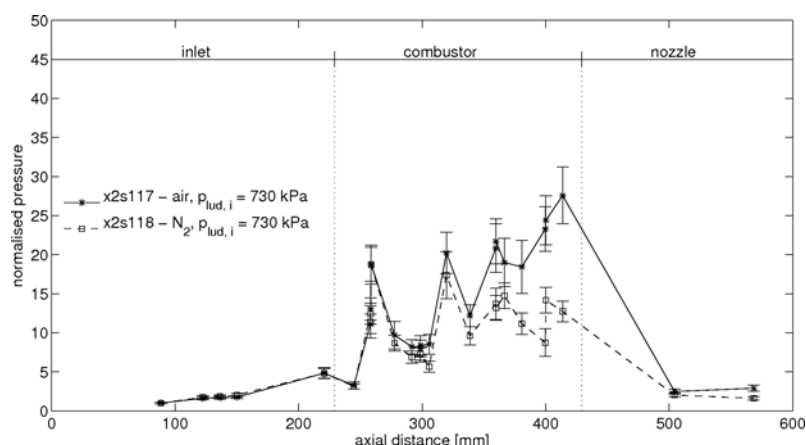


Figure D.3: Combined uncertainties in pressure measurements due to different effects for combustion effects, using an initial Ludwieg fill pressure of 730 kPa at $400 \mu\text{s}$.

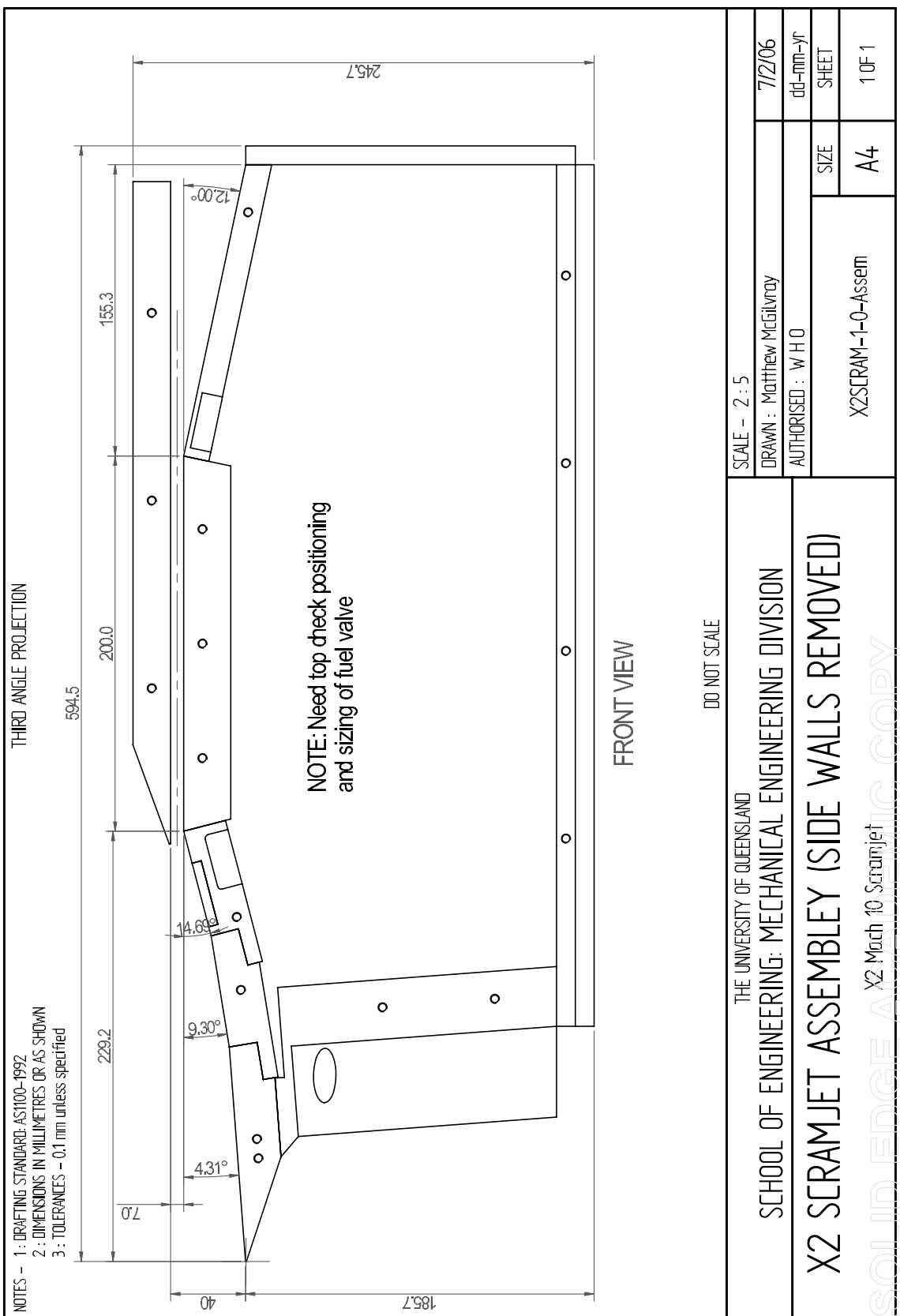
APPENDIX E

Scramjet Physical Design Drawings

The manufacturing drawings are presented within this Appendix. A list of the drawings in order can be found in Table E.

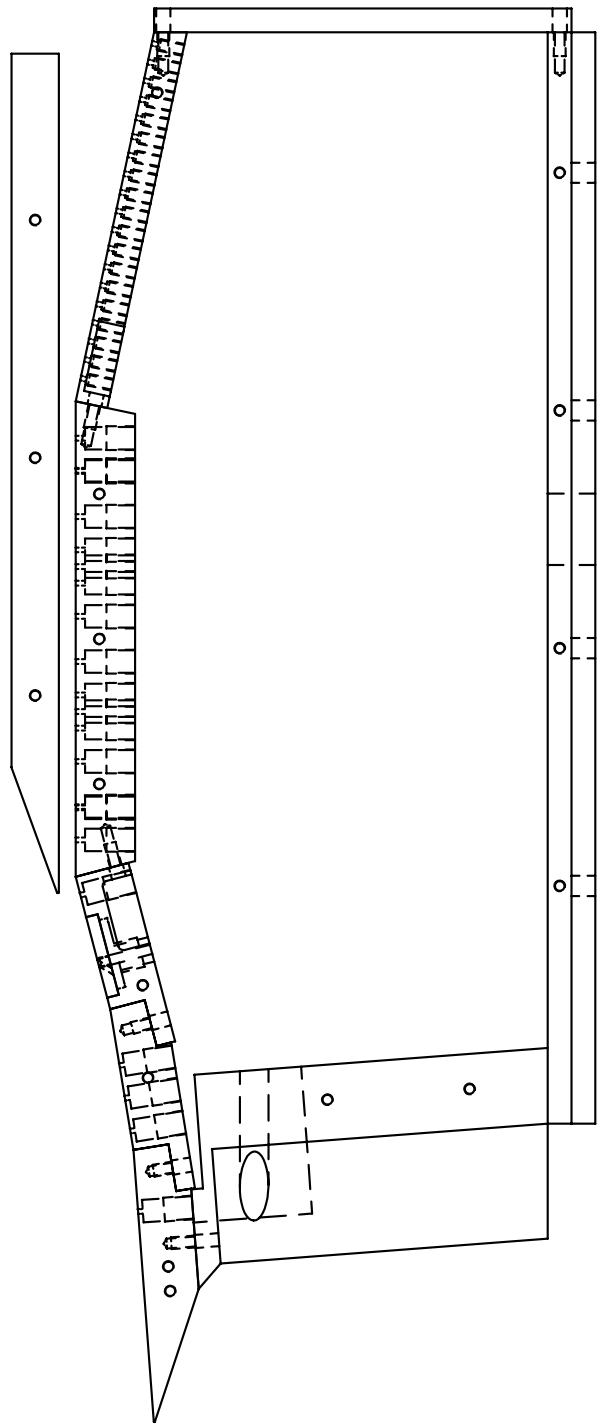
Table E.1: List of drawings for scramjet.

- 1) Assembly drawing (1 side wall off)
- 2) Assembly drawing (sectioned view, side walls off)
- 3) Assembly drawing (sectioned view, side wall on)
- 4) Assembly drawing (isometric view)
- 5) Back plate
- 6) Bottom plate
- 7) Combustor plate
- 8) Combustor plate (pressure transducer locations)
- 9) Cowl
- 10) Front shield
- 11) Injection plate
- 12) Intake surface 1
- 13) Intake surface 2
- 14) Intake surface 3
- 15) Side wall
- 16) Side wall (mounting hole locations)
- 17) Side wall cover
- 18) Thrust surface



NOTES -
1 : DRAFTING STANDARD AS1100-1992
2 : DIMENSIONS IN MILLIMETRES OR AS SHOWN
3 : TOLERANCES - 0.1 mm unless specified

THIRD ANGLE PROJECTION



DO NOT SCALE

THE UNIVERSITY OF QUEENSLAND SCHOOL OF ENGINEERING: MECHANICAL ENGINEERING DIVISION X2 SCRAMJET ASSEMBLY II (SIDE WALLS REMOVED)	SCALE - 2 : 5
DRAWN : Matthew McGilvray	7/2/06
AUTHORISED : W H O	dd-mm-yy
X2SCRAM-1-0-Assem_b	SHEET SIZE A4 10F1

SCRAMJET ASSEMBLY II (SIDE WALLS REMOVED)
X2 SCRAMJET ASSEMBLY II (SIDE WALLS REMOVED)

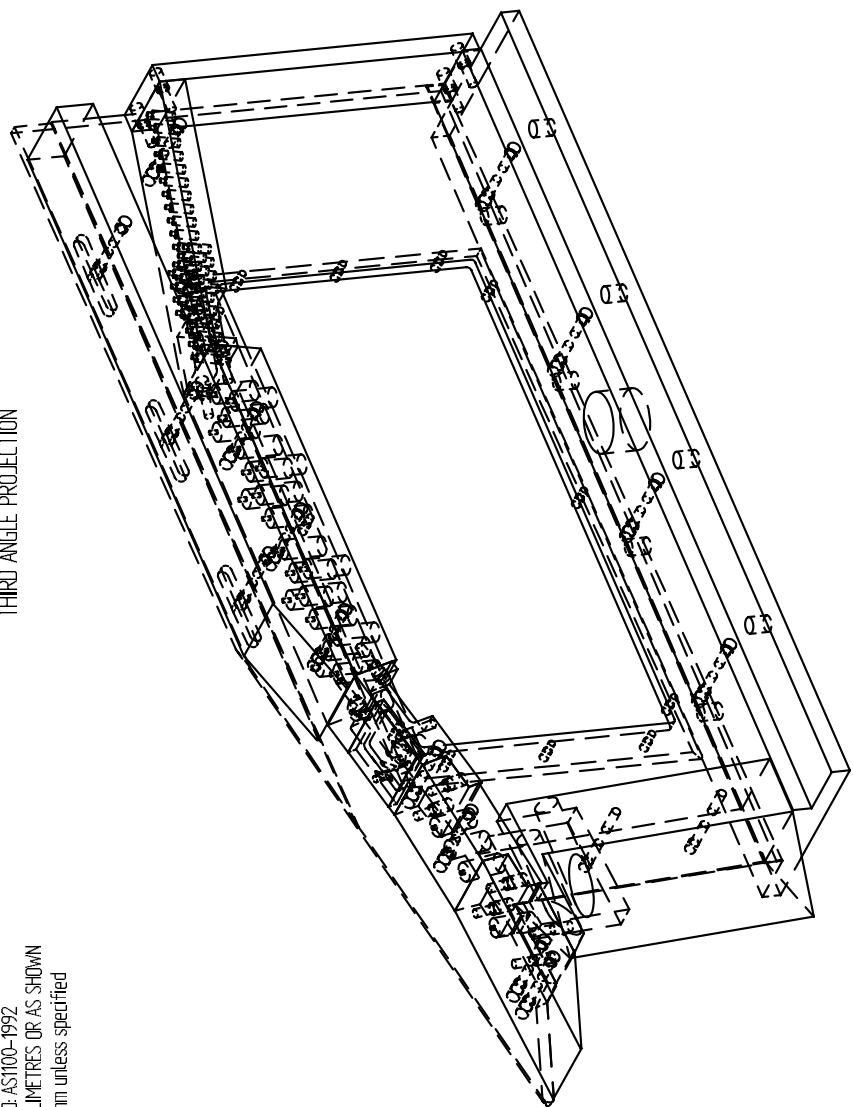
NOTES -
1 : DRAFTING STANDARD AS1100-1992
2 : DIMENSIONS IN MILLIMETRES OR AS SHOWN
3 : TOLERANCES - 0.1 mm unless specified

THIRD ANGLE PROJECTION		DO NOT SCALE	
SCALE -	2 : 5	DRAWN : Matthew McGlynn	7/2/06
AUTHORISED : W H O		dd-mm-yy	SHEET
XZSCRAM-1-0-Assem_Lc	SIZE	A4	1 OF 1
X2 SCRAMJET ASSEMBLY III (SIDE WALLS)		SCHOOL OF ENGINEERING: MECHANICAL ENGINEERING DIVISION THE UNIVERSITY OF QUEENSLAND	

SCRAMJET ASSEMBLY III (SIDE WALLS)
X2 SCRAMJET ASSEMBLY III (SIDE WALLS)

NOTES -
1 : DRAFTING STANDARD AS/NZS100-1992
2 : DIMENSIONS IN MILLIMETRES OR AS SHOWN
3 : TOLERANCES - 0.1 mm unless specified

THIRD ANGLE PROJECTION



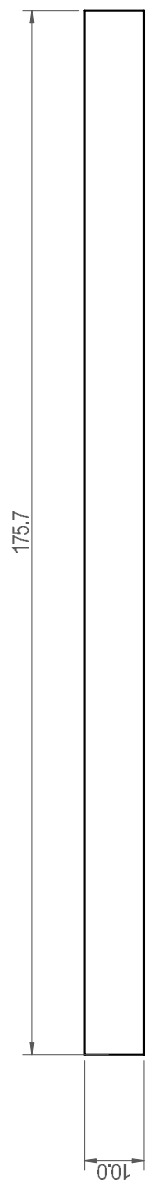
DO NOT SCALE

THE UNIVERSITY OF QUEENSLAND SCHOOL OF ENGINEERING: MECHANICAL ENGINEERING DIVISION X2 SCRAMJET ASSEMBLY IV (ISOMETRIC)	SCALE - 2 : 5	DRAWN : Matthew McGilvray	7/2/06
X2SCRAM-1-0-Assem_LC	A4	SIZE	dd-mm-yr SHEET
X2	10	Scramjet	10F1

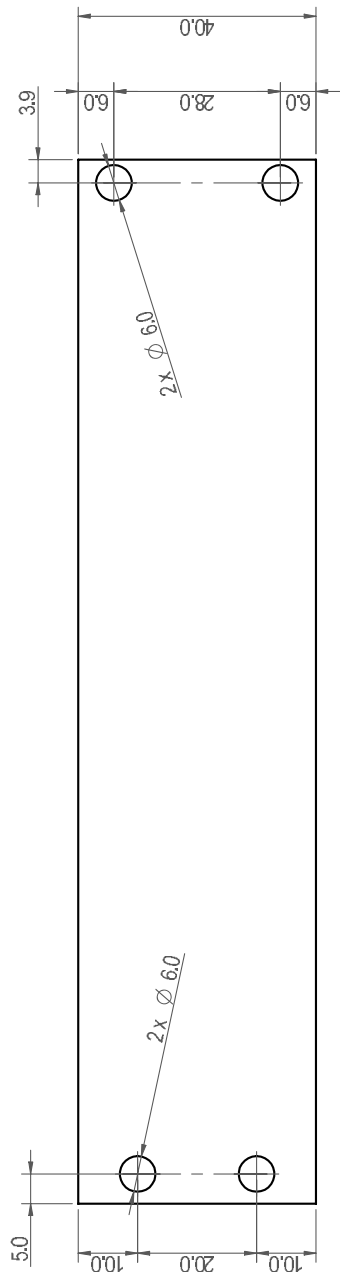
SCRAMJET ASSEMBLY COPY

NOTES -
 1 : DRAFTING STANDARD: AS1100-1992
 2 : DIMENSIONS IN MILLIMETRES OR AS SHOWN
 3 : TOLERANCES - 0.1 mm unless specified

THIRD ANGLE PROJECTION



TOP VIEW



FRONT VIEW

NO. OFF - 1
 MATERIAL - MILD STEEL
 CONDITION - AS SUPPLIED
 SURFACE FINISH - AS PROCESSED
 SURFACE TREATMENT - AS PROCESSED

DO NOT SCALE

THE UNIVERSITY OF QUEENSLAND	SCALE - 1 : 1
SCHOOL OF ENGINEERING: MECHANICAL ENGINEERING DIVISION	DRAWN : Matthew McGlynn 2/2/06
X2 SCRAMJET BACK PLATE DETAILS	AUTHORISED : W H O dd-mm-yy
X2SCRAM-1-0-Back-plate	SIZE : A4
	1 OF 1

SCRAMJET BACK PLATE DETAILS

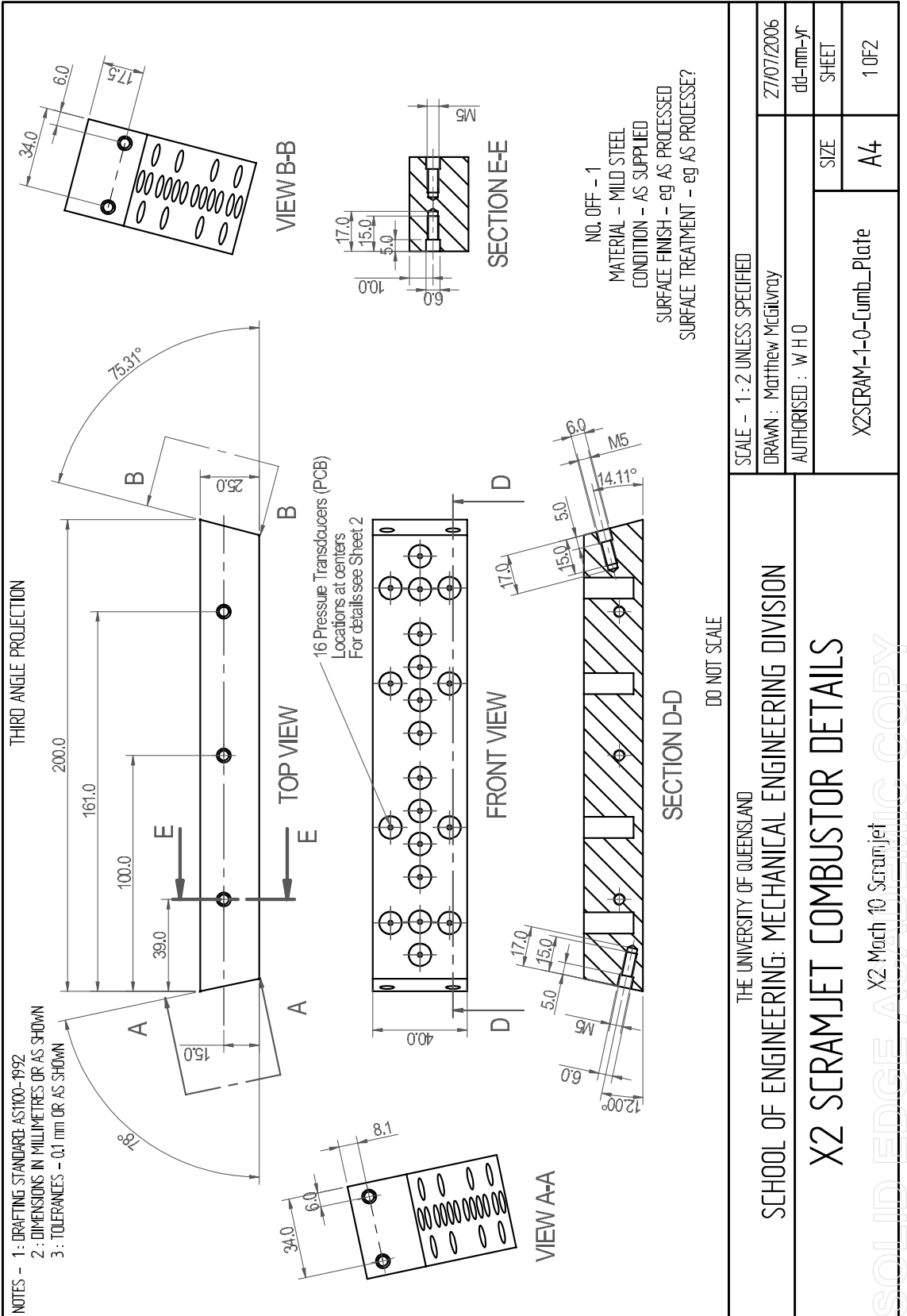
NOTES -
1 : DRAFTING STANDARD: AS100-1992
2 : DIMENSIONS IN MILLIMETRES OR AS SHOWN
3 : TOLERANCES - 0.1 mm OR AS SHOWN

THIRD ANGLE PROJECTION

3 : TOLERANCES - 0.1 mm OR AS SHOWN

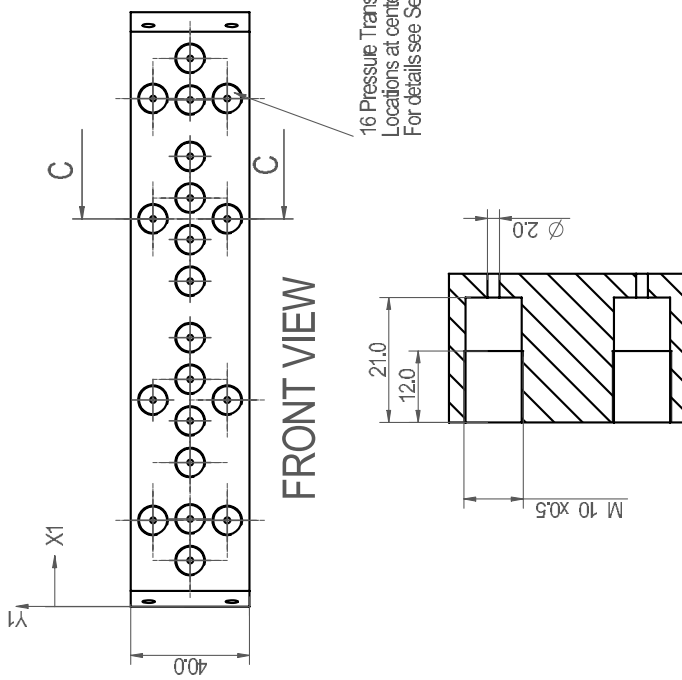
3 : TOLERANCES - 0.1 mm OR AS SHOWN

3 : TOLERANCES - 0.1 mm OR AS SHOWN



NOTES -
 1: DRAFTING STANDARD AS1000-1992
 2: DIMENSIONS IN MILLIMETRES OR AS SHOWN
 3: TOLERANCES - 0.1 mm OR AS SHOWN

THIRD ANGLE PROJECTION

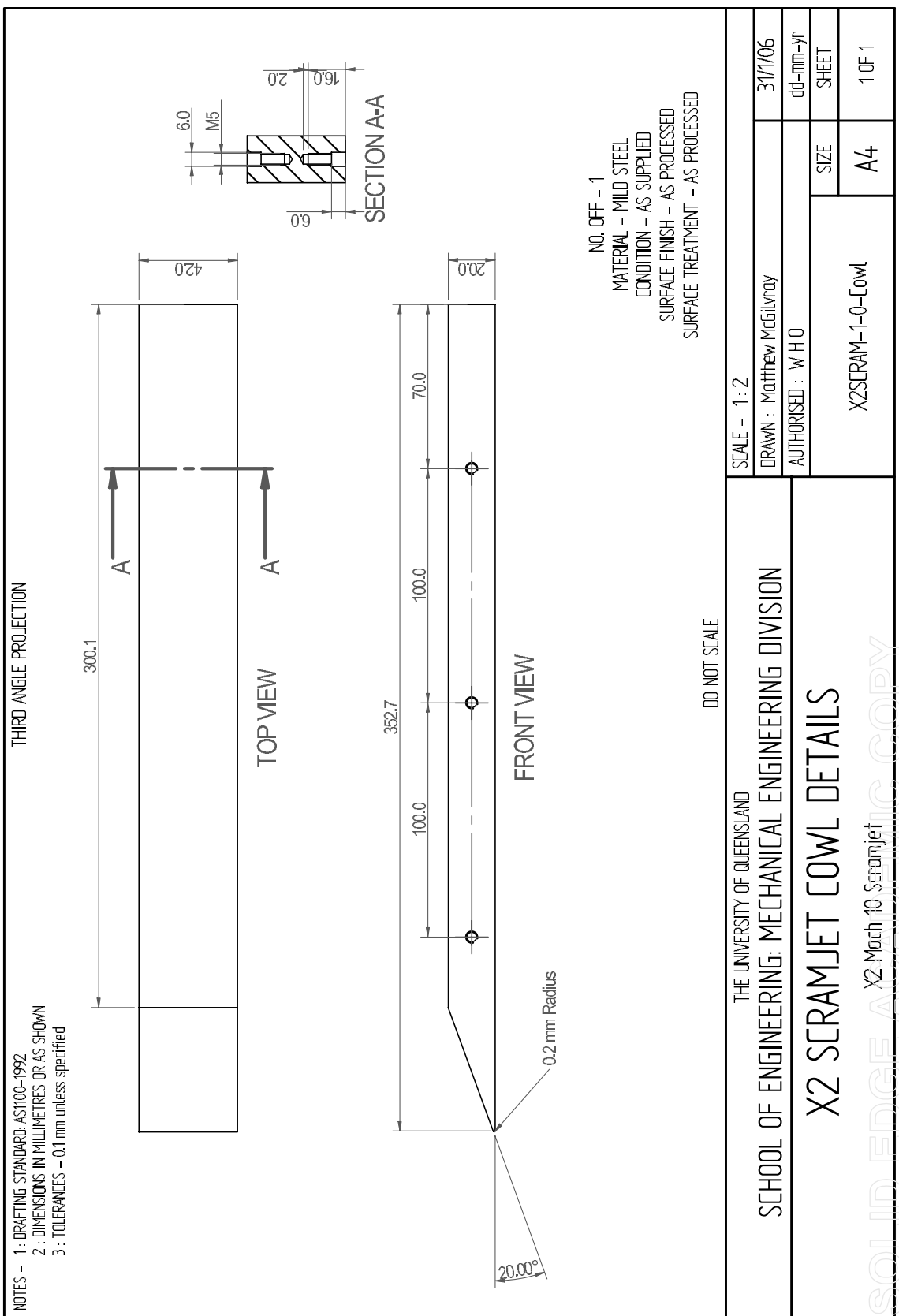


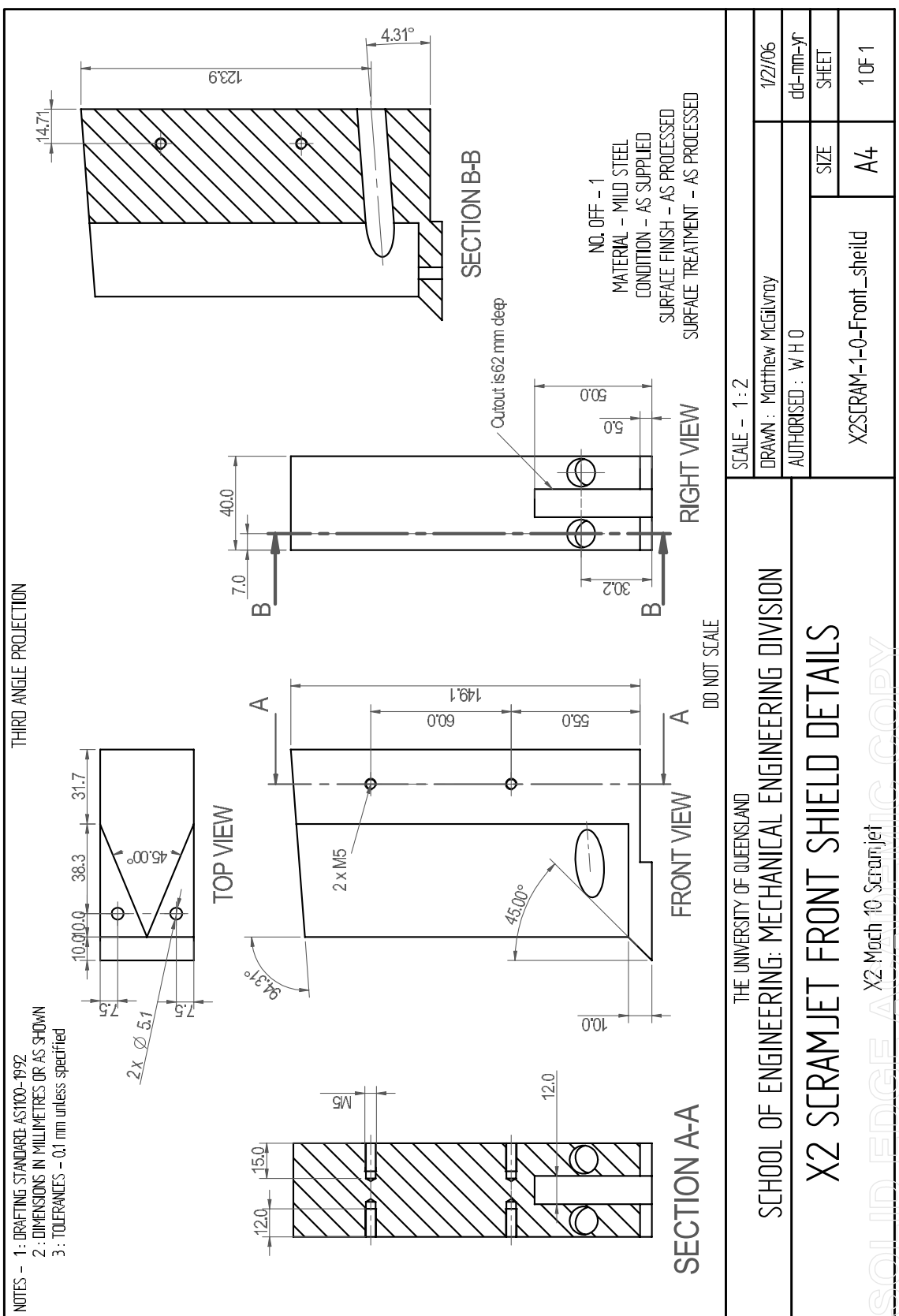
Hole Table	
X	Y
15.5	20
29	32.5
29.5	20
29	75
48.5	20
62.5	20
69.5	32.5
69.5	75
76.5	20
90.5	20
109.5	20

NO. OFF - 1
MATERIAL - MILD STEEL
CONDITION - AS SUPPLIED
SURFACE FINISH - AS PROCESSED
SURFACE TREATMENT - AS PROCESSED

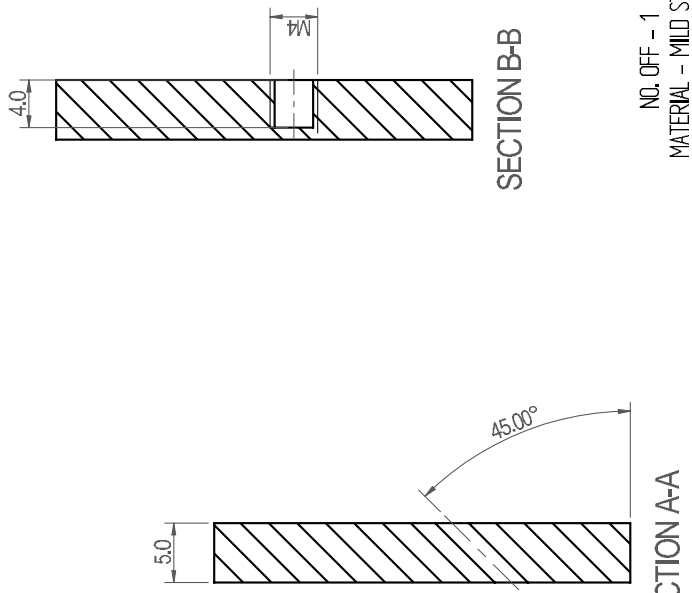
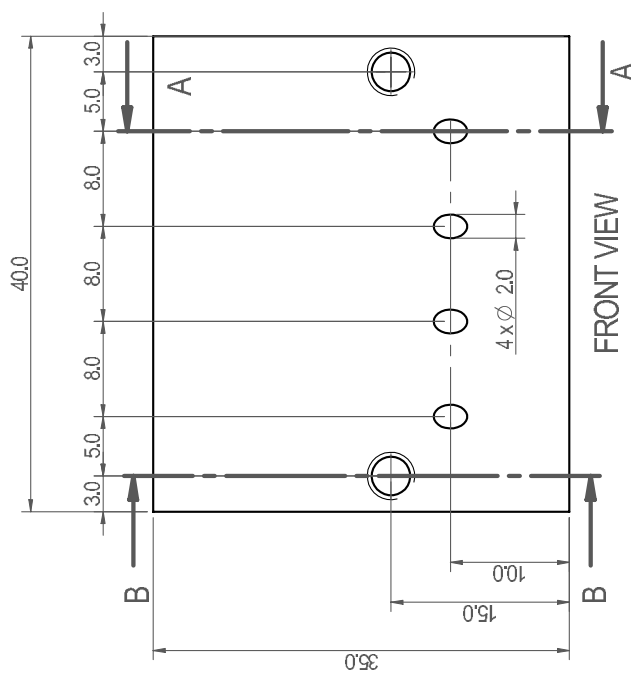
DO NOT SCALE

THE UNIVERSITY OF QUEENSLAND SCHOOL OF ENGINEERING: MECHANICAL ENGINEERING DIVISION	SCALE - 1:2 UNLESS SPECIFIED DRAWN : Matthew McElroy AUTHORISED : W H O	dd-mm-yy SHEET
X2 SCRAMJET COMBUSTOR DETAILS	X2SCRAM-1-0-Cumb_Plate	A4 2 OF 2





NOTES -
 1 : DRAFTING STANDARD: AS1100-1992
 2 : DIMENSIONS IN MILLIMETRES OR AS SHOWN
 3 : TOLERANCES - 0.1 mm unless specified

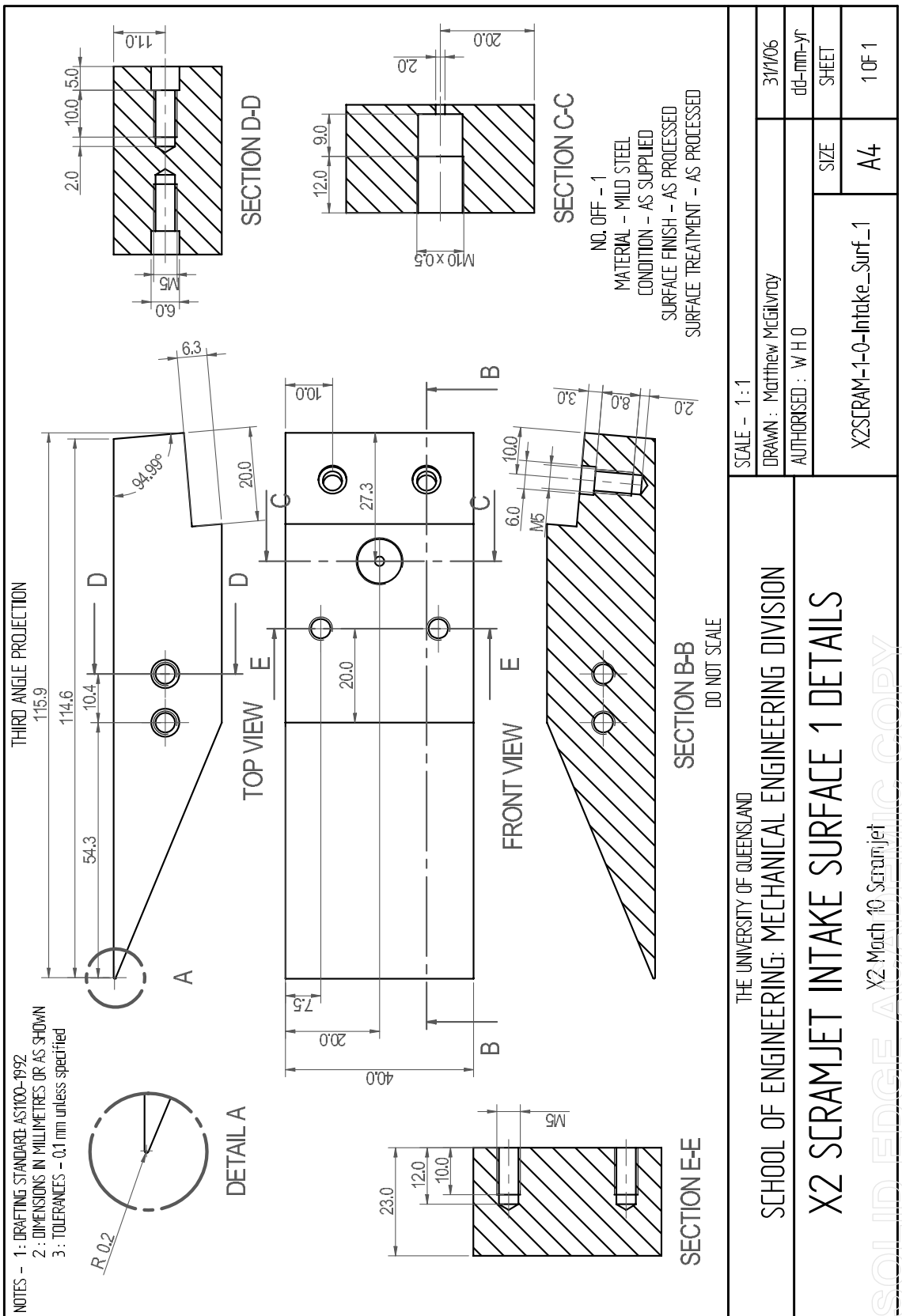


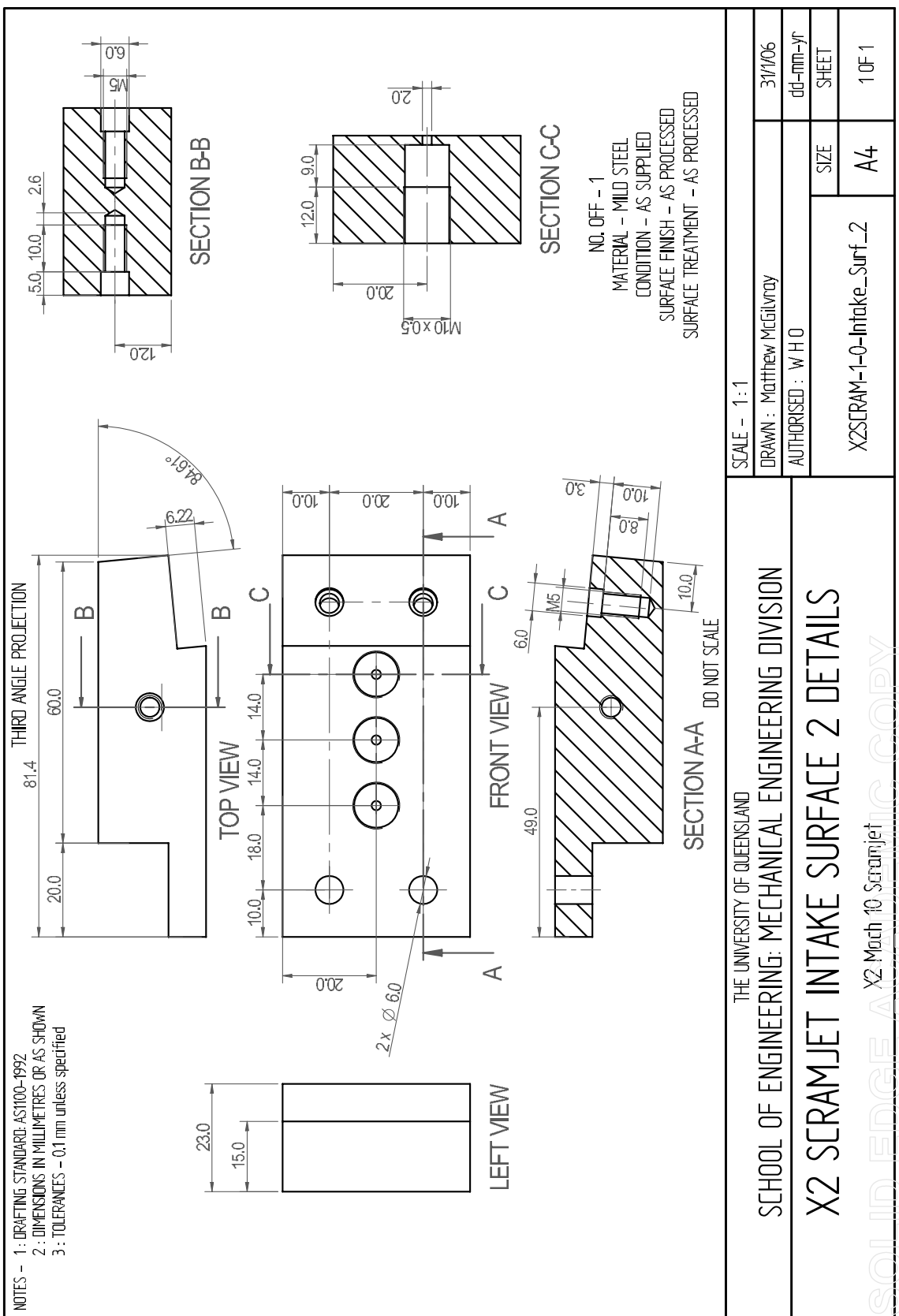
DO NOT SCALE

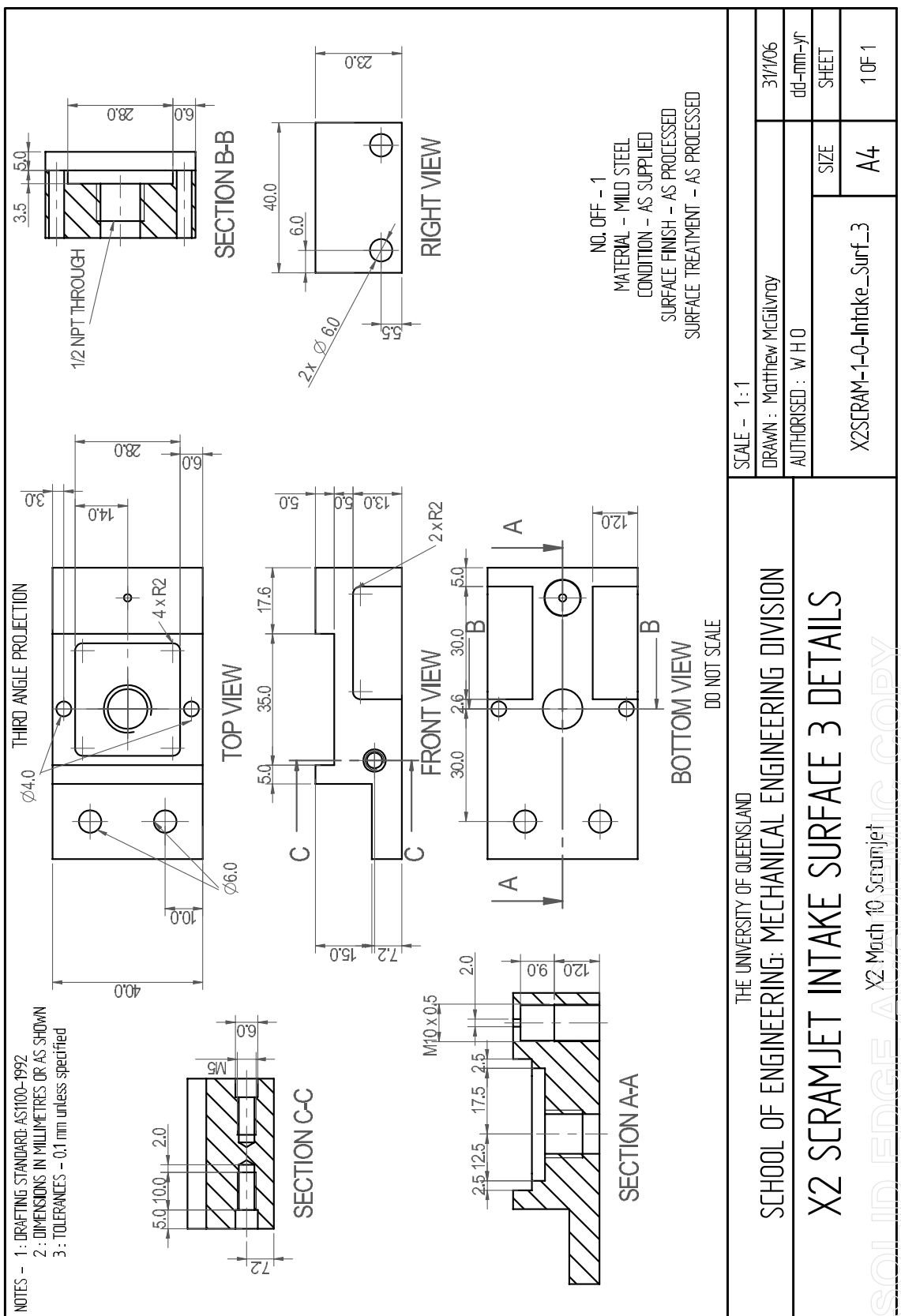
NO. OFF - 1
 MATERIAL - MILD STEEL
 CONDITION - AS SUPPLIED
 SURFACE FINISH - AS PROCESSED
 SURFACE TREATMENT - AS PROCESSED

THE UNIVERSITY OF QUEENSLAND	SCALE - 1:2
SCHOOL OF ENGINEERING: MECHANICAL ENGINEERING DIVISION	DRAWN : Matthew McGlynn 31/10/06
X2 SCRAMJET INJECTION PLATE DETAILS	AUTHORISED : W H O dd-mm-yy
X2SCRAM-1-0-Injection_plate	SIZE : A4
	10F1

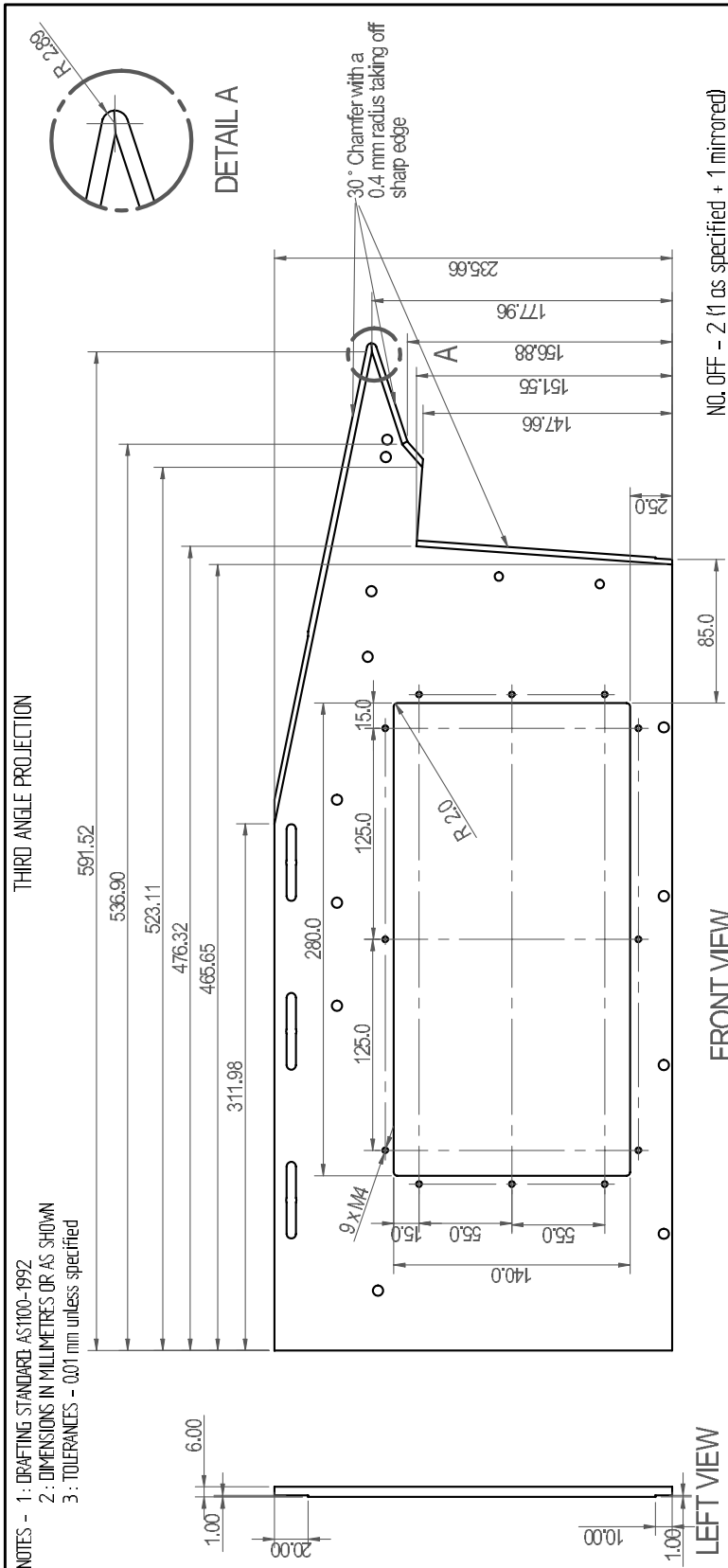
~~solid edge A2 Mach 10 Scramjet~~ copy







NOTES -
 1: DRAFTING STANDARD AS1100-1992
 2: DIMENSIONS IN MILLIMETRES OR AS SHOWN
 3: TOLERANCES - 0.01 mm unless specified



NO. OFF - 2 (as specified + 1 mirrored)
 MATERIAL - MILD STEEL
 CONDITION - AS SUPPLIED
 SURFACE FINISH - AS PROCESSED
 SURFACE TREATMENT - AS PROCESSED

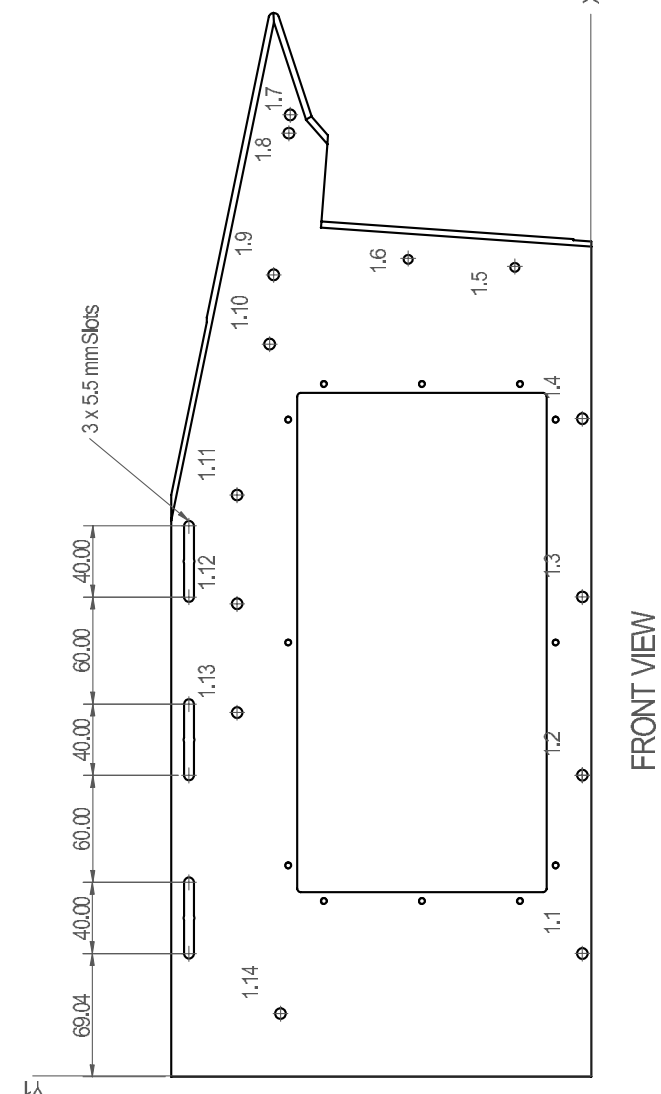
DO NOT SCALE

SCALE - 3 : 10	DRAWN : Matthew McElroy	2/2/06
AUTHORISED : W H O	dd-mm-yy	SIZE SHEET
X2SCRAM-1-0-Side_wall_A	A4	10F 2

THE UNIVERSITY OF QUEENSLAND
 SCHOOL OF ENGINEERING: MECHANICAL ENGINEERING DIVISION
X2 SCRAMJET SIDE WALL A DETAILS
 SOLID EDGE A X2 March 10 Scramjet

NOTES - 1: DRAFTING STANDARD AS1100-1992
 2: DIMENSIONS IN MILLIMETRES OR AS SHOWN
 3: TOLERANCES - .001 mm unless specified

THIRD ANGLE PROJECTION



DO NOT SCALE

THE UNIVERSITY OF QUEENSLAND
 SCHOOL OF ENGINEERING: MECHANICAL ENGINEERING DIVISION
X2 SCRAMJET SIDE WALL A DETAILS
 SOLID EDGE A X2 March 10 Scramjet

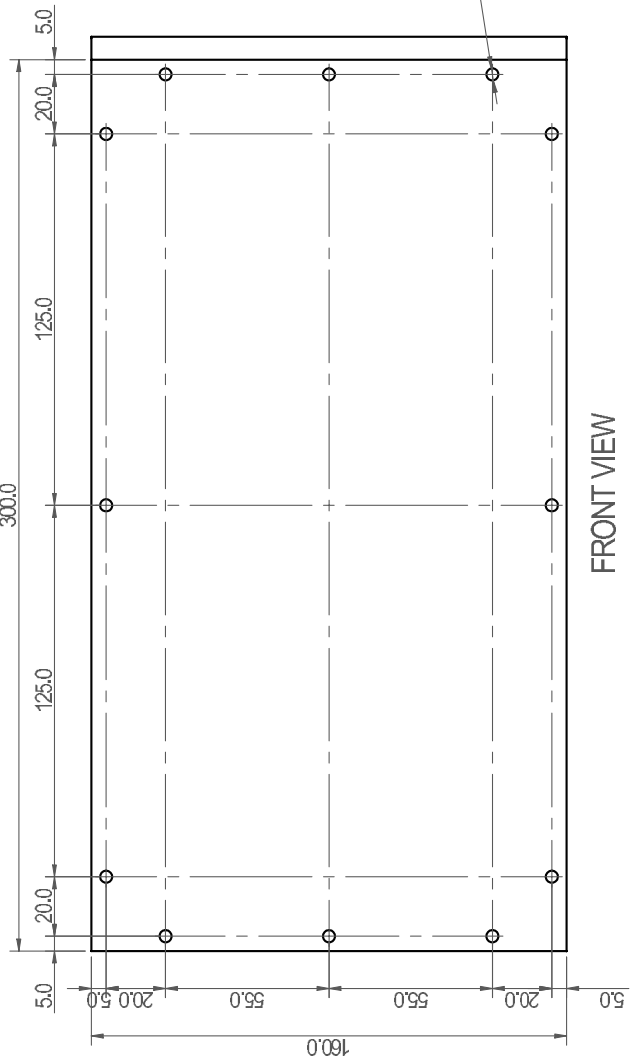
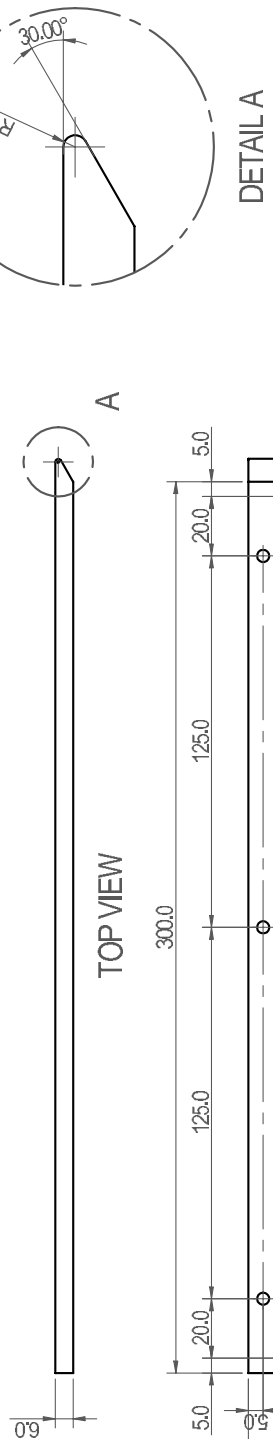
Hole Table			
Hole	X	Y	Size
11	69.12	5	$\phi 6.1$
12	169.12	5	$\phi 6.1$
13	269.12	5	$\phi 6.1$
14	369.12	5	$\phi 6.1$
15	453.96	42.88	$\phi 5.1$
16	558.47	102.71	$\phi 5.1$
17	539.54	163.85	$\phi 6.1$
18	529.21	169.63	$\phi 6.1$
19	449.79	178.19	$\phi 6.1$
1.10	440.93	180.41	$\phi 6.1$
1.11	326.25	198.66	$\phi 6.1$
1.12	265.25	198.66	$\phi 6.1$
1.13	204.25	198.66	$\phi 6.1$
1.14	35.53	174.34	$\phi 6.1$

SCALE - 3 : 10	DRAWN : Matthew McElroy	2/2/06
AUTHORISED : WHO	dd-mm-yy	dd-mm-yy
X2SCRAM-1-0-Side_wall_A	SIZE A4	SHEET 2 OF 2

NOTES -

- 1 : DRAFTING STANDARD: ASME B10.1-1992**
- 2 : DIMENSIONS IN MILLIMETRES OR AS SHOWN**
- 3 : TOLERANCES - 0.1 mm unless specified**

THIRD ANGLE PROJECTION



10 of 10

SCALE - 1:2

DRAWN : Matthew McGillivray	9/2006
AUTHORISED : WHO	dd-mm-yy
	SHEET
X2SERAM-1-0-Side_wall_cover	A4
	1 OF 1

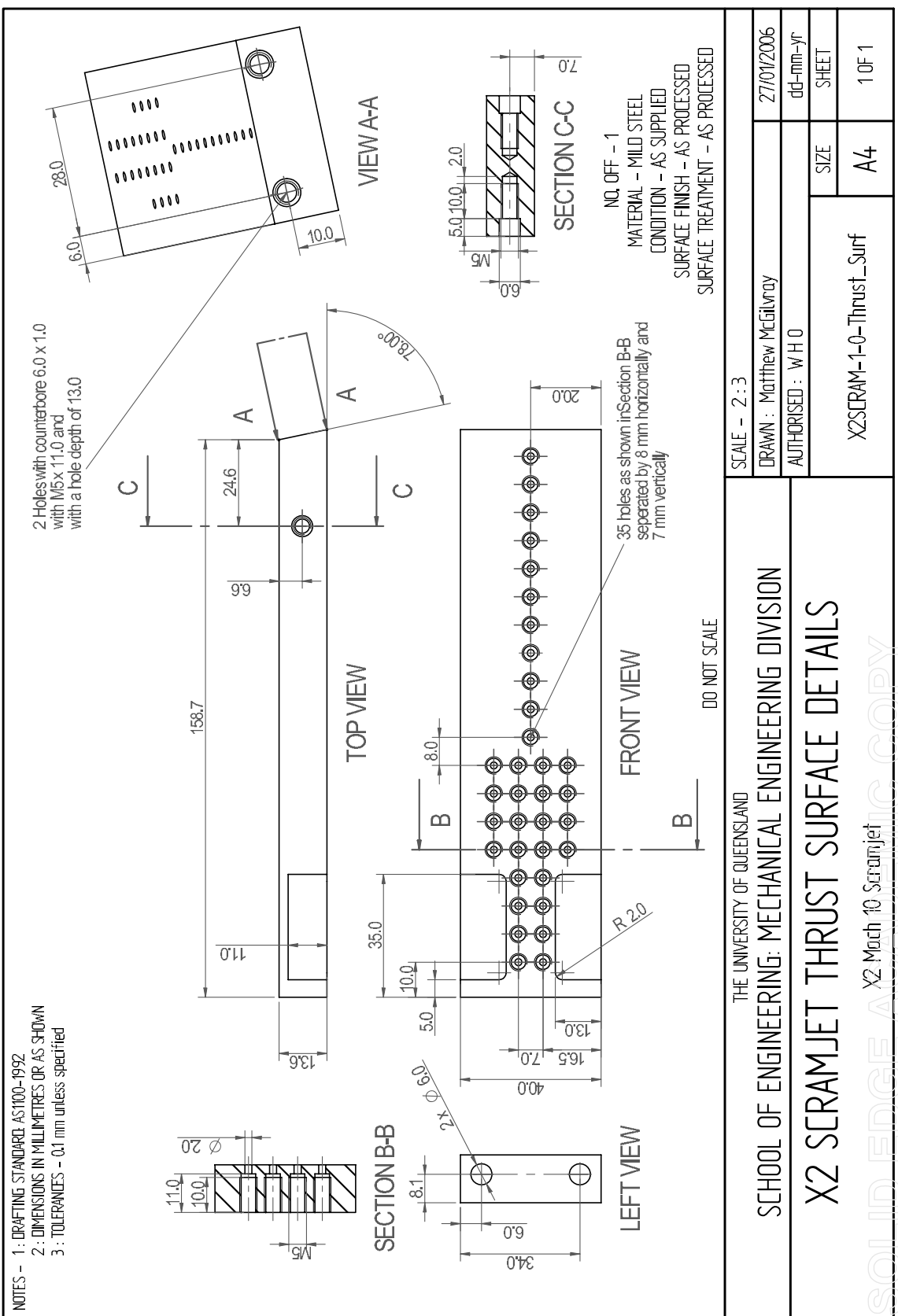
THE UNIVERSITY OF QUEENSLAND

SCHOOL OF ENGINEERING: MECHANICAL ENGINEERING DIVISION

X2 SCRAMJET SIDE WALL COVER

SOLID EDGE AERODYNICS COPY

THE UNIVERSITY OF QUEENSLAND		SCALE - 1:2	9/2/06
SCHOOL OF ENGINEERING: MECHANICAL ENGINEERING DIVISION		DRAWN : Matthew McIlvray	dd-mm-yy
		AUTHORISED : WHO	SHEET
X2 SCRAMJET SIDE WALL COVER		X2SCRAM-1-0-Side_wall_cover	A4
DO NOT SCROLL			



Scramjet Pressure Transducer Calibration

Table F.1 presents the calibrations of the Kulites taken while in-situ. Using the calibration procedure described by Odam [197], the PCB pressure transducers used during the testing of the scramjet where tested. Table F.2 shows the manufacturers calibration and the recalibration. Also shown are notes for transducers that misbehaved during the course of testing. Both of these tables show the locations of the transducers and the channel on which they where recorded.

Table F.1: Calibration results of Kulite pressure transducers used in scramjet testing.

name	location [mm]	serial number	channel	manufacturer calibration	experimental calibration
KUL_1	447.2	R66-16	A 610	5.84E-04	5.8403E-04
KUL_2	463.2	R65-36	A 620	5.84E-04	5.8365E-04
KUL_3	487.2	R66-11	A 630	5.82E-04	5.8245E-04
KUL_4	495.2	R65-40	A 710	5.84E-04	5.8424E-04
KUL_5	511.2	R65-35	A 130	5.84E-04	5.8478E-04
KUL_6	575.2	R65-39	A 430	5.83E-04	5.8298E-04
KUL_7	519.2	R65-37	A 720	5.85E-04	5.8356E-04
KUL_8	543.2	R65-38	A 730	5.81E-04	5.8345E-04

Table F.2: Calibration results of PCB pressure transducers used in scramjet testing.

name	location [mm]	serial number	channel	manufacturer calibration	experimental calibration
IA_1C_1	88.5	7944	B 110	6.8730E-03	6.4011E-03
IB_1C_2	122.5	19171	B 120	1.3348E-02	6.8130E-03
IB_2C_3	136.3	19179	B 130	7.2257E-03	7.7635E-03
IB_3C_4	150.1	7942	B 210	7.3370E-04	6.5863E-03
IC_1C_5	-	7437	B 220	1.4800E-03	1.6917E-03
IC_2C_6	220.7	9906	B 230	7.3485E-04	7.1277E-04
CO_1C_7	244.7	7453	B 310	1.5394E-03	1.5644E-03
CO_2L_8	258.2	7432	B 320	1.3905E-03	1.3232E-03
CO_2C_9	258.7	7443	B 330	1.4950E-03	1.4829E-03
CO_2R_10	258.2	7440	B 410	1.4456E-03	1.4691E-03
CO_3C_11	277.7	7435	B 420	1.4920E-03	1.4338E-03
CO_4C_12	291.7	7438	B 430	1.5616E-03	1.4878E-03
CO_5L_13	298.7	19126	B 510	1.4477E-02	1.3602E-02
CO_5R_14	298.7	19272	B 520	1.4616E-02	1.4853E-02
CO_6C_15	305.7	7431	B 530	1.4688E-03	1.3841E-03
CO_7C_16	319.7	12492	B 610	1.4720E-03	1.4548E-03
CO_8C_17	338.7	7430	B 620	1.4471E-03	1.4706E-03
CO_9C_18	347.7	19629	B 630	1.4281E-02	2.2727E-03
CO_10L_19	359.7	22236	B 710	1.4200E-02	6.6590E-03
CO_10R_20	359.7	19269	B 720	1.4230E-02	1.4461E-02
CO_11C_21	366.7	7441	B 730	1.4804E-03	1.5044E-03
CO_12C_22	380.7	7441	A 510	1.4804E-03	1.5044E-03
CO_13R_23	399.7	15302	A 520	1.5805E-02	1.1399E-02
CO_13C_24	400.2	7447	A 530	1.5848E-03	1.6105E-03
CO_13L_25	399.7	19278	A 310	1.4461E-02	1.4358E-02
CO_14C_26	413.7	9602	A 120	1.5374E-02	1.2091E-02
TP_1L_27	504.4	7451	A 130	1.5210E-03	1.5457E-03
TP_2L_28	568.4	2675	A 710	6.6473E-04	6.7552E-04
pitotR_29	-	7446	A 730	1.4456E-03	1.4691E-03
pitotL_30	-	11062	A 720	3.7416E-03	3.7416E-03

APPENDIX G

Scramjet Normalisation Pressure

Table G.1 presents the pressure used in normalisation of scramjet. It is taken on the first transducer, located on the first wedge on the scramjet intake.

Table G.1: Pressure at IA-C1 used in normalisation for each shot presented.

shot	p_{norm} [kPa]	p_{norm} [kPa]	p_{norm} [kPa]
	250 μs	400 μs	550 μs
x2s117	5.360	4.761	4.963
x2s118	5.090	4.838	4.958
x2s119	4.612	4.289	4.723
x2s121	4.591	4.638	4.897
x2s122	4.935	4.504	4.696
x2s124	4.513	4.228	4.737
x2s125	4.617	4.608	4.812
x2s128	5.230	4.211	4.336
x2s137	3.885	4.180	3.974
x2s149	5.045	4.800	5.215
x2s155	4.553	4.648	5.120
x2s156	5.317	4.978	5.115
x2s158	4.834	4.508	4.776
x2s159	4.252	4.616	4.963
x2s160	4.704	4.691	5.064